# Computational Fluid Dynamics

# Computational Fluid Dynamics

Edited by

Hyoung Woo OH

*Intech*

Published by Intech

**Intech**
Olajnica 19/2, 32000 Vukovar, Croatia


Free online edition of this book you can find under www.sciyo.com
Additional copies can be obtained from:
publication@sciyo.com

First published January 2010
Printed in India

Technical Editor: Teodora Smiljanic

Computational Fluid Dynamics, Edited by Hyoung Woo OH
p. cm.
ISBN 978-953-7619-59-6

# Preface

This book is intended to serve as a reference text for advanced scientists and research engineers to solve a variety of fluid flow problems using computational fluid dynamics (CFD). Each chapter arises from a collection of research papers and discussions contributed by the practiced experts in the field of fluid mechanics. This material has encompassed a wide range of CFD applications concerning computational scheme, turbulence modeling and its simulation, multiphase flow modeling, unsteady-flow computation, and industrial applications of CFD.

Editor

**Hyoung Woo OH**
*Chungju National University*
*Korea*

# Contents

1

# Applications of CFD in Natural Gas Processing and Transportation

Majid Abedinzadegan Abdi[1], Esam Jassim,
Mohammad Haghighi and Yuri Muzychka
[1]*Memorial University of Newfoundland, St. John's, Newfoundland and Labrador, Canada*

## 1. Introduction

In this chapter, two examples of CFD applications in natural gas processing and transportation are presented. A commercial software package (Fluent) was used in these studies. The purpose of the studies is briefly discussed, the methodology outlined and boundary conditions and problem specifications are concisely described for each case. The results of investigations and comparisons with experimental tests and literature data are presented to demonstrate how CFD can be applied to practical situations.

## 2. Flow of real gas in supersonic nozzles

The demand for natural gas has encouraged the energy industry toward the discovery of remote offshore reservoirs. Consequently new technologies have to be developed to efficiently produce and transport natural gas to consumption centers. Common design challenges in all gas processing methods for offshore applications are the compactness and reliability of process equipment. Supersonic nozzles have been introduced as an alternative to treat natural gas for offshore applications and to meet the offshore requirements (Hengwei et al. 2005, Alfyorov et al. 2005, Okimoto et al., 2002, Karimi & Abedinzadegan Abdi, 2006, Brouwer & Epsom, 2003). In a supersonic separator the gas temperature is lowered based on the principle of gas expansion where no refrigerant is needed. The compact design of supersonic nozzles is a major advantage over traditional means of natural gas treating technologies particularly for offshore applications. The gas speed in this device is very high preventing fouling or deposition of solids and ice. Refrigeration is self-induced therefore no heat is transferred through the walls and unlike external refrigeration systems, no inhibitor injection and inhibitor recovery system are necessary. Intensive water dew points down to -50 to -60 $^{o}$C can be achieved without any cryogenic cooling or use of solid adsorption techniques.

### 2.1 Problem description

Application of CFD technique is demonstrated to predict the behaviour of high pressure natural gas flowing through supersonic nozzles. Supersonic nozzles were selected as it was noticed that there was a potential for these nozzles for applications in natural gas processing industries and very few simulation analysis had been published in the open literature. The

nozzle considered here is a de Laval geometry composed of two sections: the convergent section (subsonic zone) and the divergent section (supersonic zone). However, we also address two other de Laval modified geometries, which are of interest in solid/liquid particles separation; namely throat section (critical zone) with extended constant area throat, and throat section with extended U-shape throat.

The function of the convergent part is to keep the flow uniform and parallel as well as to accelerate the gas. Within the converging section leading to the throat area, the gas is accelerated so that the sonic velocity is reached at the throat and the convergent curvature keeps the gradient in velocity of the flow uniform. In practical conditions, in order to get the sonic speed at the throat, it is required that the inlet diameter is kept larger than $\sqrt{5}$ of the throat diameter (Man et al., 1997) although in some cases the ratio of inlet to throat diameter is apparently less (Arina, 2004).

When the gas reaches the throat, the divergent part of the nozzle can further accelerate the flow depending on the outlet condition. This results in a decrease in pressure and temperature as well as increase in gas velocity. It is likely that under certain conditions the flow cannot expand isentropically to the exit pressure; therefore, an irreversible discontinuity, called a shockwave, can occur.

The shockwave is an abrupt disturbance that causes discontinuous and irreversible changes in fluid properties, such as speed (changing from supersonic to subsonic), pressure, temperature, and density. As a result of the gradients in temperature and velocity that are created by the shock, heat is transferred and energy is dissipated within the gas. These processes are thermodynamically irreversible. As the shock thickness is very small, the cross sectional areas at the upstream and downstream of the shock are considered equal and the energy or heat loss is negligible. The shock can also interact with the boundary layer and this can delay the transition from supersonic flow to subsonic flow even further. The increase of pressure across a shock is an indication of the shock strength that can lead to a sound wave considered as a shockwave of minimum strength.

### 2.2 Basis of CFD simulation

The geometry was modeled using two-dimensional axisymmetric grids. The total pressure and temperature for fully developed turbulent flow were imposed at the nozzle inlet, and no-slip condition was applied at wall boundaries. At the exit plane, ambient pressure and temperature were identified. CFD calculations were carried out using SIMPLEC algorithm and the central differencing scheme.

For turbulent flow model, the k-ε model was used here due to its frequent use for industrial applications, its relative accuracy, and its incorporation in most commercial CFD codes (Pope, 2000).

### 2.3 Results and discussions

#### 2.3.1 de *Laval nozzles*

Since most of published research has been concerned with the Laval nozzle, we validated our results by applying the numerical technique for such geometry and compared our results with the most recent available data (Arina, 2004; and Molleson & Stasenko, 2005) before proceeding and applying it to the modified nozzle systems.

Molleson and Stasenko (2005) performed their investigation for a nozzle whose geometry is shown in Figure 1-a. Their working fluid was methane at 70 bar inlet stagnation pressure

and 250 K inlet stagnation temperature while the value of exit Mach number according to their supersonic exit radii was 1.2. The SRK EOS model was used in their study. We used the same geometry and conditions in comparison of the sonic condition and in studying of the effect of a real gas model on the sonic position; MBWR was used as the thermodynamic model.

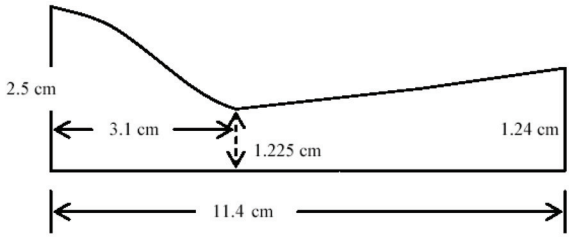


(a) (Molleson et al., 2005)

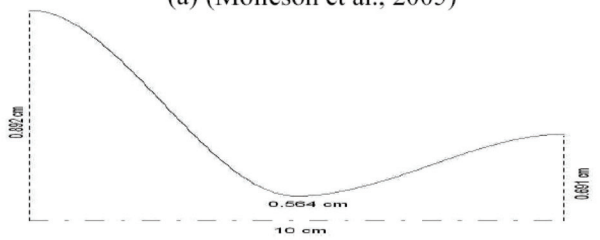


(b) (Arina, 2004)

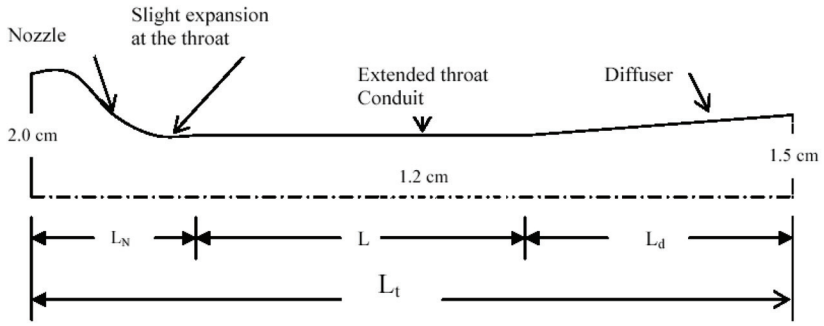


(c) System configuration for long-neck (long constant area/extended throat) Laval nozzle

Fig. 1. Nozzle geometries studied in the research

Figure 2 shows the variation of Mach number with position in real case and the comparison with results obtained from the work of Molleson and Stasenko (2005). One can see that choke (sonic velocity, M=1) occurs at the throat regardless of the EOS used. Also, our results are in very good agreement with their results. The second comparison was performed to

validate our simulation on capturing shockwave position. The comparison is done with recent available data (Arina, 2004). The geometry used in the comparison, shown in Figure 1-b, is adopted from Arina's work (2004). The working fluid was $CO_2$. The dimensions of the assumed Laval-nozzle are:

$$A(x) = 2.5 + 3\left(\frac{x}{x_{th}} - 1.5\right)\left(\frac{x}{x_{th}}\right)^2 \quad \text{for} \quad x \le x_{th}\,, \tag{1}$$

$$A(x) = 3.5 - \frac{x}{x_{th}}\left(6 - 4.5\frac{x}{x_{th}} + \left(\frac{x}{x_{th}}\right)^2\right) \quad \text{for} \quad x \ge x_{th}\,. \tag{2}$$

Where, $A_{\text{throat}}$= 1 $cm^2$, length= 10 $cm$ and the throat placed at $x_{\text{th}}$= 5 $cm$.

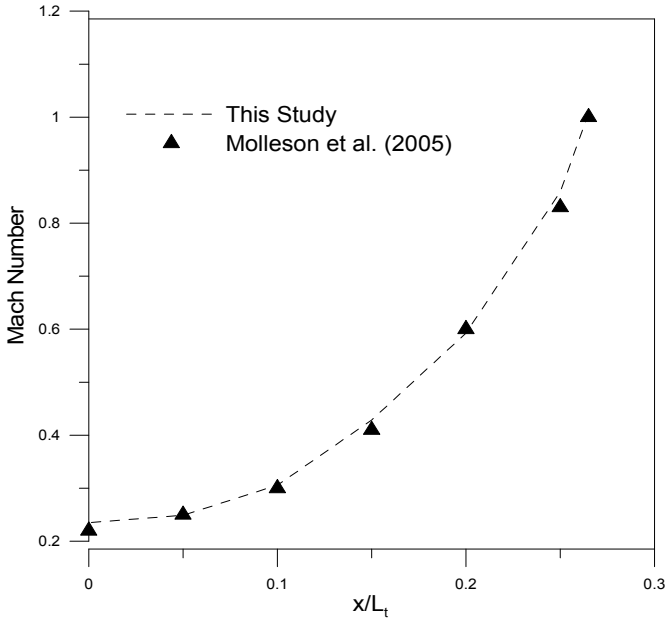


Fig. 2. Comparison of Mach numbers upstream of choke region in the Laval nozzle

Since Arina's simulation was performed near $CO_2$ condensation conditions, for which $T$= $1.001T_c$ and $\rho = \rho_c$, we compared our results for a perfect gas case as the FLUENT real gas basis could not predict multiphase conditions. The exit pressure was 83% of the inlet pressure. Our numerical results displayed the same behaviour when similar conditions and working fluids were applied as seen in Figure 3.

2.3.1.1 Real gas vs. Ideal gas assumption

The significance of using real gas models can be more clearly shown when comparison of the location of the shockwave within the Laval nozzle is made for two different gases: methane and nitrogen. At high pressures, the former compressibility factor significantly changes whereas the compressibility for the latter has almost the equivalent value of perfect gases.

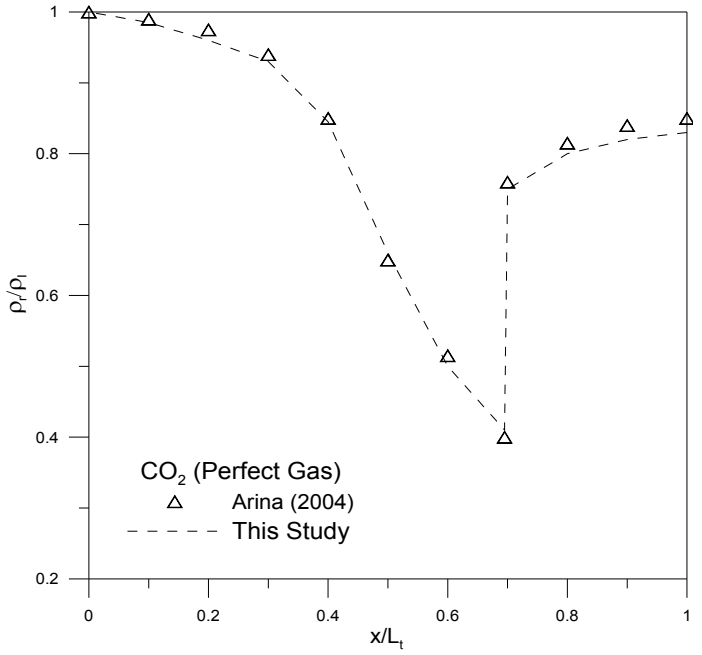


Fig. 3. Comparison of density ratios in the Laval nozzle under perfect gas conditions

2.3.1.2 Shockwave location

The real gas model predicts the shockwave location earlier than the ideal gas model for both gases. However, the differential distance between the ideal and real shock positions is different. In fact, when the ideal gas model is used, shock occurs earlier for nitrogen, see Figure 4-a. On the contrary, the real gas model predicts an opposite behaviour as shown in Figure 4-b. This example proves very clearly that ignoring the real gas effects can obviously lead to misleading results.

2.3.1.3 Real gas effects for a different configuration

The new configuration of the nozzle system designed for natural gas application consists of three different parts: an inlet nozzle (converging part ending to a throat and a slight expansion), diffuser (diverging part, gas final expansion and exit), and a conduit with constant area between these two parts. This latter part does not exist in conventional Laval nozzles where the diffuser or diverging part starts right after the throat and continues uniformly right up to the exit point. The description of the new system is shown in Figure 1-c.

Boundary conditions were chosen in such a way that the inlet pressure was predicted. Hence, we chose mass flow rate and temperature as the inlet boundary conditions while pressure and temperature were chosen for outlet boundary conditions. The working fluid was pure methane, mass flow rate was 430 kg/minute, stagnation temperature at the inlet and outlet were 293 and 280 K, respectively and the stagnation pressure at the outlet was assumed 7 MPa. The stagnation pressure at the inlet was to be predicted. The results of simulation are discussed as follows:

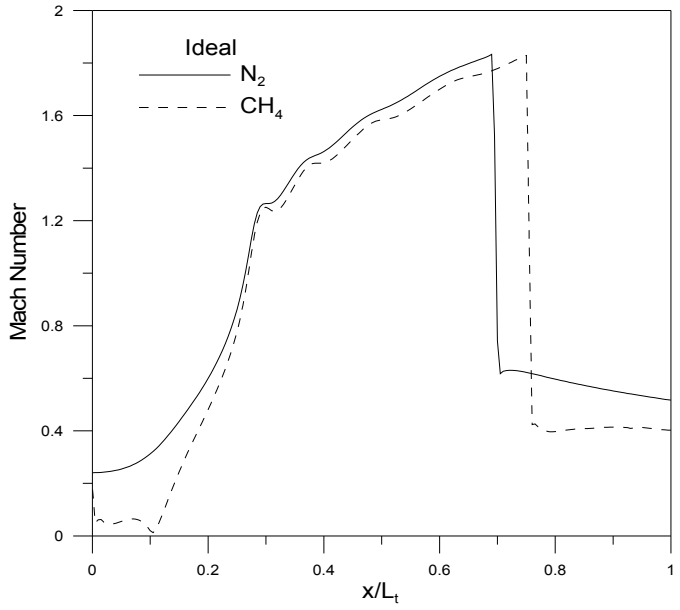


(a)

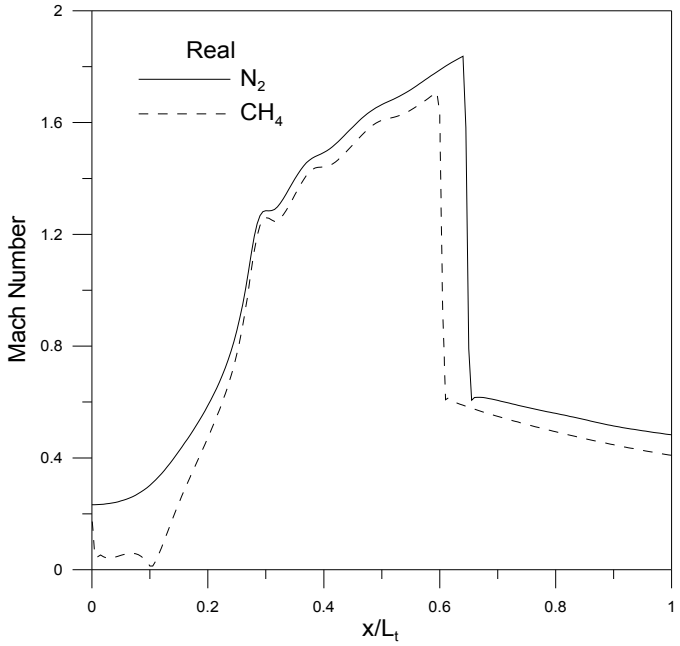


(b)

Fig. 4. Comparison of shock position for nitrogen and methane under (a) ideal and (b) real gas conditions

**Density.** By looking at any fluid textbook, one can see that the conservation of momentum equation directly or indirectly contains density terms in each component. Thus, flow structure is severely affected by any deviation in density calculation. To realize how this deviation will affect the predictions in the nozzle, a graph of the density ratio (real/ideal) along the nozzle system is plotted (see Figure 5). It is evident how erroneous the results might get if the perfect gas model is used, particularly in the vicinity of the shockwave. A large spike of density variations is seen close to the shockwave.

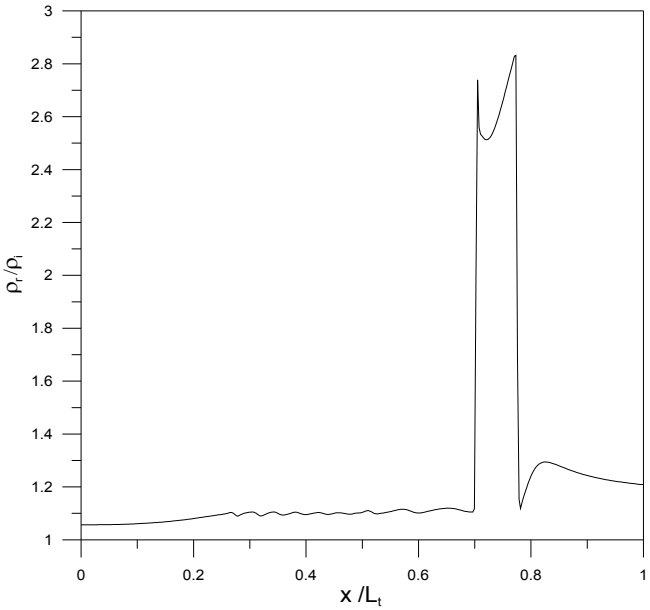


Fig. 5. Centerline density ratio for real gas (methane) simulation in an extended throat nozzle

**Inlet Pressure.** As mentioned earlier, our numerical solution predicts the inlet pressure for the given mass flow rate, outlet pressure and outlet temperature. Figure 6 represents static pressure distribution at the axis. One can see that a significant difference between the real and perfect gas at the inlet pressure is obtained. The real gas model predicts lower required inlet pressure for a given mass flow rate. Thus, better pressure recovery may be obtained. The real gas simulation predicts pressure recoveries in excess of 10% over those predicted by the perfect gas model. Also, the difference between real and ideal static pressures forces the calculation of total pressure to diverge. The errors in evaluating the total pressure and temperature can lead to incorrect predictions for friction loss, work and heat transfer. The differences between the predictions of ideal and real gas models for total pressure and total temperature are considerable. These discrepancies can result in incorrect values for friction losses and other calculated parameters.

**Temperature.** Static temperature decreases during the isentropic expansion process. Figure 7 illustrates the longitudinal variation of static temperature along the insulated wall. It is clearly shown that the temperature reduction in the real gas case is larger than the ideal case. Thus, ideal gas simulation can lead to erroneous results in predicting the potential phase change.

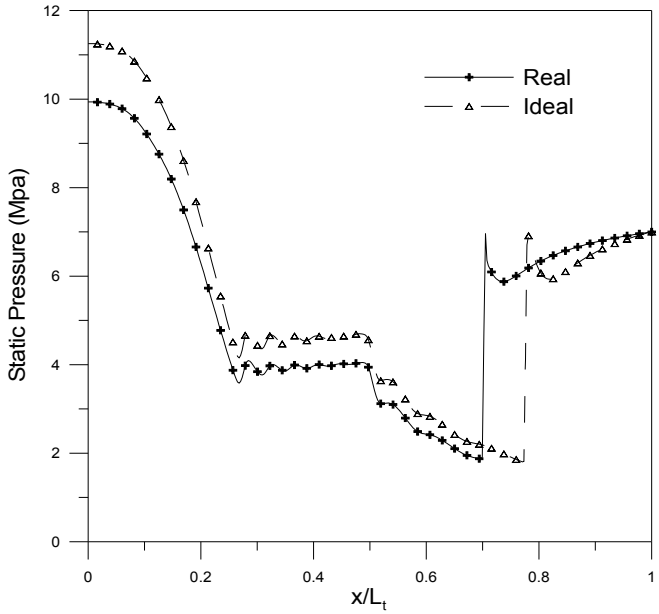


Fig. 6. Centerline static pressure for real gas (methane) simulation in an extended throat nozzle

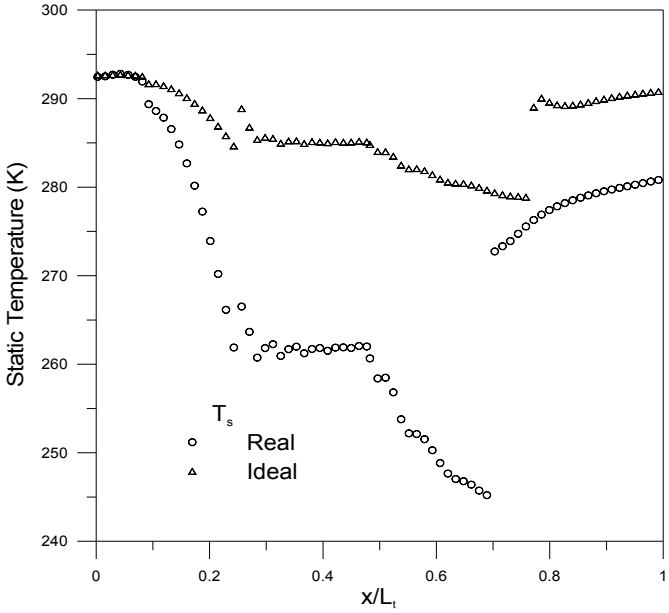


Fig. 7. Wall static temperature distribution for real gas (methane) simulation in an extended throat nozzle

Theoretically, stagnation temperature should retain its value across the shock when the nozzle is insulated. Such conclusion is true when perfect gas law is used as the thermodynamic model. However, the real gas model predicts different conditions in which the stagnation temperature may vary. Stagnation temperature in the real gas case varies across the shock because the specific heat is now varied across the shock as well. Thus, for adiabatic process;

$$\int_{T_{01}}^{T_{02}} Cp(T_0).dT_0 = 0 \tag{3}$$

This means that $T_{02} \neq T_{01}$ across the shockwave.

As a conclusion of modelling of supersonic nozzles using real gas models and discussion of the effect of real gas on the flow of natural gas through these nozzles, the choice of thermodynamic model can substantially affect the modelling results. This includes the position of shockwave, the fluid properties and conditions after the shock, and the work/heat transferred across the system.

### 2.3.2 de *Laval nozzles* with extended straight throat

In this section the influence of geometry on the flow of natural gas through the supersonic nozzle is presented. As mentioned in Section 2.3.1, the nozzle is composed of three sections: the convergent section (subsonic zone), the extended throat section (critical zone) and the divergent section (supersonic zone).

The governing equations are derived from the basic conservation laws including mass (continuity), momentum, and the first and second laws of thermodynamics and the use of a quite suitable real gas Equation of State (EOS).

2.3.2.1 Geometry Influence

**Choke location:** The flow reaches sonic condition at the throat, expands in the slight diverging/expansion section of the nozzle (~ 0.04 *m*), passes through the constant cross-section area, and finally moves across the diffuser within which the shock occurs. The flow downstream of the shock is subsonic. Thus a pressure recovery occurs. The base Fluent simulation cannot predict any phase change therefore it is assumed that no condensation will occur as the gas passes through the nozzle. Gas dynamics parameters for real and ideal flow are presented in Figures 8. The Figure indicates that no sensible variation is predicted in longitudinal Mach number, especially in the inlet/converging part. The vertical line $x=x^*$ confirms that, for both cases, the Mach number value of unity is obtained at the critical cross section of the nozzle. This conclusion agreed very well with the predictions in recent studies (Arina, 2004, Molleson & Stasenko, 2005, and Drikakis & Tsangaris, 1993). It can, therefore, be concluded that the sonic position always occurs at the throat and is independent of the nozzle geometry and gas thermodynamic model.

**Shock position**: A shock wave occurs in the diffuser part of the system that leads to a change in the flow from supersonic to subsonic. The real gas model predicts the shock location earlier as concluded in Section 2.3.1. Arina (2004) compared several real gas EOS with the corresponding perfect gas model. He concluded that all the real gas models predict a similar flow in the convergent part, while the shock position is slightly varying from one model to another. However, his conclusion was built on a Laval nozzle and inert gases (air) which behave almost ideally even at high pressures. It can also be concluded that

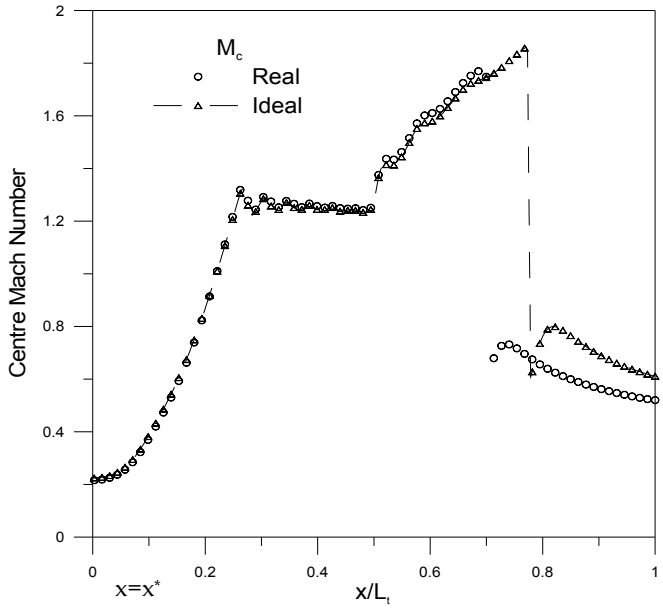


Fig. 8. Centerline Mach number for real vs. ideal methane simulation in an extended throat nozzle

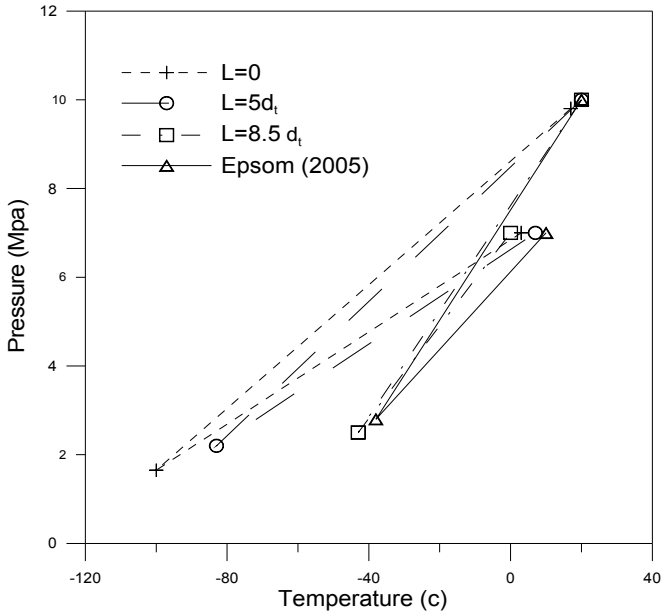


Fig. 9. Pressure-temperature chart for real gas (methane) simulation in an extended throat nozzle

thermodynamic models and the system's geometry play the most significant roles in predicting the shock position. Hence, the more accurate EOS would result in a closer prediction of the shock location and behaviour.

**Length of Constant Cross Section Area Conduit:** In order to separate liquid particles from natural gas and place instruments to control the shock wave location, Twister Inc. (Epsom, 2005) uses an extended constant area throat within the area just before the diffuser section of the Laval nozzle. Although the exact dimension and geometry of the Twister's nozzle are unknown, we studied the effect of the length of the constant cross section area conduit by selecting several length-to-diameter ($L/d_t$) ratios. The results of the simulation are plotted on a Pressure-Temperature (P-T) chart as shown in Figure 9. We could produce the same P-T chart as the Twister (Epsom, 2005) by changing the length of the conduit part by adjusting the ($L/d_t$) parameter. This indicates that, in addition to the nozzle outlet pressure, by adjusting the channel length, the minimum temperature of the system and shock position can be controlled.

**Mesh generation**

The quality of the mesh plays a significant role in the accuracy and stability of the numerical computation. The issue of grid quality is concerned with the ability of a particular discretization scheme to accurately represent the continuous governing equations on a given grid. The final accuracy and efficiency of any numerical solution are highly dependent on the particular meshing strategies and the mesh density distribution employed. The key to an efficient overall numerical solution remains in a good matching of the strengths and weaknesses of the grid generation and flow solution techniques and the maintaining of a strong and favourable interplay between these two phases of the solution procedure. Obviously, the goal of any numerical simulation should be the optimization of both the discretization scheme as well as the grid generation scheme.

Although accuracy increases with finer grids, the CPU and memory requirements to compute the solution and post-process the results also increase. Of many solutions to such deficiency -adaptive grid refinement can be used to increase and/or decrease grid density based on the evolving flow field, and thus provides the potential for more economical use of grid points and hence reduced time and resource requirements. Multigrid strategy also represents another recent powerful technique which takes a more comprehensive approach to the general problem of numerically simulating a physical phenomenon by closely coupling the grid generation and numerical solution aspects. The idea of a Multigrid algorithm, which was considered in the present numerical technique, is to accelerate the convergence of a set of fine-grid discrete equations by computing corrections to these equations on a coarser grid (Peyret, 1996), where the computation can be performed more economically. This process is applied recursively to an entire set of coarse-grid levels. Each Multigrid cycle begins on the finest grid level and cycles through the various levels up to the coarsest mesh. At this stage the computed corrections are successively interpolated back to the finest level and the cycle is repeated. The accuracy of the final discretization is solely determined by the fine-grid discretization, and the coarser levels may be viewed simply as artefacts employed to accelerate convergence.

The dependence of the accuracy on the quality of the grid can be reduced if more grid metric information is included. However, grid dependency studies (Drikakis & Tsangaris, 1993) have shown that finer meshes do not necessarily influence the accuracy of the solution in the case of the axisymmetric nozzle flow. This conclusion was also reached in our

simulation when three different numbers of mesh cells, 1882, 5533 and 11 832 cells, were selected. Table 1 shows the number of iterations that led to convergence with respect to total mass error in inlet/outlet mass flow for each case. It is clearly shown that finer grid did not significantly affect the iteration steps for convergence. In fact, for coarser grids (i.e. 1882 cell), convergence occurred even faster (~1500 steps). However the position of shock changed and became stabilized after the number of iterations was doubled. The uncertainty of shock spot forces us to choose finer grids, especially since the shock wave is considered as one of the large gradient regions that requires grids to be fine enough to minimize the change in the flow variables from cell to cell. Due to the difficulties in determining the location of the shock in advance, one should strive to achieve a high-quality mesh over the entire flow domain. Hence, we considered 5533 grid cells as the computational mesh for the present study to endorse smooth variations of flow properties across shock region. Convergence occurred after a certain number of iteration steps and varied for real and ideal gas models. For example convergence for real gas non-swirl case occurred after 3182 iterations with an error in inlet/outlet mass flow of about $4.8\text{x}10^{-4}$ %. Table 2 shows the number of iterations that led to convergence with residual errors for continuity, energy, $k$ and $\varepsilon$ equations for non-swirl real and ideal cases.

| No. of Cells | No. of Iterations | % errors in mass flow |
|---|---|---|
| 1 882 | 3 030 | $9.8\times10^{-3}$ |
| 5 533 | 3 182 | $4.8\times10^{-4}$ |
| 11 832 | 3 500 | $3.2\times10^{-1}$ |

Table 1. Number of iterations that led to convergence for simulation cases with total mass error in inlet and outlet mass flow

| Case | % Error of Inlet/Outlet Mass Balance | Number of Iteration Steps | Continuity | Energy | $k$ | $\varepsilon$ |
|---|---|---|---|---|---|---|
| Ideal | $2.0\times10^{-4}$ | 9 230 | $2.40\times10^{-3}$ | $1.90\times10^{-3}$ | $8.50\times10^{-6}$ | $9.60\times10^{-6}$ |
| Real | $4.8\times10^{-4}$ | 3 182 | $5.85\times10^{-4}$ | $5.58\times10^{-4}$ | $5.58\times10^{-5}$ | $6.03\times10^{-5}$ |

Table 2. Number of iterations that led to convergence with residual errors for continuity, energy, $k$ and $\varepsilon$ equations for non-swirl real and ideal cases

#### 2.3.3 de Laval nozzles with extended U-shape throat

The purpose of this section is to find alternative designs to the swirling flow of gas through the Laval nozzle configuration that was discussed earlier in search of better separation performances. As a result, the Laval nozzle with extended U-shaped section was proposed. The proposed nozzle is composed of three sections:

1. The convergent subsonic section that experiences a slight divergence after the throat to accommodate for the supersonic flow of the gas.
2. The U-shaped extended throat through which the centrifugal force exerted on the particles is expected to provide the intended separation between phases (gas-liquid, gas-solid, or gas-solid-liquid).
3. The divergent section that provides the cross-sectional growth required for pressure recovery.

The design parameters in this study included the ratio of the inside diameter of the throat to that of the U-shaped section, the curvature radius of the U-shaped section, and the inlet and outlet pressures. System variables that were used in the analysis were position of the shock, gas velocity inside the U-shaped section, and consequently the centrifugal acceleration experienced by the gas flowing inside that section used as a measurement of the level of phase separation the device could deliver.
Simulations were based on the inviscid flow of methane as process fluid. The governing equations were those of the conservation laws (mass, momentum, and energy) along with an appropriate thermodynamic model to predict gas properties.
As no experimental results are available for evaluation purposes, a pilot test is under development that uses compressed air as process fluid. The test results will then be compared to those of the CFD simulations performed under the same conditions to evaluate the computer models.

2.3.3.1 Throat diameter ratio

As it was shown in the previous section, the flow always reaches sonic velocity at the throat. The slight divergence after the throat and before the U-shaped section is to allow the flow to reach supersonic velocity. Assuming pressure drop across the nozzle is large enough, the value of the Mach number at the entrance to the U-shaped section depends solely on the ratio of the diameter at this point to that of the throat. Since the purpose of the U-shaped section is to take advantage of the supersonic flow in a circular path, it is important that the shock takes place in the diverging section. It must be noted that despite the diameter of the nozzle is constant throughout the U-shaped section, a shock wave may take place inside that section due to the loss of energy in the U-shaped section.
The U-shaped section to throat diameter ratio of 1.2 was determined to be most effective in this study. This means that the constant cross-section area of the U-shaped section has a diameter of 1.2 times the diameter of the throat where the choke takes place. It is important to realize that this ratio is not the only factor that determines the position of the shock. Other parameters involved are the U-shaped section curvature radius and outlet back pressure.

2.3.3.2 U-shaped section curvature radius

The curvature radius of the U-shaped section has two converse effects on the flow. Increasing the radius of the curvature allows the gas to pass through it with faster velocity and higher Mach number without triggering a shock wave, but at the same time reduces the centrifugal acceleration (Bird, 1924). This is easily shown by the kinematic expression of tangential acceleration:

$$a_{\text{tangential}} = \frac{V^2}{r} \tag{4}$$

It may be concluded that since velocity is raised to the power of two in this equation, its value overweighs the negative value of increased radius. It should be noted though that an important feature of such supersonic separators is their relatively small size, and a rather large radius of curvature will compromise this characteristic. After vigilant study of several designs with various curvature radii, it was determined that a U-shaped section with a decreasing radius profile would be the best configuration for this design. The curvature profile shown in Figure 10 was therefore developed for the U-shaped section of the nozzle.

The radius of this profile is 40 units in the beginning (lower left section) and decreases continuously until it reaches 5 units in the end (upper section).

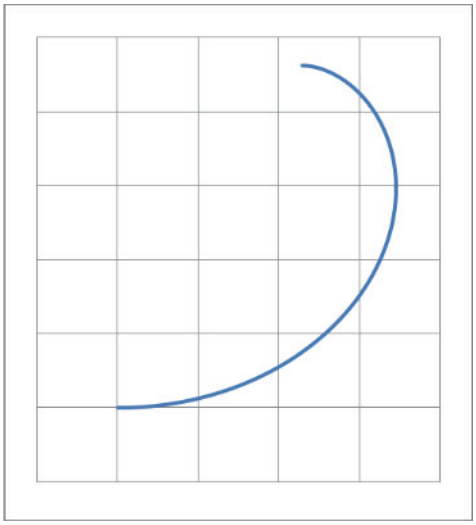

Fig. 10. A typical variable curvature proposed for the U-shaped section of the Laval nozzle.

2.3.3.3 Inlet pressure/Outlet back pressure

The outlet back pressure in this study was chosen to be the atmospheric pressure. The inlet pressure as well as the flow rate of the gas through the device were hence the other parameters affecting the pressure drop through the nozzle and consequently the position of the shock wave.

2.3.3.4 Particle Separation

Particle separation, as it was mentioned before, is due to the centrifugal force that is exerted on the flow as it passes through the U-shaped section with high velocity. The particles (e.g. micron size liquid droplets) are forced towards the outermost wall in the U-shaped section and may be extracted via a side channel that is installed in an appropriate position. Figure11 shows the values of centrifugal acceleration along this section as it is experienced by the flow. The acceleration is calculated from Equation (4). The graph is generated from the CFD simulation results for the geometry shown in Figure 12 when an inlet pressure of 345 kPa (50 psia) was imposed. It can be seen in the graph that the particles experience centrifugal accelerations of up to 36,000,000 $m/s^2$ in this particular configuration. That is the equivalent of approximately 3.7 million $g$.

2.3.3.5 Shockwave position

The position of the shockwave is very important for the performance of such separators. The shockwave should not take place before or through the U-shaped section as it was explained before. It is also important that the shock does not occur too far into the diverging section. This is because the farther into this section the shock takes place, it requires more differential pressure driving force across the device and therefore results in a greater pressure loss. It is crucial that the shock occurs as early as possible in the diverging section.

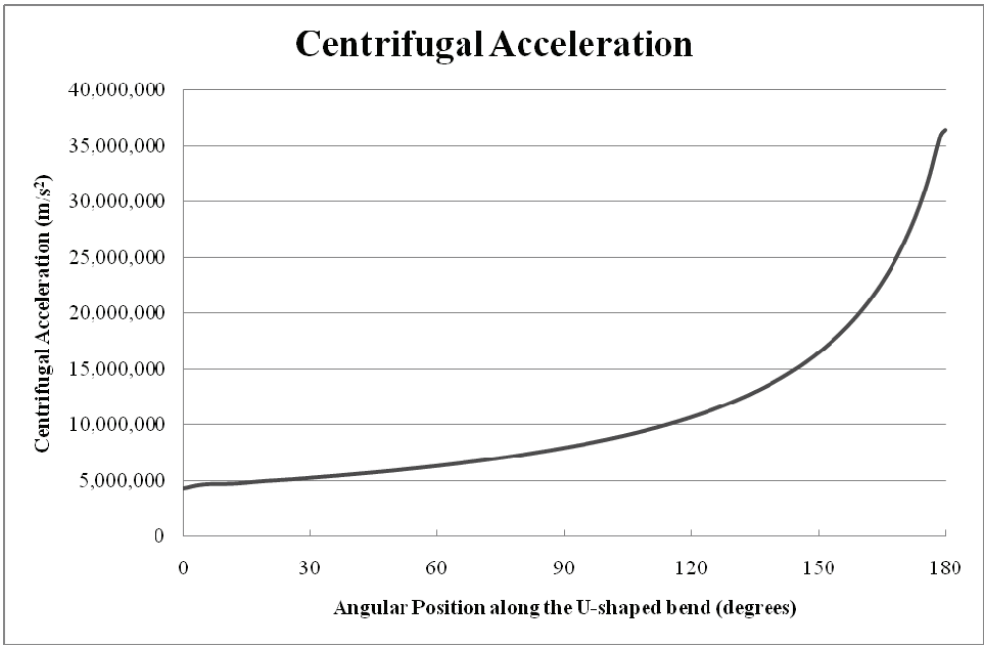


Fig. 11. Variation of centrifugal acceleration as a function of position along the U-shaped section in the proposed Laval nozzle.

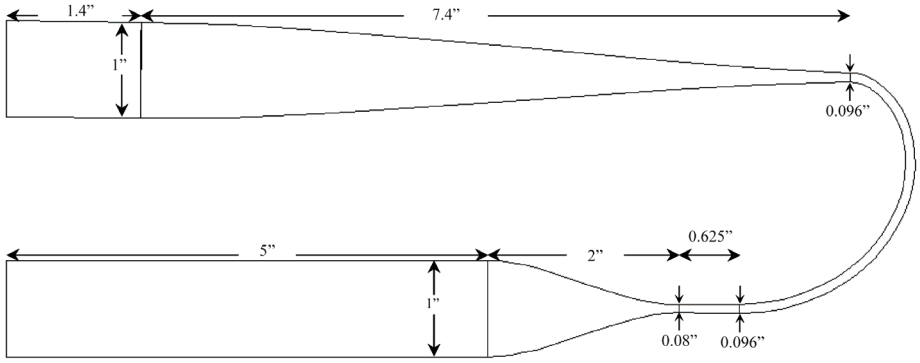


Fig. 12. A typical design configuration of the proposed Laval nozzle.

This property is one of the properties that were used to adjust the design and operating conditions of the separator. The position of the shockwave can be monitored through many different methods such as pressure profiling and velocity profiling. The most effective and accurate method that became available through the CFD package's post processing capabilities was the use of Mach number contours across the device. Theses contours clearly show the position of the shockwave as well as its shape and intensity (see Figure 13).

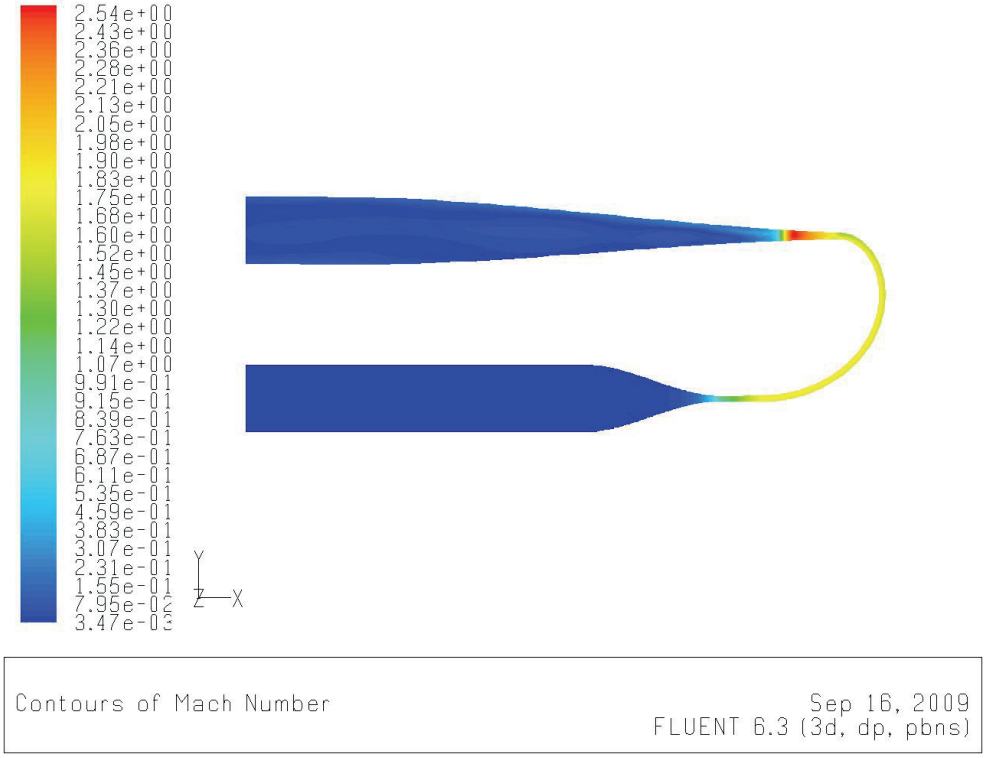


Fig. 13. Mach number filled contours showing the position of the shock wave.

2.3.3.6 Separation channel position

One important design parameter is to determine where the side channel to separate the flow of particles from the main gas flow should be placed. This can also be easily determined using the post processing features of the CFD package. Figure 14 is a volume density contour, precisely showing where most of the higher density particles are accumulated along the U-shaped section.

2.3.3.7 Mesh Generation

As it was mentioned previously, the quality of the mesh is a key factor in the accuracy and stability of a numerical (finite volume) analysis. Various characteristic properties of the geometry itself, types of fluids involved, and the amount of available memory and processing capability are some of the parameters that contribute to the final selection of a specific mesh design. A combination of wedge shaped and tetrahedral elements was chosen to represent the geometry in Figure 12. The geometry was divided into 6 sections as it can be seen in Figure 15. All sections were meshed using wedge shaped elements except section 2 which was meshed using tetrahedral elements due to the high gradient of cross-sectional area. Section 1 is only a simple pipe and its purpose is to stabilize the flow of gas before it enters the nozzle system. The meshing of this section therefore does not require a very fine quality. The mesh elements in this section are wedges with a length of $5.08\times10^{-3}$ m (0.2″) and

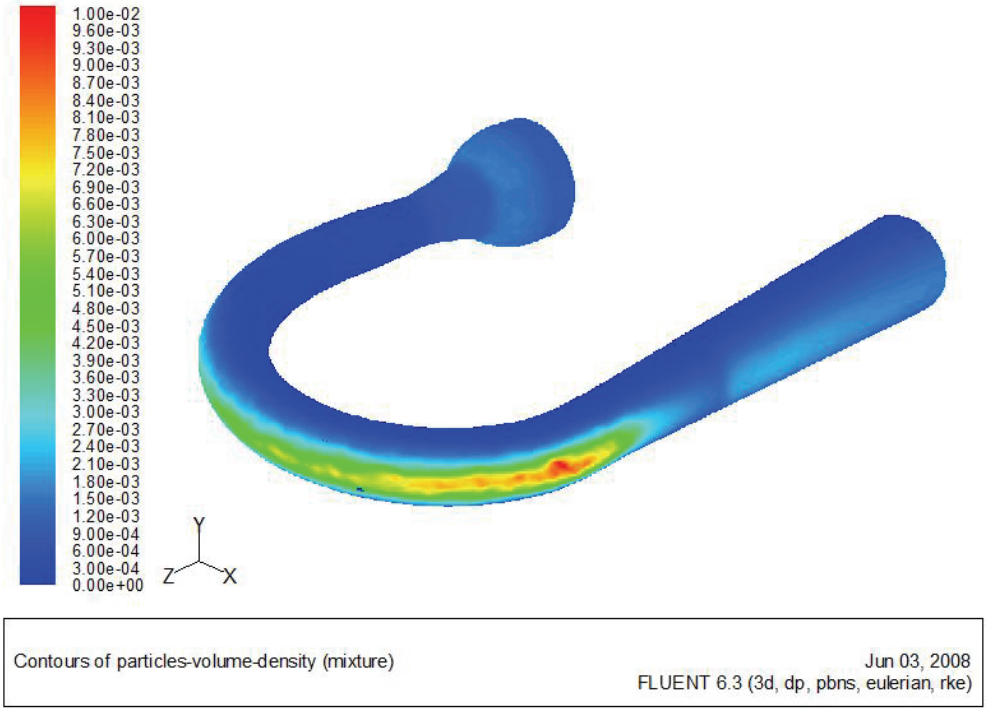


Fig. 14. A typical contour of the particles volume density showing where a side channel should be positioned to separate most of the particles

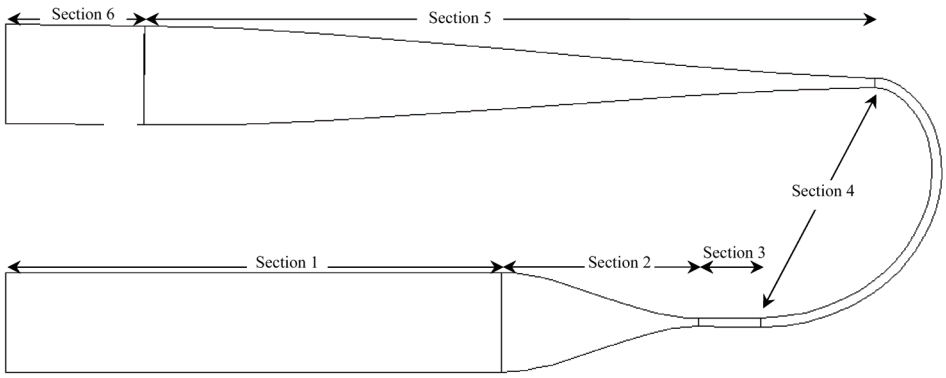


Fig. 15. Geometry divisions for meshing purposes.

equilateral triangular bases with edges of $2.54\times10^{-3}$ m (0.1″) (see Figure 16). Section 2 is the converging section of the nozzle and is meshed with a shrinking tetrahedral scheme (Figures 17 and 18). This method ensures the stability of the geometry through the

numerical analysis and links the coarse mesh of section 1 to the fine mesh of section 3. Section 3 is the slight divergence after the throat that accommodates for the supersonic flow of the gas and hence requires a very fine mesh quality to ensure the accuracy of the results. The meshing scheme is again a wedge type element that grows laterally as the cross section increases. The meshes are arranged so that there are 60 elements on the cross sectional perimeter at each point. This means that the wedge bases have lateral sizes of $1.016\times10^{-4}$ m (0.004″) in the beginning (right after the throat) and $1.27\times10^{-4}$ m (0.005″) in the end (right before the U-shaped section). A length of $2.54\times10^{-4}$ m (0.01″) is kept constant throughout this section. Section 4 is the U-shaped section. Wedge elements advance into this section with the same base sizes and lengths of $5.08\times10^{-4}$ m (0.02″). The wedges grow in section 5 until they reach a base size of $2.54\times10^{-3}$ m (0.1″) and length of $5.08\times10^{-3}$ m (0.2″) at the end of this section to merge in with section 6 that is the equivalent of section 1 and the mesh elements remain the same throughout this section. It is important to note that since the fluids being studied are gaseous and of high velocities, the effects of boundary layers may be neglected and hence no extra care is directed towards that area.

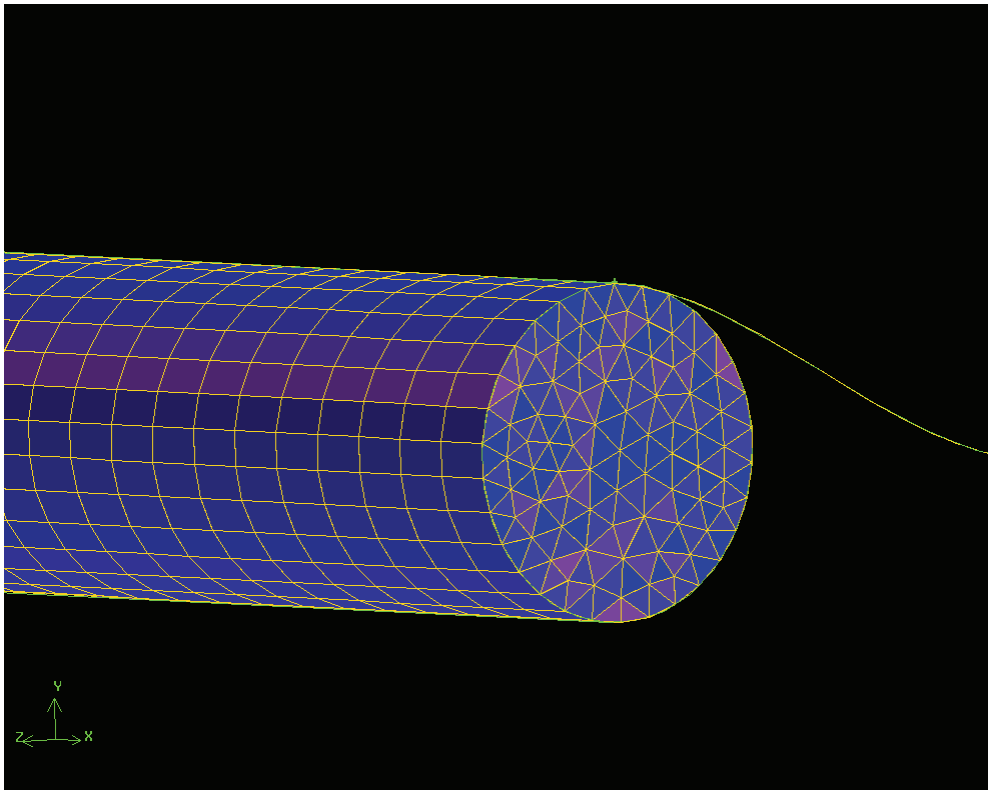


Fig. 16. Wedge shaped mesh elements forming the inlet stabilizing section of the device (Section 1).

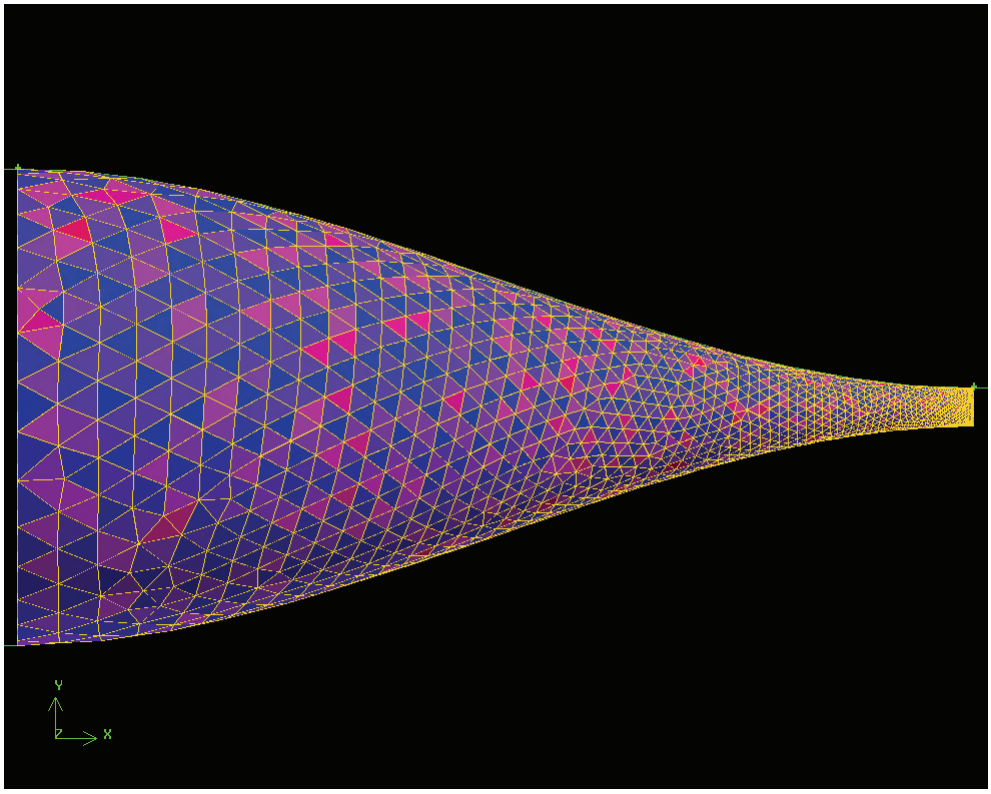


Fig. 17. Tetrahedral mesh elements in the converging section of the nozzle (Section 2). The element volumes shrink as they get closer to the throat.

2.3.3.8 Experimental apparatus

The novel nature of this study and the lack of external data inflicted the need to carry out laboratory pilot tests in order to evaluate the results of CFD simulations. The idea was to create a nozzle system similar to those that had been simulated through which high pressure gas would flow. Pressure, temperature, and flow rate measurements would be made and the results would be compared to those of the CFD simulations of the same system. The geometry chosen for this test was the geometry shown in Figure 12 and the process gas was compressed air. Two symmetrical halves of the proposed geometry was machined out of two blocks of aluminum and put together to form the desired pathways. Since it is significantly important that the flow is not disturbed by any bodily imperfection or hindrance, direct pressure and temperature measurement was not an option. Small size channels were created at several points along the pathway to enable the placement of measurement probes outside the fluid's pathway. As can be seen in Figure 19, there are 12 pressure measurement points and 4 temperature measurement points. Figure 20 shows the schematic setup of the pilot test. Measurements are currently being performed and the data is yet to be analyzed, but the preliminary results are in good agreement with the simulations.

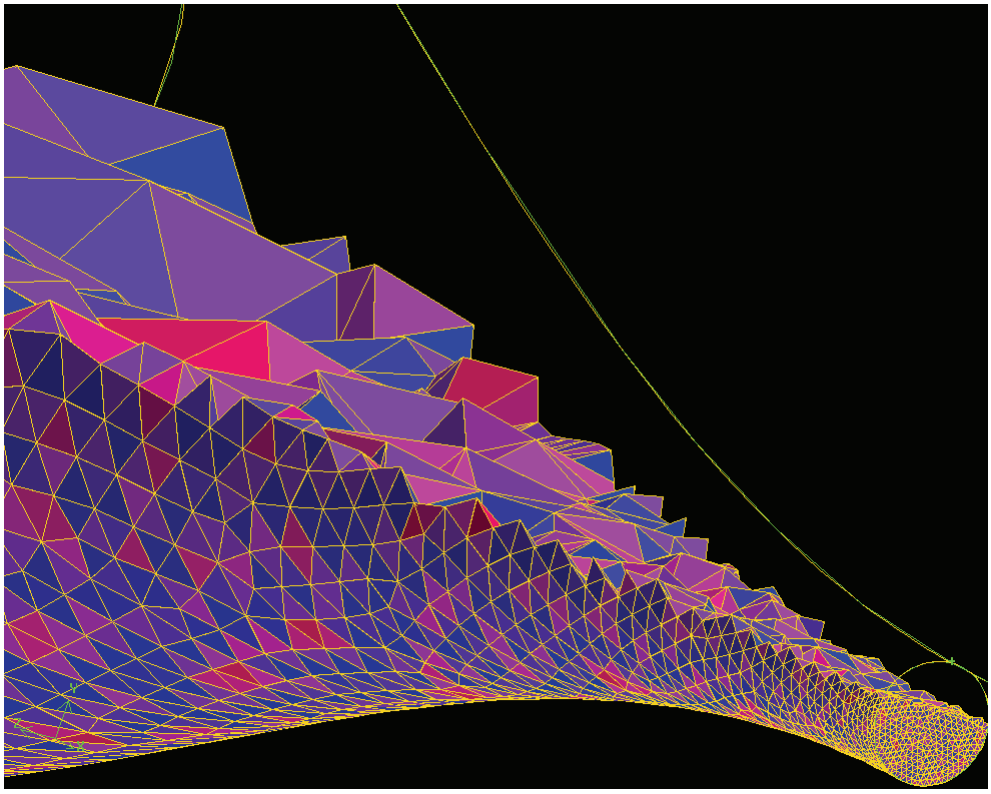

Fig. 18. A planar cut view of the mesh elements in the converging section of the nozzle (Section 2)

## 3. Cold jet release from high pressure marine CNG tanks

Cold jet is a result of a high pressure leak through a wall crack or valve stem or any other opening caused by an accident or failure to a high pressure device. Computational Fluid Dynamics, CFD, was used to study the phenomena and its effect on the surrounding equipment.

### 3.1 Problem description

The cold jet is developed when a fluid under high pressure and quite low temperature conditions is propelled to the ambient conditions through a crack or any leak opening. The very low temperature created due to this effect can influence the material's strength of construction of the high pressure containers/vessels or pipe systems carrying the gas. Very few studies have been conducted on this area while the demand is growing in the industry for such studies.

The low temperature can make ordinary carbon steel to become very brittle and lead to instant failure of high pressure tanks or pipelines and subsequent explosion. The jet can also extend to other adjacent equipment, parts, and pieces and influence their strength and

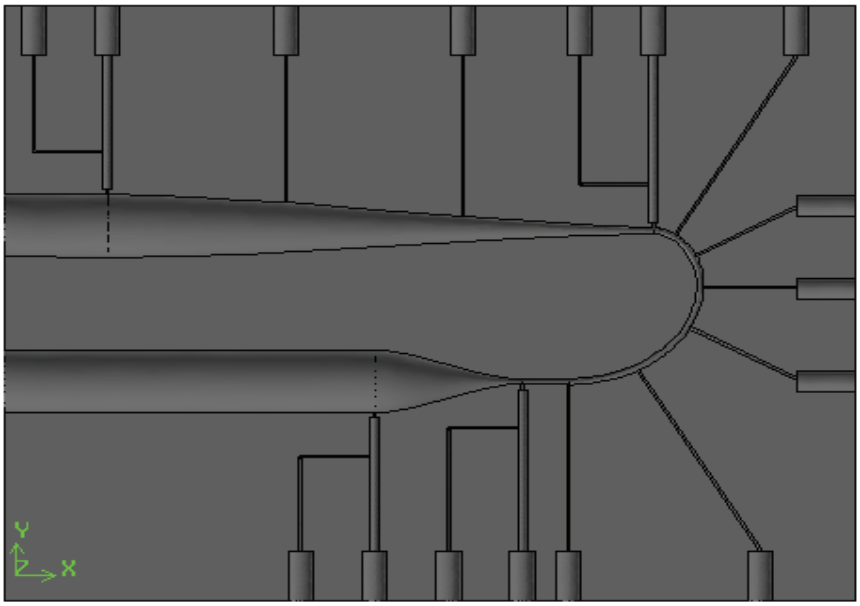


Fig. 19. The bottom piece of the pilot test nozzle system. The 4 thicker channels are designed to accommodate for temperature probes. All other channels are for pressure measurements.

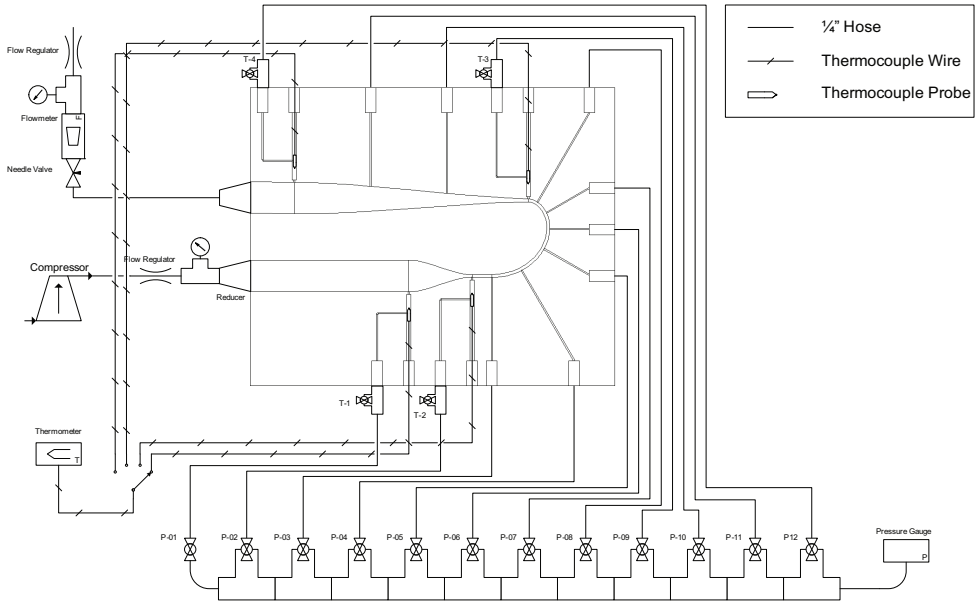


Fig. 20. Process flow diagram describing the schematic setup of the test pilot set-up

integrity due to temperature variations. The result of such study will provide an improved insight for any failure and stress analysis when such problems are encountered.
In this study, the behaviour of flow through the crack, the temperature distribution around the crack, and the influence of the jet to the adjacent walls have been reviewed.
The computational fluid dynamics technique was used to study the behaviour of high pressure natural gas when it flows through accidental cracks. The following themes are of interest in this study and will be discussed in this section:

- Flow behaviour through the crack
- Temperature distribution around the crack
- The influence of the jet to the adjacent walls

### 3.2 System configuration and simulation

The actual shape of the crack can be very irregular however for our analyses and to simplify the simulation a convergent nozzle with the geometry shown in Figure 21 was chosen. The conditions of the natural gas (methane) in the high pressure cylinders are: pressure 122 bars and temperature -8 ºC (265K), the thickness of the cylinder was 19 mm.

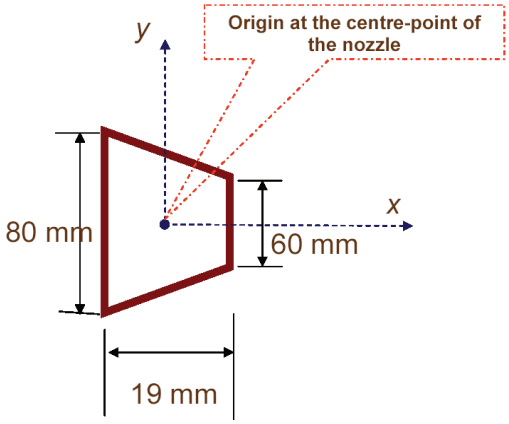


Fig. 21. Crack Geometry assumed to be convergent nozzle

### 3.3 Crack simulation and results

Figure 22 shows the Mach number variation along the crack wall. The choke flow conditions occur at the crack's exit point, which agrees well with the principles of thermodynamics. The distance is from the mid-point of the nozzle on the x-axis as seen in the Figure 21.
Wall static temperature variation shown in Figure 23 illustrates that the temperature decreases smoothly along the crack then declines very sharply near the exit, explaining the abrupt drop in pressure at crack exit.

#### 3.3.1 Wall simulation around the crack

Temperature contours of the area around the crack can be generated by simulating the flow through the crack in a 2-D environment. Figure 24 shows the temperature contours on the outer wall surface of the tank at the crack exit. As can be seen the severe temperature differentials can pose thermal stress to the material and may cause fatigue and failure on the wall.

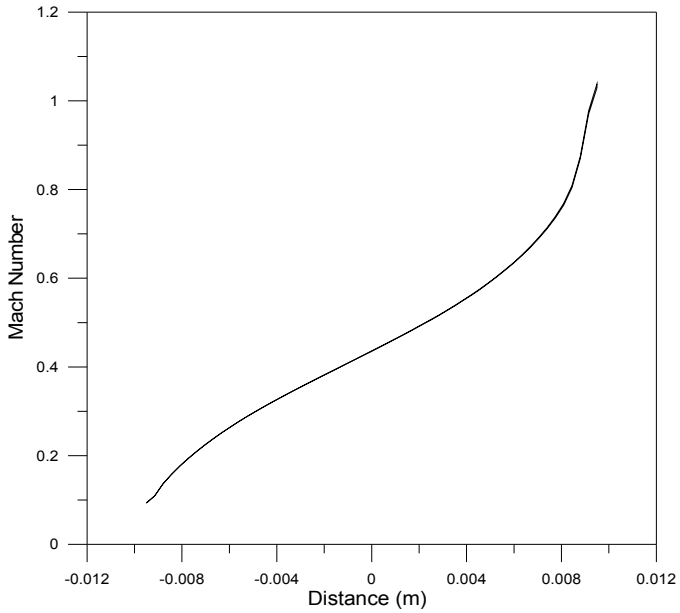


Fig. 22. Flow Mach number at centerline of the Crack

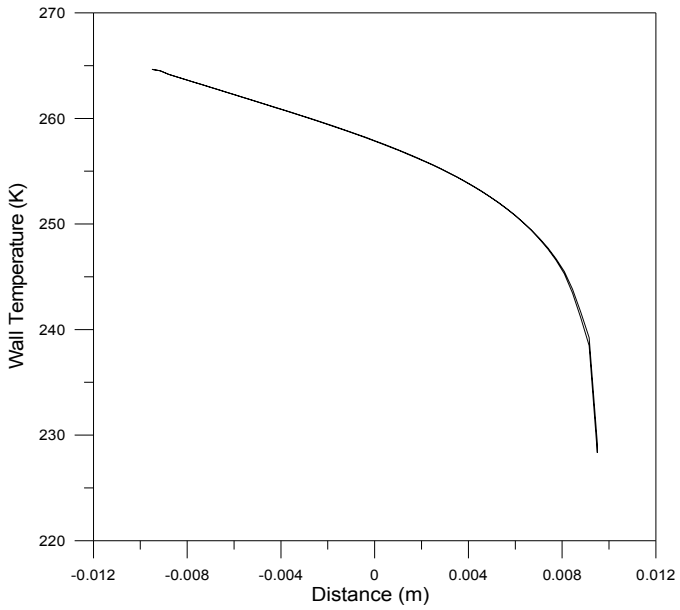


Fig. 23. Temperature variation at the inner surface of the crack

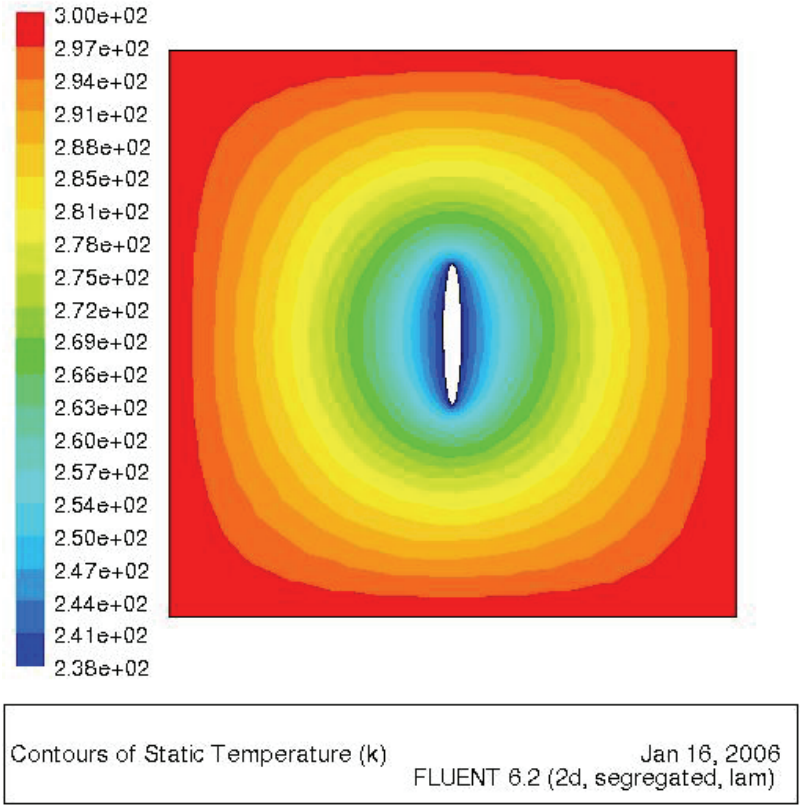


Fig. 24. Temperature contours around the crack

### 3.4 Jet simulation and results

In this section, we simulated a jet of natural gas developing outside a tank hitting a stationary wall some distant apart. Jet velocity contours are shown in Figure 25. One can recognize the impinging region and how the flow direction changes because of stagnation spot. The altered stream strikes the wall of the adjacent components (here another tank with the same height) and leaves a certain area that is exposed to impingement under less strength. Thus the temperature of this area becomes relatively higher.

It is concluded from the simulation that temperature distribution along the adjacent wall can be divided into three regions, Figures (26a, 26b):

1. Impinging point vicinity
2. Sharp variation region
3. Mild variation region

As seen in the jet velocity profile near the adjacent wall in Figure 25, the flow slightly alters then severely changes its direction to become parallel to the wall as it moves closer. Thus there is a certain distance on the wall that stagnation or circulated flow (eddies) are in contact with the wall. Hence the temperature of this region decreases sharply from a certain value (at stagnation spot) then increases gently along the rest of distance on the wall.

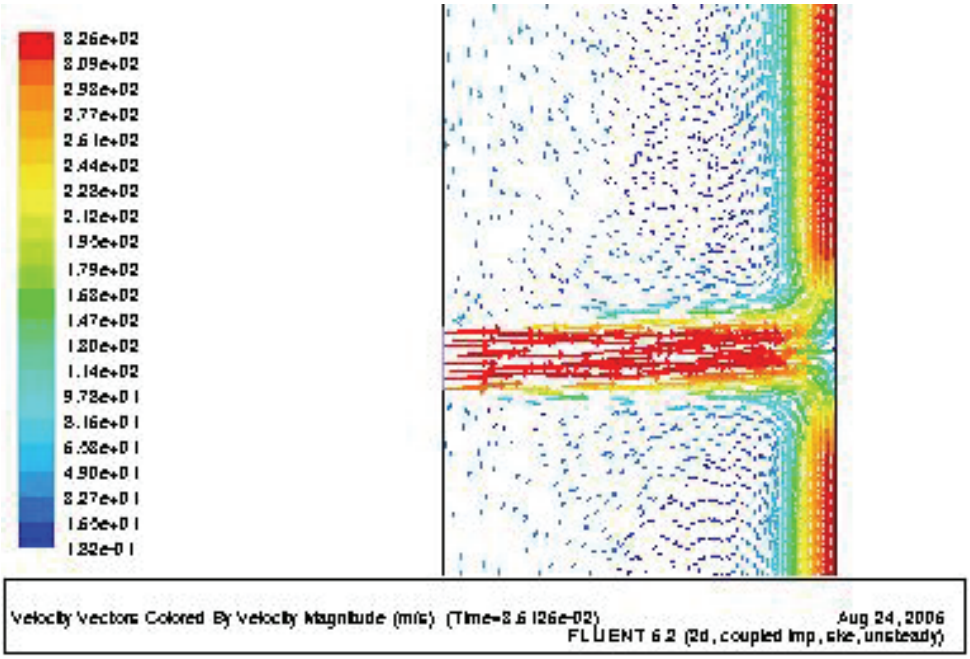


Fig. 25. Jet velocity vector caused by impinging with adjacent wall

## 4. Conclusions

Main conclusions can be summarized as follows:

- Shockwave has been studied using the CFD approach. The effects of real gas properties on the flow behavior were also addressed. It is crucial to beware of the real gas fluid behavior when analyzing high pressure natural gas flow systems. The assumption of a perfect gas may give rise to significant errors. Comparison between perfect and real gas models was implemented to present the errors involved when real properties in calculating heat, work, and other thermal processes are ignored. The results of CFD simulation runs conducted for different gases showed that the ideal gas assumption would lead to serious misrepresentation of the flow field, including the position of shockwave and severe miscalculations in the design of supersonic devices.
  The influence of geometry and vorticity were studied. Since the addition of a channel within the Laval nozzle is of interest in separating liquid particles, various lengths of such extended constant area regions, which connect the nozzle part with the diffuser part, have been selected. Results showed that variation of the channel length would impact the position of the shock wave and the minimum temperature of the system, which in turn influence the quantity and quality of droplets if condensation occurs. Swirls are formed when the fluid enters the nozzle semi-tangentially. Strength of vorticity and its behavior were addressed because the centrifugal force is responsible for particle separation due to the very high centrifugal acceleration induced within the nozzle throat. This acceleration is in the order of 105 or 106 times the acceleration of

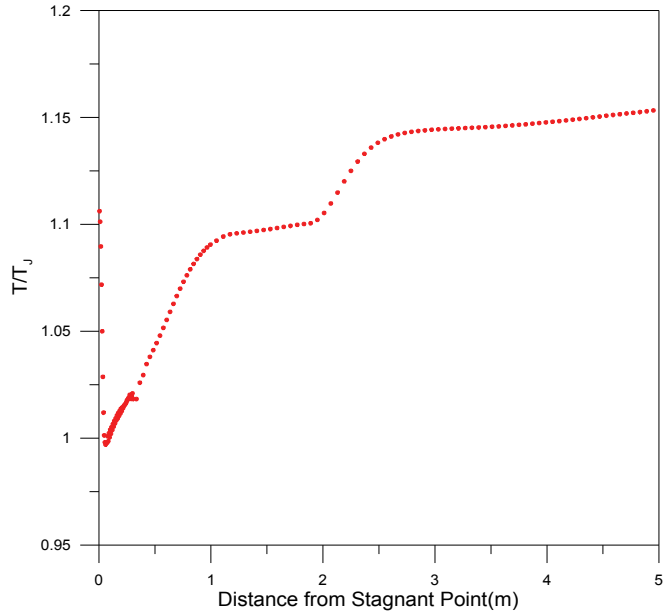


(a)

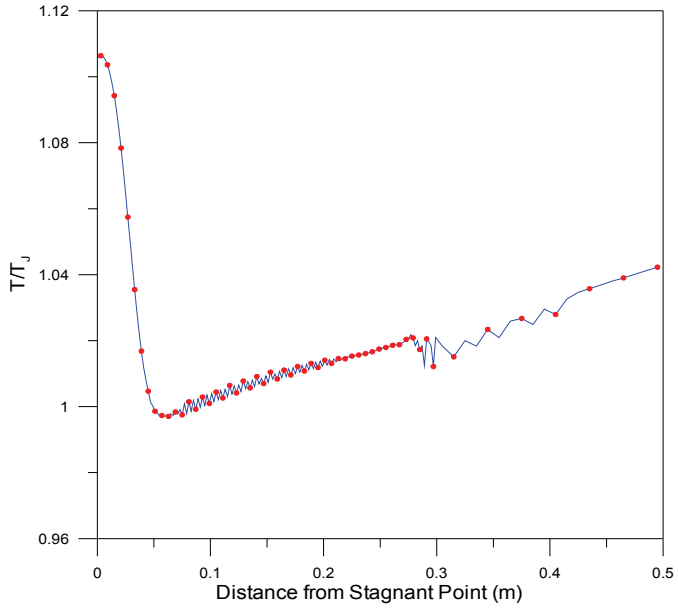


(b)

Fig. 26. Wall temperature ratio as a function of distance from stagnant point: a. Temperature profile at the adjacent wall; b. Enlarged portion wall temperature profile at the stagnant region

gravity and can induce separation of particles as small as several tenths of a macron in diameter. Furthermore, it is very important to have a sound understanding of pressure losses across the system, as these losses influence the economy of supersonic nozzles in natural gas processing. as the loss of pressure has to be compensated by costly compression facilities. In our further work, we will include the multiphase as well as multi-component fluid systems where the behavior of the natural gas in the system can be analyzed with more accuracy.

- It is concluded at this point that the alternate configuration of nozzle with an extended U-shaped section can deliver better separation performances than the original swirling flow of gas in a straight nozzle. Although the centrifugal acceleration levels observed here are highly dependent on the geometry size (curvature radius), it can be speculated that very powerful centrifugal forces can be achieved in a full size separator of this type. Despite the lack of external data, the CFD simulations have proven to be significantly reliable. The practical application of this system may look far away, but the use of CFD simulations has shown great potential and encouraging results.

CFD simulation is a very efficient technique to study the flow of high pressure gas through complex geometries and sophisticated simulations such as impinging region. This study showed how CFD could be used in analyzing such phenomena with elucidation that gives it a robust position among other algorithms. The selection of the right thermodynamic model is very crucial in simulating natural gas flow under high pressure and low temperature conditions. Results show that divergent geometry of the crack changes the flow from subsonic to supersonic flow. Hence, irreversibility is clearly affecting the properties of the flow through the crack. CFD simulation for cold jet concluded that adjacent components will be affected by the jet. The temperature varies according to the impinging phenomena in both shapes, however the temperature difference between the jet and adjacent wall is relatively higher in divergent shape than convergent. Further, heat exchange due to collision of jet with the adjacent storage tanks shows significant effects on the temperature distribution.

## 5. Acknowledgement

Financial support provided by the Centre for Marine Compressed Natural Gas (CMCNG) Inc., Unconventional Gas Supply Program of the Natural Resource Canada (NRCAN), and Atlantic Canada Opportunity Agency (ACOA) to finance various process engineering projects within the CMCNG as well as the presented work in this article is appreciated.

## 6. References

Alfyorov, V., Bagirov, L., Dmitriev, L., Feygin, V., Imayev S., Lacey, J. R., 2005. Supersonic Nozzle Efficiently Separates Natural Gas Components. Oil and Gas Journal. 103(20), 53-58.

Arina R., 2004. Numerical Simulation of Near-Critical Fluids. Applied Numerical Mathematics 51(4), 409-426.

Bai-Shi-I, 1961. An Introduction into Theory of Compressible Liquid Flow, Moscow: Izd. Inostrannoi Literatury, (Russ. Transl.)

Bird, R.B., 1924. Transport Phenomena. John Wiley & Sons, New York; USA.

Brouwer, J.M., Epsom, H. D., 2003. Twister Supersonic Gas Conditioning for Unmanned Platforms and Sub sea Gas Processing Source. Offshore Europe Conference - Proceedings, Aberdeen, UK, pp. 219-225.

Carvero, C., and Satta, A., 2000. A CFD Model for Real Gas Flow. ASME paper, GT-518.

Crocko, L., 1950. One-Dimensional Consideration of the Gas Dynamics of Time-Independent Flows, in Fundamentals of Gas Dynamics, H.W. Emmons, Ed., Princeton: Princeton University Press, Princeton, USA.

Drikakis, D., Tsangaris, S., 1993. Real Gas Effect for Compressible Nozzle Flows. Journal of Fluid Engineering. 115(117), 115-120.

Ginzburg, I. P., 1939. Uch. Zap. Leningr. Gos. University, no. 42, pp. 5.

Hengwei, L., Zhonggliang, L., Yongxun, F., Keyu, G., and Tingmin,Y., 2005. Characteristic of a Supersonic Swirling Dehydration System of Natural Gas. Chinese Journal of Chemical Eng., 13(1), 9-12.

Kouremenos, D. A., 1986. Normal Shockwaves of Real Gases and the Generalized Isentropic Exponent. Forschung im Ingenieurwesen, 52(1), 23-31.

Karimi, A., and Abedinzadegan Abdi, M., 2006. Selective Removal of Water from Supercritical Natural Gas. SPE 100442, Proceedings of the SPE Gas Technology Symposium, Calgary, Alberta, Canada, 15-18.

Man, H. C., Duan, J., Yue, T. M., 1997. Design and Characteristic Analysis of Supersonic Nozzle for High Pressure Laser Cutting. Journal of Materials Processing Technology, 63(1-3), 217-222.

Molleson, G.V. and Stasenko, A. L., 2005. An Axisymmetric Flow of a Mixture of Real Gases with a Condensing Component. High Temperature, 43(3), 422-430.

Okimoto, F., Brouwer, J. M., 2002. Supersonic Gas Conditioning. World Oil, 223(8), 89-91.

Peng, D. Y., and Robinson, D. B., 1976. A New Two-Constant Equation of State. Ind. Eng. Chem. Fundam., 15, 59-64.

Pope, S. B., 2000. Turbulent Flows. Cambridge University Press. Cambridge, USA.

Redlich, O., and Kwong, J. N. S., 1949. On the Thermodynamics of Solutions. V. An Equation of State. Fugacities of Gaseous Solutions. Chem. Rev., 44, 233-244.

Saad M. A., 1993. Compressible Fluid Flow. 2nd Edition, Prentice-Hall, Inc., New Jersey, USA.

Soave, G., 1972. Equilibrium Constants from a Modified Redlich-Kwong Equation of State. Chemical Engineering Science, 27(6), 1197-1203.

Wark, K., 1995. Advanced Thermodynamics for Engineers. McGraw-Hill Series, New York, USA

# 2

# CFD Two Fluid Model for Adiabatic and Boiling Bubbly Flows in Ducts

Martin Lopez de Bertodano and Deoras Prabhudharwadkar
*School of Nuclear Engineering, Purdue University*
*USA*

## 1. Introduction

The predictions of the CFD Two Fluid Model for bubbly flows in ducts depend on constitutive relations for various interfacial and wall transfer terms. The objective is to use state-of-the-art data covering a wide range of experimental conditions to validate the constitutive relations for two cases of practical interest: adiabatic flows and subcooled and saturated boiling flows. The key to the validation is that all the data was obtained with either double conductivity or double optical needle probes to measure the bubble sizes.

This chapter is divided into two parts. The first part considers adiabatic flows where the interfacial and wall momentum transfer is represented by various forces acting between the two phases and between the wall and each phase. There is a considerable amount of work on the development of constitutive relations for these forces in the open literature. However, these relations have been derived under special flow conditions which may not hold in general. Hence, every force term needs to be calibrated and this introduces the closure coefficients which are dependent on the flow conditions. The air-water experimental validation and calibration of lift, wall and turbulent diffusion forces, which determine the distribution of void fraction in the direction normal to the flow, is carried out.

The second part describes the implementation and validation of heat and mass transfer models required for boiling flows. In particular the wall heat transfer model is based on splitting the wall heat flux into three components: single phase convection, evaporation at the bubble surface and quenching after bubble departure. The evaporation and quenching components depend on three parameters: bubble nucleation site density, bubble departure diameter, and bubble departure frequency. These parameters depend on complex physical phenomena that are not completely understood. However, a considerable amount of experimental data, scaling and various models exist for each one. Nevertheless, it is impossible to test these three separate phenomena simultaneously and in particular the bubble departure diameter remains an open problem (Colin et al., 2009). Therefore only the other two parameters were validated and the validation was performed with two data sets where the bubble diameters were measured: one with high pressure R12 and another with water at atmospheric pressure. The high pressure Freon data corresponds to a fluid-vapor density ratio which is equivalent to that of water-steam at 150 bar. Thus the liquid to vapour density ratio between Freon and water data varies over two orders of magnitude. The surface tension also varies over a wide range from 0.0017 to 0.057 N/m. The ratio of the flow channel hydraulic diameter to the bubble diameter encountered during these simulations

varied from 4 to 40. As anticipated, the two-fluid model performs very well when bubbles are small compared to the channel width. However, appropriate modifications have to be made to the two-fluid model to account for cases where the bubbles are too large.
The constitutive relations remain the main limitation of any Two Fluid Model. In particular the present model lacks constitutive relations for the bubble size at the wall and in the bulk. Hopefully, current research such as the development of interfacial area transport models (e.g., Ishii & Hibiki, 2006) will help to resolve this shortcoming in the foreseeable future.
The commercial CFD code ANSYS CFX (version 11 for adiabatic and 12-beta for boiling flows) was used for all the simulations reported in this chapter.

## 2. Nomenclature

| | |
|---|---|
| $a_i$ | Interfacial Area Concentration |
| $C_D$ | Drag Coefficient |
| $C_{VM}$ | Coefficient of Virtual Mass (0.5) |
| $D_b$ | Bubble Diameter |
| $D_{dep}$ | Bubble departure diameter |
| $f_{dep}$ | Bubble departure frequency |
| $\underline{g}$ | Gravitational Acceleration |
| $j_L$ | Superficial Velocity of Liquid |
| $j_G$ | Superficial Velocity of Gas |
| k | Turbulence Kinetic Energy |
| $\underline{M}_{ki}$ | Interfacial Momentum Source |
| $\Delta m_k$ | Interfacial Mass Source |
| $n_{site}$ | Nucleation site density |
| $q''$ | Heat Flux |
| $\underline{\overline{v}}_k$ | Velocity (vector) |
| $\underline{\overline{v}}_R$ | Relative Velocity (vector) |
| $T$ | Temperature |
| $e_k$ | Enthalpy of the phase $k$ |
| $G$ | Mass Flux |
| $p_k$, $P$ | Pressure |

**Greek Symbols**

| | |
|---|---|
| $\alpha_k$ | Volume Fraction of $k^{th}$ phase |
| $\alpha$ | Void Fraction |
| ε | Dissipation of Turbulence Kinetic Energy |
| $\rho_k$ | Density |
| $\tau$ | Time constant |
| $\underline{\underline{\tau}}_k^{Re}$ | Turbulent (Reynolds) Stress |
| $\mu$ | Dynamic viscosity |
| $\lambda$ | Thermal Conductivity |

**Superscript**

| | |
|---|---|
| $D$ | Drag |
| $TD$ | Turbulent Diffusion |
| $L$ | Lift |
| $W$ | Wall |

**Subscript**

| | |
|---|---|
| $k$ | Phase identifier |
| $1, l, f, L$ | Continuous (Liquid) Phase |
| $2, g, G$ | Dispersed (Gas) Phase |
| $dep$ | Departure |
| $t$ | Turbulent |

## 3. Two fluid model mass and momentum equations

**Mass Conservation**

The ensemble averaged two-fluid model continuity equations (Ishii & Hibiki, 2006) governing the motion of $n$ fields, $k$ = 1 to $n$, has the following form:

$$\frac{\partial}{\partial t}\alpha_k \rho_k + \nabla \cdot \alpha_k \rho_k \underline{\overline{v}}_k = \Delta m_k \tag{1}$$

For the bubbly flow analyzed during this study, the two-fluid model is comprised of two fields: liquid continuous (k = 1) and dispersed bubbles (k = 2) and the mass transfer across the interface is zero for adiabatic flows.

**Momentum conservation**

$$\frac{\partial}{\partial t}\alpha_k \rho_k \underline{\bar{\upsilon}}_k + \nabla \cdot \alpha_k \rho_k \underline{\bar{\upsilon}}_k \underline{\bar{\upsilon}}_k = -\alpha_k \nabla p_k + \nabla \cdot \alpha_k \left( \underline{\underline{\tau}}_k + \underline{\underline{\tau}}_k^{\mathrm{Re}} \right)$$

$$+ \alpha_k \rho_k \underline{g} + \underline{\underline{M}}_{ki} + \sum_j \Delta m_{k,j} \underline{\bar{\upsilon}}_j \tag{2}$$

The interfacial momentum transfer force comprises of force terms due to drag, turbulent diffusion, lift and a wall force:

$$\underline{M}_{ki} = \underline{M}_{ki}^{D} + \underline{M}_{ki}^{TD} + \underline{M}_{ki}^{L} + \underline{M}_{ki}^{W} \tag{3}$$

Other forces like the Virtual Mass force and Basset force are also present but are assumed to be negligible.

**Drag force**

The drag force of the bubbles is given by,

$$M_2^D = -\frac{3}{4}\alpha\rho_1 \frac{C_D}{D_b} \left| \underline{\bar{\upsilon}}_R \right| \underline{\bar{\upsilon}}_R \tag{4}$$

The drag coefficient is given by the Ishii-Zuber correlation (1979). The relative velocity is given by $\underline{\bar{\upsilon}}_R = \underline{\bar{\upsilon}}_2 - \underline{\bar{\upsilon}}_1$.

**Lift force**

The lift force is given by (Auton, 1987):

$$\underline{M}_2^L = -C_L \rho_1 \alpha \left( \upsilon_2 - \upsilon_1 \right) \times \left( \nabla \times \upsilon_1 \right) \tag{5}$$

The lift coefficient used for the calculations is $C_L$ = 0.1 (Lopez de Bertodano, 1992). This value is of the same order as the experimental value (Tomiyama et al., 2002) for a bubble in Couette flow ($C_L$ = 0.288).

**Wall force**

The wall force model accounts for the effect that keeps the centers of the bubbles no closer than approximately one bubble radius from the wall. This force is important when the lift force is present. It is given by (Antal et al., 1991):

$$\underline{M}_2^W = C_{wall} \rho_1 \alpha \left| \upsilon_2 - \upsilon_1 \right|^2 \underline{n}, \quad C_{wall} = \min\left\{ 0, -\left( \frac{c_{w1}}{D_b} + \frac{c_{w2}}{y_{wall}} \right) \right\} \tag{6}$$

where $\underline{n}$ and $y_{wall}$ are the normal inward vector and the distance from the wall respectively. The values for the coefficients that are used in the CFD code CFX are:

$c_{w1}$ = -0.01 and $c_{w2}$ = 0.05. Note that the ratio $|c_{w2}/c_{w1}|$ determines the thickness of a layer next to the wall (in terms of the bubble diameter) in which the wall force is applicable.

**Turbulent Diffusion force**

The turbulent diffusion force is not yet well understood. The turbulent diffusion force model (Lopez de Bertodano, 1998) is based on a probability distribution function analysis of the two-fluid model (Reeks, 1991) which has the following form:

$$\underline{M}_2^{TD} = -(\rho_2 + C_{VM}\rho_1)\frac{\tau_c}{\tau_b}\left(\frac{\tau_c}{\tau_c+\tau_b}\right)\ \overline{\underline{\upsilon}'_1\underline{\upsilon}'_1}\cdot\nabla\alpha \tag{7}$$

The time constant of the bubbles is derived from the equation of motion of a single bubble as:

$$\tau_b = \frac{4}{3}\frac{(\rho_2+\rho_1 C_{VM})}{\rho_1 C_D}\frac{D_b}{\upsilon_R} \cong \frac{4}{3}\frac{C_{VM}}{C_D}\frac{D_b}{\upsilon_R} \tag{8}$$

The time constant of the turbulent eddies is proportional to the turnover time of the eddies and it is calculated according to the model by Mostafa and Mongia (1988):

$$\tau_{c1} = 0.35\ \frac{k}{\varepsilon} \tag{9}$$

The effect of eddy cross over is accounted for by a simple model when the particle is moving very fast with respect to the eddies, the time constant is given by:

$$\tau_{c2} = \frac{\lambda_e}{\underline{\upsilon}_R} \tag{10}$$

where $\lambda_e$ is the Eulerian length scale of the eddies. The effective time constant is obtained combining equations (9) and (10) as:

$$\frac{1}{\tau_c} = \frac{1}{\tau_{c1}} + \frac{1}{\tau_{c2}} \tag{11}$$

This approximation has the right asymptotic behavior at both extremes when the bubbles are very small or very large. The model given by equations (7) to (11) may be simplified under several hypothetical asymptotic conditions. We consider two cases:

*Case 1* - For $\tau_c >> \tau_d$, $\tau_{c1} << \tau_{c2}$ it can be shown that equation (7) is equivalent to the turbulent diffusion force model obtained by Lopez de Bertodano et. al. (2006):

$$\underline{M}_2^{TD} = -\frac{1}{\tau_b}(\rho_2 + C_{VM}\rho_1)\nu_2\ \nabla\alpha \tag{12}$$

where $\nu_2$ is the turbulent diffusivity of the bubbles. This equation was used by Lopez de Bertodano (2006) to model the diffusion of small bubbles by the very large vortices generated by cap bubbles in cap-bubbly flow. This model scales like $\upsilon'(\propto \upsilon)$ and is adequate when the turbulence is bubble induced. However for shear induced turbulence a diffusion model with stronger flow dependence is needed.

*Case 2* - For $\tau_{c1} >> \tau_{c2}$ it can be shown that equation (7) is equivalent to the model of Lopez de Bertodano et al. (1994a) for the diffusion of bubbles in turbulent duct flow, which is implemented in CFX as:

$$\underline{M}_2^{TD} = - C_{TD}\rho_1 k_1 \nabla \alpha , \tag{13}$$

where the turbulent diffusion coefficient used for the present calculations is $C_{TD}$ = 0.25. This model scales like $k \propto \upsilon'^2$ ($\propto \upsilon^2$) which provides more diffusion at higher flow velocities in the case of shear induced turbulence.

**Turbulence Transport**

The closure for the Reynolds stresses in equation (2) is based on the two-phase *k*-ε model developed by Lopez de Bertodano et al. (1994b). This model assumes that the shear induced (SI) and bubble induced (BI) turbulent stresses are added together:

$$\underline{\underline{\tau}}_k^{\mathrm{Re}} = \left(\underline{\underline{\tau}}_k^{\mathrm{Re}}\right)_{SI} + \left(\underline{\underline{\tau}}_k^{\mathrm{Re}}\right)_{BI} \tag{14}$$

The equivalent expression for the turbulent diffusivity of momentum of the liquid phase is given by Sato et al. (1981):

$$\nu_1 = C_\mu \frac{k^2}{\varepsilon} + C_{DB}\alpha D_b \upsilon_R \tag{15}$$

where the first term on the RHS corresponds to the *k*-ε model for the shear induced diffusivity and the second term corresponds to Sato et al.'s (1981) model for the bubble induced diffusivity. The coefficient $C_\mu$ = 0.09 is the standard value for the *k*-ε model. However, the coefficient $C_{DB}$ can be adjusted to fit the velocity profile data. A value of 0.6 is used for $C_{DB}$ in the present simulations. Standard *k*-ε model transport equations are used for the continuous phase. For the dispersed phase, the kinematic eddy viscosity is assumed to be equal to that of continuous phase, and hence no turbulence transport equations are needed.

## 4. Adiabatic CFD model assessment with atmospheric air-water data

**Experimental data and CFD model**

Serizawa et al. (1986) performed measurements of void fraction and interfacial area concentration in upward air water bubbly flow in a 30 mm diameter tube. A double conductivity probe was used to measure void fraction and interfacial area concentration. The radial profiles of void fraction and interfacial area concentration were obtained at 2.5 m axial distance from the inlet. The flow rates covered the range $j_L$ = 0.5 - 5 m/s and $j_G$ = 0 - 0.54 m/s.

The data set was used to compare the spatial distribution of void fraction. In particular the two-fluid model assessment was done with Experiment III data for $j_L \leq 2$ m/s, which was the range of interest for the present study.

The CFD calculations were performed with CFX-11. Geometric modeling and meshing was done using the meshing software GAMBIT. Following the CFX guidelines a one-node, 2-

degree slice of the pipe was adopted as the solution domain as shown in Fig. 1. A hexahedral mesh with 30 uniform radial elements and 150 uniform axial elements was selected after performing a mesh sensitivity study. The mesh is shown in Fig. 1.

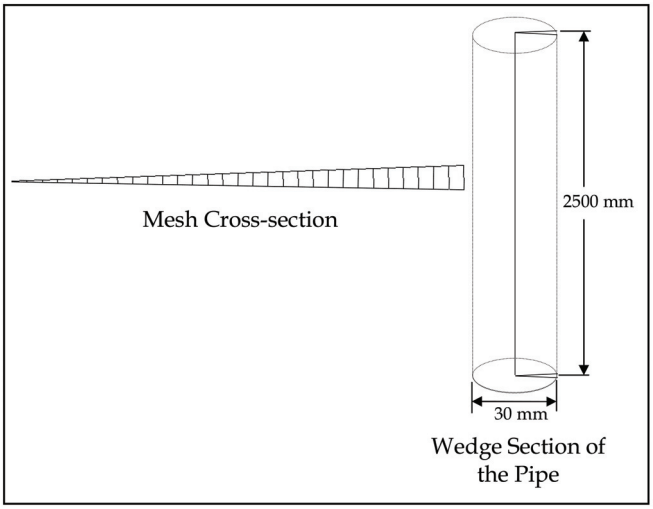


Fig. 1. The Computational Domain and Typical CFX Mesh

**Turbulent Diffusion Force Model Comparison**

The two turbulent diffusion force models described in the previous section were compared. The effect of the turbulent diffusion models is shown in Fig. 2. The two models available in CFX correspond to the models discussed in the section describing the turbulent diffusion force of the two-fluid model. The model of Lopez de Bertodano et. al. (2006) (i.e., Case 1) is similar to the *Favre Averaged Drag Model* of CFX and the *Lopez de Bertodano Model* of CFX is the model discussed in Case 2.

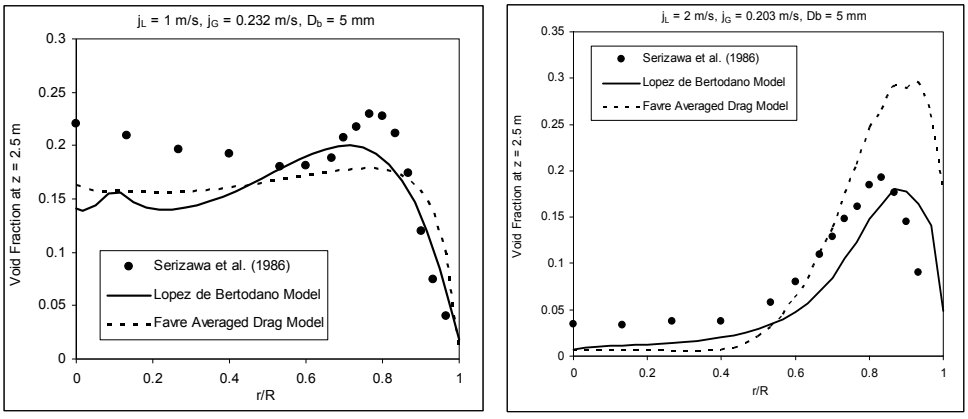


Fig. 2. Turbulent Diffusion Model Comparison for $j_L$ = 1 m/s and 2 m/s

The results with these two models did not differ much at $j_L$ = 1 m/s. A typical result at 1 m/s is shown in Fig. 2. However, Fig. 2 shows that at 2 m/s the *k* dependent model (i.e., Case 2) with $C_{TD}$ = 0.25 is a significant improvement over the Favre type model (i.e., Case 1). The previously discussed inadequacy of the Case 1 model to produce sufficient diffusion for shear induced turbulence is evident in the figure and therefore the *Lopez de Bertodano Model* of CFX was selected for all further simulations.

**Wall Force Model Comparison**

Calculations were performed for two sets of wall force parameters, viz. Antal et al. (1991) ($C_{w1}$ = -0.01, $C_{w2}$ = 0.05) and Krepper and Prasser (2000) ($C_{w1}$ = -0.0064, $C_{w2}$ = 0.016). The uncertainties in the wall force are very significant and these two sets of parameters are used as the two bounds. The bubble size used for the calculations is $D_b$ = 5 mm., which is bigger than the reported value of 3 mm. This is done so because the bubbles are oblate and the measurements correspond to the smaller diameter, whereas the distance from the wall is determined by the larger diameter.

Figures 3 to 5 show the prediction obtained using the two wall force models. A general trend noticed here is that the averaged experimental void fraction is higher than the computed results for all cases and the deviation is more for $j_L$ = 1.5 m/s and 2 m/s cases. This has a significant impact and it is the main reason why data is consistently higher than the calculated results in the center of the pipe. One explanation for this systematic discrepancy could be that the volumetric gas flow rates were measured at the inlet pressure instead of atmospheric pressure, and in such case correcting the computations for the effect of pressure would give better results. However, this has not been done here.

It can be seen from Figures 3-5 that the effect of the wall force coefficients is significant both in the prediction of the wall peak and in the void distribution in the far wall region. In general, the wall peak data is bounded by Antal et al.'s coefficients from below and Krepper and Prasser's coefficients from above.

Fig. 3 shows comparisons for $j_L$ = 1.0 m/s. At this lower liquid flux, the void distribution is primarily controlled by the lift and the wall forces. The higher void fraction case (Fig. 3) shows that there is a wall peak in the near wall region and relatively uniform void distribution in the far wall region which implies that the turbulent diffusion force has a

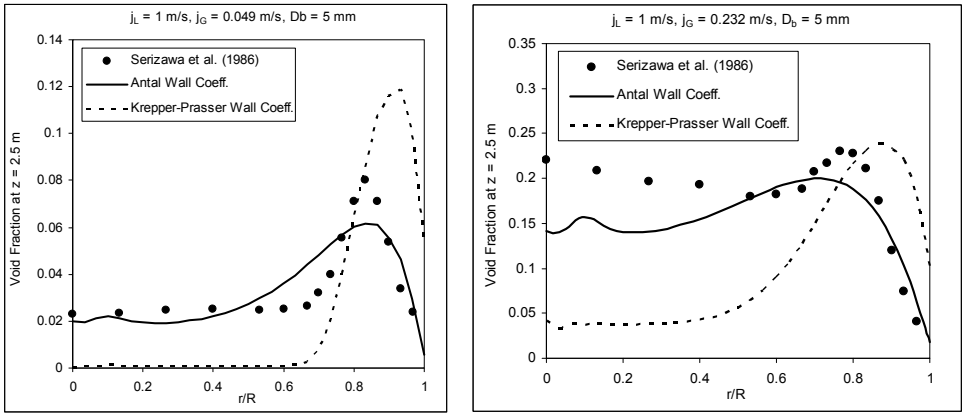


Fig. 3. Wall Force Model Comparison ($j_L$ = 1 m/s)

negligible effect. It is clear from the comparisons that Krepper and Prasser's coefficients underestimate the void fraction in the region away from wall.
For $j_L$ = 1.5 m/s, Krepper and Prasser's coefficients predict the wall peaks accurately (Fig. 4) but the void fraction in the far wall region is under predicted. For the $j_G$ = 0.083 m/s, the far wall region void fraction is well predicted with Antal et al's coefficients.

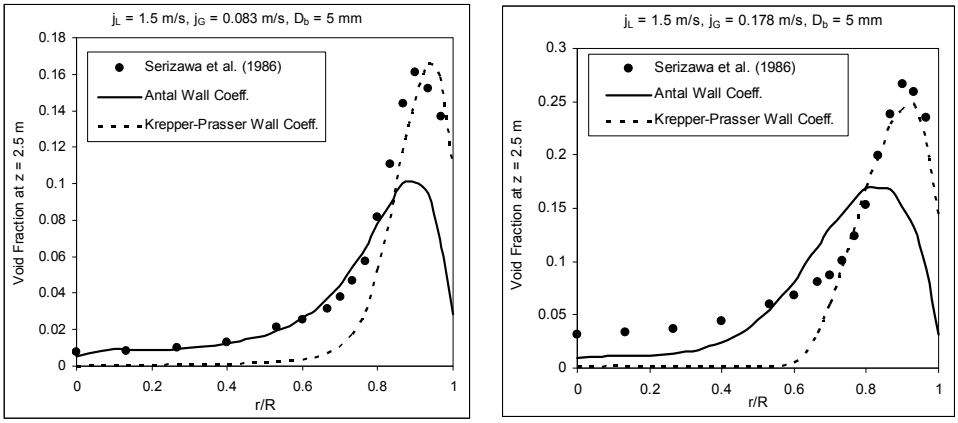


Fig. 4. Wall Force Model Comparison ($j_L$ = 1.5 m/s)

For $j_L$ = 2 m/s, the data shows that the void peak moves further away from the wall than that in $j_L$ = 1.5 m/s. This effect cannot be predicted by the present model without making some significant changes to the lift coefficient and it is an unresolved problem of two-phase flow CFD as of now. The void peak magnitude and bulk void fraction is better predicted by Antal et al.'s coefficients (Fig. 5).

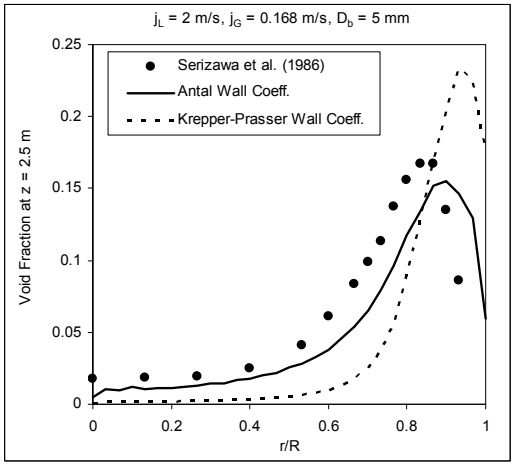


Fig. 5. Wall Force Model Comparison ($j_L$ = 2 m/s)

Thus, Antal et al.'s coefficients predict the wall peak magnitude and the trend of the void distribution in the far-wall region quite well. Furthermore, the far-wall results indicate that

the turbulent diffusion force model is satisfactory. As a result of this study, following models were selected for the further analysis using One-Group IATE.

1. Turbulence Diffusion Force: *Lopez de Bertodano Model* of CFX ($C_{TD}$ = 0.25)
2. Wall Force Model Coefficients: Antal et al's (1991) coefficients. ($c_{w1}$ = -0.01, $c_{w2}$ = 0.05)
3. Lift Force: $C_L$ = 0.1.

## 5. Two fluid model energy equation

**Energy conservation**

$$\frac{\partial}{\partial t}\alpha_k\,\rho_k\,e_k \;+\; \nabla\cdot\alpha_k\,\rho_k\,\underline{\bar{\upsilon}}_k\,e_k = \;-\nabla\cdot\left[\alpha_k\left(\underline{q''_k}+\underline{q''^{\,\mathrm{Re}}_k}\right)\right]$$

$$+\,p\left[\frac{\partial\alpha_k}{\partial t}+\nabla\cdot\left(\alpha_k\underline{\bar{\upsilon}}_k\right)\right]+\Delta m_k\,H_{ki}+q_{ki} \tag{16}$$

$$\underline{q''_k}=-\lambda_k\nabla T_k\,,\;\underline{q''^{\,\mathrm{Re}}_k}=-\frac{\rho_k\,\nu_{tk}}{\mathrm{Pr}_t}\nabla e_k \tag{17}$$

where, $\lambda_k$ is the thermal conductivity and $\nu_{tk}$ is the turbulent viscosity for phase $k$. $\mathrm{Pr}_t$ is the turbulent Prandtl number, $H_{ki}$ is the mean enthalpy of phase $k$ near interfaces, and $q_{ki}$ is the interfacial heat flux whose closure is described in detail later. In the present calculations of subcooled boiling, the vapor generated was assumed to be at saturated temperature and hence was treated as isothermal phase.

**Interfacial heat transfer**

The interface to liquid heat transfer ($k$=$l$) is expressed as,

$$q_{li}=h_{li}a_i\left(T_{sat}-T_l\right), \tag{18}$$

where, $h_{li}$ is the heat transfer coefficient between the liquid and the interface, closed as follows,

$$h_{li}=\frac{\lambda_l}{d_s}Nu\,, \tag{19}$$

In the above equation, $\lambda_l$ is the liquid thermal conductivity and $d_s$ is a length scale which is assumed equal to the bubble diameter. The Nusselt number ($Nu$) in the above closure equation is given by following expression (Ranz & Marshall, 1952):

$$Nu=2+0.6\,\mathrm{Re}_b^{0.5}\,\mathrm{Pr}_l^{0.33} \tag{20}$$

Reynolds number ($\mathrm{Re}_b$) used in the above closures is defined as,

$$\mathrm{Re}_b=\frac{D_b\left|\underline{\bar{\upsilon}}_R\right|}{\nu_l} \tag{21}$$

The interfacial mass transfer is given as,

$$\dot{m}_{cond,L} = \max\left(\frac{h_{li}\left(T_{sat} - T_l\right)a_i}{H_{\lg}}, 0\right), \quad \dot{m}_{evap,L} = \min\left(\frac{h_{li}\left(T_{sat} - T_l\right)a_i}{H_{\lg}}, 0\right) \tag{22}$$

where, $H_{lg}$ is the latent heat of phase change.

**Wall heat transfer**

Wall heat transfer is the most important aspect of boiling as it provides the sources for energy and phase mass balance equations. Most wall heat transfer models are based on partitioning the wall heat flux into three components. In particular, the multidimensional CFD model by Kurul and Podowski (1990) has been implemented in the CFX-12 beta version (Egorov & Menter, 2004) and some of the details of this implementation are reported in the next section.

The three components of the wall heat flux are:

a. Evaporation heat flux ($q_e$) – The part of heat flux utilized in formation of vapor at the wall,
b. Forced convection to the liquid ($q_c$),
c. Wall quenching by liquid phase (transient conduction) ($q_q$) – This accounts for the heat transfer to the subcooled liquid that replaces the detached bubble at the wall.

**The CFD Wall Boiling Model**

The wall surface is assumed to be split into two parts ($A_1$, $A_2$) each under the influence of one phase. Fraction $A_2$ is influenced by the vapour bubbles formed on the wall and participates in the evaporation and quenching heat transfer. Fraction $A_1$ is the remaining part of the wall surface, ($A_1$=1–$A_2$) and participates in the convective heat transfer to the liquid. $A_1$ and $A_2$ are related to the nucleation site density per unit wall area ($n_{site}$) and to the influence area of a single bubble forming at the wall nucleation site. The CFX-12 model assumes, that the diameter of the bubble influence zone is twice as big as the bubble departure diameter ($a$ = 2).

$$A_2 = \frac{\pi}{4}\left(a \cdot D_{dep}\right)^2 \cdot n_{site}, \; A_1 = 1 - A_2, \tag{23}$$

*Evaporation Heat Flux:*

The evaporation heat flux is obtained from the rate of vapor generation at the wall which is given as a product of mass of a bubble at detachment, the detachment (departure) frequency and the nucleation site density,

$$\dot{m}_e = \frac{\pi D_{dep}^3}{6}\rho_G f_{dep} n_{site}, \tag{24}$$

and,

$$q_e = \dot{m}_e h_{\lg}, \tag{25}$$

The specification of evaporation heat flux using above equation requires closure for bubble departure diameter, bubble departure frequency and the site density. The default model in CFX uses following closure relations:

The bubble departure diameter is given by the empirical correlation of Tolubinsky and Kostanchuk (1970), the Nucleation Site Density is obtained using the correlations of Lemmart and Chawla (1977) and the departure frequency is closed using the simplest available expression (Cole, 1960), which uses a characteristic bubble velocity (terminal velocity of bubble rise) and a characteristic bubble size (departure diameter).
The frequency of bubble departure obtained by Cole (1960) was derived under the assumption of bubble moving with terminal velocity once detached from the surface. This is a fair assumption for pool boiling scenario at low heat fluxes where bubble detachment is hydrodynamically governed, but may not be accurate for flow boiling at high heat fluxes where the thermodynamics governs the bubble growth and detachment. The closure relations are given below

$$D_{dep} = D_{ref} \exp\left(-\left(T_{sat} - T_{liq}\right)\Big/ T_{ref}\right),\ D_{ref} = 0.6\ mm,\ T_{ref} = 45\ K \tag{26}$$

$$n_{site} = n_{ref}\ \left((T_{wall} - T_{sat}) / \Delta T_{ref}\right)^{1.805},\ n_{ref} = 7.9384 \times 10^5\ m^{-2},\ \Delta T_{ref} = 10\ K \tag{27}$$

$$f_{dep} = \sqrt{\frac{4g\Delta\rho}{3D_{dep}\rho_{liq}}} \tag{28}$$

An alternative to the Lemmart and Chawla (1977) correlation for the nucleation site density is the correlation of Kocamustaffaogullari and Ishii (1983) validated against water data for 0-50 bar. The Kocamustaffaogullari-Ishii (K-I) correlation relates the site density to the wall superheat as follows:

$$n^*_{site} = R^{*-4.4}_c f\left(\rho^*\right), \tag{29}$$

where,

$$n^*_{site} = n_{site} D^2_{dep}, \tag{30}$$

$$R^*_c = R_C / (D_{dep} / 2) \tag{31}$$

$R_c$ is the critical radius of the surface cavity which represents a minimum cavity size which can be activated at a given wall superheat. $R_c$ is given as,

$$R_C = \frac{2\sigma\left(1 + \left(\rho_g / \rho_f\right)\right)\Big/ P}{\left(\exp\left(h_{fg}\Delta T_{sat,e} / \left(R T_g T_{sat}\right)\right) - 1\right)}. \tag{32}$$

Under the following conditions:

$$\rho_g << \rho_l, \quad h_{fg}(T_g - T_{sat}) / \left(R T_g T_{sat}\right) << 1, \tag{33}$$

$R_c$ can be simplified as,

$$R_C = 2\sigma T_{sat} / \left(\rho_g h_{fg} \Delta T_{sat,e}\right). \tag{34}$$

The density dependent parameter in equation (29) is given as,

$$f\left(\rho^*\right)=2.157\times10^{-7}\rho^{*-3.2}\left(1+0.0049\rho^*\right)^{4.13}$$
$$\rho^*=\left(\rho_l-\rho_g\right)\Big/\rho_g \quad . \tag{35}$$

The effective wall superheat in equation (32) is usually less than the actual wall superheat. The reason for this is as follows. A bubble nucleated at the wall grows through a liquid film adjacent to the wall where a considerably high temperature gradient exists. So, in reality, it experiences a lower mean superheat than the wall superheat. In case of pool boiling, the difference is not significant and the superheat based on the wall temperature can be taken as the effective superheat. In case of forced convective boiling, there exists a steeper temperature gradient in the near wall field due to thermal boundary layer. Hence, the effective superheat experienced by the bubble is smaller than the actual wall superheat and it is given as,

$$\Delta T_{sat,e}=S\Delta T_{sat} \text{ where, } \Delta T_{sat}=T_w-T_{sat}\,. \tag{36}$$

The multiplier $S$ in the above equation is the superheat suppression factor and is given as (Chen, 1966),

$$S=1\Big/\left(1+1.5\times10^{-5}\,\mathrm{Re}_{TP}\right) \tag{37}$$

The two-phase Reynolds number is given as,

$$\mathrm{Re}_{TP}=\left[G(1-x)d_h/\mu_l\right]F^{1.25} \tag{38}$$

$$\begin{aligned} F&=1.0 \ , for\ X_{tt}\geq10\\ &=2.35\left(0.213+1/X_{tt}\right)^{0.736}, for\ X_{tt}<10\end{aligned} \tag{39}$$

The Martinelli parameter can be approximated as,

$$X_{tt}=\left(\frac{1-x}{x}\right)^{0.9}\left(\frac{\rho_g}{\rho_l}\right)^{0.5}\left(\frac{\mu_f}{\mu_g}\right)^{0.1} \tag{40}$$

Thus, equations (29)-(40) represent the complete model of Kocamustafaogullari-Ishii (1983), which has been implemented in CFX-12 for the present study.

*Quenching Heat Flux:*

As mentioned previously, the quenching heat flux is the component of wall heat flux utilized to heat the cold liquid replacing the detached bubble adjacent to the heated wall. In order to evaluate this component, Mikic and Rohsenow (1969) used an analytical approach starting with transient conduction in semi-infinite medium with heated wall being the only boundary where temperature is specified.

$$\frac{\partial T(x,t)}{\partial t}=\alpha\frac{\partial^2T(x,t)}{\partial x^2};\ T(x,0)=T_\infty, T(0,t)=T_w, T(\infty,t)=T_\infty \tag{41}$$

The above equation has a solution of the form,

$$\frac{T_w - T}{T_w - T_\infty} = erf\left(\frac{x}{2\sqrt{\alpha t}}\right) \tag{42}$$

The heat flux at the wall boundary can be obtained as,

$$q''(0,t) = -\lambda_l \left.\frac{\partial T}{\partial x}\right|_{(0,t)} = \frac{\lambda_l (T_w - T_\infty)}{\sqrt{\pi \alpha t}} \tag{43}$$

The above heat flux is averaged over a "characteristic" time period which is approximated by the inverse of bubble departure frequency. This leads to the original closure for quenching heat flux [Mikic & Rohsenow, 1969].

$$\overline{q''} = f_{dep} \int_0^{1/f_{dep}} q''(0,t)\, dt = 2\lambda_l \sqrt{\frac{f_{dep}}{\pi \alpha}} (T_w - T_\infty) = h_q (T_w - T_\infty) \tag{44}$$

Kurul and Podowski (1990) made minor modification to the above expression with an assumption that quenching occurs between detachment of one bubble and appearance of next bubble (nucleation), and this time was assumed to be 80% of the detachment period. This is the final form of quenching heat transfer closure of the CFX-12 model.

$$h_q = 2\lambda_l f \sqrt{\frac{t_w}{\pi \alpha}};\ \ t_w = \frac{0.8}{f_{dep}} \tag{45}$$

$$q_q = A_2 h_q (T_w - T_\infty) \tag{46}$$

*Single Phase Convection Heat Flux:*

This is evaluated under the standard assumption of a logarithmic temperature profile across the turbulent boundary layer (Kader (1981), ANSYS CFX Solver Theory Guide (2006)).

$$q_{w,1ph} = \frac{\rho_l C_{p,l} u^*}{T^+} (T_w - T_{liq}) \tag{47}$$

$$\begin{gathered} T^+ = \mathrm{Pr}_l y^* e^{-\Gamma} + \left(2.12 \ln(y^*) + \beta\right) e^{-1/\Gamma};\ \beta = f(\mathrm{Pr}_l), \Gamma = f(y^*) \\ u^* = C_\mu^{1/4} k_l^{1/2}, y^* = \rho_l u^* \Delta y / \mu_l \end{gathered} \tag{48}$$

where, $\Delta y$ is the distance of the wall adjacent node from the wall, $k_l$ is the liquid turbulence kinetic energy. In the above equation $\beta$ is a function of liquid Prandtl number and $\Gamma$ is a function of $y^*$(ANSYS CFX Solver Theory Guide (2006)).
The convective heat flux component through the liquid area fraction is thus given as,

$$q_c = A_{1f} h_c (T_w - T_{liq}),\ h_c = \frac{\rho_l C_{p,l} u^*}{T^+} \tag{49}$$

It should be noted here that all the wall heat flux model correlations above use a liquid temperature ($T_{liq}$). The single phase heat transfer correlation above uses the wall adjacent node temperature. However, in the bubble departure diameter and the quenching heat transfer correlations which were based on one-dimensional models, the liquid temperature refers to the bulk mean temperature. As a good estimate, CFX approximates this temperature with the temperature at a fixed $y^*$ (250). This is done in order to have a mesh size independent evaluation of wall heat flux partitions.

## 6. Boiling CFD Model assessment with high pressure R12 data

**Experimental data and CFD model**

Morel et al. (2003) performed boiling experiments in a vertical pipe of 19.2 mm internal diameter and a length of 5 m. The pipe had a heated section of 3.5 m preceded by and followed by unheated lengths of 1 m and 0.5 m respectively. The input parameters for the four tests reported were as summarized in Table 1. The liquid-vapor density ratio in these experiments corresponds to that for water-steam at 95-150 bar.
Radial Profiles of Void Fraction, Liquid Temperature and Interfacial Area Concentration were measured. Dual sensor fiber optics probes were used to measure void fraction and interfacial area concentration. Miniature thermocouples were used to measure the fluid temperature.
The CFD calculations were performed with CFX-12. Geometric modeling and meshing was done using the meshing software GAMBIT. A 2° wedge of the pipe is used as the domain. The mesh had 20 radial and 250 axial uniformly spaced elements. Fig. 6 shows the domain and cross-section of the mesh used.

| Parameter | Test1 (Deb5) | Test2 (Deb6) | Test3 (Deb13) | Test4 (Deb10) |
|---|---|---|---|---|
| Mass Flux (kg/m$^2$) | 1986 | 1984.9 | 2980.9 | 2027.0 |
| Pressure (bar) | 26.15 | 26.15 | 26.17 | 14.59 |
| Inlet Subcooling ($^o$C) | 18.12 | 16.11 | 18.12 | 23.24 |
| Heat flux (W/m$^2$) | 73.89 | 73.89 | 109.42 | 76.24 |

Table 1. Simulation input parameters for R12 tests

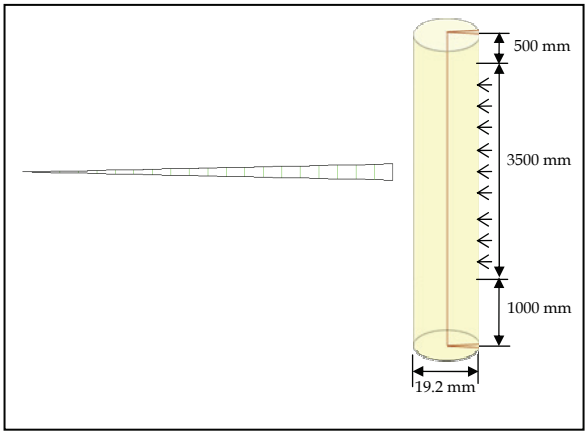


Fig. 6. Domain and Mesh for R12 boiling simulation case

**Comparisons**

All the data sets include radial profiles of bubble diameter. Note that with Freon at these test pressures, the surface tension is 0.0017 N/m for 26 bar which results in very small bubble sizes (i.e., 0.5 mm). Instead of using bubble size correlations for the CFD calculations the mean of the measured radial profile value is used for the bubble diameter in the bulk, whereas, the value measured at the wall is used as the departure bubble size (Fig. 7).

It was found during all the cases that a better match with experimental data is obtained with the coefficient of the turbulent diffusion force $C_{TD}$ = 0.5 instead of the value obtained for adiabatic air water flows, $C_{TD}$ = 0.25. This change may be attributed to bubble diameters in these cases which are one order of magnitude smaller than that in atmospheric air-water systems (Prabhudharwadkar et al., 2009). Therefore there are more interactions of the bubbles with smaller turbulent eddies. Two comparisons are presented below for this particular benchmark problem: the nucleation site density model comparison and the bubble size model comparison.

Fig. 8 shows the prediction of radial variation of void fraction obtained using two different site density models. The Lemmart-Chawla (1977) model which is used in CFX was found to under-estimate the void fraction in all the cases. Kocamustafaogullari-Ishii model (termed as

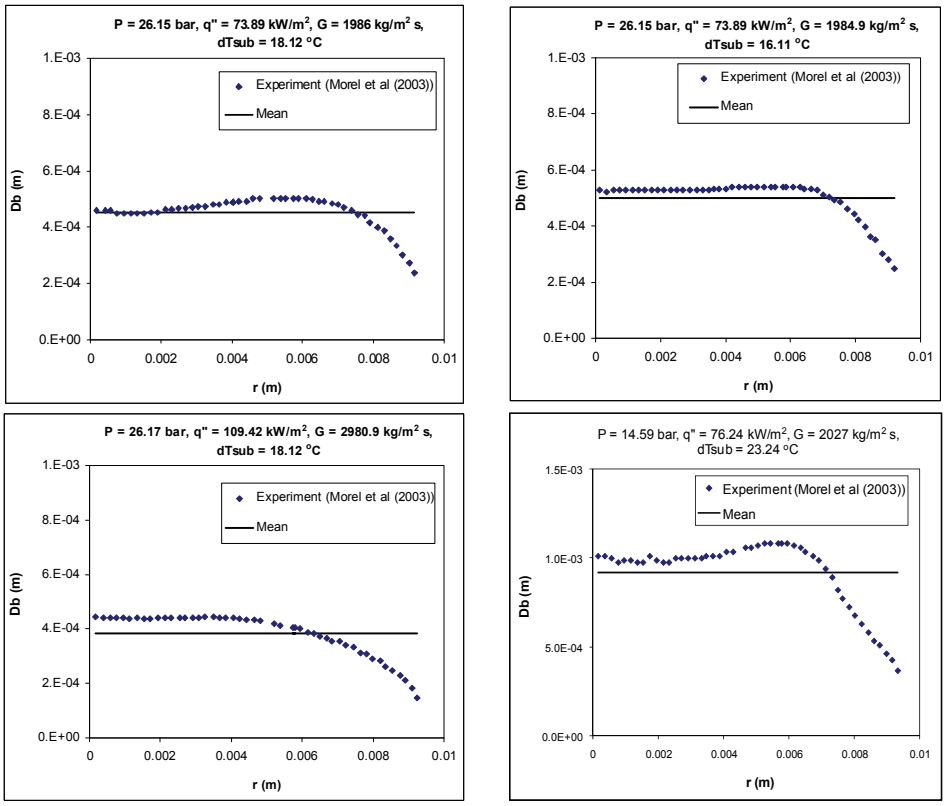


Fig. 7. Bubble diameter approximation for the simulations

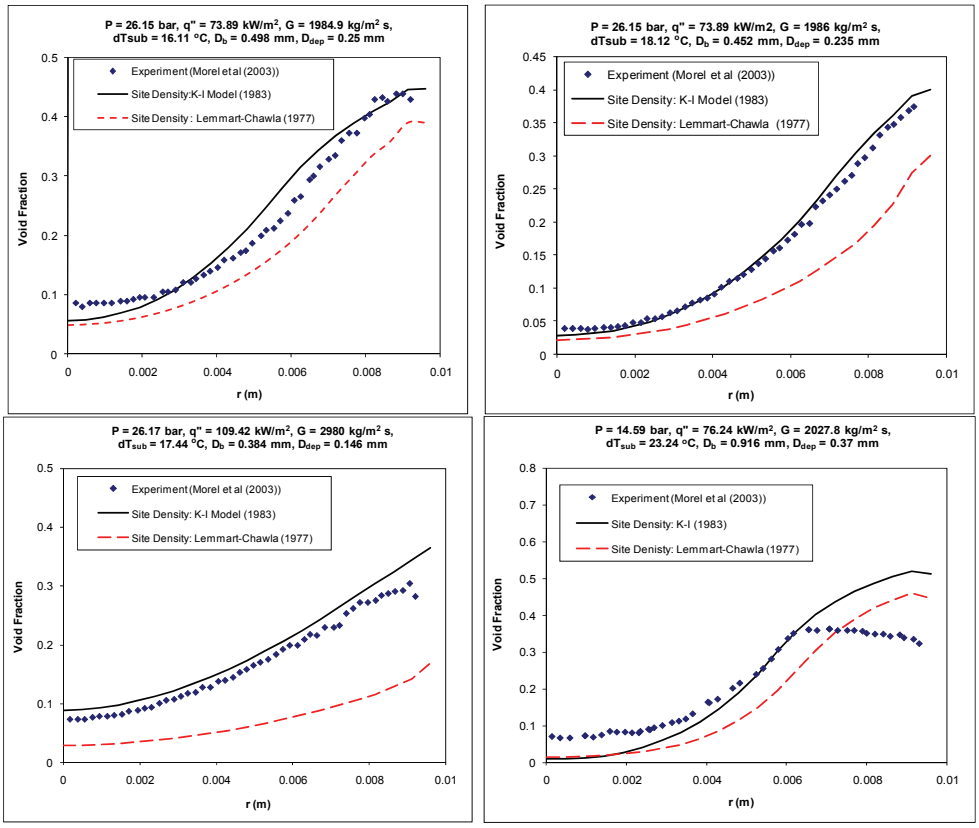


Fig. 8. Void Fraction prediction using the two Nucleation Site Density models

K-I Model in the figures below) predicted the data well in all the cases. The prediction however deteriorated at low pressure data (P = 14.59 bar) and this needs further investigation.
Fig. 9 shows the prediction of radial profiles of interfacial area concentration (IAC). The IAC is obtained using the expression for the Sauter mean diameter:

$$a_i = 6\alpha / D_b \tag{50}$$

As the bubble diameter is assumed to be uniform, the deviation of the CFD values from the experimental data near the wall, where the bubble diameter is smaller, is justified.
Fig. 10 shows prediction of liquid temperature for the first two cases (for which data is available). The simulation results show a good match with the experimental data in the bulk. However, towards the wall, the results with Lemmart-Chawla correlation showed steeper rise in temperature which caused over-prediction in this region.
Fig. 11 shows the bubble diameter prediction using the CFX default bubble departure diameter model with the Kurul and Podowski (1990) correlation for the bubble size in the bulk of the flow. The bubble departure diameter and the bulk diameter predicted by the models are approximately three times higher than the actual value, leading to a very high rate of vapor generation. This results in over-prediction of void fraction as shown in Fig. 11.

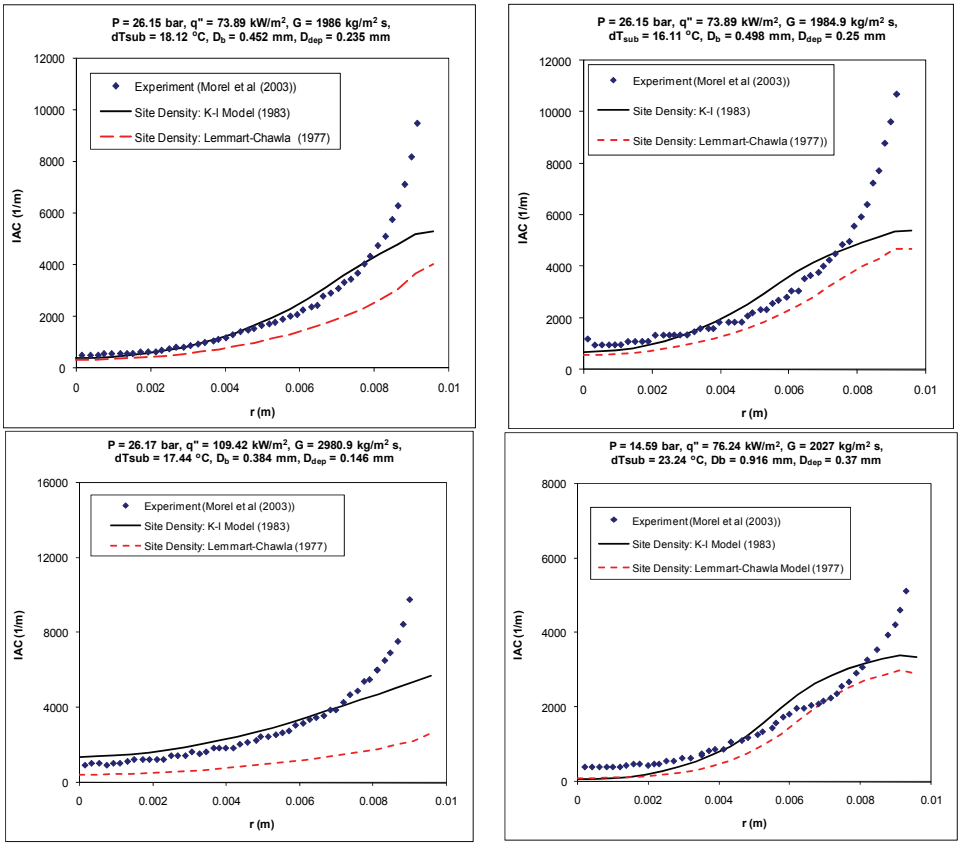


Fig. 9. Interfacial Area Concentration prediction using the two Nucleation Site Density models

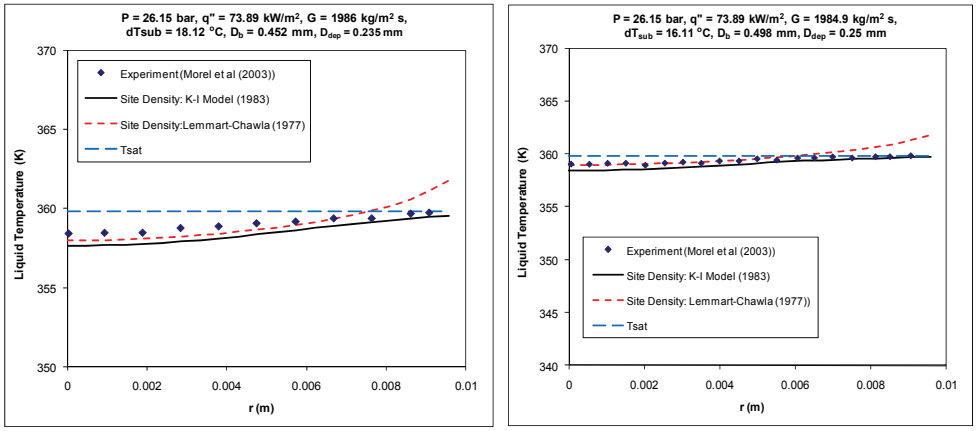


Fig. 10. Liquid Temperature prediction using the two Nucleation Site Density models

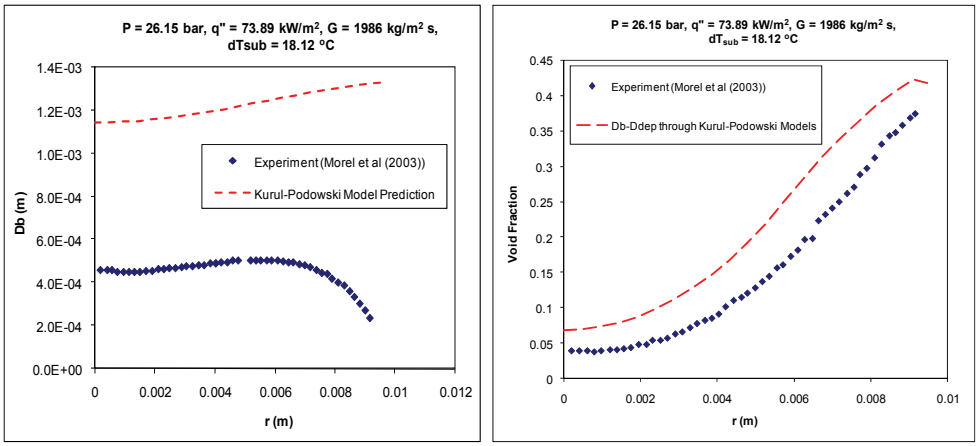


Fig. 11. Bubble diameter prediction using Kurul-Podowski model and void fraction prediction.

## 7. Subcooled boiling CFD model assessment with atmospheric water data

### Experimental data and CFD model

Lee et al. (2002) performed subcooled boiling experiments in a vertical annulus having a 19 mm diameter heating rod placed inside a tube with internal diameter of 37.5 mm. The total length of the test section was 2.37 m. The central heated length of 1.67 m was preceded and followed by unheated portions of 0.188 m and 0.518 m respectively as shown in Fig. 12.

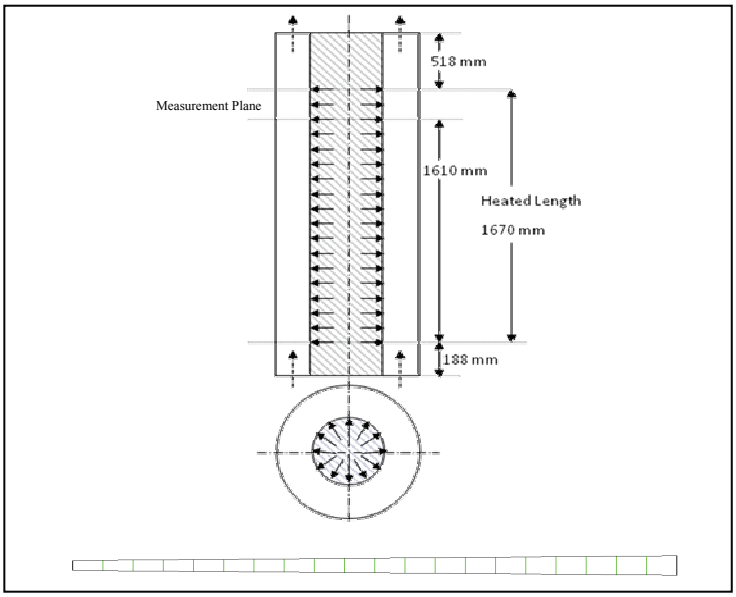


Fig. 12. Domain and Mesh for water boiling simulation case

Yeoh and Tu (2005) have reported two cases for this experiment where the bubble diameter measurements have been done. These two cases were selected for the analysis here. The input parameters for the two tests reported are summarized in Table 2 below.

| Parameter | Test1 | Test2 |
|---|---|---|
| Mass Flux (kg/m$^2$) | 474 | 1059.2 |
| Pressure (bar) | 1.42 | 1.43 |
| Inlet Subcooling ($^o$C) | 13.11 | 17.82 |
| Heat flux (kW/m$^2$) | 152.9 | 251.5 |

Table 2. Simulation input parameters for water boiling tests

Radial profiles of void fraction, vapor velocity and liquid velocity were measured at 1.61 m downstream of the start of the heated section. Two-point conductivity probe was used to measure void fraction and bubble velocity. Pitot tube was used for liquid velocity measurements with a correction factor for two phase flow.

The CFD calculations were performed with CFX-12. Geometric modeling and meshing was done using the meshing software GAMBIT. A 2° wedge of the annulus is used as the domain. The mesh had 20 radial and 142 axial uniformly spaced elements. Fig. 12 shows the domain and cross-section of the mesh used.

The bubble diameter measurements for the two cases are shown below in Fig. 13. It must be noted here that although a variation in the bubble size has been measured along the radial direction, however, the bubble layer is one bubble thick and the bubble size is of the order of 4-5 mm which occupies almost half of the annulus gap. This means the departure size can be assumed the same as the bubble size, which is equal to the maximum size of bubble measured across the cross-section. Hence, a bubble size (bulk and departure) of 4.7 mm is used in the low heat flux case and that of 4.1 mm is used in high heat flux case.

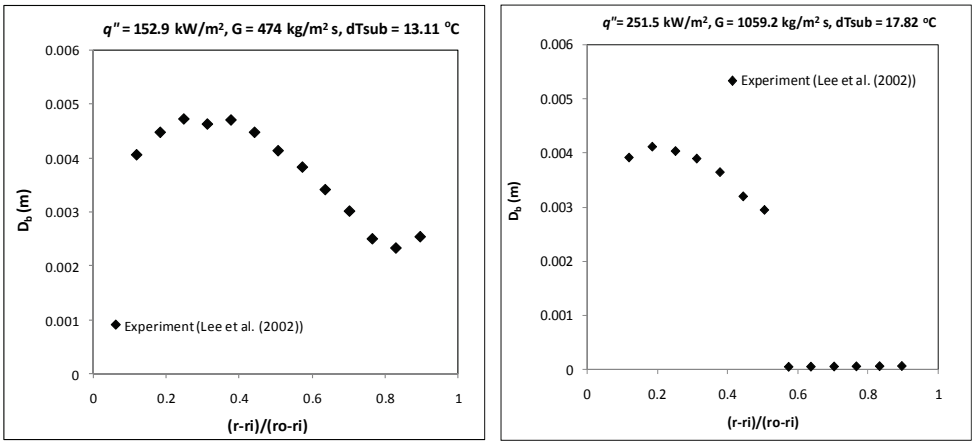


Fig. 13. Bubble Diameter data for the water boiling tests

The site density model comparison was done for these two cases also and the void fraction comparison is shown below in Fig. 14. It can be seen that the Lemmart-Chawla correlation over-predicted the void fraction at the wall by a significant margin. Although results using

K-I model did not accurately match the void fraction distribution, the wall void fraction was consistently better predicted.

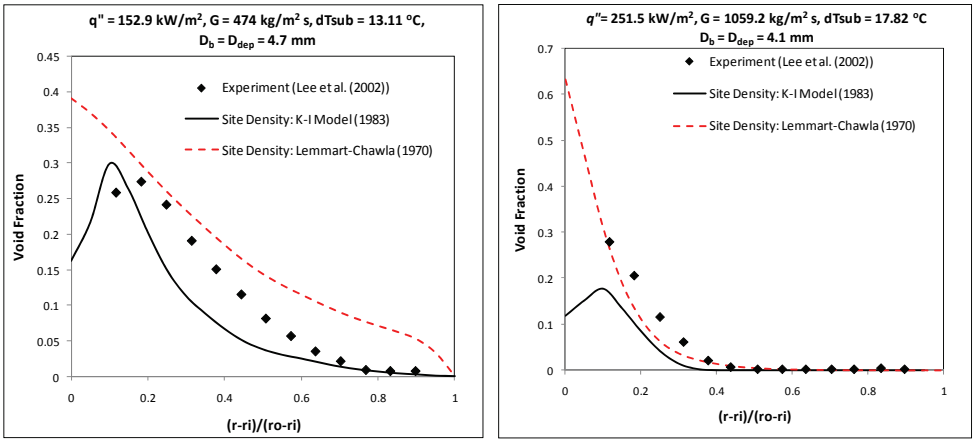


Fig. 14. Void Fraction prediction using different site density models (Water Data)

It is to be noted here that the K-I model did a better job even at the high pressure data and hence appears to be better than the Lemmart-Chawla model.

**Modifications of the Two-Fluid model**

As stated earlier, in this problem, the bubble size is comparable to the annulus gap width and hence further modifications were made to the two-fluid model to improve the results:

1. Addition of a wall drag force: The bubble moves touching the wall and hence experiences the shear due to the liquid velocity gradient near the wall. In such cases the bubble is further slowed by an additional wall drag which is essentially an additional shear stress on the bubble which is moving in the liquid shear layer. A model for this wall drag force has been derived by Lahey et al. (1993) and is given as follows:

$$\underline{M}_2^{WD} = -\underline{M}_1^{WD} = -C_{DW}\frac{\rho_l}{100D_b}\alpha\left|\bar{\underline{v}}_l\right|\bar{\underline{v}}_g \tag{51}$$

   The value suggested for $C_{DW}$ is 1.

2. Exclusion of Turbulent Dispersion: The turbulent dispersion force accounts for transverse dispersion of bubbles due to interaction with turbulent eddies. However, in the present case where there exists only one bubble across the cross-section, such a diffusion model is invalid and hence this force is turned off.

Fig. 15 shows the void fraction prediction for the two cases where the wall drag is included. It can be noticed that the wall drag effect is more in the high mass flux case. This is due to the fact that wall drag is comparable to the interfacial drag in this case.

Fig. 16 shows the void fraction predictions after turning off turbulent dispersion ($\underline{M}^{TD}$) force. The peak void fraction increased substantially in both cases but it also resulted in slight narrowing of the vapor boundary layer near the boiling wall. Overall, the two modifications to the two-fluid model improved the results. However, these computations based on a model where the void distribution is the result of the balance between the lift and wall

forces are not correct in a strict sense because the thickness of the bubble layer is determined instead by the diameter of one bubble. This fundamental problem has been addressed by Moraga et al. (2006).

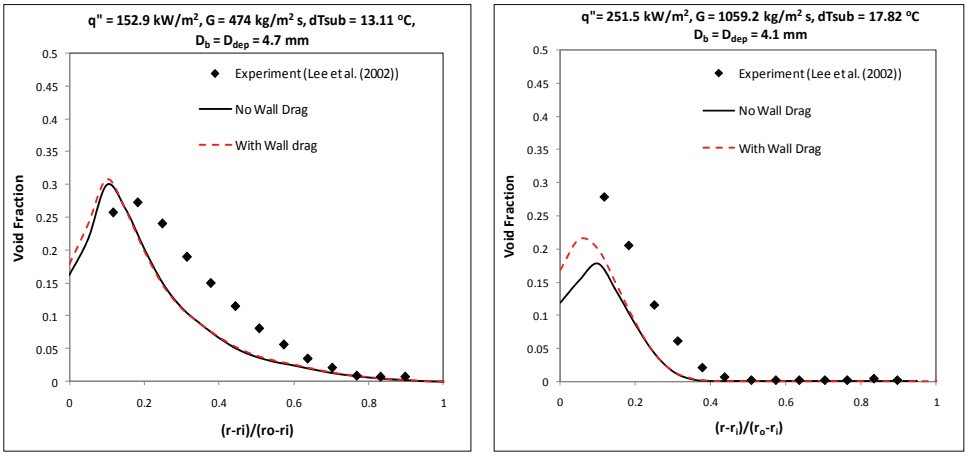


Fig. 15. Void Fraction predictions after including the wall drag term

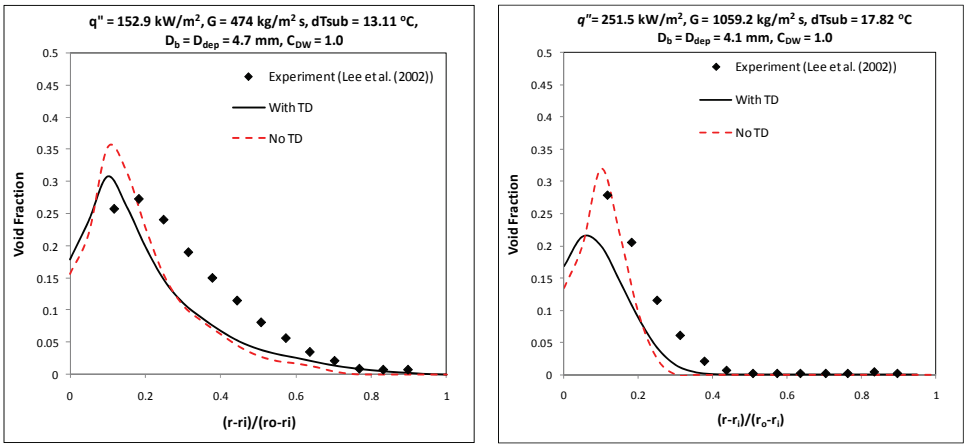


Fig. 16. Void Fraction predictions after excluding turbulent dispersion

Fig. 17 shows the vapor velocity comparison with two simulations, viz., the original two-fluid model and with wall drag and no turbulent dispersion. The low flux case showed no significant difference in the three cases. A deviation near the outer wall in the no TD case can be neglected since this region has no vapor. The vapor velocity did not change much even in the high flux case but showed a slight reduction when wall drag was added.

With this benchmark the two-fluid model with the wall-boiling module was validated over a wide range of pressures (~1-150 water-steam equivalent bar). It is worth noting again that the low pressure case presented above has a large bubble size (i.e., half the annulus size) which makes the two-fluid model constitutive relations invalid in a strict sense. Despite this shortcoming, the results are acceptable.

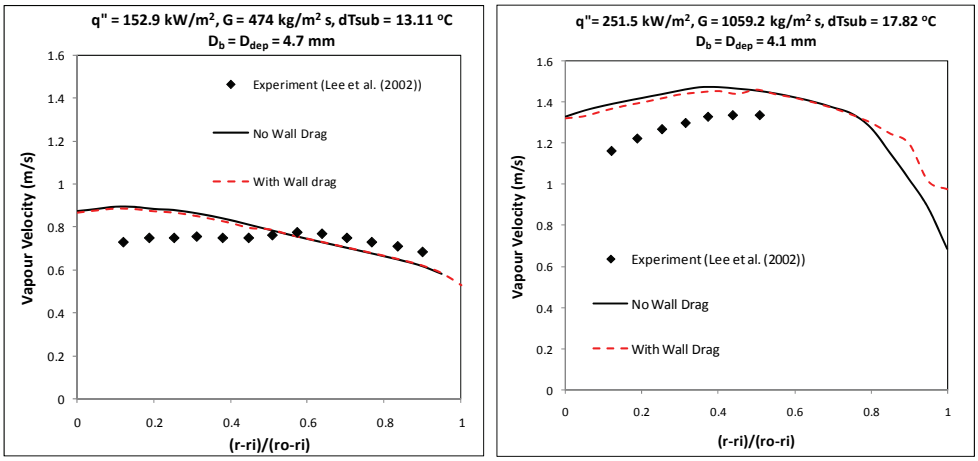


Fig. 17. Vapor velocity predictions without and with two-fluid model modifications

## 8. Conclusions

Several CFD Two Fluid Model constitutive relations were assessed with experimental data over a wide range of conditions for adiabatic and boiling flows to provide a guideline to choose the constitutive models.

For the air-water adiabatic flow data Auton's (1987) formulation of the lift force was found appropriate for the prediction of the void fraction profiles. The turbulent diffusion force given by the Lopez de Bertodano et al. (1994a) produced satisfactory results, especially at higher liquid fluxes. Two sets of coefficients for Antal et. al.'s (1991) wall force were compared and it was found that Antal et al.'s coefficients produced more consistent predictions and with the combination of selected lift and turbulent diffusion models, it produced overall better predictions throughout the pipe cross-section. The interfacial momentum models selected using adiabatic data were then used for the boiling flow comparisons with satisfactory results.

For the high pressure R12 boiling flow data the nucleation site density model by Kocamustaffaogullari and Ishii (1983) and the bubble departure frequency model of Cole (1960) were found to predict the data well. For the atmospheric pressure subcooled boiling water data set, where the bubble size is about half the flow channel width and where the thickness of the bubble layer is one bubble diameter, use of a wall drag force and elimination of the turbulent diffusion force improved the predictions.

The present model does not include constitutive relations for the bubble size at the wall nor in the bulk. These remain as open problems to be resolved in the future.

## 9. References

Antal, S.; Lahey, R. & Flaherty, J. (1991). Analysis of phase distribution in fully-developed laminar bubbly two phase flow. *International Journal of Multiphase Flow*, Vol. 17, No. 5, pp 635-652, ISSN 0022-1120.

ANSYS CFX Solver Theory Guide (2006). ANSYS CFX Release 11.0.

Auton, T. R. (1987). The Lift Force on a Spherical Body in a Rotational Flow. *Journal of Fluid Mechanics*, Vol. 183, pp. 199–213, ISSN 1469-7645.

Chen, J.C. (1966). Correlation for boiling heat transfer to saturated fluids in convective flow. *Industrial and Engineering Chemistry Process Design and Development*, Vol. 5, No. 3, pp. 322–329. ISSN 0196-4305.

Cole, R. (1960). A Photographic Study of Pool Boiling In the Region of the Critical Heat Flux. *AIChE Journal*, Vol. 6, No. 4, pp. 533- 534, ISSN 0001-1541.

Colin, C.; Legendre, D.; Yoshikawa, H. & Montout, M. (2009). Hydrodynamics of bubble detachment in convective boiling, *Proceedings of the 7th ECI International Conference on Boiling Heat Transfer (BOILING 2009)*, Florianopolis-SC-Brazil.

Egorov, Y. & Menter, F. (2004). Experimental Implementation of the RPI Wall Boiling Model in CFX-11. Ansys Cfx, Staudenfeldweg 12, 83624 Otterfing, Germany.

Ishii, M. & Hibiki, T. (2006). *Thermo-fluid Dynamics of Two-phase Flow*, Springer, ISBN 0-387-28321-8, United States.

Ishii, M. & Zuber N. (1979). Drag coefficient and relative velocity in bubbly, droplet or particulate flows. *AIChE Journal*, Vol. 25, No.5, pp. 843-855, ISSN 0001-1541.

Kader, B.A. (1981). Temperature and concentration profiles in fully turbulent boundary layers. *International Journal of Heat and Mass Transfer*, Vol. 24, No. 9, pp. 1541-1544.

Kocamustafaogullari G. & Ishii M. (1983). Interfacial area and Nucleation Site Density in boiling systems. *International Journal of Heat and Mass Transfer*, Vol. 26, No. 9, pp. 1377-1397, ISSN 0017-9310.

Krepper, E. & Prasser, H-M. (2000). Measurements and CFD Simulations of bubbly flow in a vertical pipe, *AMIFESF Workshop*, Computing Methods in Two-Phase Flow, pp. 1-8.

Kurul, N. & Podowski, M. Z. (1990). Multidimensional effects in forced convection subcooled boiling, *Proceedings of the Ninth International Heat Transfer Conference*, pp. 21-26, Jerusalem, Israel, Hemisphere Publishing Company.

Lahey, R.T. Jr.; Bertodano M. & Jones O.C., Jr. (1993). Phase distribution in complex geometry conduits. *Nuclear Engineering and Design*, Vol. 141, No. 2, pp. 177-201, ISSN 0029-5493.

Lee T.H.; Park G.C. & Lee D.J. (2002). Local flow characteristics of subcooled boiling flow of water in a vertical concentric annulus. *International Journal of Multiphase Flow*, Vol. 28, No. 8, pp. 1351-1368, ISSN 0301-9322.

Lemmert, M. & Chawla, J.M. (1977). Influence of flow velocity on surface boiling heat transfer coefficient, In: Hahne, E., Grigull, U. (Eds.), *Heat Transfer in Boiling*, pp. 237–247, Hemisphere Publishing Corporation, ISBN 0-12-314450-7.

Lopez de Bertodano, M.A., *Turbulent bubbly two-phase flow in a triangular duct*, PhD Thesis, Rensselaer Polytechnic Institute, Troy, NY, U.S.A, 1992.

Lopez de Bertodano, M. A.; R. T. Lahey, Jr. & O. C. Jones (1994a). Phase distribution in bubbly two-phase flow in vertical ducts. *International Journal of Multiphase Flow*, Vol. 20, No. 5, pp. 805-818, ISSN 0301-9322.

Lopez de Bertodano, M. A.; R. T. Lahey, Jr. & O. C. Jones (1994b). Development of a k-epsilon model for bubbly two-phase flow. *Journal of Fluids Engineering*, Vol. 116, No. 1, pp. 128-134, ISSN 0098-2202.

Lopez de Bertodano, M. (1998). Two fluid model for two-phase turbulent jets. *Nuclear Engineering and Design*, Vol. 179, No. 1, pp. 65-74, ISSN 0029-5493.

Lopez de Bertodano, M.; Ishii, M.; Sun, X. & Ulke, A. (2006). Phase distribution in the cap bubble regime in a duct. *Journal of Fluids Engineering*, Vol. 128, No. 4, pp. 811-818.

Mikic B.B. & Rohsenow W.M. (1969). A new correlation of pool-boiling data including the fact of heating surface characteristics. *ASME Journal of Heat Transfer*, Vol. 91, pp. 245–250, ISSN 0022-1481.

Moraga, F.J.; A.E. Larreteguy; D.A. Drew & R.T. Lahey Jr. (2006). A center-averaged two-fluid model for wall-bounded bubbly flows. *Computers & Fluids*, Vol. 35, No. 4, pp. 429–461, ISSN 0045-7930.

Morel C.; Yao W. & Bestion D. (2003). Three dimensional modeling of boiling flow for the NEPTUNE code. *Proceedings of the 10th International Topical Meeting on Nuclear Reactor Thermal Hydraulics*, Seoul, Korea.

Mostafa, A.A. & Mongia, H.C. (1988). On the interactions of particles and turbulent fluid flow. *Int. J. Heat Mass Transfer*, Vol. 31, No. 10, pp. 2063-2075, ISSN 0017-9310.

Prabhudharwadkar D.M.; Bailey C.A.; Lopez de Bertodano M.A. & Buchanan Jr, J.R. (2009). Two-Fluid CFD model of adiabatic air-water upward bubbly flow through a vertical pipe with a One-Group Interfacial Area Transport Equation, *Proceedings of the ASME 2009 Fluids Engineering Division Summer Meeting*, Vail, Colorado, USA.

Ranz, W.E. & Marshall, W.R. (1952). Evaporation from drops. *Chemical Engineering Progress*, Vol. 48, No. 3, pp. 141-146, ISSN 0360-7275.

Reeks, M. W. (1991). On a kinetic equation for the transport of particles in turbulent flows. *Phys. Fluids A*, Vol. 3, No. 3, pp. 446-456, ISSN 1070-6631.

Sato, Y.; Sadatomi, M. & Sekoguchi, K. (1981). Momentum and heat Transfer in Two-phase Bubble Flow-II. *International Journal of Multiphase Flow,* Vol. 7, No. 2, pp. 179-190, ISSN 0301-9322.

Serizawa, A.; Kataoka, I. & Michiyoshi, I. (1986). Phase Distribution in Bubbly Flow, Data Set No. 24, *Proceedings of the Second International Workshop on Two-Phase FlowFundamentals,* Troy, NY, USA.

Tolubinsky, V.I. & Kostanchuk, D.M. (1970). Vapor bubbles growth rate and heat transfer intensity at subcooled water boiling, *Proceedings of the 4th International Heat Transfer Conference*, Vol. 5, Paris, France. (Paper No. B-2.8).

Tomiyama, A.; Tamai, H.; Zun, I. & Hosokawa, S. (2002). Transverse migration of single bubbles in simple shear flows. *Chemical Engineering Science*, Vol. 57, No.11, pp. 1849-1858, ISSN 0009-2509.

Yeoh, G.H. & Tu, J.Y. (2005). A unified model considering force balances for departing vapour bubbles and population balance in subcooled boiling flow. *Nuclear Engineering and Design*, Vol. 235, No. 10, pp. 1251-1265, ISSN 0029-5493.

# 3

# Contaminant Dispersion Within and Around Poultry Houses Using Computational Fluid Dynamics[1]

Sourabh R. Pawar, John M. Cimbala, Eileen F. Wheeler and Darla V. Lindberg
*The Pennsylvania State University, USA*

## 1. Introduction

The United States poultry industry is the world's largest producer and exporter of poultry meat. U.S. consumption of poultry meat (broilers, other chicken, and turkey) is considerably higher than either beef or pork, but less than total red meat consumption. The U.S. is also a major egg producer; egg consumption has been reported to be around six eggs per person per week in the country [1]. Poultry producers worldwide depend on sustaining good flock health to remain competitive in both national and international trade. Thousands of chickens are often housed inside a single poultry house, and if one chicken is affected by an airborne virus, then the remaining chickens inside the poultry house have a high chance of getting the disease. This leads to rapid spread of disease within and outside the poultry house and it represents huge economic loss for the producers and companies involved. Therefore, monitoring and control of airborne particles are important issues. The most common diseases are the ones caused by the avian respiratory viruses, including avian influenza, Newcastle disease, Paramyxovirus type 2 and Paramyxovirus type 3, infectious bronchitis, and infectious laryngotrachitis [2] [3] [4]. These respiratory viruses have been documented to cause major disease outbreaks in poultry. Awareness of potential disease transmission from farms and expectations for proactive responsibility for managing those emissions is under scrutiny by neighbors, regulators, retailers, and environmental interest groups. Measuring and quantifying virus particles is very important from the point of view of control and prevention of epidemic outbreaks. This in turn depends upon understanding the impact of mechanical and biological environments.

Ventilation schemes in poultry houses are used to provide cooling during warm weather and to improve air quality during cold weather. Ventilation thus affects the particle distribution within and emissions from poultry houses. Ventilation air movement can be

---

[1] This chapter was written by invitation as an extension to a journal article written by the authors:
Pawar, S. R., Cimbala, J. M. Wheeler, E. F., and Lindberg, D. V. Analysis of Poultry House Ventilation using Computational Fluid Dynamics. *Transactions of the ASABE*, Vol. 50, Number 4, pp. 1373-1382, September 2007.
Funding from the Penn State Indoor Environment Center is acknowledged.

natural (due to difference in temperature or wind) or forced (due to fans). Natural or forced flow of air through properly sized and managed ventilation openings should continuously replace contaminated air with fresh outside air [5]. Almost all commercial-scale poultry houses use forced ventilation during cold and mild weather, with the majority using fans year-round. This air exchange helps to control relative humidity, reduce dust particles carrying disease pathogens, interrupt the aerobiological transmission pathways, and decrease or dilute the concentration of ammonia and other air pollutants, as well as carbon dioxide. Maintaining a clean and dry environment is essential to reducing molds and associated toxins that contribute to respiratory or digestive problems, which are threats to animal and human health.

Poultry birds are warm-blooded and therefore give off heat. The thermal plume produced by a typical laying hen is visualized with the Schlieren imaging technique in Figure 1. Air currents caused by thermal buoyancy can either enhance or inhibit the forced flow ventilation system, depending on inlet and outlet area and location, height difference between the inlet and outlet, and difference between inside and outside air temperatures [6]. For example, natural air currents may disrupt forced-ventilation air currents at times of relatively low air exchange such as during cold and mild weather. On the other hand, utilizing the "stack effect" (hot air rises) through thermal buoyancy for natural ventilation can provide the primary air exchange needed during some seasons of the year [7] [8]. Thermal buoyancy happens naturally, and the effect of thermal buoyancy can be used to increase the effectiveness of the ventilation system. This is one of the issues considered in this article while proposing a new ventilation system.

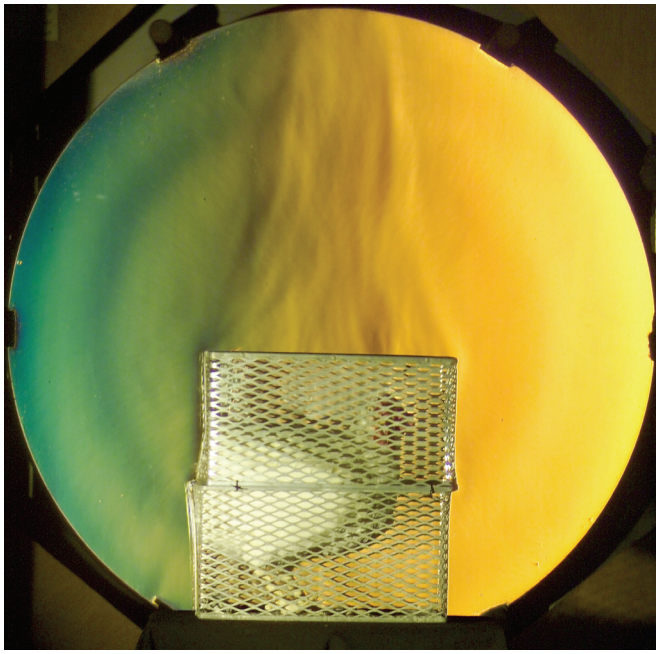

Fig. 1. Schlieren image of a hen in a cage showing the rising thermal plume. *Courtesy: Penn State Gas Dynamics Lab*.

Poultry farms fall into two general categories based on the product produced: egg or meat facilities. Meat birds (broilers, turkeys, etc.) are raised on the floor with litter as a manure management material. Most egg-laying hens are housed in stacked cages with the manure dropping through the cage floor. There are two common egg-laying hen house designs, each based on the strategy to manage the manure as a nutrient-rich byproduct. About two-thirds of the hen houses in the USA are "high-rise," two-story facilities where the hens are housed upstairs in cages staggered over each other so that manure drops down to the lower story. Accumulated manure is removed once or twice a year as needed for crops. Fresh air is introduced to the facility upstairs to benefit the hens and exhausted downstairs after being used to dry the manure. Most newly constructed hen houses are "manure-belt" houses where a conveyor belt under each cage collects manure for daily or bi-weekly removal from the hen house to a separate storage. With cages stacked directly over each other and both upstairs and downstairs occupied with hens, there can be 50-100% more hens in a manure-belt house than in the same size high-rise facility. With the adoption of manure-belt cage configuration, the hot weather ventilation usually employs a "wind-tunnel" strategy. Cold and mild weather ventilation is the same in both high-rise and manure-belt houses, albeit with increased ventilation rate in the latter due to the increased number of birds. The present analysis evaluates airflow conditions in relation to the potential for disease spread in a manure-belt house similar to that shown in Figure 2.

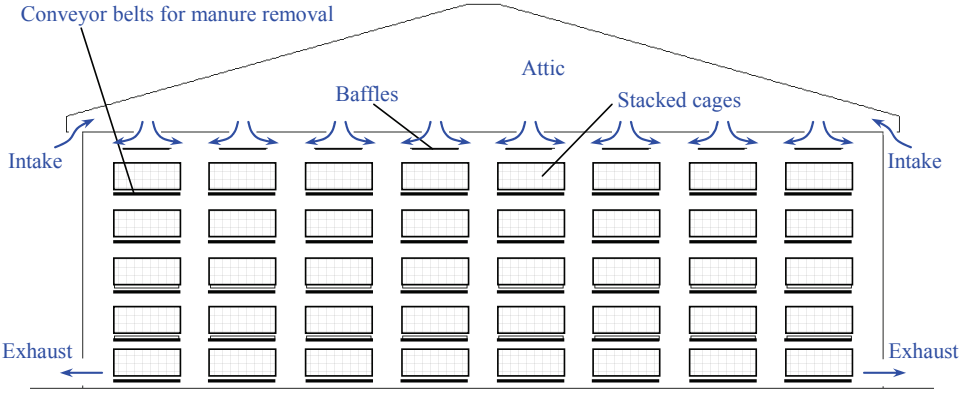


Fig. 2. Cross-sectional slice through a manure-belt equipped hen house with a traditional, downward flow ventilation scheme.

In the event of epidemic outbreak at poultry production facilities, air quality control and decreased contamination spread downwind is of fundamental importance. In this article computational fluid dynamics (CFD) is used to monitor the flow of particles and test the effectiveness of ventilation systems. CFD can be defined as the process of determining a numerical solution to the governing equations of fluid flow while advancing the solution through space and/or time in a computationally modeled domain in order to obtain a numerical description of the flow field of interest. The governing equations can be solved either by writing in-house codes or by using commercial software codes that are designed to give optimum performance and a convenient user interface. In the present research, the commercially available CFD computer software package FLUENT [9] (now part of ANSYS) was used. FLUENT is a three-dimensional finite-volume CFD code, capable of using

structured, unstructured, and hybrid grids. It can handle both laminar and Reynolds-averaged turbulent flows, steady and unsteady flows, compressible and incompressible flows, and the transport of contaminant species and particles. To create the geometry and to mesh the computational domain, software accompanying FLUENT called GAMBIT [10] was used. In this work various ventilation scenarios in egg-laying hen houses, in various wind conditions, with both particulate and gaseous contaminants introduced at various locations in the house were studied (a gaseous contaminant introduced at one location is presented here). In particular, a modified ventilation scheme that may reduce the spread of airborne contaminants within the hen house and also to adjacent hen houses was proposed and tested.

Prior to this work, a CFD study of agricultural ventilation characteristics has been reported for greenhouse [11] temperature distributions using FLUENT and of air velocity and ammonia distribution in swine barns [12] and internal climate of broiler houses [13]. Virtual chickens have been included in simulations of internal climate [14].

## 2. Geometry and modeling

The typical hen house in the U.S. is 50-ft wide and 500-ft long, with 16-ft high walls. It has a shallow 4/12 slope on the roof. The hens are housed inside cages which are typically 1.5 ft in depth and 1.2 ft in height. A single, two-story manure-belt hen house may accommodate 150,000 or more birds. There are usually 6 to 8 tiers of cages, stacked on top of each other. The tiers run the entire length of the 500-ft barn. In a poultry facility there are 2 to 8 hen houses arranged side-by-side in a row. There is at least 50 ft of air space between two adjacent houses. This space is required to allow fire truck access and to reduce fire spread. The building separation is also an attempt to have fresh air supply for each house. The reason the separation distance is minimized is to reduce cost of the egg conveying system that connects all houses to the egg handling facility at each farm.

### 2.1 Cage, conveyer belt and tier assembly

The cages that house the hens are of the wire mesh type as shown in Figure 3. The feeding system and the egg conveyor system are attached to the front of the cages. A wide conveyor belt runs under each row of cages to collect manure, which is transported to a separate storage building. In the CFD simulations, the wire mesh cages were modeled as porous walls and the hens inside an individual cage were modeled together as a single block with constant heat flux corresponding to their body temperature. The conveyor belt was modeled as a rectangular wall in between two tiers. The tier system and its model are shown in Figure 4 along with the cage modeling.

### 2.2 Ventilation schemes and modeling their components

Negative pressure ventilation is used in hen housing. Fans discharge air from a tightly-constructed building envelope that is under a slight negative pressure (vacuum typically 0.05 to 0.10 inches water) so that fresh air enters at planned inlet openings. In this chapter two ventilation schemes are studied and compared with respect to simulated-virus spread and effectiveness in maintaining temperatures uniformly within the building. The first ventilation scheme is the traditional one used in the United States and the second one is the proposed scheme in which the air flow is in a direction exactly opposite to the first one.

Fig. 3. Cage over manure conveyer belt.

With either ventilation scheme, the volume of air exchange is increased by turning on more fans with the inlet opening size increased to maintain a constant static pressure difference between interior and exterior conditions. When less air exchange is needed, fans are turned off to reduce the volume of air movement through the hen house, and the baffle inlet is closed partially to maintain the constant static pressure difference. In different weather conditions different air flow rates are required; e.g., more flow rate per hen is required in hot weather conditions as compared to cold weather conditions. The same (existing) control system can also be used for the proposed ventilation scheme. There is an automated mechanism that controls the baffle inlet opening according to the temperature-controlled airflow rate inside the hen house. The baffles and their adjustment system are shown in Figure 5.

Of interest is the effect of ventilation on the spread of disease-causing viruses within the hen house and to the neighboring hen houses. The important questions to be answered are: a) If one hen in the house gets infected, how are the other hens affected? b) How does the infection of a hen in one house affect the hens in neighboring houses? These questions remained unanswered until now due to absence of air flow modeling inside and discharge from the poultry houses.

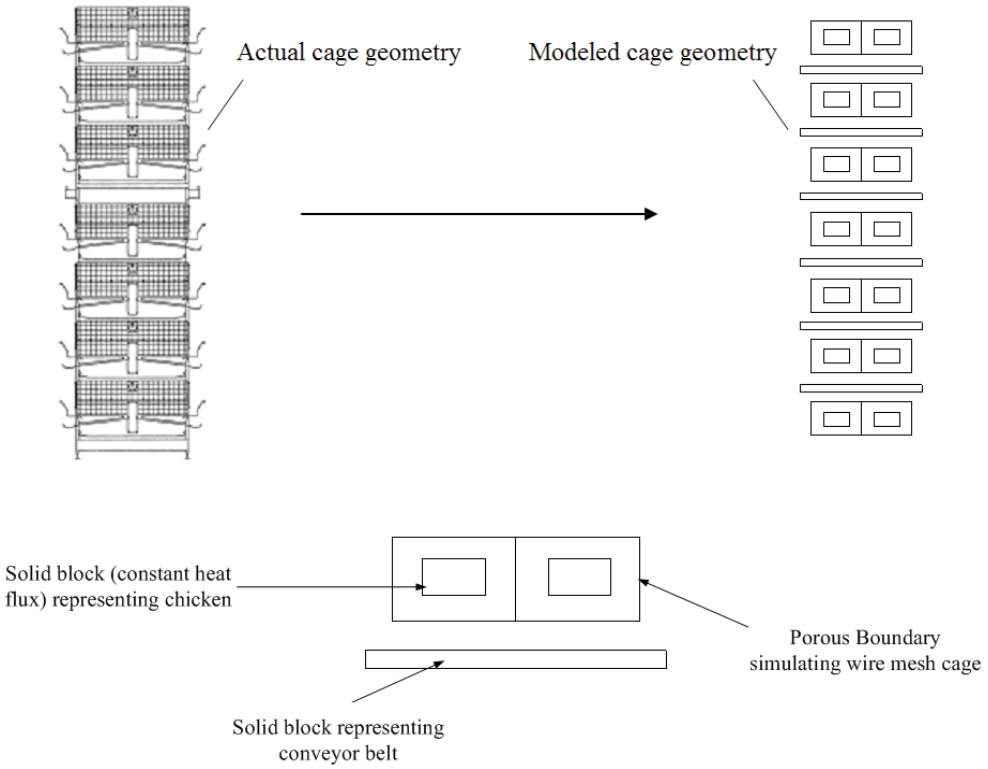


Fig. 4. Cage, conveyer belt and 7-cage tier assembly modeling.

#### 2.2.1 Traditional ventilation scheme: downward flow

In this type of ventilation system the air flow is from top to bottom as practiced in high-rise hen houses and manure-belt houses during all but hot weather. Fresh air comes into the attic space at the eaves between the roof and the wall through a 2 to 3 ft continuous opening along the length of the building. Within the attic floor there are slot openings above each cage-row to distribute fresh air uniformly across the upper level of the hen house. Each slot opening has a horizontal baffle to direct incoming air along the ceiling. The air is exhausted outside using fans placed about 3 ft above ground on the lower story of the barn. The ventilation fans are shown in Figure 6. The eave on one side of the poultry house is shown in Figure 7. The problem with this ventilation approach is that the direction of air flow (top to bottom) is against the natural tendency of warm air from the hens to rise, as was shown in Figure 1.

#### 2.2.2 Proposed ventilation scheme: upward flow

In this ventilation system the air flow is exactly opposite to that of the previous traditional scheme. In this case the flow comes in from the bottom of the barn and it is vented out using fans placed in the attic, at the top of the roof. This type of ventilation system assists the thermal plume produced by the hens rather than opposing it. It is shown in Figure 8.

Fig. 5. Horizontal baffle with inlet slot above it is adjustable to match inlet area to air flow capacity of operating fans.

Fig. 6. Fan Arrangement on lower story of hen house. Small extension of building near background has a set of six fans protected to reduce light entry into the building.

Fig. 7. Open eave along entire length of the poultry house to allow air entry to attic space prior to distribution to building interior.

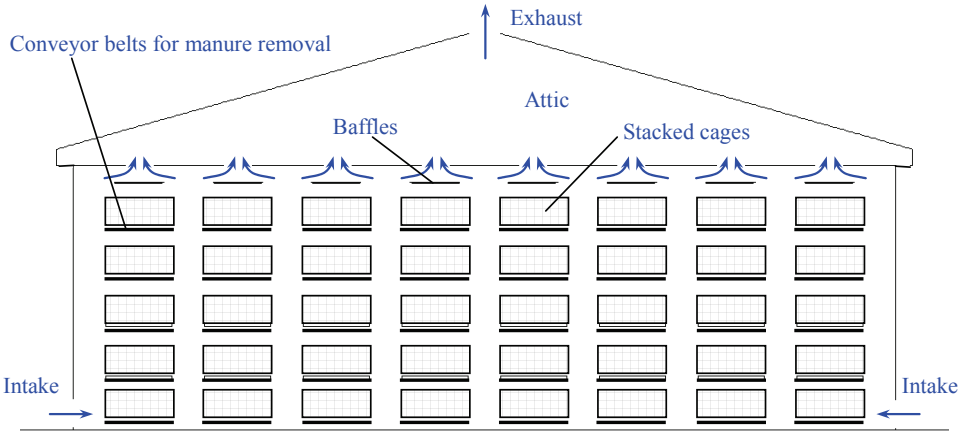


Fig. 8. Proposed ventilation scheme airflow from bottom to top of house.

### 2.3 Final 2-D geometry with dimensions

Incorporating all the above mentioned features, the final 2-D geometry shown in Figure 9 was created and used for the CFD simulation. This geometry was extruded in the third dimension (out of the page in Figure 9) to create the three-dimensional geometry.

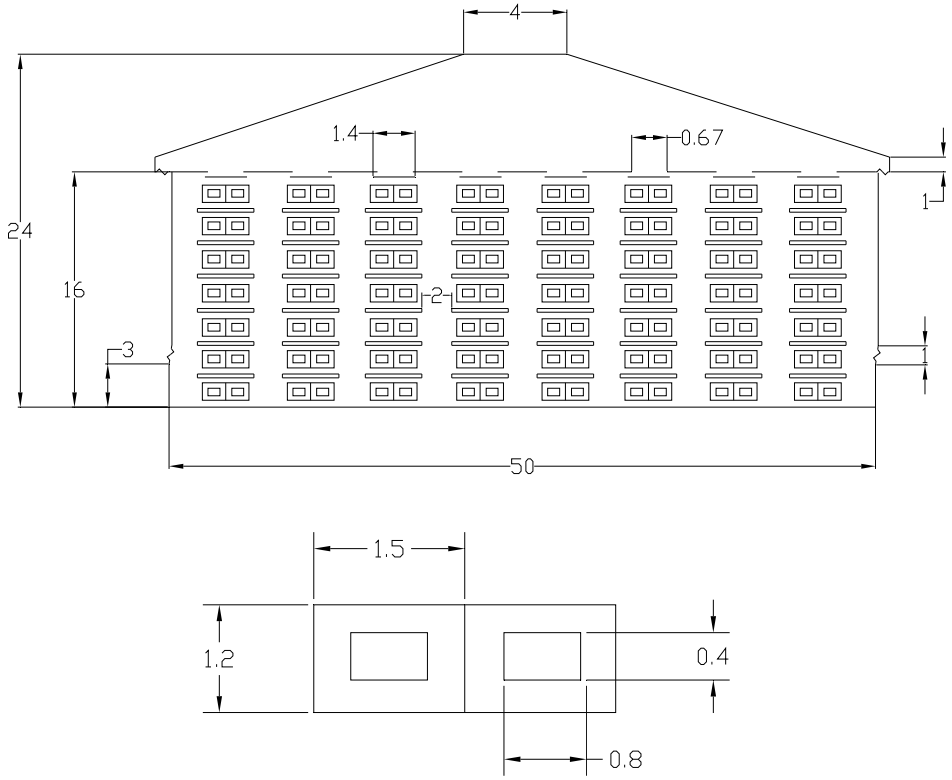


Fig. 9. Two-dimensional simulation model (top) and details of the cages (bottom) with dimensions in feet (cage dimension reference: the Big Dutchman Manual).

## 3. Meshing (grid generation)

In CFD analysis, the geometry (developed in section 2.3) is first enclosed in a computational domain. The size of the domain is determined by various factors. The "approach length" (distance from the start of the domain to the left-most wall of the building) must be sufficiently long so that the inlet flow is sufficiently developed before it reaches the building. The top and right boundaries of the domain are placed such that reverse flow is avoided. In this work only two hen houses are modeled side by side, as in Figure 10, assuming that the flow and thermal interactions would be similar if there were additional barns on the site. The domain extends several barn widths downstream since eddies are created downstream of the buildings. These eddies need to be captured and contained inside the computational domain to avoid reverse flow at the outflow boundary.

The next and the most fundamental consideration in CFD is that of discretization, which involves the process of transforming continuous models and equations into forms suitable for numerical analysis and implementation on a computer. In this case the discretization is initiated by dividing the spatial domain into small cells (finite volumes) to form a volume mesh or grid. Then by using a suitable algorithm/solver, the discretized equations of

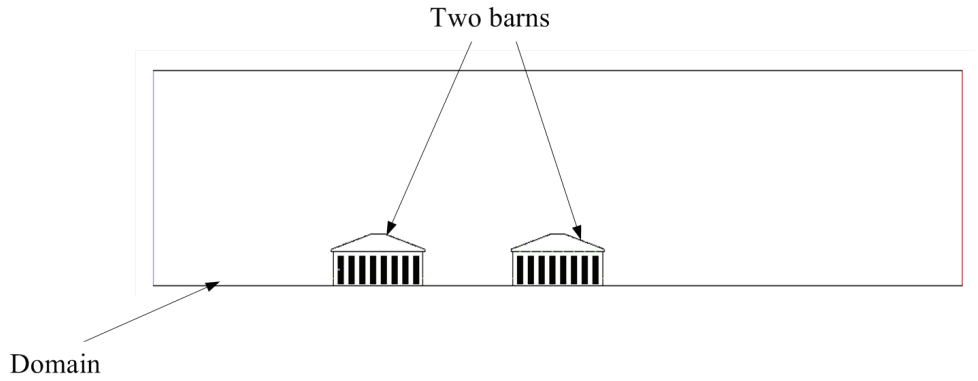


Fig. 10. Domain for 2-D mesh.

motion (conservation of mass, energy, and the Navier-Stokes equation of linear momentum) are solved. In FLUENT, the mesh can be regular (quadrilateral cells in 2-D or hexahedral cells in 3-D), irregular (triangular or quadrilateral cells in 2-D or pyramidal volumes in 3-D), or a combination of these (hybrid grid). Information about each cell must be stored separately in memory.

In GAMBIT for the 2-D case, two primary elements are used to mesh faces, namely, quadrilateral and triangular. The quadrilateral elements can be combined with four types of meshes: map, sub map, pave, and tri primitive. Triangular elements can be used only with the pave type. The final result of meshing the domain using the above mentioned elements is shown in Figure 11.

In the mesh for the region of interest, which is the interior of the barn, the grid is fine, i.e., the number of nodes for edges in the interior of the barn is dense. The grid becomes progressively more coarse as focus is shifted away from the barn. This is evident in Figure 11. In 2-D meshes, the quad-map (structured) scheme is usually preferred as it requires fewer cells for a given area and hence less storage space is required.

## 4. Boundary conditions

The next step in CFD analysis is specification of boundary conditions. In the 2-D model the left edge of the domain is a velocity inlet. Velocity inlet boundary conditions are used to define the flow velocity, along with all relevant scalar properties of the flow (such as temperature, turbulence properties, etc.), at flow inlets. The right edge is a pressure outlet where a static (gauge) pressure needs to be specified. The base (ground) and the top part of the domain are walls. The top part of the domain is specified as a zero shear wall. This is done to avoid reverse flow out of the top of the domain and also to keep the height of the domain and thus the number of required grid points as low as possible. This does not significantly affect the flow/thermal characteristics near the barn. The domain with boundary conditions is shown in Figure 12.

The top surface of the roof is a wall for Case 1, the traditional ventilation system (air flow from top to bottom). It is a fan for Case 2, the alternate ventilation system (air flow from bottom to top). The fan boundary condition is a lumped parameter model in which a pressure jump is enforced across the boundary; it is used to determine the impact of a fan

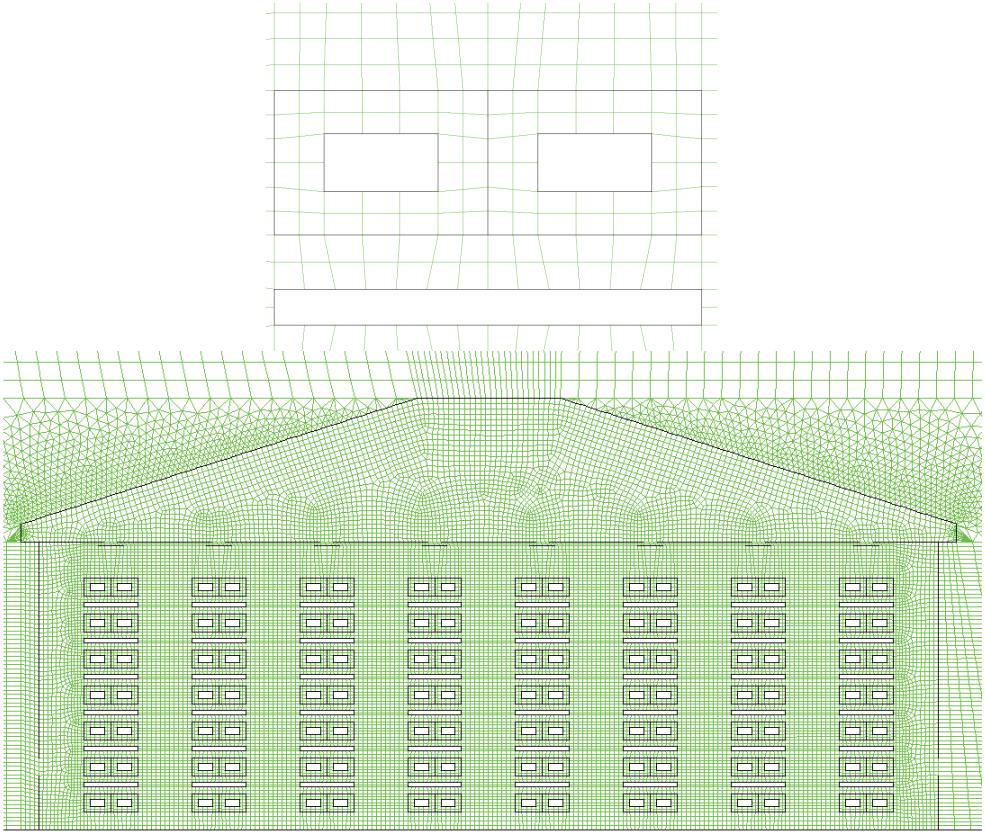

Fig. 11. Details of the 2-D mesh around a cage (top) and in the entire building (bottom).

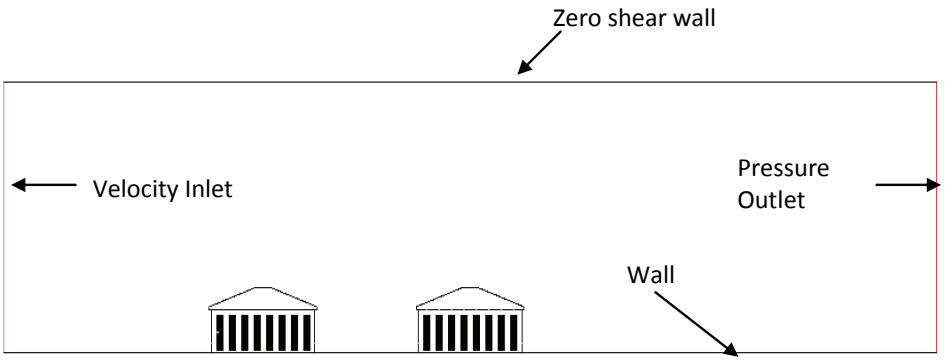


Fig. 12. Boundary conditions for the 2-D computational domain.

with known characteristics upon some larger flow field. The slanting edges of the roof are walls. The eave, the portion projecting out of the side walls of the barn, is an interior face for

Case 1 and it is a wall for Case 2. This interior boundary is considered as a part of the mesh and the flow is not affected due to it. The slots in the attic space for air are also specified as interior. The baffles are specified as walls. The sides of the barn are walls except for a slot which is a fan for Case 1 and interior for Case 2. The base (floor) of the barn is a wall. The cage is a wire mesh so the boundary condition specified for it is a porous jump. Porous jump conditions are used to model a thin "membrane" that has known velocity/pressure-drop characteristics. The wires used in the mesh are thin, and it is assumed that the cages are 80% open. Nothing needs to be specified for interior boundary conditions. The solid block representing the hens is a wall. The conveyor belt is a wall. These boundary conditions are summarized in Figure 13.

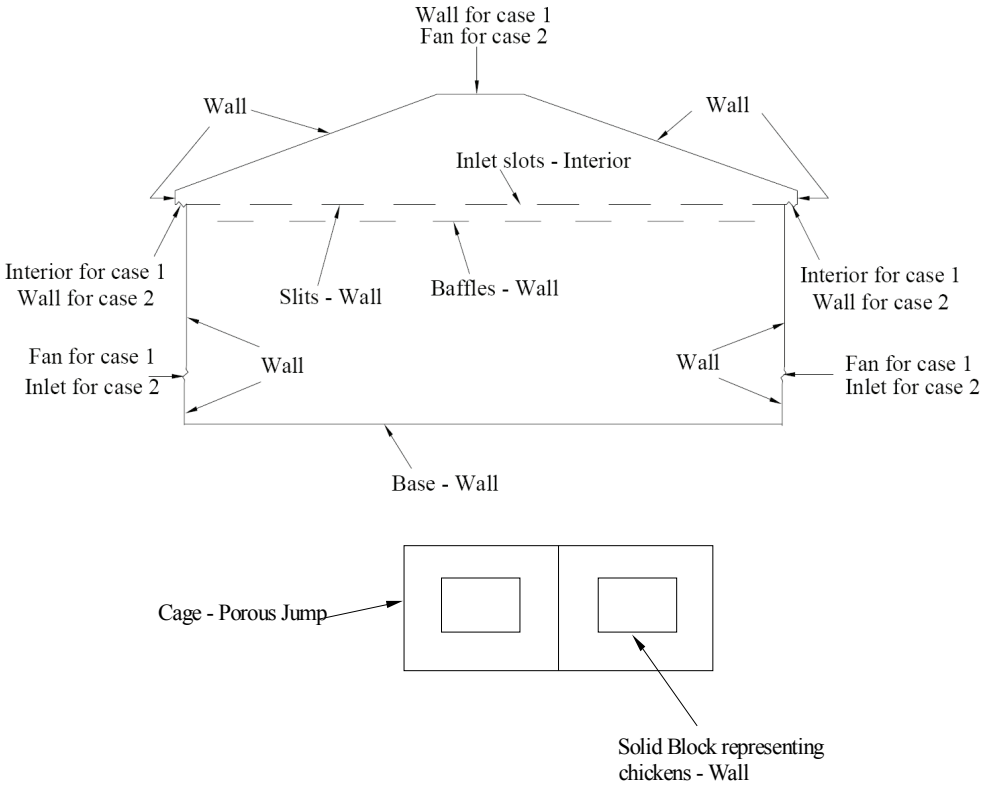


Fig. 13. Boundary conditions for the 2-D poultry house (top) and cage (bottom).

For one particular case to be discussed in detail, the walls are specified as no-slip walls with zero heat flux/constant temperature (300K). The blocks representing the hens are no-slip walls with a constant heat flux of 6.577 W/m$^2$ (calculation shown below). The left edge/face of the domain is specified as a velocity inlet with velocity magnitude of 1.0 m/s normal to the boundary, inlet temperature of 300 K, turbulence kinetic energy (TKE) = 0.01 m$^2$/s$^2$, turbulence dissipation rate (TDR or $\varepsilon$) = 0.01 m$^2$/s$^3$, and a species mass fraction of zero (pure air). The ammonia inlet (analogous to the infected hen) is a velocity inlet condition applied

to a particular block of hens. The velocity magnitude is 0.010 m/s normal to the boundary, the species mass fraction is unity (100% ammonia), and the rest of the parameters remain the same. The right edge/face of the domain is a pressure outlet. The gauge pressure is zero Pa, backflow total temperature is 300K, TKE is 0.01 $m^2/s^2$, TDR is 0.01 $m^2/s^3$ and the species mass fraction is zero. For Case 1 two fans per barn (sides of the barn) are specified and for Case 2 only one fan per barn (roof top of the barn) is specified. The pressure difference across the fan is specified as 24.9 Pa (0.10 inch of water column).

### 4.1 Calculation of parameters for boundary conditions

The hens inside the cage, which are represented by a block, are modeled as either a constant heat flux wall or as a constant temperature wall. The constant heat flux boundary condition is preferred since it is more representative.

#### 4.1.1 Constant heat flux case

The basal metabolic rate for warm blooded animals like chickens can be approximated by the following empirical equation,

$$\dot{M}_b \text{ (in watts)} = 3.39\left(m_b^{0.75}\right) \tag{1}$$

where $m_b$ is the animal body mass in kg. For example, a typical hen has a mass of $m_b$ = 3.0 lbm (1.36 kg), and thus $\dot{M}_b = 4.28$ W. If there are 8 hens per cage, the heat generated per cage is 34.2 W. For unit depth the heat flux is given by

$$\text{Heat flux} = \frac{\text{Total heat generated}}{\text{perimeter} \times 1 \text{ m}} \tag{2}$$

where the perimeter is 5.2 m in the present case. Thus, the heat flux is calculated to be 6.58 $W/m^2$.

#### 4.1.2 Constant temperature case

Two hen body temperatures were considered in the modeling, depending on the conditions of the outside air temperature:

a. Mild and cold atmospheric conditions: Hen skin temperature set to 68°F.
b. Hot atmospheric conditions (outdoor temperature above 70°F): Hen skin temperature set to ambient temperature + 5°F

#### 4.1.3 Baffle openings for mild atmospheric conditions

The required air flow rate in the hen house was calculated as follows:

$$\begin{aligned} \text{Required air flow rate} = &\left(\text{flow rate per lbf}\right) \\ &\times\left(\text{weight of one chicken}\right) \\ &\times\left(\text{number of chickens in the barn}\right) \end{aligned} \tag{3}$$

For the mild conditions studied in detail here, the flow rate per pound was taken to be 1.0 cubic feet per minute (CFM) per lbf, the weight of one hen was estimated as 3.0 lbf, and the

number of hens in the barn was 158,000. Thus, the required air flow rate was 474,000 CFM. At the inlet (at the attic floor, which is also the hen house ceiling), the standard design is to provide 1.7 ft² of inlet area per 1000 CFM of fan capacity. So the required inlet area for 474,000 CFM was 805.8 ft². This area was divided between eight inlets in the attic. Thus, the required area per inlet was approximately 100 ft². Since the length of the barn was 500 ft, the baffle opening was set to 0.20 ft. The static pressure difference across the fan was set to 0.10 inches of water column (24.9 Pa).

#### 4.1.4 Pressure drop across the wire mesh cage

Instead of meshing the cages (which would require an extremely fine computational mesh), a porous jump boundary condition was applied in the CFD model in place of the cages. The pressure drop across a wire mesh or screen is calculated as

$$\Delta p = K_L\left(\frac{1}{2}\rho V_2^2\right) \tag{4}$$

where $K_L$ is the loss factor, $\rho$ is the density of the air, taken to be 1.25 kg/m³, and $V_2$ is the velocity of the air through the open area of the mesh. However, the loss factor needs to be estimated. The velocity through the mesh is calculated as follows, using Figure 14 as a guide:

$$V_2 = V_1 \times \frac{A_1}{A_2} = \frac{s}{s-d} \tag{5}$$

where $V_1$ is the air velocity before the mesh. To determine the pressure drop, the Bernoulli equation (ignoring elevation differences) is applied,

$$\frac{p_1}{\rho g} + \frac{V_1^2}{2g} = \frac{p_2}{\rho g} + \frac{V_2^2}{2g} \tag{6}$$

or,

$$\Delta p = p_1 - p_2 = \frac{\rho}{2}\left(V_2^2 - V_1^2\right) \tag{7}$$

Once the pressure drop is estimated, the loss factor is calculated from Equation 4. FLUENT uses an *adjusted* loss factor which is calculated as

$$K'_L = K_L \times \frac{V_2^2}{V_1^2} \tag{8}$$

Finally, the pressure jump coefficient is given by

$$C_2 = \frac{K'_L}{\text{thickness}} \tag{9}$$

where the thickness in the denominator of Equation (9) is the thickness of wire in the wire mesh – the thickness across the porous jump. For the particular case discussed here, $C_2$ =

201.2 per meter. FLUENT's default value of face permeability ($1.0 \times 10^{10}$ m$^2$) was used, and the porous medium thickness was specified as 1.0 mm.

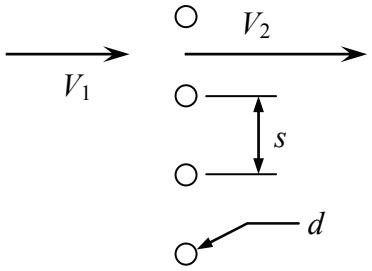


Fig. 14. Simplification of the cage wire mesh, used to calculate porous jump parameters.

## 5. CFD setup and results

For the results reported here, the CFD solver FLUENT was set up to run in 2-D double precision mode. We also ran three-dimensional cases, not shown here, with similar results [15]. The mesh was imported from the grid generator GAMBIT. The segregated solver was used. The $k-\varepsilon$ model was used for turbulence; the constants used are given in Table 1.

| | |
|---|---|
| $C_{2,\varepsilon}$ | 1.9 |
| TKE Prandtl number | 1 |
| TDR Prandtl number | 1.2 |
| Energy Prandtl number | 0.85 |
| Wall Prandtl number | 0.85 |
| Turbulent Schmidt number | 0.7 |

Table 1. Constants used in FLUENT

For simulating the spread of airborne virus an air/ammonia mixture was used. The thermal conductivity of the mixture was specified to be 0.025 W/m-K and the viscosity was $1.72 \times 10^{-5}$ kg/m-s. The mass diffusivity was $2.88 \times 10^{-5}$ m$^2$/s. The density was calculated using the ideal gas law, and the specific heat was calculated using the mixing law. The species model was enabled without volumetric reactions. The under-relaxation factors and discretization methods are summarized in Tables 2 and 3.

The operating conditions were then specified. The operating pressure was set to 101,325 Pa and the operating temperature was set to 288.16 K. Also, gravity was enabled and the gravitational acceleration was specified as 9.81 m/s$^2$ in the negative $y$-direction (down). The boundary conditions were specified using the parameters calculated above. The flow field was initialized using the values listed in Table 4.

| Variable | Under-relaxation factor |
|---|---|
| Pressure | 0.15 |
| Density | 1 |
| Body forces | 1 |
| Momentum | 0.35 |
| Turbulence kinetic energy | 0.4 |
| Turbulence dissipation rate (TDR) | 0.4 |
| Turbulent viscosity | 1 |
| Species | 1 |
| Energy | 1 |

Table 2. Under-relaxation factors

| Variable | Method |
|---|---|
| Pressure | Standard |
| Density | Second-order upwind |
| Momentum | Second-order upwind |
| TKE | Second-order upwind |
| TDR | Second-order upwind |
| Species | Second-order upwind |
| Energy | Second-order upwind |

Table 3. Discretization methods

| Variable | Initialized value |
|---|---|
| Gauge pressure | 0 Pa |
| $x$ velocity component | 0 m/s |
| $y$ velocity component | 0 m/s |
| TKE | 0.01 $m^2/s^2$ |
| TDR | 0.01 $m^2/s^3$ |
| $NH_3$ | 0 |
| Temperature | 300K |

Table 4. Flow-field initialization values

The iteration procedure was then started. The FLUENT solution was allowed to converge, i.e., the residuals decrease below the convergence criteria set for them. After this, post-processing was performed. In particular, contour plots and vector plots of several variables were generated. For the case of particulate contaminants (not presented here), the particle

injection/tracking capability of FLUENT was utilized, whereby particle paths are tracked using a Runge-Kutta scheme after the particles are injected from specified surfaces. For gaseous contaminants, FLUENT has multiple species capability, and mass fraction contour plots are readily generated.

As an example of gaseous contaminant diffusion, Figure 15 shows a comparison of ammonia mass fraction contours for both ventilation schemes. The hen in the fourth cage in the first (left-most) column of the first (upstream) poultry house was considered to be affected by a disease. The scale of this contour plot is clipped at a mass fraction of 0.1. The figure shows the spread of contaminant for both cases and the amount of contaminant that passes out of the upstream barn and enters into the downstream barn. Figure 16 shows diffusion contours inside the upstream barn. The white region is a region with very high concentration of contaminant (off the scale). Figure 17 shows the diffusion contours inside the downstream barn. This illustrates spread of contaminant from the upstream barn to the downstream one.

Figure 18 shows a comparison of temperature contours for the two cases. The air enters at ambient temperature and the temperature variations are caused by the body heat given off by the hens. Figure 19 shows temperature variations inside the upstream poultry house, which is an indicator of ventilation system performance. The temperature values are in Kelvin (K).

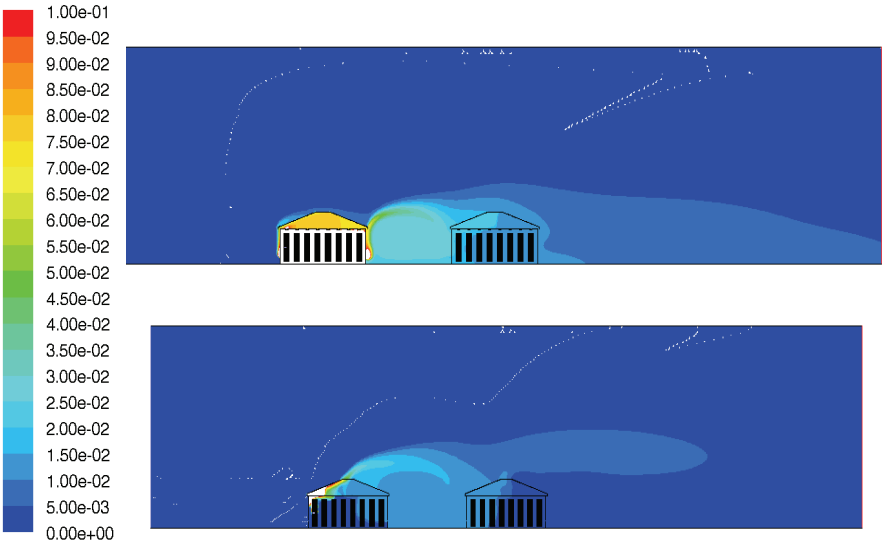


Fig. 15. Comparison of species diffusion contours inside the domain for Case 1 (downward flow) in the top image and Case 2 (upward flow) in the bottom image.

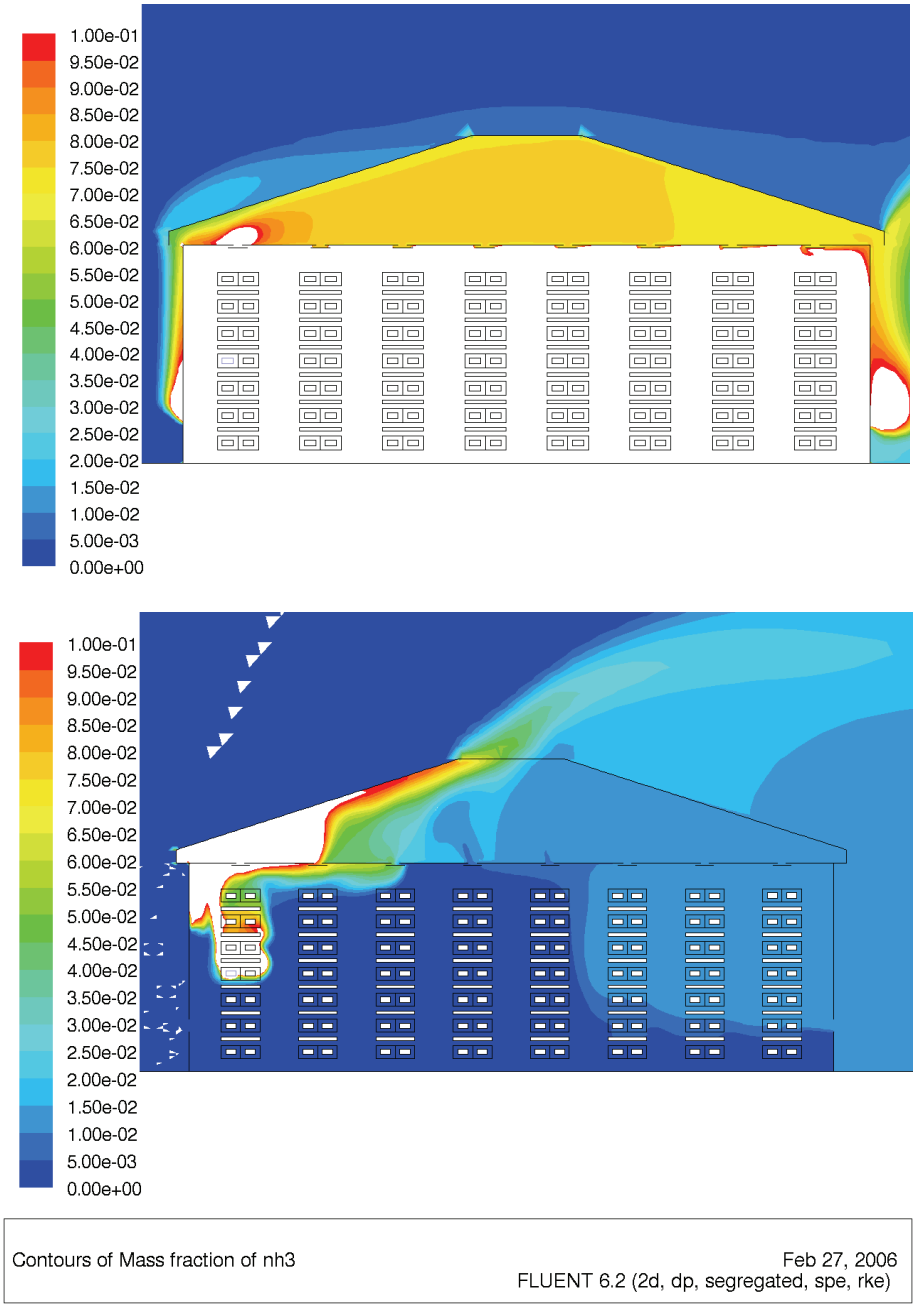


Fig. 16. Comparison of species diffusion contours inside the upstream poultry house for Case 1 (downward flow) in the top image and Case 2 (upward flow) in the bottom image.

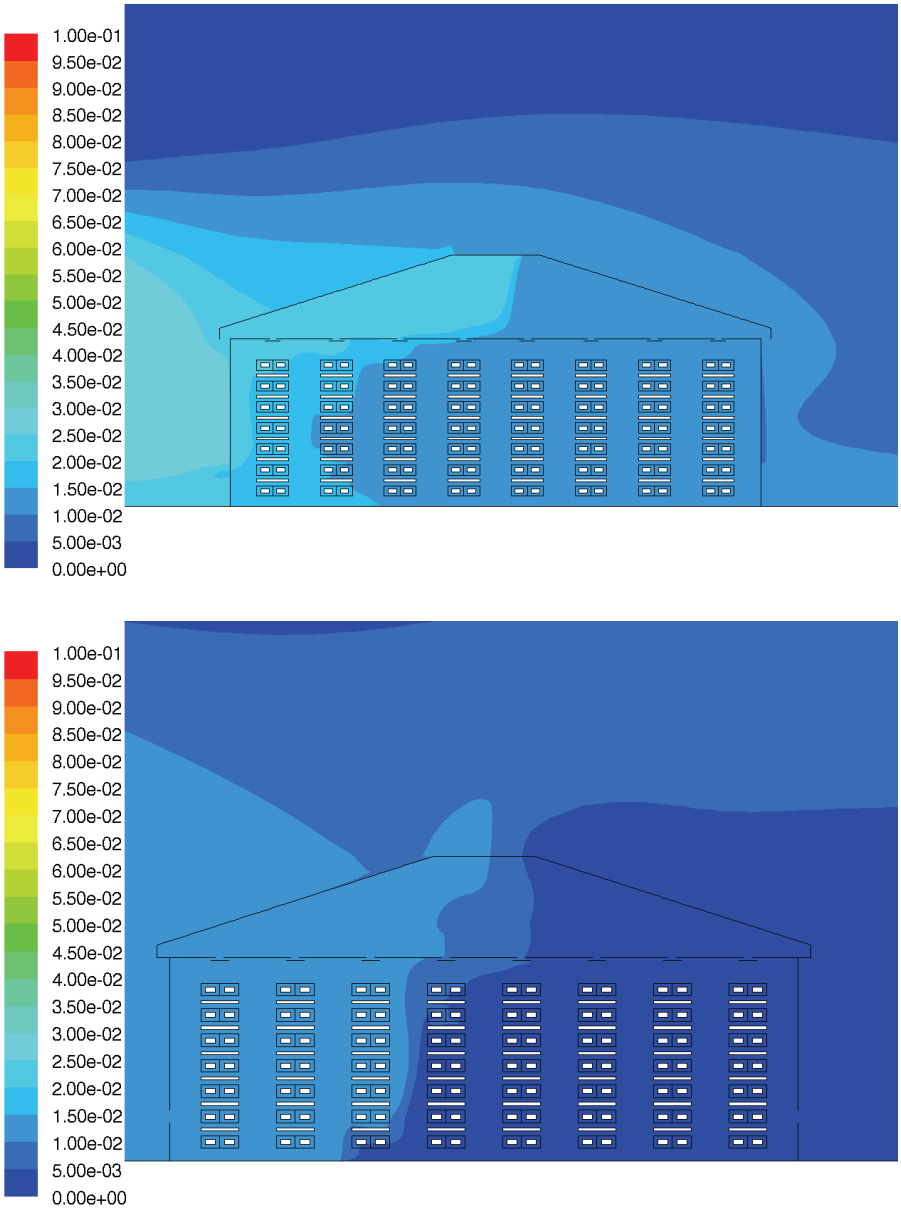


Fig. 17. Comparison of species diffusion contours inside the downstream poultry house for Case 1 (downward flow) in the top image and Case 2 (upward flow) in the bottom image.

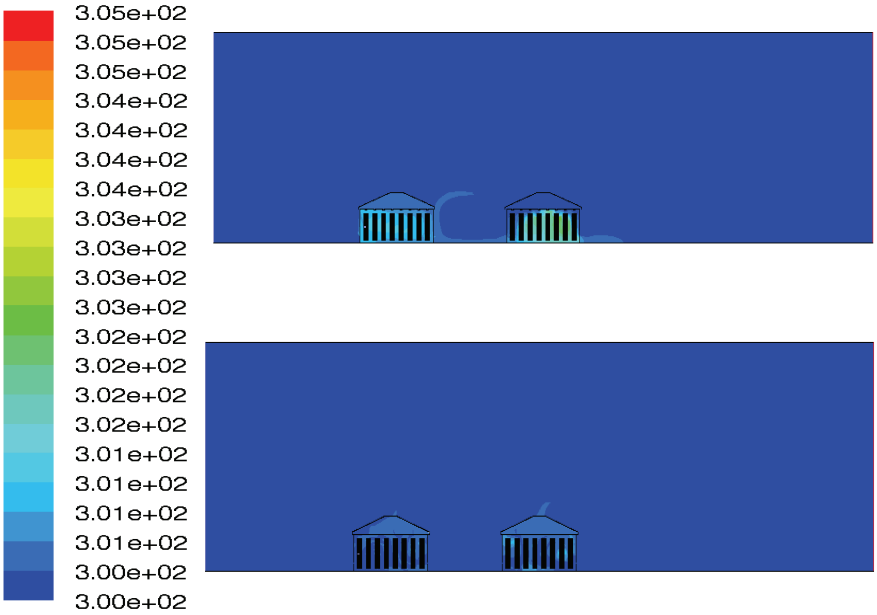


Fig. 18. Comparison of temperature contours in the entire computational domain for Case 1 (downward flow) in the top image and Case 2 (upward flow) in the bottom image.

## 6. Observations, conclusions, and future scope

The main objective of this article was to compare the two ventilation schemes from the view point of air quality and ventilation characteristics. Therefore, only species diffusion contours and temperature contours were analyzed. Species diffusion contours are good indicators for performance of ventilation schemes from the view point of air quality. It has been assumed that the hen in cage 4 of the first row of the upstream poultry house has been affected by a disease, i.e., the contaminant is injected from this cage. For the species diffusion contours the scale has been clipped to a range of 0-0.1 mass fraction. The white region indicates high concentrations of the contaminant. The contaminant coming out of the upstream poultry house affects the downstream poultry house much more in downward flow (Case 1) than in upward flow (Case 2) as shown in Figures 15, 16, and 17. This is primarily due to fan position in both cases. The outlets of fans for downward flow oppose each other and due to this the air exhausted outside through the outlet of the upstream poultry house rises and enters the inlet of the adjacent poultry house. In upward flow the fans are placed on the roof so that the exhaust air is ejected directly up and above the adjacent poultry houses and does

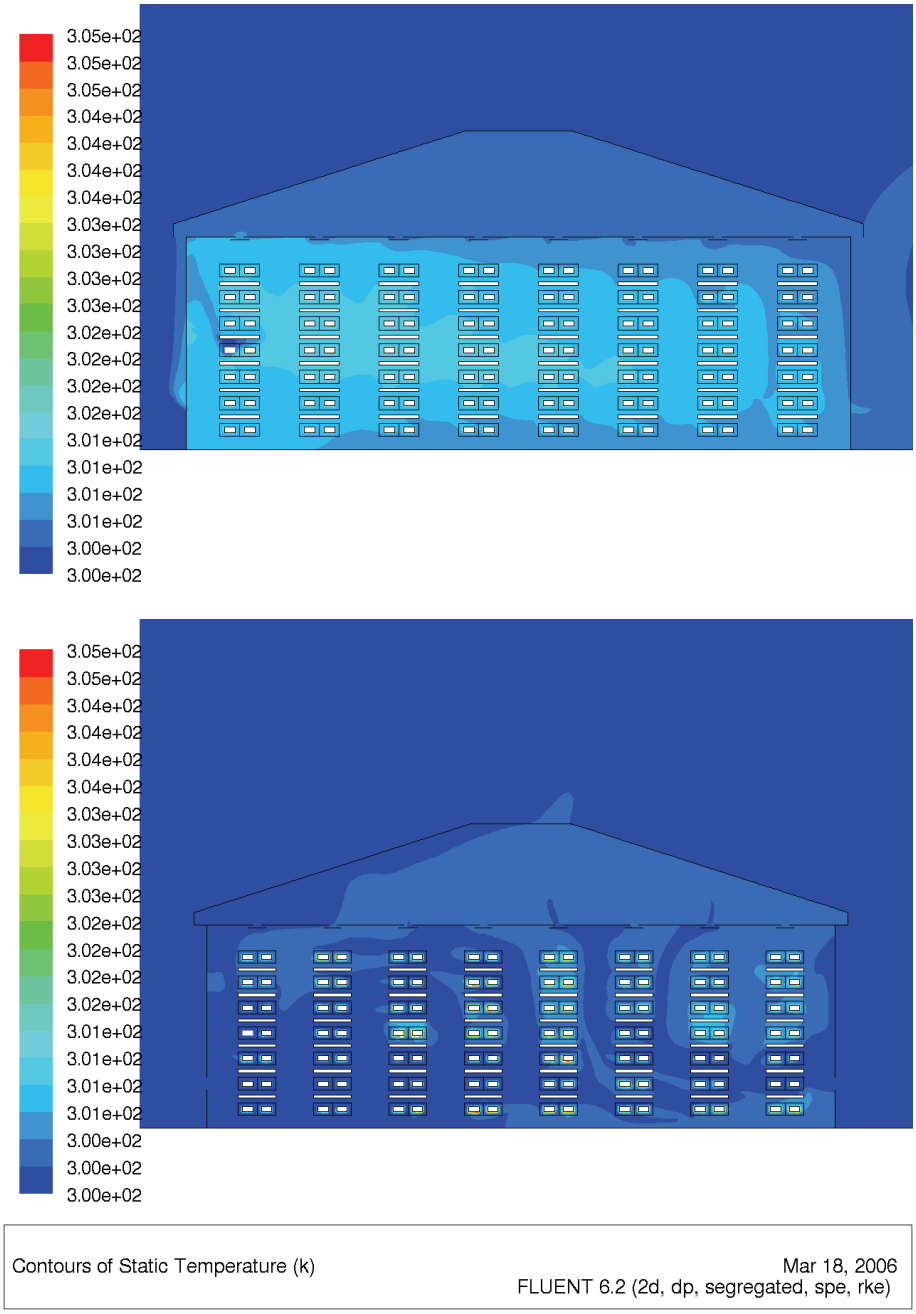


Fig. 19. Comparison of temperature contours inside the upstream poultry house for Case 1 (downward flow) in the top image and Case 2 (upward flow) in the bottom image.

not interfere significantly with the inlets of the downstream poultry houses. (The minimal amount of species diffusing from poultry house 1 to poultry house 2 in Case 2 results partly from the domain height being limited in FLUENT.) Due to this, the contaminant spread from the upstream poultry house to the downstream one is much less with upward flow than with downward flow. Inside the upstream poultry house it is also observed that contaminant diffusion is much less for upward flow as compared to downward flow. In Figure 16 it is observed that for downward flow the entire interior of the poultry house is colored white which indicates high concentration of contaminant inside the poultry house. In upward flow the diffusion of the contaminant inside the poultry house is restricted to a few regions and the concentration of the contaminant in these regions is low. This is because the rising warm plume of air in Case 2 naturally flows upward, carrying the contaminant with it and out the exhaust. In Case 1, however, the air flow tends to diffuse the contaminant inside the poultry house because the direction of flow is opposite to the natural thermal plumes from the hens.

Comparison of the temperature contours for both ventilation schemes in Figures 18 and 19 shows that the ventilation system in upward flow is more effective than that in downward flow. The temperature contours in downward flow are predominantly light blue in color which indicates that the temperature is greater than the ambient outdoor temperature. On the other hand, the temperature contours for upward flow are predominantly dark blue which is nearly equal to the outside air temperature. One of the primary purposes of a ventilation system is to control temperature and thus from this view point the ventilation scheme in upward flow is better than that in downward flow. The temperature variations inside the poultry house occur due to heat produced by the hens because of their warm body temperatures. This process occurs via the thermal plumes generated by the hens. The airflow in Case 1 is from top to bottom and this direction opposes the naturally rising thermal plume. Due to this effect, the heat gets redistributed inside the poultry house and impairs the effectiveness of this ventilation scheme. On the other hand, in Case 2 the airflow is from bottom to top which is in the same direction as the naturally rising thermal plume. So in this scheme the thermal plume assists the airflow, heat is effectively carried out of the poultry house, and the temperature inside is maintained at a cooler level.

The present CFD simulations reveal that the cold and mild weather ventilation system in use in the United States, downward flow, for manure-belt cage hen houses is not effective from the view point of air quality and distribution. On the other hand, upward flow provides more effective ventilation in relation to diminishing disease spread. The ineffectiveness of the current system from an air quality viewpoint could be crucial if an outbreak of an airborne virus, for example avian influenza, were to occur. Upward flow is much better at containing contaminant and restricting spread. To support the CFD results, experimentation with an empty poultry house and a tracer gas such as sulfur hexafluoride ($SF_6$) should be done. There are optimizations needed to improve the practical application of the simple reversal of air flow depicted here. For example the upward flow case will be strengthened with an inlet system to more uniformly introduce fresh air to the hens, attic redesign to reduce the potential for condensation of moist warm exhaust air, and elimination of baffles at entry to the attic space. Also, an economic analysis with regard to financial implications of changing from the existing system to the new system needs to be done.

Further studies could be done from the disease spread and containment point of view. Using data from virologists regarding the concentration of a particular airborne virus required to affect living beings and the life of such viruses, effective quarantine techniques could be developed. For this purpose the results of species diffusion can be used to find concentration in particular areas and appropriate quarantine measures can be taken. Using a similar approach, other poultry house architectures could also be investigated. One example of an alternative structure is the double envelope system wherein an interior wall with pores is installed inside the side walls. Air is moved from the building interior into the envelope through the pores, and passes through this envelope space to be exhausted at the top of the building. Also, other ventilation approaches such as the hot-weather wind-tunnel ventilation system could be analyzed using CFD.

## 7. References

[1] Economic Research service (ERS): http://www.ers.usda.gov/briefing/poultry/

[2] Jia, W.K., K. Parrish, C.R., and Naqi, S.A. A novel variant of avian infectious bronchitis virus resulting from recombination among three different strains. *Archives of Virology*, Vol. 140, No. 2, pp. 259-271, 1995.

[3] Mondal, S.P., Lucio-Martinez, B. Naqi, S.A., Isolation and characterization of a novel antigenic subtype of infectious bronchitis virus serotype DE072. *Avian Dis*., Vol. 45, No. 4, pp. 1054-1059, 2001.

[4] Gelb, J.J., Ladman, B.S., Tamayo, M. Gonzalez, M., Sivandandan, V., Novel infectious bronchitis virus S1 genotypes in Mexico 1998-1999. *Avian Dis*., Vol. 45, No. 4, pp. 1060-1063, 2001.

[5] Ford, B., Diaz, C., Hewitt, M. Passive downdraught cooling - architectural integration in Seville. *PLEA Conference Proceedings: Architecture City, Environment*, Cambridge: James & James, 2000.

[6] Givoni, B., Passive and Low Energy Cooling of Buildings. 1994, New York: Van Nostrand Reinhold.

[7] Fathy, H., Natural Energy and Vernacular Architecture. 1986, Chicago: University of Chicago Press.

[8] Alvarez, S. Full scale experiments in EXPO '92 the bioclimatic rotunda. *PLEA Ninth Conference Proceedings*, Seville, Spain, 1991.

[9] FLUENT User's Guide, Ver. 6.0, Lebanon, N.H., Fluent Inc. 2005.

[10] GAMBIT User's Guide, Ver. 2.0, Lebanon, N.H., Fluent Inc. 2005.

[11] Lee I. B. and Short T. H. Verification of Computational Fluid Dynamic Temperature Simulations in a Full-Scale Naturally Ventilated Greenhouse. ASAE, October 2000.

[12] Sun H., Stowell R.R., Keener H.M., Michel Jr. F.C., Two-Dimensional CFD modeling of air velocity and ammonia distribution in high – rise hog building, *Trans. ASAE*, Vol. 45, No. 5, pp. 1559-1568, 2002.

[13] Lee I.B., You B.K., Choi K.H., Jeun J.G., Kim G.W., Study of internal climate for naturally and mechanically ventilated broiler houses, ASAE Paper No. 034060, St. Joseph, Mich, 2003.

[14] Aerts J.M., Berckmans D., A virtual chicken for climate control design: Static and Dynamic simulations of heat losses, *Trans. ASAE*, Vol. 47. No. 5, pp. 1765-1772, 2004.

[15] Pawar, S. Air Quality and Ventilation Analysis of Poultry Houses using Computational Fluid Dynamics, M.S. Thesis, The Pennsylvania State University, Dept. of Mech. and Nuc. Engr., May 2006.

4

# Investigation of Mixing in Shear Thinning Fluids Using Computational Fluid Dynamics

Farhad Ein-Mozaffari and Simant R. Upreti
*Ryerson University, Toronto*
*Canada*

## 1. Introduction

Mixing is an important unit operation employed in several industries such as chemical, biochemical, pharmaceutical, cosmetic, polymer, mineral, petrochemical, food, wastewater treatment, and pulp and paper (Zlokarnik, 2001). Crucial for industrial scale-up, understanding mixing is still difficult for non-Newtonian fluids (Zlokarnik, 2006), especially for the ubiquitous shear-thinning fluids possessing yield stress.

Yield-stress fluids start to flow when the imposed shear stress exceeds a particular threshold yield stress. This threshold is due to the structured networks, which form at low shear rates but break down at high shear rates (Macosko, 1994). Many slurries of fine particles, certain polymer and biopolymer solutions, wastewater sludge, pulp suspension, and food substances like margarine and ketchup exhibit yield stress (Elson, 1988). Mixing of such fluids result in the formation of a well mixed region called cavern around the impeller, and essentially stagnant or slow moving fluids elsewhere in the vessel. Thus, the prediction of the cavern size becomes very important in evaluating the extent and quality of mixing. When the cavern size is small, stagnant zones prevail causing poor heat and mass transfer, high temperature gradients, and oxygen deficiency for example in aeration processes (Solomon et al., 1981).

The conventional evaluation of mixing is done through experiments with different impellers, vessel geometries, and fluid rheology. This approach is usually expensive, time consuming, and difficult. Moreover, the resulting empirical correlations are suitable only for the specific systems thus investigated. In this regard, Computational Fluid Dynamics (CFD) offers a better alternative. Using CFD, one can examine various parameters of the mixing process in shorter times and with less expense; an otherwise uphill task with the conventional experimental approach.

During the last two decades, CFD has become an important tool for understanding the flow phenomena (Armenante et al., 1997), developing of new processes, and optimizing the existing processes (Sahu et al., 1998). The capability of CFD to satisfactorily forecast mixing behavior in terms of mixing time, power consumption, flow pattern, and velocity profiles has been considered as a successful achievement. A distinct advantage of CFD is that, once a validated solution is obtained, it can provide valuable information that would not be easy to obtain experimentally. The objective of this work is to present recent developments in using CFD to investigate the mixing of shear-thinning fluids possessing yield stress.

## 2. CFD modeling of the mixing vessel

The laminar flow of a fluid in an isothermal mixing tank with a rotating impeller is described by the following continuity and momentum equations (Patankar, 1980; Ranade, 2002):

$$\frac{\partial \rho}{\partial t} = -\nabla . \rho \boldsymbol{v} \tag{1}$$

$$\frac{\partial (\rho \boldsymbol{v})}{\partial t} = -\nabla \cdot \left( \rho \boldsymbol{v} \boldsymbol{v} \right) - \nabla p + \nabla \cdot \boldsymbol{\tau} + \rho \boldsymbol{g} + \boldsymbol{F} \tag{2}$$

where $\rho$, $p$, $\boldsymbol{v}$, $\boldsymbol{g}$, $\boldsymbol{F}$ and $\boldsymbol{\tau}$ respectively are the fluid density, pressure, velocity, gravity, external force, and the stress tensor given by

$$\boldsymbol{\tau} = \mu \left[ \left( \nabla \boldsymbol{v} \right) + \left( \nabla \boldsymbol{v} \right)^T - \frac{2}{3} \left( \nabla \cdot \boldsymbol{v} \right) \boldsymbol{I} \right] \tag{3}$$

In the above equation, $\mu$ is the molecular viscosity, and $\boldsymbol{I}$ is the unit tensor. For incompressible fluids, the stress tensor is given by

$$\boldsymbol{\tau} = \mu \left[ \left( \nabla \boldsymbol{v} \right) + \left( \nabla \boldsymbol{v} \right)^T \right] = \mu \boldsymbol{D} \tag{4}$$

where $\boldsymbol{D}$ is the rate-of-strain tensor. For multidimensional flow of non-Newtonian fluids, the apparent viscosity ($\mu$) is a function of all three invariants of the rate of deformation tensor. However, the first invariant is zero for incompressible fluids, and the third invariant is negligible for shearing flows (Bird et al., 2002). Thus, for the incompressible non-Newtonian fluids, $\mu$ is a function of shear rate, which is given by

$$\dot{\gamma} = \sqrt{\frac{1}{2} \left( \boldsymbol{D} : \boldsymbol{D} \right)} \tag{5}$$

It can be seen that $\dot{\gamma}$ is related to the second invariant of $\boldsymbol{D}$.

### 2.1 The rheological model

Equations (1)–(5) need a rheological model to calculate the apparent viscosity of the non-Newtonian fluid. For shear-thinning fluids with yield stress, the following Herschel-Bulkley model has been widely used by the researchers (Macosko, 1994):

$$\mu = \frac{\tau_y}{\dot{\gamma}} + k \left| \dot{\gamma} \right|^{n-1} \tag{6}$$

where $\tau_y$ is the yield stress, $k$ is the consistency index, and $n$ is the flow behavior index. Table 1 lists the rheological parameters of aqueous xanthan gum solution, which is a widely used Herschel-Bulkley fluid (Whitcomb & Macosko, 1978; Galindo et al., 1989; Xuewu et al., 1996; Renaud et al., 2005).

The Herschel-Bulkley model causes numerical instability when the non-Newtonian viscosity blows up at small shear rates (Ford et al., 2006; Pakzad et al., 2008a; Saeed et al., 2008). This problem is surmounted by the modified Herschel-Bulkley model given by

$$\mu = \begin{cases} \mu_0 \quad \text{for} \quad \tau \le \tau_y \\ \dfrac{1}{\dot{\gamma}}\left[\tau_y + k\left(\dot{\gamma}^n - \left(\dfrac{\tau_y}{\mu_0}\right)^n\right)\right] \quad \text{for} \quad \tau > \tau_y \end{cases} \tag{7}$$

where $\mu_0$ is the yielding viscosity. The model considers the fluid to be very viscous with viscosity $\mu_0$ for the shear stress $\tau \le \tau_y$, and describes the fluid behavior by a power law model for $\tau > \tau_y$ (Ford et al., 2006; Pakzad et al., 2008a; Saeed et al., 2008).

| xanthan gum concentration (%) | $k$ (Pa.s$^n$) | $n$ | $\tau_y$ (Pa) |
|---|---|---|---|
| 0.5 | 3 | 0.11 | 1.79 |
| 1.0 | 8 | 0.12 | 5.25 |
| 1.5 | 14 | 0.14 | 7.46 |

Table 1. Rheological properties of xanthan gum solutions (Saeed & Ein-Mozaffari, 2008)

### 2.2 Simulation of impeller rotation

The following four methods exist for the simulation of impeller rotation in a mixing vessel:

**The black box method** requires the experimentally-determined boundary conditions on the impeller swept surface (Ranade, 1995). Hence, this method is limited by the availability of experimental data. Moreover, the availability of experimental data does not warrant the same flow field for all alternative mixing systems (Rutherford et al., 1996). The flow between the impeller blades cannot be simulated using this method.

**The Multiple Reference Frame (MRF) method** is an approach allowing for the modeling of baffled tanks with complex rotating, or stationary internals (Luo et al., 1994). A rotating frame (i.e. co-ordinate system) is used for the region containing the rotating components while a stationary frame is used for stationary regions. In the rotating frame containing the impeller, the impeller is at rest. In the stationary frame containing the tank walls and baffles, the walls and baffles are also at rest. The momentum equations inside the rotating frame is solved in the frame of the enclosed impeller while those outside are solved in the stationary frame. A steady transfer of information is made at the MRF interface as the solution progresses.

Consider the rotating frame at position $r_0$ relative to the stationary frame as shown in Figure 1. The rotating frame has the angular velocity $\boldsymbol{\omega}$. The position vector $\boldsymbol{r}$ from the origin of the rotating frame locates any arbitrary point in the fluid domain. The fluid velocities can then be transformed from the stationary frame to the rotating frame using

$$\boldsymbol{v}_{\mathrm{r}} = \boldsymbol{v} - \boldsymbol{u}_{\mathrm{r}} \tag{8}$$

where $\boldsymbol{v}_{\mathrm{r}}$ is the relative velocity viewed from the rotating frame, $\boldsymbol{v}$ is the absolute velocity viewed from the stationary frame, and $\boldsymbol{u}_{\mathrm{r}}$ is the "whirl" velocity due to the moving frame given by

$$\boldsymbol{u}_{\mathrm{r}} = \boldsymbol{\omega} \times \boldsymbol{r} \tag{9}$$

When the equation of motion is transferred to the rotating reference frame, the continuity and momentum equations respectively become

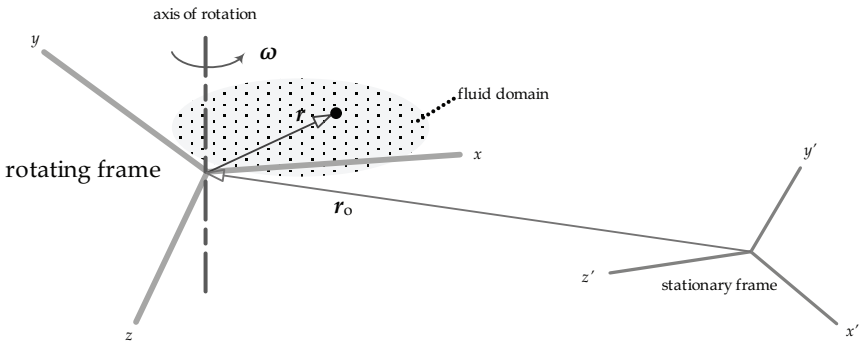


Fig. 1. The rotating and stationary frames

$$\frac{\partial \rho}{\partial t} = -\nabla . \rho \boldsymbol{v}_{\mathrm{r}} \tag{10}$$

and

$$\frac{\partial (\rho \boldsymbol{v}_{\mathrm{r}})}{\partial t} = -\nabla . \left( \rho \boldsymbol{v}_{\mathrm{r}} \boldsymbol{v}_{\mathrm{r}} \right) - \rho \left( 2\boldsymbol{\omega} \times \boldsymbol{v}_{\mathrm{r}} + \boldsymbol{\omega} \times \boldsymbol{\omega} \times \boldsymbol{r} \right) - \nabla p + \nabla . \boldsymbol{\tau}_{\mathrm{r}} + \rho \boldsymbol{g} + \boldsymbol{F} \tag{11}$$

where $\left( 2\boldsymbol{\omega} \times \boldsymbol{v}_{\mathrm{r}} \right)$ and $\left( \boldsymbol{\omega} \times \boldsymbol{\omega} \times \boldsymbol{r} \right)$ respectively are the Coriolis and centripetal accelerations, and $\boldsymbol{\tau}_{\mathrm{r}}$ is the stress tensor based on $\boldsymbol{v}_{\mathrm{r}}$. The momentum equation for the absolute velocity is

$$\frac{\partial (\rho \boldsymbol{v})}{\partial t} = -\nabla . \left( \rho \boldsymbol{v}_{r} \boldsymbol{v} \right) - \rho \left( \boldsymbol{\omega} \times \boldsymbol{v} \right) - \nabla p + \nabla . \boldsymbol{\tau} + \rho \boldsymbol{g} + \boldsymbol{F} \tag{12}$$

where $\left( \boldsymbol{\omega} \times \boldsymbol{v} \right)$ embodies the Coriolis and centripetal accelerations. The MRF method is recommended for simulations in which impeller-baffle interaction is weak. With this method, the rotating frame section extends radially from the centerline or shaft out to a position that is about midway between the blade's tip and baffles. Axially, that section extends above and below the impeller. In the circumferential direction, the section extends around the entire vessel.

**The sliding mesh method** is the most rigorous and informative solution method for stirred tank simulations. It provides a time-dependent description of the periodic interaction between impellers and baffles (Luo et al., 1993). The grid surrounding the rotating components physically moves during the simulations, while the stationary grid remains static. The velocity of the impeller and shaft relative to the moving mesh region is zero as is the velocity of the tank, baffles, and other internals in the stationary mesh region. The motion of the impeller is realistically modeled because the surrounding grid moves as well, enabling accurate simulation of the impeller-baffle interaction. The motion of the grid is not continuous, but it is in small discrete steps. After each such motion, the set of transport equations is solved in an iterative process until convergence is reached.

**The snapshot method** is based on snapshots of flow in a stirred tank in which the relative position of the impeller and baffles is fixed (Ranade & Dommeti, 1996; Ranade, 2002). The impeller blades are considered as solid walls, and the flow is simulated using stationary

frame in a fixed blade position. Simulations are performed at different blade positions, and the results averaged. Like the MRF method, the entire domain is divided into two regions. In the impeller region, time-dependent terms are approximated in terms of spatial derivatives. In the outer region, the relatively small time derivative terms can be neglected.
Upon comparing numerical predictions obtained from applying different impeller modeling methodologies, several investigators observed that steady state methods such as MRF can

i. provide reasonable predictions to flow field features and power consumption (Jaworski et al., 2001; Bujalski et al., 2002; Kelly & Gigas, 2003; Khopkar et al., 2004; Aubin et al., 2004; Sommerfeld & Decker, 2004; Khopkar et al., 2006), and
ii. save about one-seventh of the CPU-time (Brucato et al., 1998).

## 3. CFD model validation

For the mixing of shear-thinning fluids with yield stress, CFD model validation is typically done by comparing the CFD-predicted power number, and velocity field with the experimental counterparts (Ihejirica & Ein-Mozaffari, 2007; Saeed et al., 2007; Pakzad et al., 2008b; Ein-Mozaffari & Upreti, 2009).
Figure 2 depicts the impeller power number as a function of Reynolds number (Re) for the Lightnin A200 impeller in the mixing of xanthan gum solution, which is a shear-thinning fluid with yield stress (Saeed et al., 2008).

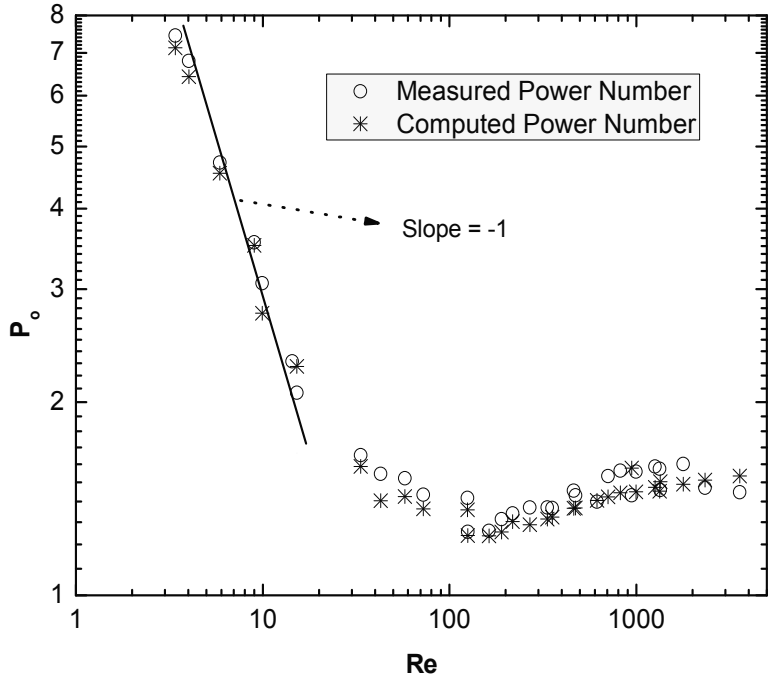


Fig. 2. Power number as a function of Reynolds number for the Lightnin A200 impeller

The power number is given by the following equation:

$$P_0 = \frac{P}{\rho N^3 D^5} \tag{13}$$

where $P$, $N$, D, and $\rho$ respectively are power, impeller speed, impeller diameter, and fluid density. The Reynolds number is given by

$$\mathrm{Re} = \frac{\rho N^2 D^2 k_s}{\tau_y + k(k_s N)^n} \tag{14}$$

where $\tau_y$ is related to the average shear rate $\dot{\gamma}$ via the Herschel-Bulkley model as

$$\eta = \frac{\tau}{\dot{\gamma}} = \frac{\tau}{k_s N} = \frac{\tau_y + k(k_s N)^n}{k_s N} \tag{15}$$

and the average $\dot{\gamma}$ is given as follows (Metzner & Otto, 1957):

$$\dot{\gamma} = k_s N \tag{16}$$

The results illustrated in Figure 2 show a very good agreement between calculated power number and the experimentally determined values. At Re < 10 (the laminar regime), power number is inversely proportional to Re.

**Comparison of velocity field** To experimentally determine the velocity field, Ultrasonic Doppler Velocimetry (UDV) has been effectively used in the mixing of shear-thinning fluids with yield stress using different impellers (Ein-Mozaffari et al., 2007a, Ihejirika & Ein-Mozaffari, 2007; Saeed et al., 2008; Pakzad et al., 2008b; Ein-Mozaffari & Upreti, 2009). UDV is a non-invasive method of measuring velocity profiles (Asher, 1983), which is very useful in industrial applications. It utilizes pulsed ultrasonic echography together with the detection of the instantaneous frequency of the detected echo to obtain spatial information, and Doppler shift frequency. The latter provides the magnitude and direction of the velocity vector (Takeda, 1991). Compared to the conventional Doppler anemometry, and particle image velocimetry, UDV offers the following benefits (Takeda, 1986,1995; Williams, 1986; McClements, 1990): (i) more efficient flow mapping, (ii) applicability to opaque liquids, and (iii) the recording of the spatio-temporal velocity.

Figure 3 shows a comparison of the velocity data (axial and radial velocities) from the UDV measurements with the velocities computed using CFD for the Scaba 6SRGT impeller in the mixing of xanthan gum solution, which is an opaque shear-thinning fluid possessing yield stress (Pakzad et al., 2008b). It is observed that the CFD calculations pick up the features of the flow field, and the computed velocities agree well with the measured data.

## 4. Estimation of the cavern size

As mentioned earlier, the mixing of shear-thinning fluids with yield stress results in the formation of a well-mixed region called cavern around the impeller, and regions of stagnant or slow moving fluids elsewhere in the vessel.

The term cavern was introduced by Wichterle and Wein (1975) in the investigation of mixing of extremely shear thinning suspensions of finely divided particulate solids.

Solomon et al. (1981) modeled a spherical cavern assuming that the power dissipated by the impeller is transmitted through the fluid to the cavern wall, the shear stress at the cavern

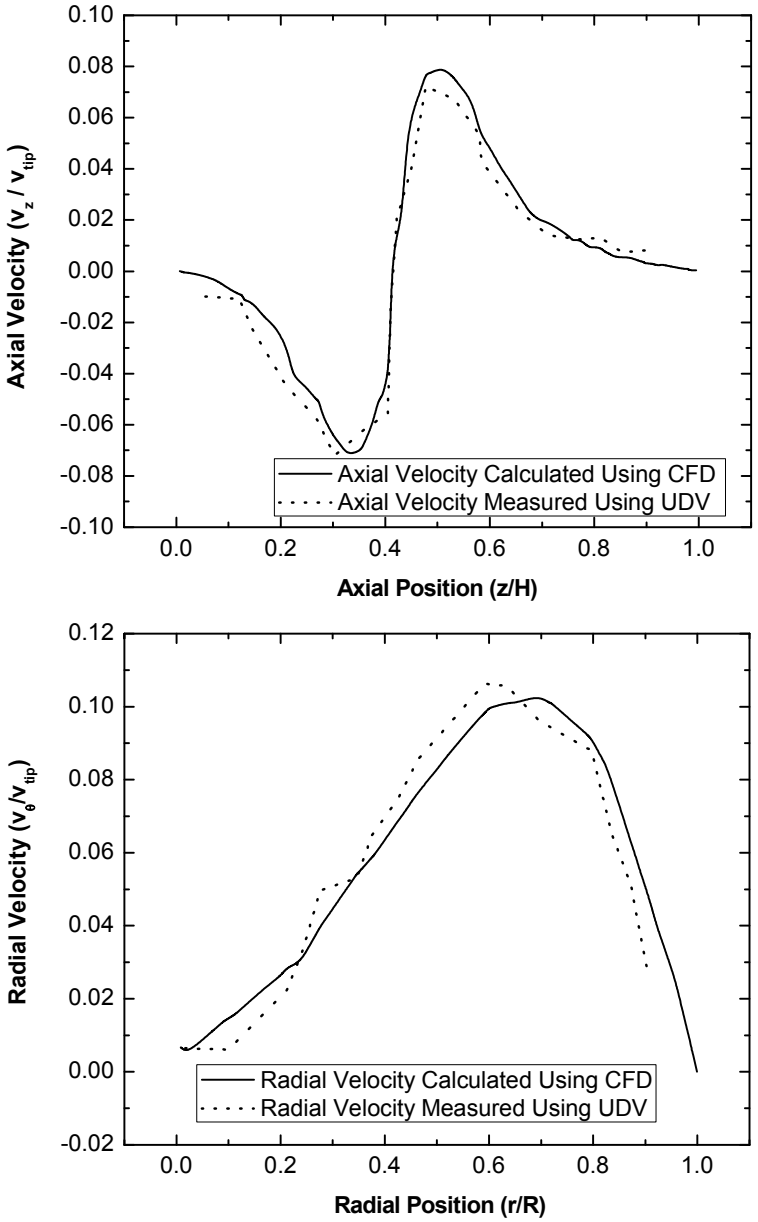


Fig. 3. (a) axial and (b) radial velocity profiles generated by the Scaba 6SRGT impeller at Re = 80.9

boundary equals the fluid yield stress, and the predominant motion of the fluid within the cavern is tangential. Elson et al. (1986, 1988) modified that for a more appropriate cylindrical cavern. A cylindrical cavern model was also proposed by Hirata & Aoshima (1994,1996). Amanullah et al. (1998) developed a mathematical model for a torus-shaped cavern. This model considers the total momentum imparted by the impeller as the sum of both tangential and axial shear components transported to the cavern boundary by the pumping action of the impeller. Wilkens et al. (2005) empirically developed an elliptical torus model neglecting the axial force to predict the cavern diameter and height, and using the yield stress of the fluid to define the cavern boundary. Table 2 lists these cavern models.

| Model | Reference |
|---|---|
| $\left(\frac{D_c}{D}\right)^2 \propto \frac{\rho N^2 D^2}{\tau_y}$ | Witchterle and Wein (1975, 1981) |
| $\left(\frac{D_c}{D}\right)^3 = \left(\frac{4P_0}{\pi^3}\right)\left(\frac{\rho N^2 D^2}{\tau_y}\right) = \frac{4}{\pi^3} P_0 \mathrm{Re}_y$ | Solomon et al. (1981) |
| $\left(\frac{D_c}{D}\right)^3 = \left(\frac{1.36 P_o}{\pi^2}\right)\left(\frac{\rho N^2 D^2}{\tau_y}\right) = \frac{1.36}{\pi^2} P_o \mathrm{Re}_y$ | Elson et al. (1986) |
| $\left(\frac{D_c}{D}\right)^3 = \frac{P_0 \mathrm{Re}_y}{\left(H_c / D_c + 1/3\right)\pi^2}$ | Elson (1988) |
| $\left(\frac{D_c}{D}\right)^3 = \left(\frac{4\alpha^2 P_0}{\pi}\right)\left(\frac{\mathrm{Re}_y{}^2}{\mathrm{Re}}\right)\left(\frac{H_c}{D_c}\right)$ | Hirata & Aoshima (1995, 1996) |
| $\left(\frac{D_c}{D}\right)^2 = \frac{1}{\pi}\left(\frac{\rho N^2 D^2}{\tau_y}\right)\sqrt{N_f^2 + \left(\frac{4P_0}{3\pi}\right)^2}$ | Amanullah et al. (1998) |
| $D_c = \alpha\left(\frac{P_0 N^2 D^5}{2\pi}\right)^{1/3}, \; H_c = \beta\left(\frac{P_0 N^2 D^5}{2\pi}\right)^{1/3}$ | Wilkens et al. (2005) |

Table 2. Various models proposed for cavern size

The contours of velocity magnitude generated CFD simulations can be used to analyze the formation of cavern around the impeller (Pakzad et al., 2008a; Saeed et al., 2008; Pakzad et al, 2008b; Ein-Mozaffari & Upreti, 2009). The boundary velocity for the cavern is considered to be $0.01 v_{tip}$, where $v_{tip}$ is the impeller tip velocity. Thus, the fluid velocity is greater than $0.01 v_{tip}$ within the cavern, and less than $0.01 v_{tip}$ in the surrounding. Pakzad et al. (2008a) employed CFD to measure the size of the cavern generated around the Scaba 6SRGT impeller in the mixing of xanthan gum solution. Figure 4 shows the formation of cavern around the Scaba 6SRGT impeller for Re equal to 30 and 110 (Pakzad, 2007). To validate the CFD results for the cavern size, Pakzad et al. (2008a) used the Electrical Resistance Tomography (ERT) to measure the cavern diameter. ERT is a non-intrusive technique to interrogate the three dimensional concentration fields inside the mixing tanks. It enables effective measurements of the homogeneity and flow pattern inside the mixing vessel.

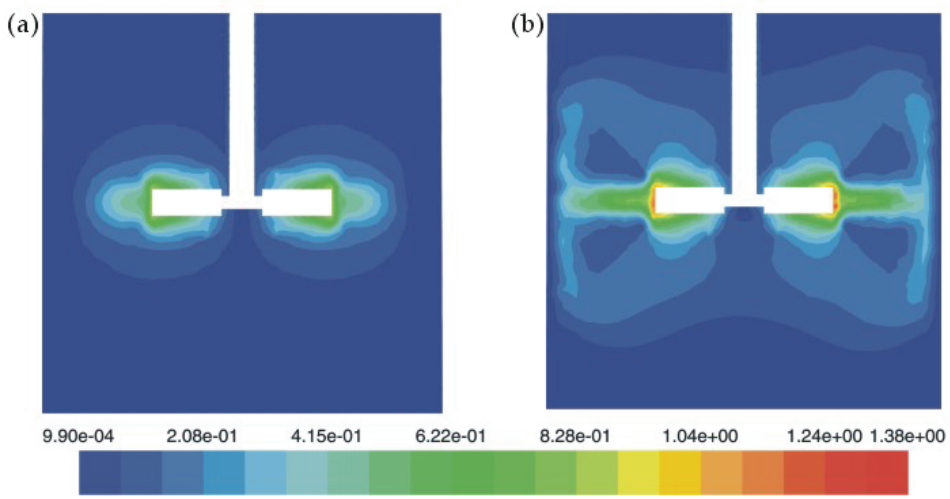


Fig. 4. Cavern formation at (a) Re = 30 and (b) Re = 110 around the Scaba 6SRGT impeller in the mixing of xanthan gum solution

Based on the CFD and ERT results, it was observed that the cavern can be represented by a right circular cylinder. Figure 5 shows the dimensionless cavern diameter ($D_c/D$) versus dimensionless $P_0\mathrm{Re}_y$ for the Scaba 6SRGT impeller. These results show good agreement between calculated cavern diameter using CFD, and the experimentally counterpart

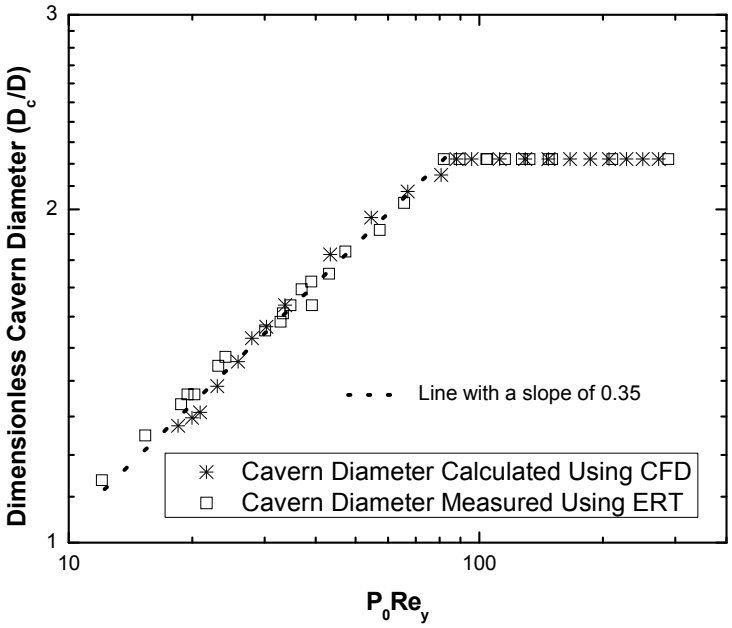


Fig. 5. Cavern diameter as a function of $P_0\mathrm{Re}_y$ for the Scaba 6SRGT impeller

determined using ERT. It can be seen that for $P_0\mathrm{Re}_y$ greater than 80, the cavern reached the vessel walls ($D_c = T$) and $D_c/D$ remained constant. The slope of the line was 0.35 for $P_0\mathrm{Re}_y$ less than 80.
The cylindrical model (Elson, 1988) predicts a theoretical slope of 0.33 from a log-log plot of $D_c/D$ versus $P_0\mathrm{Re}_y$ (see Table 2). Thus, the CFD predictions show a good agreement with the Elson model as well. Further, Pakzad et al. (2008a) found that the ratio of the cavern height $H_c$ to $D_c$ stayed at 0.48 until the cavern reached the tank wall with $D_c = T$. After that happened, the height of the cavern increased with the impeller speed such that

$$\frac{H_C}{D_C} \propto N^{0.58} \tag{17}$$

This result is in good agreement with that reported by Galindo & Nienow (1993) for the Scaba 6SRGT impeller.
In addition, Ein-Mozaffari & Upreti (2009) also used CFD simulations to analyze the shape and the size of cavern generated around three axial-flow impellers: marine propeller, pitched blade turbine, and Lightnin A310 impeller.
Their CFD results were in good agreement with those reported by Galindo & Nienow (1992) for the axial-flow Lightnin A315 impeller.

## 5. Calculation of impeller flow number

The rotary motion of the impeller has a pumping effect: the liquid is drawn towards the impeller and then pumped away from it, with the outgoing flow having a predominant radial, axial, or an intermediate direction. The high-velocity outgoing flow entrains the neighboring liquid into motion, thus the overall circulating liquid combines both the pumped out and the entrained liquid.
In order to assess the pumping capacity of the impeller at different operating conditions, the impeller flow number and the circulation number must be evaluated. Saeed et al. (2009) used CFD to calculate the flow and circulation numbers for three axial-flow impellers in the mixing of a shear-thinning fluid with yield stress. The pumping flowrate encompassing the impeller swept volume is given by (Mishra et al., 1998)

$$Q_P = 2\pi \int_0^{D/2} \left(rv_z\right)\Big|_{z_1} \mathrm{d}r + \pi D \int_{z_1}^{z_2} v_r\Big|_{D/2} \mathrm{d}z \tag{18}$$

where $D$, $v_r$ and $v_z$ respectively are impeller diameter, radial velocity, and axial velocity; and $z_1$ and $z_2$ are the boundaries of the impeller-swept volume in the axial direction. The second term in Equation (18) is negligible for the axial flow impellers (Patwardhan & Joshi, 1999; Kumaresan & Joshi, 2006). Thus, the flow number (Fl) can be estimated for axial flow impellers from the following equation using $Q_P$:

$$\mathrm{Fl} = \frac{Q_P}{ND^3} = \frac{2\pi}{ND^3} \int_0^{D/2} rv_z \mathrm{d}r \tag{19}$$

Saeed et al. (2008) have utilized the axial velocities obtained using CFD to calculate the flow numbers for Lightnin A100, A200, and A310 impellers (Table 3).

| | Impeller | | |
|---|---|---|---|
| **Parameter** | **A100** | **A200** | **A310** |
| Power Number | 0.66 | 1.16 | 0.40 |
| Flow Number | 0.42 | 0.47 | 0.37 |
| Circulation Number | 0.89 | 0.92 | 0.77 |
| Pumping Efficiency | 0.636 | 0.405 | 0.925 |
| Circulation Efficiency | 1.348 | 0.793 | 2.139 |

Table 3. Specifications of three axial-flow impellers (Saeed et al. 2008)

It must be mentioned that the flow numbers shown in Table 3 for xanthan gum solution are less than those reported in literature for water. Other researchers have reported that the impeller flow number is a function of the rheologial properties of the fluid (e.g. viscosity and yield stress). Jaworski & Nienow (1993) found that the impeller flow number for carboxymethyl cellulose solutions was lower than that for water, and Mavros et al. (1996) showed that as liquid viscosity increased the impeller flow rate decreased. Using measured velocity profiles across the impeller, Ein-Mozaffari et al. (2007a) found that the pulp suspension yield stress increased (by increasing fibre mass concentration, or fibre length) with the decrease in Fl.

The circulation number for an axial flow impeller is defined as follows (Ranade & Dommeti, 1996; Aubin et al., 2001):

$$\mathrm{Fl_c} = \frac{Q_\mathrm{c}}{ND^3} = \frac{2\pi}{ND^3}\int_0^{r|_{v_z}} \left(rv_z\right)\Big|_{z_1} \mathrm{d}r \tag{20}$$

where $Q_c$ is overall liquid circulation generated in impeller swept volume and includes flow entrained by impeller discharge, and $r|_{v_z}$ is the radius where the axial flow velocity reverses from downward to upward direction in the downward pumping impellers. Table 3 shows the circulation numbers calculated using CFD for three axial flow impellers in the mixing of xanthan gum solution (Saeed, 2007; Saeed et al., 2008).

The impeller pumping efficiency ($\eta_\mathrm{P}$) and circulation efficiency ($\eta_c$) can be used to compare the performances of the different impellers in the mixing of shear-thinning fluids possessing yield stress (Mishra et al, 1998; Aubin et al., 2001):

$$\eta_\mathrm{P} = \mathrm{Fl} / P_0 \tag{21}$$

$$\eta_\mathrm{c} = \mathrm{Fl_c} / P_0 \tag{22}$$

The pumping and circulation efficiencies computed by CFD for the Lightnin A100, A200, and A310 impellers in the mixing of the xanthan gum solution are listed in Table 3 (Saeed, 2007). These results show that the A310 impeller is superior to the rest.

Pakzad et al. (2008b) employed CFD to measure the impeller flow number as a function of Reynolds number for a radial-flow impeller used for the mixing of a shear-thinning fluid with yield stress. For a radial-flow impeller, the first term in Equation (18) is negligible. Thus, the impeller flow number for a radial-flow impeller is defined by:

$$\mathrm{Fl} = \frac{Q_\mathrm{P}}{ND^3} = \frac{\pi}{ND^2}\int_{z_1}^{z_2} v_r\big|_{D/2}\mathrm{d}z \tag{23}$$

Figure 6 depicts the impeller flow number versus Re for the radial-flow Scaba 6SRGT impeller utilized for the mixing of the xanthan gum solution (Pakzad et al., 2008b).

## 6. Analysis of mixing time

Mixing time is a key variable, which provides a powerful way to evaluate mixing effectiveness, and compare mixing systems (Paul et al, 2004). It is defined as the time elapsed between the instant when a tracer of similar rheological properties as the bulk fluid is added, and the instant at which the vessel contents attain a specified degree of uniformity (Harnby et al., 1997); usually the expected equilibrium tracer concentration.
If there is no tracer initially present in the vessel, then the mixing time, $t_m$, can be defined as the time between tracer addition to the time when

$$\frac{|C - C_\infty|}{C_\infty} = m \tag{24}$$

where $C$ is the tracer concentration, $C_\infty$ is its equilibrium value, and $m$ is the maximum acceptable deviation from homogeneous conditions (Ihejirica & Ein-Mozaffari, 2007).

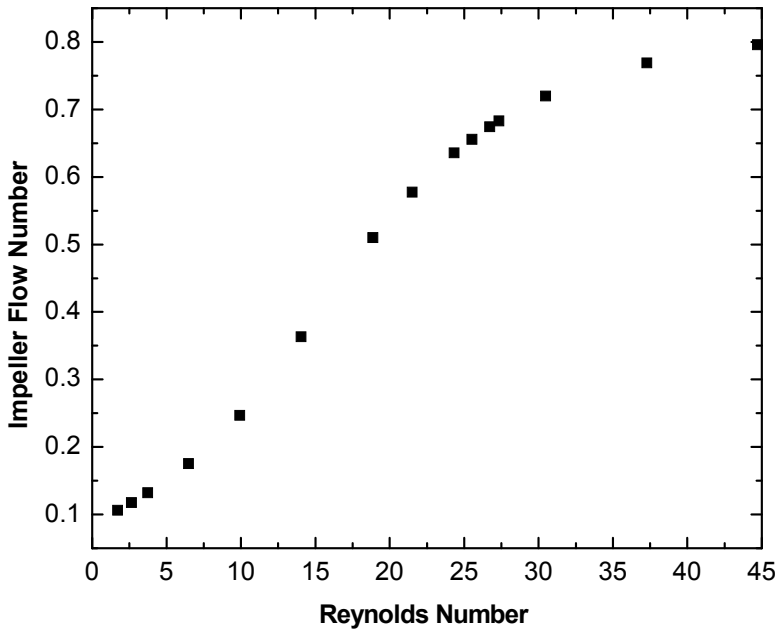


Fig. 6. Impeller flow number as a function of Re for the mixing of the xanthan gum solution with the Scaba 6SRGT impeller

The mixing time can be obtained through experiments as well as CFD. Some of the experimental methods are not applicable for the opaque fluids, and the probe techniques have the disadvantage of affecting the flow pattern inside the tank. The advantage of CFD is that it provides comprehensive data not easily obtained from the experimental techniques.

To simulate the mixing times after the convergence of the flow field through CFD, the unsteady state transport of an inert tracer superimposed on the calculated flow field is monitored until complete homogenization is achieved. Assuming tracer distribution by convection and diffusion, the unsteady distribution of the tracer is determined by solving the species transport equation (Ein-Mozaffari & Upreti, 2009)

$$\frac{\partial}{\partial t}(\rho m_t) = -\nabla \cdot (\rho v m_t) + \nabla \cdot (\Gamma \nabla m_t) \tag{25}$$

where $m_t$ is the mass fraction of the tracer species, $v$ is the mean velocity vector, and $\Gamma$ is the molecular diffusivity. $\Gamma$ has negligible effect on the tracer distribution possibly because the insignificant contribution of molecular diffusion to the overall tracer dispersion (Montante et al., 2005). Some researchers also find that the effect of the molecular diffusivity is negligible in the mixing of non-Newtonian fluids in the laminar regime (Saeed et al., 2007; Ihejirika & Ein-Mozaffari, 2007; Ein-Mozaffari & Upreti, 2009).

Pakzad (2007) used CFD to predict the mixing time for the agitation of the shear-thinning fluid possessing yield stress with a Scaba 6SRGT impeller. The tracer concentration was monitored at four locations as depicted in Figure 7. The tracer concentration $C$ was normalized using the tracer concentration at time equal to infinity ($C_\infty$), which represents a perfectly mixed condition, to give a normalized tracer concentration ($C / C_\infty$). The mixing system was considered homogeneous when the normalized tracer concentrations at all four monitoring points were equal to one. The mixing time was defined as the time required for the normalized tracer concentrations at all four monitoring points to reach 95% of the steady state value (Figure 8).

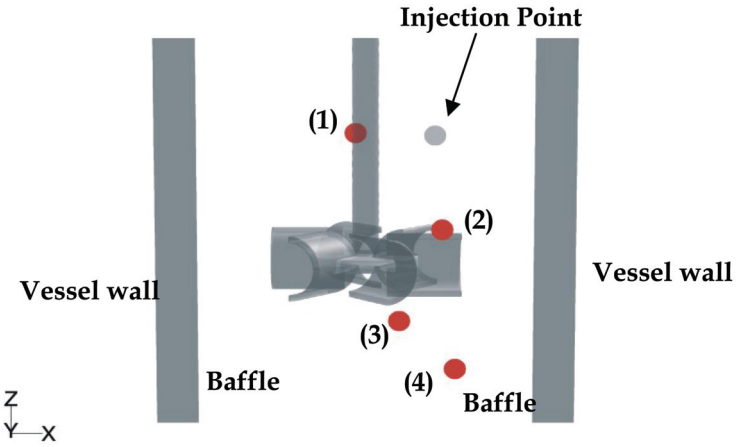


Fig. 7. Injection point and four monitoring locations (1, 2, 3, and 4) used to predict $t_m$

To evaluate the accuracy of this technique, Pakzad (2007) compared the mixing time values computed by the CFD model with those measured through electrical resistance tomography (ERT) for xanthan gum solution. Figure 9 shows that although the CFD model underpredicted the mixing time for the shear-thinning fluid possessing yield stress, there was a reasonable agreement between the CFD and ERT results.

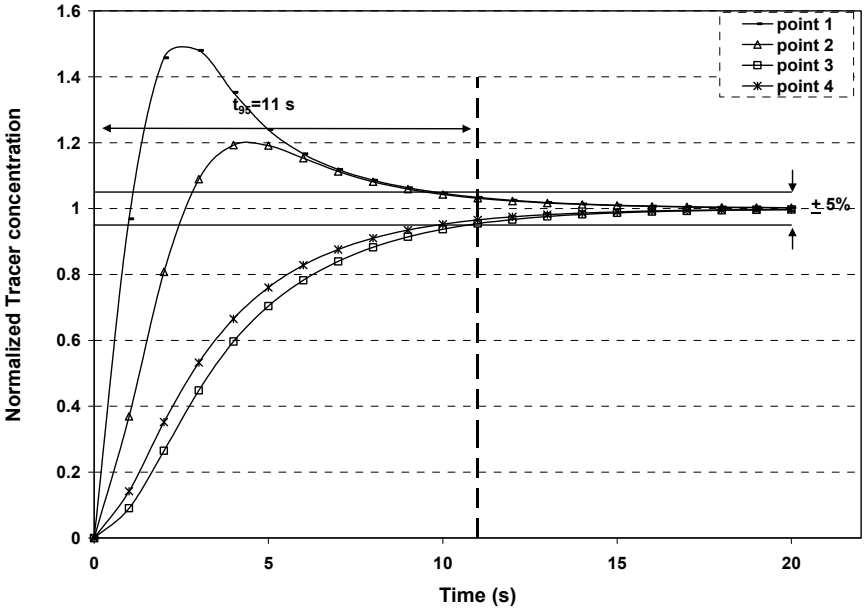


Fig. 8. Normalized tracer concentration versus time for four monitoring points

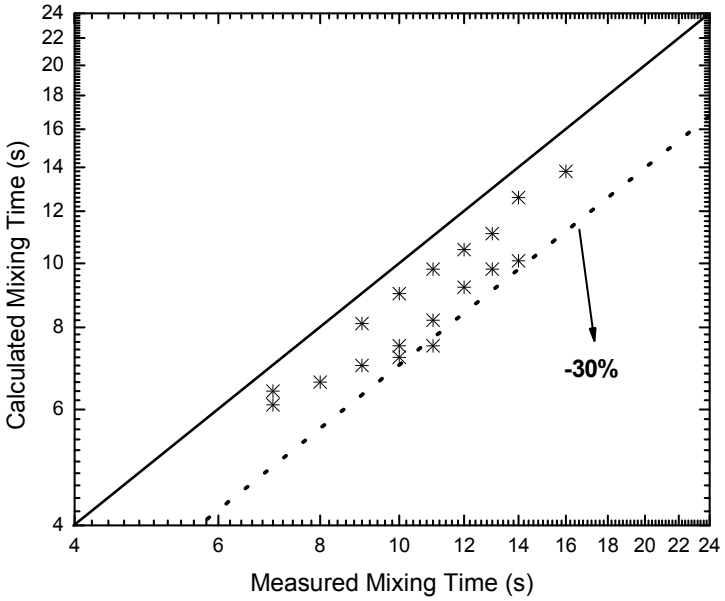


Fig. 9. Calculated versus measured mixing time for the xanthan gum solution agitated with a Scaba 6SRGT impeller

Ihejirika & Ein-Mozaffari (2007) utilized CFD technique to investigate the effect of impeller pumping direction on the mixing performance for a pseudoplastic fluid with yield stress agitated in a cylindrical tank equipped with a helical ribbon impeller. To achieve this goal, they used the following two parameters: (i) the dimensionless mixing time $Nt_m$, and (ii) the performance rating given by $Pt_m^2/(\eta D^3)$. While $Nt_m$ represents the number of revolutions of the agitator required to achieve a specified level of homogeneity (Kappel, 1979; Delaplace et al., 2000), $Pt_m^2/(\eta D^3)$ is a function of the mixing time Reynolds number given by $D^2\rho/(\eta t_m)$ (Tatterson, 1991).

The authors showed that $Nt_m$ was a constant for a specific geometry of close clearance impellers such as helical ribbons in the laminar flow regime. The average $Nt_m$ value for the helical ribbon pumping upwards was 27 as compared to an average value of 33 in the downward pumping mode. From the definition of $Nt_m$, it is clear that in pumping downwards, the impeller requires more rotations to achieve the desired level of uniformity. This translates into longer mixing times.

The performance rating $Pt_m^2/(\eta D^3)$ represents energy divided by the volumetric performance of the mixing equipment. It allows the decision as to which impeller exhibits the lowest specific power consumption in mixing a given fluid with required mixing intensity in a vessel of given volume. Figure 10 depicts the performance rating versus the mixing time Reynolds number (Ihejirica & Ein-Mozaffari, 2007) obtained for a helical ribbon impeller used for the agitation of xanthan gum solution. It can be seen that the helical ribbon impeller pumping upwards is the more efficient mode of operation because this pumping direction gives lower values of $Pt_m^2/(\eta D^3)$ in the entire operating flow regime.

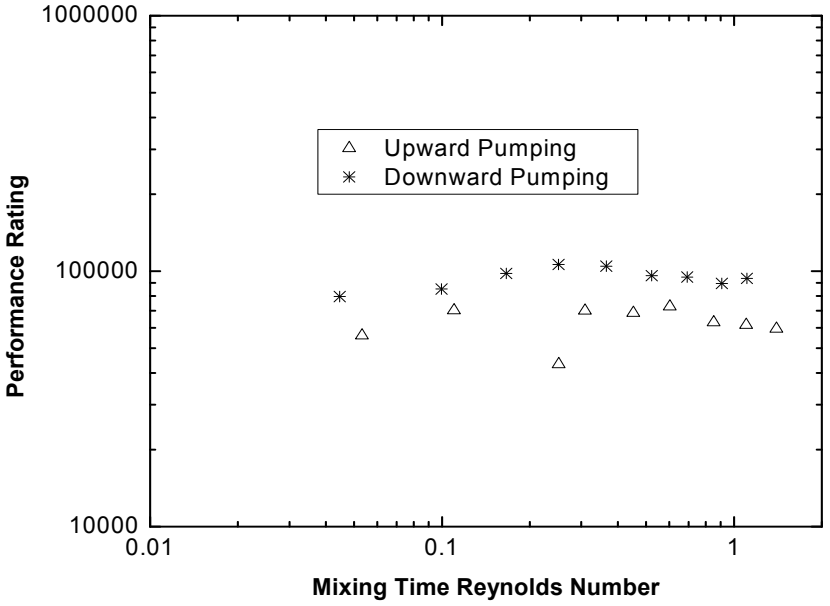


Fig. 10. Performance rating versus mixing time Reynolds number for helical ribbon impeller

Saeed et al. (2007) employed the CFD technique to estimate the mixing time in the mixing of the pulp suspension with a side-entering Lightnin A310 impeller in a rectangular chest. Pulp suspension is a shear-thinning fluid possessing yield stress whose rheology was approximated using Herschel-Bulkley model. The authors showed that the mixing time computed from CFD simulation was the following function of the impeller momentum flux (Figure 11):

$$t_{\mathrm{m}} = 17.21(N^2D^4)^{-1.03} \tag{26}$$

The impeller momentum flux, which is proportional to $N^2D^4$, was introduced by Fox & Gex (1956) for mixing time correlation and used by Yackel (1990) for designing agitated pulp stock chests. This parameter was correlated with the mixing time ($t_{\mathrm{m}}$) of pulp suspension by Ein-Mozaffari et al. (2003).

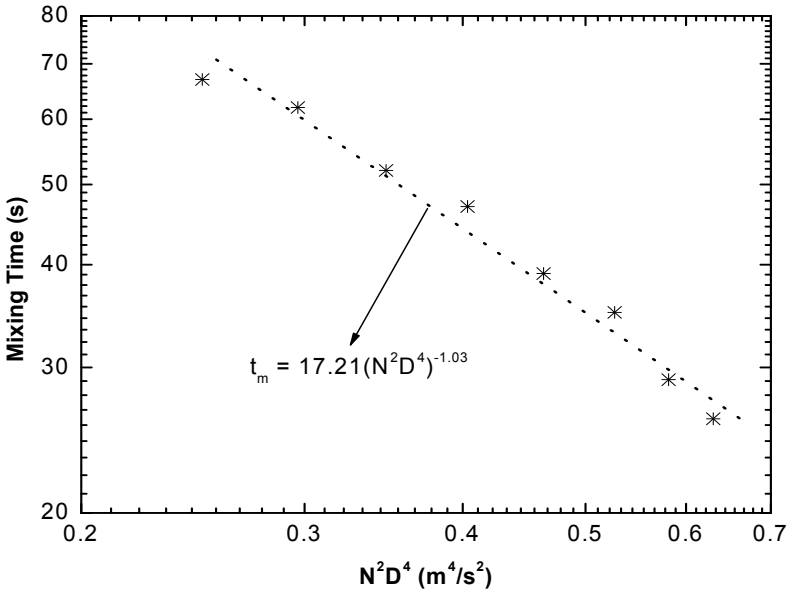


Fig. 11. Mixing time as a function of $N^2D^4$ for pulp suspension agitated in a rectangular chest equipped with a side-entering Lightnin A310 impeller

Ein-Mozaffari & Upreti (2009) utilized CFD to evaluate the performances of three axial-flow impellers (pitched blade turbine (PBT), marine propeller, and Lightnin A310) in the mixing of shear-thinning fluids with yield stress. To achieve this goal, they calculated mixing time and impeller specific power (power/mass) through CFD. Figure 12 illustrates mixing time versus specific power for these three impellers used for the mixing of xanthan gum solution. It can be seen that for a given power input, the A310 impeller achieved homogenization in the shortest time. The results also show that the pitched blade turbine (PBT) gives longer mixing times compared to the marine propeller, and A310 impeller at a specific power input. Thus, in order to minimize the mixing time, an impeller with a large pumping efficiency such as the A310 impeller should be chosen for the mixing of shear-thinning fluids with yield stress.

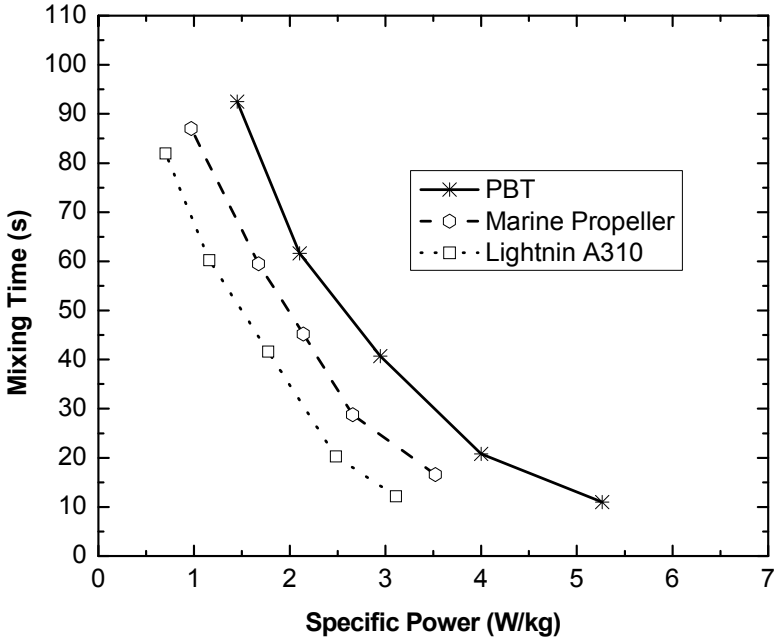


Fig. 12. Mixing time versus specific power for three axial-flow impellers used for the agitation of xanthan gum solution

## 7. Analysis of the continuous-flow mixing of shear-thinning fluids possessing yield stress

Continuous mixing has numerous advantages over the batch mixing since continuous operations allow high production rates, enhanced process control, and reduce operation times by eliminating pump-out, filling and between-cycle cleaning. Continuous-flow mixing is a vital component to many processes including polymerization, fermentation, waste water treatment, and pulp and paper manufacturing. Shear thinning fluids with yield stress are commonly encountered in the aforementioned processes (Saeed & Ein-Mozaffari, 2008; Saeed et al., 2008).

Continuous-flow mixers have traditionally been designed based upon ideal flow assumption (Levenspiel, 1998). However, the complex rheology displayed by the non-Newtonian fluids can create considerable deviation from ideal mixing. Dynamic tests conducted on those mixing vessels show that the non-ideal flow such as channelling, recirculation, and dead zones significantly affect the performance of the continuous mixing processes (Ein-Mozaffari et al., 2003b, 2004a, and 2004b). A dynamic model incorporating the effect of these non-ideal flows was proposed by Ein-Mozaffari (2002) for continuous-flow mixing processes. This model allows for two parallel flow paths through the mixing vessel:

i. the channelling zone comprising the first order transfer function with a delay, and
ii. the mixing zone comprising the first order transfer function with a delay, and feedback for recirculation (Figure 13).

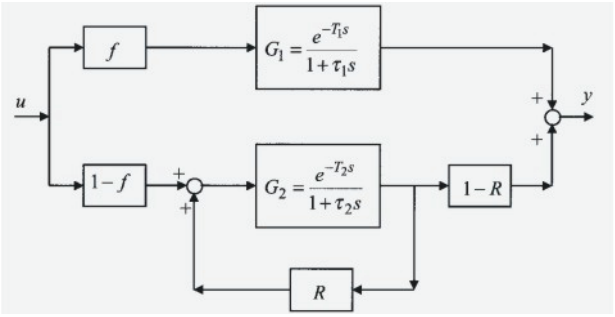


Fig. 13. Block diagram of the continuous-flow mixing processes

The combined transfer function for flow paths in a continuous time domain can be expressed mathematically as follows:

$$G = \frac{f\, e^{-T_1 s}}{1+\tau_1 s} + \frac{(1-f)\,(1-R)\, e^{-T_2 s}\left(1+\tau_2 s\right)^{-1}}{1-R\, e^{T_2 s}\left(1+\tau_2 s\right)^{-1}} \tag{27}$$

where $G$ is the transfer function of the vessel, $f$ is the portion of the fluid channelled in the mixing tank, and $R$ is the portion of the fluid recirculated within the mixing vessel. $\tau_1$ and $\tau_2$ are the time constants for the channelling and mixing zones. $T_1$ and $T_2$ are the time delays for the channelling and agitated zone, respectively.

The identification experiment is performed through exciting the system by the frequency-modulated random binary signal and observing the input and output signals over a time interval (Ein-Mozaffari, 2003b). By measuring the input-output signals of the mixing vessel, the dynamic model parameters can be estimated using a numerical method developed by Kammer et al. (2005). Two distinct stages were used for the identification in this method: an efficient but less accurate least squares minimization for the optimal delays followed by an accurate gradient search for all parameters. Although this algorithm did not ensure convergence to the global minimum, a Monte Carlo simulation showed very encouraging results. Later on, a hybrid genetic algorithm bridged that gap and identified the mixing parameters with high accuracies (Upreti & Ein-Mozaffari, 2006; Patel et al., 2008).

Since the dynamic tests conducted on both lab-scale and industrial-scale mixing vessels are costly and time-consuming, Saeed (2007) and Saeed et al. (2008) utilized CFD to study the dynamic behavior of the continuous-flow mixing processes. Fluent was used to simulate xanthan gum flow within the continuous mixing vessel under steady state. Boundary conditions imposed on the system included: (i) non-slip at the vessel wall and baffles, (ii) zero normal velocity at the free surface, (iii) inflow boundary condition for vessel inlet, defining inlet velocity from the volumetric flow rate of the feed, i.e. $v = 4Q/(\pi d^2)$ where $Q$ is volumetric flow rate, and $d$ is the inlet diameter of the pipe; and (iv) outflow boundary condition for vessel outlet, implying zero normal diffusive flux for all flow variables (Versteeg & Malalasekera, 2007).

To simulate the dynamic test after the convergence of the flow field through CFD, a user defined function (UDF), written in C programming language, was linked to Fluent solver (Saeed, 2007). The UDF defines the time at which the tracer was continuously injected to the mixing vessel. The UDF was linked to the inlet as a boundary condition that specifies the

tracer concentration in the inlet stream. Outlet concentration was recorded for comparison with experimental data later. Mass fraction of tracer in UDF was set to the values analogous to the conductivity of the random binary excitation signal used in the experimental work (Saeed et al., 2008). In order to evaluate the CFD ability to predict the dynamic behavior of the continuous-flow mixers, experimental and CFD input-output conductivity curves for tracer injections were compared against each other in Figure 14 (Saeed, 2007; Saeed et al., 2008).

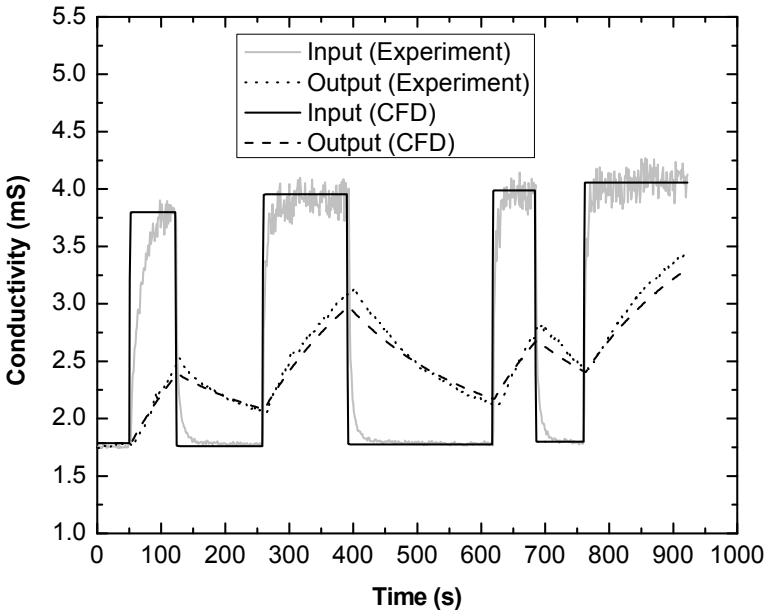


Fig. 14. Input and output signals in flow situations containing insignificant channelling

The noise associated with measured input signals was excluded from input signals used in CFD simulations. The output response predicted by CFD demonstrated good agreement with the experimental response. However, the authors observed that the signal output computed using CFD deviated from measured output in flow situations containing significant channelling (Figure 15). Similar observations were reported for the mixing of pulp suspension in a rectangular chest equipped with a side-entering impeller (Ford et al., 2006).

Two parameters have been widely used to quantify the performance of the continuous-flow mixing process: (i) the extent of channelling $f$ in the vessel, and (ii) and the ratio of the fully-mixed volume $V_{\mathrm{fm}}$ to the total volume $V_{\mathrm{t}}$ of the fluid in the mixing tank (Ein-Mozaffari et al., 2004a, 2004b, 2005, 2007b). The fraction of fully-mixed volume is given by

$$\frac{V_{\mathrm{fm}}}{V_{\mathrm{t}}} = \frac{Q\tau_2\left(1-f\right)}{V_{\mathrm{t}}} \tag{28}$$

where $Q$ is the solution flow rate through the mixing vessel. Table 4 compares CFD and experimental results for the extent of channelling and fully-mixed volume at two different

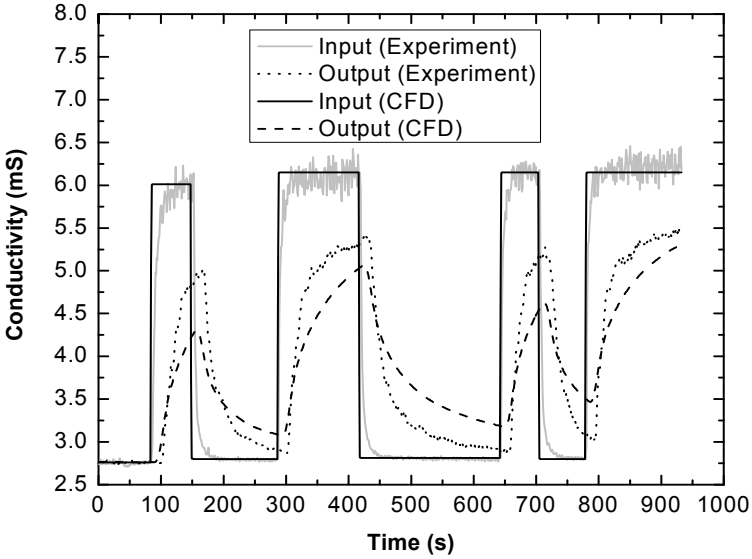


Fig. 15. Input – output signals in flow situations containing significant channeling

xanthan gum concentrations (Saeed, 2007; Saeed et al., 2008). It can be seen that the CFD results are in a good agreement with the experimentally determined values.

Saeed et al. (2008) used CFD to investigate the effect of impeller type on the dynamic behavior of the continuous-flow mixing of xanthan gum solution. Table 5 summarizes the extent of channelling and fully mixed volume for three axial-flow impellers (Lightnin A100, A200, and A310). A comparison of CFD and experimental data in this table reveals that the A310 impeller was able to reduce channelling and increase fully-mixed volume in the vessel. They concluded that in order to minimize the extent of channelling and dead volume in a continuous-flow mixer, an impeller with a large pumping and circulation efficiency such as A310 should be chosen.

| | **0.5% xanthan gum** | | **1.5% xanthan gum** | |
|---|---|---|---|---|
| **Parameter** | **Experiment** | **CFD** | **Experiment** | **CFD** |
| $f$ | 0.09 | 0.07 | 0.18 | 0.15 |
| $V_{fm} / V_t$ | 0.91 | 0.94 | 0.83 | 0.87 |

Table 4. Extent of channelling and fully-mixed volume at two different xanthan gum concentrations

| | $f$ | | $V_{fm} / V_t$ | |
|---|---|---|---|---|
| **Impeller** | **Experiment** | **CFD** | **Experiment** | **CFD** |
| A100 | 0.17 | 0.13 | 0.91 | 0.98 |
| A200 | 0.19 | 0.15 | 0.88 | 0.93 |
| A310 | 0.15 | 0.10 | 0.97 | 0.98 |

Table 5. Extent of channeling and fully-mixed volume for three axial-flow impellers

Ein-Mozaffari et al.(2005), Saeed & Ein-Mozaffari (2008), and Saeed et al. (2008) explored the effect of cavern formation around the impeller on the dynamic behavior of the continuous-flow mixing of the shear-thinning fluids possessing yield stress. They found that the size of the cavern generated around the impeller has a significant effect on the extent of non-ideal flow in continuous mixing of fluids with yield stress. As the impeller speed increases, the cavern surface moves towards the tank wall and the fluid surface within the mixing vessel.When the cavern does not reach the vessel wall and fluid surface, a high percentage of the feed stream will be channelled easily to the exit without being entrained in the impeller flow. Thus, the continuous-flow mixing system is prone to a high level of non-ideal flow.

## 8. Conclusion

This chapter presented the application of Computational Fluid Dynamics (CFD) along with stat-of-the-art experimental techniques of Ultrasonic Doppler Velocimetry (UDV), and Electrical Resistance Tomography (ERT) to capture the mixing of shear-thinning fluids with yield stress. The mathematical underpinnings of the CFD approach, and the experimental methods were elaborated. To demonstrate the utility of CFD, we included the results of relevant investigations juxtaposing the CFD simulations against the experimental tests of mixing the shear thinning fluids.

## 9. References

Amanullah, A.; Hjorth, S.A. & Nienow, A.W. (1998). A new mathematical model to predict cavern diameters in highly shear thinning, power law liquids using axial flow impellers. *Chem. Eng. Sci.*, Vol. 53, No. 3, 455-469.

Armenante, P.M.; Luo, C.; Chou, C.C.; Fort, I. & Medek, J. (1997). Velocity profiles in a closed, unbaffled vessel: comparison between experimental ldv data and numerical cfd prediction. *Chem. Eng. Sci.*, Vol. 52, No. 20, 3483-3492.

Asher, R.C. (1983). Ultrasonic sensors in the chemical and process industries. *J. Phys. E: Sci. Instrum.*, Vol. 16, No. 10, 959-963.

Aubin, J.; Mavros, P.; Fletcher, D.F.; Bertrand, J. & Xuereb, C. (2001). Effect of axial agitator configuration (up-pumping, down-pumping, reverse-rotation) on flow patterns generated in stirred vessels. *Chem. Eng. Res. Des.*, Vol. 79, No. 8, 845-856.

Aubin, J.; Fletcher, D.F. & Xuereb, C. (2004). Modeling turbulent flow in stirred tanks with cfd: the influence of the modeling approach, turbulent model and numerical scheme. *J. Exp. Thermal Fluid Sci.*, Vol. 28, No. 5, 431-445.

Bird, R.B.; Stewart, W. E. & Lightfoot E.N. (2002). *Transport Phenomena*. John Wiley & Sons, New York.

Brucato, A.; Ciofalo, M.; Grisafi, F. & Micale, G. (1998). Numerical prediction of flow fields in baffled vessels: a comparison of alternative modeling approaches. *Chem. Eng. Sci.*, Vol. 53, No. 21, 3653-3684.

Bujalski, W.; Jaworski, Z. & Nienow, A.W. (2002). CFD study of homogenization with dual rushton turbines - comparison with experimental results: Part II: The multiple reference frame, *Chem. Eng. Res. Des.*, Vol. 80, No. 1, 97-104.

Delaplace, G.; Leuliet, J.C. & Relandeau, V. (2000). Circulation and mixing times for helical ribbon impellers: Review and experiments, *Exp. Fluids*, Vol. 28, 170-182.

Ein-Mozaffari, F. (2002). *Macroscale Mixing and Dynamic Behavior of Agitated Pulp Stock Chests*. Ph.D. Thesis, University of British Columbia, Vancouver.

Ein-Mozaffari, F.; Dumont, G.A. & Bennington, C.P.J. (2003a). Performance and design of agitated pulp stock chests. *Appita J.*, Vol. 56, No. 2, 127-133.

Ein-Mozaffari, F.; Kammer, L.C.; Dumont, G.A. & Bennington, C.P.J. (2003b). Dynamic modeling of agitated pulp stock chests. *TAPPI J.*, Vol. 2, No. 9, 13-17.

Ein-Mozaffari, F.; Kammer, L.C.; Dumont G.A. & Bennington, C.P.J. (2004a). The effect of operating conditions and design parameters on the dynamic behavior of agitated pulp stock chests. *Can. J. Chem. Eng.*, Vol. 82, No. 1, 154-161.

Ein-Mozaffari, F.; Bennington C.P.J. & Dumont, G.A. (2004b). Dynamic mixing in industrial agitated stock chests. *J. Pulp Paper Can.*, Vo. 105, No. 5, 41-45.

Ein-Mozaffari, F; Bennington C.P.J. & Dumont, G.A. (2005). Suspension yield stress and the dynamic response of agitated pulp chests. *Chem. Eng. Sci.*, Vol. 60, No. 8, 2399-2408.

Ein-Mozaffari, F.; Bennington, C.P.J.; Dumont, G.A. & Buckingham, D. (2007a). Measuring flow velocity in pulp suspension mixing using ultrasonic doppler velocimetry. *Chem. Eng. Res. Des.*, No. 85, No. A5, 591-597.

Ein-Mozaffari, F.; Bennington, C.P.J. & Dumont, G.A. (2007b). Optimization of rectangular pulp stock mixing chest dimensions using dynamic tests. *TAPPI J.*, Vol. 6, No. 2, 24-30.

Ein-Mozaffari, F. & Upreti, S.R. (2009). using ultrasonic doppler velocimetry and CFD modeling to investigate the mixing of non-newtonian fluids possessing yield stress. *Chem. Eng. Res. Des.*, Vo. 87, No. 4, 515-523.

Elson, T.P. (1988). Mixing of fluids possessing a yield stress, *Proceedings of 6th European Conference on Mixing*, pp. 485-492, Pavia. Italy, 1988, AIDIC.

Elson, T.P.; Cheesman, D.J. & Nienow, A.W. (1986). X-Ray studies of cavern sizes and mixing performance with fluids possessing a yield stress. *Chem. Eng. Sci.*, Vol. 41, No.10, 2555-2562.

Ford, C.; Ein-Mozaffari, F.; Bennington, C.P.J. & Taghipour, F. (2006). simulation of mixing dynamics in agitated pulp stock chests using CFD. *AIChE J.*, Vol. 52, No. 10, 3562-3569.

Fox, E.A. & Gex, V.E. (1956). Single-phase blending of liquids. *AIChE J.*, Vol. 2, No. 4, 539-544.

Galindo, E. & Nienow, A.W. (1992). Mixing of highly viscous simulated xanthan fermentation broths with the lightnin a-315 impeller. *Biotechnol. Prog.*, Vol. 8, No. 3, 223-239.

Galindo, E. & Nienow, A.W. (1993). The performance of the Scaba 6SRGT agitator in the mixing of simulated xanthan gum broths. *Chem. Eng. Technol.*, Vol. 16, No. 2, 102-108.

Galindo, E.; Torrestiana, B. & García-Rejón, A. (1989). Rheological characterization of xanthan fermentation broths and their reconstituted solutions. *Bioproc. Eng.*, Vol. 4, 113-118.

Harnby, N.; Edwards, M.F. & Nienow, A.W. (1997). *Mixing in the Process Industries*, Butterworth-Heinemann, Boston.

Hirata, Y. & Aoshima, Y. (1994). Flow characteristics and power consumption in an agitated shear-thinning plastic fluid. *IChem. E. Symp.*, Vol. 136, 415-422.

Hirata, Y. & Aoshima, Y. (1996). Formation and growth of cavern in yield stress fluids agitated under baffled and non-Newtonian conditions. *Chem. Eng. Res. Des.*, Vol. 74, 438-444.

Ihejirika, I. & Ein-Mozaffari, F. (2007). Using CFD and ultrasonic velocimetry to study the mixing of pseudoplastic fluids with a helical ribbon impeller. *Chem. Eng. Tech.*, Vol. 30, No. 5, 606-614.

Jaworski, Z. & Nienow A.W. (1993). An LDA study of the hydrodynamics of caverns formed in a yield stress fluid agitated by a hydrofoil impeller. *Proceedings of CHISA 93*, paper H.6.2, Prague, 1993.

Jaworski, Z.; Dyster, K.N. & Nienow, A.W. (2001). The effect of size, location and pumping direction of pitched blades turbine impellers on flow patters: LDA measurements & CFD predictions. *Chem. Eng. Res. Des.*, Vol. 79, No. 8, 887-894.

Kammer, L.C.; Ein-Mozaffari, F.; Dumont, G.A. & Bennington, C.P.J. (2005). Identification of channellng and recirculation parameters of agitated pulp stock chests. *J. Process Control*, Vol. 15, No. 1, 31-38.

Kappel, M. (1979). Development and application of a method for measuring the mixture quality of miscible liquids: Application of the new method for highly viscous Newtonian liquids. *Int. Chem. Eng.*, Vol. 19, 571-590.

Kelly, W. & Gigas, B., (2003). Using CFD to predict the behavior of power law fluids near axial- flow impellers operating in the transitional flow regime. *Chem. Eng. Sci.*, Vol. 58, No. 10, 2141-2152.

Khopkar, A.R.; Mavros, P.; Ranade, V.V. & Bertrand, J. (2004). Simulation of flow generated by an axial flow impeller-bath and continuous operation. *Chem. Eng. Res Des.*, Vol. 82, No. 6, 737-751.

Khopkar, A.R.; Kasat, G.R.; Pandit, A.B. & Ranade, V.V. (2006). Computational fluid dynamics simulation of the solid suspension in a stirred slurry reactor. *Ind. Eng. Chem. Res.*, Vol. 45, No. 12, 4416-4428.

Kumaresan, T. & Joshi, J.B. (2006). Effect of impeller design on the flow pattern and mixing in stirred tanks, *Chem. Eng. J.*, Vol. 115, No. 3, 173-193.

Levenspiel, O., (1998). *Chemical Reaction Engineering*. John Wiley & Sons, New York.

Luo, J.Y.; Gosman, A.D.; Issa, R.I.; Middleton, J.C. & Fitzgerald, M.K. (1993). Full flow field computation of mixing in baffle stirred vessels. *Chem. Eng. Res. Des.*, Vol. 71, 342-344.

Luo, J.Y.; Gosman, A.D. & Issa, R.I. (1994). Prediction of impeller-induced flows in mixing vessels using multiple frames of reference. *Inst. Chem. Eng. Sympo. Ser.*, Vol. 136, 549-556.

Macosko, C.W. (1994). *Rheology: Principles, Measurements and Applications*, Wiley-VCH, New York.

Mavros, P.; Xuereb, C. & Bertrand, J. (1996). Determination of 3-D flow fields in agitated vessels by laser-doppler velocimetry. effect of impeller type and liquid viscosity on liquid flow patterns. *Chem. Eng. Res. Des.*, Vol. 74, 658-668.

McClements, D.J.; Povery, M.J.W. & Jury, M. (1990). Ultrasonic characterization of a food emulsion, *Ultrasonics*, Vol. 28, No. 4, 266-271.

Metzner, A.B. & Otto, R. E. (1957) Agitation of non-Newtonian fluids. *AIChE J.*, Vol. 3, No. 1, 3-10.

Mishra, V.P.; Dyster, K.N.; Jaworski, Z.; Nienow, A.W. & Mckemmie, J. (1998). A Study of an Up- and a Down-Pumping Wide Bade Hydrofoil Impeller: Part I. LAD Measurements, Can. J. Chem. Eng., Vol. 76, No. 3, 577-588.

Montante, G.; Mostek, M.; Jahoda, M. & Magelli. F. (2005). CFD Simulations and Experimental Validation of Homogenization Curves and Mixing Time in Stirred Newtonian and Pseudoplastic Liquids, Chem. Eng. Sci., Vol. 60, No. (8), 2427-2437.

Pakzad, L. (2007). Using Electrical Resistance Tomography (ERT) and Computational Fluid Dynamics (CFD) to Study the Mixing of Pseudoplastic Fluids with a Scaba 6SRGT Impeller. M.A.Sc. Thesis, Ryerson University, Toronto.

Pakzad, L.; Ein-Mozaffari, F. & Chan, P. (2008a). Using Electrical Resistance Tomography and Computational Fluid Dynamics Modeling to Study the Formation of Cavern in the Mixing of Pseudoplastic Fluids Possessing Yield Stress. Chem. Eng. Sci., Vol. 63, No. 9, 2508-2522.

Pakzad, L.; Ein-Mozaffari, F. & Chan, P. (2008b). Using Computational Fluid Dynamics Modeling to Study the Mixing of Pseudoplastic Fluids with a Scaba 6SRGT Impeller. Chem. Eng. Proc., Vol. 47, No. 12, 2218-2227.

Patel, H.; Ein-Mozaffari, F. & Upreti, S.R. (2008). Continuous Time Domain Characterization of Mixing in Agitated Pulp Chests. TAPPI J., Vol. 7, No. 5, 4-10.

Patwardhan, A.W. & Joshi, J.B. (1999). Relation between Flow Pattern and Blending in Stirred Tanks, Ind. Eng. Chem. Res., Vol. 38, No. 8, 3131-3143.

Paul, E.L.; Atiemo-Obeng, V. & Kresta, S.M. (2004). Handbook of industrial mixing: science & practice, Wiley-Interscience, New York.

Ranade, V.V. (1995). Computational Fluid Dynamics for Reactor Engineering. Rev. in Chem. Eng., Vol. 11, 229-284.

Ranade, V.V. (2002). Computational Flow Modeling for Chemical Reactor Engineering, Academic Press, San Diego.

Ranade, V.V. & Dommeti, S.M.S. (1996). Computational Snapshot of Flow Generated by Axial Impellers in Baffled Stirred Vessels. Chem. Eng. Res. Des., Vol. 74,476-484.

Renaud, M.; Belgacem, M.N.; Rinaudo, M. (2005). Rheological Behavior of Polysaccharide Aqueous Solutions. Polymer, Vol. 46, No. 4, 12348–12358.

Rutherford, K.; Mahmoudi, S.M.S.; Lee, K.C. & Yianneskis, M. (1996). The Influence of Rushton Impeller Blade and Disk Thickness on the Mixing Characteristics of Stirred Vessels. Chem. Eng. Res. Des., Vol. 74, 369-378.

Saeed, S. (2007). Dynamic and CFD Modeling of a Continuous-Flow Mixer Using Fluids with Yield Stress, M.A.Sc. Thesis, Ryerson University, Toronto.

Saeed, S.; Ein-Mozaffari, F. & Upreti, S.R. (2007). Using Computational Fluid Dynamics Modeling and Ultrasonic Doppler Velocimetry to Study Pulp Suspension Mixing. Ind. Eng. Chem. Res., Vol. 46, No. 7, 2172-2179.

Saeed, S. & Ein-Mozaffari, F. (2008). Using Dynamic Tests to Study the Continuous Mixing of Xanthan Gum Solutions. J. Chem. Technol. Biotechnol., Vol. 83, No. 4, 559-568.

Saeed, S.; Ein-Mozaffari, F. & Upreti, S.R. (2008). Using Computational Fluid Dynemics to Study the Dynamic Behavior of the Continuous Mixing of Herschel-Bulkley Fluids. Ind. Eng. Chem. Res., Vol. 47, No. 19, 7465-7475.

Sahu, A.K.; Kummar, P. & Joshi, J.B. (1998). Simulation of Flow in Stirred Vessels with Axial Flow Impellers: Zonal Modeling and Optimization of Parameter. Ind. Eng. Chem. Res., Vol. 37, No. 6, 2116-2130.

Solomon, J.; Elson, T.P. & Niewnow, A.W. (1981). Cavern Sizes in Agitated Fluids with a Yield Stress, Chem. Eng. Commun., Vol. 11, No. 1, 143-164.

Sommerfeld, M. & Decker, S., (2004). State of the Art and Future Trends in CFD Simulation of Stirred Vessel Hydrodynamics. Chem. Eng, Technol., Vol. 27, No. 3, 215-224.

Takeda, Y. (1986). Velocity Profile Measurement by Ultrasound Doppler Shift Method. Int. J. Heat Fluid Flow, Vol. 7, No. 4, 313-318.

Takeda, Y. (1991). Development of an Ultrasound Velocity Profile Monitor. Nucl. Eng. Des., Vol. 126, No. 2, 277-284.

Takeda, Y. (1995). Velocity Profile Measurement by Ultrasonic Doppler Method. Exp. Therm. Fluid Sci., Vol. 10, No. 4, 444-453.

Tatterson, G.B. (1991). Fluid Mixing and Gas Dispersion in Agitated Tanks, McGraw-Hill, Toronto.

Upreti, S.R. & Ein-Mozaffari, F. (2006). Identification of Dynamic Characterization Parameters of Agitated Pulp Chests Using a Hybrid Genetic Algorithm. Chem. Eng. Res. Des., Vol. 84, No. 3, 221-230.

Versteeg, H.K., & Malalasekera, W. (2007). An Introduction to Computational Fluid Mechanics – The Finite Volume Method, Pearson Prentice Hall, New York.

Whitcomb, P.J. & Macosko, C.W. (1978). Rheology of xanthan gum. J. Rheol., Vol. 22, No. 5, 493–505.

Wilkens, R.J.; Miller, J.D.; Plummer, J.R.; Dietz, D.C. & Myers, K.J. (2005). New Techniques for Measuring and Modeling Cavern Dimensions in a Bingham Plastic Fluid. Chem. Eng. Sci., Vol. 60, No. 19, 5269-5275.

Williams, R.P. (1986). On the Relationship between Velocity Distribution and Power Spectrum of Scattered Radiation in Doppler Ultrasound Measurements on Moving Suspensions, Ultrasonics, Vol. 24, No. 4, 197-200.

Wichterle, K. & Wein, O. (1975). Agitation of Concentrated Suspensions, Proceedings of CHISA 75, Paper B4.6, Prague, Czechoslovakia, 1975.

Xuewu, Z.; Xin, L.; Dexiang, G.; Wei, Z.; Tong, Z. & Yonghong, M. (1996). Rheological Models for Xanthan Gum. J. Food Eng., Vol. 21, No. 2, 203-209.

Yackel, D.C. (1990). Pulp and Paper Agitation: The History, Mechanics and Process, TAPPI Press, Atlanta.

Zlokarnik, M. (2001). Stirring: Theory and Practice, Wiley-VCH, Weinheim.
Zlokarnik, M. (2006). Scale-up in Chemical Engineering, Wiley-VCH, Weinheim.

# 5

# Turbulence, Vibrations, Noise and Fluid Instabilities. Practical Approach.

Dr. Carlos Gavilán Moreno
*Cofrentes N.P.P. Iberdrola S.A.*
*Spain*

## 1. Introduction

Colloquially speaking, turbulence in any language means disorderly, incomprehensible, and of course, unpredictable movement. Consequently, we encounter expressions that employ the word turbulence in social and economic contexts; in aviation whenever there are abnormalities in the air, and even in psychology and the behavioural sciences in reference to turbulent conduct, or a turbulent life, in the sense of a dissolute existence. Thus has the word turbulence become associated with chaos, unpredictability, high energy, uncontrollable movement: dissipation. All of the foregoing concepts have their source in the world of hydrodynamics, or fluid mechanics.

In fluid mechanics, turbulence refers to disturbance in a flow, which under other circumstances would be ordered, and as such would be laminar. These disturbances exert an effect on the flow itself, as well as on the elements it contains, or which are submerged in it. The process that is taking place in the flow in question is also affected. As a result, they possess beneficial properties in some fields, and harmful ones in others. For example, turbulence improves processes in which mixing, heat exchange, etc., are involved. However, it demands greater energy from pumps and fans, reduces turbine efficiency and makes noise in valves and gives rise to vibrations and instabilities in pipes, and other elements.

The study of turbulence and its related effects is a mental process; one that begins with great frustration and goes on to destroy heretofore accepted theories and assumptions, finally ending up in irremediable chaos. "I am an old man now, and when I die and go to heaven, there are two matters on which I hope for enlightenment. One is the quantum electrodynamics, and the other is the turbulent motion of fluids. An about the former I am rather optimistic" (Attributed to Horace Lamb).

Nonetheless, some progress has been made in turbulence knowledge, modelling and prediction. (Kolmogorov, 1941). This chapter will deal briefly with these advances, as well as with the effects of turbulence on practical applications. In this sense, reference will be made to noise effects and modelling, as well as to flow vibration and instabilities provoked by turbulence. (Gavilán 2008, Gavilán 2009).

## 2. Turbulence.

Of itself, turbulence is a concept that points to unpredictability and chaos. For our purposes, we will deal with this concept as it applies to fluid mechanics. Therefore, we will be dealing

with turbulent flow. Throughout what follows, the terms *turbulence* and *turbulent flow* will be understood as synonymous. Some texts treat the terms *turbulence* and *vortex* as analogous, however, this seems to be rather simplistic. For the purposes of this work, it seems best to take the concept of turbulence in its broadest sense possible.

Historically, fluid mechanics has been treated in two different ways, namely, in accordance with the Euler approach, or pursuant to the Lagrange approach. The Eulerian method is static, given that upon fixing a point, fluid variations are determined on the effect they have on this point at any given time. On the other hand, the Lagrangian method is dynamic, given that it follows the fluid. In this way, variations in the properties of the fluid in question are observed and/or calculated by following a particle at every single moment over a period of time.

The Eulerian method is the one most employed, above all, in recent times, by means of numerical methods, such as that of finite elements, infinites, finite volumes, etc. Notwithstanding, there is great interest in the Lagrangian method or approach, given that it is one that is compatible with methods that do not use mesh or points. (Oñate, E; et al. 1996)

Throughout history, there have been two currents of thought as regards the treatment of turbulence. One is the so-called deterministic approach, which consists of solving the Navier-Stokes equation, with the relevant simplifications, (Euler, Bernoulli) practically exclusively via the use of numbers. The other approach is statistical. The work of Kolmogorov stands out in this field; work which will be dealt with below, given its later influence on numerical methods and the results of same. Apart from the Eulerian or Lagrangian methods, classic turbulent fluid theory will be dealt with in Section 2.1, whereas the statistical or stochastic approach will be dealt with in Section 2.2, in clear reference to Kolmogorov's theory. (Kolmogorov, 1941).

### 2.1 General theory

This section provides a brief and concise exposition of successive fluid flow approaches designed to respond to the presence of anomalies that were later referred to as *turbulence*, and which gave rise to the concept of turbulent fluid. Furthermore, the equations given enable the visualisation of the turbulence in question and its later development. A Eulerian and deterministic focus will be followed in this section.

Working in reverse to the historical approach, the fluid flow equation formulated by Navier-Stokes in 1820 is given; firstly, because it is the most general one, and secondly, because, of itself, its solution can represent the turbulent flow equation.

$$\frac{\partial u_i}{\partial t} + \sum_{j=1}^{n} u_j \frac{\partial u_i}{\partial x_j} = \upsilon \Delta u_i - \frac{\partial p}{\partial x_i} + f_i(x,t) \tag{1}$$

$$div\vec{u} = \sum_{i=1}^{n} \frac{\partial u_i}{\partial x_i} = 0 \tag{2}$$

$$u(x,0) = u^0(x) \tag{3}$$

Where $u_i$ stands for the velocity components at each point and at each moment in time, $\upsilon$ is the viscosity, $p$ is the pressure at each point and at each moment in time, and $f_i$ refers to the external forces at each point and at each moment in time. By annulling the viscosity and its effects, we get Euler's fluid flow equation announced in 1750.

$$\frac{\partial u_i}{\partial t} + \sum_{j=1}^{n} u_j \frac{\partial u_i}{\partial x_j} = -\frac{\partial p}{\partial x_i} + f_i(x,t) \tag{4}$$

$$div\vec{u} = \sum_{i=1}^{n} \frac{\partial u_i}{\partial x_i} = 0 \tag{5}$$

$$u(x,0) = u^0(x) \tag{6}$$

In addition to this simplification, if we make the fluid stationary, so that:

$$\frac{\partial u}{\partial t} = 0 \tag{7}$$

we get the first Bernoulli theorem announced in 1738.

$$\frac{D}{Dt}\left(p + \rho \cdot \phi + \rho \frac{u^2}{2}\right) = 0 \tag{8}$$

The solving of these equations, given their simplifications and context conditions, provide us with a field of speeds and pressures for a fluid in movement. Indeed, as regards the Navier-Stokes equation, it can be solved and turbulences and instabilities determined by employing powerful numerical solution methods, such as that of the finite element.

Thus, the equations that govern fluid movement. By means of these two equations, particularly the last two (those of Euler and Bernoulli), it was observed that, under certain conditions, the results did not correspond to reality, on account of a certain problem of disorder developing in the fluid and its flow. Only the accurate and numerical solving of the Navier-Stokes equation can exactly reproduce these phenomena. To this end, resort must be had to potent computational fluid dynamic (CFD) software. Notwithstanding, in 1883, Osborne Reynolds discovered a parameter that predicted or anticipated the chaotic and turbulent of the fluid: the Reynolds number.

$$Re = \frac{\rho \cdot v_s \cdot D}{\mu} = \frac{v_s \cdot D}{\upsilon} \tag{9}$$

Thus was it established that the flow is stationary, and therefore laminar, for Re<2000 values, a fact which meant that the solutions given by Bernoulli and Euler were very accurate. For values of 2000<Re<4000 the system was deemed to be in transition, and therefore, not stationary. The functions that work best are those of Euler and Navier-Stokes. This turbulence undergoes three phases or states of development.

A. Growth of coherent bidimensional vortices[1].
B. Joining of Vortices
C. Separation of vortices and turbulent state in 3D

Finally, if completely turbulent, the fluid is non-stationary and tri-dimensinal for values of Re>4000. These solutions are only possible by means of using the Navier-Stokes equations.

In conclusion, only the numerical solution of the Navier-Stokes equation provides a solution that considers turbulence. Nevertheless, there are other processes and approaches that will be developed in Section 2.3. Turbulence is, therefore, produced by the interaction of the fluid with geometry, by the loss of energy due to viscosity, by density variations caused by temperature, or other factors, such as changes in speed, or all of these at once. Consequently,

[1] These are referred to as coherent because the vorticity is concentrated and the fluid flows around as if it were a solid obstacle. It keeps its shape for longer than a single rotation.

the turbulent flow is unpredictable and chaotic in the sense that it depends on a host of small variations in the initial conditions and these disturbances are amplified in such a way that it becomes possible to predict them in space and time. Another of its features is its great capacity for mixing and, lastly, that it affects at various scales and wavelengths. It could be said that together, fluid, structure and context conditions, constitute a non-linear, non-stationary dynamic system. Its most noteworthy characteristic is its sensitivity to the initial conditions and its self-similarity, which will serve as a staring point to develop Kolmogorov's theory.

In the 19th and 20th centuries, several researchers devoted great efforts to studying turbulence under certain, extremely particular conditions. Examples of such turbulence or instabilities are to those of Von Karman, Kevin-Helmotz, Raleygh-Bernard, and so on.

### 2.2 Kolmogorov´s theory

Kolmogorov's theory cannot be dealt with without first mentioning the spectral analysis of turbulence, or the application of Fourier's analysis to the study of turbulence. Fourier's theory decomposes the fluctuations into sinusoidal components and studies the distribution of the turbulent energy along several wavelengths. In this way it becomes possible to get several scales of turbulence and their evolution in time. This technique works and produces acceptable results when turbulence is homogenous. Under this condition, accurate equations can be determined for the speed spectrum and for the transferring of energy between difference scales of turbulence, as well as the dissipation of turbulent energy due to viscosity. The simplest development assumes that there is no average speed gradient, in such a way that the turbulence interacts with itself, with the energy dropping by itself. Neither energy sources nor sinks are taken into account.

To start, we assume that the speed of a particle in the fluid can be decomposed into an average speed plus a fluctuation component.

$$U_i = \overline{U}_\iota + u_i \tag{10}$$

$R_{ij}$ is defined as the speed correlation function by the expression:

$$R_{ij}(x, x', t) = \overline{u(x,t)_\iota u(x',t)_J} \tag{11}$$

Given that we assume homogenous turbulence, $R_{ij}$ is only a function of the distance $r$, which is the distance between $x$ and $x'$:

$$R_{ij}(r, t) = \overline{u(x,t)_\iota u(x',t)_J} \tag{12}$$

Therefore, we assume that the value of the correlation function tends to zero when the radius tends to the infinite. We now define a spectral function $\Phi_{ij}$ as the Fourier transform of the correlation function in 3D:

$$\emptyset_{ij}(k,t) = \frac{1}{(2\pi)^3} \int R_{ij}(r,t) \cdot e^{-ikr} \cdot d^3k \tag{13}$$

This spectral function, which will form the spectral matrix, depends on time and on the wave number $k$, which is a vector. The turbulent kinetic energy can be expressed as:

$$\frac{1}{2}\overline{u_\iota u_\iota} = \frac{1}{2}R_{ij}(0,t) = \frac{1}{2}\int \emptyset_{ii}(k,t)d^3k \tag{14}$$

The magnitude of the vector of the wave number $k=[k]$ is the inverse of the length, thus the length is $k^{-1}$. Therefore, if $L$ is a characteristic scale of turbulence, the $L^{-1}$ value of the wave number represents the higher scales of turbulence, where all the turbulent kinetic energy is contained. The spectral function, $\Phi_{ij,}$ describes the energy distribution in relation to wave numbers. It has a maximum value of $[k]=L^{-1}$, which drops to zero when $[k]$ tends to the infinite. The evolution of kinetic energy is defined as:

$$E = 2\pi k^2 \emptyset_{ii} \tag{15}$$

As far as the evolution of the $k$ energy value is concerned, this can be seen in the following figure (Figure 1).

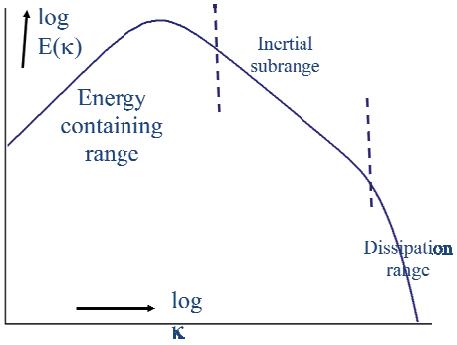


Fig. 1. Energy ranges.

This is where the term, or value, $\eta$ comes in, referring to Kolmogorov's scale, which determines the scale point at which energy dissipation by viscosity is most significant. We will use the following equation for Kolmogorov's theory:

$$\frac{\partial E}{\partial t} = T - 2 \cdot \upsilon \cdot k^2 E \tag{16}$$

That is to say, the energy and its evolution in time will be a function of that which is transferred and that which is dissipated. Integrating it from k=0 to a greater, or finite, as well as limited, value gives us:

$$\frac{d}{dt}\int_0^k E(k'.t)dk' = -\aleph(k,t) - 2\upsilon \int_0^k k'^2 E(k',t)dk' \tag{17}$$

Where:

$$\aleph(k,t) = -\int_0^k T(k',t)dk' = \int_k^\infty T(k',t)dk' \tag{18}$$

This can be interpreted as follows:

"Energy changes in wave numbers below $k$ on account of the interchange with larger wavelengths through the energy spectral fluid and the dissipation caused by viscosity forces on its own wavelength"

Kolmogorov holds that turbulence properties in the inertial range, above $\eta$, only depend on the energy spectral fluid, in such a way that:

$$\aleph = \bar{\varepsilon} \tag{19}$$

The idea behind this is that the transfer cascade evolves towards lower scales, leaving the spectral fluid as a fixed parameter. Consequently, the energy equation now stands at:

$$E(k,t) = C \cdot \varepsilon^{-\frac{2}{3}} \cdot k^{-\frac{5}{3}} \tag{20}$$

where *C* is a Kolmogorov constant, considered as a universal, the value of which is 1.5 when $L^{-1} << k << \eta^{-1}$ and the *Re* (Reynolds number) is high. Thus, beyond the inertial scale wave numbers, we have the dissipation range numbers, as shown in Figure 2.

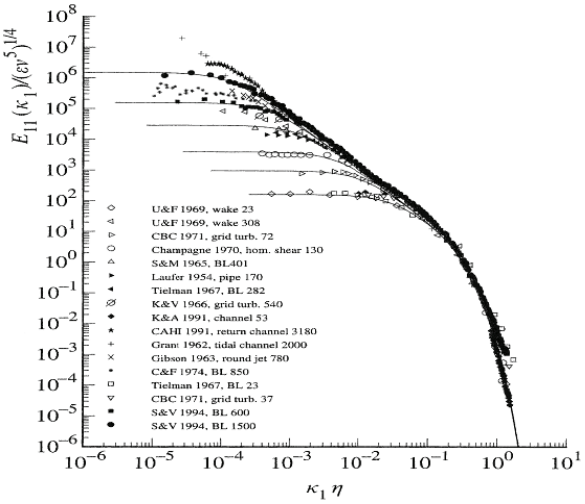


Fig. 2. Kolmogorov scales and data from several tests.

This range is only determined by the $\eta$ parameter, which only has a dependence parameter, as shown by the equation (21).

$$\eta = \left(\frac{\upsilon}{\varepsilon}\right)^{\frac{1}{4}} \tag{21}$$

This Kolmogorov derived value gives the size of the smallest turbulence dissipation scale. The dissipation range energy expression now becomes:

$$E(k,t) = \varepsilon^{\frac{1}{4}}\upsilon^{\frac{5}{4}} \cdot F(k\eta) \tag{22}$$

where $F(\cdot)$ is also a universal function.
We will define the Kolmogorov time and speed scale factor with the $\varepsilon$ y $\upsilon$ parameters, which determine the behaviour of the flow in the dissipation range:

$$t_\eta = \left(\frac{\upsilon}{\varepsilon}\right)^{\frac{1}{2}} \tag{23}$$

$$u_\eta = (\upsilon \cdot \varepsilon)^{\frac{1}{4}} \tag{24}$$

Thus, the Kolmogorov theory completes the spectral analysis. The theory postulates high Reynolds number values. The small turbulence scales are assumed that serve to balance and be controlled by the average energy flow, which is generated in the inertial scale and which equals the dissipation rate. Furthermore, Kolmogorov's theory universally predicts speed properties and their differences for small separations, as well as their correlations and spectre, only depending on the $\upsilon$ y $\varepsilon$ parameters. Kolmogorov also marked the boundary between the transferred or contained energy range (inertial range) and the dissipative structures by way of the following expression:

$$\frac{L}{\eta} = f(Re^{3/4}) \tag{25}$$

Therefore, given a Reynolds number, the lower scales are not sensitive to the turbulent flow in which they find themselves. Nevertheless, the lower scales are intimately related to the flow, with their properties varying substantially depending on the specific flow. These concepts will form the basis for future methods of modelling and solving fluid movement problems, such as *k*-$\varepsilon$ and Large Eddy Simulation (LES) models.

### 2.3 Simulation of turbulent fluids.

As is well known, Navier, L.H.H. and Stokes, G.G derived fluid movement equations over 150 years ago. This equation, along with that of continuity, provides an answer to any fluid movement problem.

The solution and determination of the speed field is, therefore, nothing more than discretising the domain and the differential equations and applying context conditions in order to repeatedly solve the system formed until achieving convergence. This is the so-called Direct Numerical Solution (DNS). Nonetheless, this simple method is only useful in simple geometries, given that otherwise, the time calculation would be so big as to make any simulation unfeasible. This defect arises noticeably when we design fluid-structure (FIS) models. Consequently, other models need to be found, which are lest costly computationally speaking.

The most common solution to the high number of elements required by the former simulation method, DNS, is to use weighted, or weighting, techniques. In this way, modelling is done on a small scale expecting that the solution will respond to the flow as a whole. This is the idea that underlies the so-called Reynolds Averaged Navier-Stokes (RANS). It must be assumed that the speed of a turbulent flow can be described as follows:

$$\vec{u} = \bar{\vec{u}} + \overrightarrow{u'} \tag{26}$$

That is to say, as the sum of an average speed plus a fluctuating component on this average speed. The following is an example of the application of this assumption. It refers to the 2D modelling of a turbulent flow on a flat plate, the Navier Stokes (NS) equation for which is given below:

$$\rho\left(\frac{\partial u_x}{\partial t} + u_x\frac{\partial u_x}{\partial x} + u_x\frac{\partial u_x}{\partial y}\right) = \mu\frac{\partial^2 u_x}{\partial y^2} \tag{27}$$

replacing

$$\rho\left(\overline{u_x}\frac{\partial \overline{u_x}}{\partial x} + \overline{u_x}\frac{\partial \overline{u_x}}{\partial y}\right) = \mu\frac{\partial^2 \overline{u_x}}{\partial y^2} - \rho\frac{\partial}{\partial y}\overline{u'_x u'_y} \tag{28}$$

The difficulty of this expression and of all those assuming equation (28) is that an analytical expression of the term is required:

$$\rho \frac{\partial}{\partial y} \overline{u'_x u'_y} \tag{29}$$

known as Reynold Stress. In order to avoid this difficulty, the kinetic energy ($k$) and the dissipation rate ($\varepsilon$) are modelled. This gives rise to a well known model: the $k$- $\varepsilon$ model.
The simplification consists of the following:

$$\rho \cdot \overline{u'_x u'_y} = \mu_{turb} \frac{\partial \overline{u_x}}{\partial y} \tag{30}$$

where, moreover,

$$\mu_{turb} = \frac{C_k \cdot k^2}{\varepsilon} \tag{31}$$

by replacing all of this, in the proposed movement equation, the result is as follows:

$$\left(\overline{u_x} \frac{\partial \overline{u_x}}{\partial x} + \overline{u_y} \frac{\partial \overline{u_x}}{\partial y}\right) = \upsilon \frac{\partial^2 \overline{u_x}}{\partial y^2} - \frac{C_k \cdot k^2}{\varepsilon} \frac{\partial \overline{u_x}}{\partial y} \tag{32}$$

This $k$- $\varepsilon$ model has a big advantage over the DNS model in that it takes less time to compute. This model provides acceptable solutions when flow fluctuations are not very important. When the flow motor, or the problem, to be studied has to do with pressure fluctuation, that is to say, external flow Flow Induced Vibrations (FIV), the RANS model is unviable, given that it does not provide quality solutions. There are several RANS model variations, the main features of which are shown in Table 1.

| Method | Strengths | Weaknesses |
|---|---|---|
| Spalart-Allmaras | A one-equation model, which provides less computational effort than most other models. Produced for external flow over airfoils but is increasing in popularity for turbo machinery applications. Performs well for attached wall-bounded flows with weakly complex boundary layers. | Weak for adverse pressure gradients that produce boundary layer separation. Since it is relatively new, it has a lack of submodels available. |
| RNG k-ε | Possesses many of the same characteristics as the standard k-ε, but uses mathematical group theory to determine the previously empirical constants. It performs better for moderately complex flows like jet impingement. | Subject to limitations due to isotropic eddy viscosity assumptions. |
| Reynolds Stress Model (RSM) | Highly rooted in the physics by solving a transport equation for each Reynolds stress. | Requires much more computational effort than any other technique |

Table 1. RANS submodels, strengths and weaknesses.

Lastly, there is a model that lies halfway between the RANS and DNS. The DNS model has been seen to represent the real circumstance and disturbances very well. On the other hand, though the RANS model is extremely comfortable computationally speaking, it does not represent turbulence or disturbances very well. The so-called Large Eddy Simulation (LES) model provides instantaneous solutions, as does the DNS model, while at the same time containing models and simplifications such as those in the RANS model. The LES model solves the Navier-Stokes equation as does the DNS model, but the equations are spatially filtered, or refined. This filtering or refining of the equations means that the flow is determined at a characteristic scale, and is modelled afterwards at lower scales. It is the application of Kolmogorov's theory to non-stochastic numerical models.

This succession of modelling and refining is due to the fact that big eddies behave anisotropically and, therefore, must be calculated, whereas smaller eddies behave isotropically and can, as such, be treated statistically. Thus, the mesh is such that the majority of energy is contained in big eddies and calculated directly, the rest is assigned in a weighted manner to flow as a whole.

The bigger the Reynolds number, the bigger the cost in this LES model. Mathematically, the model is based on the $\Phi$ flow being formed by two superimposed flows:

$$\phi = \bar{\phi} + \phi' \tag{33}$$

the mesh flow, or the grand scale flow, $\bar{\phi}$

the sub-mesh flow, or the small scale flow $\phi'$

The grand scale (GS) flow is calculated as follows:

$$\overline{\phi(x)} = \int \phi(x')G(x,x')dx' \tag{34}$$

where

$$G(x,x') = \begin{Bmatrix} \frac{1}{v} & \sqrt{x}\epsilon\Delta v \\ 0 & resto \end{Bmatrix} \tag{35}$$

then replacing

$$\overline{\phi(x)} = \frac{1}{v}\int \phi(x')dx' \tag{36}$$

By applying these assumptions to the flow movement equation

$$\frac{\partial \overline{u_i}}{\partial t} + \frac{\partial}{\partial x}\left(\overline{u_i}\overline{u_j}\right) = -\frac{1}{\rho}\frac{\partial}{\partial x}\bar{p} + v\frac{\partial^2 \overline{u_i}}{\partial x_j^2} + \tau_{ij} \tag{37}$$

$$\tau_{ij} = \overline{u_i u_j} - \overline{u_i}\cdot\overline{u_j} \tag{38}$$

the latter term is modelled on the sub-mesh, or on the SGS sub-model and the accuracy of the model rests on the idea that lower speeds than the mesh are homogenous and, therefore, can be modelled with great accuracy. The aim of the LES method is to solve the majority of the flow and to model only a small part of it. Thus, the LES method strikes a balance between mesh size and accuracy. Figure 3, in which the solution for a turbulent flow in a pipe compares the RANS method with the LES one, provides an explanatory example.

These are practically the general models that are used in flow simulation and fluid movement. Notwithstanding, there are variations of these basic methods depending on the application in question.

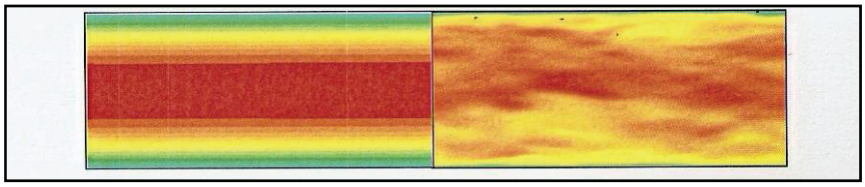

Fig. 3. Solutions of the same problem with a RANS model (on the left) and LES model (on the right).

Quite clearly, discretisations can be Eulerian, or Lagrangian, in such a way as to respond to both forms of tackling problems concerning fluid dynamics.

## 3. General effects of the turbulence. (FIC)

Having introduced turbulence, the turbulent flow and its equations and simulations, the question arises as to what can turbulence do? What are its possible effects? To answer these questions, first off it is necessary to decide whether the effects in question are general or local, that is to say, whether they are provoked by the turbulent flow or, on the contrary, are caused by turbulence or instabilities. The latter will be dealt with in Sections 4, 5 and 6, while the general effects are considered below.

Numerous studies have been carried out highlighting the benefits of turbulence with respect to miscibility, diffusion and heat exchange, though it can also have harmful effects. Here we are going to deal with the phenomenon of spontaneous cavitation, and its effects, in turbulent flow. Specifically, our aim is to study the effect of the change of speed caused by vorticity and pressure due to load loss on account of turbulence in high energy turbulent fluids near saturation point, such as, for example, feed water in power stations.

Firstly, we are going to define a non-dimensional parameter, which is called the cavitation number.

$$Ca = \frac{Pa - Pv}{\frac{1}{2}\rho v^2} \tag{39}$$

where:

$P_a$ is the local or system pressure;

$P_v$ is the vaporization pressure at system temperature;

$P$ is the fluid density at system temperature;

$V$ is the fluid speed.

Cavitation will occur when the parameter value is low. There is a limit value that corresponds to a determined speed, for each temperature and pressure, below which cavitation is ensured.

Speed can be defined in a turbulent flow as follows:

$$u_T(t) = u_m + \delta u(t) \tag{40}$$

That is to say, an average value and a fluctuation or oscillation component. Moreover, turbulence intensity is defined as:

$$u'^2(t) = \frac{1}{T}\int_0^T u_T(t)^2 dt \tag{41}$$

replacing the equation *40* in the equation 39 gives:

$$Ca = \frac{Pa - Pv}{\frac{1}{2}\rho(u_m^2(t) + 2 \cdot u_m(t) \cdot \delta u(t) + \delta u^2(t))} \tag{42}$$

If we assume that $\delta u(t)$ is proportional to the standard deviation of the measured values in the speed system, and that in turn, this standard deviation is a function of the average speed, (Gavilán, C.J. 2008) we find that:

- $\delta u(t)$ is zero for low speeds, therefore, the *Y* expression is accurate and can be applied to all fluid points. Moreover, the Bernoulli and Euler theorem is applicable, therefore, there will be no spontaneous cavitation, unless the average speed changes.
- For high speeds, $\delta u(t) >> 0$, there may be some speed values at which *Ca* is lower than the average value, and therefore, spontaneous cavitation may occur.

This effect will be called Fluid Induced Cavitation (FIC), given that, although cavitation is associated with turbulence, in turbo-machines or rotary pumps, little attention is paid to spontaneous cavitation due to the effect of turbulence on fluid systems. This effect is not widely known, though it is most definitely of great importance when dealing with fluids that are working very near the vaporization limit, or to put it more clearly, when the system pressure is very near the fluid vapour pressure at working temperature. This is particularly important for thermal power plants, or energy producing stations. In such facilities, the liquid is heated before entering the vaporization element; if there are elements that make the pressure fall, such as elbows, T's, filters, etc. in the conditions prior to vaporization, the numerator of equation 39 drops, reducing the *Ca* value, thus representing a high risk situation. In the same way, if we have elements in which the speed rises, such as jet pumps, venturi tubes, and other restrictions, the denominator increases, in such a way that the *Ca* value falls, thus increasing the risk of cavitation.

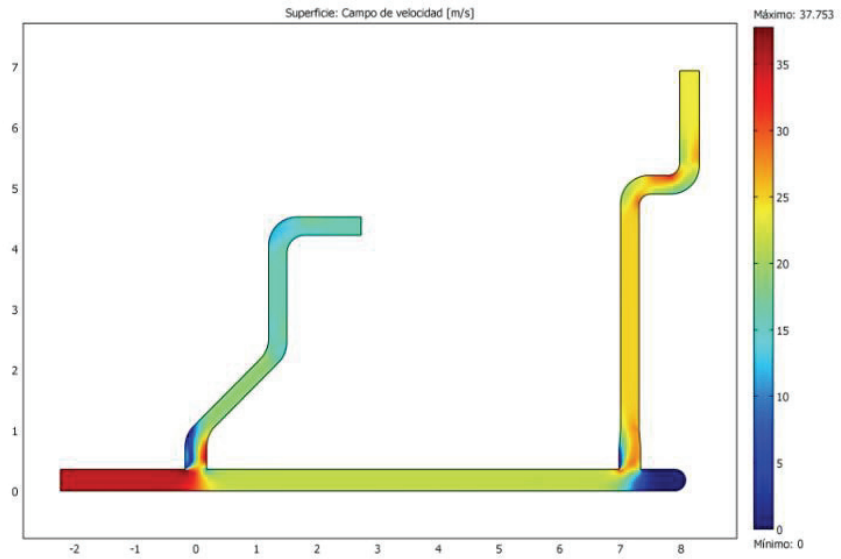


Fig. 4. Flow in pipe system.

Cavitation, which elsewhere and in other fora is referred to as *flashing*, is a vibration and noise - FIV and FIN - and may even manage to change the flow pattern, and therefore, cause FII flow instabilities. Other effects also need to be taken into account, such as the presence of erosion-corrosion, in what is, in principle, a single-phase fluid. Furthermore, if there are stable cavitation conditions, and a real and permanent void ratio is established, pump cavitation is ensured, even when this should not occur according to the calculations.
There are other reasons for possible cavitation, such as variations in the density and vapour pressure parameters on account of changes in the pressure and temperature conditions.
Let us have a look at a real example. Figure 4 shows the case of feed water speed in a pipe to an electricity-generating installation boiler. If we calculate the *Ca* parameter between two points, A and B, already having the average, or tendency, speed and the real one, we see that their *Ca* values are different. After the *Ca*, *v* and *p* values have been calculated in several situations, if we extrapolate them, there is such a turbulent speed value that it provokes spontaneous cavitation (Figure 5). Therefore, there is a speed limit for each flow at which spontaneous cavitation occurs, which coincides with the asymptotic value.

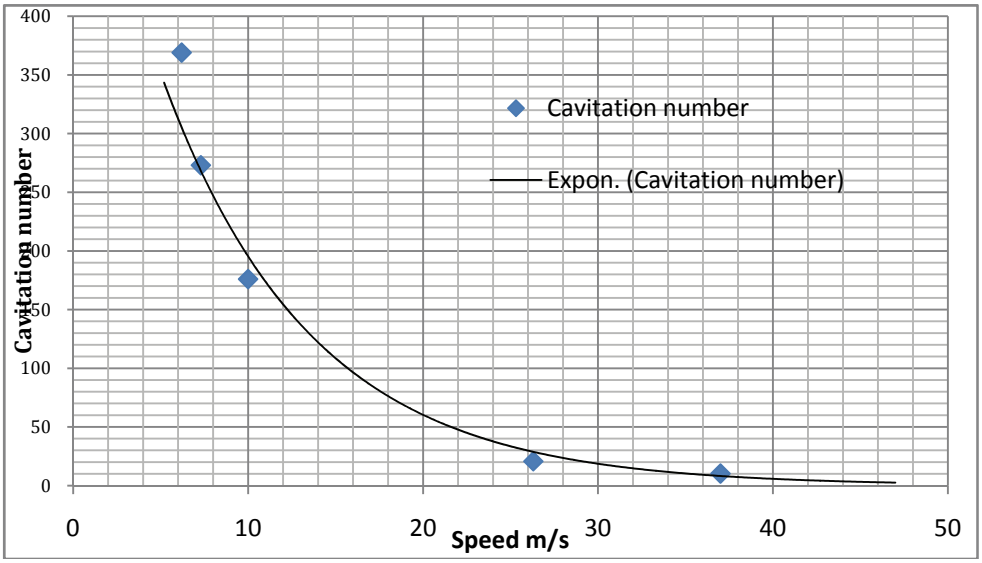


Fig. 5. Cavitation number versus flow speed.

The cavitation effect is not completely harmful, given that occasionally it is provoked by means of the speed of the fluid around a vehicle in such a way that movement resistance is very low and energy is saved in the movement, the fluid entry length is increased, or the energy is increased on knocking against another object in the fluid. This is the case of the supercavitating torpedoes used by the Russian navy.

## 4. Fluid Induced Vibration. (FIV)

There are lots of books and articles that have dealt with this subject. Strictly speaking, the term was only coined in the 1980's. In truth, this case study is a particular case of fluid-

structure interaction. Interest in this subject lies in the fact that the source of vibration is dissipated energy caused by turbulence, or in other cases, by eddies that produce oscillating lift forces that impregnate objects immersed in the fluid with a vibratory movement.
There are two basic FIV mechanisms:

- a self-induced vibrating mechanism
- a forced vibration mechanism.

Mathematically speaking, this is true. Nevertheless, the subject is somewhat wider than this might suggest, as can be seen from the following classification, which provides us with a more complete view. (Figure 6).

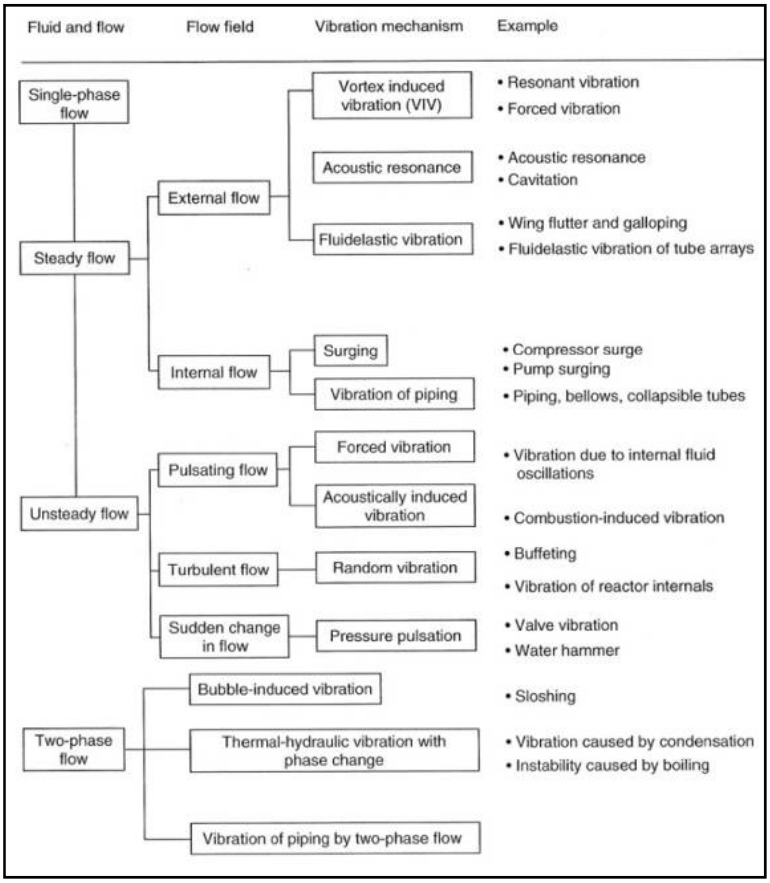


Fig. 6. Vibration mechanism.

As far as we are concerned, two of the most important effects, or examples, as regards nuclear plants of the Boiling Water Reactor (BWR) type, are those that reflect the influence of FIV on reactor internals. That is to say, on single-phase fluids in a non-stationary operating system with turbulent flow, and in the case of a bi-phase flow, those that are subject to FIV on account of the vibrations caused by the phase change, which may even go as far as to cause thermo-hydraulic instabilities.

Therefore, we will analyse two examples, fuel element vibrations in a flow with phase change and vibration induced by the leak flow in a BWR's jet pumps.
In the latter case, the jet pump FIV can be modelled as a vibration induced by the external axial flow. This is so because the leak flow through the Slip-Joint is deemed to be external to the mixer, as can be seen from Figure 7.

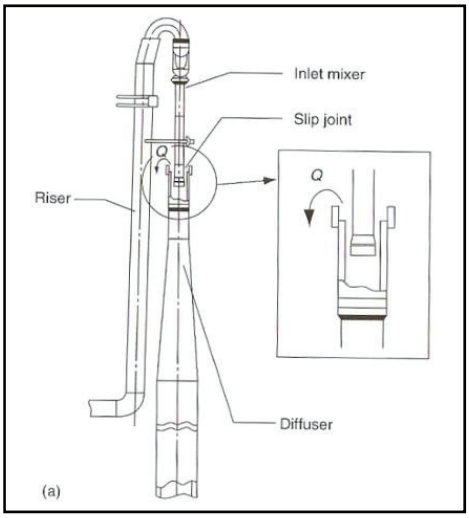


Fig. 7. JetPump and Slipjoint leak.

Thus, the model will be an axial flow cylinder, as described by Chen and Wambsganss (1970). The turbulent flow in the exterior, axial fluid gives rise to uneven pressure distribution on the outer wall of the pipe. Thus, on lacking balance it possesses resulting transverse forces. Moreover, as it is neither a permanent nor a stationary situation, the continuous change in pressure distribution over time, in space and in axial length, produces vibrations. The situation described is that which is shown in Figure 8.

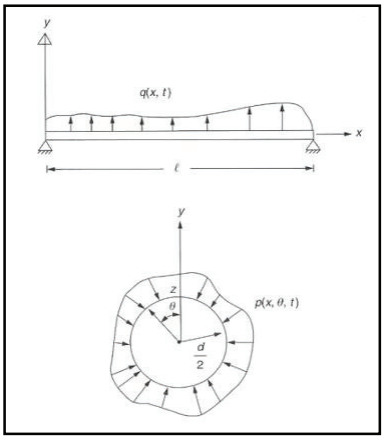


Fig. 8. Pressure distribution in an external flow pattern.

The Corcos (1963) model is used to analyse this type of situation. The model is expressed by:

$$\psi_{pp}(w, z_1, z_2, \theta_1, \theta_2) = \phi_{pp}(w) \cdot A\left(\frac{w|z_2 - z_1|}{V_c}\right) \cdot B\left(\frac{w \cdot D \cdot |\theta_2 - \theta_1|}{2 \cdot V_c}\right) \cdot e^{iw\frac{w|z_2 - z_1|}{V_c}} \quad (43)$$

where $\psi_{pp}$ is the cross-spectral density of the pressure field, $\varphi_{pp}$ is the pressure power spectrum at the point, $A$ and $B$ are spatial functions and $V_c$ is the convection speed.
$\varphi_{pp}$ value is given by:

$$\phi_{pp}(fr) = \begin{Bmatrix} 0.272 \cdot 10^{-5} / fr^{0.25} \; si \; fr < 5 \\ 22.75 \cdot 10^{-5} / fr^{3} \; si \; fr > 5 \end{Bmatrix} \quad (44)$$

where $f_r$ is the reduced frequency, which is given by the following, where $Dh$ is the hydraulic diameter:

$$fr = \frac{f \cdot Dh}{V} = \frac{w \cdot Dh}{2 \cdot \pi \cdot V} \quad (45)$$

The convection speed of the limit layer is given by:

$$\frac{V_c}{V} = 0.6 + 0.4e^{\left(-2.2 \cdot \frac{w \cdot \delta}{V}\right)} \quad (46)$$

where

$$\delta = \frac{Dh}{2(n+1)} \quad (47)$$

$$n = 0.125 \cdot m^3 - 0.181 \cdot m^2 + 0.625 \cdot m + 5.851 \quad (48)$$

$$m = \log(Re) - 3 \quad (49)$$

Lastly, the vibration amplitude is given by the approximations:

$$y_{rms} = \begin{Bmatrix} V^{1.5} \; si \; fr < 0.2 \\ V^2 \; si \; 0.2 < fr < 3.5 \\ V^3 si \; 3.5 < fr \end{Bmatrix} \quad (50)$$

These equations result in the generation of transversal forces, which move the mixer parts, the elbows and the riser. Moreover, as a result of its geometrical configuration, mode 3 vibration causes damage as a result of the stress at the first fixed point of the system, which is the joint between the riser and its support. Indeed, it is this stress that provokes breakages. A detail of the turbulence associated with the simulation of slipjoint leak can be seen in Figure 9.
In general, the Païdousis (1973) model is the equation used for industrial settings.
As far as FIV caused by external flow with phase change is concerned, its study and development can basically be put down to the nuclear industry, after the development of boiling water reactors. At such plants, boiling occurs on the external part of fuel rods in the upflow. This study was later extended to the steam generator pipes of pressurised water reactors. Figure 10.

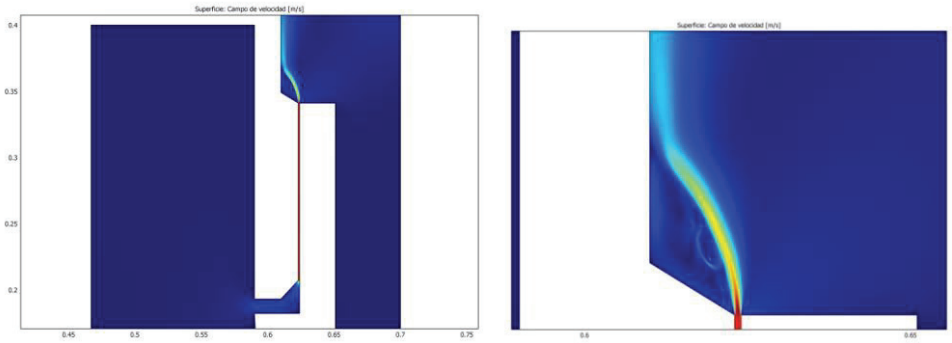

Fig. 9. Simulated Slipjoint leak and vortex induced.

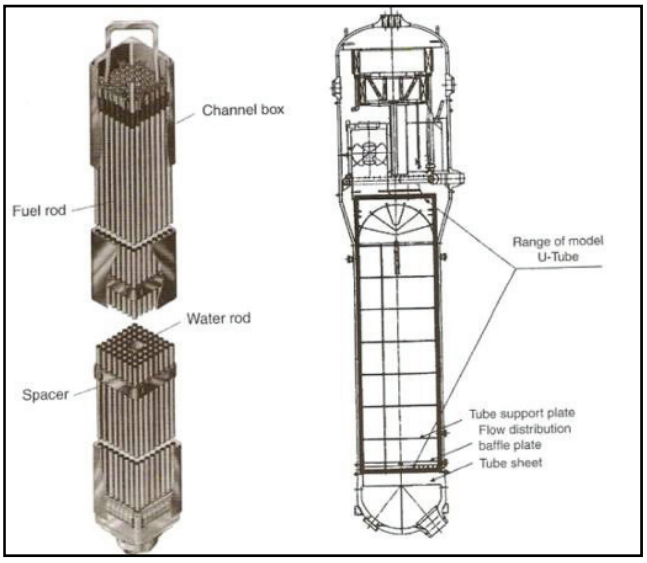


Fig. 10. Fuel Bundle and Steam Generator.

Both studies reached the same conclusion, namely that the vibration amplitude is proportional to the mass upflow, but decreases with pressure. As far as fluid quality, or the void ratio, is concerned, two peaks can be seen, 0.1-0.25 and 0.4-0.5, which suggests that there is great dependence between vibration amplitude and the void ratio, or fluid quality.
On a BWR (Figure x) type fuel bar, it was established that the pressure power spectrum of the excitation force is proportional to $V^{1.56-2.7}$, while the amplitude is proportional to $V^{0.78-1.35}$. These values were determined in a rod test carried out by Pettigrew and Taylor [13] under the following conditions:
Pressure: 2.8-9 MPa
Mass flow: 0-4600 Kg/m²s
Power: 1-1000 Kw
Quality: 0-0.25.
Saito (2002) came to the same conclusions in another test under different conditions.

## 5. Fluid Induced Noise (FIN)

In this section, we will take a look at the noise generated by a turbulent flow. Throughout this chapter and the following sections, fluid dynamics is based on movement equations, with speed as the unknown, essential analysis value.

For this particular case of noise induced by turbulence, a change of mindframe is called for in the sense of assessing the fluid in terms of pressure, and even density. Original FIN theory and expressions are given by the Ligthhill aeroacoustic model (1952/1954), as indicated below:

$$\nabla p^2 - \frac{1}{c_0^2}\frac{\partial^2 p}{\partial t^2} = -\frac{\partial^2 T_{ij}}{\partial x_i \partial x_j} \tag{51}$$

$$T_{ij} = \rho v_i v_j \tag{52}$$

where $T_{ij}$ is the turbulent stress tensor. Whenever the fluid can be compressed, pressure variation is accompanied by density variation, the expression of which is:

$$\frac{\partial^2 \rho}{\partial^2 t} - c_0 \frac{\partial^2 \rho}{\partial x_i \partial x_j} = \rho_0 \frac{\partial^2 v_i v_j}{\partial x_i \partial x_j} \tag{53}$$

Thus, turbulence collaterally generates pressure and density variation in the fluid. By means of the turbulent stress tensor the turbulence produces variations in pressure and density. The former cause the noise, and as such, are deemed to be sound sources.

There are many practical applications of the analysis of turbulence generated noise. Two particularly curious, albeit useful ones, have solved some serious problems. The two situations in question are:

- Determination of leaks through the seat of safety relief valves from the outside by means of non-intrusive techniques.
- Element breakage due to resonance frequencies.

The first of the above situations has been used to detect safety relief valve leaks in BWR nuclear plants. The theoretical principle employed is that the seat leak flow produces turbulence which in turn generates a characteristic sound. The conceptual model is similar to the one used by Van Herpe and Creghton (1994), in which they model the fluid flow through a conduit with a restriction inside. These researchers came to the conclusion that the acoustic power, dB, is proportional to the speed in the conduit and to the passage diameter determined by the restricting element. Consequently, an SRV leak can be detected by means of sound and its register, but also by its evolution. The latter claim is based on the tests done by EPRI on this particular study NP-2444-SY. In this study, the frequency band is established at which the leak is best detected, 40-55 KHz, as well as the complete detection interval, 30-60KHz. Likewise, the author holds that regular monitoring can establish drift and trend patterns, the development mathematical law of which is that determined by Van Herpe y Creghton (1994).

The other case refers to the catastrophic breakages of steam dryers at BWR plants due to an acoustically sourced resonance. (Figure 11).

After the failure of the Quad cities dryer, a study was carried out on the loads to which it was subject. In none of the cases did the operating loads justify the breakage, or degradation, of the component. Consequently, a study was made of the vibratory or pulsatory phenomena, by measuring the vibrations at the component and the passage of

pressure along the main steam lines. Acoustic excitation coming from the main steam lines is the current model. (Figure 12).

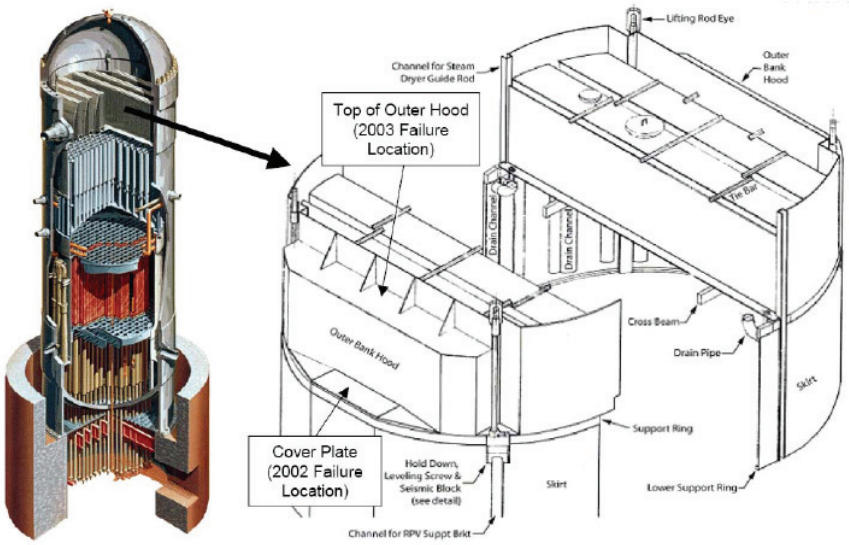


Fig. 11. BWR vessel and Steam dryer detail. (Cracked areas)

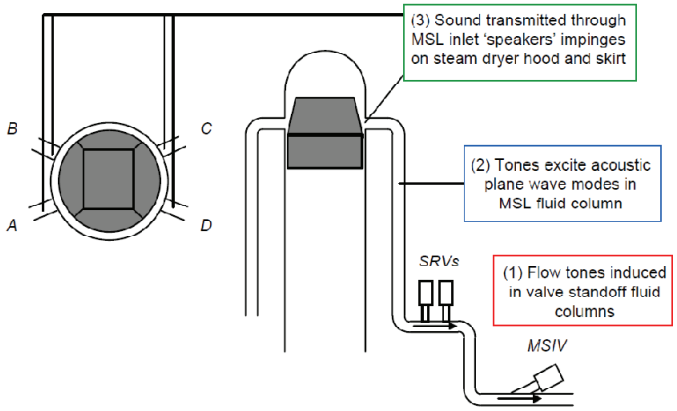


Fig. 12. MSL, SRV's and the main characteristic of the sound transmission.

Acoustic excitation is produced in the main steam lines as a result of the turbulence generated at the SRV connections, instrumentation connections, equalising header, etc… (Figure 13)

This turbulence, which in general, manifests itself as vortices or eddies will, in the Von Karman sense, give off a determined frequency. Moreover, the lower scale turbulence will have its own frequency in accordance with the Lighthill model. Thus, the pressure waves that are generated with a defined frequency will constitute an external dryer load that increase its total dynamic load. (Figure 14).

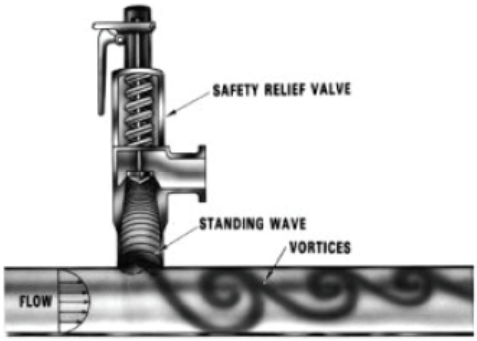


Fig. 13. Singing branch. Vortex Sheeding.

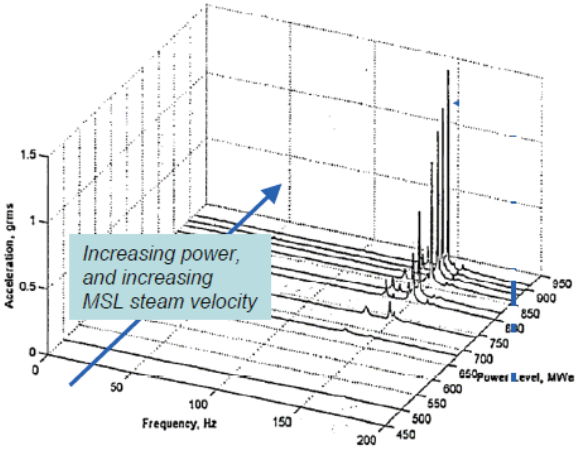


Fig. 14. Frequency dependency of the power and acceleration of the induced load.

Moreover, this load with be pulsatory in nature and will have a determined frequency, thus, if it coincides with a natural dryer frequency, the pressure effects are amplified, exceeding the resistance of the material, in some cases breaking, in others causing cracks.

As can be seen, there are frequencies in Figure 14 that coincide with certain natural ones of parts of the dryer (Figure 15). Consequently, there will certainly be damage. The only variable will be time and the power of the vibration due to the reactor power. Notwithstanding, the solution to the problem is to be found at the same source as the excitation, namely, by studying the turbulence. It has been proven that by changing the geometry of the SRV connection, this changes the spectrum frequency, and consequently, the effect on the dryer. (Figure 16).

In line with the practical focus followed in this chapter, there are reduced analytical studies that make it possible, in a T-type geometry, to predict and check the existence of acoustic excitation applied to steam pipes.

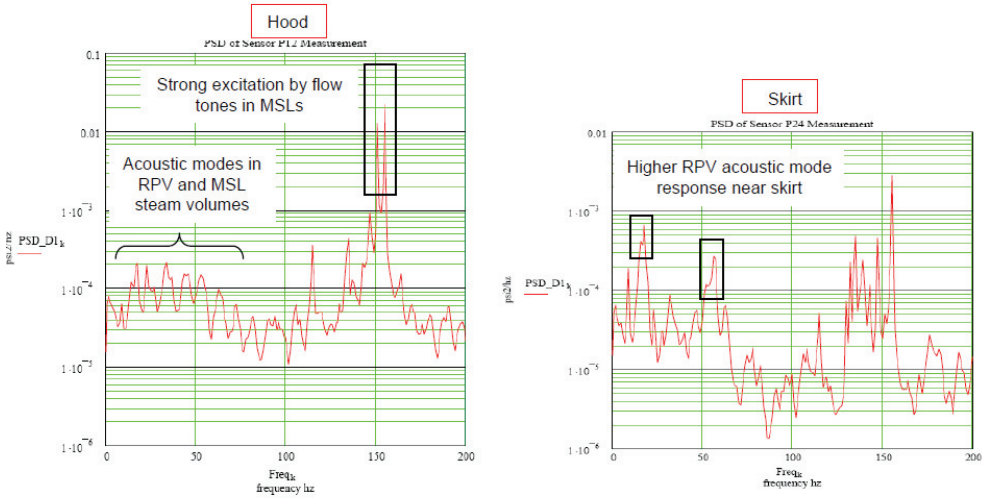


Fig. 15. Natural frequencies of the steam dryer Hood and skirt.

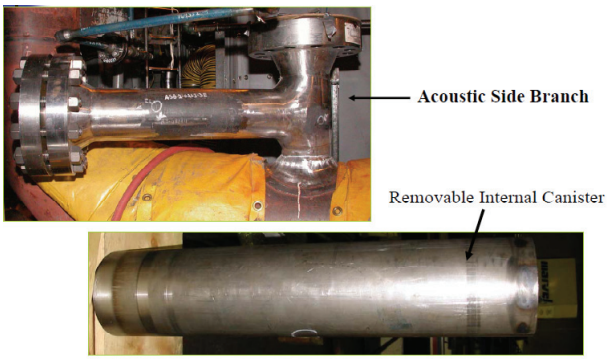


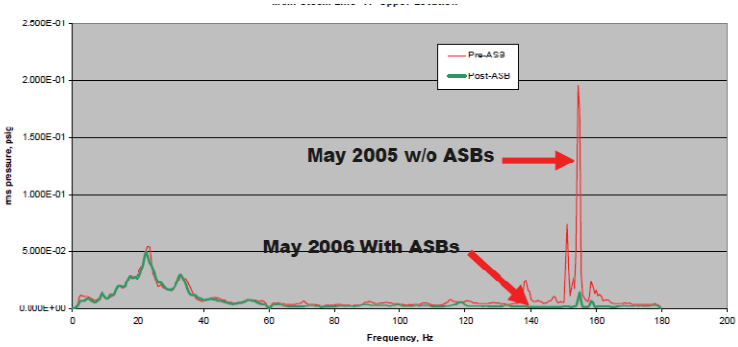


Fig. 16. Acoustic side branch, and the effect on the pressure, or load.

The mathematical expression is:

$$S_0 = \frac{a \cdot N \cdot (d+r)}{4 \cdot L \cdot V_0} \tag{54}$$

where:
$S_0$ is the Stroudhal number;
$a$ is the speed of sound in a fluid medium;
$N$ takes on value of 1 and 3;
$d$ is the branch diameter;
$r$ is the branch curve radius at its connection to the main line;
$L$ is the branch length;
$V_0$ is the main line speed.
The assessment is carried out in accordance with the Strouhal number, defined by the equation $x$, if the value lies within the 0.25-0.60 interval, for which it can be said that there is a big likelihood of acoustic excitation appearing. The frequency estimate can be approximated by the following function:

$$S_0 = \frac{f_s \cdot d}{V_0} \tag{55}$$

## 6. Fluid induced instabilities.

In this section, we are going to deal with fluid instabilities, though more specifically with that which makes the flow bistable, given that this represents a transition within the turbulent system. Notwithstanding, what follows is a brief description of other instabilities about which references and studies abound. Turbulent flow, as has been above, is a generalised process, whereas instability is different. This is an unexpected situation, and one which, in principle, should not be happening. Quite often it is associated with the local formation of turbulence in a laminar, ordered flow. The most widely known instabilities model and study turbulence of this type of situation, but there are other instabilities in a turbulent flow that cause changes to the flow pattern. As with turbulent flow and its transition, instabilities possess factors that give rise to same, which are:

- Fluid-structure interaction: Remodels the flow
  - Von Karman
  - Stroudhal
- Density or viscosity variations
  - Raleigh-Taylor
  - Plateau-Railegh
  - Ritchmyer-Meshkov
- Speed difference
  - Kevin-Heltmotz.
- Increase in turbulence intensity
  - Bistable flow.

All of these instabilities exert different effects on the structure that is either immersed in them, or that contains the flow, such as vibrations, noise or change in process flow values. The latter, is of itself only an instability, albeit a very perculiar one, thus it will be dealt with separately. The others, given their spatial characteristics, have been dealt with separately in Sections 4 and 5.

Presented here is an important advance on the investigation of the bistable flow phenomenon inside a boiling water reactor (BWR) vessel. The study of the flow time series concludes that the phenomenon of the bistable flow is a particular case of transitions induced by turbulence. Afterwards the phenomenon is identified, simulated and the model is validated. The real behaviour is reproduced using the mathematical model, which has given excellent results. Therefore the bistable flow is an instability that comes by transitions induced by turbulent flows and vortex.

During this analysis a new technique was used to characterize the phenomenon. The new technique was the Hilbert´s transform. The conclusion that came from this last study is that:

- The bistable flow is non linear and non stationary
- The bistable flow is produced when the plant is near the coast down and the flow is the maximum
- There is a relationship between the average value of the flow and the bistability.
- The bistable flow has two attractors structure.

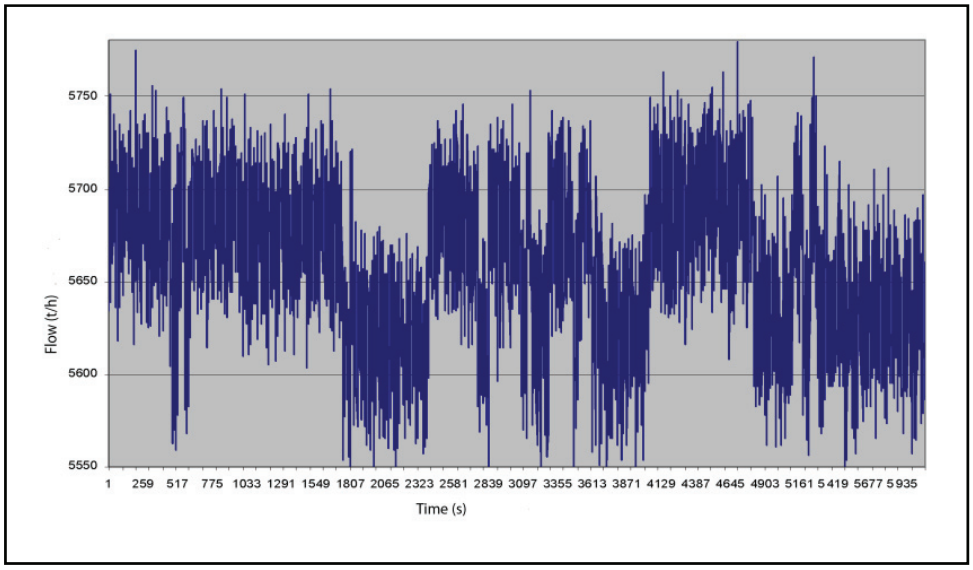


Fig. 17. Flow rate time series of in the recirculation loop. Bistable event.

One of the most absurd process features is that the white noise can induce order in a system that is non linear and non stationary, is not in equilibrium. That is, a chaotic system can be ordered by itself. This is called vibration resonance (Horsthemke, 2005), with transitions induced by noise. In this case the word noise and turbulence will be similar. So this phenomenon is modeled by the Laugevin´s equation (56).

$$\dot{x}_i = f(x_i) + g(x_i)\cdot\varepsilon(t) + \frac{D}{2\cdot d}\Sigma\left(x_j - x_i\right) + A\cos(w\cdot t) + B\cos(\Omega\cdot t) \tag{56}$$

Where:

x(t)i is the state of the i-esim oscillation.

ε(t) it is a gaussian noise zero-averaged an non correlated.

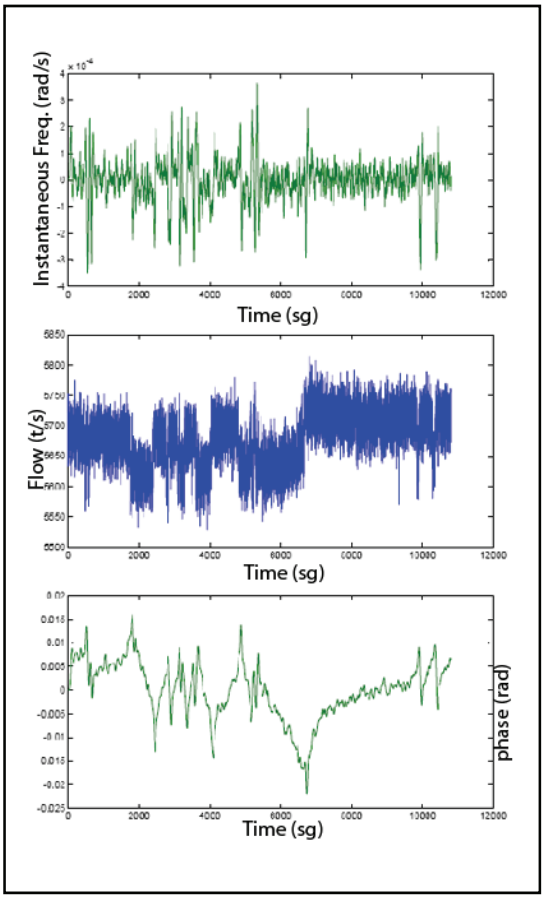


Fig. 18. Results of the Hilbert´s Transform. Real Time series (central), Phase (bottom), Inst. Frequency (upper)

The last terms in the equation, represent the external and periodic forces represented as low frequency and amplitude A, and another of high frequency with amplitude B.
For the case under study the expressions of the functions g(x) and f(x) are:

$$g(x) = K1x \tag{57}$$

$$f(x) = -K2x - K3x3(7) \tag{58}$$

For the above-mentioned the equation of the flow would be in the way:

$$\dot{x}_i = \varepsilon \cdot K_1 \cdot x - K_2 \cdot x - K_3 x^3 + \sqrt{\eta} \cdot \zeta \tag{59}$$

Resuming:

$$\dot{x}_i = x(\varepsilon \cdot K_1 - K_2) - K_3 x^3 + \sqrt{\eta} \cdot \zeta \tag{60}$$

Simplifying:

$$\dot{x}_i = x \cdot K_1^{'} - K_3 x^3 + \sqrt{\eta} \cdot \zeta \tag{61}$$

Where:
x(t) is the flow and $\zeta$ is the zero averaged and non-correlated noise white. The parameters K1' and. K3 will be calculated to determine the times in those that, statistically, the system is in each value, or also called escape times.
To determine the values of the K´s factors it must be consider that:

- The averaged value of the flow is 5650 t/h and if there´s no noise or turbulence the results of the equation (61) are zero.
- The averages deviations of the average value must be +50 and -50 t/h.

The values of the parameters expressed in the equation (61) and that are coherent with the previous premises are given by the table 2.

| Parameter | Value |
|---|---|
| K1` | 0.0052 |
| K2 | 8e-11 |
| η | 0.1797 |
| Desv. Typical Noise | 40 |

Table 2. Values of parameter to equation (58).

The realization of the equation (61), gives results such the follows, showed in figure 19 and 20.

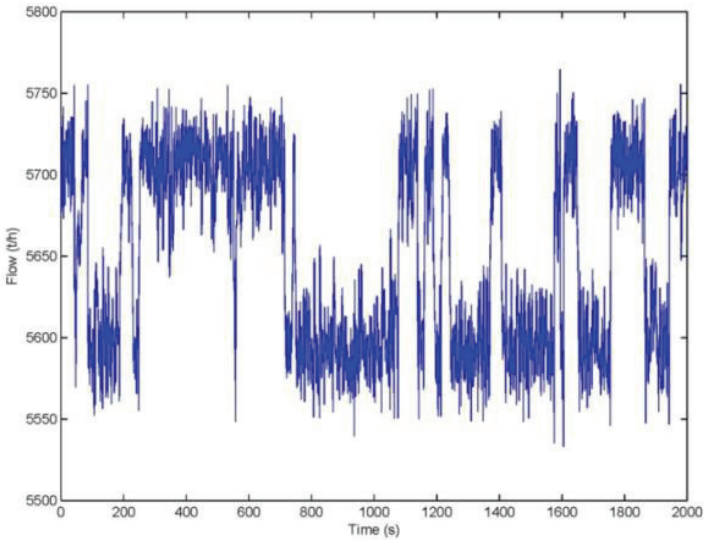


Fig. 19. Realization of the equation (61) with the parameters of the table 2.

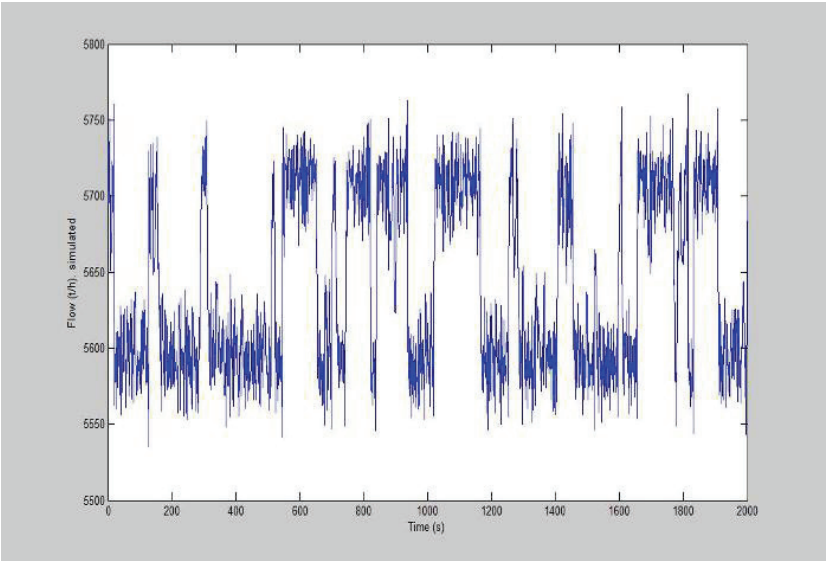


Fig. 20. Realization (2nd) of the equation (61) with the parameters of the table 2.

The previous graphics are two drawings of the flow value in sets of 2000 samples, in order to have a more representative graphic.

The difference between the simulation and the real time series is due to the measurement method that adds a new noise to the signal, but that noise is not important to the phenomenon. The flow is measured by the difference of pressure in an elbow, so in this method the centrifugal force has to be measured and then the mass flow.

The validation is based in two steps. The first step is the generation of the histogram, autocorrelation graphic and the spectral density graphic (figures 21, 22 and 23) to compare with the results showed in the characterization previous work done by Gavilán (2007). And the second is the evaluation of the phase diagram given by the Hilbert´s transform over the simulated data and the comparison with the real data phase

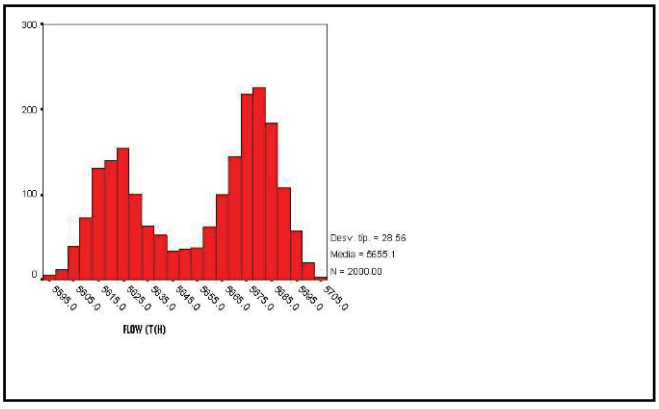


Fig. 21. Simulated time serie Histogram. (2000 seconds)

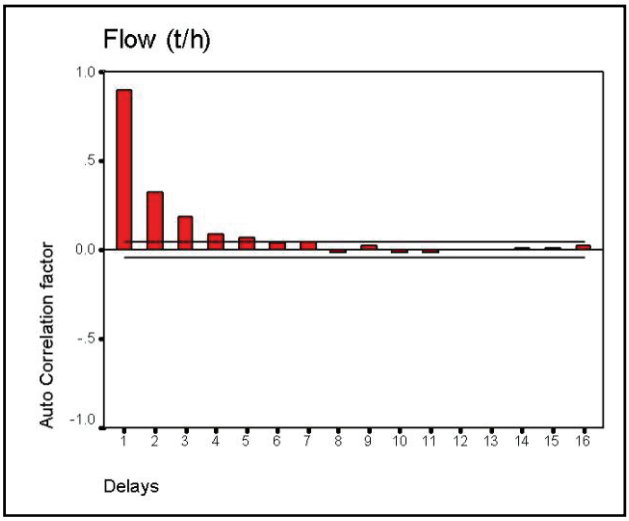


Fig. 22. Simulated time serie Autocorrelation factor

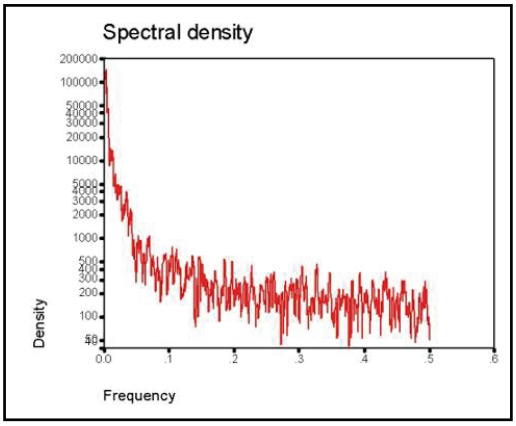


Fig. 23. Simulated time serie Spectrogram.

The statistic parameters of the simulated series, (from figures 21, 22 and 23) are coherent with the results found by Gavilán (2007) in the characterization of the bistable flow signal.

To conclude the validation method, is necessary to check if the simulated time series have the same characteristics as the real one in the Hilbert´s sense. So to compare is necessary to repeat the Hilbert´s transform but now to the simulated time series. The results are showed in the figure 24.

In the figure 124, y can be observed the structure of two attractors in the phase, and in the instantaneous frequency. The law for the transitions between one and the other attractor, in the phase space, is an arcos(K(t)) and the instantaneous frequency is the derivate of it. If we compare the figures17, 18, 19, 20 and 24 can be concluded that the simulated series adjust fairly to the real one. The adjustment appears very qualitative but must remember that the relationship in statistical.

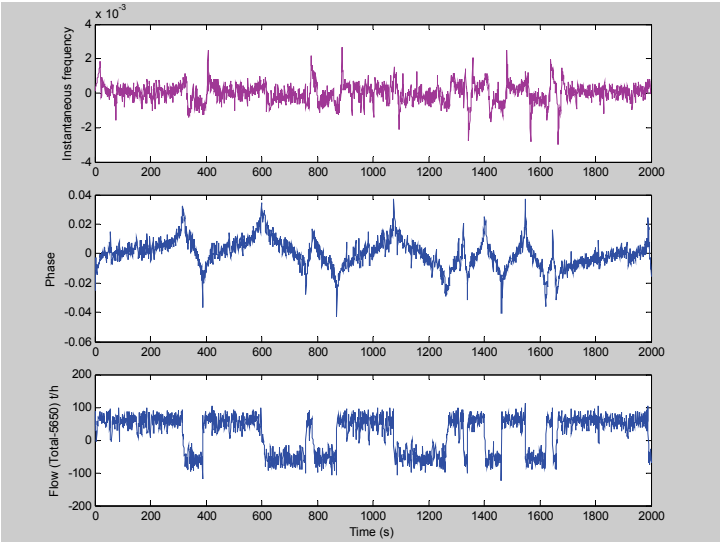


Fig. 24. Results of Hilbert´s transform to simulated data.

The characterization of the bistable flow results in, that is non linear and non stationary process. The bistable flow can be evaluated and characterized, properly using the Hilbert´s Transform.

The bistable flow appears under some operative conditions without change in the values of control variables, so is associated to an internal variation. The variation is due to the turbulence that is a self oscillatory process in a continuous medium. The development of a turbulence event is the birth of an attractor in the space of the phase. The turbulence is a convective process because it doesn´t increase indefinitely but rather it evolve to water bellow. All those conclusions about the turbulence justify that the flow change the average value of the speed and then the value of the flow taking one of the two values of the attractor.

The turbulence is an unstructured process, because there´s no pattern in it. The Fourier transform gives poor results when is used so that´s the reason why the turbulence is associated to a noise, and sometimes to a white noise. The phenomenon of bistable flow is a turbulence induced transition process, because the reason of the jumping between two flow values is the turbulence. Because turbulence and noise are physically the same, mathematically the phenomenon can be simulated with a noise-induced transition model.

The simulation gives us, a low error simulated time series that had the same statistical parameters than the original. And the other idea is that the bistable flow only appears in a finite region of the flow space, because there´s only a set of values of the turbulence and flow that induce the bistable behavior. In the same idea, the noise (turbulence) has only one value to induce the bistable flow. The characteristics parameter of the noise is the average that must be zero, and the standard deviation that has a relationship with the value of flow, and only in a small interval of values produce the bistable flow (table 3, figure 25). The relationship between the noise standard deviation and the flow depends in every installation because depends on the hardware but in this case can be modeled by the equation (62).

$$StdDev(F) = 30.02 + \frac{A}{\frac{B^2}{Flow(t/h)^2} - 1} \tag{62}$$

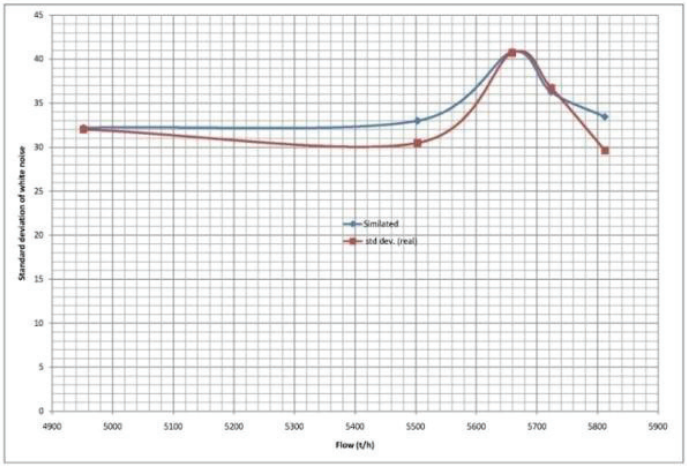


Fig. 25. Relationship between average flow and noise typical deviation.

| Interval Time | Min. Flow (t/h) | Max. Flow(t/h) | Average Error | Typical Deviation | R2 adjusts lineal | Bistability |
|---|---|---|---|---|---|---|
| 300-1200 | 4423.9 | 5479.2 | 4.17 | 32.01 | 0.9844 | No |
| 1500-3000 | 5323.3 | 5682.9 | -41.01 | 30.47 | 0.7952 | No |
| 3001-10000 | 5492.7 | 5825.7 | 0.091 | 40.71 | 0.5011 | Yes |
| 10001-13000 | 5579.9 | 5867.7 | 0.055 | 36.72 | 0.2972 | Yes, smaller |
| 13001-15000 | 5695.3 | 5929.5 | 0.0455 | 29.63 | 0.1482 | Residual |

Table 3. Parameters of several intervals of flow and conditions.

## 7. Conclusion

This chapter has shown that turbulence exercises several effects in the industrial setting, and except for those of diffusion, or mixture, all the others are both harmful and give rise to problems. Given its variety and applicability, it is not easy to discover the reason for a component failure. Sometimes, only an in-depth analysis of the problem from the perspective of turbulence can serve to clarify a case that defies normal analyses.

Therefore, a thorough grounding in fluid mechanics is needed to solve the problems related to turbulence. Furthermore, a knowledge of computer fluid flow modelling tools, which

involves so-called Computational Fluid Dynamics (CFD), represents a great advance in the knowledge of the turbulent behaviour of fluids in movement. Notwithstanding, all is not science and mathematics, given that turbulence is chaos, and therefore, there will always be a certain druidic facet in those professionals given to working in this field.
As an end to this chapter, we provide a summary table (Table 4) that can serve as a guide to locating what effect may be producing the turbulence, with the aim in mind of better focusing the subsequent analyses.

| **Fluid type // condition** | **Turbulence effect** | **Affected area** |
|---|---|---|
| Single-phase // Saturated fluid | Cavitation | Venturi tubes and geometry changes |
| Single-phase fluid | Instability | Connection geometry |
| | Noise // Acoustic Excitation | Connection geometry |
| Fluid structure | Vibration | Elements submerged in the current |
| | Noise // Acoustic Excitation | Elements submerged in the current |

Table 4. Summary of fluid type and effects.

Lastly, a look at the use of CFD´s. The use of this type of tool does not ensure the success of the study, given that employing it a preliminary analysis needs to be done and the following defined:

- Model type (LES, RANS, DNS…)
- Minimum modelling scale (Kolmogorov)
- Analysis type (permanent or provisional system)
- Variable to be simulated (density, pressure or speed)

Otherwise, the results from the computer will be nothing more that a nicely coloured drawing, without any coherent information.

> *"Linearity is an idea sought after, yearned for and forced by the human mind. It is a reflection of our condition as animal. Only by accepting, assimilating and understanding the chaos of the world that surrounds us, will we truly ascend to the rational condition."*

## 8. References

United Stated Nuclear Regulatory Commision. (1986). Anomaluos behavior of recirculation loop flow in jet pump BWR plants, Information. *notice No. 86-110*. Washington.

A. Nuñez Carrera, E. Martinez-Mendez, G. Espinosa Paredes (2006), Análisis del fenómeno de flujo biestable de la central Nucleoeléctrica de Laguna Verde. *Proceedings of the 2006 Congreso Internacional Buenos Aires. LAS/ANS.*

C.J Gavilán Moreno (2007). El flujo biestable en lazos de recirculación de una central BWR. Analisis y caracterización. *Proceeding of the XXXIII Reunión anual de la Sociedad Nuclear Española.*

C.J. Gavilan Moreno, (2008) Analysis and simulation of the flow signal in the recirculation loop of a nuclear power station during a bistable flow event. *Nuclear engineering and Design*. Vol 238, Issue 10, pp-2754-2760.

C.J, Gavilán Moreno (2009) Hydraulic study on recirculation loops using computational fluid dynamics (CFD). Design optimization and turbulence reduction. *Nuclear Engineering and Design,* Volume 239, Issue 3, pp 434-441

N.E Huang, Introduction to the Hilbert-Huang transform and its related mathematical problems. *Goodard Institute for Analysis dates*. NASA.

S. Ziada, S. Shine. (1999). Strouhal numbers of flow excited acoustic resonance of closed side brances. *Journal of fluids and structures*. Vol 13. 127-142.

R.M. Baldwin H.R. Simmons.(1986). Flow induced vibration in safety relief valves. *Journal of pressure vessel technology*. Vol.108. Pp. 267-272.

O.C. Zienkiewicz; R.L. Taylor (2004) *El método de los elementos finitos. Vol. 3, dinámica de fluidos*. Ed. CIMNE.

K. Morgan, E. Oñate, J. Periaux, J. Peraire and O (1993) *Finite element in fluids. New trends and applications.* Ed. CIMNE.

Lesieur. M (2008) *Turbulence in fluids* Ed. Springer.

Horsthemke & Lefever (2005). *Noise Induced Transitions.* Ed. Springer series in Sinergetics.

White, Frank M. (2008) *Mecánica de fluidos*. Ed. McGraw-Hill.

D'Agostino-Salvatore Eds (2007) *Fluid Dynamics of Cavitation and Cavitating Turbopumps*. Ed. SpringerWien NewYork.

Persson, Per-Olof. (2002) *Implementation of finite element based Navier Stokes Solver.* 2094 Project.

Bigersson, F.; Finnveden, S. ; Robert, G. (2004) Modelling turbulence induced vibration in pipes with a spectral finite element method. *Journal of sound and vibration.* Vol 278. Pp 749-772.

Kolmogorov, A.N. (1941) The local structure of turbulence in incompressible viscous fluid for very larger Reynolds numbers. *Proc. R. Soc Lond. A.* Vol 434, pp 9-13.

Roshko, A. (2000) On the problem of turbulence. *Current Science*, Vol 76, No 6, pp 834-839.

Dassé, J.; Mendez, S.; Nicoud, F () Large-Eddy Simulation of Acoustic Response of a perforated plate. *American Institute of Aeroanutics.*

Van Herpe,F.; Crighton, D.G. (1994) Noise generation by turbulent flow in ducts. *Journal de Physique III,* Vol 4. Pp 947-950.

Davies, P.; Holland, K.R.; (2004) Flow Noise generation in expansion chambers. *Procc of the Institute of Acoustic.* Vol. 26. Pt. 2, pp 206-213.

Hamakawa, H. et all (2006) Effects of flow induced Acoustic resonance on vortex shedding form Staggered tube banks. *JSME International Journal.* Series B, Vol. 49, No. 1, pp 142-151.

Chen, S.S.; Wambsganss, Jr. M.W. (1970) Response of a flexible rod to near field flow noise. *Proceedings of the conference on flow induced vibrations in reactor system components.* ANL-7685 Argonne National Laboratory.

Corcos, G.M. (1963) Resolution of pressure in turbulence. *J. Acoustic Soc. Am*. Vol 35, No 2 pp 192-199.

Païdoussis, M.P. (1973) Dynamics of cylindrical structures subjected to axial flow. *Journal of Sound and vibration. Vol.* 29, No 3, pp 365-385.

Saito, N. et all. (2002) BWR 9x9 Type Rod Assembly Thermal Hydraulic Test (2) – Hydraulic Vibration Test. *10th International Conf. on Nuclear Engineering*. ICONE10-22557.

Lighthill M. J., (1952) On Sound Generated Aerodynamically. I. General Theory, *Proc. R. Soc. Lond*. A 211 pp. 564-587.

Lighthill M. J., (1954) On Sound Generated Aerodynamically. II. Turbulence as a Source of Sound, *Proc. R. Soc. Lond*. A 222 pp. 1-32.

# 6

# CFD-based Evaluation of Interfacial Flows

Kei Ito[1], Hiroyuki Ohshima[1], Takaaki Sakai[1] and Tomoaki Kunugi[2]
[1]*Japan Atomic Energy Agency*
[2]*Kyoto University*
*Japan*

## 1. Introduction

Gas-liquid two-phase flows with interfacial deformations have been studied in various scientific and industrial fields. However, owing to the complexity of interfacial transient behaviors, the full understanding of gas-liquid two-phase flows is extremely difficult. For example, the occurrence condition of gas entrainment (GE) from free surface is not yet clarified even though a number of studies have been conducted by a lot of researchers. Unexpected GE phenomena often cause problems with equipments or troubles in plant operations (e.g. pump failure) and suppression of their occurrences by flow optimization is strongly required from the viewpoints of operation rates and safety. Therefore, the high-level understanding of interfacial flows is very important and should be achieved appropriately based on mechanistic considerations.
In this Chapter, the authors propose two methodologies to evaluate the GE phenomena in fast reactors (FRs) as an example of interfacial flows. One is a CFD-based prediction methodology (Sakai et al., 2008) and the other is a high-precision numerical simulation of interfacial flows. In the CFD-based prediction methodology, a transient numerical simulation is performed on a relatively coarse computational mesh arrangement to evaluate flow patterns in FRs as the first step. Then, a theoretical flow model is applied to the CFD result to specify local vortical flows which may cause the GE phenomena. In this procedure, two GE-related parameters, i.e. the interfacial dent and downward velocity gradient, are utilized as the indicators of the occurrence of the GE phenomena. On the other hand, several numerical algorithms are developed to achieve the high-precision numerical simulation of interfacial flows. In the development, an unstructured mesh scheme is employed because the accurate geometrical modeling of the structural components in a gas-liquid two-phase flow is important to simulate complicated interfacial deformations in the flow. In addition, as an interface-tracking algorithm, a high-precision volume-of-fluid algorithm is newly developed on unstructured meshes. The formulations of momentum and pressure calculations are also discussed and improved to be physically appropriate at gas-liquid interfaces. These two methodologies are applied to the evaluation of the GE phenomena in experiments. As a result, it is confirmed that both methodologies can evaluate the occurrence conditions of the GE phenomena properly.

## 2. Brief description of GE phenomena

The GE phenomena can be observed in a lot of industrial plants with gas-liquid interfaces, e.g. pump sump. Therefore, the GE phenomena have been studied theoretically and

experimentally in many years (Maier, 1998). In the experiments, the onset condition of the GE phenomena in a reservoir tank or main pipe with branch pipe was investigated in detail. As a result, the onset conditions of the GE phenomena are summarized as the function of Froude number (*Fr*) (Zuber, 1980):

$$\frac{H_{GE}}{d_b} = b_1 Fr^{b_2}, \tag{1}$$

where $H_{GE}$ is the critical interfacial height of the GE phenomena, $d_b$ is the diameter of a branch. $b_1$ and $b_2$ are the constants determined depending on the geometrical configurations in each experimental apparatus. Froude number is defined as

$$Fr = \frac{v_d}{\sqrt{\frac{\Delta\rho}{\rho_l} g d_b}}, \tag{2}$$

where $v_d$ is the liquid velocity (suction velocity) in a branch, $\rho_l$ is the liquid density, $\Delta\rho$ is the density difference between liquid and gas phases and $g$ is the gravitational acceleration. Equation 1 can be derived from theoretical considerations with the Bernoulli equation (Craya, 1949), i.e. Eq. 1 implies the energy conservation law between potential and kinetic energies. Therefore, Eq. 1 is widely accepted among researchers of the GE phenomena.

The authors are interested in the GE phenomena at the gas-liquid interface in the primary circuit of FRs. It is well known that FR cycle technologies are expected to provide realistic solutions to global issues of energy resources and environmental conservations because they are efficient for not only the reduction of carbon dioxide emission but also the effective use of limited resources (Nagata, 2008). However, large-scale FRs have positive void reactivity, i.e. core power increases when gas bubbles flow into the core through the primary circuit. Moreover, gas bubbles in the primary circuit may cause the performance degradation of the heat exchangers. Therefore, the GE phenomena should be suppressed to reduce the number of the gas bubbles in the primary circuit and to achieve the stable operation (without power disturbances) of FRs. The GE phenomena in FRs are caused at the gas-liquid interface in an upper plenum region of the reactor vessel (the region located above the core). As showin in Fig. 1, the GE phenomena in FRs have been classified into three patterns, i.e. waterfall, interfacial disturbance and vortical flow types (Eguchi et al., 1984). Former two patterns can be suppressed by reducing the horizontal velocity at the gas-liquid interface. However, the GE phenomena caused by vortical flows is very difficult to determine a suppression criterion because the vortical flows at the gas-liquid interface are formed very locally and transiently. In fact, most vortical flows are initiated as the wake flows behind obstacles at the gas-liquid interface, e.g. inlet and/or outlet pipes in the upper plenum region, and intensified by interacting with local downward flows. Therefore, the suppression criterion of the GE phenomena caused by vortical flows should be determined based on local complicated flow patterns. In this case, a rather simple equation like Eq. (1) can not be applied to the evaluation of the GE phenomena and the property of vortical flows should be considered to the evaluation (Daggett & Keulegan, 1974). The authors propose two methodologies to evaluate the GE phenomena caused by vortical flows in FRs.

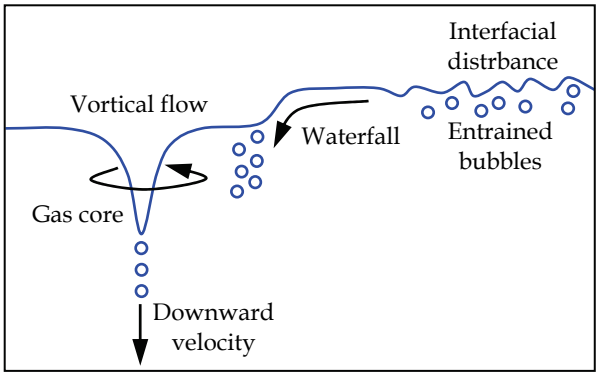


Fig. 1. GE phenomena in FRs

## 3. CFD-based prediction methodology

### 3.1 Basic concept

For the evaluation of the GE phenomena in FRs, complicated flows (vortical flows) which cause the GE phenomena have to be understood appropriately. However, it is highly difficult to predict the vortical flow patterns in complicated geometrical system configurations of FRs. In this case, CFD can be the efficient tool to evaluate the vortical flows in such a complicated FR system. Therefore, the authors propose a GE evaluation methodology in combination with CFD results (CFD-based prediction methodology) (Sakai et al., 2008). In the CFD-based prediction methodology, first, a transient numerical simulation of vortical flows is performed on a relatively coarse mesh to reduce the computational cost. For the same reason, interfacial deformations are not considered and the interfaces are modeled as the free-slip walls in the transient numerical simulation. Owing to these simplifications, the vortical flows can not be reproduced completely in the CFD result. Then, a theoretical flow model is applied to the CFD result to compensate for the mesh coarseness and to determine the strengths of each vortical flow. In the CFD-based prediction methodology, the Burgers theory (Burgers, 1948) is employed to calculate the gas core length (interfacial dent caused by the vortical flow) which is an important indicator to evaluate the GE phenomena.

### 3.2 Vortical flow model

In the CFD-based prediction methodology, the Burgers theory is employed as a vortical flow model. The Burgers theory is derived as a strict solution of the axisymmetric Navier-Stokes (N-S) equation:

$$u_r = -\frac{1}{2}\alpha r, \tag{3}$$

$$u_\theta = \frac{\Gamma_\infty}{2\pi r}\left[1 - \exp\left\{-\left(\frac{r}{r_0}\right)^2\right\}\right], \tag{4}$$

$$u_z = \alpha\left(z - h_\infty\right), \tag{5}$$

where $r$, $\theta$ and $z$ show the radial, tangential and axial directions, respectively ($u_r$, $u_\theta$ and $u_z$ are the velocity components of each direction). $\alpha$ is the downward velocity gradient, $r_0$ is the specific radius of a vortical flow and $h_\infty$ is the standard interfacial height at the far point from the vortical flow. Here, $\alpha$ and $r_0$ are related theoretically as

$$r_0 = 2\sqrt{\upsilon/\alpha}\,. \tag{6}$$

From the momentum balance equation in radial and axial directions, the equation of interfacial shape can be obtained as

$$g\frac{dh}{dr} = \frac{u_\theta^2}{r}, \tag{7}$$

where $h$ is the interfacial height. Here, Eq. 7 is based on the assumption that the advection terms in the N-S equation is negligible compared to the pressure or gravitational term (Andersen et al., 2003). By substituting Eq. 4 into Eq. 7, the gas core length (the interfacial dent at the center of the vortical flow) is calculated as

$$L_{gc} = \frac{\log 2}{g}\left(\frac{\alpha\Gamma_\infty}{2\pi\upsilon}\right)^2, \tag{8}$$

where $L_{gc}$ is the gas core length, $\Gamma_\infty$ is the circulation (at the free vortical flow region) of a vortical flow and $\upsilon$ is the dynamic viscosity of liquid phase. In Eq. 8, $\alpha$ and $\Gamma_\infty$ are necessary to calculate the gas core length. Therefore, in the CFD-based prediction methodology, these values are calculated by using the CFD result. As the first step of the calculation procedure, the second invariant of the velocity deformation tensor is calculated at the gas-liquid interface based on the CFD result to evaluate the strength of each vortical flow (Hunts et al., 1988). In this stage, vortical flows are extracted as the regions with negative second invariant, and the centers of each vortical flow are determined as the points with the minimum second invariant. For the strong vortical flows (with highly negative second invariant) which may causes the GE phenomena, the calculated second invariant is used again to determine the outer edges of each strong vortical flow. The initial outer edge is determined as the isoline of the second invariant with the value of zero. The reference circulation is calculated along the initial outer edge as

$$\Gamma_\infty = \int_C \vec{u}d\vec{s}, \tag{9}$$

where $\vec{u}$ is the velocity vector and the integral path $C$ is determined as the outer edge ($d\vec{s}$ is the local tangential vector on $C$). Then, the outer edge is expanded radially, step by step, from the initial one to that twice larger than the initial one, and the circulation values are calculated on each expanded outer edge. Finally, to pick up the conservative value of the circulation, the maximum value is selected as the circulation of the vortical flow. On the other hand, the downward velocity gradient is calculated on the initial outer edge (isoline of the second invariant with the value of zero) as

$$\alpha = \frac{\int_C \vec{u}\cdot\vec{n}_C ds}{A}, \tag{10}$$

where $\vec{n}_C$ is the unit vector normal to the outer edge (*C*) and *A* is the area of the inner region (surrounded by the outer edge). *ds* is the local length of the outer edge. Eq. 10 shows the averaged downward velocity gradient in the inner region which is calculated as the averaged horizontal inlet flow rate into the inner region. By substituting these two calculated parameters into Eq. 7, the gas core length can be calculated based on the Burgers theory.

### 3.3 Two types of GE phenomena

In the FRs, the generation of the vortical flow with strong downward velocity is the key of the occurrence of the GE phenomena. Therefore, this flow pattern is modeled in two simple experiments to investigate types of the GE phenomena. Those simple experiments are performed by utilizing a cylindrical vessel which has an outlet pipe installed on the center of the bottom of the vessel. As for the working fluids, water and air at room temperature are employed in those simple experiments.

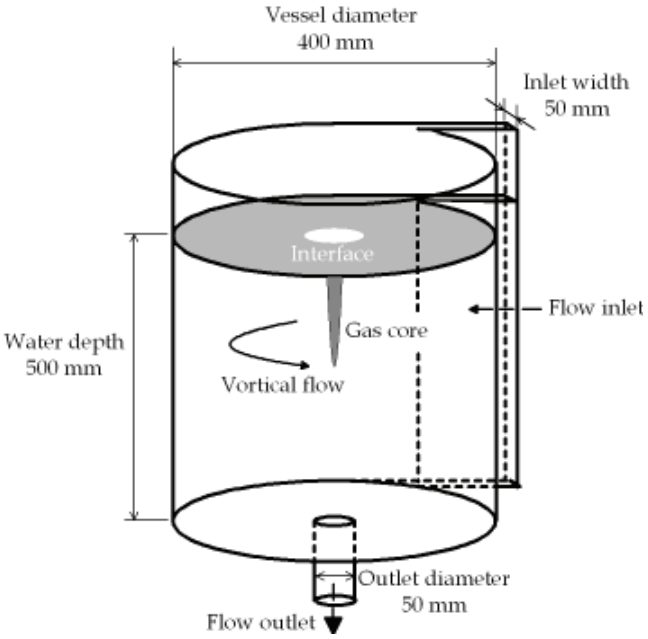


Fig. 2. Schematic view of Moriya's experimental apparatus

The first experiment was performed by Moriya (Moriya, 1998). As shown in Fig. 2, the inner diameter of the cylindrical vessel and outlet pipe are 400 and 50 mm, respectively. The water depth is kept at 500 mm. The water is driven by a pump and flowed into the cylindrical vessel in tangential direction through a rectangular inlet with the width of 40 mm. In the cylindrical vessel, a vortical flow is caused by this inlet flow and intensified by the downward flow towards the outlet pipe on the bottom of the vessel. Therefore, the strength of the vortical flow increases and the gas core became longer as the inlet flow rate increases. Finally, the GE phenomena occur when the tip of the gas core reached the outlet pipe. Then, a ring-plate whose inner and outer diameters were 100 and 400 mm was set on the gas-liquid interface to investigate the change in the GE phenomena. As a result, it was found

that the ring-plate made the downward velocity gradient near the gas core higher and caused bubble pinch-off from the tip of the gas core.
The second experiment was performed by Monji (Monji et al., 2004). For this experiment, a cylindrical vessel similar to the Moriya's (without a ring-plate) is employed. The inner diameter of the cylindrical vessel and outlet pipe are 200 and 12.5 mm, respectively. The water depth is kept at 250 mm and the width of the rectangular inlet is 20 mm. A vortical flow and gas core are generated in the cylindrical vessel with the same mechanism as the Moriya's experiment. In this (Monji's) experiment, typical bubble pinch-off from the tip of gas core was observed as shown in Fig.3 by utilizing a micro-scope. This bubble pinch-off occurred continuously from the gas core. In this case, the gas core length was only about 60 mm and the tip of the gas core had the diameter of approximately 0.5 mm.

Fig. 3. Bubble pinch-off type of GE phenomena

From the results of these two experiments, the authors define the two types of the GE phenomena, i.e. a) elongated gas core type and b) bubble pinch-off type. It is evident that the elongated gas core type is caused by a strong vortical flow which makes the gas core length longer than a liquid depth. In addition, the experimental results show that the strong downward velocity gradient near the tip of a gas core can cause the bubble pinch-off. Therefore, in the CFD-based prediction methodology, the gas core length and downward velocity gradient should be considered as the indicators to evaluate two types of the GE phenomena.

### 3.4 Onset conditions of GE phenomena

In the CFD-based prediction methodology, the gas core length and downward velocity gradient are evaluated by Eqs. 8 and 10, respectively. However, it is necessary to determine the criteria of the GE occurrences for the prediction of the GE phenomena. In this section, the criteria are determined based on the CFD results of the simple experiments (like the Moriya's or Monji's experiment).
In this study, the CFD of the Monji's, Moriya's and Sakai's (Sakai et al., 1997) experiments are performed under the boundary conditions consistent with the experimental conditions. For the CFD of those experiments, the authors utilize the FLUENT code. In the CFD, the 2nd order up-wind scheme is applied for the advection term of the N-S equation, and the turbulent model is not employed to diminish the model dependency to the CFD result. In addition, the interfacial deformation model is not employed to reduce the computational cost, and the gas-liquid interface is treated as a flat free-slip wall. Figure 4 shows the computational mesh for the CFD of the Monji's experiment, which is subdivided by only

hexahedral cells. As for boundary conditions, the uniform velocity condition is applied to the inlet, and the constant pressure condition is applied to the outlet. The transient CFD is performed for over 100 seconds to obtain the quasi-steady result.

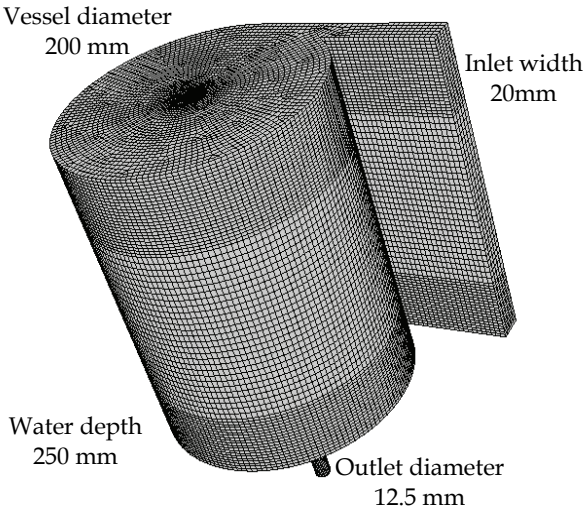


Fig. 4. Computational mesh for CFD of Monji's experiment

Figure 5 shows the comparison of the circumferential velocity distributions in the experimental and CFD results. It is evident that the CFD result agrees well with the experimental result in the free vortical flow regions, and therefore, the circulation can be evaluated accurately by Eq. 9 in the CFD-based prediction methodology. The CFD of the Moriya's experiments is also performed and the downward velocity distribution in the CFD result is compared to the experimental result. As shown in Fig. 6, the CFD can not reproduce the experimental result near the center of the vortical flow. However, the CFD results approach to the experimental results as the radius from the center of the vortical flow

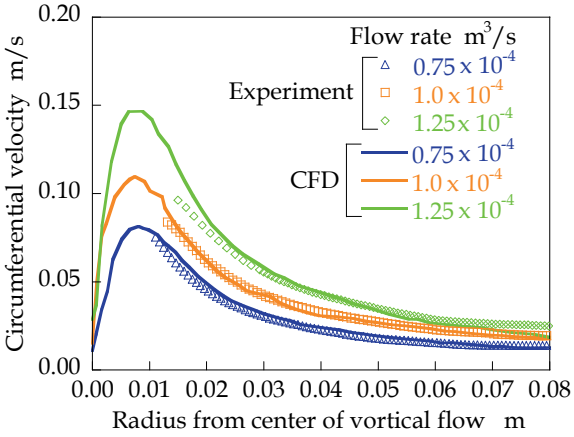


Fig. 5. Cicumferential velocity in CFD result of Moji's experiment

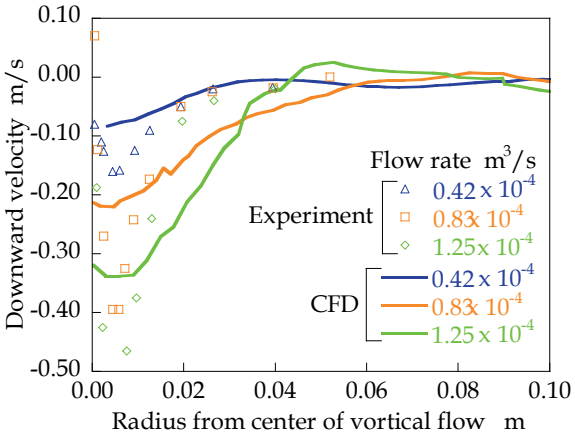


Fig. 6. Downward velocity in CFD result of Moriya's experiment

increases and the downward velocities converge to zero. This behavior shows that the areas of the regions with non-zero downward velocity are the almost same in the CFD and experimental results near the center of the vortical flow. Therefore, the averaged downward velocity can be evaluated accurately by Eq. 10 in the CFD-based prediction methodology.

Figure 7 shows the gas core length evaluated by the CFD-based prediction methodology. In this figure, two non-dimensional numbers are introduced to organize the CFD results, which are defined as

$$\alpha^* = \frac{\alpha \upsilon}{g h_\infty}, \tag{11}$$

$$\Gamma^* = \frac{\Gamma_\infty}{\upsilon}, \tag{12}$$

In reference to Eq. 8, the ratio of the gas core length to the liquid depth (non-dimensional gas core length) can be written as

$$\frac{L_{gc}}{h_\infty} = K \cdot \alpha^* \cdot \Gamma_\infty^{*2}, \tag{13}$$

where $K$ is 4.389 × $10^{-3}$. Therefore, the lateral axis of Fig. 7 is proportional to the non-dimensional gas core length evaluated by the CFD-based prediction methodology, and the vertical axis shows the non-dimensional gas core length in the experimental results (the subscripts EXP and CFD show the experimental result and the values evaluated based on the CFD result, respectively). From these definitions, it is apparent that the elongated gas core type GE phenomena occur when the non-dimensional gas core length excesses unity. Therefore, the indicator of the elongated gas core type of the GE phenomena should be determined based on Eq. 13 if the CFD-based prediction methodology can evaluate the non-dimensional gas core length exactly. In that case, the plots have to lie on the line of the Burgers theory (the red bold line in Fig. 7). Actually, the plots are scattered almost within the range from one-third to three-times of the Burgers theory (the error bars of the lateral

values show the transient fluctuation in CFD results). Therefore, the authors determine the first onset condition for the elongated gas core type of the GE phenomena as

$$\alpha^*_{CFD}\left(\Gamma^*_\infty\right)^2_{CFD} < 76. \tag{14}$$

Equation 14 is derived from Eq. 13 with the consideration of the three times allowance, and is shown by the red left dotted line in Fig. 6. By employing this criterion, the occurrences of the elongated gas core type of the GE phenomena can be predicted with appropriate conservativeness.

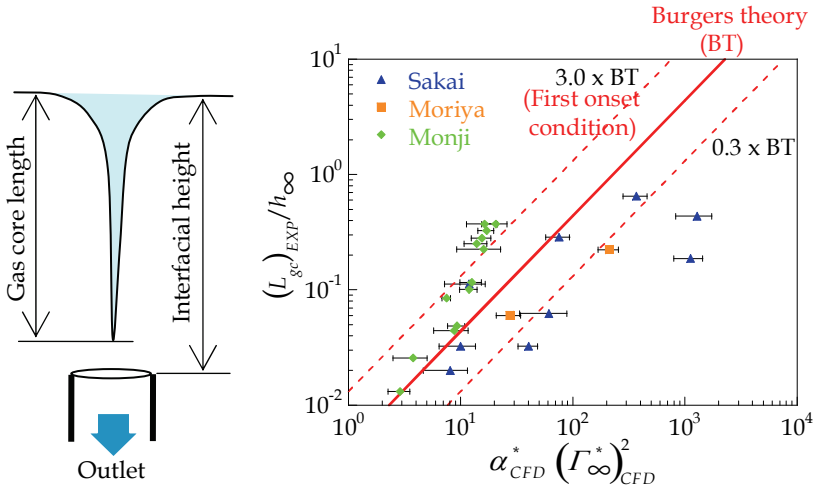


Fig. 7. Prediction accuracy of gas core length

Figure 8 shows the downward velocity gradient evaluated by the CFD-based prediction methodology. As mentioned in Section 3.3, it is apparent that the bubble pinch-off type of

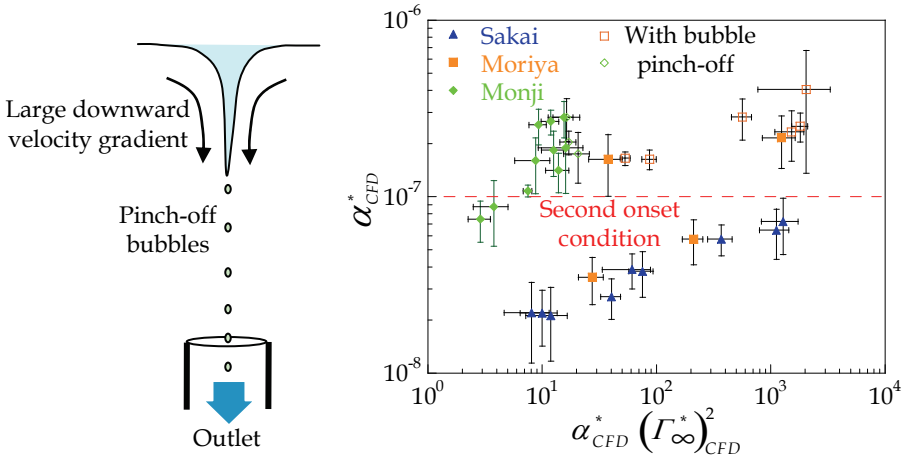


Fig. 8. Bubble pinch-off behavior

the GE phenomena (open plots) occurs when the downward velocity gradient becomes large. Therefore, the authors determine the second onset condition for the bubble pinch-off type of the GE phenomena empirically as

$$\alpha^*_{CFD} < 10^{-7}. \tag{15}$$

The occurrence of the GE phenomena in FRs is predicted by using these two conditions (Eqs. 14 and 15).

### 3.5 Application to GE phenomena in FRs

For the validation of the CFD-based prediction methodology, the GE phenomena in a 1/1.8 scale partial model (Kimura et al., 2008) are evaluated. Figure 9 shows the 1/1.8 scale partial model in which the geometrical configurations of the FR system components, e.g. the pipes, are reproduced accurately. The dipped plate (horizontal plate) is also reproduced in the model to reduce the horizontal velocity at the interface for the prevention of the waterfall and interfacial disturbance. In this model, the inlet horizontal flow generate wake flows (vortical flows) behind the pipes and the vortical flows are intensified by interacting with the suction flow around the pipes toward the gaps between the pipes and dipped plate. The experiments were performed under several conditions for inlet and suction velocities and/or liquid depth.

In this study, the evaluation of the GE phenomena by the CFD-based prediction methodology is performed in terms of the rated and GE conditions. Under the rated condition, the inlet and suction velocities are set to be the rated condition in FRs, and the liquid depth is also determined from the rated condition in FRs. In the experiment under the rated condition, no strong vortical flow was observed, and therefore, no GE phenomenon was observed. On the other hand, under the GE condition, the inlet and suction velocities are enhanced to five times rated condition, and the liquid depth is reduced to about half of the rated condition. Owing to this very severe condition setting, the GE phenomena were observed in the experiment under the GE condition.

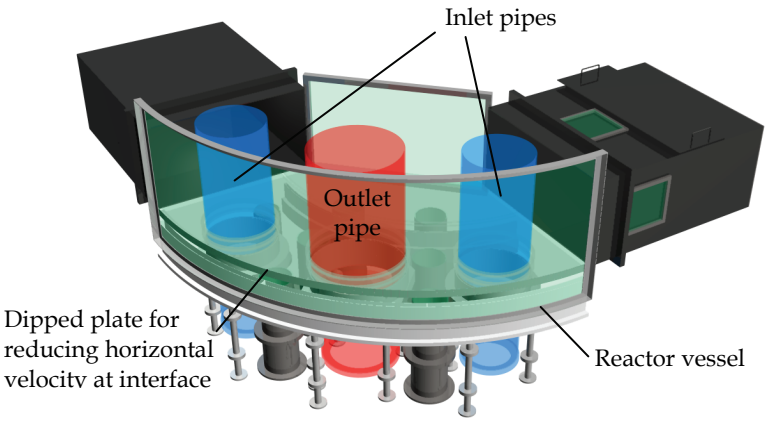


Fig. 9. 1/1.8 scale partial model

The CFD of the 1/1.8 scale partial model is performed by utilizing the FLUENT code. To simulate the complicated flow pattern in the 1/1.8 scale partial model, the RNG

(renormalization group) $k$-$\varepsilon$ turbulent model is employed in the CFD. It should be mentioned that relatively coarse computational mesh (cell size is about twenty or thirty millimeters) is employed to reduce the computational cost.
Figure 10 shows the evaluation results of the GE phenomena under the two conditions (Uchibori et al., 2006). In the figures, the vertical dotted line shows the indicator of the elongated gas core type of the GE phenomena (Eq. 14) and the horizontal one is the indicator of the bubble pinch-off type of the GE phenomena (Eq. 15). It is evident that no GE phenomenon is evaluated under the rated condition, and the occurrence of the GE phenomena is predicted under the GE condition. This tendency agrees with the experimental results, and therefore, it is confirmed that the CFD-based prediction methodology can evaluate the GE phenomena in FRs accurately.

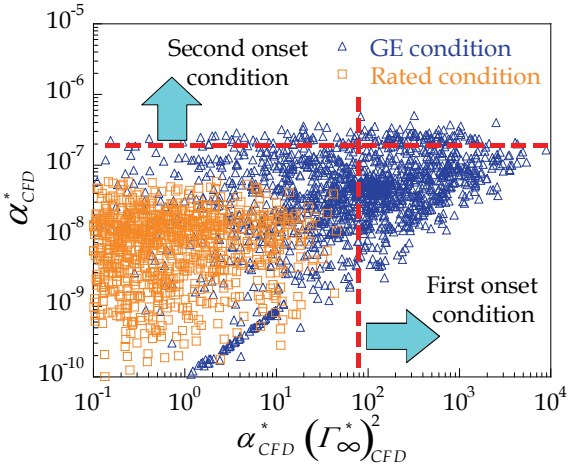


Fig. 10. Assessment of GE occurrence by CFD-based prediction methodology

### 3.6 Improvement of CFD-based prediction methodology

The CFD-based prediction methodology is very effective for the evaluation of the GE phenomena in FRs. However, some physical mechanisms are neglected in the CFD-based prediction methodology for the simplification. For example, the surface tension is not included in Eq. 7, and therefore, gas core lengths can be overestimated by Eq. 8. Recently, the authors have developed the improved CFD-based prediction methodology by introducing the surface tension (Ito et al., 2008). In this improved methodology, the mechanical balance equation between the centrifugal, gravitational and surface tension forces (Andersen et al. 2003) is employed instead of Eq. 7. The mechanical balance equation is written as

$$g\frac{dh}{dr}=\frac{u_\theta^2}{r}-\frac{\sigma}{\rho}\frac{d\kappa}{dr}, \tag{16}$$

where $s$ is the surface tension coefficient. The interfacial curvature $\kappa$ is calculated as

$$\kappa=\frac{h'}{r\left\{1+\left(h'\right)^2\right\}^{1/2}}+\frac{h''}{\left\{1+\left(h'\right)^2\right\}^{3/2}}, \tag{17}$$

where $h' = dh/dr$, $h'' = d^2h/dr^2$. Then, the gas core length with the consideration of the surface tension is calculated as

$$L_{gc} = \frac{\log 2}{g}\left(\frac{\Gamma_\infty}{2\pi r_0}\right)^2 - \frac{4\sigma W}{\rho g r_0}. \tag{18}$$

where $W$ is the function of the Froude and Weber numbers. The improved CFD-based prediction methodology has been applied to the GE phenomena in the Monji's simple experiment conducted under the several fluid temperatures or surfactant coefficient concentrations. As a result, the effect of the fluid property (the dynamic viscosity and/or surface tension coefficient) was evaluated accurately by the improved CFD-based prediction methodology.

## 4. High-precision numerical simulation of interfacial flow

### 4.1 General description of high-precision numerical simulation algorithm

In order to reproduce the GE phenomena, the authors have developed high-precision numerical simulation algorithms for gas-liquid two-phase flows. In the development, two key issues are addressed for the simulation of the GE phenomena in FRs. One is the accurate geometrical modeling of the structural components in the gas-liquid two-phase flow, which is important to simulate accurately vortical flows generated near the structural components. This issue is addressed by employing an unstructured mesh. The other issues is the accurate simulation of interfacial dynamics (interfacial deformation), which is addressed by developing an interface-tracking algorithm based on the high-precision volume-of-fluid algorithm on unstructured meshes (Ito et al., 2007). The physically appropriate formulations of momentum and pressure calculations near a gas-liquid interface are also derived to consider the physical mechanisms correctly in numerical simulations (Ito & Kunugi, 2009).

### 4.2 Development of high-precision volume-of-fluid algorithm on unstructured meshes

In this study, a high-precision volume-of-fluid algorithm, i.e. the PLIC (Piecewise Linear Interface Calculation) algorithm (Youngs, 1982) is chosen as the interface-tracking algorithm owing to its high accuracy on numerical simulations of interfacial dynamics. In the volume-of-fluid algorithm, the following transport equation is solved to track interfacial dynamic behaviors:

$$\frac{\partial f}{\partial t} + \vec{u} \cdot \nabla f = 0, \tag{19}$$

where $f$ is the volume fraction of the interested fluid in a cell with the range from zero to unity, i.e. $f$ is unity if a cell is filled with liquid; $f$ is zero if a cell is filled with gas; $f$ is between zero and unity if an interface is located in a cell. To enhance the simulation accuracy, the PLIC algorithm is employed to calculate Eq. 19. In the procedures of the PLIC algorithm, the calculation of the volume fraction by Eq. 19 is as follows:

1. an unit vector normal to the interface ($\vec{n}$) in an interfacial cell is calculated based on the volume fraction distribution at time level $n$ ($f^n$);
2. a segment of the interface is reconstructed as a piecewise linear line;

3. volume fraction transports through cell-faces on the interfacial cell are calculated based on the location of the reconstructed interface;
4. the volume fraction distribution at time level $n + 1$ ($f^{n+1}$) is determined.

The PLIC algorithm and its modifications (e.g. Harvie & Fletcher, 2000; Kunugi, 2001; Renardy & Renardy, 2002; Pilliod & Puckett, 2004) have been applied to a lot of numerical simulations of various multi-phase flows.

Then, to address the requirement for the accurate geometrical modeling of complicated spatial configurations, an unstructured mesh scheme was employed, so that the authors improve the PLIC algorithm originally developed on structured meshes to be available even on unstructured meshes. In concrete terms, the algorithms for the calculation of the unit vector normal to an interface, reconstruction of an interface, calculation of volume fraction transports through cell-faces and surface tension model are newly developed with high accuracies on unstructured meshes. Usually, the unit vector normal to an interface ($\vec{n}$) is calculated based on the derivatives of a given volume fraction distribution. In this study, the Gauss-Green theorem (Kim et al., 2003) is utilized to achieve the derivative calculation on unstructured meshes. Therefore, the non-unit vector is calculated in an interfacial cell as

$$\vec{n} = \frac{1}{V_c}\int_{\Sigma} f_f d\vec{A} = \frac{1}{V_c}\sum_{f} f_f \vec{A}_f \tag{20}$$

where $V_c$ is the cell volume and $\vec{A}$ is the area vector normal to a cell-face, which shows the area of the cell-face by its norm. Subscripts $f$ shows the cell-face value, and $f_f$ is interpolated from the given cell values. The summation in Eq. 20 is operated on all cell-faces on a cell. The unit vector is obtained by subdividing the calculated vector by the norm of the vector. It is confirmed that this calculation algorithm is robust and accurate even on unstructured meshes. In the interface reconstruction algorithm, a gas-liquid interface is reconstructed as a piecewise linear line in an interfacial cell, which is normal to the unit vector ($\vec{n}$) and is located so that the partial volume of the interfacial cell determined by the reconstructed interface coincides with the liquid (or gas) volume in the cell. In general, this reconstruction procedure is accomplished by the Newton-Raphson algorithm, i.e. an iterative algorithm (Rider & Kothe, 1998). However, a direct calculation algorithm, i.e. a non-iterative algorithm, in which a cubic equation is solved to determine the location of the reconstructed interface, has been developed on a structured mesh, and it is reported that the direct calculation algorithm provides more accurate solutions with the reduced computational cost (Scardvelli & Zaleski, 2000). Furthermore, the direct calculation algorithm was extended to two-dimensional unstructured meshes and succeeded in reducing the computational costs also on unstructured meshes (Yang & James, 2006). In this study, the authors newly develop the direct calculation algorithm on three-dimensional unstructured meshes. In addition, to achieve more accurate calculation of an interfacial curvature compared to the conventional calculation algorithm, i.e. the CSF (Continuum Surface Force) algorithm (Brackbill, 1992), the RDF (Reconstructed Distance Function) algorithm (Cummins et al., 2005) is extended to unstructured cells. To establish the volume conservation property violated by the excess or too little transport of the volume fraction, the volume conservative algorithm is developed by introducing the physics-basis correction algorithm.

As the verifications of the developed PLIC algorithm on unstructured meshes, the slotted-disk revolution problem (Zalesak, 1979) is solved on structured and unstructured meshes. The simulation results of the slotted-disk revolution problem by various volume-of-fluid

algorithms are well summarized by Rudman (Rudman, 1997). Therefore, the numerical simulations are performed under the same simulation conditions as Rudman's. Figure 11 shows the simulation conditions. In a 4.0 x 4.0 simulation domain, a slotted-disk with the radius of 0.5 and the vertical slot width of 0.12 is located. Initially, the volume fraction is set to be unity in the slotted-disk and zero outside the slotted-disk. Then, the slotted-disk is revolved around the domain center (2.0, 2.0) in counterclockwise direction. After one revolution, the volume function distribution is compared to the initial distribution to evaluate the numerical error.

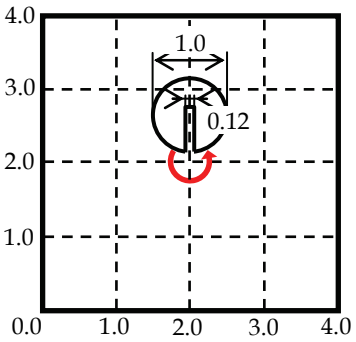


Fig. 11. Rudman's simulation conditions of slotted-disk revolution problem

Table 1 shows the simulation results. The structured mesh consists of 40,000 uniform square cells with the size of 2.0 x 2.0, and the unstructured mesh consists of about 40,000 irregular (triangular) cells. Upper four simulation results on the table are obtained by Rudman. On the structured mesh, it is evident that the developed PLIC algorithm shows much better simulation accuracy than the conventional volume-of-fluid algorithms, i.e. the SLIC (Simple Line Interface Calculation) algorithm (Noh & Woodward, 1976), the SOLA-VOF algorithm (Hirt & Nichols, 1981) and the FCT-VOF algorithm (Rudman, 1997). Moreover, the developed PLIC algorithm provides slightly more accurate simulation result than the original PLIC algorithm (Youngs, 1982). Therefore, the developed PLIC algorithm is confirmed to have the capability to simulate interfacial dynamic behaviors accurately. On the unstructured mesh, the simulation accuracy of the developed PLIC algorithm is much higher than that of the CICSAM (Compressive Interface Capturing Scheme for Arbitrary Meshes) (Ubbink & Issa, 1999) algorithm. However, the numerical error on the unstructured mesh is about 1.4 times larger than that on the structured mesh because the volume conservation property is highly violated by the excess or too little transport from the distorted cells on the unstructured mesh. Therefore, the numerical error is reduced to only 1.15 times larger than that on the structured mesh by employing the volume conservative algorithm. It should be mentioned that the volume conservative algorithm is efficient also for stabilizing the numerical simulations with large time increments (as shown in Fig. 12).

### 4.3 Physically appropriate formulations

To simulate interfacial dynamics accurately, it is necessary to employ not only the high-precision interface-tracking algorithm but also the physically appropriate formulations of the two-phase flow near a gas-liquid interface. Therefore, physics-basis considerations are conducted for the mechanical balance at a gas-liquid interface. In this study, the authors

| Algorithm | Computational mesh | Numerical error |
|---|---|---|
| SLIC | Structured | 8.38 x $10^{-2}$ |
| SOLA-VOF | | 9.62 x $10^{-2}$ |
| FCT-VOF | | 3.29 x $10^{-2}$ |
| PLIC | | 1.09 x $10^{-2}$ |
| Present | | 1.07 x $10^{-2}$ |
| Present | Unstructured | 2.02 x $10^{-2}$ |
| CICSAM | | 1.50 x $10^{-2}$ |
| Present (volume conservative) | | 1.23 x $10^{-2}$ |

Table 1. Numerical error in slotted-disk revolution problem

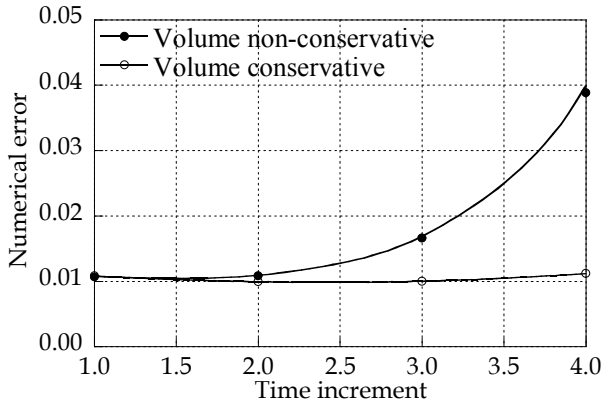


Fig. 12. Comparison of volume conservative and non-conservative algorithms

improve the formulations of momentum transport and pressure gradient at a gas-liquid interface.

In usual numerical simulations, the velocity at an interfacial cell is defined as a mass-weighted average of the gas and liquid velocities:

$$\vec{u} = \frac{\vec{u}_g \rho_g (1-f) V_c + \vec{u}_l \rho_l f V_c}{\rho V_c} = \frac{\vec{m}}{\rho} \tag{21}$$

where $\vec{u}$ and $\vec{m}$ the velocity and momentum vectors, respectively. The subscripts $g$ and $l$ shows the gas and liquid phases. This formulation is valid when the ratio of the liquid density to the gas density is small. However, in the numerical simulations of actual gas-liquid two-phase flows, the density ratio becomes about 1,000, and the liquid velocity dominates the velocity at an interfacial cell owing to the large density even when the volume fraction is small. Therefore, a physically appropriate formulation is derived to simulate momentum transport mechanism accurately. In the physically appropriate formulation, the velocity and momentum are defined independently

$$\vec{u} = (1-f)\vec{u}_g + f\vec{u}_l, \tag{22}$$

$$\vec{m} = (1-f)\rho_g \vec{u}_g + f\rho_l \vec{u}_l. \tag{23}$$

It is apparent that the velocity calculated by Eq. 22 is density-free and the volume-weighted average of the gas and liquid velocities. To validate the physically appropriate formulation, a rising gas bubble in liquid is simulated. As a result, the unphysical pressure distribution around the gas bubble caused by the usual formulation is eliminated successfully by the improved formulation (as shown in Fig. 13).

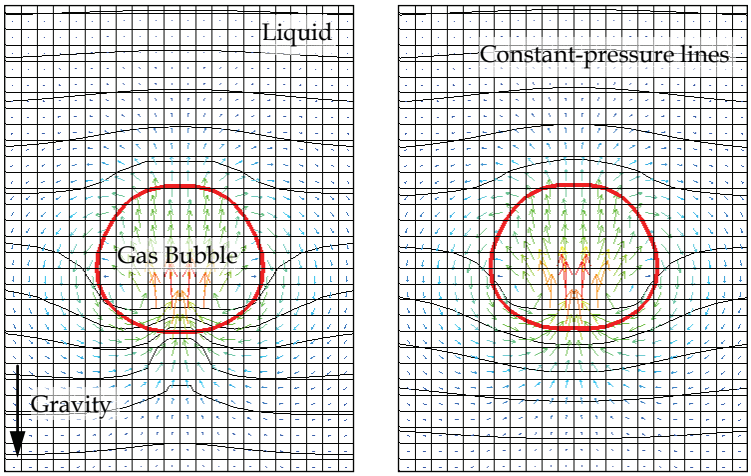


Fig. 13. Pressure distributions near interface of rising gas bubble: (a) Unphysical distribution caused by conventional algorithm, (b) Physically appropriate distribution with improved formulation

The other improvement is necessary to satisfy the mechanically appropriate balance between pressure and surface tension at a gas-liquid interface. In usual numerical simulations, the pressure gradient at an interfacial cell is defined as

$$\nabla p = \sum_{adjacent} \beta p, \tag{24}$$

where $p$ is the pressure. The summation is performed on all adjacent cells to an interfacial cell, and $\beta$ is the weighting factor for each adjacent cell. Equation 24 shows that the pressure gradient at an interfacial cell is calculated from the pressure distribution around the interfacial cell. However, the surface tension is calculated locally at an interfacial cell, and therefore, the balance between pressure and surface tension at the interfacial cell is not satisfied. The authors improved the formulation of the pressure gradient at an interfacial cell (Eq. 24) to be physically appropriate formulation which is consistent with the calculation of the surface tension at the interfacial cell. In the physically appropriate formulation, the pressure gradient at an interfacial cell is calculated as

$$p_f = p + (\nabla p)^t \cdot \frac{\vec{r}_f}{2}, \tag{25}$$

$$\frac{F-(\nabla p)^t}{\rho}=\frac{\sum_{sides}\gamma F-(\nabla p)_f}{\rho_f}, \tag{26}$$

$$\nabla p=\frac{\sum_f \vec{A}_f p_f}{V_c}, \tag{27}$$

where $F$ is the surface tension and $(\nabla p)^t$ is the temporal pressure gradient for the calculation of $p_f$. $\vec{r}_f$ is the vector joining the cell-center of an interfacial cell to the cell-face-center on the interfacial cell. The summation in Eq. 26 is the interpolation from the cells on both sides of a cell-face to the cell-face, and $\gamma$ is the weighting factor. The left side hand of Eq. 26 shows that the mechanical balance between pressure gradient and surface tension at an interfacial cell, and the right hand side shows the balance on a cell-face. In other words, the temporal pressure gradient at an interfacial cell becomes the same as the surface tension at the interfacial cell when the mechanical balance between pressure gradient and surface tension is satisfied on all cell-faces on the interfacial cell. Moreover, the mechanical balance on cell-faces can be satisfied easily because both the pressure gradient and surface tension are calculated locally on cell-faces. Therefore, above equations eliminate almost the numerical error in the usual calculation of the pressure gradient at an interfacial cell. To validate the improved formulation, a rising gas bubble in liquid is simulated again. Figure 14 shows the simulation result of velocity distribution around the bubble. The discontinuous velocity distribution caused by the usual formulation is eliminated completely by the improved formulation.

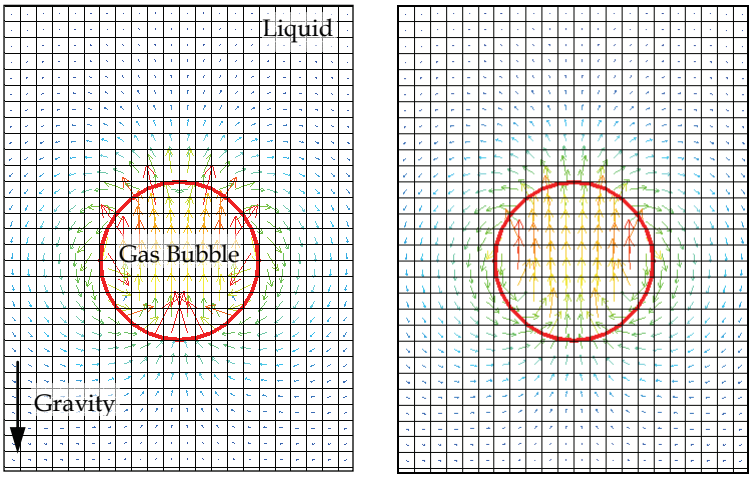


Fig. 14. Velocity distributions near interface of rising gas bubble: (a) Unphysical distribution caused by conventional algorithm, (b) Physically appropriate distribution with improved formulation

### 4.4 Numerical simulation of GE phenomena

The developed high-precision numerical simulation algorithms are validated by simulating the GE phenomena in a simple experiment (Ito et al. 2009). Figure 15 shows the

experimental apparatus (Okamoto et al., 2004) which is a rectangular channel with the width of 0.20 m in which a square rod with the edge length of 50 mm and square suction pipe with the inner edge length of 10 mm are installed. The liquid depth in the rectangular channel is 0.15 m. Working fluids are water and air at room temperature.

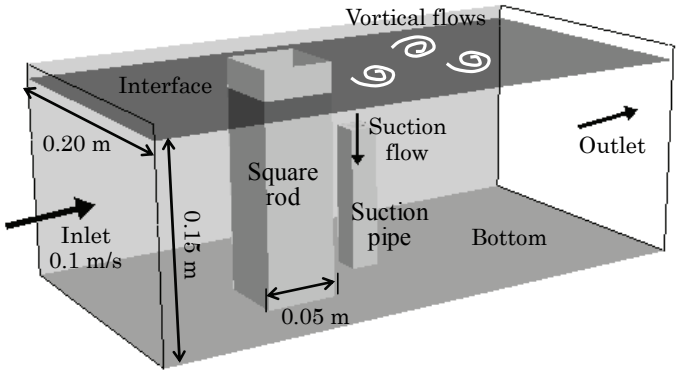


Fig. 15. Schematic view of Okamoto's experimental apparatus

In the rectangular channel, uniform inlet flow (0.10 m/s) from the left boundary (in Fig. 15) generates a wake flow behind the square rod when the inlet flow goes through the square rod. In the wake flow, a vortical flow is generated and advected downstream. Then, when the vortical flow passes across the region near the suction pipe, the vortical flow interacts with the suction (downward) flow (4.0 m/s in the suction pipe), and the vortical flow is intensified rapidly. Furthermore, a gas core is generated on the gas-liquid interface accompanied by this intensification of the vortical flow. Finally, when the gas core is elongated enough along the core of the vortical flow, the GE phenomena occur, i.e. the gas is entrained into the suction pipe.

In the numerical simulation, first, a computational mesh is generated carefully to simulate the GE phenomena accurately. Figure 16 shows the computational mesh. In this computational mesh, fine cells with the horizontal size of about 1.0 mm are applied to the region near the suction pipe in which the GE phenomena occur. In addition, to simulate the transient behavior of a vortical flow accurately, unstructured hexahedral cells with the horizontal size of about 3.0 mm are also applied to the regions around the square rod and that between the square rod and the suction pipe. Furthermore, the vertical size of cells is refined near the gas-liquid interface to reproduce interfacial dynamic behaviors. As for boundary conditions, uniform velocity conditions are applied to the inlet and suction boundaries. On the outlet boundary, hydrostatic pressure distribution is employed. The simulation algorithms employed in this chapter is summarized in Table 2.

In the numerical simulation, the development of the vortical flow and the elongation of the gas core are investigated carefully. As a result, the vortical flow develops upward from the suction mouth to the gas-liquid interface by interacting with the strong downward flow near the suction mouth. Then, the rapid gas core elongation along the center of the developed vortical flow starts when the high vortical velocity reached the gas-liquid interface. Finally, the gas core reaches the suction mouth and the GE phenomena (entrainment of the gas bubbles into the suction pipe) occur (as shown in Fig. 17). After a

| | | |
|---|---|---|
| General discritization scheme | Finite volume algorithm (Collocated variable arrangement) | |
| Velocity-pressure coupling | SMAC | |
| Discritization schemes for each term in the N-S equation | Unsteady term | 1st order Euler |
| | Advection term | 2nd order upwind |
| | Diffusion term | 2nd order central |
| Interface tracking scheme | PLIC | |
| Momentum transport | Eqs. 22 and 23 | |
| Pressure gradient | Eqs. 25, 26 and 27 | |

Table 2. General description of high-precision numerical simulation algorithms

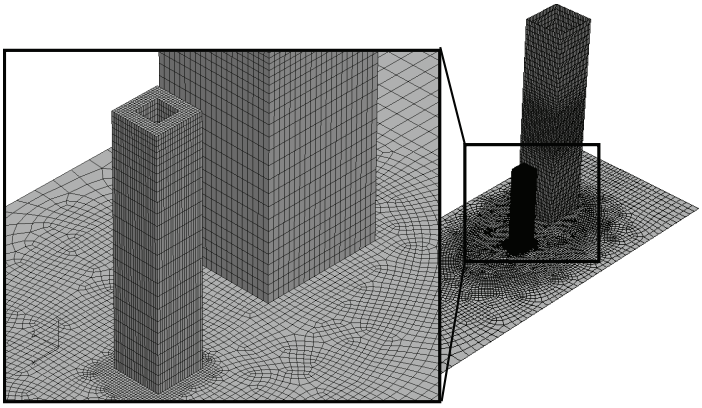

Fig. 16. Simulation mesh of Okamoto's experimental apparatus

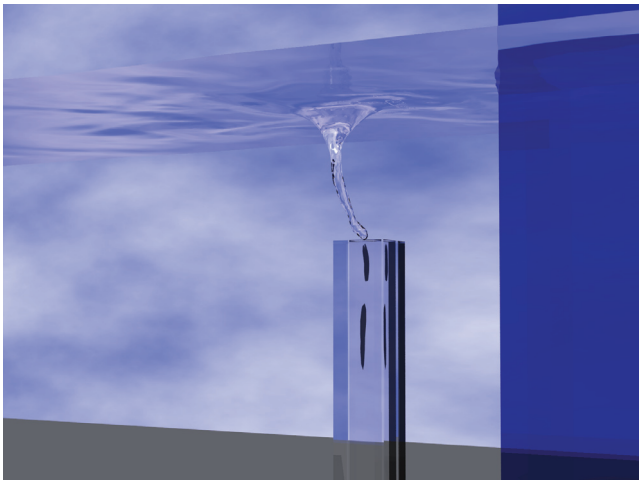

Fig. 17. Photorealistic visualization of GE phenomena

short period of the GE phenomena, the vortical flow is advected downstream, and the gas core length decreases rapidly. In this stage, the bubble pinch-off from the tip of the attenuating gas core is observed.

This GE phenomena observed in the simulation result is compared to the experimental result. In Fig. 18, it is evident that the very thin gas core provided in the experimental result is reproduced in the simulation result. In addition, as for the elongation of the gas core, the

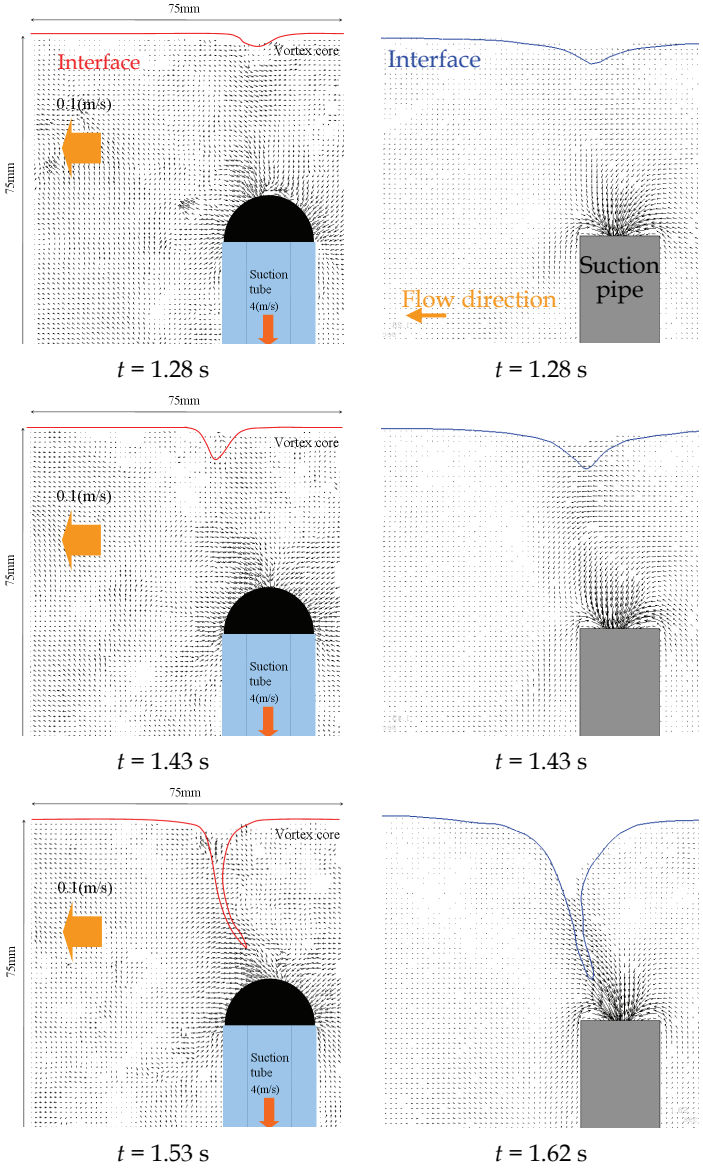


Fig. 18. Comparison of gas core elongation behavior in experimental and simulation results

simulation result shows clearly that the gas core is elongated along the region with the high downward velocity when the downward velocity develops toward the gas-liquid interface. This tendency is observed also in the experimental result and is reported by Okamoto (Okamoto et al., 2004) as the occurrence mechanism of the GE phenomena in the simple experiment. Therefore, it is confirmed that the GE phenomena in the simulation result is induced by the same mechanism as that in the experiment. From these simulation results, the developed high-precision numerical simulation algorithms are validated to be capable of reproducing the GE phenomena.

## 5. Conclusion

As an example of the evaluation of interfacial flows, two methodologies were proposed for the evaluation of the GE phenomena. One is the CFD-based prediction methodology and the other is the high-precision numerical simulation of interfacial flows.

In the development of the CFD-based prediction methodology, the vortical flow model was firstly constructed based on the Burgers theory. Then, the accuracy of the CFD results, which are obtained on relatively coarse computational mesh without considering interfacial deformations for the reduction of the computational costs, was discussed to determine the occurrence indicators of the two types of the GE phenomena, i.e. the elongated gas core type and the bubble pinch-off type. In this study, the gas core length was selected as the indicator of the elongated gas core type with considering the three times allowance. On the other hand, the downward velocity gradient was determined empirically as the indicator of the bubble pinch-off type. Finally, the developed CFD-based prediction methodology was applied to the evaluation of the GE phenomena in an experiment using 1/1.8 scale partial model of the upper plenum in reactor vessel of a large-scale FR. As a result, the GE occurrence observed in the 1/1.8 scale partial model experiment was evaluated correctly by the CFD-based prediction methodology. Therefore, it was confirmed that the CFD-based prediction methodology can evaluate the GE phenomena properly with relatively low computational costs.

In the development of the high-precision numerical simulation algorithms, the high-precision volume-of-fluid algorithm, i.e. the PLIC algorithm, was employed as the interface-tracking algorithm. Then, to satisfy the requirement for accurate geometrical modeling of complicated spatial configurations, an unstructured mesh scheme was employed, so that the PLIC algorithm was newly developed on unstructured meshes. Namely, the algorithms for the calculation of the unit vector normal to an interface, reconstruction of an interface, volume fraction transport through cell-faces and surface tension were newly developed for high accurate simulations on unstructured meshes. In addition, to establish the volume conservation property violated by the excess or too little transport of the volume fraction, the volume conservative algorithm was developed by introducing the physics-basis correction algorithm. Physics-basis considerations were also conducted for mechanical balances at gas-liquid interfaces. By defining momentum and velocity independently at gas-liquid interfaces, the physically appropriate formulation of momentum transport was derived, which can eliminate unphysical behaviors near the gas-liquid interfaces caused by conventional formulations. Furthermore, the improvement was necessary to satisfy the mechanically appropriate balances between pressure and surface tension at gas-liquid interfaces, so that the physically appropriate formulation was also derived for the pressure gradient calculation at gas-liquid interfaces. As the verification of the developed PLIC

algorithm, the slotted-disk revolution problem was solved on the unstructured mesh, and the simulation result showed that the accurate interface-tracking could be achieved even on unstructured meshes. The volume conservation algorithm was also confirmed to be efficient to enhance highly the simulation accuracy on unstructured meshes. Finally, the GE phenomena in the simple experiment were simulated. For the numerical simulation, the unstructured mesh was carefully considered to determine the size of cells in the central region of the vortical flow. In the simulation result, the GE phenomena observed in the experiment was reproduced successfully. In particular, the shape of the elongated gas core was very similar with the experimental result. Therefore, it was validated that the high-precision numerical simulation algorithms developed in this study could simulate accurately the transient behaviors of the GE phenomena.

## 6. References

Andersen, A.; Bohr, T.; Stenum, B.; Juul Rasmussen, J. & Lautrup, B. (2003). Anatomy of a bathtub vortex, *Physical Review Letters*, Vol. 91, No. 10, 104502-1-104502-4.

Brackbill, J. U. D.; Kothe, B. & Zemach, C. (1992). A continuum method for modeling surface tension, *J. Comput. Phys.*, Vol. 100, Issue. 2, 335-354.

Burgers, J. M. (1948). A mathematical model illustrating the theory of turbulence, In: *Advance in applied mechanics,* Mises, R. & Karman, T., Eds., 171-199, Academic Press, New York.

Craya, A. (1949). Theoretical research on the flow of nonhomogeneous fluids, *La Houille Blanche,* Vol. 4, 22-55.

Cummins, S. J.; Francois M. M. & Kothe, D. B. (2005). Estimating curvature from volume fractions, *Computer & Structure,* Vol. 83, 425-434.

Daggett, L. L. & Keulegan, G. H. (1974). Similitude in free-surface vortex formations, *Journal of the Hydraulics Division, Proceedings of the ASCE,* Vol. 100, HY8.

Eguchi, Y.; Yamamoto, K.; Funada, T.; Tanaka, N.; Moriya, S.; Tanimoto, K.; Ogura, K.; Suzuki, K. & Maekawa, I. (1984). Gas entrainment in the IHX of top-entry loop-type LMFBR, *Nuclear Engineering and Design,* Vol. 146, 373-381.

Harvie, D. J. E. & Fletcher, D. F. (2000). A new volume of fluid advection algorithm: the Stream scheme, *Journal of Computational Physics,* Vol. 162, 1-32.

Hirt, C. W. & Nichols, D. B. (1981). Volume of fluid (VOF) method for the dynamics of free boundaries, *Journal of Computational Physics,* Vol. 39, 201-205.

Hunt, J.; Wray, A. & Moin, P. (1988). Eddies, stream and convergence zones in turbulent flows, *Center for Turbulence Research report*, CTR-S88.

Ito, K.; Yamamoto, Y. & Kunugi, T. (2007). Development of numerical method for simulation of gas entrainment phenomena, *Proceedings of the Twelfth International Topical Meeting on Nuclear Reactor Thermal Hydraulics*, No. 121, Sheraton station square, September 2007, Pittsburgh, PA.

Ito, K.; Eguchi, Y.; Monji, H.; Ohshima, H.; Uchibori, A. & Xu, Y. (2008). Improvement of gas entrainment evaluation method –introduction of surface tension effect–, *Proceedings of Sixth Japan-Korea Symposium on Nuclear Thermal Hydraulics and Safety*, No. N6P1052, Bankoku-shinryokan, November 2008, Okinawa, Japan.

Ito, K.; Kunugi, T.; Ohshima, H. & Kawamura, T. (2009) Formulations and validations of a high-precision volume-of-fluid algorithm on non-orthogonal meshes for numerical

simulations of gas entrainment phenomena, *Journal of Nuclear Science and Technology,* Vol. 46, 366-373.

Ito. K & Kunugi, T. Appropriate formulations for velocity and pressure calculations at gas-liquid interface with collocated variable arrangement, *Journal of Fluid Science and Technology* (submitted).

Kim, S. E.; Makarov, B. & Caraeni, D. (2003) A multi-dimensional linear reconstruction scheme for arbitrary unstructured grids, *Proceedings of 16th AIAA Computational Fluid Dynamics Conference*, pp. 1436-1446, June 2003, Orlando, FL.

Kimura, N.; Ezure, T.; Tobita, A. & Kamide, H. (2008). Experimental study on gas entrainment at free surface in reactor vessel of a compact sodium-cooled fast reactor, *Journal of Nuclear Science and Technology,* Vol. 45, 1053-1062.

Kunugi, T. (2001). MARS for multiphase calculation, *Computational Fluid Dynamics Journal,* Vol. 19, 563-571.

Maier, M. R. (1998). Onsets of liquid and gas entrainment during discharge from a stratified air-water region through two horizontal side branches with centerlines falling in an inclined plane, *Master of Science Thesis*, University of Manitoba.

Monji, H.; Akimoto, T.; Miwa, D. & Kamide, H. (2004). Unsteady behavior of gas entraining vortex on free surface in cylindrical vessel, *Proceedings of Fourth Japan-Korea Symposium on Nuclear Thermal Hydraulics and Safety*, pp. 190-194, Hokkaido University, November 2004, Sapporo, Japan.

Moriya, S. (1998). Estimation of hydraulic characteristics of free surface vortices on the basis of extension vortex theory and fine model test measurements, *CRIEPI Abiko Research Laboratory Report,* No. U97072 (in Japanese).

Nagata, T. (2008). Early commercialization of fast reactor cycle in Japan, *Proceedings of the 16th Pacific Basin Nuclear Conference*, October 2008, Aomori, Japan.

Noh, W. F. & Woodward, P. (1976). SLIC (simple line interface calculation), *Lecture Notes in Physics,* van der Vooren, A. I. & Zandbergen, P. J., Eds., 330-340, Springer-Verlag.

Okamoto, K.; Takeyama, K. & Iida, M. (2004). Dynamic PIV measurement for the transient behavior of a free-surface vortex, *Proceedings of Fourth Japan-Korea Symposium on Nuclear Thermal Hydraulics and Safety*, pp. 186-189, Hokkaido University, November 2004, Sapporo, Japan.

Pilliod, J. E. & Puckett, E. G. (2004). Second-order accurate volume-of-fluid algorithms for tracking material interfaces, *Journal of Computational Physics,* Vol. 199, 465-502.

Renardy, Y. & Renardy, M. (2002). PROST: A parabolic reconstruction of surface tension for the volume-of-fluid method, *Journal of Computational Physics,* Vol. 183, 400–421.

Rider, W. & Kothe, D. B. (1998). Reconstructing volume tracking, *Journal of Computational Physics,* Vol. 141, 112-152.

Rudman, M. (1997). Volume-tracking methods for interfacial flow calculations, *International Journal for Numerical Methods in Fluids,* Vol. 24, 671-691.

Sakai, S.; Madarame, H. & Okamoto, K. (1997). Measurement of flow distribution around a bathtub vortex, *Transaction of the Japan Society of Mechanical Engineers, Series B*, Vol. 63, No. 614, 3223-3230 (in Japanese).

Sakai, T.; Eguchi, Y.; Monji, H.; Ito, K. & Ohshima, H. (2008). Proposal of design criteria for gas entrainment from vortex dimples based on a computational fluid dynamics method, *Heat Transfer Engineering,* Vol. 29, 731-739.

Scardvelli, R. & Zaleski, S. (2000). Analytical relations connecting linear interface and volume functions in rectangular grids, *Journal of Computational Physics,* Vol. 164, 228-237.

Ubbink, O. & Issa, R. I. (1999). A method for capturing sharp fluid interfaces on arbitrary meshes, *Journal of Computational Physics,* Vol. 153, 26-50.

Uchibori, A.; Sakai, T. & Ohshima, H. (2006). Numerical prediction of gas entrainment in the 1/1.8 scaled partial model of the upper plenum, *Proceedings of Fifth Japan-Korea Symposium on Nuclear Thermal Hydraulics and Safety*, pp. 414-420, Ramada Plaza Hotel, November 2006, Jeju, Korea.

Yang, X. & James, A. J. (2006). Analytic relations for reconstructing piecewise linear interfaces in triangular and tetrahedral grids, *Journal of Computational Physics,* Vol. 214, 41-54.

Youngs, D. L. (1982). Time-dependent multi-material flow with large fluid distortion, *Numerical Methods for Fluid Dynamics,* Morton, K. W. & Baines, M. J. Eds., 273-486, American Press, New York.

Zalesak, S. T. (1979). Fully multidimensional flux-corrected transport algorithm for fluids, *Journal of Computational Physics,* Vol. 31, 335-362.

Zuber, N. (1980). Problems in modeling of small break LOCA, *Nuclear Regulatory Commission Report,* NUREG-0724.

7

# Numerical Simulation of Flow in Erlenmeyer Shaken Flask

Liu Tianzhong[1], Su Ge[2], Li Jing[3], Qi Xiangming[4] and Zhan Xiaobei[3]
[1]*Qingdao Institute of Bioenergy and Bioprocess Technology, China Academy of Sciences,Qingdao 266101,*
[2]*College of Material Science and Engineering, Ocean University of China,Qingdao 266101,*
[3]*China Key Laboratory of Industrial Biotechnology, Ministry of Education, School of Biotechnology, Jiangnan University, Wuxi 214122,*
[4]*College of Food Science and Engineering, Ocean University of China,Qingdao 266003, China*

## 1. Introduction

By far most of all biotechnological experiments are carried out in shaken bioreactors [1,2]. Every laboratory bioprocess development developing in early stages are relied on parallel thousands of experiments in shaken flasks to determine optimal medium composition or to find an suitable microbial strain due to the great experimental simplicity of the apparatus. Furthermore, it can also helpful for decisive and orienteering decisions on experimental conditions. However, shaken flask experiments could only provide phenomenal conditions such as rotary speed which reflects mixing and oxygen requirement degree in aeration process, it could not quantify important engineering parameters like the volumetric power consumption [3], the oxygen transfer capacity [4-6] or the hydro-mechanical stress [7,8] which would be more crucial for process scale-up. Thus such parameters have to be determined through empirical or semi-empirical equations or depended on pilot experiments. This facts is doubtfully wakened the reliability of shaken results and also prolong the period of bioprocess through laboratory to industrial process. To gain deeper understanding of the afore mentioned mechanisms on a theoretical basis, the geometry, i.e. the contour and spatial distribution of the rotating liquid mass moving inside a shaken Erlenmeyer flask is of crucial importance. The liquid distribution gives important information about the momentum transfer area, which is the contact area between the liquid mass and the flask inner wall, and the mass transfer area, which is the surface exposed to the surrounding air, including the film on the flask wall [4]. B¨uchs et.al [9] have setup the liquid distribution model flow characterization of liquid in shaken flask to calculated the liquid distribution, and validated with photography. However their calculation based simply liquid shape did not consider the liquid surface bend or sunk during rotation, thus the calculated maximum height of liquid approached has a little difference with experimental results, and also this model could not calculate the gas-liquid interface which may important for oxygen transfer.

Computational fluid dynamics (CFD) is a novel method to investigate the flow behavior with low cost, independent on container geometry. It can also provide more details which could not be obtained by experiments. Many commercial CFD softwares such as Phoenics, Fluent, CFX, StarCD have presented excellent success in simulation for both process and apparatus.

This work aims at proving dynamic fluid kinetic model with dynamic mesh of shaken flask, to calculate the liquid distribution, contact area between the liquid mass and the flask wall and energy dissipation etc. in shake flasks to provide the information required to investigate momentum and gas/liquid mass transfer and volumetric power consumption. All the work was carried out with Fluent 6.2 in this work.

## 2. Model formulation

### 2.1 Basic concepts of shaken movement

Most commonly shake flasks are agitated by orbital shaking machines. Figure. 1 illustrates the physic description of this shaking motion. The shake flask performs a circular translatoric movement with the radius equal to half the shaking diameter keeping its orientation relative to the surrounding. This movement is synthesized by a superposition of two individual movements. The first movement is the angular velocity $\omega_1$ of the circular translatoric movement with the shaking radius around the center of the shaking motion (shaft 1), which is related to as the shaking frequency of the shaking machine, N.

$$\omega_1 = 2\pi N$$

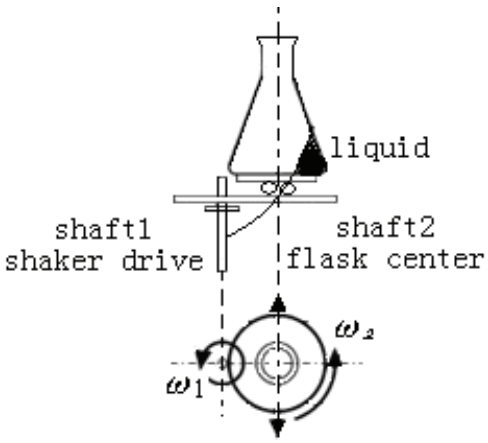


Fig. 1. Theoretical partition of shake flask movement: superposition of circular translatoric and rotational movement.

The second movement is the rotation counteracted the first rotation to keep the shake flask's spatial orientation around the flask center (shaft 2). Therefore: $\omega_2 = -\omega_1$, driven by the centrifugal field of the first rotation ($-\omega_1$).Thus, in shaken flask, the liquid will move in ellipses in caterian coordinate system, as described as equation 1 and 2.

$$\frac{x^2}{a^2}+\frac{y^2}{b^2}=1 \tag{1}$$

$$\begin{aligned} U_X &= ab\omega\times\frac{\Lambda\cdot\cos(\omega t)-\Pi\cdot\sin(\omega t)}{\Lambda^2} \\ U_Y &= ab\omega\times\frac{\Lambda\cdot\sin(\omega t)-\Pi\cdot\cos(\omega t)}{\Lambda^2} \end{aligned} \tag{2}$$

Where, $\omega$ is the angular velocity, t is the rotation time. a and b are radius in shaft 1 and shaft 2 axial respectively. Parameters $\Lambda$ and $\Pi$ are defined in equation (3).

$$\begin{aligned} \Lambda &= \sqrt{a^2\cos^2(\omega t)+b^2\sin^2(\omega t)} \\ \Pi &= \frac{b^2-a^2}{2\Lambda}\sin(2\omega t) \end{aligned} \tag{3}$$

For most Erlenmeyer shaken flask is designed as circular radius, so $a$ equals $b$, the movement equation can be simplified as equation (4) and (5).

$$x^2+y^2=a^2 \tag{4}$$

$$\begin{aligned} Ux &= a\omega\cos(\omega t) \\ Uy &= a\omega\sin(\omega t) \end{aligned} \tag{5}$$

### 2.2 Model for flow dynamics

In most cases, there are two phases of both gas and liquid in shaken flask, and there is little entanglement between both of them, gas phase and liquid phase are always separated with little exchange. As the results, Volume of Fluid Model of Eularian model is more practical for the description of motion in shaken flask.

**Continua equations:**

In VOF model, the interface between phases is determined by the volume void of one or more phase in the multiphase system. The continua equation of phase $q$ is as follow.

$$\frac{1}{\rho_q}\left[\frac{\partial}{\partial t}(a_q\rho_q)+\nabla\cdot(a_q\rho_q\vec{\upsilon}_q)\right]=S_{aq}+\sum_{p=1}^{n}(\dot{m}_{pq}-\dot{m}_{qp}) \tag{6}$$

In which, $\rho_q$ and $a_q$ presents density and volume void for q phase respectively. $p$ presents all phases excluding $q$ phase in calculation region, and $S_{aq}$ is the resource item. $m_{pq}$ states the exchange from p phase and q phase. $m_{qp}$ states the exchange from $q$ phase and $p$ phase. In this case, if all the phase exchanges are neglected, then equation (6) can be rewritten as equation (7).

$$\frac{1}{\rho_q}\left[\frac{\partial}{\partial t}(a_q\rho_q)+\nabla\cdot(a_q\rho_q\vec{\upsilon}_q)\right]=0 \tag{7}$$

Further, the normalized condition of phase volume void is written as in equation (8).

$$\sum_{q=1}^{n} a_q = 1 \tag{8}$$

**Momentum equations:**

VOF model takes all phases sharing same moving velocity, so the momentum equation is as follow.

$$\frac{\partial}{\partial t}(\rho\vec{v}) + \nabla\cdot(\rho\vec{v}\vec{v}) = -\nabla p + \nabla\cdot[\mu(\nabla\vec{v} + \nabla\vec{v}^T)] + \rho\vec{g} + \vec{F} \tag{9}$$

In which, the density and viscosity are the weighted mean values calculated as follows:

$$\rho = \sum a_q \rho_q \tag{10}$$

$$\mu = \sum a_q \mu_q \tag{11}$$

*F* presents all the volumetric force except gravity, as described in equation (12). In which, σ is the tension force of water, and κ,α are the Surface curvature and liquid void at gas-liquid interface respectively., *n* presents outward unit normal vector of gas-liquid interface

$$\begin{aligned} F &= \alpha_k(x)\alpha(x,t) \\ k &= \frac{1}{|n|}[(\frac{n}{|n|}\cdot\nabla] - \nabla\cdot n] \end{aligned} \tag{12}$$

**Turbulent modl equations:**

Due to the rotation, the turbulent flow mostly is eddy flow, a modified turbulent model of RNG *k*-ε [10] in equation (13) and (14) are used in the work.

$$\frac{\partial}{\partial t}(\rho k) + \nabla\cdot(\rho k\vec{v}) = \nabla\cdot(\alpha_k\mu_{eff}\nabla k) + G_k + G_b - \rho\varepsilon - Y_M + S_k \tag{13}$$

$$\frac{\partial}{\partial t}(\rho\varepsilon) + \nabla\cdot(\rho\varepsilon\vec{v}) = \nabla\cdot(\alpha_\varepsilon\mu_{eff}\nabla\varepsilon) + c_{1\varepsilon}\frac{\varepsilon}{k}(G_k + c_{3\varepsilon}G_b) - c_{2\varepsilon}\frac{\varepsilon^2}{k} - R_\varepsilon + S_\varepsilon \tag{14}$$

$$c_{1\varepsilon} = 1.42, c_{2\varepsilon} = 1.68, \alpha_k = \alpha_\varepsilon \approx 1.39 \tag{15}$$

Where, $G_k$ is turbulent kinetic energy by average velocity gradient, and *Gb* presents buoyancy production for turbulent kinetic energy. $Y_M$ is contributed by the fluctuate expansion item for compressible flow, $\alpha_k$ and $\alpha_e$ are the reciprocal of effective Prandtl number for *k* and ε respectively. $S_k$ and *S*ε are volumetric source items. *P* and $\mu$ are weighted mean density and viscosity as defined previously in equations (10) and (11).

Incompressible flow with outer resource input is taken in this work, thus, $G_b = 0$, $Y_M = 0$ and $S_k = S\ \varepsilon = 0$.

The effective viscosity $\mu_{eff}$ in RNG k-ε model is related as in equation (13).

$$d\left(\frac{\rho^2}{\sqrt{\varepsilon\mu}}\right)=1.72\frac{\hat{\upsilon}}{\sqrt{\hat{\upsilon}^3-1+C_\upsilon}}d\hat{\upsilon} \tag{13}$$

$$\hat{\upsilon}=\frac{\mu_{eff}}{\mu},C_\upsilon\approx 10 \tag{14}$$

$R_\varepsilon$ in equation (14) was given in equation (15).

$$R_\varepsilon=\frac{C_\mu\rho\eta^3(1-\frac{\eta}{\eta_0})\varepsilon^2}{1+\beta\eta^3}\frac{\varepsilon^2}{k} \tag{15}$$

$$\eta=S\frac{k}{\varepsilon},\eta_0=4.38,\beta=0.01 \tag{16}$$

## 3. Geometry structure and calculation strategy

### 3.1 Geometry structure and mesh

The geometry structure of shaken flask is a unbaffled shake flask with a nominal volume of 250mL (Schott, Mainz, Germany), the same as Büchs used[9]. The shaker is orbital shakers with rotary diameter of 5cm. In order to decrease the calculation capacity, only the bottom half of flask with 5cm height as shown in figure 2, was considered because all the liquid is distributed in the zone and upper gas phase would not make difference for the liquid distribution when rotation.

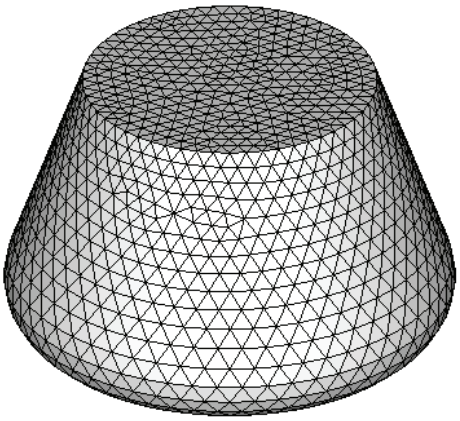

Fig. 2. Schematic diagram of the simulation zone of the flask

The mesh of the calculation zone was plotted with Grid type by Gambit3.20. Grid independence study was preliminary carried out with three different mesh densities of close (49919), middle (29779) and coarse (12490), and found middle (29779) mesh cells was reasonable economic mesh good results. In order to enhance the convergence during iteration, smooth treatment of mesh was carried out to decrease the maximum skewness.

### 3.2 Dynamic mesh strategy

In CFD calculation, the quality of mesh would produce important effects on convergence and calculation efficiency. However, for those cases bearing moving boundary, the movement of the boundary would cause mesh cell stretched and skewed, worsen the quality of interior mesh cells related with moving area. In fluent, such problem was modified by DM technique. The principle of DM is based on local remeshing with size function strategy. In which, those cells of which the cell skewness or length scale is bigger than maximum cell skewness or maximum length scale , respectively would be labred and reunited first, and then remeshed to new required mesh cells according to size function factor $\gamma$. The size function factor $\gamma$ is determined according to equation (17). More details of DM technique can be refereed in the help documents for Fluent 6.20[11].

$$\gamma = \begin{cases} 1 + md_b^{1+2n}, m > 0 \\ 1 + md_b^{\frac{1}{1-n}}, m < 0 \end{cases} \tag{17}$$

### 3.3 Calculation conditions

The density and viscosity for both water and air are 1.225 kg·m$^{-3}$, 1.7894×10$^{-5}$ Pa·s, 1000 kg·m$^{-3}$, 0.001 Pa·s respectively. Surface tension of water is 0.072 N·m.

In the simulation, water load of 15ml, 25ml and 35ml were investigated under different rotation speed of 100rpm, 150rpm, 200rpm and 250rpm respectively.

The equations were solved with 1st implicit with standard wall function and wall adhesion[12].The pressure interpolation scheme adopted was PRESTO (Pressure staggered option), which is useful for predicting highly swirling flow characteristics prevailing inside the flask. In order to reduce the effects of numerical diffusion, higher order discretization schemes are recommended. Accordingly, a third order accurate QUICK scheme was used for spatial discretization.

Fixed time step, Δt was used in the whole calculation, which was determined by equation (18).

$$\Delta t \le \frac{\Delta L}{u} \tag{18}$$

Where, ΔL is the cell length of the cell connected moving boundary. It cab be estimated as 0.005m in this work. u is the maximum tangular velocity of shaken flask. As the results, $\Delta t \le 0.003s$ in this mesh system. Here $\Delta t = 0.001s$ was adopted in all of the calculations.

The convergence criteria is 10$^{-3}$ in residual error. In our calculation, all the flow under different water load and rotation speed would arrive "steady state" in 2 second rotary time.

## 4. Results and discussion

### 4.1 Validation of the CFD results

The liquid shape and distribution in shaken flask with 25ml water load and rotation speed of both 250rpm (A) and 150rpm(B) by CFD simulation and by experimental and simplified model[9] calculated results were shown in figure 3. It can be observed that the simulated liquid distribution and shape have a good agreement with referred photographes[9] (A1,A2; B1,B2). The minor difference is possibly by the difference of viscosity in referred and this

simulation. Bigger water viscosity could prevent the crawl of water during rotation, thus the maximum height of water crawl is a little smaller than this work.

### 4.2 The periodical position change of liquid phase

Figure 4 gives the periodical position change of liquid during rotation of 150rpm, 25ml water load. The same reference coordinate system was adopted for the nine angular positions. It can be found that as the flow arrived steady state, liquid in flask would periodically scan the relatively flask wall without any shape changes. It well agrees with the observation of flask movement.

### 4.3 Liquid phase shape

The rotation of shaken flask would produce centrifugal force to push water moving towards flask wall. Figure 5 gives the liquid shape under different rotation speeds with 25ml water load. Obviously, higher the rotation speed is, bigger the centrifugal force is and then smaller surface the water contact with the bottom surface of flask, and higher the water crawls to flask wall. Though the shaken flask is geometric symmetry, and the liquid phase position was changed periodically, the shape of water was not symmetrical. It is the combination effects of liquid rotary inertia and wall adhesion. Furthermore, with the increase of rotation speed, the gas-liquid interface would depressed deterioratedly, which means bigger area for gas-liquid contact.

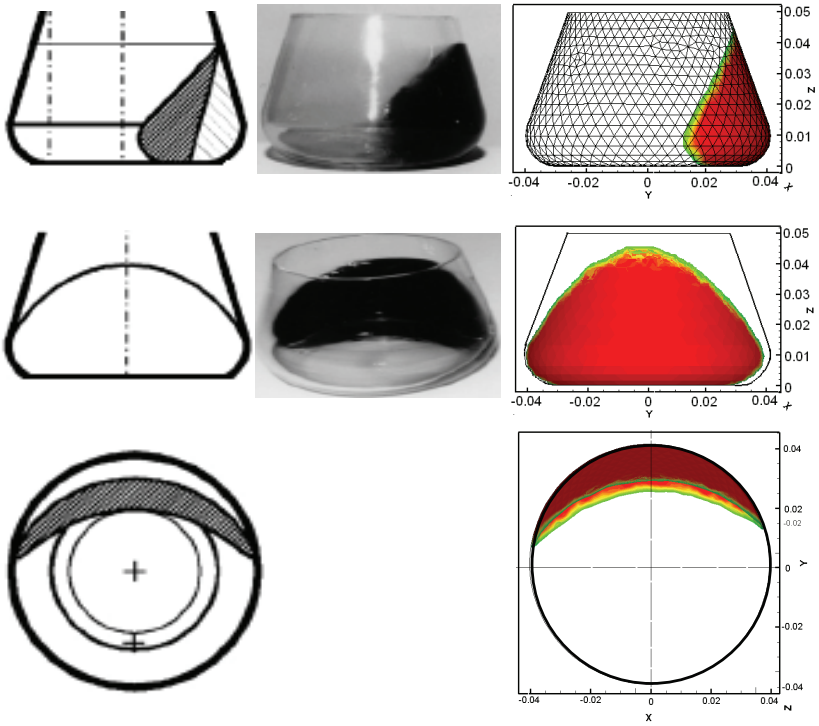


A1 A2 A3

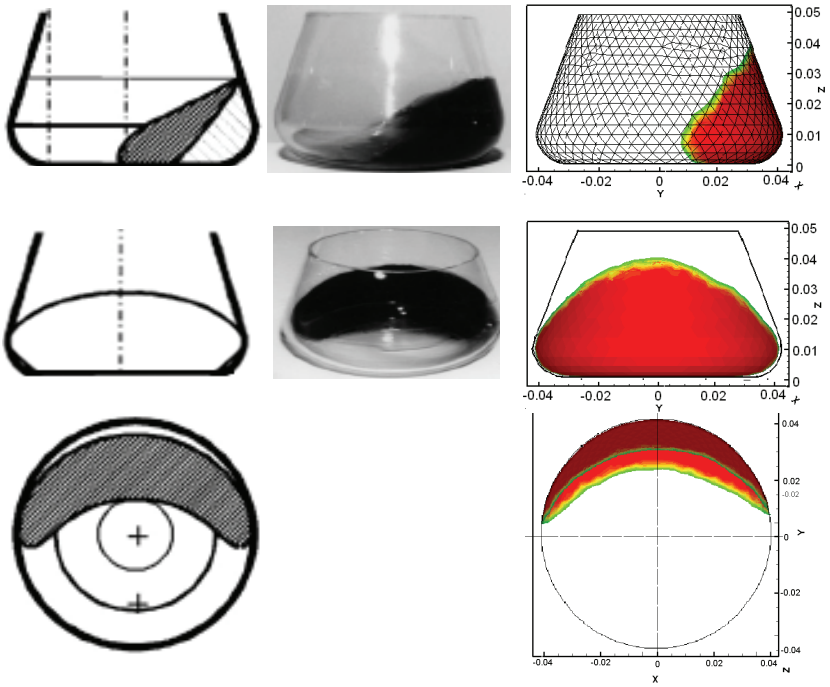


Fig. 3. Simulated and referred liquid distribution in a 250mL shaken flask.
Operating conditions: (A) $V_L$ =25mL, N = 250 rpm, $d_0$ = 5 cm. (B) $V_L$ =25mL, N = 150 rpm, $d_0$ = 5 cm. In which, A1, A2 and B1, B2 are from reference [8], A3 and B3 are the results of this work. It should be mentioned that the viscosity of referred data is 0.01 Pa·s, ten times of the viscosity in this simulation.

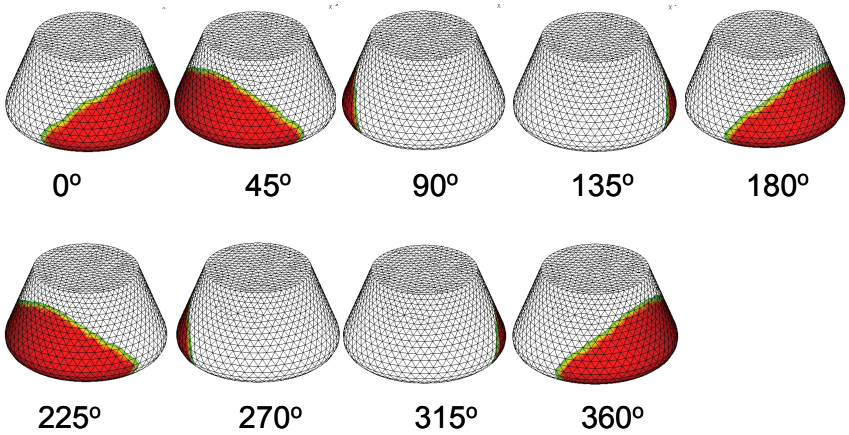


Fig. 4. The liquid position changes in one rotation period of shaken flask with 25ml water load under 150rpm rotation speed.

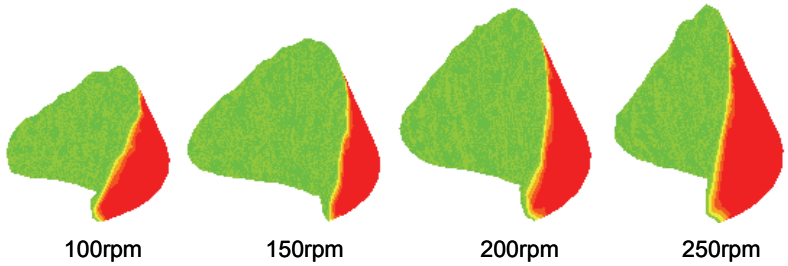


Fig. 5. The liquid phase shape influenced by rotation speed with 25ml water load

### 4.4 Maximum height of liquid approached

As described previously, due to the rotation, liquid would be rejected outwards and crawled along flask wall. The effects of water load and rotation speeds on the maximum height of liquid approached are plotted in figure 6. It can be found that with the increase of both rotation speed and water load, the maximum height of liquid approached would also increase obviously. However, the increase of the maximum liquid height would dropoff due to the gravity limits when bigger rotation speed.

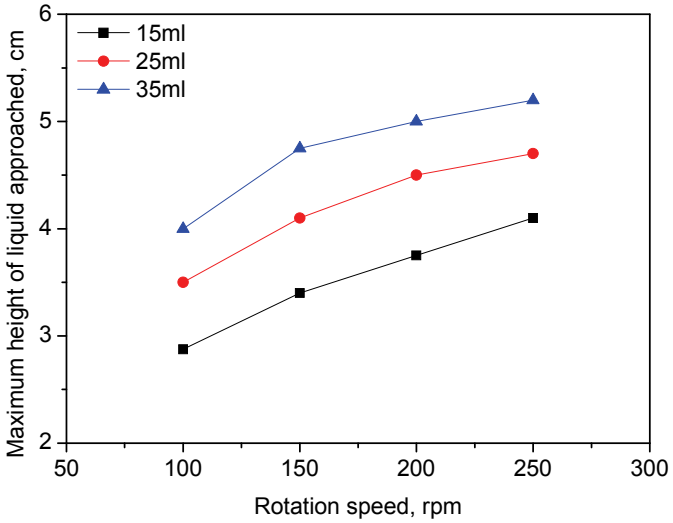


Fig. 6. Effect of liquid loading and rotation speed on the maximum height of liquid approached

### 4.5 Gas-liquid interfacial area

In shaken flask, the mass transfer is mainly dominated by the gas-liquid interfacial area. Bigger gas-liquid interfacial area always indicates good mass transfer, increasing rotation

speed is a conventional method to improve mass transfer, such as oxygen supply for fermentation in shaken flask. Figure 7 presents the influences of both water load and rotation on gas-liquid interfacial area. It can be found, compared with water load, higher rotation speed does not lead to a bigger gas-liquid interfacial area, especially when the rotation speed is bigger than 150rpm. In fact, in most fermentation experiments in shaken flask, 150-200rpm rotation speed is a conventional choice. Too big rotation speed could not improve gas-liquid mass transfer obviously. More water load gives a rise of gas-liquid interfacial area, but it should be limited to the liquid crawls height on the wall in practice.

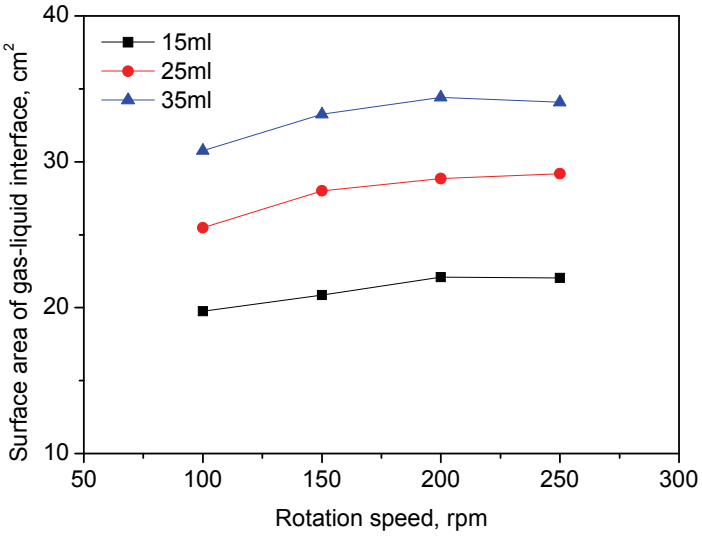


Fig. 7. Effects of rotation speed and water load on the gas-liquid interfacial area

### 4.6 Turbulent kinetic dissipation rate and volumetric power consumption

The rotation of liquid in shaken flask is produced by the power input from orbital shaking machine. How many the power consumed and how about the energy dissipated in flask are of interests to understand both mixing transfer and scale-up of bioprocess.

According to the turbulent model, turbulent intensity (I) is defined as in equation (19).

$$I = \frac{\upsilon'}{\upsilon_{avg}} \tag{19}$$

In which, $\upsilon'$ is the .root mean square of turbulent fluctuation velocity, and $\upsilon_{avg}$ presents the averaged flow velocity. The random fluctuation of micelles causes turbulence. So I indicates the degree of fluctuation and interaction between fluid micelles. Figure 8 gives the influences of rotation speed and water load on turbulent intensity. Higher rotation speed and more water load would almost linearly increase turbulent intensity, as the results, liquid mixing is better.

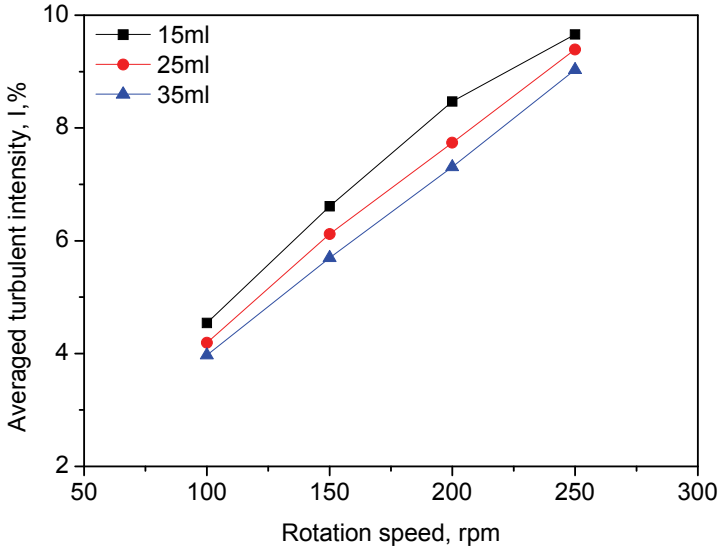


Fig. 8. Changes of turbulent intensity with different rotation speed and water load

Figure 9 plotted the changes of turbulent kinetic dissipation rates with different rotation speed and water load. It can be found that with the increase of rotation speed and water load, the averaged turbulent kinetic dissipation rates also increase greatly. Relatively, the influence of rotation speed is bigger on it. It is easy to understand that bigger rotation speed of shaken flask would input more power in it, such power mostly is dissipated by the collision between micelles in turbulent flow.

In most bioprocess, power consumption is usually taken as an effective criterion for process scaleup. Precisely understand of the power consumption in small apparatus or bench would help to improve the reliability of scaleup process and diminish pilot step. However, more details of power consumption of shaken flask are difficult, and in most cases, the power consumption in unbaffled Erlenmeyer flasks is calculated by empirical approach. Generally, the mechanical power introduced into the shake flask reactor during rotating motion is described as follows by Büchs et al. [13,14].

$$P = M(2\pi N) \tag{19}$$

Where, P is the power input to flask, M is the net torque, and N is the shaken frequency ($min^{-1}$). Following the definition of the torque, the dimensionless power number for shake flasks is defined by Büchs et al. [14] as the modified Newton number:

$$Ne' = \frac{P}{\rho N^3 d^4 V_L^{1/3}} \tag{20}$$

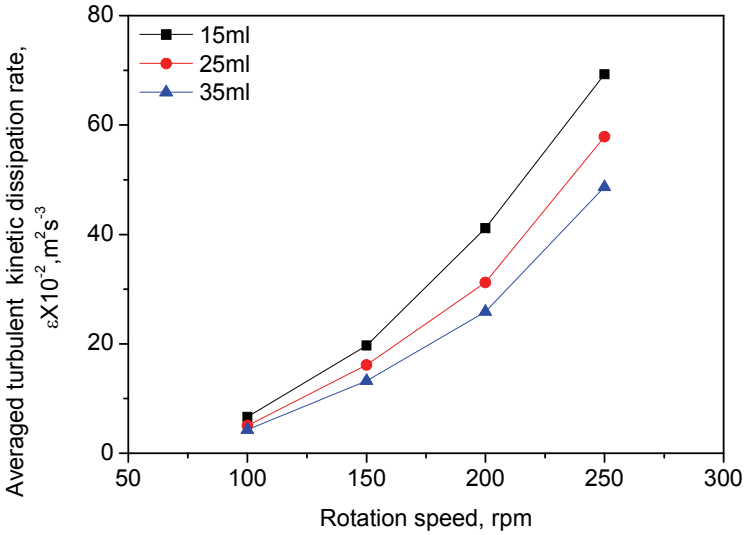


Fig. 10. Changes of turbulent kinetic dissipation rates with different rotation speed and liquid load

Moreover, the Reynolds number for shake flask is defined as

$$\mathrm{Re} = \frac{\rho N d^2}{\mu} \tag{21}$$

and a relationship for dimensionless power in unbaffled shaken flasks is given by Büchs et al.[15]:

$$Ne' = 70\,\mathrm{Re}^{-1} + 25\,\mathrm{Re}^{-0.6} + 1.5\,\mathrm{Re}^{-0.2} \tag{22}$$

Thus, the volumetric power consumption in unbaffled shaken flask $P/V_L$ ($W/m^3$) can be calculated. On the other hand, according to the definition of turbulent kinetic dissipation rate ε, it means power consumption per unit mass. So $\varepsilon\rho_L$ would also presents the volumetric power consumption rates The empirical approached results of $P/V_L$ by equation (19-22) and averaged $\varepsilon\rho_L$ by CFD simulation of all the cases of rotation speeds and water loads, is plotted in figure 11. It can be found that they both have a good linear relationship as in equation (20), and both the rotation speed and water load make no influence on the relationship.

$$\varepsilon\rho_L = 0.629\frac{P}{V_L} \tag{20}$$

It means that the empirical value of volumetric power consumption $P/V_L$ ($W/m^3$) is much bigger than volumetric power consumption $\varepsilon\rho_L$ ($W/m^3$) by CFD. It should be noted that

$\varepsilon\rho_L$ is really dissipated by rotary liquid. Thus, $\varepsilon\rho_L$, or $0.629\frac{P}{V_L}$ by empirical approach is more practical as the power input criterion for scale-up of bioprocess directly from shaken flask.

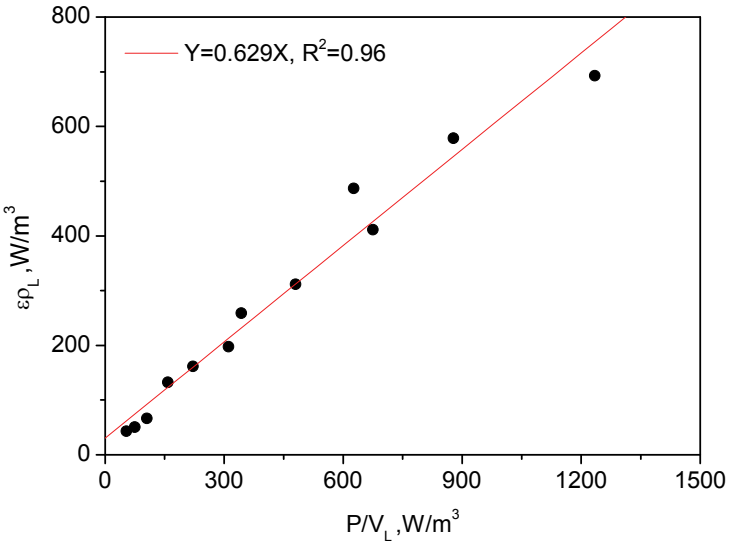


Fig. 11. The relationship between volumetric power consumptions by empirical approach and CFD simulation.

## 5. Conclusion

A fluid dynamic model was prepared to calculate the flow behaviors in an Erlenmeyer shaken flask with a volume of 250mL moving in a shaker based on the combination of volume of fluid (VOF) model and RNG k-ε turbulence model. The numerical simulation was carried out using a commercial computational fluid dynamics software, Fluent, implementing the technique of Dynamic Mesh (DM). The effects of four different rotation speeds and three water load on the flow were investigated. The simulated results of liquid shape and distribution well agreed with experimental morphology in reference[9]. As the motion approached steady state, liquid would periodically traverse shaken flask wall with wall crawl driven by the centrifugal force and gravity without change of liquid shape and distribution. The shape of water was not symmetrical due the liquid rotary inertia and wall adhesion. The increase of both rotation speed and water load would give a rise of the maximum height of liquid approached Compared with water load, higher rotation speed does not lead to a bigger gas-liquid interfacial area, especially when the rotation speed is bigger than 150rpm. Bigger rotation speed and more water load would almost linearly increase the turbulent intensity to improve liquid mixing. With the increase of rotation speed and water load, the averaged turbulent kinetic dissipation rates also increase greatly.

In order to under stand the power consumption in shaken flask, volumetric power consumption by empirical approach and CFD simulation were compared and it is found that there is good linear relationship between them without any influence by rotation speed and water load. And the empirical value of volumetric power consumption $P/V_L$ ($W/m^3$) is much bigger than volumetric power consumption $\varepsilon\rho_L$ ($W/m^3$) by CFD, probably indicating that $\varepsilon\rho_L$ by CFD, or $0.629\frac{P}{V_L}$ by empirical approach is more practical as the power input criterion for scale-up of bioprocess directly from shaken flask.

## 6. Notation

$A$ – Gas-liquid interface area, $cm^2$

$a$ , $b$ – Length in elliptical axis in x and y directions

$H$ – Maximum liquid height approached

$I$ – Turbulent intensity, %

$k$ – Turbulent kinetic energy, $m^2 \bullet s^{-2}$

$M$ – Net torque,

$m$ – Mutation rate of size function

$N$ – Rotation speed, rpm

$Ne'$ – Modified Newton number

$n$ – Mutation gradient of size function

$P$ – Power input, W

$Re$ – Reynolds number

$t$ – Rotary time of shaken flask, s

$U_x$, $U_y$ – Linear velocities of shaken flask in x and y directions, $m \bullet s^{-1}$

$u$ – Maximum linear velocities of shaken flask, $m \bullet s^{-1}$

$V_L$ – Water load volume in flask, mL

$v$ – Liquid flow velocity, $m \bullet s^{-1}$

$v'$, $v_{avg}$ – Fluctuation and averaged velocity of liquid, $m \bullet s^{-1}$

$a$ – Volume void of fluid phases

$\gamma$ – Size function factor

$\varepsilon$ – Turbulent kinetic dissipation rate, $m^2 \cdot s^{-3}$

$\mu$ – Fluid viscosity of each phase weighted average, Pa•s

$\mu_{eff}$ – Effective viscosity, Pa•s

$\rho$ – Fluid density of each phase weighted average, $kg \cdot m^{-3}$

$\omega$ – Rotation angular velocity of flask, $rad \cdot s^{-1}$

**Subscripts**

p – The p phase

q – The qphase

## 7. References

[1] Freedman D., The shaker in bioengineering, Proc. Biochem. 1969, 2:35–40.

[2] Huang X., Liu M., Gong B., Zeng X., Zhang S. and Cao Z., Expression of site-directed mutant glutamine synthetase and enzymatic glutamine production. Journal of Chemical Industry and Engineering(China). 2008, 59(6): 1479-1484

[3] B¨uchs J., Maier U., Milbradt C., Zoels B., Power consumption in shaking flasks on rotary shaking machines: I. Power consumption measurements in unbaffled flasks at low liquid viscosity, Biotechnol. Bioeng. 2000, 68:589–593.

[4] Maier U., Büchs J., Characterisation of the gas–liquid mass transfer in shaking bioreactors, Biochem. Eng. J. 2001, 7 (2): 99–107.

[5] Maier U., Losen M., Büchs J., Advances in understanding and modeling the gas–liquid mass transfer in shake flasks, Biochem. Eng. J. 2004,17 (3): 155–167.

[6] Fan D., Yu J., Research on fermentation scale-up bases on the OUR obtained from shake flask. Chinese Journal of Biotechnology. 1996, 12(3): 301-306

[7] Büchs J., Zoels B., Evaluation of maximum to specific power consumption ratio in shaking bioreactors, J. Chem. Eng. J. 2001,34 (5): 647–653.

[8] Peter C.P., Suzuki Y., Büchs J., Hydromechanical stress in shake flasks: Correlation for the maximum local energy dissipation rate, Biotechnol. Bioeng. 2006,93 (6): 1164–1176.

[9] Büchs J., Maier U., Lotter S., Peter C. P.. Calculating liquid distribution in shake flasks on rotary shakers at waterlike viscosities. Biochemical Engineering Journal 2007, 34: 200–208

[10] Yakhot V., Orszag S.A., Renormalization group analysis of turbulence (I): Basic theory Journal of Scientific Computing, 1996 , 1 (1): 3211

[11] http://202.118.250.111:8080/fluent/Fluent60_help/index.htm

[12] Brackbill J U, Kot he D B , Zemach C., A continuum method for modeling surface tension. Journal of Computational Physics. 1992, 100 (2): 335-354

[13] Cyril P. Peter, Suzuki Y., Rachinskiy K., Lotter S. and Büchs J., Volumetric power consumption in baffled shake flasks. Chemical Engineering Science. 2006,61: 3771 – 3779

[14] Büchs, J., Maier, U., Milbradt, C., Zoels, B., Power consumption in shaking flasks on rotary shaking machines: I. Power consumption measurement in unbaffled flasks at low liquid viscosity. Biotechnology and Bioengineering. 2000a, 68 (6), 589-593.

[15] Büchs, J., Maier, U., Milbradt, C., Zoels, B., Power consumption in shaking flasks on rotary shaking machines: II. Nondimensional escription of specific power consumption and flow regimes in unbaffled flasks at elevated liquid viscosity. Biotechnology and Bioengineering. 2000b.68 (6): 594-601.

# 8

# Application of Computational Fluid Dynamics to the Study of Designed Green Features for Sustainable Buildings

Cheuk Ming Mak
*Department of Building Services Engineering, The Hong Kong Polytechnic University*
*Hong Kong, China*

## 1. Introduction

Continuing urbanisation has implications on preservation of our common resources and has caused global and mirco-environmental pollution. It affects our public health and causes damage to the prospects of future generations. Although the timely provision of resources and environmental mitigation measures could resolve some of the issues, others may require fundamental reconsiderations of the implications on long-term sustainability. The understanding of the benefits of sustainability development in urbanisation and its implementation in the practice of building design is of importance for the long-term sustainability of a city.

Natural ventilation is increasingly being used in modern urbanised residential buildings to minimise the consumption of non-renewable energy and the reliance on active means for environmental control. Increased consciousness of the environmental problems has aroused people's interest of sustainable urbanisation, especially the application of green features in buildings. Green features are architectural features used to mitigate migration of various air-borne pollutants and to moderate the transport of heat, air and transmission of daylight from outside to indoor environment in an advantageous way [Mak et al., 2005a]. Green features such as a windcatcher [Li & Mak, 2007], wing walls [Mak et al., 2005a; Mak et al., 2007], skygardens [Niu et al., 2005] and balconies have made use of natural ventilation in residential buildings for increasing ventilation rate. However, the ventilation performance of these green features is not fully understood.

In recent years, Computational Fluid Dynamics (CFD) has been widely used to study building airflow and the indoor environment, as well as the wind environment. An overview of applications in ventilation [Chen, 2009] has indicated that the CFD models were a most popular tool used to predict ventilation performance of buildings. CFD can be used to perform combined simulation of the wind environment around the buildings and the airflow inside the buildings [Awbi, 1989; Chen & Srebric, 2000; Chow, 1996; Jones & Whittle, 1992; Niu & Kooi, 1992] and modelling of different green features to study their ventilation performance since it can provide detailed airflow velocity distribution and thermal conditions. For most applications of ventilation and turbulence flow, the results have been approved to be useful and reasonably accurate. CFD has therefore become a reliable tool for flow analysis in buildings. It is believed that natural ventilation in buildings can be

enhanced through the incorporation of appropriate green features in sustainable development such that there is a potential saving in non-renewable energy consumption in buildings.

A commercial CFD package FLUENT has been applied to various research works and found to be useful [Bojic et al., 2001; Mak et al., 2005b; Mak & Oldham, 1998a; Mak & Oldham, 1998b; Mak & Yik Francis, 2002; Niu et al., 2005]. FLUENT has been adopted by the author and his research partners [Li & Mak, 2007, ; Li et al., 2006; Mak et al., 2007] to study the performance of two designed green features including windcathcer and wing walls used for sustainable buildings. This chapter will introduce the numerical simulation of these two green features. The CFD numerical technique used including geometry, numerical grids, boundary conditions and turbulence models will be discussed. The ventilation performance of these green features in buildings will be discussed. Other CFD applications in building services engineering such as prediction of flow-generated noise using CFD will also be briefly introduced.

## 2. Study of green features for sustainable buildings using CFD

### 2.1 Windcatcher

#### 2.1.1 Description of the windcatcher

The windcatcher system is one of the green features for providing good natural ventilation. In the modern design of windcatchers, the principles of wind effect and passive stack effect are considered in the design of the stack that is divided into two halves or four quadrants/segments with the division running the full length of the stack [Awbi & Elmualim, 2002].

The windcatcher systems were employed in buildings in the Middle East for more than three thousands years. They have different names in different parts of region [Bahadori, 1994; Elmualim et al., 2001; McCarthy, 1999]. Although more and more windcatcher systems have been applied into recent commercial buildings and residential buildings such as the Queen's Buildings at Demonfort University and the BRE office of the future [Hurdle, 2001; McCarthy, 1999; Swainson, 1997], their performance has not been fully evaluated under different climates. The experimental studies of windcatcher systems for all different cases are obviously costly and impossible. The assessment of the performance of windcatcher systems using CFD is very important for both design and improvement of the systems. Three-dimensional models of a windcatcher system have therefore been built and their performance under different wind speeds and flow directions has been studied and compared [Li & Mak, 2007].

The buildings with only one window opening usually have poor ventilation because it is difficult for wind to change its direction to enter to the interiors of the buildings, especially when the window opening is small. The windcatcher is designed for solving this problem (as shown in Figure 1 (a) and (b)). It can change the direction of wind and channel the fresh air into rooms (as shown in Figure 2). Generally, the windcatchers are installed on the roof of a building in order to increase the outdoor-indoor pressure gradient and velocity gradient, and to provide more fresh air into rooms. In order to induce more air into the interiors when the wind direction varies, the stack of the windcatcher is usually divided into two halves or four segments. A numerical modelling of the windcatcher will be discussed in the following section.

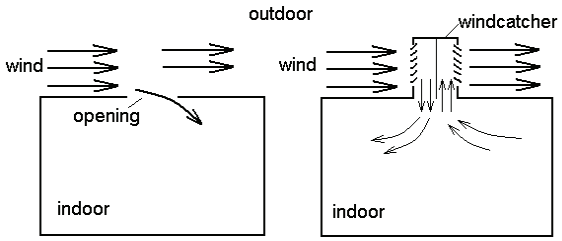


Fig. 1. Comparison of different ventilated rooms
(a) Rooms without windcatcher (b) Rooms with windcatcher

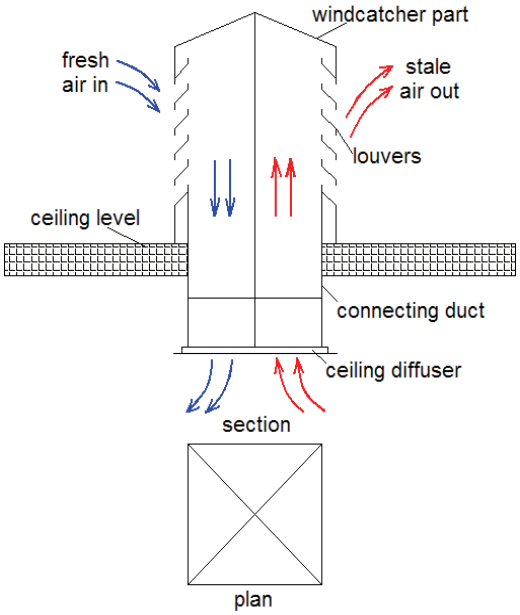


Fig. 2. The structure and principle of the windcatcher system

### 2.1.2 Numerical simulation of the windcatcher

2.1.2.1 Geometry

It can be seen in Figure 3 that a three dimensional square windcatcher model of dimension 500mm x 500mm and length of 1.0m connected to a room has been created when the wind speed varies in the range of 0.5-6m/s. The overall numerical domain size is 3.6×3.6×2m (as shown in Figure 3). In order to show the influence of the wind direction, three additional models with the incident angle α varying from 0˚ to 45˚ with an interval of 15˚ shown in Figure 4 (a), (b), (c) and (d) have been created. At the wind direction of 0˚, the performances of the windcatcher under different wind speeds v of 0.5, 1, 2, 3, 4, 5 and 6m/s were investigated. Moreover, the flow rate of air entering the room through the windcatcher under different wind directions and different wind speeds is investigated.

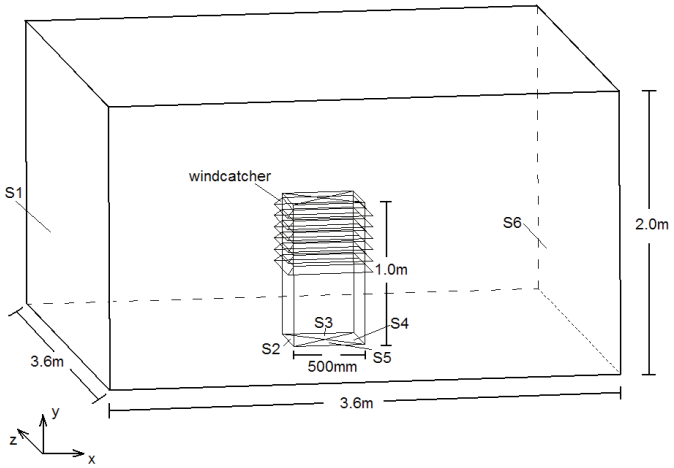


Fig. 3. The 3D model of windcatcher

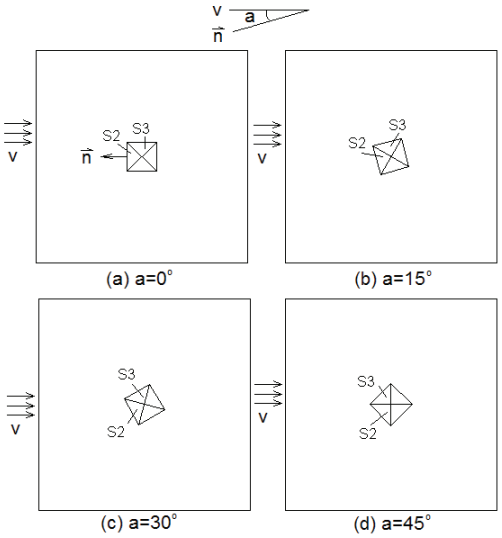


Fig. 4. Plan of the models under different wind direction

2.1.2.2 Numerical grids, turbulence model and boundary conditions

The accuracy of CFD simulation is affected by numerical schemes, turbulence model, and boundary conditions used etc. [Marakami, 2002]. It is important to set reasonable boundary and initial parameters. Since the air flow velocity in and around the windcatcher is much lower than sound velocity, the flow can be considered as incompressible and the density of air is assumed to be constant. The wind speed was specified at the inlet and wind friction along the wall is calculated using the standard wall function. S1 shown in Figure 3 was assumed to be the natural wind source and was set to be the wind velocity inlet. The turbulence intensity and the viscosity ratio of this inlet are set to be 3 and 10 respectively. S6 was assumed to be the

outlet of wind and was set to be the pressure outlet. S2, S3, S4 and S5 are the connection of the square windcatcher to the room. In the cases shown as Figure 4 (a), (b) and (c), S2 was set to be pressure outlet and others pressure inlet while in case shown as Figure (d), S2 and S3 are both set to be pressure outlet and the other two pressure inlet. The boundary conditions are based on the experiments of Awbi and Elmualim [Awbi & Elmualim, 2002]. The standard (two-equation) k-ε turbulence model was adopted. Although this turbulence model inevitably introduces some errors [Murakami, 1997], it has been chosen because the overall trend of airflow parameters such as pressure and air velocity can be reasonably predicted [Bojic et al., 2001; Mak & Oldham, 1998a; Mak & Oldham, 1998b; Murakami, 1997; Niu & Zhu, 2004]. The total number of grids in all simulation models is all around 50,000 and the maximum and minimum grid volume is about 2.7×10-4m3 and 3.2×10-7m3 respectively. Unstructured grid was used for all simulation models (as shown in Figure 5).

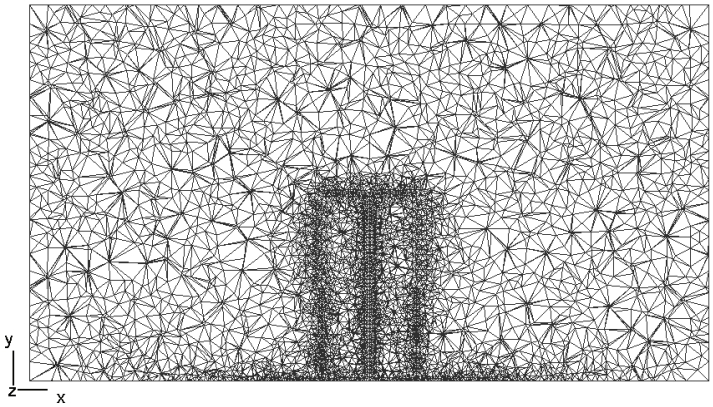


Fig. 5. Grid information of the model (cross-section)

### 2.1.3 Results and analysis

2.1.3.1 Verification of the simulation result

The numerical results are compared with the published experiment results of Awbi and Elmualim [Awbi & Elmualim, 2002]. Figure 6(a), (b), (c) and (d) show that the airflow rate Q

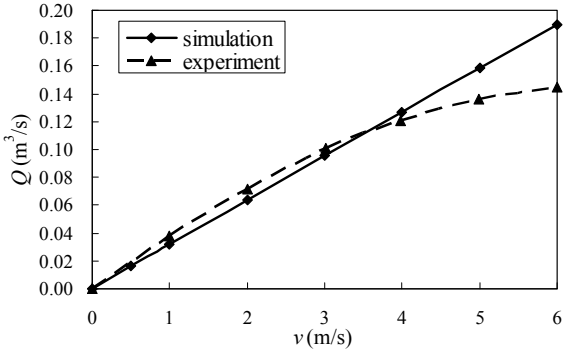


(a)

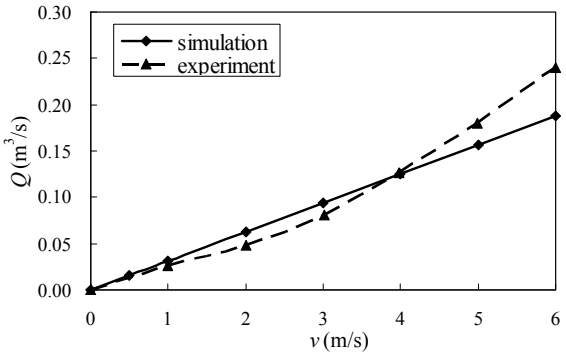


(b)

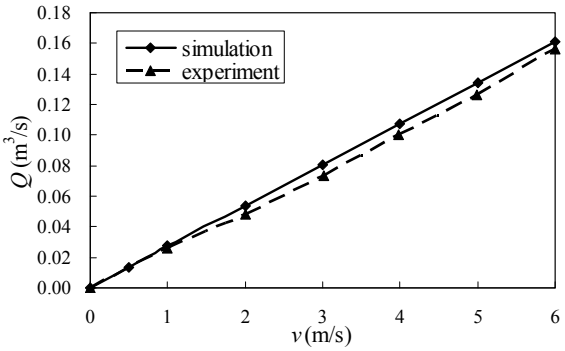


(c)

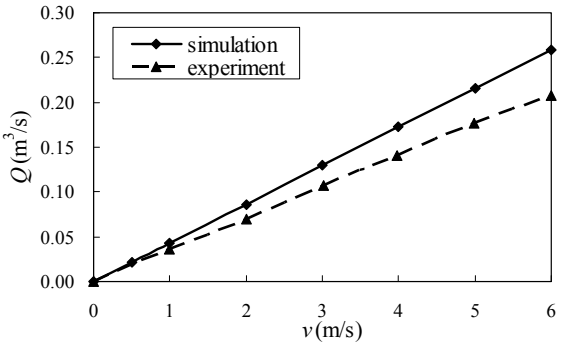


(d)

Fig. 6. Comparison of simulation and experiment results
(a) α = 0° (b) α =15° (c) α = 30° (d) α = 45° $v$=external wind speed

entering into the test room though S2 at the wind incidence angle of 0º, 15º, 30º and 45º respectively. It can be seen that the simulation results have a good agreement with the experimental results and similar trend have been obtained for the other cases. The percentage of error between the simulation results and the experiments is in the range of -5% and 30%.

2.1.3.2 Function of the windcatcher quadrants

The windcatcher has been divided into four quadrants in order to induce wind from all directions and one or two quadrants will be the air inlet of the test room while others being the outlet. To figure out the specific function of each quadrant is essential for the calculation of indoor air flow rate and the control of windcatcher system. Since it is impossible to conduct experiment to obtain velocity and pressure at every point by velocity or pressure sensors on each quadrant. CFD tool is adopted here.

The velocity distribution on the cross-section of four quadrants at the wind incidence angle of 0º, 15º, 30º and 45º is shown in Figure 7. It demonstrates that when the incidence angle α = 0º and 15º, only the windward side S2 acts as the air supply quadrant of the test room, but when α = 30º and 45º, both S2 and S5 take the responsibility of inducing wind into room as well as exhausting the indoor air out. A few of short circling flow has been observed and its influence will be studied in future work. The flow of S5 is therefore taken into consideration when calculating the indoor flow rate of 30º and 45º.

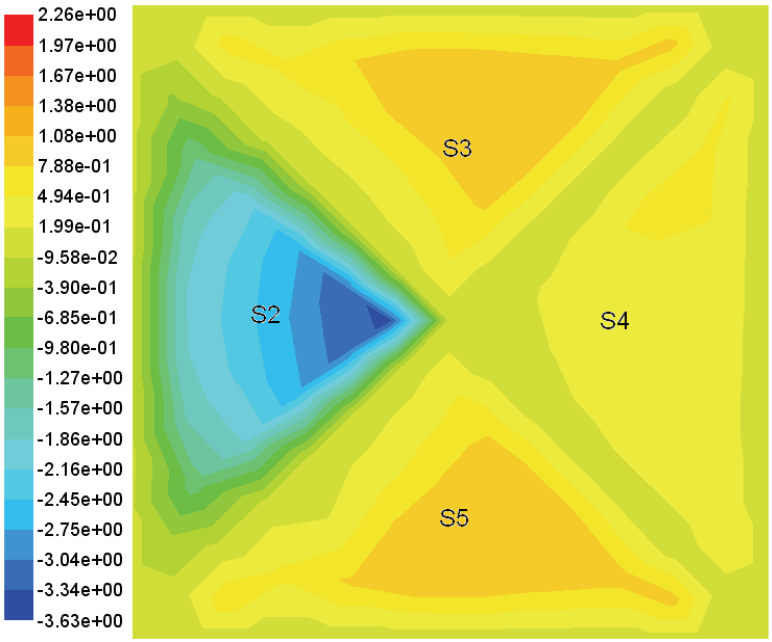


(a)

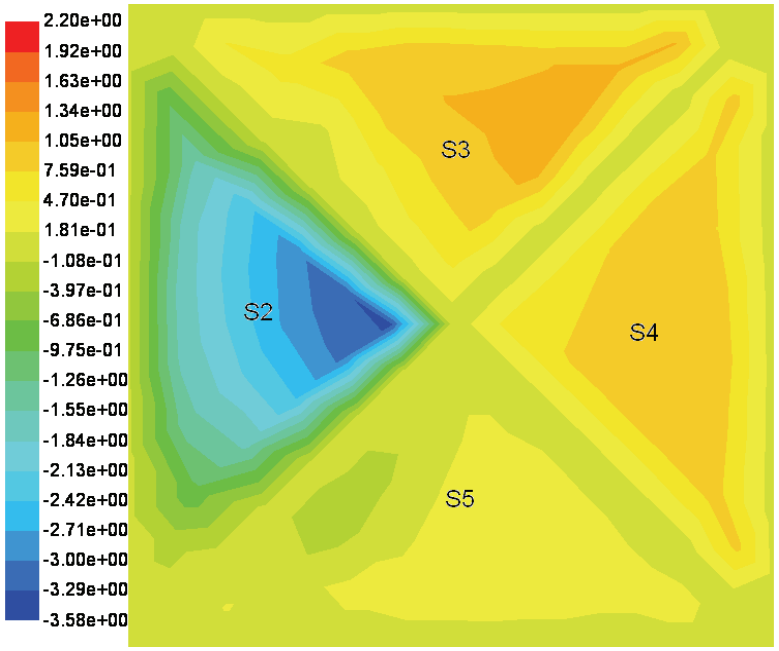
2.20e+00
1.92e+00
1.63e+00
1.34e+00
1.05e+00
7.59e-01
4.70e-01
1.81e-01
-1.08e-01
-3.97e-01
-6.86e-01
-9.75e-01
-1.26e+00
-1.55e+00
-1.84e+00
-2.13e+00
-2.42e+00
-2.71e+00
-3.00e+00
-3.29e+00
-3.58e+00
S3
S2
S4
S5

(b)

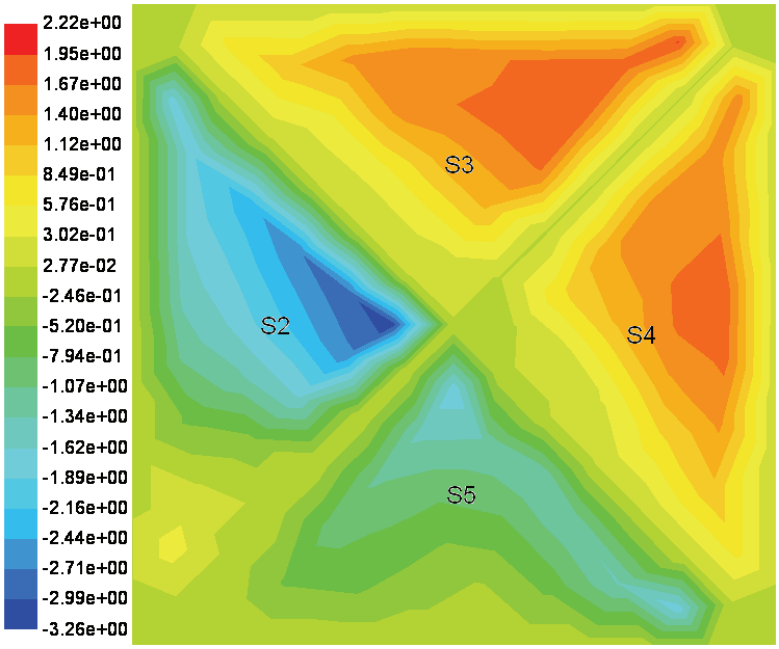
2.22e+00
1.95e+00
1.67e+00
1.40e+00
1.12e+00
8.49e-01
5.76e-01
3.02e-01
2.77e-02
-2.46e-01
-5.20e-01
-7.94e-01
-1.07e+00
-1.34e+00
-1.62e+00
-1.89e+00
-2.16e+00
-2.44e+00
-2.71e+00
-2.99e+00
-3.26e+00
S3
S2
S4
S5

(c)

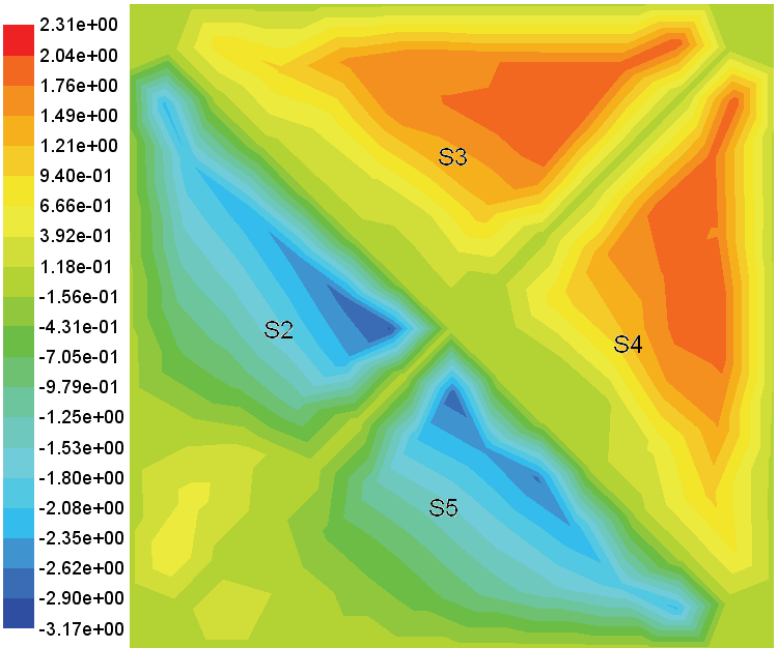


(d)

Fig. 7. Velocity distribution on the cross-section of four quadrants
(a) α = 0° (b) α =15° (c) α = 30° (d) α = 45°

2.1.3.3 Performance of the windcatcher under different wind speed

The calculated air flow rate of supply air inlet under different wind incidence angle α of 0°, 15°, 30° and 45° was found to increase with the external wind speed (as shown in Figure 8). At an angle of 0˚ the ventilation rates are generally lower than for the other three cases and at the angle of 45˚ the ventilation rate increases more quickly than other cases with the external wind speed. At α = 0°, a volumetric airflow of 0.093m3/s was achieved through the main supply quadrant for an average wind velocity of 3m/s and a maximum value of

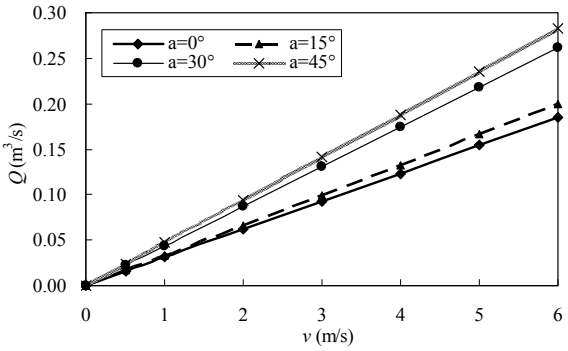


Fig. 8. The variation of ventilation rate with *v* external wind speed

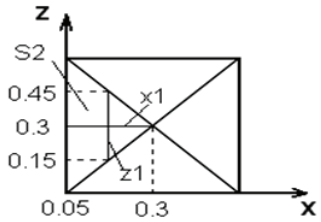


Fig. 9. Positions of x1

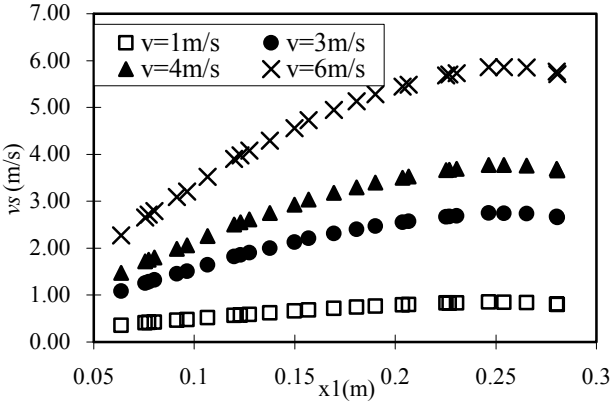


(a)

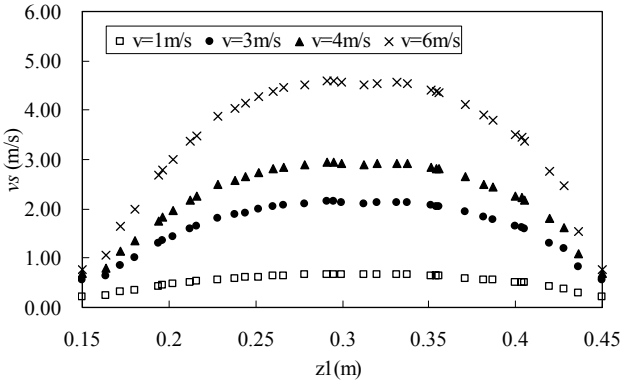


(b)

Fig. 10. The variation of air velocity when α=0°
(a) along with x1 (b) along with z1
vs=velocity of air supply into room, v=external wind speed

0.185m3/s for the external wind speed of 6m/s. At α = 45°, the maximum volumetric airflow rate reaches 0.282m3/s when there are two air supply quadrants. Since the volume

of the test room is 15.25m3, the maximum indoor air exchange rate (ACH) is about 70 and thus can keep indoor air at a healthy level in most cases.
Figure 10 (a) and (b) show the variation of wind speed along with x1 and z1 respectively when the wind incidence angle is 0˚. x1 and z1 are both in the center of the supply air inlet (as show in Figure 9). It can be seen from the figures that when the wind incidence angle is 0˚, the maximum wind speed induced into text room is close to the external wind velocity. It demonstrates that it is an effective way to induce natural fresh air into room by using a windcatcher system.

2.1.3.4 Performance of the windcatcher under different wind direction

It seems that the volumetric airflow rate increases with the external wind incidence angle (shown as Figure 8), but different result has been obtained by investigating three additional models under the wind incidence angle of 10º, 25º and 40º. The variation of ventilation rate with the wind direction when the external wind velocity v=3m/s is shown in Figure 11 and it demonstrates that airflow rate increases with the incidence angle only in the range of 10º~40º and when α is smaller than 10º or larger than 40º, the trend becomes opposite. Similar results have been observed in other cases. The installation angle of windcatcher should therefore be adjusted in order to operate better in different regions.

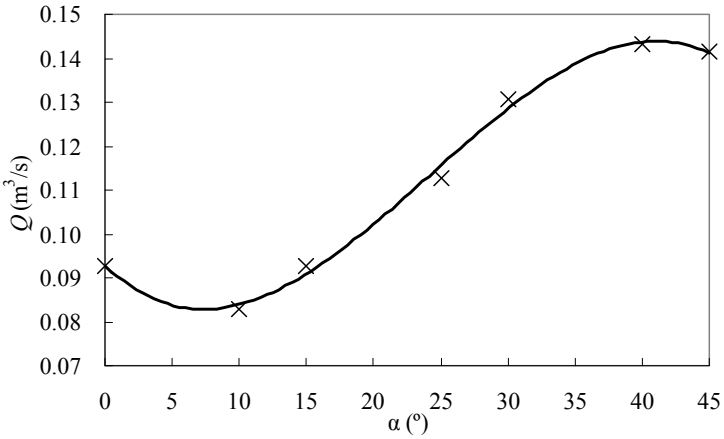


Fig. 11. The variation of ventilation rate with the wind direction

2.1.3.5 Uniformity of supply air inlet

The variance of airflow velocity into text room is used here to compare the uniformity of supply air inlet. It is defined as:

$$D(vs) = E\{[vs - E(vs)]^2\} \tag{1}$$

where E(vs) is the mathematical expectation of the supply air velocity vs and the value of vs is obtained from random points at the line x1 and z1, see Figure 9. When D(vs) increases, the uniformity of supply air becomes worse.
The results at wind velocities from 0.5 to 6m/s and wind angle of 0º and the results at wind angles from 0º to 45º and wind angle of 3m/s are shown in Figure 12(a) and (b) respectively. From these figures, it can be seen that the uniformity of supply air inlet decreases with the

external wind velocity and increases with incidence angle. Therefore, in the application of the windcatcher system, diffusers should be installed at the inlet entering the text room in order to keep the occupants comfortable.

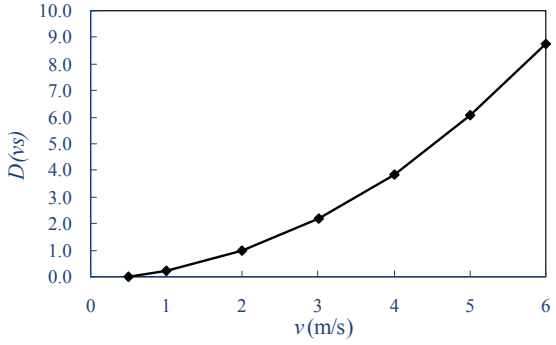


(a)

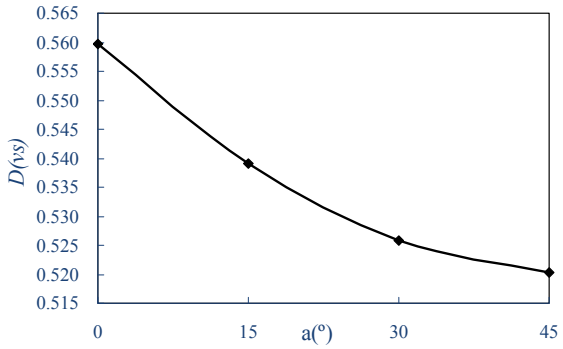


(b)

Fig. 12. The variance of air flow velocity of the air entering into the text room against external wind speeds and wind directions

### 2.2 Wing walls

#### 2.2.1 Description of the wing walls

There is a growing consciousness of the environmental performance of buildings. The use of green features in building design not only improves the environmental quality, but also reduces the consumption of non-renewable energy used in active control of indoor environment. Larger window openings in the walls of a building may provide better natural ventilation. However, it also increases the penetration of direct solar radiation into indoor environment. The use of wing wall as shown in Figure 13 is an alternative to create effective natural ventilation. Figure 13 shows the provision of wing wall in a building façade vertically between two openings. Natural ventilation is considered to be an effective passive cooling strategy in building design. In 1962 and 1968, Givoni [Givoni, 1962; Givoni, 1968] conducted experiments on room models with and without wing walls in a wind tunnel so as to study its effect on natural ventilation. He found that single-sided ventilation incorporated

with wing walls could greatly improve the internal air circulation compared with that without wing walls. Maximizing the utilization of natural ventilation therefore not only minimize the reliance on active means for environmental control, but also reduces the consumption of non-renewable energy.

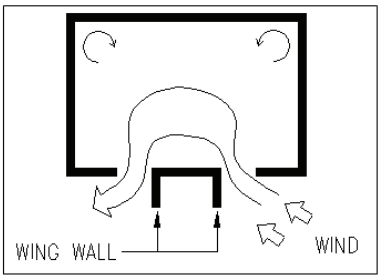


Fig. 13. Physical configuration of wing walls

### 2.2.2 Experiments of Givoni

The experiments of Givoni [Givoni, 1962; Givoni, 1968] were conducted to study air flow through room models with and without wing walls in a wind tunnel. Figure 14 and Figure 15 show the plan and side elevation of the open-throat type wind tunnel respectively. It consists of an intake section, a working section, a distribution control section, a transit section, a fan and an exit.

It can be seen in Figure 14 and Figure 15 that the intake opening has a cross section of 1.8 x 1.1m(H) and contracts to a cross section of 1.5 x 0.8m(H), over a length of 0.9m. The working section is 2.22x1.2m(H). The distribution control section contracts in cross section from 1.5x0.8m(H) to 0.8x0.6m(H) and contains five vertical louvers whose angle can be adjusted so as to regulate flow distribution. The transit sections are used for connecting the rectangular and circular section.

The room model of dimension of 0.65x0.65x0.5m(H) with a centered window opening shown in Figure 14 and Figure 15 with dashed lines was located at the center of the wind tunnel. The window opening with dimension of 1/3 of that of the wall was created at the center of the wall of the room model facing the air flow.

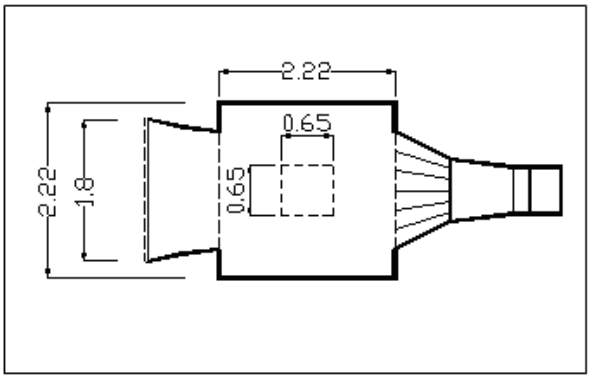


Fig. 14. Plan elevation of the wind tunnel experiments

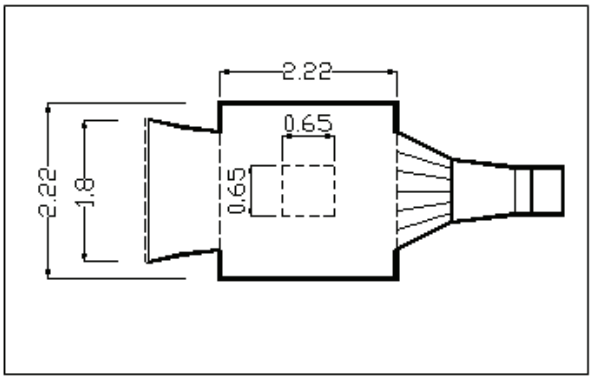


Fig. 15. Side elevation of the wind tunnel experiments

The wind tunnel was then tested with different uniform air (wind) flow velocities ranging from 1.27m/s to 3.35m/s. Different wind directions were tested with the angle of air flow incidence ranging from 0o (opening facing the air flow) to 135o with 22.5o increment. The average internal velocity based on five measurement points inside the room model was expressed in percentage based the inlet uniform air flow velocity (wind speed).

### 2.2.3 Numerical simulation of the wing walls

2.2.3.1 Geometry

There are three major parts in the FLUENT CFD code. They are: i) pre-processor, ii) solver and iii) post-processor. The pre-processor GAMBIT was applied to create 3-dimensional physical room models that are based on the experiments of Givoni. Figure 16 shows the geometry of the 3-dimensional computational domain where the room model of 0.65m x 0.65m x height 0.5m is located inside the computational domain. There are two lateral openings in the room model (Case 1). The wind angle is 0° when the lateral openings on the wall are facing the wind and their normal is in parallel to the wind as shown in Figure 16.

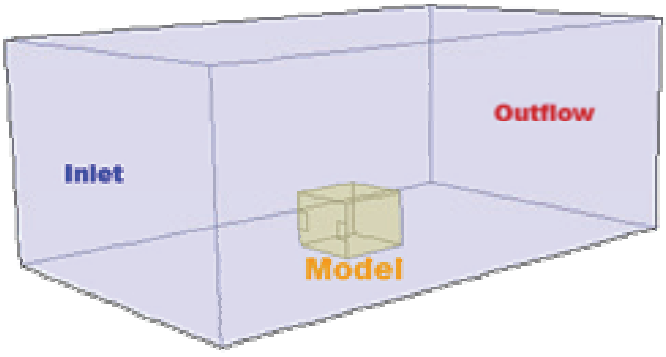


Fig. 16. Physical model for computer simulation

2.2.3.2 Numerical grids, discretization scheme, turbulence model and boundary conditions

The FLUENT CFD package is used here in modeling the natural ventilation by solving the conservation equations for mass, momentum and energy using the finite volume method. A simple standard (two-equation) k-ε turbulence model was used though it was inevitable to introduce some errors [Murakami, 1997]. The number of uniform structured grids for the 3-dimensional simulation is around 60000 – 68000 while the number of grids for the 2-dimensional simulation is around 12700. The first-order upwind discretization scheme was used. All CFD results have been checked against energy conservation. Figure 17 shows the grids of the simulated model. Figure 18 shows the model configurations for all cases at different wind angles. Table 1 and Figure 18 show the different inlet uniform wind speeds and wind angles for all cases respectively.

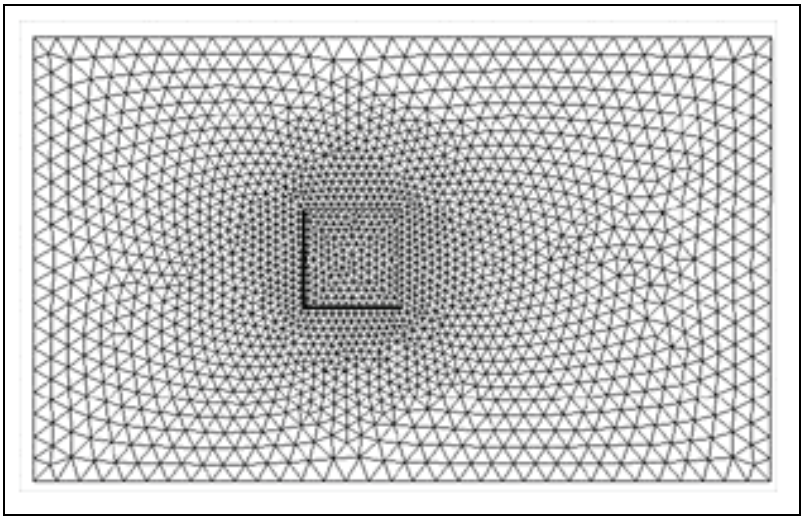

Fig. 17. Grids of the simulation model

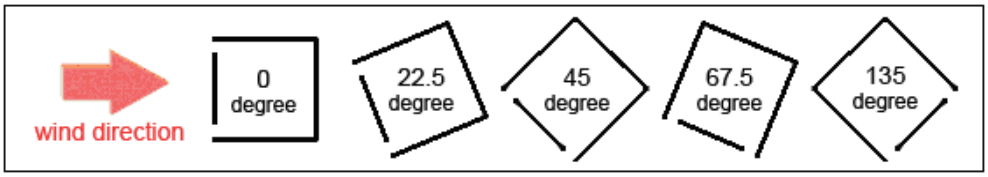


Fig. 18. Different wind angles

| Different inlet mean wind speeds (m/s) |
|---|
| 1.27 |
| 1.68 |
| 1.83 |
| 2.0 |
| 2.95 |
| 3.35 |

Table 1. Different inlet mean wind speeds

The descriptions of all three cases for the 2-dimensional and 3-dimesional CFD simulation and the wind tunnel experiments of Givoni are shown in Figure 19 and as follows:
Case 1: Two lateral openings, with total 1/3 width of wall, no vertical projections (wing wall)
Case 2: Two lateral openings, with total 1/3 width of wall and vertical projections (wing wall) of depth equal to the opening width
Case 3: Two lateral openings, with total 1/3 width of wall and vertical projections (wing wall) of depth double the opening width

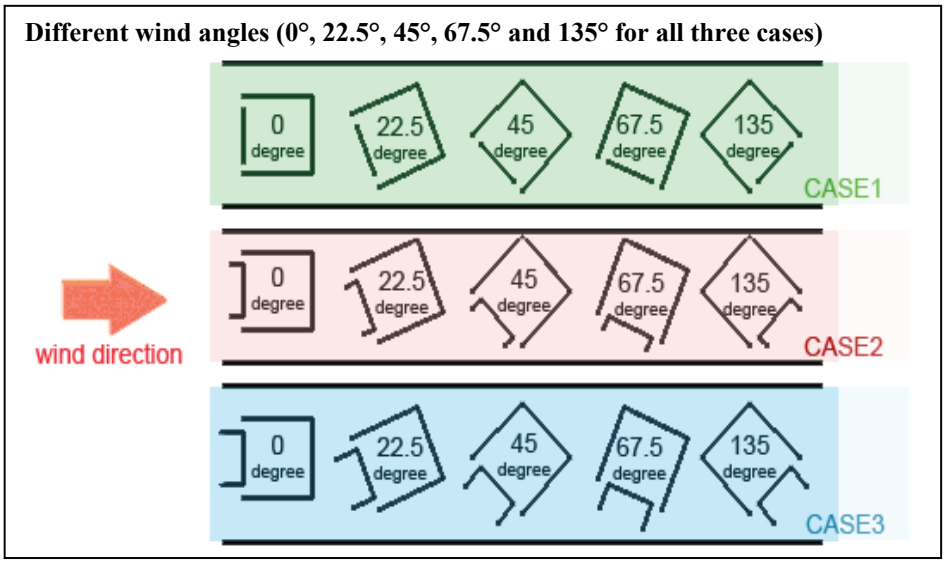


Fig. 19. Model configuration at different wind directions

Figure 20 shows the physical configuration of the room model for the three cases.

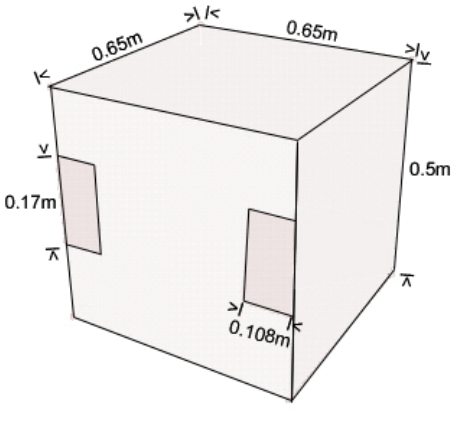


(a) Case 1: Two lateral openings, with 1/3width of wall, no vertical projections

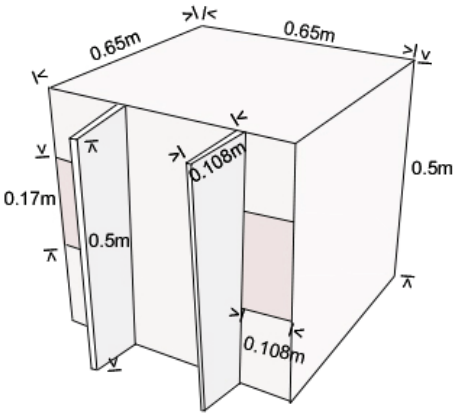


(b) Case 2: Two lateral openings, with 1/3 width of wall and vertical projections (wing walls) of depth equal to the opening width

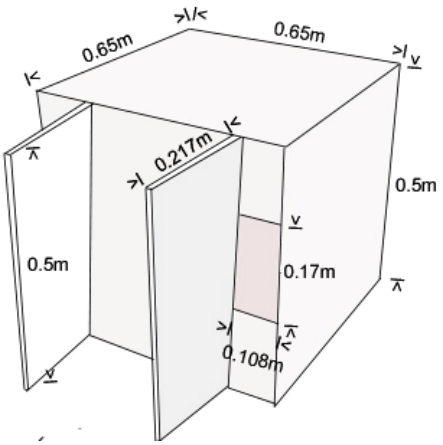


(c) Case 3: Two lateral openings, with 1/3 width of wall and vertical projections (wing walls) of depth double the opening width

Fig. 20. Physical configuration of the room model for three cases

### 2.2.4 Analysis of results

2.2.4.1 Effect of input turbulence on the CFD results

It is known the approaching turbulence levels would impact the curvature of separation on a bluff body and as a result affect the mean pressure data derived [Melbourne, 1979]. However, there is no information provided regarding the input turbulence levels used in the

experiments of Givoni [Givoni, 1962; Givoni, 1968]. As the wind tunnel experiments of Givoni were conducted at low-turbulence, different low input turbulence parameters including turbulence intensity and turbulence viscosity ratio were used in the three-dimensional simulation models shown in Table 2. It was found in Figure 21 that the variation in the incoming turbulence did not have much effect on CFD result, i.e. the mean indoor air speed relative to the uniform wind speed. In the CFD results, the mean indoor air speed could be based on all grid point values inside the room at a particular uniform wind speed while that in the experiments of Givoni [Givoni, 1962; Givoni, 1968] was only based on five selected measurement points inside the room.

| Set | Turbulence Intensity/% | Turbulence Viscosity ratio |
|---|---|---|
| A | 10 | 10 |
| B | 10 | 1 |
| C | 1 | 1 |
| D | 1 | 0.1 |
| E | 1 | 0.01 |
| F | 1 | 0.001 |
| G | 0.1 | 0.001 |

Table 2. Different input turbulence parameters

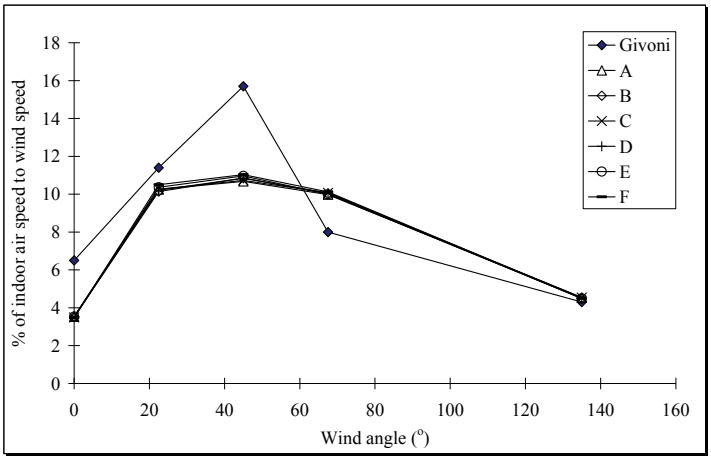


Fig. 21. Effect of different turbulence input parameters on CFD results

2.2.4.2 Effect of wing wall

It can be seen in Figure 22 and Figure 23 that the wing wall increases the air circulation in and out of the two lateral openings of the room model. Figure 24 and Figure 25 show that the wing wall increases the pressure difference between the two lateral openings. Figures 26-29 show the CFD results for the models and the experimental results of Givoni. Givoni

[Givoni, 1962; Givoni, 1968] found that the percentage of mean indoor air speed to uniform wind speed remained almost constant as the uniform wind speed varied from 1.27ms-1 to 3.35 ms-1. This percentage and the air change per hour in the CFD results were obtained by taking average all values at different wind speeds listed in Table 1. It can be seen in Figure 26 that the percentage of mean indoor air speed inside the room to the uniform wind speed is increased by the incorporation of wing wall on the wall facing the wind. Significant improvement of natural ventilation is obtained in the cases with wing wall (i.e. case 2 and 3) in both experimental results and CFD results. The increase in the mean indoor velocity in two cases with wing wall can be reached up to few times compared with those without wing wall. However, it can be seen in Figure 26 that there is no significant improvement of natural ventilation for a longer wing wall (Case 3) is used.

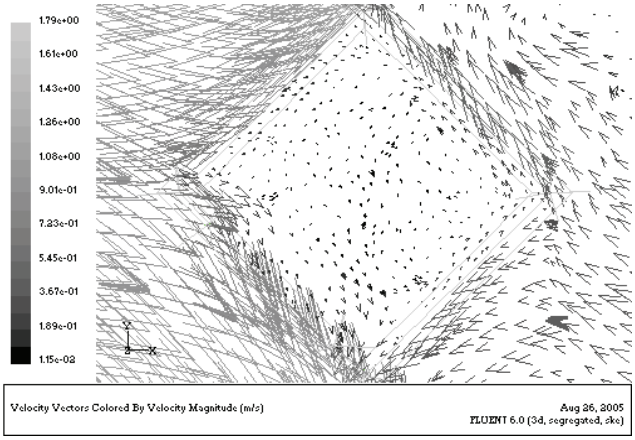


Fig. 22. Plan view of velocity vector diagram for the room model without wing wall at wind angle of 45$^{o}$ and wind speed of 1.25m/s

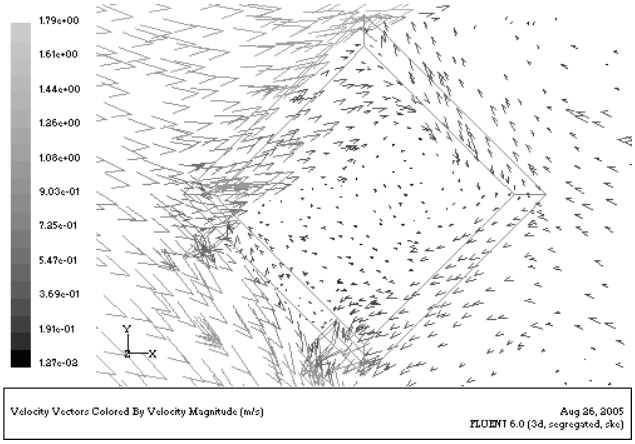


Fig. 23. Plan view of velocity vector diagram for the room model with wing wall at wind angle of 45$^{o}$ and wind speed of 1.25m/s

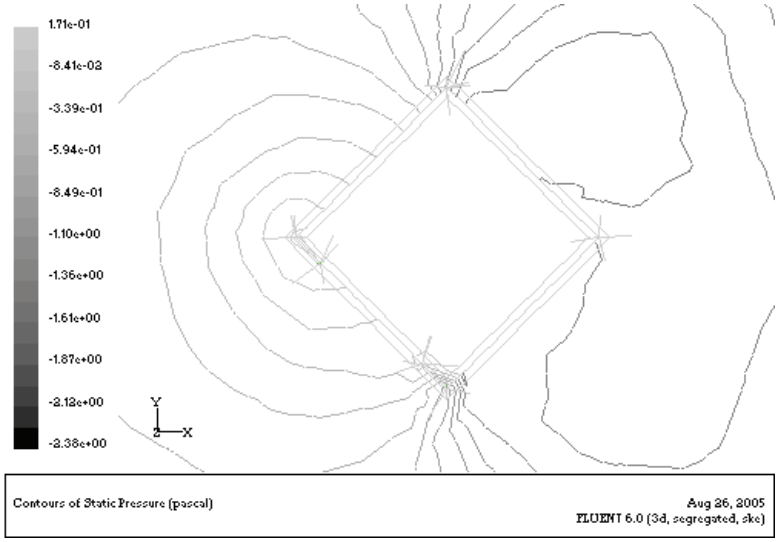


Fig. 24. Plan view of pressure contour of the room model without wing wall at wind angle of 45$^{o}$ and wind speed of 1.25m/s

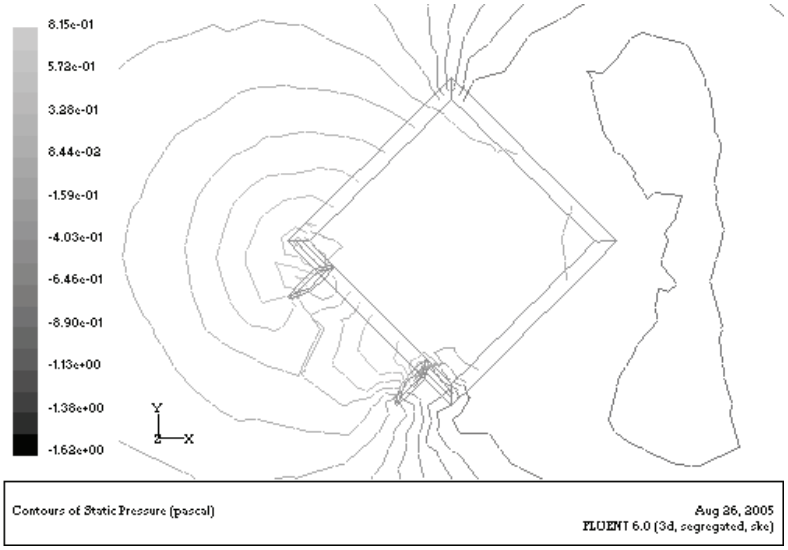


Fig. 25. Plan view of pressure contour of the room model with wing wall at wind angle of 45$^{o}$ and wind speed of 1.25m/s

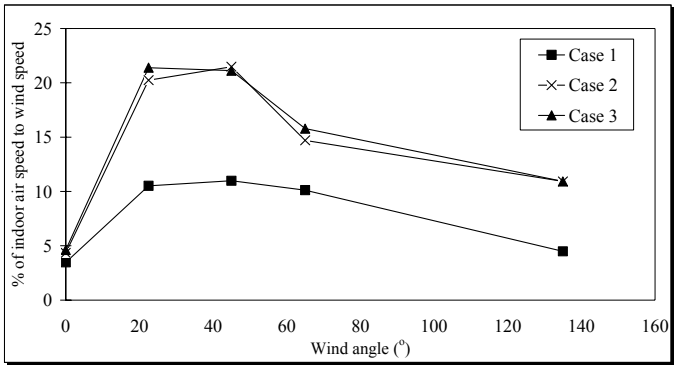


Fig. 26. Percentage of mean indoor air speed to wind speed against wind angle ranging 0° and 135° (CFD results for three cases)

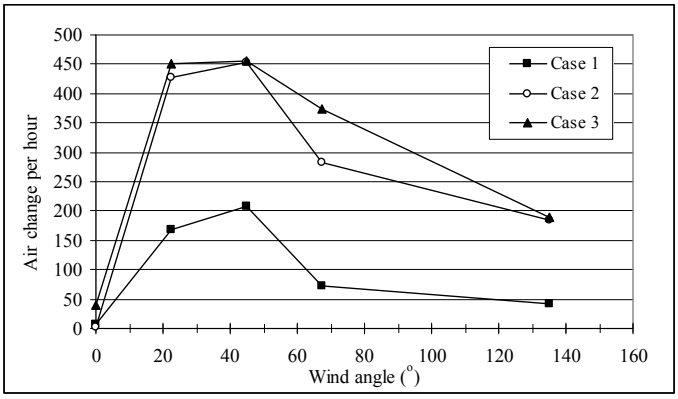


Fig. 27. Ventilation rate (in $m^3/s$) against wind angle ranging 0° and 135° (CFD results for three cases)

2.2.4.3 Performance of wing wall under different wind directions

In order to compare the CFD results with the experiments of Givoni, the percentage of mean indoor air speed to uniform wind speed was used in Figures 26, 28-30. Air change per hour was also used in Figure 27 since it is a common indicator of ventilation. It can be seen in Figure 26 and Figure 27 that there are large variations of the percentage of mean indoor air speed to wind speed and the air change per hour in case 2 and case 3 under different wind directions (i.e. wing angle ranging 0° and 135°). Highest values of the percentage of mean indoor air speed to wind speed and the ventilation rate occur at around 45°. That means although wing wall can increase the air change per hour and the mean indoor air velocity that would promote natural ventilation, its performance is greatly affected by the wind directions. Figures 26-30 all show that the wing wall has its best performance at wind angle of around 45°.

2.2.4.4 Comparison of CFD results and the experiments of Givoni

Figures 28-30 show the comparisons between CFD results and wind tunnel experiments of Givoni [Givoni, 1962; Givoni, 1968] for cases 1-3. There is no wing wall in Case 1. Case 3 has a longer wing wall than Case 2. It can be seen in the figures that the CFD results generally have similar trend to the experimental results of Givoni. The deviations may be due to the limitations of the CFD code in terms of algorithm used for the computer iterations, grid topologies, physical parameters used and turbulence models, and the measurement methods used in the experiments. Givoni [Givoni, 1962; Givoni, 1968] found that the internal velocity distribution inside the room was quite constant at the wind angle of 45° and wind speed of 1.25m/s to 3.3m/s and the mean indoor air speed was obtained by averaging speeds measured at only 5 measurement points. However, there are larger variations of internal velocity distribution in the simulation and the mean indoor air speed in the CFD results was obtained by averaging speeds at all grid points inside the rooms.

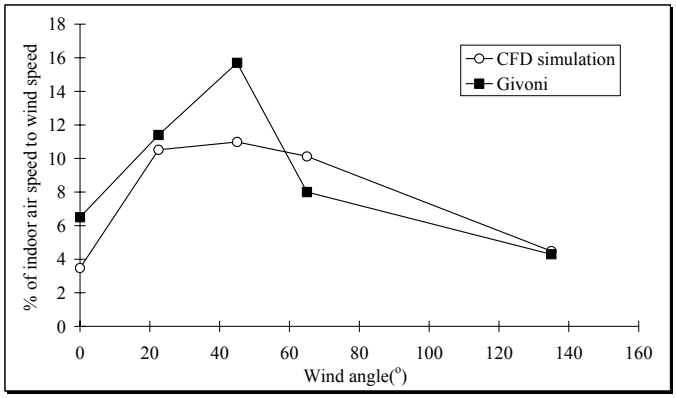


Fig. 28. Percentage of mean indoor air speed to wind speed against wind angle ranging 0° and 135° (Case 1-comparison between CFD results and the experiments of Givoni)

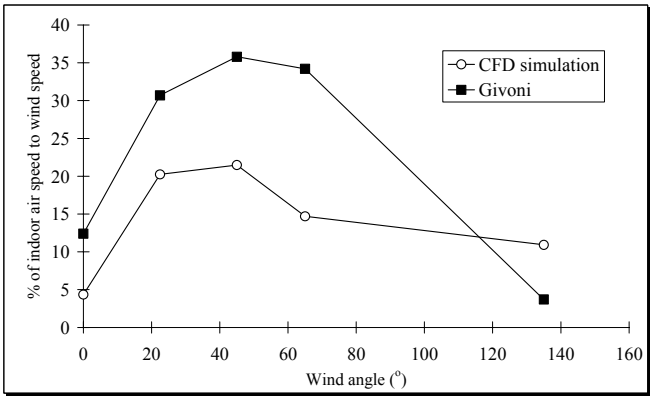


Fig. 29. Percentage of mean indoor air speed to wind speed against wind angle ranging 0° and 135° (Case 2-comparison between CFD results and the experiments of Givoni)

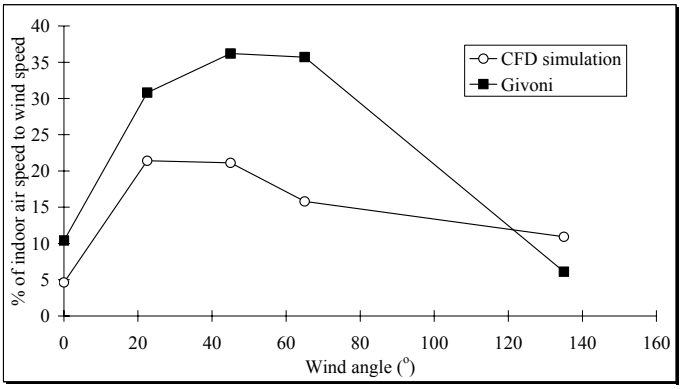


Fig. 30. Percentage of mean indoor air speed to wind speed against wind angle ranging 0° and 135° (Case 3-comparison between CFD results and the experiments of Givoni)

## 3. Other CFD applications in building services engineering (BSE)

CFD has been applied successfully to various research works in BSE [Chow, 1996] including fire engineering, smoke movement, sprinkler and hot air interaction, combustion, heating, ventilation and air-conditioning design, air-conditioned gymnasium and air-conditioned office. CFD has also been attempted to modify the predictive method of Mak et al. [Mak, 2002; Mak, 2005; Mak et al., 2009; Mak & Yang, 2000; Mak & Yang, 2002] to produce a turbulence-based predictive for flow-generated noise produced by an in-duct element in a ventilation system [Mak & Au, 2009; Mak & Oldham, 1998a; Mak & Oldham, 1998b].

## 4. Conclusions

This chapter has reviewed the numerical studies of the performance two green features used in buildings. For the performance of windcatcher, the air flow rate increases with wind speed and wind direction when incidence angle varies from $10^o$ to $40^o$ and slightly decreases when incidence angle is smaller than $10^o$ or lager than $40^o$. In all cases studied, the velocity of the supply air entering into the text room is close to the external wind speed and therefore the windcatcher system is found to be an efficient way of improving indoor ventilation. For the performance of wing walls, wing wall can promote natural ventilation by increasing the air change per hour and the mean indoor air speed relative to wind speed at various wind speeds and wind directions. The best performance is at the wind angle of around 45°. The numerical studies agree generally with the experiments of Givoni and show that wing wall can perform very well in single-sided ventilation for this type of room configurations. In summary, the numerical studies have shown that the windcatcher and the wing walls can increase the performance of natural ventilation in buildings. CFD is therefore a useful tool in studying the performance of green features used in buildings.

## 5. Acknowledgements

The writing of this chapter was fully supported by a grant from the Fcaulty of Constuction and Land Use of the Hong Kong Polytechnic University (Sustainable Urbanization Research Fund, Project No. 1-ZV4S).

## 6. References

Awbi, H.B. (1989). Application of computational fluid dynamics in room ventilation. *Building and Environment*, Vol. 24, No. 1, pp. 73-84

Awbi, H.B. & Elmualim, A.A. (2002). Full scale model windcatcher performance evaluation using a wind tunnel, *Proceedings of the World Renewable Energy Congress VII*, 2002

Bahadori, M.N. (1994). Viability of wind towers in achieving summer comfort in the hot arid regions of the Middle-East. *Renewable Energy*, Vol. 5, pp. 879-892

Bojic, M.; Lee, M. & Yik, F. (2001). Influence of a depth of a recessed space to flow due to air-conditioner heat rejection. *Energy and Buildings*, Vol. 34, No.1, pp. 33-43

Chen, Q. (2009). Ventilation performance prediction for buildings: A method overview and recent applications. *Building and Environment*, Vol. 44, pp. 848-858

Chen, Q. & Srebric, J. (2000). Application of CFD tools for indoor and outdoor environment designs. *International Journal on Architectural Science*, Vol. 1, pp. 14-29

Chow, W.K. (1996). Application of computational fluid dynamics in building services engineering. *Building and Environment*, Vol. 31, pp. 425-36

Elmualim, A.A.; Awib, H.B.; Teekaram, A.J. & Brown, R.G. (2001). Evaluating the Performance of a Windcatcher System Using Wind Tunnel Testing, *Proceedings of 22nd Annual AIVC Conference*, Vol. 1, pp. 29.1-29.12, Bath, UK, 11-14 September 2001, Air Infilteration and Ventilation Centre, INIVEEIG, Belguim

Givoni, B. (1962). Basic study of Ventilation problems in housing in hot countries. Research Report to the Ford Foundation, Building Research Station, Israel Institute of Technology, Technion, Haifa, Israel

Givoni, B. (1968). Ventilation problems in hot countries. Research Report to the Ford Foundation, Building Research Station, Israel Institute of Technology, Technion, Haifa, Israel

Hurdle, A. (2001). Is natural ventilation the new wind of change?. *Building Services and Environmental Engineers*, Vol. 24, No. 7, pp. 26-7

Jones, P.J. & Whittle, G.E. (1992). Computational fluid dynamics for building air flow prediction-current status and capabilities. *Building and Environment*, Vol. 27, No. 3, pp. 321-38

Li, L. & Mak, C.M. (2007). The assessment of the performance of a windcatcher system using computational fluid dynamics. *Building and environment*, Vol. 42, pp. 1135-41

Li, L.; Mak, C.M & You, S.J. (2006). A numerical study of the performance of a windcatcher system. *Proceedings of Sichuan-Hong Kong Joint Symposium*, pp. 34-43, Chengdu, Sichuan, China

Mak, C.M. (2002). Development of a prediction method for flow-generated noise produced by duct elements in ventilation systems. *Applied Acoustics*, Vol. 63, pp. 81-93

Mak, C.M. (2005). A prediction method for aerodynamic sound produced by multiple elements in air ducts. *Journal of Sound and Vibration*, Vol. 287, pp. 395-403

Mak, C.M. & Au W.M. (2009). A turbulence-based prediction technique for flow-generated noise produced by in-duct elements in a ventilation system. *Applied Acoustics*, Vol. 70, pp. 11-20

Mak, C.M.; Cheng, C. & Niu, J.L. (2005a). The application of computational fluid dynamics to the assessment of green features in buildings: Part 1: Wing walls. *Architectural Science Review*, Vol. 48, No. 1, pp. 121-34

Mak, C.M.; Cheng, C. & Niu, J.L. (2005b). The application of computational fluid dynamics to the assessment of green features in buildings: Part 1: Wing walls. *Architectural Science Review*, Vol. 48, No. 1, pp. 1-14

Mak, C.M.; Niu, J.L.; Lee, C.T. & Chan, K.F. (2007). A numerical simulation of wing walls using computational fluid dynamics. *Energy and Buildings*, Vol. 39, pp. 995-1002

Mak, C.M. & Oldham, D.J. (1998a). The application of computational fluid dynamics to the prediction of flow-generated noise in low speed flow ducts. Part 1: Fluctuating drag forces on a flow spoiler. *Journal of Building Acoustics*, Vol. 5, No. 2, pp. 123-41

Mak, C.M. & Oldham D.J. (1998b). The application of computational fluid dynamics to the prediction of flow-generated noise in low speed flow ducts. Part 2: Turbulence-based prediction technique. *Journal of Building Acoustics*, Vol. 5, No. 3, pp. 199-213

Mak, C.M.; Wu, J.; Ye, C. & Yang, J. (2009). Flow noise from spoilers in ducts. *Journal of the Acoustical Society of America*, Vol. 125, No. 6, pp. 3756-65

Mak, C.M. & Yang J. (2000). A prediction method for aerodynamic sound produced by closely spaced elements in air ducts. *Journal of Sound and Vibration*, Vol. 229, No. 3, pp. 743-53

Mak, C.M. & Yang J. (2002). Flow-generated noise radiated by the interaction of two strip spoilers in low speed flow ducts. *Acta Acustica united with Acustica*, Vol. 88, pp. 861-68

Mak, C.M. & Yik Francis, W.H. (2002). A study of natural ventilation in a kitchen using computational fluid dynamics (CFD). *Architectural Science Review*, Vol. 45, pp. 1-8

McCarthy, B. (1999). *Wind Towers: Details in building*, Academy Edition, John Wiley & Sons, West Sussex, UK

Melbourne, W.H. (1979). Turbulence effects on maximum surface pressures; a mechanism and possibility of reduction. *Proceedings of the Fifth International Conference on Wind Engineering*, pp. 541-51, Fort Collins, USA, July 1979, edited by Cermak, J.E.

Murakami, S. (1997). Current status and future trends in computational wind engineering. *Journal of Wind Engineering and Industrial Aerodynamics*, Vol. 67-68, pp. 3-34

Murakami, S. (2002). Setting the scene: CFD and symposium overview. *Wind and Structures*, Vol. 5, No. 2-4, pp. 83-8

Niu, J.L. & Kooi, J.V.D. (1992). Two-dimension simulation of the air flow and thermal comfort in a room with open-window and indoor cooling systems. *Energy and Buildings*, Vol. 18, No. 1, pp. 65-75

Niu, J.L.; Yuen, Y.M. & Mak, C.M. (2005). The application of Computational Fluid Dynamics to the assessment of green features in buildings: Part 2: Communal sky gardens. *Architectural Science Review*, Vol. 48, pp. 337-44

Niu, J.L. & Zhu, Z.J. (2004). Numerical study of wind flow around a CAARC Standard tall building in an atmospheric boundary layer. *ASME Journal of Fluid Engineering*, Jan 2004

Swainson, M.J. (1997). Evaluation of the potential of Solar Chimneys to Drive Natural Ventilation in Non-Domestic Buildings, Ph.D. Dissertation, Cranfield University, UK

# 9

# Unsteady Computational and Experimental Fluid Dynamics Investigations of Aerodynamic Loads of Large Optical Telescopes

Mahmoud Mamou[1], Youssef Mébarki[1] and Ali Tahi[2]
[1]*Aerodynamics Laboratory, Institute for Aerospace Research, National Research Council Ottawa, Ontario,*
[2]*Département d'Aéronautique, Faculté des Sciences de l'Ingénieur, Université Saad Dahlab-Blida,*
[1]*Canada*
[2]*Algérie*

## 1. Introduction

The present chapter includes a comprehensive literature review of flow simulations and measurements of aerodynamic loads on large optical telescopes, and a discussion on a recent computational fluid dynamics (CFD) investigation, supported by wind tunnel measurements. The investigation was performed at the National Research Council of Canada (NRC) and was focused mainly on predicting and measuring unsteady wind loads on a scaled wind tunnel model of a Very Large Optical Telescope (VLOT), and on a VLOT full-scale model housed within spherical enclosures.

Optical telescopes are usually housed in confined enclosures with apertures to limit buffeting problems caused by environmental disturbances such as wind and onsite thermal plumes or by the combined effect. In other words, the enclosures enhance the telescope pointing and tracking performance and also preserve the primary mirror optical shape by minimizing or reducing the unsteady wind loads and air circulation fluctuations inside the enclosure.

Most of the present generation telescopes are equipped with relatively small primary mirror areas that limit the light-gathering power and angular resolution. This obviously causes a detrimental effect and restrictions on the telescope performance in capturing details of distant celestial objects, which are key elements for understanding the origin of the universe. To overcome this limitation, astrophysicists are building much larger optical telescopes to allow large mirror reflecting areas. Consequently, massive and stiff supporting structures are required. As the telescopes grow in size, structural buffeting, unsteady wind loads, thermal mass, and other issues become crucial factors that must be considered in the early design phases.

The enclosure requires an opening without shielding to avoid smearing of light and electromagnetic waves, and diffraction. The boundary layer flow that starts to build up from the stagnation point on the enclosure surface up to the upstream edge of the opening, must detach and by doing so forms a free strong shear layer across the opening. Under some flow conditions, the shear layer becomes unstable and rolls up into a series of strong and distinct vortices, which impinge against the aft edge of the opening. As a result, acoustic waves are

generated, affecting the flow inside the enclosure (unsteady pressure loads) and over the opening (possible shear layer excitation). When the acoustic waves arrive near the leading edge of the opening, where the shear layer starts to build up, they excite and strengthen the newly formed vortices, which could result in aeroacoustic coupling. A strong pressure fluctuation is thus induced inside the enclosure, which in turn contributes to significant dynamic loads on the telescope structure. As the size of telescopes increases, their structural natural frequency is shifted to lower values closer to the wind loading frequencies, which collectively may impart significant structure buffeting on the telescope components.

This chapter focuses mainly on the CFD simulations of unsteady flows past a very large optical telescope structure that were conducted at the National Research Council. The CFD simulations were performed using the Lattice Boltzmann method as implemented in the commercial PowerFLOW™ solver. Unsteady viscous flow solutions were computed for various zenith and azimuth angles. The CFD simulations were performed assuming fully turbulent flows past the enclosure. For the full-scale telescope enclosure, the Reynolds number is large (about $5\times10^7$) and, according to Achenbach's results for sphere flow (1974), the assumption of fully turbulent flow can be justified.

As a high Reynolds number test was beyond the scope of this investigation, a scaled model was tested at moderate Reynolds number (about $5\times10^5$) to provide a basis for planning future tests. Although the flow conditions were strictly not matched, it was thought that the flow unsteadiness inside the enclosure would not be strongly affected by the complex flow phenomena around the exterior surface of the enclosure. Therefore, the experimental results were still expected to shed some light on the internal flow field. The validity of this assumption could be established in the future by performing more comprehensive tests, or considering advanced CFD codes allowing for automatic prediction of flow transition and separation.

The objective of the CFD investigation was to assess the capabilities of a flow solver in predicting some of the flow properties inside and outside the telescope enclosure by mimicking the wind tunnel flow conditions. Correlations were obtained between the CFD and wind tunnel (WT) data in terms of the mean pressure coefficients on the enclosure and on the primary mirror surfaces, and their standard deviations. Power spectral density analyses were also carried out for a number of pressure signals collected on the primary mirror surface. Also, infrared measurements were performed to characterize the boundary layer flow behavior around the telescope enclosure in order to determine the transition and flow separation locations, which depended on the Reynolds number, telescope roughness, turbulence level and telescope orientations. The CFD solutions affirmed that the flow inside and outside the enclosure was unsteady and massively separated on the back of the enclosure.

## 2. Review of flow simulations on large telescopes

The astrophysics community is building larger and larger telescopes, such as the Thirty Meter Telescope (TMT), in order to study the universe in greater detail (Angeli *et al.*, 2004). For such large structures, the unsteady wind loading is becoming an important factor in the telescope design phase. The wind flow around and inside the telescope enclosure can lead to many direct undesirable effects upon the "seeing" attributes of the primary mirror. The seeing factor describes how much the turbulence of the earth's atmosphere and the flow inside the telescope enclosure perturbs the images of stars as seen through the telescope. An increase in the "seeing" factor is generally associated with a degradation of the optical

performance of the telescope. The induced unsteady pressure loads on the telescope components lead to a dynamic structure deformation, causing wind buffeting that, owing to the large size of the telescope, directly affects the primary mirror as well as the secondary mirror assembly, which is usually exposed to relatively higher wind speeds and shear layer unsteadiness near the enclosure opening.

The application of CFD to predict flows and pressure loads on telescope structures can provide critical and detailed data for the design of future large optical telescopes. Most of the flow phenomena that affect the mirror seeing can be assessed by CFD within an acceptable level of accuracy.

Several CFD studies have been reported for ground-based telescopes. De Young (1996) performed time-independent airflow simulations inside the Gemini telescope enclosure. The author found that venting (airflow through vents) was most effective means of influencing flow directions inside the enclosure; particularly near the vents and across the primary mirror surface. Turbulence was present for different wind conditions and orientations; however, it was worst when the enclosure opening was facing the wind. The author also identified a strong pressure gradient across the primary mirror for different wind conditions. Similarly, using CFD, Vogiatzis *et al*. (2004) estimated the effect of unsteady wind loading on the performance of extremely large telescopes (ELT). The CFD predictions were validated against WT measurements. The study showed the existence of an unstable shear layer over the opening that caused significant pressure fluctuations inside the enclosure. The power spectral density of the normalized velocity signal, measured near the enclosure opening, showed the existence of different oscillatory mode frequencies, which agreed well with experimental data. De Young and Vogiatzis (2004) simulated steady-state airflow past very large optical telescope enclosures. The simulations were performed for an extremely large typical empty telescope enclosure, as well as for the more specific Gemini South telescope mounted on the summit of Mount Cerro Pachon. The authors reported only qualitative flow pattern results to demonstrate the feasibility and ability of CFD to simulate and predict pressure loads inside and outside the telescope enclosure.

Cho *et al*. (2001) investigated wind-buffeting effects on the Gemini 8-m primary mirror. The measurements were performed under onsite mountaintop wind conditions. Pressure data were obtained at various taps installed on the primary mirror, and the wind velocity and direction were measured at several locations inside and outside the enclosure. To assess the dynamic response of the telescope, the time history of the pressure data was used to calculate the primary mirror deformation using a finite-element method. Angeli *et al*. (2002) studied experimentally the characteristics of wind loading on the Gemini telescope. The authors found that the pressure fluctuations on the primary mirror were extremely pronounced when the mirror was pointing into the wind with a small bandwidth of the wind loading. Cho *et al*. (2003) also reported a similar study of the wind loading on the Gemini telescope. They found that the pressure fluctuations over the primary mirror were significant; however, the global wind force on the mirror was negligibly small. The average pressure on the primary mirror was mainly controlled by the airflow around the enclosure opening, and the fluctuations were caused by the turbulence generated by the enclosure structures. Quattri *et al*. (2003) performed full-scale flow simulations of wind loading on the 100-m OWL telescope using commercial CFD software. The study focused on the wind loads acting on the primary mirror with the loads predominantly induced by a nearby building situated upstream of telescope structure. Pressure signals collected at different points on the mirror surface showed that the wind pressure load at low frequencies was

reduced by the building; however, the high frequency wind pressure components increased under these conditions. Angeli *et al*. (2004) presented an integrated approach for the necessary modeling tools to estimate the performance of the TMT, which is an upgraded version of the VLOT. Among these tools, the authors emphasized the role of CFD in predicting the wind loading and buffeting, which are more crucial during the conceptual design phase of the telescope. As shown in Fig. 1, a flow simulation was performed past a generic telescope. The flow is highly unsteady, especially over the slit and behind the enclosure, and it was observed that the air pressure inside the dome is dominated by the lowest frequency of the acoustic waves generated by the unsteady free shear layer interaction with the dome slit edge.

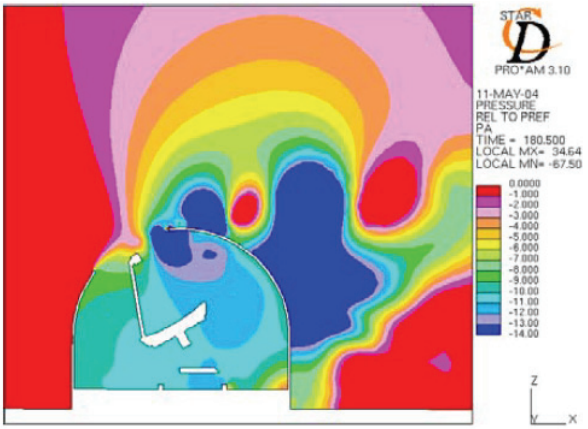


Fig. 1. A snapshot of the pressure field in and around the generic ELT dome with a Giant Segmented Mirror Telescope model inside (Angeli *et al.* (2004)

Riewaldt *et al*. (2004) also carried out an interesting and thorough wind tunnel investigation for an extremely large telescope with a 50-m primary mirror diameter. The investigation was performed on a 1:200-scale model in the boundary layer wind tunnel at the National University in Galway, Ireland. Pressure signals were measured at various locations on the primary mirror and on the enclosure. This particular study included a number of different telescope configurations: an empty enclosure, a telescope unit on its own, and a combined telescope and enclosure configuration. Aerodynamic forces and moments acting on the enclosure and on the telescope primary mirror were also measured. The authors concluded that under nominal wind conditions (12 m/s), the wind produced a large mean pressure load and significant pressure fluctuations on the primary mirror surface. In addition to the above studies, Pottebaum and MacMynowski (2006) conducted WT measurements of the flow inside an empty generic telescope enclosure with a rectangular opening. Smoke and tuft visualizations were performed to illustrate the flow patterns inside and around the enclosure. Digital particle image velocimetry data were obtained on a vertical plane near the enclosure opening to estimate the mean flow velocity and the kinetic energy fluctuations. The experimental observations and measurements again revealed the existence of a strong shear layer that formed over the enclosure opening when it was pointing into the wind. Different oscillatory mode frequencies were detected. When the enclosure opening was facing downstream, the flow was driven inside the enclosure with less rigorous unsteady

flow structures, because the mechanisms for coupling has been removed. Drilling some vents around the enclosure structure, appeared to weaken the shear layer and the amplitudes of the oscillatory modes were dampened.

MacMynowski *et al*. (2006) documented the effect of wind load and buffeting on ground-based telescopes and identified the sources that lead to better understanding the wind flow characteristics inside the telescope enclosure and past its aperture. One of the sources relies on CFD analyses using current state-of-the-art numerical techniques and advanced turbulence models. Non-vented and vented enclosure configurations were analyzed. For a non-vented enclosure, the shear layer modes are strong for given orientations, as observed in wind-tunnel and predicted by CFD results; however they are not the most important source of unsteadiness of wind loads on the telescope components. For a vented enclosure, the shear layer was weakened, resulting in low-amplitude modes. The authors reported difficulties using CFD to predict accurately the flow turbulence behavior along the telescope axis, when compared to experiment.

Quattri *et al.* (2008) performed WT measurements to characterize the wind turbulence structure and intensity inside two types of telescope enclosures with different screen positions. WT data were obtained for various wind speeds and enclosure orientations, which will certainly serve for future CFD code validations.

For airborne telescopes, Srinivasan (1997) and (2000) used a combined CFD and experimental approach for the airborne Stratospheric Observatory for Infrared Astronomy (SOFIA) to investigate the challenges related to aerodynamic and aeroacoustic problems. The telescope was housed in an open built-in cavity on a Boeing 747 aircraft fuselage. Comparisons with CFD results obtained under the wind tunnel conditions showed fairly good agreement for sound pressure levels and power spectra at various locations within the cavity and on the telescope. However, the power spectral density of the pressure signals on the telescope surface showed that the agreement between CFD and experiment was achieved within a narrow frequency bandwidth with a slight difference in signal amplitudes. Elsewhere, the discrepancy was significant. This discrepancy was probably attributed to the unresolved unsteady shear layer over the cavity aperture and to numerical dissipation of the shear layer vortices, which are responsible for the pressure tones, frequencies and amplitudes inside the telescope cavity. Also, the CFD-predicted broadband turbulence spectrum was different from the experimental data for unexplained reason.

Using unsteady RANS computations and detached eddy simulation (DES), Schmid *et al*. (2008a), (2008b) and (2009) simulated successfully the flow unsteadiness around and inside the airborne SOFIA telescope (see Fig. 2). For the DES approach, the region across the telescope aperture, where the shear layer spans the cavity opening, was solved using large eddy simulation (LES), as displayed in Fig. 3. Both unsteady Reynolds-averaged Navier-Stokes (URANS) models and DES predicted fairly well all the oscillatory modes and their frequency and amplitude, when compared to experiment. As expected, in general, the results from the DES simulations were in excellent agreement with experimental data. To reduce the sound pressure level inside the telescope cavity, the authors incorporated a few pairs of vortex generators on the front edge of the cavity, which served to thicken and to stabilize the shear layer and thus mitigate the pressure fluctuations inside the cavity. Also, to avoid any acoustic resonance, the authors found that by adding baffles inside the cavity or changing the shape of the cavity, the frequencies of the acoustic modes could be shifted to lower or higher values.

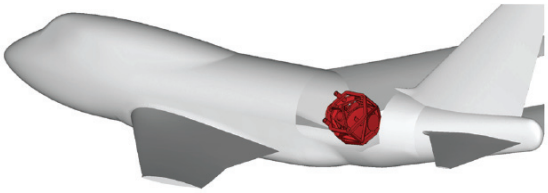

Fig. 2. SOFIA telescope carried on the Boeing 747SP (Schmid *et al*., 2009)

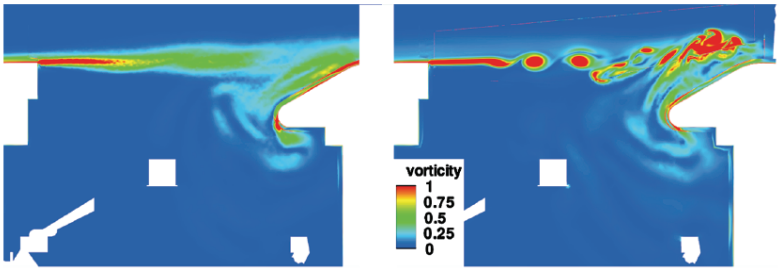


a) b)

Fig. 3. Snapshots of the predicted vorticity patterns across the cavity opening: a) URANS and b) DES (Schmid *et al*., 2009)

Coming back to the ground-based telescope discussion, which represents the main focus of the present chapter, a campaign of scaled-model wind-tunnel measurements and CFD simulations was undertaken at the National Research Council of Canada to estimate wind loads on a very large optical telescope (VLOT) housed within a spherical calotte. The tests were performed for various wind speeds to examine Reynolds number effects, and VLOT orientations, see Cooper *et al*. (2005) and (2004a). The measurements revealed the existence of significant pressure fluctuations inside the enclosure owing to the formation of a shear layer across the enclosure opening. As many as four modal frequencies were detected, depending on the wind speed. The number of modal frequencies decreased with increasing wind speed. The mean pressure inside the enclosure and on the primary mirror surface was roughly uniform. Later on, the effect of the enclosure venting was investigated experimentally by Cooper *et al*. (2004b) by drilling two rows of circular vents around the enclosure. The amplitude of the periodic pressure fluctuations that were measured in Cooper *et al*. (2005) was significantly reduced. The shear layer oscillatory modes were reduced to a single mode with smaller pressure fluctuation amplitude.

In parallel with the aforementioned experimental studies, Mamou *et al*. (2004a-b) and Tahi *et al*. (2005a) numerically investigated the wind loads on a full-scale and scaled model. Comparisons with WT measurements (Cooper *et al*., 2005) showed good agreement for the mean pressure on the enclosure inside and outside surfaces as well on the primary mirror surface. However, some discrepancies between CFD and WT data were observed for the pressure fluctuations and the oscillatory modal frequencies. It was believed that these discrepancies could be attributed to several possible sources. One possible error was the scaling effects, as the CFD solutions were obtained for a full-scale model that corresponded to a Reynolds number that was two orders of magnitude greater than that at the wind tunnel conditions. Second, the viscous effects of the wind tunnel floor were neglected. Since

an inviscid boundary condition was used in the simulations, the horseshoe vortex was not simulated. Third, the flow simulations were run at a relatively higher Mach number (i.e. large time step) to speed up the computations owing to the large grid size of the computational domain. The specification of a high Mach number in the flow simulation has no influence on the compressibility effects. Finally, the freestream flow conditions of Mount Mona Kea used in the CFD simulations were different from those imposed in the wind tunnel.

To understand better the reasons for the differences, Mamou *et al.* (2004c) performed additional CFD simulations based on the scaled model and using the same flow conditions reported in Cooper *et al*. (2005). Non-slip conditions were considered for the floor to account for the formation of a boundary layer that could affect the pressure distribution and the flow field near the enclosure base. Higher simulation Mach numbers and the wind tunnel Mach number were both used. Tahi *et al*. (2005a) also conducted a CFD analysis to predict the wind loading on the primary mirror surface for a 30-m VLOT telescope (an upsized VLOT configuration) with a vented enclosure. The results showed that the pressure fluctuations, when compared to the sealed enclosure configuration, decreased considerably, while the mean pressure on the primary mirror increased. Tahi *et al.* (2005b) also performed detailed and thorough comparisons between CFD predictions and WT measurements for different VLOT configurations and wind conditions. The comparisons were focused mainly on the effect of the pressure wind loads on the primary mirror of the telescope. Grid sensitivity and Mach number effects were reported for a given configuration. It was found that the cause for the discrepancy between CFD and WT data was attributed to the Mach number effect. Using the wind tunnel Mach number, the predicted flow unsteadiness inside the enclosure was in good agreement with the experimental data. Overall, for the approaches, there was a good agreement between the mean pressure coefficients predicted by CFD and those measured on the primary mirror surface.

According to previous CFD simulations studies for flows past ground-based telescopes housed in enclosures, the big challenge is to predict the pressure loads and flow unsteadiness behavior over the primary and secondary mirrors units. As the enclosure opening is subject to unstable shear layer flows, the vortex-structure interactional effects must be well resolved. Unstable shear layers usually lead to the formation of a series of strong vortices (Kelvin–Helmholtz) that are very difficult to simulate or maintain owing to the numerical dissipation effect, which smears the vortices, increases their size and reduces their intensity. To capture well this type of flow behavior, high-order numerical schemes or severe grid refinement is required to reduce the numerical dissipation to an acceptable level. Obviously, grid refinement leads to prohibitive computation times, and the solution becomes impossible to achieve owing to the scale of large telescopes. Also, vortices and structure interaction are a source of acoustic wave generation. These waves are usually three-dimensional and propagate everywhere in the flow domain at the local speed of sound. For cavity flows, there is a mutual interference between aerodynamic and acoustic effects. In other words, acoustic waves affect the shear layer aerodynamics through acoustic excitation, and in turn the shear layer aerodynamics affects the generation of the acoustic waves. Besides these numerical simulation challenges, acoustic waves are also very difficult to maintain and trace owing to their small pressure amplitudes and thickness. Capturing the acoustic waves in the flow domain relies on intensive grid refinement and numerical dissipation mitigation using high-order numerical schemes and relatively small time steps. Obviously, these requirements can render the CFD computations unpractical. The incompressible form of the Navier-Stokes equations is not suitable for cavity free-shear-

layer flow simulations as, besides the inevitable numerical dissipation problem, the acoustic-aerodynamic interaction cannot be addressed.

## 3. Wind tunnel test

### 3.1 Model

A 1:100 scale model of the VLOT was tested in the NRC 0.9×0.9 m pilot wind tunnel in the ¾ open-jet configuration (Fig. 4). The tunnel has an air jet 1.0 m wide and 0.8 m high.

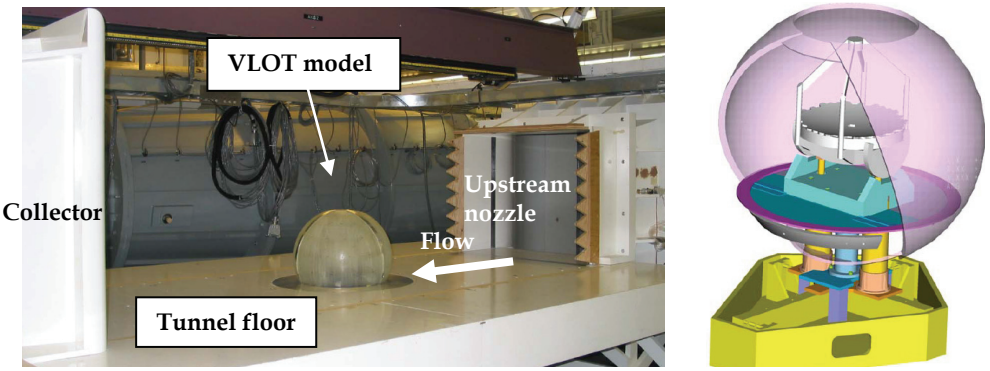


Fig. 4. a) VLOT 1:100 scale model installed in the NRC 0.9×0.9 m open-jet pilot wind tunnel, b) VLOT CAD model and balance assembly (Cooper *et al.*, 2005)

The VLOT model, manufactured using the stereolithography apparatus (SLA) process, included an internal mirror and a spherical enclosure (see Fig. 5). The model external diameter was $D$ = 0.51 m, with a circular opening of 0.24 m diameter at the top of the external enclosure. The measured average roughness height on the VLOT model was 0.13 mm, giving $kr/D = 25.5\times10^{-5}$. The model was mounted on the floor turntable of the test section (see Fig. 4b). The model installation permitted adjustment of the zenith angle $\phi$ by 15° increments between 0° and 45°, while the floor turntable allowed continuous variations in the azimuth direction $0° \le \varphi \le 180°$. The zenith angle $\phi$=0° corresponds to when the primary mirror is pointing overhead and the azimuth angle $\varphi$=0° when the mirror is facing the upstream wind at $\phi$=90°.

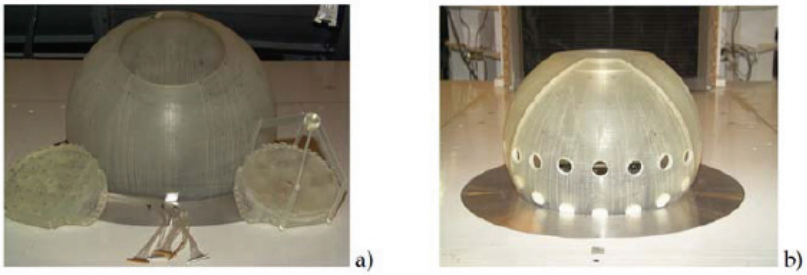


Fig. 5. VLOT wind tunnel model: (a) pressure-instrumented mirror with tubing, enclosure with tubing runs and (b) force mirror assembly (Cooper *et al.*, 2005)

### 3.2 Wind tunnel flow conditions

The wind tunnel tests were performed under atmospheric flow conditions at various wind speeds and telescope orientations. The wind speed was varied from 10 to 40 m/s, with Reynolds numbers from $3.4\times10^5$ to $13.6\times10^5$.

### 3.3 Unsteady pressure load measurements

As reported in Cooper *et al.* (2005), the enclosure and mirror surfaces were instrumented with pressure taps, as illustrated in Fig. 6. The locations of the pressure taps were described by the azimuth angle, $\theta$, within the enclosure frame. The angle $\theta = 0^o$ corresponded to the intersection line between the enclosure and the y-z plane located on the left side of the enclosure when pointing upstream; this line is indicated by column C1 on the enclosure surface (see Fig. 6a). Pressure taps in the enclosure were integrated to the structure. The pressures were scanned at 400 Hz. A few scans were done at 800 Hz to show that no additional frequency content was present above 200 Hz. The dynamic response of each pressure tube was calibrated up to 200 Hz using a white noise signal source. The resulting transfer function of each tube was used to correct for the dynamic delay and distortion resulting from the tubing response.

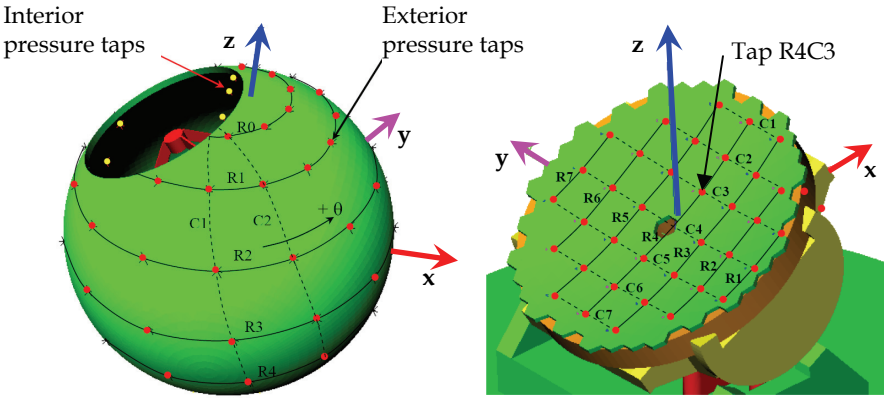


Fig. 6. Pressure taps on: (a) the exterior and interior enclosure surfaces, and (b) the primary mirror surface (Mamou *et al.*, 2008)

### 3.4 Infrared measurements

In parallel to the pressure load measurements, infrared (IR) measurements were conducted to determine the location of the transition between laminar and turbulent flow, as well as to determine the separation location on the spherical model enclosure. The Agema Thermovision 900 infrared camera used for this test had an image resolution of 136×272 pixels covering a field of view of roughly $10\times20^o$. The camera operated in the far infrared 8–12 μm wavelength and could acquire four frames per second. To improve the data quality, 16 consecutive images were averaged and stored on disk. The camera sensitivity and accuracy were $0.08^oC$ and $\pm1^oC$, respectively. The model emissivity was $\varepsilon = 0.90$. For all the test runs, the camera was positioned on the left-hand side of the test section (when facing the flow), providing an excellent side view of the model.

### 3.4.1 Principles of IR measurements

The transition detection using IR was based on the difference in convective heat transfer between the air flow and the model skin. The heat transfer is basically affected by the nature of the boundary layer. Compared with laminar flow, the heat transfer is significantly greater in the turbulent flow regime. The different levels of heat transfer become visible when the model and air temperatures are different.

In practical wind tunnel applications, artificial temperature differences between the air flow and the model can be introduced by controlling the air temperature, Mébarki (2004) and Mébarki *et al*. (2009). Two methods were used in the present study to enhance the heat transfer between the model and the air flow.

For wind speeds below 30 m/s, the tunnel was operated first at maximum speed to heat the model. Then the wind speed was reduced to the target speed and the air temperature was reduced by turning on the wind tunnel heat exchanger. During this cooling process, several images were acquired and recorded for later analysis.

For the maximum speed of 40 m/s, the tunnel heat exchanger was unable to absorb the substantial heat generated by the tunnel fan. In this case, the model was first cooled using low speed flow (~10 m/s) with the heat exchanger operating, and then the tunnel heat exchanger was turned off and the air speed was set to the maximum target speed. After a moment, the air started to heat the model.

### 3.4.2 Heat transfer computation

The convective heat transfer coefficient was estimated from the sequence of temperature images recorded during the cooling or heating processes using a one-dimensional analysis of heat transfer inside a semi-infinite medium and neglecting the heat transfer with the surrounding medium due to radiation. The objective of this computation was not to obtain accurate heat transfer data, but to gain information about relative changes of the heat transfer coefficient at the surface of the model, and therefore better identify the various flow regimes (laminar, turbulent and separation). The method of Babinsky and Edwards (1996), used here, involved the resolution of the convolution product of the surface temperature changes and time. This equation was solved in Fourier space using the convolution theorem

$$h(T - T_r) = \frac{1}{2}\sqrt{\frac{\rho\, c\, k}{\pi}} \int_0^t F(T)G(t)d\tau \tag{1}$$

with $F(T) = T - T_0$ and $G(t) = (t - \tau)^{-1/2}$.

In Eq. (2), $t$ is the time, $h$ is the convective heat transfer coefficient, $T_0$ and $T$ are the initial ($t$ = 0) and current (time $t$) model temperatures, $T_r$ is the adiabatic wall temperature of the flow computed with a recovery factor $r$ = 0.89, and $\beta$ is the thermal product given by $\beta = (\rho c\, k)^{1/2}$, where $\rho$ is the density, $c$ is the specific heat and $k$ is the thermal conductivity of the medium. In the present evaluation, the thermal characteristics of Plexiglas were used to approximate the model characteristics ($\beta$ = 570).

From the heat transfer coefficient, the Stanton number was computed as follows:

$$St = \frac{h}{\rho_{air}\, Cp\, V} \tag{2}$$

where $St$ is the Stanton number, and $\rho$, $Cp$ and $V$ are respectively the air density, specific heat at constant pressure, and velocity. Since the objective of this computation was to obtain sufficient resolution between the various flow regimes rather than accurate heat transfer data, the resulting Stanton numbers were normalized by a reference value. This reference value was based on the correlation from White (1983), giving an expression for an average Nusselt number for a sphere:

$$Nu_0 = 2 + Pr^{0.4}(0.4Re^{0.5} + 0.06Re^{2/3}) \tag{3}$$

where $Nu$ is the Nusselt number, $Pr$ is the Prandtl number ($Pr$ = 0.7 for air) and $Re$ is the Reynolds number based on the model diameter. The reference Stanton number was obtained using:

$$St_0 = Nu_0 \,/\, RePr \tag{4}$$

## 4. Computational fluid dynamics

### 4.1 VLOT CAD model

The CAD geometry of the VLOT wind tunnel model shown in Fig. 6 was used in the CFD simulations without any simplification. According to a study of flows past a rough sphere by Achenbach (1974), there is no significant difference in the drag coefficient of a sphere in smooth flow at a low supercritical Reynolds number over the range $0 \le kr/D \le 25\times10^{-5}$. For the current model surface roughness very close to $kr/D = 25\times10^{-5}$, it appears that at the test Reynolds number of Re = $4.6\times10^5$ and with low wind tunnel turbulence intensity of 0.5%, the flow is likely supercritical. Within this range $0 \le kr/D \le 25\times10^{-5}$, the mean flow conditions remain similar to those for a smooth surface. The computational domain was delineated by the model surface, wind tunnel floor and a farfield that was located 15$D$ upstream of the enclosure, 18$D$ downstream of the enclosure, 14$D$ away from the sides of the enclosure, and 30$D$ above the enclosure. Since the flow was nearly incompressible, the location of the farfield boundaries at these distances was assumed to be appropriate for the computations, and the effect of the domain boundaries on the solution was expected to be negligible. This facilitated comparisons with the WT measurements, which were corrected for blockage effect.

The freestream flow conditions used in the current simulations matched those measured in the wind tunnel, however a higher Mach number was used in three simulations. The wind tunnel floor was located at an elevation 0.125 m below the pivot telescope axis. The position of the upstream edge of the viscous floor boundary layer was calculated using a measured velocity profile at some distance upstream from the model center and applying a turbulent boundary layer approximation (McCormick, 1979). To minimize the grid size within the flow field, viscous conditions were applied only to a small region of the floor around the telescope enclosure. The upstream and downstream edges of the viscous region were fixed at 5.46$D$ and 1.75$D$ from the model position, respectively. The viscous region extended 0.9$D$ from the sides of the model.

### 4.2 Grid topology and flow solver

After defining the VLOT CAD model and the farfield, the flow domain was discretized into cubic elements called voxels. As displayed in Fig. 7, to optimize the number of voxels used

in the simulations, seven levels of variable resolution (VR) regions were created to adequately distribute the voxels according to the pertinence of the flow details around and inside the VLOT enclosure. Five levels of VR regions were created outside the enclosure and two VR region levels were created inside the enclosure. In each VR region, the grid remained Cartesian and uniform. The voxel edge length was multiplied or divided by a factor of two across the VR region interfaces. To predict accurately the pressure drag and the separation line, the grid was refined on the back of the enclosure around the telescope structure and along the observation path, as shown in Fig. 7. The grid resolution within the highest-level VR region was set to 1.1 mm.

The grid size of the entire flow domain was about 26.7 million voxels. To speed up the computations, the CFD simulations were performed in two steps. First, the solution was marched in time on a coarse mesh (about 11 million voxels), for about 100k time steps, in order to dampen rapidly the transient effects. The solution was initiated with uniform flow in the computational domain and with the stagnation condition inside the enclosure. Then, the resulting solution was mapped over to the refined mesh using linear interpolations. Then, the computations were performed until the unsteady behavior of the aerodynamic forces reached a periodic or aperiodic state.

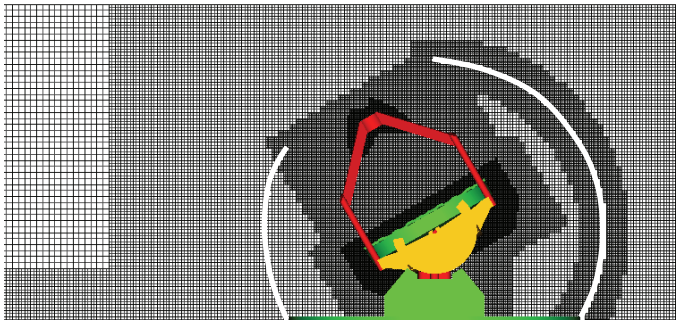

Fig. 7. Voxel distribution on a plane cutting through the telescope configuration ($\phi = 30^o$ and $\varphi = 0^o$). The enclosure cross-section is displayed in white (Mamou *et al.*, 2008)

### 4.3 Modelling of flow separation and boundary layer transition

#### 4.3.1 Modelling of flow separation

The CFD simulations were performed using the time-dependent CFD PowerFLOW™ solver. The solver uses a lattice-based approach, which is an extension of the lattice-gas/Boltzmann method (LBM). The LBM algorithm is inherently stable and with low numerical dissipation, which is suitable for acoustic wave simulation. For high Reynolds number flows, turbulence effects are modeled using the very large eddy simulation (VLES) approach based on the renormalization group theory (RNG) form of the k-ε turbulence model. It resolves the very large eddies directly (anisotropic scales of turbulence) and models the universal scales of turbulence in the dissipative and inertial ranges. The code contains wall treatments equivalent to the logarithmic law-of-the-wall with appropriate wall boundary conditions. The effects of adverse pressure gradients are simulated by modifying the local skin friction coefficient, which allows an accurate prediction of the flow separation location. The effect of the sub-grid scale turbulence is incorporated into the LBM through the eddy viscosity.

### 4.3.2 Modelling of flow transition

When three-dimensional transition occurs over non-slip surfaces and/or in free shear layers, the flow behavior is far away from being addressed by current commercial CFD codes. To resolve such complex flows, hybrid CFD techniques are required. Such techniques may involve DNS, LES and URANS simulations at the same time. DNS can be applied to a small region around the edge of the opening to track the evolution of the Tollmien–Schlichting (TS) waves, and further LES can be used to track the Kelvin-Helmholtz (KH) waves and reproduce the interactional flow mechanism as the shear layer impinges on the aft edge of the opening. In the present CFD work, the flow simulations were fully turbulent as the code does not allow for transition. Owing to the complex external flow behavior around the sphere-like enclosure, this was not a good approximation in the critical-supercritical range where the wind tunnel tests were performed. According to the discussion of Section 4.1, the assumption of fully-turbulent flow might be acceptable at the experimental Reynolds number; however, further validation simulations are desirable to assess the effect of transition occurring on an appreciable distance from stagnation. The intent of the IR investigation was to produce for future CFD code validation some experimental data concerning the transition and separation locations on the telescope configuration. However, as discussed below, the flow behavior around a base-truncated-spherical enclosure with an opening at various orientations can be quite different from that reported by Achenbach (1974) for an isolated sphere. However, from the good comparison between CFD and experimental results for the mean pressure loads on the enclosure surface and the pressure fluctuations inside the enclosure, it appears that the flow inside the enclosure was not significantly affected by the transitional and separated flow regions on the enclosure surface. Thus, running the flow simulation with fully turbulent conditions over a smooth surface was believed to be a fair assumption.

## 5. Results and discussion

In the present chapter, some CFD and experimental data are discussed for a specific configuration. Owing to the limited budget of the project and the high cost of the CFD simulations, only a few telescope configurations were performed.

### 5.1 Infrared measurement data

The intent of the infrared measurements was to visualize the boundary layer flow behavior on the external surface of the telescope enclosure, distinguishing between laminar and turbulent flows, and attached and separated flows, which could be useful for future CFD code validations.

Figure 8 shows examples of raw images obtained at a speed of $V$ = 10 m/s for the model configuration $\phi$ = 30° and $\varphi$ = 0°. At this speed, a temperature variation of 2°C to 3°C was visible, separating the laminar boundary layer from the turbulent boundary layer on the model. The image processing was performed to extract quantitative information from the IR data. Of particular interest was the location of transition and the separated flow regions at the rear of the model. For this purpose, a bi-cubic polynomial transformation was used to convert the IR image coordinate system into the model spherical coordinate system using control points on the VLOT model, with an accuracy of 1° RMS for both the zenith ($\phi$) and azimuth ($\varphi$) angles, estimated using the pressure taps on the model.

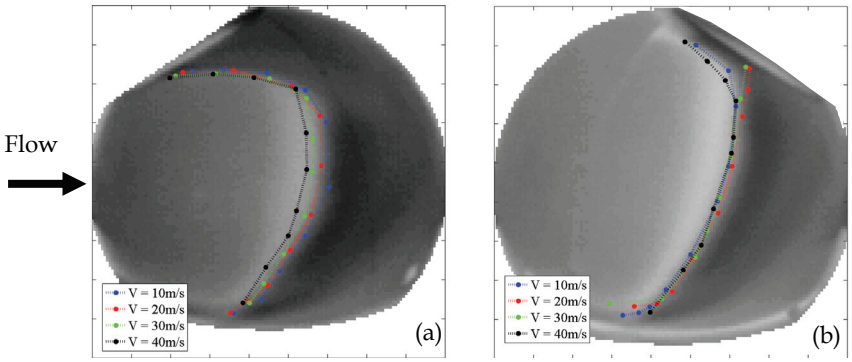


Fig. 8. Effect of wind speed on the transition locations (dotted lines) overlaid over the temperature image obtained at V = 10 m/s for two configurations: (a) model at $\phi$ = 30° and $\varphi$ = 0°, (b) model at $\phi$ =30° at $\varphi$ =180°

The IR results shown in Fig. 8 were obtained for various speeds and model azimuth positions: (a) $\varphi$ = 0° and (b) $\varphi$ = 180°. The transition locations were extracted from the temperature images and overlaid on top of the IR images recorded at $V$ = 10 m/s.

The effect of the opening on the transition location is visible when comparing the two model orientations shown in Fig. 8a and b. In the case of an azimuth of 0°, the maximum transition location, starting at $\theta$ = 15° near the centerline on the model for the minimum speed, moved forward with increasing speed by about 2.5° per 10 m/s increment (Fig. 8a). The shape of the transition line was also curved towards the front of the telescope near the external envelope opening. The laminar flow did not extend past the opening, which triggered the turbulence at an azimuth of 0°.

On the other hand, the opening did not affect the transition location much in the case of an azimuth of 180°, as shown in Fig. 8b. In this case, the maximum transition location on the model, about $\theta$ = 205°, appeared fairly insensitive to the Reynolds number, except in the vicinity of the opening. The resulting normalized Stanton number ($St/St_0$) distributions are given in Fig. 9 for model azimuth positions of 0° and 180°, with the levels indicated, unlike the raw temperature images shown in Fig. 8. From the Stanton number distributions in Fig. 9, the estimated transition and separation lines were not sensitive to the test procedure (*e.g.*, model cooling or heating).

The estimated transition lines and separation lines at the rear of the VLOT model are shown on the images. The heat transfer coefficient (and, therefore, $St$) increased suddenly as the boundary layer transitioned from laminar to turbulent. Then, as the turbulent boundary layer thickened, the skin friction was reduced and the heat transfer coefficient decreased again. In contrast, the flow separation induced a nearly constant heat transfer coefficient in the reversing flow region. Therefore, the separation region was estimated from examination of the constant Stanton number regions at the rear of the model. The attached flow extended to a maximum of about $\theta$ = 30° for $\varphi$ = 0° and $\theta$ = 210° for $\varphi$ = 180° on the model. At $V$ = 10 m/s, as displayed in Fig. 9, the estimated transition and separation lines for $\varphi$ = 0° and $\varphi$ = 180° agreed quite well with the flow visualization performed using mini-tufts on the model's surface (Cooper *et al.*, 2005), although the mini-tufts affected the surface flow behavior locally.

From the IR measurements, for the $\varphi$ = 0° case over the range of wind speeds tested, the boundary layer separated in its laminar state right at the front edge of the opening. The flow

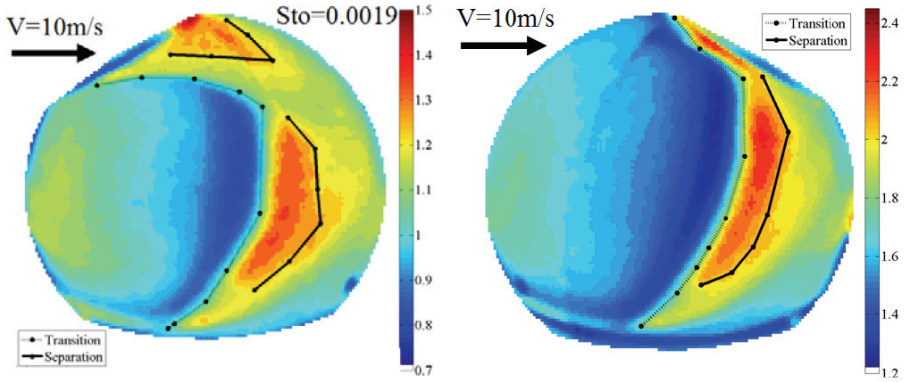


(a) (b)

Fig. 9. Stanton number ($St/St_0$) distribution and estimated transition and separation lines for a) $\varphi = 0°$ and b) $\varphi = 180°$azimuth angles

on the sides of the opening seemed to experience transition to turbulence at about mid-diameter of the opening. Beyond the aft edge of the opening, the flow appeared to be turbulent. These experimental observations reveal that the free shear layer underwent transition from the laminar to turbulent state before reaching the aft edge of the opening. The transition line might be three dimensional owing to the circular shape of the opening. Then the shear layer, before reaching the front edge to the transition location, might contain unstable TS waves that were transported into the main stream. A bit further downstream, a combination of TS and KH waves could coexist and interact, leading to a much more complex unsteady flow over the enclosure opening.

### 5.2 Unsteady wind loading measurement data

During the wind tunnel tests performed by Cooper *et al*. (2005) and (2004a-b), various wind speeds and telescope orientations were considered. When the enclosure opening was directly pointing into the wind ($\varphi = 0°$ with $0° \le \phi \le 30°$), strong pressure fluctuations were present in the enclosure, displaying one to four periodic oscillatory modes, which were mainly caused by the oscillatory nature of the shear layer forming over the enclosure opening (see Fig. 10). The number of modes decreased as the wind speed increased, which corresponded to a notable increase in the peak power-spectral-density of the pressure signal. The pressure fluctuations became significant when the Helmholtz cavity mode was excited, when all the pressure taps inside the model were excited by an almost identical unsteady pressure loading. The mean pressure inside the enclosure was almost uniform and had the magnitude of the pressure distribution of the external pressure field at the enclosure opening. It was observed that, when increasing the speed from 10 to 41 m/s, the enclosure resonance was first exited by the fourth mode, followed at higher speeds by successively lower modes. However, the first and second modes resulted in the largest pressure fluctuation amplitude inside the enclosure, as these two modes excited the enclosure at the Helmholtz frequencies. According to the averaged measurements of the interior pressure taps, the mirror surface had a pressure field almost identical to that on the enclosure interior surface. The mean and rms pressure distributions over the inner surface of the enclosure

were nearly uniform, with little or no significant phase difference observed over the mirror surface. For a vented enclosure, as seen in Fig. 10, only one oscillatory mode appeared, with its frequency slightly reduced by the ventilation effect. This indicated a weaker interaction of the shear layer with the enclosure opening edge. To illustrate the flow patterns past the telescope enclosure, smoke visualization was applied around and inside the enclosure, showing that the flow was massively separated on the back of the enclosure, while a strong horseshoe vortex was formed on the floor around the front part of the enclosure.

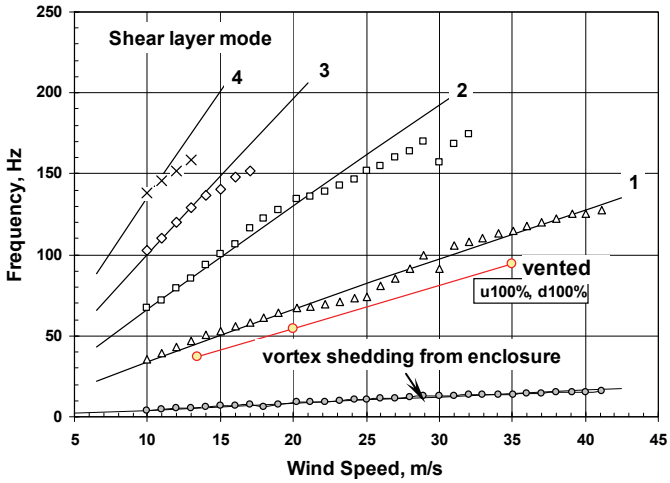


Fig. 10. Cavity oscillation behavior at $\phi = 0^o$ and $\varphi = 0^o$ for a sealed enclosure (black curves and symbols) and a vented enclosure (red curve and symbols) (Cooper *et al*., 2004b)

### 5.3 CFD results compared to experimental data

For the purpose of the CFD analysis, this section focuses on the results obtained from both wind tunnel measurements and CFD simulations at one wind speed (13.4 m/s) and four azimuthal and two zenithal orientations. In general, both experimental and CFD investigations revealed unsteady flows past the telescope structure for all orientations. The results are presented in terms of the time history of the forces, pressure coefficients, and flow patterns. For comparisons with experimental data (Cooper *et al*., 2005), mean values of the pressure coefficients and their standard deviations were computed at the pressure tap locations on the outer and inner surfaces of the enclosure, as well as on the primary mirror surface. A spectral analysis was also performed for the pressure coefficient signal collected at one (R4C3) of the pressure taps on the primary mirror surface. Grid sensitivity and time-step size refinement effects were investigated.

In the PowerFLOW™ solver, the time-step value is defined implicitly by specifying the finest voxel size, the maximum velocity, and the simulation Mach number. To speed up the computation, the simulation Mach number (*i.e.*, Ma = 0.228) was chosen to be greater than the physical Mach number (Ma = 0.0391). After solution convergence, two or three of the periodic cycles were simulated, from which statistical quantities were estimated. The simulation time step was $\Delta t$ = 22.23 μs for the coarse mesh and $\Delta t$ = 14.82 μs for the fine mesh. The coarse mesh solution was marched for 2.40 s of simulated time, and then the refined mesh solution was computed for an additional 1.596 s of simulated time.

### 5.3.1 Flow patterns

Snapshots of detailed flow patterns are illustrated in Fig. 11. On the back of the telescope enclosure, the flow was separated and several vortices were formed. Flow separation also took place at the aft edge of the opening, from which periodic vortices emanated and were shed downstream. Since a boundary layer formed on the non-slip floor a horseshoe vortex was formed and its core was clearly visible on the floor ahead of the enclosure base, as shown in Fig. 11. Over the opening, the flow was complex, where it sometimes entered the enclosure through a small area near the aft edge of the opening and spilled out from both sides of the opening. Snapshots of the vorticity magnitude field for various telescope orientations are shown in Fig. 11(a-c), when the opening was facing into the wind, and a snapshot of the static pressure field is displayed in Fig. 11d, when the opening was facing downstream. In all cases, the vorticity-time histories showed that a strong free shear layer formed across the opening, starting from the upstream edge of the opening and extending towards the aft edge. The free shear layer developed into a series of vortices that sometimes impinged on the downstream edge, leading to instantaneous changes in the pressure field inside the enclosure, and sometimes passed over the edge or entered the enclosure. When the enclosure was facing downstream, Fig. 11d, the opening was totally submerged within the separated flow region, accompanied by low pressure fluctuations inside the enclosure.

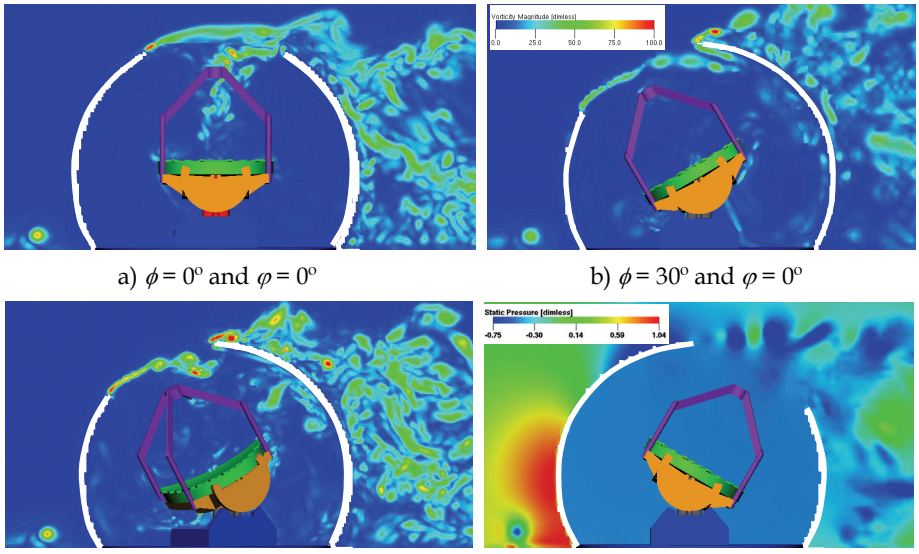


a) $\phi = 0^o$ and $\varphi = 0^o$ b) $\phi = 30^o$ and $\varphi = 0^o$

c) $\phi = 30^o$ and $\varphi = 30^o$ d) $\phi = 30^o$ and $\varphi = 180^o$

Fig. 11. Time snapshots of flow patterns colored by the vorticity magnitude (a, b and c) and the static pressure magnitude (d) on a centerline plane (Mamou *et al.*, 2004a, 2008)

Snapshot of the off-body streamlines past the enclosure shown in Fig. 12a indicates that the air stream across the opening was intermittently deflected inside and outside the enclosure, owing to the unstable shear layer that formed across the opening. A primary unsteady horseshoe vortex followed by a secondary vortex formed on the floor below the stagnation region on the enclosure. The results showed that the secondary vortex periodically grew and

decayed in size, causing the primary vortex to move slowly back and forth on the floor (time evolution not shown here). The iso-surface of the vorticity magnitude, illustrated in Fig. 12b, showed that the flow past the enclosure opening and in the wake region displayed very complex patterns. Iso-surfaces colored with the actual pressure values clearly illustrated the shape of the horseshoe vortex formed on the floor and the shape of the vortices formed along the shear layer over the enclosure opening. The vortices shed at the aft edge of the opening were also quite visible.

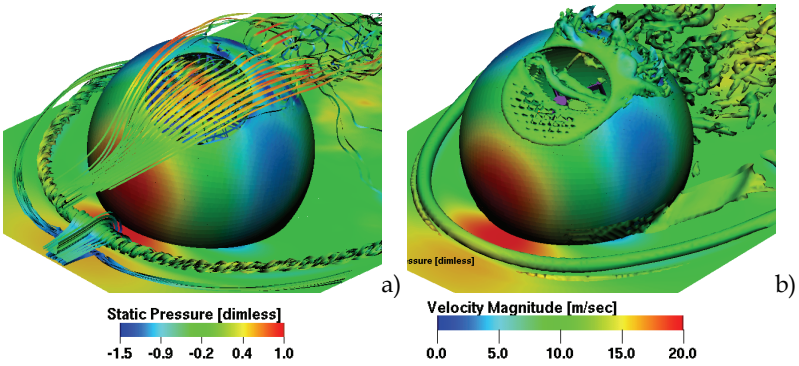


Fig. 12. a) Surface pressure and off-body streamlines colored by the velocity magnitude, b) surface pressure and vorticity iso-surfaces over the floor and the enclosure opening, colored by the static pressure field ($\phi = 30^o$ and $\varphi = 30^o$) (Mamou *et al.*, 2004a, 2008)

For a qualitative comparison between CFD predictions and experimental observations, a smoke stream was used in the wind tunnel to visualize the flow behavior around the enclosure structure. Figure 13a displays the smoke stream close to the enclosure opening when it was facing the wind ($\phi = 30^o$ and $\theta = 0^o$), showing a massive flow separation right

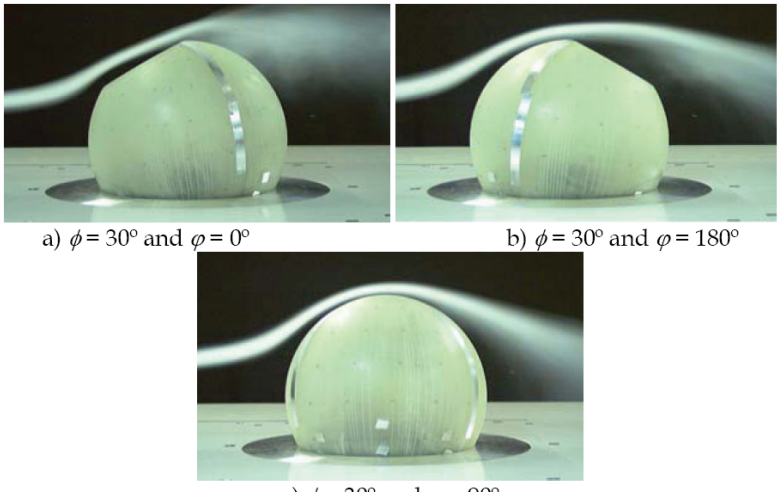

a) $\phi = 30^o$ and $\varphi = 0^o$ b) $\phi = 30^o$ and $\varphi = 180^o$

c) $\phi = 30^o$ and $\varphi = 90^o$

Fig. 13. Smoke stream close to the opening at $V = 13.4$ m/s (Cooper *et al.*, 2005)

after the aft edge of the opening. Figure 13b illustrates the smoke stream when the opening was facing downstream ($\phi$ = 30° and $\theta$ = 180°). It is clear that the enclosure opening was located within the separated flow region, in agreement with the CFD predictions in Fig. 12d. The flow behavior around the sphere-like enclosure was different from that of free sphere flow in the supercritical regime, Achenbach (1974). This is clearly visible in Fig. 13a-b, when the enclosure opening is facing upstream and downstream. The enclosure opening, combined with the floor effect, as shown by the infrared measurements (Fig. 8), had a significant effect on the loci of the separation and transition locations, which were different from those observed on a plain sphere under the same flow conditions. Nevertheless, Fig. 13c suggests that for $\varphi$ = 90°, the flow separated near $\theta$ = 120° measured from the stagnation point, consistent with the assumption of supercritical flow (see Section 4.1).

### 5.3.2 Telescope aerodynamic forces

To describe the flow unsteadiness behavior and to examine the CFD solution convergence, the time history of the telescope force coefficients (lift and drag) are presented in Fig. 14 for $\phi$ = 30° and $\varphi$ = 30°. The CFD results were obtained using the simulation Mach number. The mesh refinement had a negligible effect on the accuracy of the force history. The forces acting on the telescope were close to zero mean value, but exhibited relatively large fluctuations.

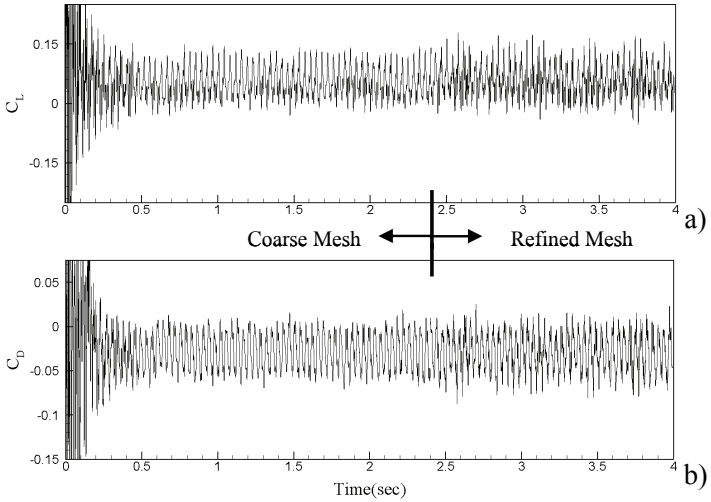


Fig. 14. CFD lift and drag force coefficients on the primary mirror assembly ($\phi$ = 30° and $\varphi$ = 30°) (Mamou *et al*., 2008)

### 5.3.3 Pressure signal and spectral analysis

The results discussed here were obtained for the $\phi$ = 30° and $\varphi$ = 30° configuration. From the CFD simulations and experimental measurements, the pressure signals collected on the primary mirror showed that the mirror surface was excited by roughly the same pressure tones. Hence, only the signal collected at pressure tap R4C3 (see Fig. 6b) is presented. Figure 15 displays the CFD predicted pressure coefficient time history compared to the

measured signal, which was filtered at 400 Hz. The CFD results were obtained using the real Mach number, which allowed capturing of the interactional effects between the shear layer and the generated acoustic waves. As can be seen from Fig. 15, the trend and the amplitude agreed very well, even though the CFD signal contained an additional low energy, high frequency component.

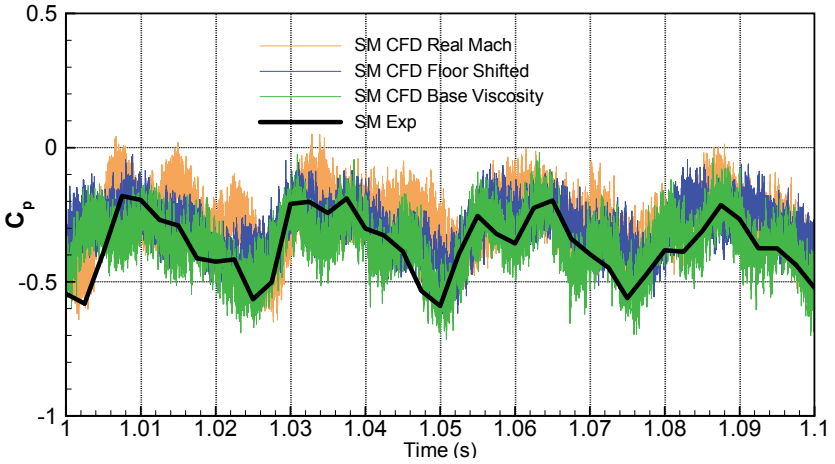


Fig. 15. Instantaneous CFD and experimental pressure coefficients collected on one of the mirror probes, R4C3 ($\phi = 30^o$ and $\varphi = 30^o$).

As shown in Fig. 16, the power spectral density of the pressure signal on the primary mirror showed a noticeable discrepancy between the CFD simulation Mach number results and the measured data. As discussed in the introduction, a number of flow simulations were performed to investigate how to resolve better the flow past the telescope and obtain a good comparison between the CFD and experimental results. Since further grid refinement did not improve the comparison (Mamou *et al*., 2008; Tahi *et al*., 2005), attention was turned to the flow solver time step definition. In the PowerFLOW™ solver, the time step size was computed using the following formula:

$$\Delta t = 0.794 Ma \frac{\Delta l}{V_\infty} \tag{5}$$

where $Ma$ is the Mach number and $\Delta l$ = 1.1 mm is the size of the finest voxel in the computational domain. The simulation Mach number used in PowerFLOW™ was approximately $Ma$ = 0.228, such that the virtual-physical time step was maximized to accelerate convergence. This was done intentionally, as it was not expected that the acoustic effects on the flow around and inside the telescope enclosure were significant. To examine the Mach number effect on the flow unsteadiness, a flow solution was obtained using the wind tunnel Mach number $Ma$ = 0.039 (real Mach number; denoted by "SM CFD Real Mach" in Fig. 15), which resulted in a smaller time step. The solution was marched for a period of 0.75 s of simulated time, starting with uniform flow outside the enclosure and a stagnation condition inside the enclosure. As expected, the simulation at the wind tunnel Mach number considerably improved the prediction of the power spectral density functions,

as shown in Fig. 16. The new results were in excellent agreement with the wind tunnel measurements obtained for the three modal frequencies. The oscillatory flow behavior over the enclosure opening and inside the enclosure was dominated mainly by the acoustic effects resulting from the interaction of the shear layer with the aft edge of the enclosure opening. When the flow solutions were computed using a Mach number greater than the physical value, the interaction between the opening shear layer and the acoustic waves that existed in the flow was severely affected.

For the simulation at the experimental Mach number, some grid adjustments were needed to improve the CFD results (pressure histories as displayed in Fig. 15), as the turbulent eddy viscosity was overestimated on the digital tunnel floor, which cut through the voxels. A simulation was run by shifting the tunnel floor up to match a complete voxel edge, and referred to as "SM CFD Floor Shifted". The results, obtained for this case, gave a better mean $C_P$ with no change to the frequency domain of the pressure signal, nor to its rms value. Another simulation run by setting a threshold for the base viscosity, denoted by "SM CFD Base Viscosity", agreed much better with the experiment in terms of the pressure signal.

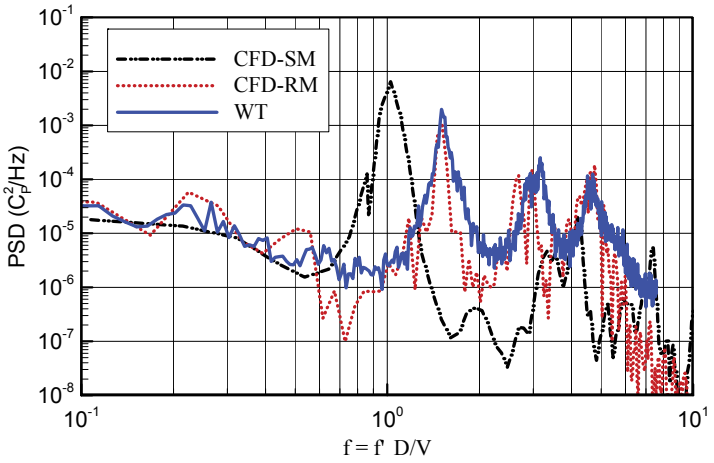


Fig. 16. CFD and experimental power density spectra pressure coefficients collected on one of the mirror probes, R4C3 ($\phi = 30^o$ and $\varphi = 30^o$) (Mamou *et al.*, 2008)

### 5.3.3 Mean and standard deviation of the pressure coefficients

The CFD mean pressure coefficients and their standard deviations for pressure tap Row 2 around the outer and the inner surfaces of the enclosure and on the primary mirror surface are compared to the measurements in Fig. 17. The plots on the left side show the $C_{Pm}$ values and the plots on the right side show the standard deviations. The CFD results obtained at the simulation Mach number are referred to as "CFD-SM" and the results obtained at the real Mach number are referred to as "CFD-RM". Overall, the mean pressure coefficients, Figs 17a, b and c, along Row 2 on the enclosure exterior and interior surface and on the primary mirror surface, respectively, showed a good agreement between the CFD predictions and measurements. According to the pressure plateau in Fig. 17a, the flow separation area on the back of the enclosure occurred within the range $0 \lesssim \theta \lesssim 100°$. For a quantitative comparison, the measured pressure coefficient uncertainty at a wind speed of

13.4 m/s was ±0.006. In Fig. 17, the uncertainty is represented by the height of the square symbols. Furthermore, good agreement was observed between the CFD and measured rms $C_P$ data displayed on the right side of Fig. 17, with some slight discrepancies close to the separated region. Inside the enclosure, the $C_{Pm}$ plots in Fig. 17b and c indicated that the mean pressure was almost uniform inside the enclosure. The amplitude of the CFD-predicted pressure fluctuations was higher than that of the wind tunnel measurements.

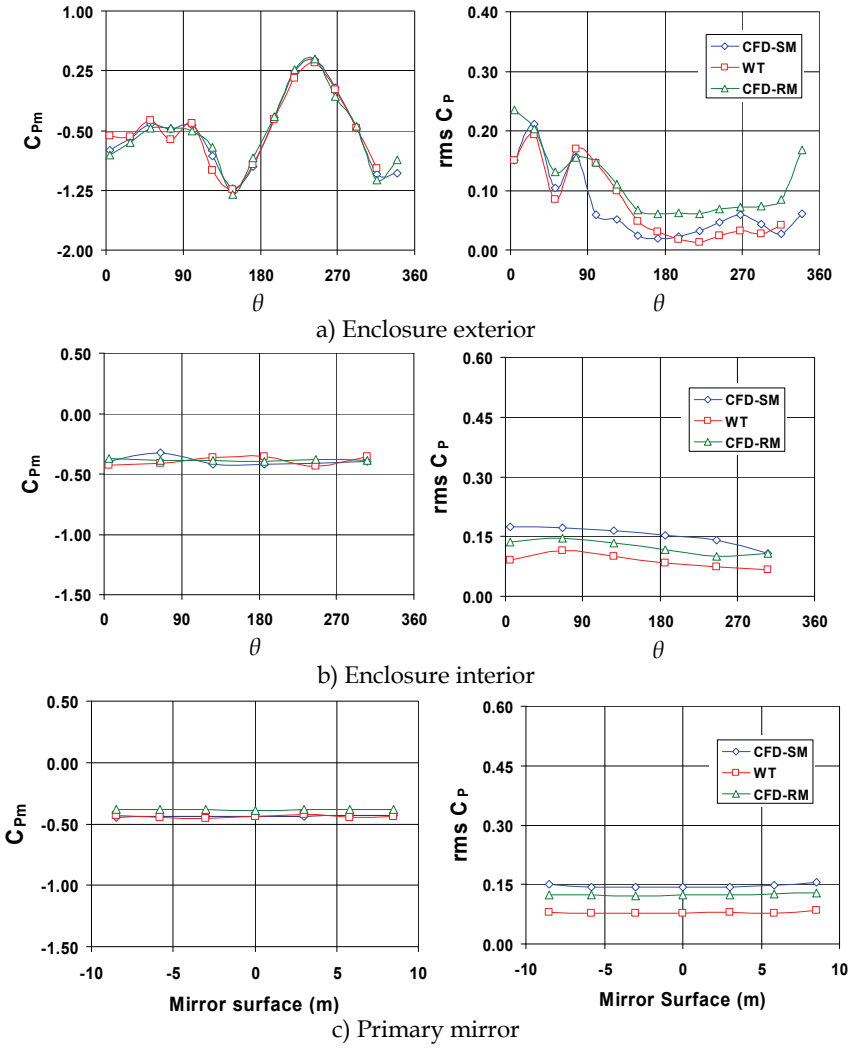


Fig. 17. Comparison between CFD and measured data: mean pressure coefficients (left) and standard deviations (right) for the Row2 pressure taps on the enclosure (a) exterior and (b) interior, and (c) the Row3 pressure taps on the primary mirror surface ($\phi$ = 30° and $\varphi$ = 30°) (Mamou *et al.*, 2008)

As in the case of the pressure loads on the enclosure interior surface, the mean pressure over the primary mirror surface was uniform. The rms $C_{Pm}$ values on the primary mirror were slightly overestimated by the CFD predictions. This is probably due to the three-dimensional effect of the opening free shear layer, which was not accurately simulated. Figure 17a shows two peaks of the rms $C_{P,}$ which corresponded to the loci of strong and large vortices formed on the back of the enclosure, as shown in Fig. 18. The real Mach number simulation showed much better agreement with experiment for the rms $C_{Pm}$ inside the enclosure.

Figure 19 presents a comparison between the CFD and the WT data for the $C_{Pm}$ and the rms $C_P$ variations on the exterior surface of the enclosure for Row2 of the pressure probes. The results were obtained for $\phi$=30° and $\varphi$=0°. A good agreement between CFD and WT data was obtained for the $C_{Pm}$. The rms $C_P$ trend was well captured, indicating two distinct high

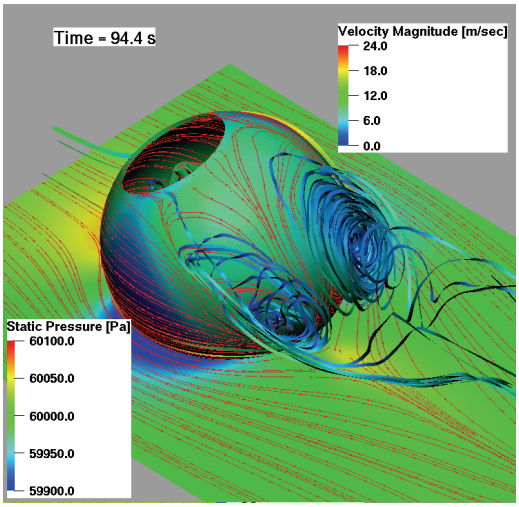


Fig. 18. Snapshot of the off-body streamlines within the separated region behind the enclosure ($\phi$ = 30° and $\varphi$ = 30°) (Mamou *et al.*, 2004a)

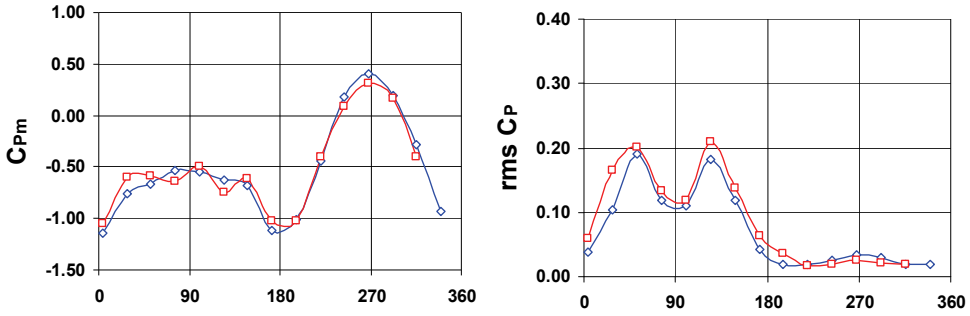


Fig. 19. Comparison between CFD and measured data: mean pressure coefficients (left) and standard deviations (right) for the Row2 pressure taps on the enclosure exterior ($\phi$=30° and $\varphi$=0°) (Mamou *et al.*, 2004a)

fluctuation peaks, which were the signature of the presence of two strong vortical flows inside the separated region $30° \leq \theta \leq 150°$. The predicted separation point for Row2 was in agreement with the mean pressure measured data and the IR measurements displayed in Fig. 9a.
For the vented enclosure configuration, the measurements revealed that the pressure tones inside the enclosure were reduced to one oscillatory mode, with a lower pressure fluctuation amplitude. Similar results were predicted by the CFD simulations performed on a 30-m full-scale telescope (Mamou *et al.*, 2004a). Only one row of vents was opened. The streamlines displayed in Fig. 19a-b show that the air flowed through the front vents and exited from the rear ones and through the enclosure opening. This obviously created a large flow circulation inside the enclosure and on the primary mirror surface, as displayed in Fig. 19b-c. The CFD results showed that, as the air flowed outwards through the enclosure opening, the free shear layer was lifted somewhat, causing less interaction with the aft edge of the opening. Also, the pressure inside the enclosure increased owing to reduced suction effects caused by the airflow through the vents.

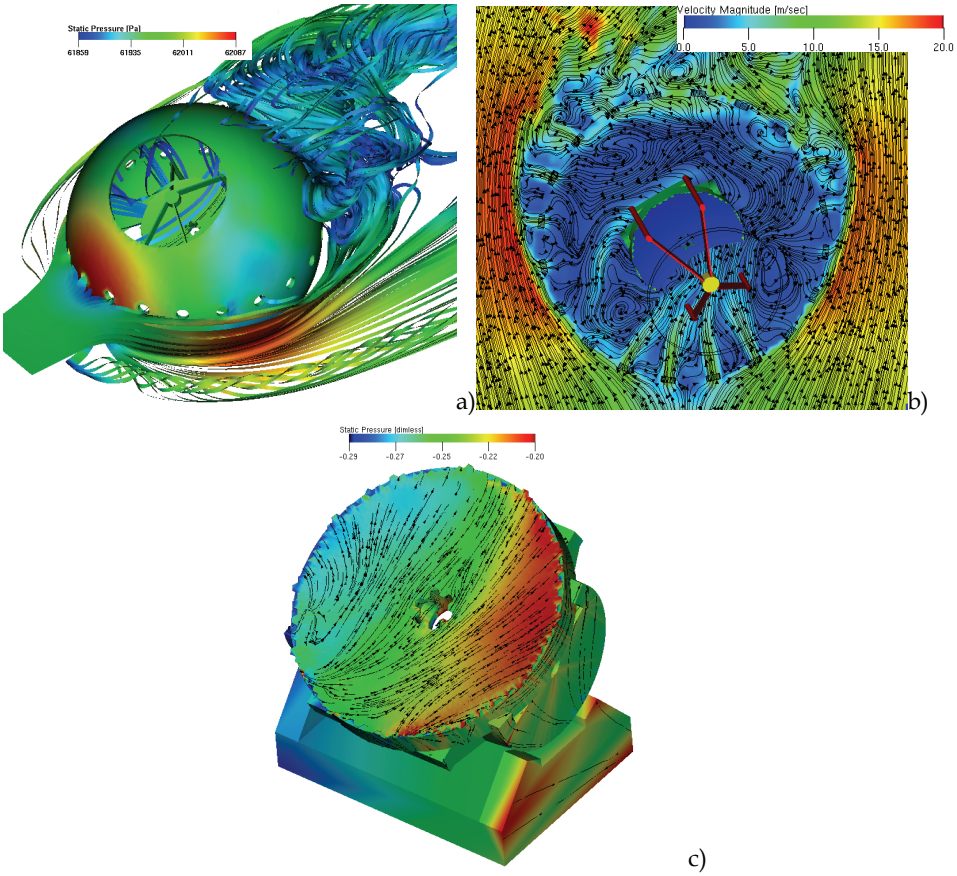


Fig. 19. a) Off-body streamlines through the enclosure vents, b) streamlines on a horizontal cutting plane through the enclosure vents, c) streamlines on the primary mirror surface ($\phi = 30^o$ and $\varphi = 30^o$)

## 6. Conclusion

The importance of applying computational fluid dynamics (CFD) for large optical telescope flow analyses in the early design phase was emphasized and some critical challenges for accurate flow field prediction were drawn. Also, a thorough literature review was performed specifically on the role of CFD that can play towards accurate prediction of pressure loads on telescopes structure. Some recent CFD and experimental investigations, on a scaled model of a very large optical telescope housed within a spherical enclosure, were performed and led to the following remarks.

In general, when the enclosure opening was facing into the wind, both the CFD and measured data revealed that the flow was highly unsteady inside and outside the enclosure, causing unsteady wind loads on the enclosure and the telescope structure. Outside the enclosure, owing to the formation of a boundary layer over the floor, a distinct unsteady horseshoe vortex was formed. A strong shear layer was noted to evolve across the enclosure opening. The shear layer was decidedly unstable, and tended to roll up into a series of small vortices that interacted with the aft edge of the enclosure opening, resulting in large pressure fluctuations on the primary mirror surface. The mean pressure inside the enclosure was roughly uniform. The flow was separated on the back of the enclosure, starting from the aft edge of the enclosure opening towards the floor.

A spectral analysis of the pressure signal on the primary mirror surface showed the existence of at least three principal oscillatory modes. Owing to the elevated Mach number used for most of the simulations, the first CFD mode frequency was understandably under-estimated. However, when the actual wind tunnel Mach number was used in the simulations, the spectral analysis showed excellent agreement between the CFD and measured data, demonstrating the relevance of simulating appropriately the acoustic waves generated by the interaction of the shear layer vortices with the enclosure opening edge. Good comparisons were also obtained between the CFD predictions and the measurements for the mean pressure coefficients and their standard deviations around and inside the enclosure surfaces and on the primary mirror surface. For the purposes of this study, the level of agreement obtained with the experimentally observed phenomena justifies the assumption of a hydraulically smooth enclosure surface and fully turbulent flow.

Despite the good agreement between CFD and experimental results for the flow behavior inside the enclosure, the flow physics around the enclosure external surface was not properly simulated by assuming fully turbulent flows, as the infrared measurements showed a large laminar run on the front region of the enclosure, followed by transition, fully turbulent flows, and finally separated flows. Furthermore, from the smoke visualization and infrared measurements, it appeared that the flow around the enclosure was strongly affected by the tunnel floor, causing an unsteady horseshoe vortex to form, and by the enclosure opening, which disrupted the transition and separation locations expected on sphere flows in the supercritical regime. These have the effect of delaying the transition location and triggering earlier flow separation.

For bodies with a high sensitivity to the boundary layer state, such as a spherical enclosure, there is a need to simulate transition, even in the high Reynolds number case. Future work involving high Reynolds number tests and CFD simulations using hybrid and zonal DNS, LES and URANS simulations is required to address properly these flow phenomena.

## 7. References

Achenbach, E. (1974) The effect of surface roughness and blockage on the flow past spheres, J. Fluid Mech. (1974), vol. 65, part 1, pp 113-125.

Angeli, G.Z.; Cho, M.K.; Sheehan, M. & Stepp, L.M. (2002). Charaterization of wind loading of telescopes, SPIE procedding, Vol. 4757 "Integrated Modeling of Telescopes", Lund, Sweden, Feb. 2002, pp. 72-83.

Angeli, G.Z.; Dunn, J.; Roberts, S.; MacMynowski, D.; Segurson, A; Vogiatzis, K. & Fitzsimmons, J. (2004). Modeling tools to estimate the performance of the Thirty Meter Telescope: an integrated approach, Proceedings SPIE, Vol. 5497, pp. 237-250, 2004 Glasgow, Scotland, United Kingdom.

Babinsky, H. & Edwards, J.A. (1996) *Automatic liquid crystal thermography for transient heat transfer in hypersonic flow*, Experiments in Fluids, 21 (4) pp. 227-236, 1996.

Cho, M.K.; Stepp, L.M.; Angeli, G.Z. & Smith, D.R. (2003). Wind loading of large telescopes, Proc. SPIE, Vol. 4837, 352 (2003), Thursday 22 August 2002 , Waikoloa, HI, USA

Cho, M.K.; Stepp, L. & Kim, S. (2001). Wind buffeting on the Gemini 8m primary mirrors, Proc. SPIE 4444, 302 (2001).

Cooper, K.R.; Farrell, I.; Leclerc, G.; Franchi, G.; Vezzaro, N.; & Fitzsimmons, J. (2005). A wind tunnel test on the HIA very large optical telescope: Phase 0 - mean and unsteady pressure measurements, NRC-IAR-LR-AL-2005-0038, NRC Canada, 2005.

Cooper, K.R. & Fitzsimmons, J. (2004a). An example of cavity resonance in a ground-based structure, Fifth International Colloquium on Bluff Body Aerodynamics and Applications, Ottawa, Canada, pp. 115-118, 2004.

Cooper, K.R.; Farrell, I.; Fitzsimmons, J.; Chu, V. & Vezzaro, N. (2004b) A wind tunnel test on the HIA very large optical telescope: Phase 0 - Vented enclosure mean and unsteady mirror pressures and mean mirror loads. NRC-IAR-LR-AL-2005-0039 , NRC Canada, 2004.

De Young, D.S. (1996). Numerical simulations of airflow in telescope enclosure, *Astronomical Journal*, Vol. 112, No. 6, pp. 2896-2908

De Young, D.S. & Vogiatzis, K. (2004). Numerical simulations of airflow in very large telescope enclosures, Proc. SPIE, Second Backaskog Workshop on Extremely Large Telescopes, Vol. 5382 p. 379-387, 2004.

Hubner, J.P.; Carroll, B.F. & Schanze, K.S. (2002) Heat transfer measurements in hypersonic flow using luminescent coating techniques, Journal of Thermophysics and Heat Transfer, Vol. 16, No 4, 2002, pp. 516-522

MacMynowski, D.G.; Vogiatzis, K.; Angeli, G.Z.; Fitzsimmons, J. & Nelson, J.E. (2006) Wind loads on ground-based telescopes. *Applied Optics*, Vol. 45, No. 30, pp. 7912-7923, 20 October 2006.

Mamou, M.; Tahi, A.; Benmeddour, A.; Cooper, K.R,.; Abdallah, I.; Khalid, M. & Fitzsimmons, J. (2008). Computational fluid dynamics simulations and wind tunnel measurements of unsteady wind loads on a scaled model of a very large optical telescope. *Journal of Wind Engineering & Industrial Aerodynamics*, Vol. 96, Issue 2, pp. 257-288, ISSN

Mamou, M.; Benmeddour, A. & Khalid, M. (2004a) Computational fluid dynamics analysis of the HIA very large optical telescope: Phase 0 - full scale mean and unsteady pressure and loads predictions, NRC-IAR-LTR-AL-2004-0022, NRC Canada, 2004.

Mamou, M.; Cooper, K.R.; Benmeddour, A.; Khalid, M.; Fitzsimmons, J. & Sengupta, R. (2004b) CFD and wind tunnel studies of wind loading of the Canadian very large optical telescope, *Fifth International Colloquium on Bluff Body Aerodynamics and Applications*, Ottawa, Canada, pp. 119-122, 2004.

Mamou, M.; Tahi, A.; Abdallah, I.; Benmeddour, A. & Khalid, M. (2004c) Computational fluid dynamics analysis of the very large optical telescope – mean and unsteady pressure and loads predictions, NRC-IAR-LTR-AL-2004-0200, NRC Canada, 2004.

McCormick, B.W.: Aerodynamics, Aeronautics, and Flight Mechanics, John Wiley & Sons Edition, 1979.

Mébarki, Y. (2004) Transition detection on the iSun solar racecar from McGill University in the NRC 9-meter wind tunnel using infrared thermography, NRC LML LM-AL-2004-0081

Mébarki, Y.; Mamou, M. & Genest, M. (2009) Infrared measurements of transition location on the CRIAQ project morphing wing model. NRC-IAR-LTR-AL-2009-075.

Pottebaum, T. & MacMynowski, D.G. (2006). Wind tunnel testing of vented and unvented hemispherical telescope enclosure, J. Fluids and Structures, Vol. 22, 2006, pp. 3-19.

PowerFLOW™ explanatory notes http://www.exa.com

Quattri, M.; Koch, F.; Noethe, L.; Bonnet, A.C. & Noelting S. (2003). OWL wind loading characterization: a preliminary study, Proceedings of SPIE, Vol. 4840 Future Giant Telescopes, January 2003, pp. 459-470.

Quattri, M.; Haase, R.; Barreto Cabrera, M.; Friend Monasterio, E.; Codina, R.; Gonzalez Hernandez, M. & Reyes, M. (2008) Wind turbulence struture inside telescope enclosures. Proc. SPIE, Vol. 7017, 70170O (2008), 26 June 2008, Marseille, France.

Riewaldt., H.; McNamara, K. & Wang, X. (2004) Euro50 Wind tunnel study, Euro50 Technical Report No. 3, LUND Observatory and National University of Ireland, 2004.

Tahi, A.; Benmeddour, A.; Mamou, M. & Khalid, M. (2005a) Computational fluid dynamics analysis of the HIA 30m (TMT) very large optical telescope (VLOT) with vented enclosure: mean and unsteady pressure and loads predictions, NRC-IAR-LTR-AL-2005-0007, NRC Canada, 2005.

Tahi , A.; Benmeddour, A.; Mamou, M.; Khalid, M.; Cooper, K.R.; Fitzsimmons, J.; Freed, D. & Sengupta, R. (2005b) Computational aerodynamic analyses of different Canadian very large optical telescope configurations, AIAA-2005-5095, 23rd AIAA Applied Aerodynamics Conference, Toronto, Canada, June 2005.

Schmid, S.; Lutz, T. & Kramer, E. (2008a) Simulation of the flow around the stratospheric observatory for infrared astronomy SOFIA using URANS and DES, chapter in the Book on High Performance Computing in Science and Engineering, *Garching/Munich 2007 Publisher Springer Berlin Heidelberg* ISBN 978-3-540-69181-5, Part IV pp. 365-375, October 22, 2008.

Schmid, S.; Lutz, T.; Kramer, E. & Kuhn, T. (2008b) Passive control of the flow around the stratospheric observatory for infrared astronomy. *26th AIAA Applied Aerodynamics Conference AIAA* 2008-6717, 18 - 21 August 2008, Honolulu, Hawaii, August 2008.

Schmid, S.; Lutz, T.; Kramer, E. & Kuhn, T. (2009) Passive Control of the Flow Around the Stratospheric Observatory for Infrared Astronomy. *Journal of Aircraft*, Vol. 46, No. 4, July–August 2009.

Srinivasan, G.R. (1997) Unsteady flowfield and cavity acoustics of the stratospheric observatory for infrared astronomy. *Journal of Spacecraft and Rockets*, Vol. 34, No. 3, pp. 372-378, May–June 1997.

Srinivasan, G.R. (2000) Acoustics and unsteady flow of telescope cavity in an airplane. Journal of Aircraft Vol. 37, No. 2, pp. 274-281, March–April 2000.

Vogiatzis, K.; Segurson, A.; & Angeli, G.Z. (2004). Estimating the effect of wind loading on extremely large telescope performance using computational fluid dynamics, *Proc. SPIE Modeling and Systems Engineering for Astronomy,* Vol. 5497, pp. 311-320, 2004. Thursday 24th June 2004, Glasgow, Scotland, United Kingdom

White, F.M. (1983) Heat Transfer, Addison Wesley Educational Publishers Inc., 1983

# 10

# Application of Computational Fluid Dynamics to Practical Design and Performance Analysis of Turbomachinery

Hyoung Woo OH
*Chungju National University*
*Korea*

## 1. Introduction

Over the past several decades, the meanline analysis method based on the conventional empirical loss correlations, assuming that the flow characteristics averaged over the cross-section of flow passage could represent the three-dimensional flow phenomena through the passage of turbomachinery, has been widely employed to determine the overall geometric design variables for each component of turbomachinery and to predict the on and off-design performance characteristics.
With the relentless increase in computing power, however, the computational fluid dynamics (CFD) techniques have remarkably progressed in the last decade, and CFD becomes commonly used not only as a design tool to improve the flow dynamic performance of specific components of turbomachinery but also as a virtual test rig to numerically experiment on a working prototype of the new/existing model.
This Chapter demonstrates how the meanline and CFD analyses can be applied to carrying out the hydraulic design optimization and performance analysis of a mixed-flow pump with the non-dimensional specific-speed ($N_s$) of 2.44. Although the present article focuses on the incompressible flow machine, which falls into the regime of mixed-flow pumps with the non-dimensional specific-speed in the range of 1.9 to 2.5, the following procedure presented herein can be used efficiently as a practical design and analysis guide for general purpose turbomachinery.

## 2. Experimental apparatus for hydraulic performance

The Maritime and Ocean Engineering Research Institute (MOERI) constructed an apparatus (Fig. 1) to simulate the performance characteristics of the mixed-flow pump and conducted experiments on the hydraulic performance for the head rise, input power, pump efficiency versus flowrate, and the cavitation characteristics. The pump flowrate is calculated from the pressure difference across a downstream nozzle. Wall static pressures at the inlet and outlet planes are averaged in a manifold with four duct taps. The bulk total pressure, delivered head, is derived from the wall static pressure measurements and from the assumption of uniform velocity at the inflow and outflow stations. The input power is obtained from the torque transducer and impeller rotational speed readings. Uncertainties are ±1% for head, flowrate, and shaft torque and ±1 r/min for shaft speed.

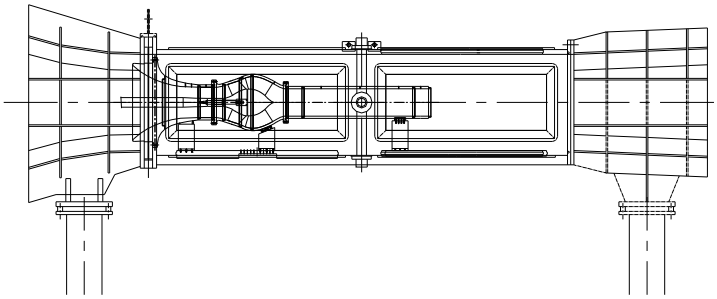

(a)

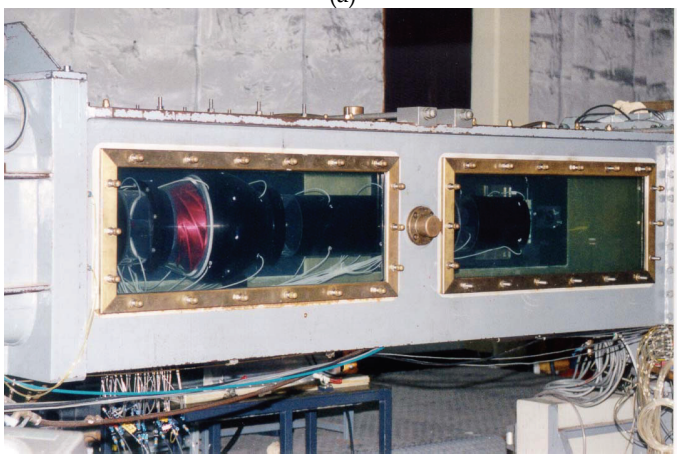

(b)

Fig. 1. Performance test rig: (a) schematic diagram and (b) view of test section section

## 3. Conceptual design considerations

In order to accomplish the specific geometric modeling of a three-dimensional configuration of turbomachinery, the overall configuration data have to be first specified, i.e. the inlet and outlet blade angles and other design variables for each component in the meridional plane have to be determined from the preliminary design process.

Most of the preliminary design and performance analyses of turbomachinery are still essentially empirical. General principles on the design theories of fluid machinery based on empirical loss correlations have been well described in a number of references (Aungier, 2000; Japikse, 1994; Neumann, 2005; Stepanoff, 1993). However, because the open literature provides only the ranges of design variables such as the ratios of inlet to outlet diameters, the inlet and outlet blade angles as a design guide, the specific values of the design variables in the recommended ranges have to be determined to achieve a design point performance target by design engineers' own past experience.

The present study adopted the meanline design code (Oh & Kim, 2001) in order to carry out the conceptual design optimization of a mixed-flow pump. This program states the loss of mixed-flow pump efficiency as an objective function and then deals with a nonlinear

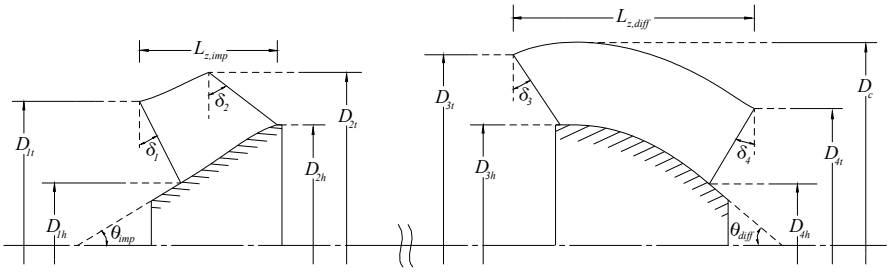


Fig. 2. Meridional cross-section of mixed-flow pump with geometric parameters

constrained optimization problem – most of the geometric and fluid dynamic design constraints herein are, unfortunately, based on the industrial field data and designer's database. Figure 2 depicts the overall meridional configuration of a mixed-flow pump system with representative geometric parameters. Taking account of the design target in this study, the pump system should satisfy the performance of the head coefficient ($\psi \equiv 6.5\times gH/(\Omega^2 D_{in}^2)$ where $g$ is the gravitational acceleration [m/s$^2$], $H$ is the pump total head [m], $\Omega$ is the rotational speed [rad/s], and $D_{in}$ is the inlet duct diameter [m]) 0.557 at the flow coefficient ($\phi \equiv 5\times Q/(\Omega D_{in}^3)$ where $Q$ is the volume flow [m$^3$/s]) 0.747 as a mixed-flow pump with the non-dimensional specific-speed of 2.44. The non-dimensional specific-diameter ($D_s$) of the mixed-flow pump preliminarily optimized by using the meanline analysis is 1.79, which lies on the collected field data (Balje, 1981) of efficient turbomachines (Fig. 3). This confirms that the present conceptual design optimization for the meridional

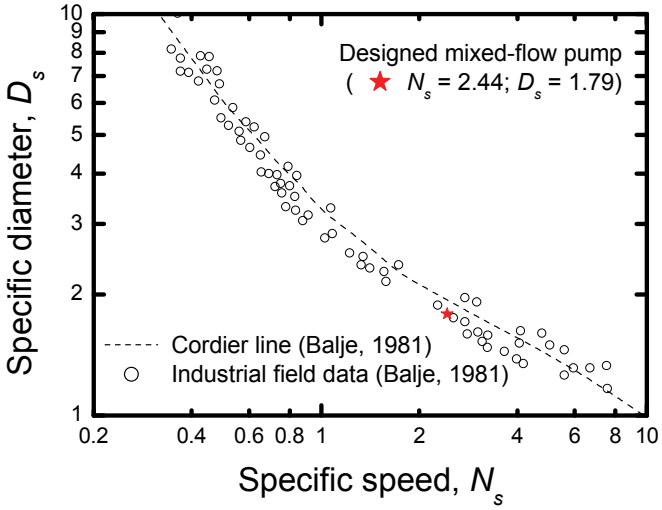


Fig. 3. Specific-speed and specific-diameter diagram

configuration has been accomplished within the reliable design regime. As a reference, the Cordier line (Balje, 1981), which is a fair curve through the field data in the statistical sense, is represented in Fig. 3.

## 4. Detailed design optimization and performance analysis using CFD

### 4.1 Overview of design process

The detailed design work on the impeller and diffuser blades proceeds in consideration of the overall meridional geometric data determined from conceptual design optimization. The present study decides the three-dimensional configuration by using a well-established commercial CFD package (ANSYS 12.0 Turbo System, 2009), whose predictive capabilities to analyze the performance characteristics of a variety of turbomachines have already been validated in the open literature and industrial applications, that enables the user to create a new blade geometry and to analyze the three-dimensional viscous flow phenomena within the blade passage in a graphical environment. Investigating the internal flow dynamics and the performance characteristics of a pump system, the iterative design process is continued until geometric feasibility is reached.

Some representative design factors to be first considered in accomplishing detailed design optimization can be briefly stated as follows: The blade angles along the streamline should be distributed in such a way that the blade-loadings, i.e. the static pressure difference between the blade upper and lower surfaces, are optimized along the blade surface and the incidence, defined as flow angle minus blade angle, has to be designed to improve the pump efficiency and the pump performance at the off-design points. In the case of diffuser, to suppress the energy dissipation due to the exit swirl, the blading has to be achieved to minimize the rotational velocity component at the exit of diffuser.

Newly designed impeller and diffuser for a mixed-flow pump in accordance with the above detailed design procedure are illustrated in Fig. 4.

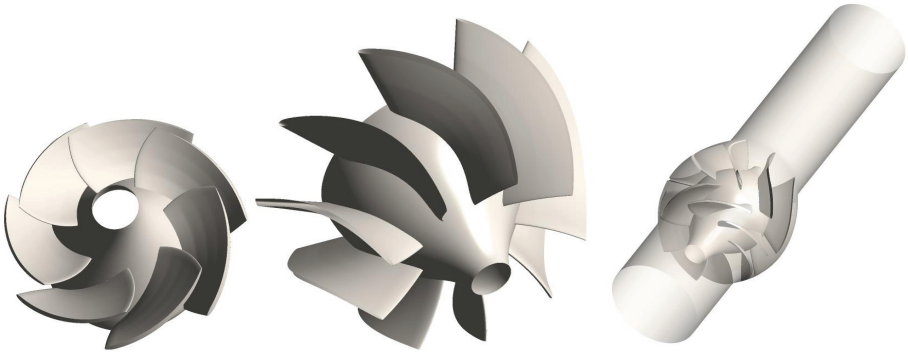

Fig. 4. Three-dimensional modeling: impeller (left), diffuser (middle), and a mixed-flow pump stage for computation (right)

### 4.2 Computational aspects

The right side of Fig. 4 shows the three-dimensional modeling for the performance analysis of a mixed-flow pump stage. The computational domain is divided into the inlet duct, the unshrouded-impeller with tip-clearance, the diffuser, and the outlet duct parts, with a total

number of 1 237 287 nodes and 1 176 622 hexahedral elements, of which the size next to the wall boundary has been determined to meet the required condition, $y^+ \leq \sim 3$, for highly accurate boundary-layer simulation. This grid system as shown in Fig. 5 is used for all subsequent computations. In order to remove the dependence of the solution on the grid density, the simulations were run on a number of meshes of different mesh refinement such as 1 031 877, 1 237 287, 1 248 185, and 1 344 297 nodes.

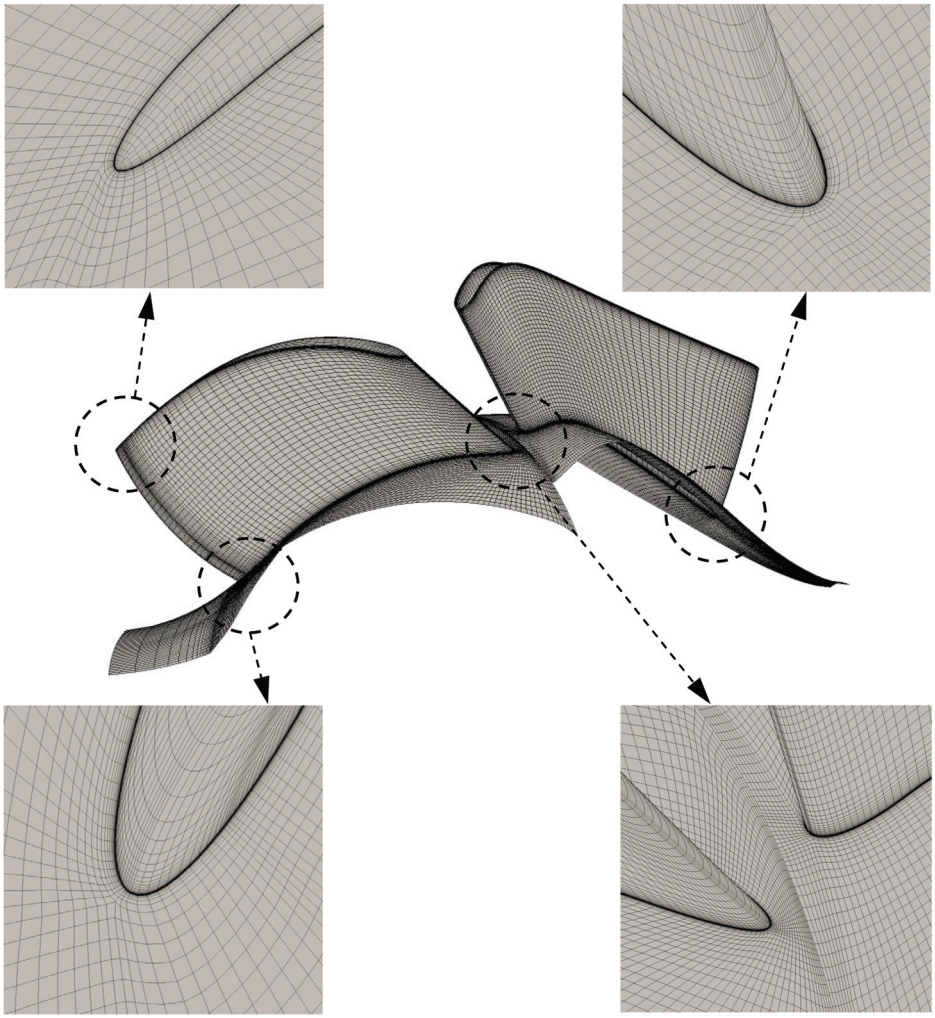

Fig. 5. View of computational mesh for impeller and diffuser

The numerical analysis of three-dimensional steady-state turbulent flow based on the Reynolds-averaged Navier-Stokes equations has been performed using the $k$-$\omega$ based shear stress transport model to give accurate predictions of the onset and the amount of flow separation.

As for the boundary conditions, the total pressure was prescribed at the inflow boundary, whereas the mass flowrate was specified at the outlet section of the pump stage. The inlet duct, diffuser, and outlet duct were set as absolute stationary. The surfaces of the unshrouded-impeller blade and hub were the relative stationary except for the impeller shroud casing wall, which was modeled as stationary in the absolute frame of reference. All computations have been carried out using water at 25 ˚C as a working fluid.
A multiple frame of reference calculation with a general grid interface, which permits non-matching of node location, element type, surface extent, surface shape, and flow physics across the connection, solves a series of both rotating and stationary components, and the flow passing through the frame-change interface called a stage or mixing-plane interface is calculated by averaging the flux in the circumferential direction, although the variation in the meridional plane is preserved. Moreover, the rotationally periodic boundary conditions for each component with one blade passage are implemented in order to reduce the computational mesh size of the mixed-flow pump stage.

### 4.3 Internal flow characteristics at design flow and off-design performance curves

A computational study has been carried out to determine the performance characteristics of a mixed-flow pump under the normal operating conditions. Figures 6 to 8 show the representative flow dynamic phenomena for the design flowrate in a mixed-flow pump developed by the present design and analysis method. Here, the notation 'ii' means the interface between the inlet duct and the impeller, and 'id' does the interface between the impeller and the diffuser. In addition, 'do' denotes the interface between the diffuser and the outlet duct. Figure 6(a) illustrates the computed streamwise static and total pressure (normalized by the atmospheric pressure) distributions through the flow passage in the pump stage. The overall performance curves gradually increase and then level out. Observing the static pressure distribution in the diffuser part, the static pressure rises as the flow diffuses because of the expansion of flow area, and the local flow acceleration caused by the curvature near the hub region of the diffuser exit leads to a slight fall in the static pressure distribution.
In order to decrease the total pressure loss, i.e. the energy dissipation due to the exit swirls of a pump stage, or to improve the pump efficiency, the rotational (or tangential) component of the absolute velocity through the diffuser and outlet duct passages has to be minimized. As can be seen in Fig. 6(b), the calculated absolute flow angle (measured from the meridional plane) remains satisfactorily constant at around -2.1˚, which represents that the diffuser blading has been obtained to eliminate the swirling flow in the outlet of the pump stage.
Figures 7(a) and 8(a) show that the blade-loadings for the static pressure (normalized by the atmospheric pressure) are ideally distributed along the streamlines of the impeller and the diffuser over the blade-span, although the flow reversal phenomena appear near the exit regions, which is substantially regarded as the flow separation. In Figs. 7(b) to (d), the relative flow streamlines on the impeller blade surfaces have been well optimized without any separation lines. However, the elliptic configuration for the impeller trailing edge and the centrifugal force induced by the impeller rotation give rise to the flow separation along the trailing edge, and the secondary flows due to vortex-curling over the impeller blade tip affect the flow separation on the pressure surface of impeller near around 75% blade-span.

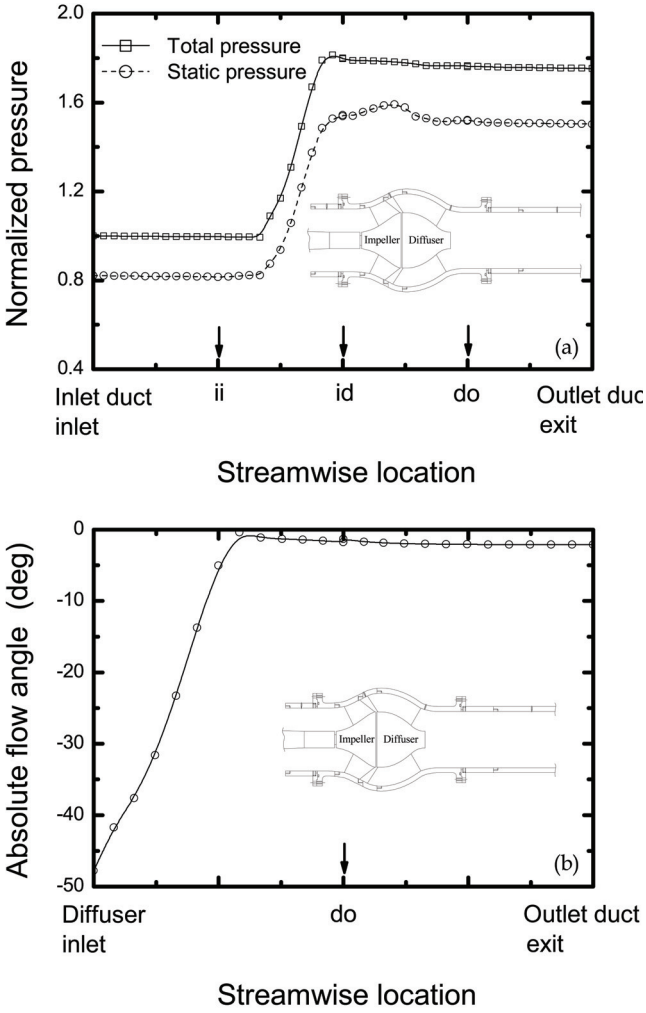


Fig. 6. Streamwise flow characteristics of a mixed-flow pump: (a) static and total pressure distributions, and (b) absolute flow angle distribution

As for the absolute streamlines on the diffuser blade, it is observed from Figs. 8(b) to (d) that except at the pressure side, the excessive flow separation appears near the exit hub region of the suction side, which is due to the adverse pressure gradient along the streamwise direction and the curvature around the exit hub region of the diffuser passage.

A comparison between the computed and measured performance characteristic curves of a mixed-flow pump is illustrated in Fig. 9. Here is the torque coefficient ($\tau$) defined as $30\times\acute{W}/(\rho\,\Omega^3 D_{in}^5)$ where $\acute{W}$ is the input power [W] and $\rho$ is the fluid density [kg/m$^3$], and the pump efficiency ($\eta$) defined as $\rho\,gHQ/\acute{W}$. As shown in this figure, the experimental data agree very satisfactorily with the predicted performance curves in a range of operating flow conditions.

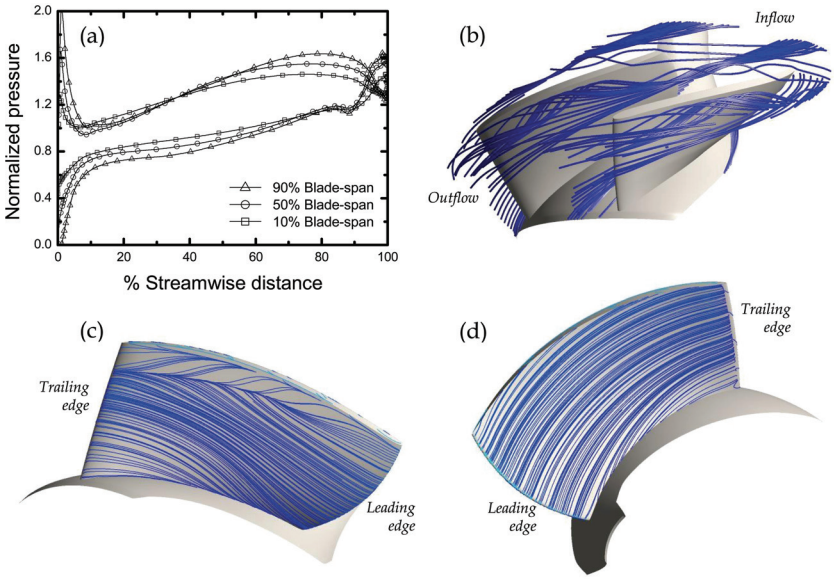


Fig. 7. Flow dynamic phenomena around the impeller blade: (a) blade-loading distributions (b) streamtubes for the overall flow, (c) streamline distribution on the pressure side, and (d) streamline distribution on the suction side

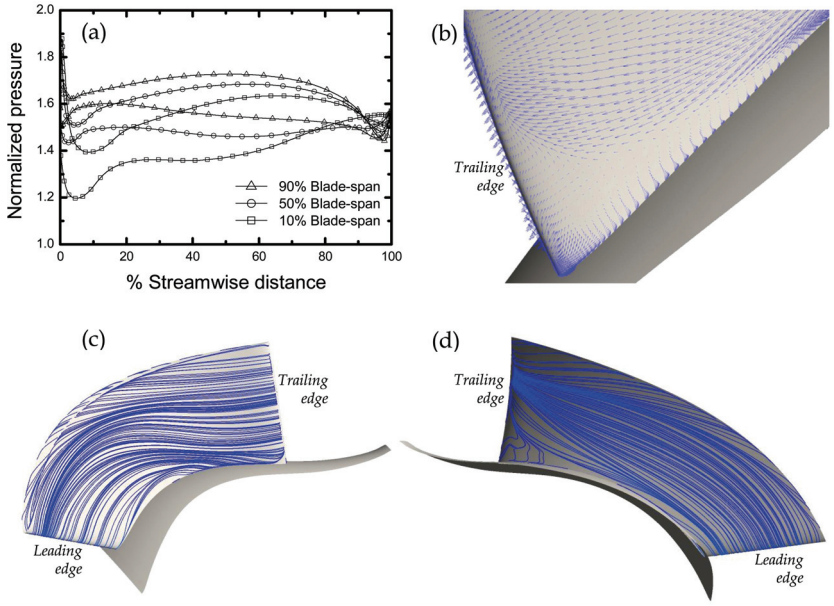


Fig. 8. Flow dynamic phenomena around the diffuser blade: (a) blade-loading distributions, (b) velocity vectors near the exit hub of the suction side, (c) streamline distribution on the pressure side, and (d) streamline distribution on the suction side

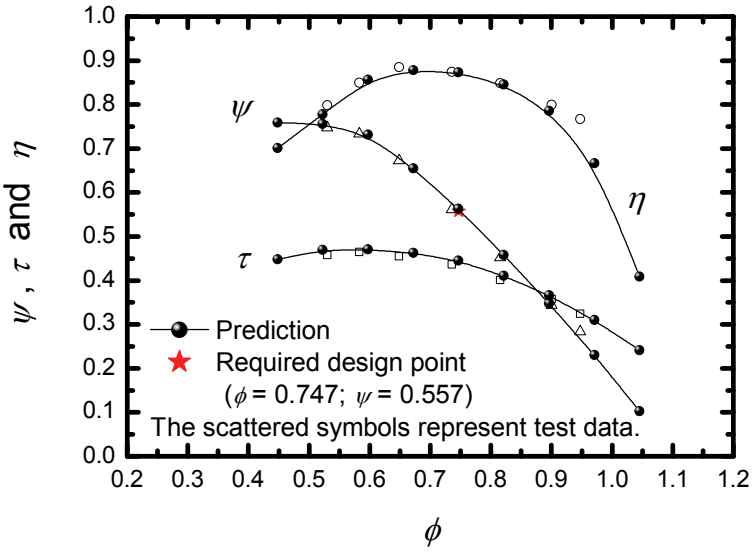


Fig. 9. The performance characteristic curves of a mixed-flow pump

#### 4.4 Cavitation performance characteristics

Generally, cavitation occurs in the liquid system when the local absolute static pressure in a flowing liquid is reduced to or below the vapour pressure of the liquid, thereby forming vapour bubbles. The bubbles suddenly collapse as they are convected to a high-pressure region. The consequent high-pressure impact may lead to hardware damage, e.g. local pitting and erosion, and emit noise in the form of sharp crackling sounds. Cavitation may also degrade the performance characteristics of hydraulic machinery.

Figure 10 demonstrates the cavitation performance characteristic curves of a mixed-flow pump developed by the present optimal design method, considering the highest pump efficiency. In order to investigate the flow dynamics of cavitation for the near-design flowrate ($\phi$ = 0.738 in Fig. 10) under the design pump speed, the side-view of the cavitating flow along the impeller blade has been photographed through the window of the test facility and compared with the isosurface plots, generated by the CFD code, for the vapour fraction of the fluid. In this figure, the cavitation parameter ($\sigma$) is defined as the ratio of the net positive suction head (NPSH) to the pump total head. At case (1), a small amount of cavitation, the inception of cavitation, occurs at the tip vortex generated by the tip of the impeller leading edge. With further reduction up to case (4) in the cavitation parameter, the tip-vortex cavitation has been more produced; the generated pump head still remains, however, constant without severe performance degradation. When the NPSH reaches a sufficiently low value over the knee of nearly constant head coefficient (for case (6)), the distortion of the flow pattern, by mixing more tip-vortex and face sheet cavitation with the

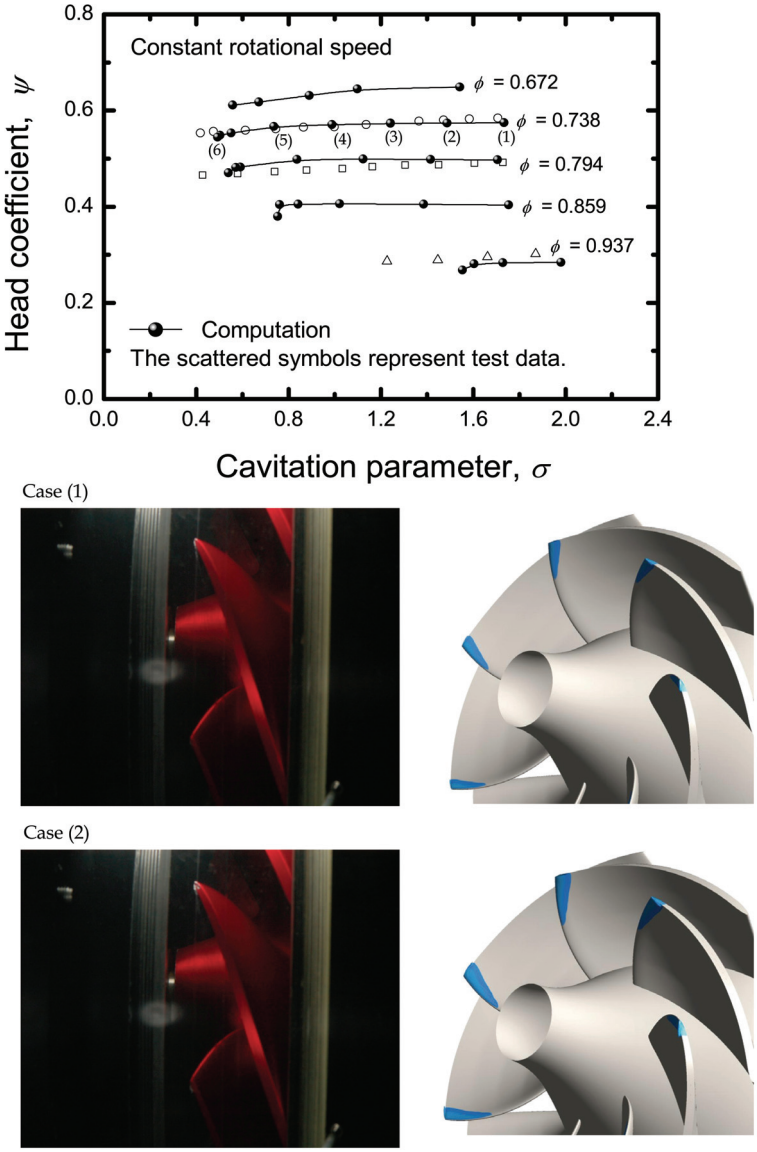


Fig. 10. Cavitation performance characteristics of a mixed-flow pump: NPSH curves

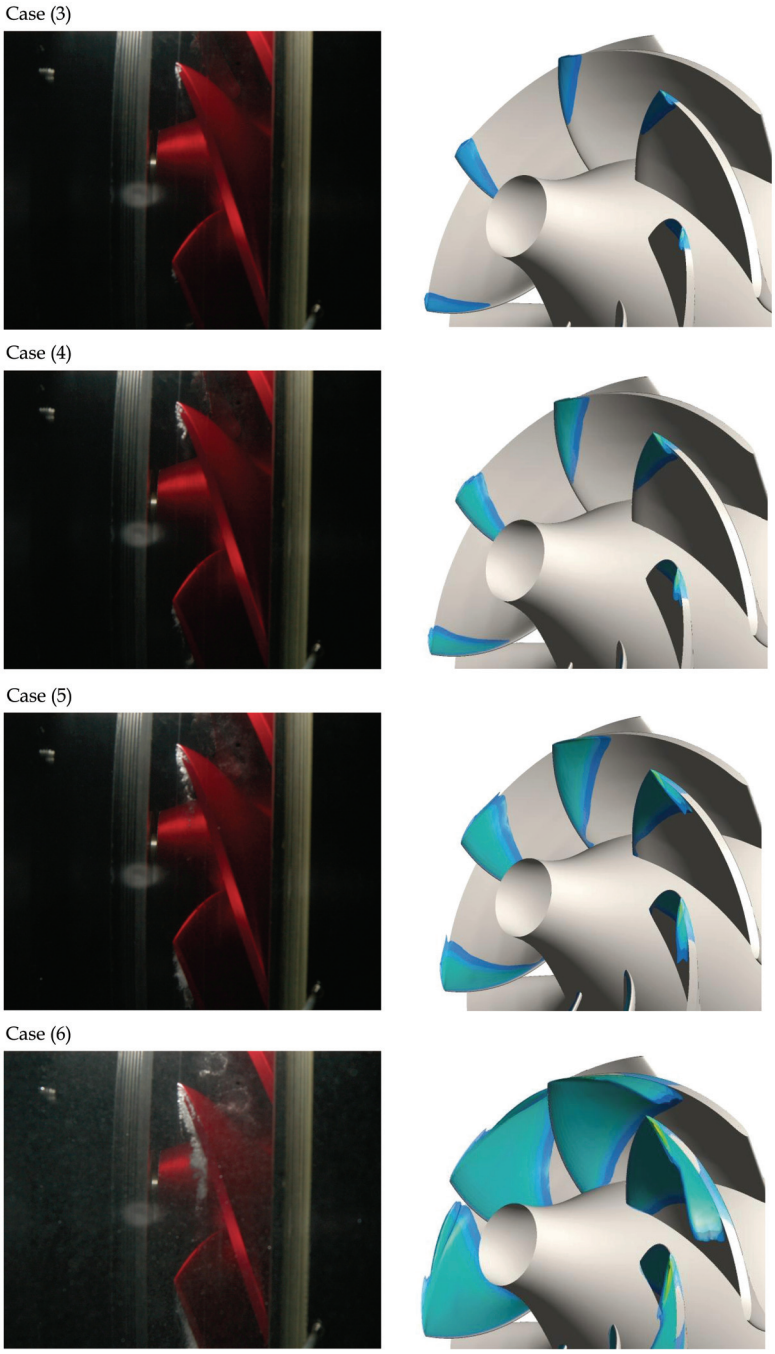


Fig. 10. (continued)

main flow between the impeller blades, extends across the flow channel and consequently leads to a sudden decrease in the total pressure rise. Comparing with the computational results, it is observed that the cavitating region is spread out over the suction surface as well as the leading edge of the impeller blade. By repeating the above procedure for several off-design flowrates under the same rotational speed, the suction performance curves, NPSH versus pump head, have been constructed as shown in Fig. 10. It can be seen that the cavitation performance curves predicted by the CFD code are in good agreement with the measured data. Meanwhile, it is worth noting that the cavitation on the diffuser blade surface has not appeared for the cavitating flow regimes, which means that the diffuser blade design, taking the flow angle leaving the rotating impeller into account, has been successfully carried out in this study.

Every pump has a critical NPSH, i.e. the required net positive suction head ($NPSH_R$), which is defined as the minimum NPSH necessary to avoid cavitation in the pump. Typically, the $NPSH_R$ is defined as the situation in which the total head decreases by some arbitrarily selected percentage, usually about 3 to 5%, due to cavitation. Although the pump system operates under the NPSH safety margin, it does not ensure the absence of cavitation, i.e. there might be light cavitation that does not give rise to severe hardware damage. However, further reduction in the $NPSH_R$ will lead to a major deterioration in the hydraulic performance.

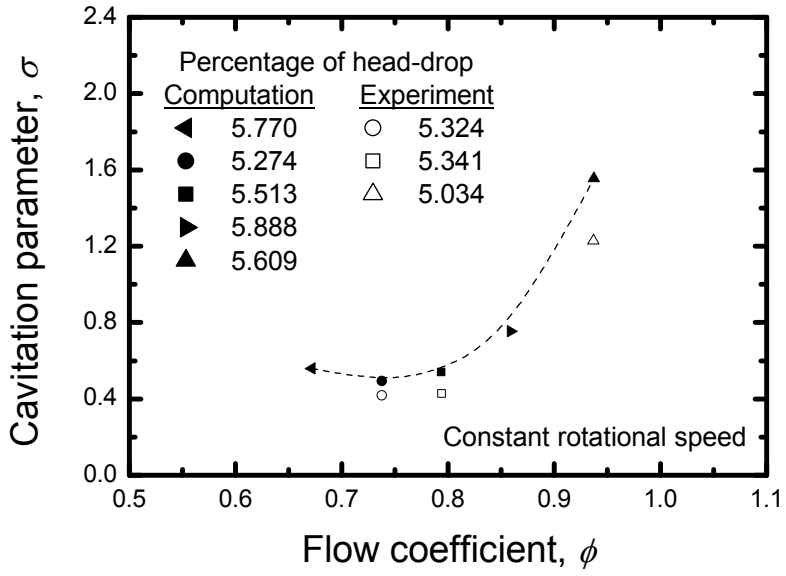


Fig. 11. Cavitation performance characteristics of a mixed-flow pump: $NPSH_R$ curve

This article employs an about 5% head-drop criterion to define the $NPSH_R$ for a mixed-flow pump. Figure 11 shows the performance characteristic curves for the $NPSH_R$ under the operating flowrate conditions. From this figure, it is noted that the $NPSH_R$ for a newly designed pump with the highest pump efficiency is minimized near the design flowrate regime.

## 5. Conclusions

A practical design and performance analysis procedure of a mixed-flow pump, in which the conceptual approach to turbomachinery design using the meanline analysis is followed by the detailed design and analysis based on the verified CFD code, has been presented in this Chapter. Performance curves predicted by a coupled CFD code were compared with the experimental data of a designed, hydrodynamically efficient, mixed-flow pump. The results agree fairly well with the measured performance curves over the entire operating conditions. A study for the cavitation performance characteristic curves of a mixed-flow pump has also been successfully carried out, although further research is definitely needed to suppress the tip-vortex cavitation under the normal condition.
The design and predictive procedure, including cavitation, employed throughout this study can serve as a reliable tool for the detailed design optimization and assist in the understanding of the operational characteristics of general purpose hydraulic and compressible flow turbomachinery.

## 6. Acknowledgements

The author would like to thank Dr. E S YOON of the Korea Institute of Machinery and Materials (KIMM) for his advice and support and it is also gratefully acknowledged that Dr. K S KIM and Dr. J W AHN of the Maritime and Ocean Engineering Research Institute (MOERI) provide the experimental data for a mixed-flow pump to publish this Chapter.

## 7. References

Aungier, R. H. (2000). *Centrifugal Compressors: A Strategy for Aerodynamic Design and Analysis,* American Society of Mechanical Engineers Press, ISBN 0791800938, New York

Balje, O. E. (1981). *Turbomachines: A Guide to Design, Selection, and Theory,* John Wiley, ISBN 0471060364, New York

Japikse, D. (1994). *Introduction to Turbomachinery,* Concepts ETI, ISBN 0933283067, Norwich

Neumann, B. (2005). *The Interaction between Geometry and Performance of a Centrifugal Pump,* John Wiley, ISBN 0852987552, New York

Oh, H. W. & Kim, K-Y. (2001). Conceptual design optimization of mixed-flow pump impellers using mean streamline analysis. *Proc. IMechE*, *Part A: J. Power and Energy*, 215, A1, 133-138, ISSN 09576509

Stepanoff, A. J. (1993). *Centrifugal and Axial Flow Pumps: Theory, Design, and Application,* Krieger Publishing Company, ISBN 0894647237, Florida

# 11

# Hydrodynamic Simulation of Cyclone Separators

Utikar[1], R., Darmawan[1], N., Tade[1], M., Li[1], Q, Evans[2], G., Glenny[3], M. and Pareek[1], V.
[1]*Department of Chemical Engineering, Curtin University of Technology, Perth, WA 6845,*
[2]*Centre for Advanced Particle Processing, University of Newcastle, Callaghan, NSW 2308,*
[3]*BP Kwinana Refinery Pty Ltd, Mason Road, Kwinana, WA 6167,*
*Australia*

## 1. Introduction

Cyclone separators are commonly used for separating dispersed solid particles from gas phase. These devices have simple construction; are relatively inexpensive to fabricate and operate with moderate pressure losses. Therefore, they are widely used in many engineering processes such as dryers, reactors, advanced coal utilization such as pressurized and circulating fluidized bed combustion and particularly for removal of catalyst from gases in petroleum refinery such as in fluid catalytic cracker (FCC). Despite its simple operation, the fluid dynamics and flow structures in a cyclone separator are very complex. The driving force for particle separation in a cyclone separator is the strong swirling turbulent flow. The gas and the solid particles enter through a tangential inlet at the upper part of the cyclone. The tangential inlet produces a swirling motion of gas, which pushes the particles to the cyclone wall and then both phases swirl down over the cyclone wall. The solid particles leave the cyclone through a duct at the base of the apex of the inverted cone while the gas swirls upward in the middle of the cone and leaves the cyclone from the vortex finder. The swirling motion provides a centrifugal force to the particles while turbulence disperses the particles in the gas phase which increases the possibility of the particle entrainment. Therefore, the performance of a cyclone separator is determined by the turbulence characteristics and particle-particle interaction.

Experimental and numerical studies have been carried out in the last few decades to develop a better understanding of the flow field inside the cyclone separators. In the early years, empirical models were built (e.g. Shepherd & Lapple, 1939; Lapple, 1951; Barth, 1956; Tengbergen, 1965; Sproul, 1970; Leith & Licht, 1972; Blachman & Lippmann, 1974; Dietz, 1981 and Saltzmann, 1984) to predict the performance of industrial cyclones. However, these models were built based on the data from much smaller sampling cyclones therefore; they could not achieve desired efficiency on industrial scales as the industrial cyclone operates in the turbulent regime while sampling cyclones operate under the transitional conditions. One of the major drawbacks of these empirical models is the fact that they ignore two critical factors that determine the performance of a cyclone namely the unsteadiness and asymmetry. Many flow phenomena such as high turbulence, flow reversal, high

vorticity, circulating zones and downflow also occur. The empirical models do not include these phenomena in their analysis and hence are limited in their application. Computational fluid dynamics (CFD) models on the other hand can accurately capture these aspects and thus can take a significant role in analyzing the hydrodynamics of cyclone separators. A validated CFD model can be a valuable tool in developing optimal design for a given set of operating conditions. However, cyclone separators pose a peculiar fluid flow problem. The flow in cyclone separators is characterized by an inherently unsteady, highly anisotropic turbulent field in a confined, strongly swirling flow. A successful simulation requires proper resolution of these flow features. Time dependent turbulence approaches such as large eddy simulation (LES) or direct numerical simulation (DNS) should be used for such flows. However, these techniques are computationally intensive and although possible, are not practical for many industrial applications. Several attempts have been made to overcome this drawback. Turbulence models based on higher-order closure, like the Reynolds Stress Model, RSM, along with unsteady Reynolds averaged Navier – Stokes (RANS) formulation have shown reasonable prediction capabilities (Jakirlic & Hanjalic, 2002). The presence of solids poses additional complexity and multiphase models need to be used to resolve the flow of both the phases.

In this chapter we review the CFD simulations for cyclone separators. Important cyclone characteristics such as the collection efficiency, pressure and velocity fields have been discussed and compared with the experimental data. Several significant parameters such as the effect of geometrical designs, inlet velocity, particle diameter and particle loading, high temperature and pressure have also been analysed. The chapter discusses peculiar features of the cyclone separator and analyses relative performance of various models. Finally an example of how CFD can be used to investigate the erosion in a cyclone separator is presented before outlining general recommendations and future developments in cyclone design.

## 2. Basic design of cyclone separators

A cyclone separator uses inertial and gravitational forces to separate particulate matter from gas. Accordingly various designs have been proposed in literature (Dirgo & Leith, 1986). Figure 1 shows a schematic of widely used inverse flow cyclone and depicts main parts and dimensions. The particle laden gas enters the cyclone separator with a high rotational velocity. Different inlet configurations like tangential, scroll, helicoidal and axial exist to provide high rotational velocity. Of these, the tangential and scroll configurations are most frequent. The rotational flow then descends near the wall through the cyclone body and conical part until a reversal in the axial velocity making the gas flow in the upwards direction. Where this occurs is called as the vortex end position. The upward rotating flow continues along the cyclone axis forming a double vortex structure. The inner vortex finally leads the flow to exit through a central duct, called the vortex finder. The vortex finder protrudes within the cyclone body. It serves both in shielding the inner vortex from the high inlet velocity and stabilizing its swirling motion. The solids are separated due to the centrifugal force and descend helicoidally along the cyclone walls and leave the equipment through the exit duct.

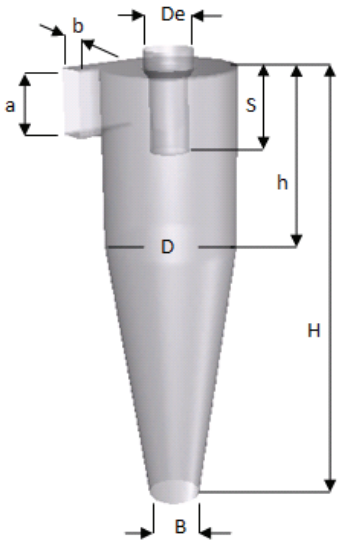


Fig. 1. Typical design of cyclone separator

| Source | Stairmand (1951) | Stairmand (1951) | Lapple (1951) | Swift (1969) | Swift (1969) | Swift (1969) |
|---|---|---|---|---|---|---|
| Duty | High efficiency | High throughput | General purpose | High efficiency | General purpose | High throughput |
| D | 1 | 1 | 1 | 1 | 1 | 1 |
| a/D | 0.5 | 0.75 | 0.5 | 0.44 | 0.5 | 0.8 |
| b/D | 0.2 | 0.375 | 0.25 | 0.21 | 0.25 | 0.35 |
| De/D | 0.5 | 0.75 | 0.5 | 0.4 | 0.5 | 0.75 |
| S/D | 0.5 | 0.875 | 0.625 | 0.5 | 0.6 | 0.85 |
| h/D | 1.5 | 1.5 | 1 | 1.4 | 1.75 | 1.7 |
| H/D | 4 | 4 | 4 | 3.9 | 3.75 | 3.7 |
| B/D | 0.375 | 0.375 | 0.25 | 0.4 | 0.4 | 0.4 |

Table 1. Standard Geometrical Design of Industrial Cyclone Separator

For convenience, the dimensions of various cyclone parts are usually stated in dimensionless form as a ratio to the cyclone diameter, D. This method allows a comparison between the cyclone designs, without using the actual size of each individual part. Table 1 lists a few examples of industrial cyclone types (Leith and Licht, 1972). A more comprehensive range of designs can be found in Cortes and Gil (2007). The performance of a cyclone separator is measured in terms of the collection efficiency defined as the fraction of solids separated and the pressure drop. By nature, the flow in a cyclone separator is multiphase (gas–solid) and shows strong gas–solid–solid interactions. The gas–solid interactions can only be neglected at very low solid loadings. Early CFD models focused on single phase flow and turbulence interactions inside the cyclone. Multiphase CFD simulations that account for the gas–solid and gas–solid–solid interactions and its immediate results concerning cut sizes and grade-efficiency are relatively scarce in the

literature. The subsequent sections discuss available CFD models and their predictive capabilities with respect to the flow field, pressure drop and collection efficiency.

## 3. Computational fluid dynamics models for cyclone separators

The flow inside a cyclone separator is inherently complex and poses many practical difficulties for numerical simulations. The primary difficulty arises from the fact that the turbulence observed in cyclones is highly anisotropic. This renders most of the first order turbulence closures, like the popular k-ε model, unusable for reliable prediction of the flow characteristics. Several attempts were made to overcome this limitation. Boysan et al. (1982, 1983) were one of the first to report CFD studies of cyclone flows. These early studies realized that the standard k-ε turbulence model is not able to accurately simulate this kind of flow and that at least a second-order closure, e.g., RSM is needed to capture the anisotropy and achieve realistic simulations of cyclone flows. The authors found reasonable agreement between the experimental data and simulations using a mixed algebraic-differential, stationary RSM. Many studies have since been performed to capture the turbulence characteristics accurately. The next section will review these in detail.

Selection of numerical parameters, especially the discretization of the advection terms, poses an additional difficulty and plays an important role on the accuracy of simulations. First order discretization is prone to numerical diffusion and often produces misleading results in cyclone separator simulations. The use of hexahedral grids for the main flow region (Harasek et al., 2004) and a second order accurate advection scheme (Bunyawanichakul et al. 2006) has shown a significant improvement in CFD predictions. The flow in a cyclone separator is characterized by unsteady structures like secondary eddies and the precessing vortex core (PVC). An adequate resolution in space and time is necessary to capture these dynamic features. Early CFD studies focused on the steady state solution of the flow (Boysan et al. 1982) due to limited availability of computational power and low spatial resolution that resulted into artificial dampening of instabilities. With increasing computational power, unsteady state simulations with a sufficiently resolved mesh have become standard (Derksen et al. 2006).

Finally, the complexity arises from the presence of solids and their interaction with the gas phase flow. Two approaches, namely the Eulerian-Eulerian approach and the Eulerian-Lagrangian approach have been adopted in the literature to predict the multiphase flow. In the Eulerian–Eulerian approach both the solid particles and the fluid are treated as the interpenetrating continua. The governing equations are then formulated and solved for each phase. This approach can account for the complex phenomena such as the agglomeration and break-up by using a population balance model. The Eulerian-Eulerian approach requires that the interactions between the phases are modelled and are accounted for. These interactions are not yet well understood. The Eulerian-Eulerian approach also requires a specification of the boundary conditions for the particulate phase mutual interaction between particles, and interactions with the wall. In many situations, this information is not readily available. Due to these inherent drawbacks this approach has found limited application in cyclone separator simulation (See for example, Meier et al. 1998 and Qian et al. 2006).

In the Eulerian-Lagrangian approach, particle trajectories are obtained by integrating the equation of motion for individual particles, whereas, the gas flow is modelled using the Navier-Stokes equation. The flow structures in dispersed two-phase flows are a direct result

of the interactions between the two phases. Accordingly, a classification based on the importance of the interaction mechanisms has been proposed (Elghobashi, 1994). Depending on the existence of mutual, significant interaction between particles, two different regimes namely dilute and dense two-phase flow can be distinguished (See figure 2). For $\alpha_p < 10^{-6}$ and $L/d_p > 80$, the influence of particles on the gas can be neglected. This is known as ''one-way coupling''. The influence of the particle phase is pronounced at higher volume fractions and has to be accounted for. This is known as ''two way coupling''. For larger particles at higher volume fraction ($\alpha_p > 10^{-3}$, $L/d_p < 8$), the interparticle interactions become important, both through the physical collisions and indirect influence on the nearby flow field. The collisions can lead to coalescence and break-up, which must then be considered. This regime is frequently called the ''four-way coupling''regime. The Eulerian-Lagrangian approach is more suited to dilute flows with one- or two-way coupling. The approach is free of numerical diffusion, is less influenced by other errors and is more stable for the flows with large gradients in particle velocity. The treatment of realistic poly-dispersed particle systems is also straightforward. These attributes make Eulerian-Langrangian approach more suitable for the simulation of gas – particle in cyclone separators. The Eulerian-Lagrangian approach is discussed in section 1.3.2.

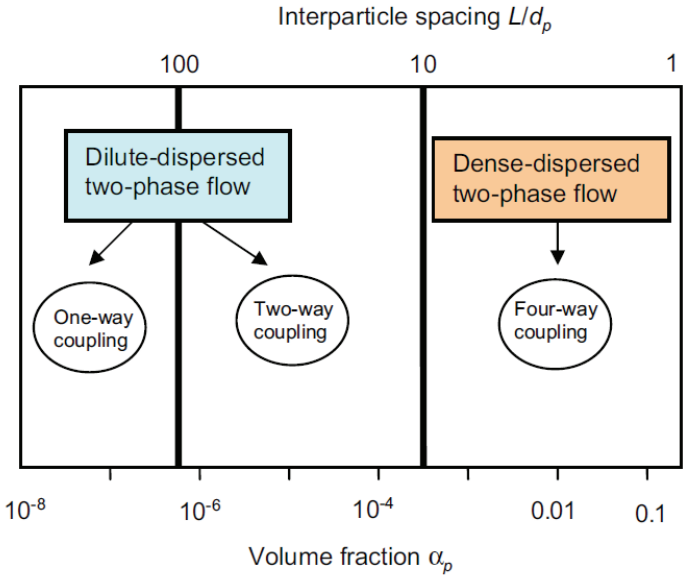


Fig. 2. Regimes of dispersed two-phase flow as a function of the particle volume fraction/interparticle spacing. Adapted from Elghobashi, 1994.

### 3.1 Choice of turbulence model

The preceding discussion makes it clear that the choice of the turbulence model is the most critical aspect of CFD simulation of cyclone separators. An appropriate turbulence model should be selected to resolve these flow features. As mentioned previously, the models based on first order turbulence closure have a limited ability for capturing the real flow. Generally it is thought that at least a second-order closure is needed to capture the

anisotropy and achieve realistic simulations (Hoekstra et al., 1999). While stressing the need for a higher order turbulence model, one needs to keep in mind that as we resolve larger ranges of time and length scales, the computational requirements escalate tremendously. A trade-off between the accuracy and speed of computation is therefore needed for practical simulations.

Of the three available approaches to capture the turbulent characteristics, namely RANS, LES and DNS, RANS approach are the oldest approach to turbulence modeling. In the unsteady RANS, an ensemble averaged version of the governing equations that also includes transient terms is solved. Turbulence closure can be accomplished either by applying the Boussinesq hypothesis, i.e. using an algebraic equation for the Reynolds stresses or by using the Reynolds stress model (RSM), i.e. by solving the transport equations for the Reynolds stresses. In the LES approach, the smaller eddies are filtered and are modeled using a sub-grid scale model, while the larger energy carrying eddies are simulated. The DNS solves fully-resolved Navier – Stokes equations. All of the relevant scales of turbulent motion are captured in direct numerical simulation. This approach is extremely expensive even for simple problems on modern computing machines. Until sufficient computational power is available, the DNS will be feasible only for model problems; leaving the simulation of industrial problems to LES and RANS approaches. Although LES of full-size equipment is possible, it is still costly partly due to the escalating computational cost near the wall region. The unsteady RANS approaches are comparatively far less expensive.

Within the RANS approach, comparative studies have been performed for different turbulence models. Hoekstra et al. (1999) compared the relative performance of the k-ε model, RNG k-ε model (a variation of the k-ε model based on renormalization group theory) and Launder, Reece, Rodi and Gibson (LRRG) models (a differential RSM model). The simulations were compared with Laser Doppler Anemometry (LDA) velocity measurements. Tests were performed with three different vortex finder diameters, which produced three different swirl numbers. The results for the tangential velocity are shown in Figure 3. For all runs, the k-ε model predicted only the inner vertex structure clearly contradicting the experimental observations showed two distinguishing vortices. The RNG k-ε model showed significant improvement, while the RSM exhibited the best behavior. Pant et al. (2002) and Sommerfeld and Ho (2003) have also reported similar observations. Gimbun et al. (2005) studied the effect of temperature and inlet velocity on the cyclone pressure drop. They compared four different empirical models, the k-ε model, and the RSM with the experimental data. Their study of the effect of the inlet velocity on the pressure drop found that the RSM gave the closest agreement with the experimental results. The superiority of the RSM over other models has been established by Meier et al. (1999), Xiang et al. (2005), Qian et al. (2006), Wan et al. (2008) and Kaya et al. (2009). These investigations of various characteristics of cyclone separator flow field, such as velocity profiles, pressure drop, effect of particle size, mass loading, separation efficiency, effect of pressure and temperature, have reemphasized the ability of the RSM for realistic prediction of the flow field inside cyclone separators.

Although, the superiority of the RSM over the other models has been established, it is still not clear which is the most suitable form of the RSM for cyclone separator simulations as both algebraic and differential RSMs have been employed. Between these two, the differential form of the RSM is more accurate and should be preferred over the algebraic

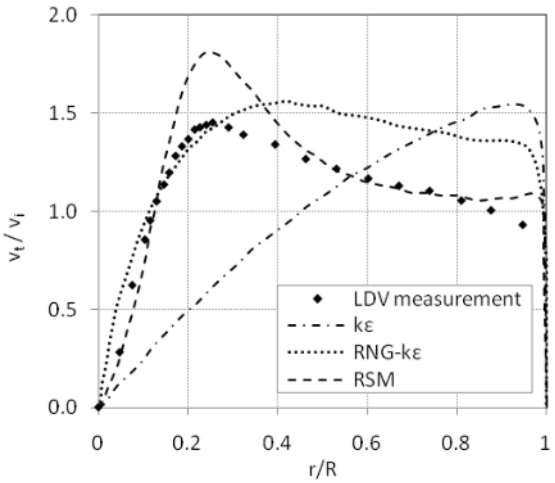


Fig. 3. Comparison of tangential velocity profiles (Adapted from Hoekstra et al., 1999)

form when the extra cost of the calculation is affordable (Hogg & Leschziner, 1989). Within the differential RSMs, the difference between a basic and an advanced differential RSM is also of relevance. For example, Grotjans et al. (1999) compared the predictions of various turbulence models with LDA measurements for the tangential velocity profile in an industrial hydrocyclone. Turbulence models including two differential RSM implementations, the basic Launder, Reece, Rodi (LRR) implementation and the advanced Speziale, Sarkar and Gatski (SSG) implementation along with the standard k-ε and a k-ε model modified to account for the streamline curvature (the k-ε cc model) were tested. They found the flow field to be highly sensitive to the model choice, whereas the pressure distribution predictions were relatively robust. The typical Rankine profile was obtained only by means of the RSMs. The SSG model produced more acceptable results compared to the LRR model in the lower part of the cyclone. The LRR model also underpredicted tangential velocity near the cyclone center.

Despite a number of advances, the ability of unsteady RANS simulations with advanced RSM to accurately predict complex flow structures has not been fully established. Only relatively stable and ordered flows have been simulated. In order to fully establish their viability for cyclone separator simulations, these models should be tested for conditions of highly incoherent and variable PVC. Meanwhile, LES simulation of swirling and cyclone flows is presently becoming a new standard (Derksen, 2008). Derksen and van den Akker (2000) were among the first to simulate the PVC phenomenon by means of LES simulations. The capabilities of LES to simulate the turbulent flow in a cyclone separator have been reported by Shalaby et al. (2005), Derksen (2003), Derksen et al. (2006) and Shalaby et al. (2008). Early simulations (Derksen & van den Akker, 2000) were limited to small scale cyclones at a moderate inlet Reynolds number. With increasing computational power, simulation of industrial scale equipment (with Re = 280000) have been reported (Derksen et al. 2006). The LES approach seems to offer a very realistic simulation. However due to the scale and complexity of today's industrial cyclone separator simulations, the unsteady RANS approach with higher order turbulence closures is the only practical approach that

offers affordable realistic predictions of flow inside cyclone. It is only a matter of time that resolved simulations using LES will become the preferred alternative. The behavior of particles and their interaction with continuous phase is paramount in cyclone separators and should be accounted for regardless of the turbulence models.

### 3.2 Eulerian–Lagrangian approach for multiphase flow

The Eulerian-Lagrangian approach is generally more suitable for cyclone separator simulation over the Eulerian-Eulerian approach. In the Eulerian-Lagrangian approach, the gas is treated as a continuum while the solid phase is resolved by tracking individual solid particles (Lagrangian tracking) through the flow field. Lagrangian tracking essentially applied the Newton's second law of motion to a particle to determine its position. The forces generally considered are the drag force, gravity buoyancy, virtual mass and Basset forces. For cyclone separators only the drag and gravity forces are of significance due to the large gas-particle density ratio. Of these, drag force, due to the relative slip between the particle and gas, is the dominating force and is typically modeled using an empirical correlation like the Morsi Alexander model (Morsi & Alexander, 1972).

Depending on the volume fraction, either one-way or two-way coupling is applied to account for the interactions between the two phases. For dilute flows, the gas phase flow is not influenced by the solid flow and Lagrangian tracking decoupled from the gas flow calculation is sufficient. The advantage of this is that the Lagrangian tracking can be performed as a post-processing step as a calculation using the converged and time averaged single phase simulation. To achieve a statically meaningful solution in the simulation, a large number of tracked particles (at least $3 \times 10^5$ particles) are required (Sturgess et al., 1985). Furthermore, the time averaged gas flow field smooth out all the turbulent fluctuations. Only particles of large size will behave as exclusively influenced by the time-averaged gas flow. While very small particles will tend to fluctuate following turbulent fluctuations (known as turbulent diffusion) of the gas velocity there will be a complete range of intermediate behaviors between these two extremes. Turbulence fluctuations are random functions of space and time and several ways are available to accommodate them, mostly by including additional terms in the time averaged equation. Amongst these, the stochastic discrete random walk model is the most popular. In this model a prefixed probability distribution of velocity is assumed. The equation of motion for the discrete velocities and particle sizes is solved and the average of the forces is obtained (Gosman & Ioannides, 1981). The Stochastic Lagrangian model has been used successfully by many researchers including Yuu et al. (1978), Boysan et al. (1982), Hoekstra et al. (1999), Sommerfeld and Ho (2003) and Wang et al. (2006). The one-way coupling approach assumes negligible effect of particles on the gas flow. As a result of the collection process, high local solid concentration is observed in the near wall regions. These regions are not effectively modelled using one-way coupling. Hence in most of the Lagrangian tracking results the computational simulations show larger cut-sizes than those observed experimentally.

The effectiveness of the LES to accurately predict the gas flow field in cyclone separators has been established (Derksen, 2003). Subsequently, the Lagrangian tracking has been applied to calculate the particle flow in the LES simulations (Narsimha et al., 2006). The dynamic nature and enormous quantity of time dependent data generated by the LES prohibits post-priori calculation of the Lagrangian tracking and demands instantaneous tracking of a large number of particles. Moreover, since all the turbulence length scales are not fully resolved, the stochastic model for turbulent particle diffusion still needs to be applied. This leads to an

extremely intensive method for predicting the cyclone performance. Several alternatives have been proposed, based on average, frozen and periodic LES-velocity fields. Amongst these methods, the periodic approximation produces closest match to experimental data, however, it is the most costly costly method in terms of computational requiremnts. Using this approximation, the simulation results are much closer to the experimental data than the classical Lagrangian tracking (Derksen, 2003).

Depending on the particle size distribution, agglomeration may also become an important factor in predicting the cyclone efficiency. Particle sizes ranging from 1 to 10 μm tend to agglomerate due to the turbulent flow. For this range of particle size the turbulence induced motion is more dominant compared to that of both Brownian motion and gravitational motions. Van der Waal forces are considerably strong enough between the particles to result in particle agglomeration and bigger size particles. Sommerfeld and Ho (2003) observed that the separation efficiency increased considerably for smaller particles in an agglomerating regime. Although, the predictions were not in a perfect agreement with the measurements regarding the grade efficiency curve, they revealed the importance of particle agglomeration on the total separation efficiency.

At higher solid concentrations, the interactions between the two phases become significant and a two-way coupling for the momentum between the particulate and fluid phases needs to be considered. Traditionally, the particle-source-in cell (PSIC) model (Crowe et al. 1977) is used for this purpose. In this model, the flow field is calculated first without the particle-phase source terms until a converged solution is achieved. A large number of ''parcels'' (i.e. discrete particles representing large groups with the same properties) are then tracked through the flow field. The source terms are then obtained from these tracks for a second Eulerian calculation of the gas flow. The procedure is repeated iteratively until convergence is achieved. The accuracy of this method depends on the number of parcels. Typically a minimum of 10000 to 20000 parcels are used. Computational effort also escalates as the number of particles needed to represent the dispersed phase increases. For this reason, two-way coupling therefore is still uncommon. Derksen et al. (2008) studied the effect of mass loading on the gas flow and solid particle motion in a Stairmand high efficiency cyclone separator using a two-way coupled Eulerian-Lagrangian simulation. They observed that compared to one-way coupling the two-way coupled simulation yield higher overall efficiencies. They found that the dependence of the separation efficiency on the inlet solid loading is the result of two competitive two effects namely, the attenuation of the swirl, which lowers the efficiency due to a lowered centrifugal force, and the attenuation of turbulence, which augments the efficiency through a decreased turbulent diffusion of particles.

The standard Lagrangian approach neglects the particle-particle interactions. However at higher solid concentration, these interactions must be included. The discrete element method (DEM) solves the force balance on individual particles and takes into consideration both the particle-particle and particle-gas interactions and has been used to simulate the motion of particles for highly dense flows (Zhu et al. 2007). This approach gives information about the position and velocities of individual particles. Conventional DEM approaches assume a simplified flow field and are not suitable for simulating the particle flow in cyclone separators. Recent advances in DEM and its coupling with the CFD codes has allowed simulation of particle flow within complex flow fields (e.g. Chu et al. 2009), but at this stage the method remains very costly and is limited by the number and size of particles.

## 4. Cyclone flow and pressure fields

The collection efficiency and pressure drop performance of the cyclone separator are a direct result of the flow patterns of gas and solid and pressure field inside the cyclone. In a time-averaged basis, the dominant flow feature in a cyclone separator is a vortical flow that can be described as the Rankine vortex, which is a combination of a free outer vortex and a forced inner vortex. Apart from the inlet gas velocity and geometrical parameters, the wall friction and solid loading also influence the strength of the vortex. The empirical models often neglect the later two aspects and hence are limited in their application. Computational modelling is needed to resolve the velocity and pressure fields (Kim et al., 1990, Hoekstra et al., 1999, Ma et al., 2000, Slack et al. 2000 and Solero et al 2002).

### 4.1 Axial velocity

The axial velocity of the gas phase is a major influence in the transportation of particles to the collection device. Empirical models based on the double vortex structure postulate radially constant values for the downward flow in the outer vortex and upward flow in the inner vortex. Both these values are zero at the axial position where the vortex ends. In reality, the profiles are not flat but exhibit maxima and minima. Typically the downward flow shows a maximum near the walls, while the upward flow shows either a maximum or a minimum at the symmetry axis. The diameter of the swirl of gas entering the vortex finder is larger than the vortex finder diameter itself. Consequently, the gas velocity expected to increase and peak at the vortex finder either on the centre or at the sides. This results in an inverted V or an inverted W shaped profile as seen in figures 4a and 4b for the inner vortex. The V pattern forms an axial velocity maximum at the vortex core of the cyclone while the W pattern forms an axial velocity maximum at the vortex finder radius with a minimum at the vortex core.

Figures 4a and 4b show the axial velocity profile in a cyclone separator at a horizontal position of 0.125 m below the vortex finder for two $D_e/D$ ratios of 0.3 and 0.375, respectively. It can be seen that with relatively small difference in the dimensionless length parameters, the axial velocity in the inner vortex region shift from a V pattern to a W pattern. Harasek et al. (2008) studied this phenomenon by investigating the effect of the vortex finder diameter on the axial velocity profile. Their simulation findings could not determine the conditions when there is a transition in the velocity profile. For smaller $D_e/D$ ratio ($< 0.45$) the V shaped axial velocity is more stable was dominant. They also observed temporary W patterns due to turbulent fluctuations. At higher $D_e/D$ ratio ($> 0.53$), the possibility of back flow occurring increases and the air from outside is more likely to be drawn into the core due to the low pressure at the centre of the vortex. Thus, a W pattern is more stable.

The $D_e/D$ ratio is not the only factor that affects the axial velocity profile. The downstream exit conditions, at both gas and particle outlets, have been shown to significantly affect the reversed flow to the vortex finder and the whole internal flow. For example, Hoffmann et al. (1996) showed that for cyclone separators with diplegs, the upward flow has a V-shape profile. This was confirmed by the numerical study by Velilla (2005). The V-shape profile is expected to have greater separation efficiency due to a narrower ascending flow region with higher swirl. Some observation by Wang et al. (2006) and Liu et al. (2006) indicate that the centre of the upward flow does not always coincide with the centre of the geometrical cyclone. This is attributed to the chaotic flow within the cyclone. In such cases, an eccentric vortex finder can be designed to reduce the pressure drop and weaken the chaotic flow.

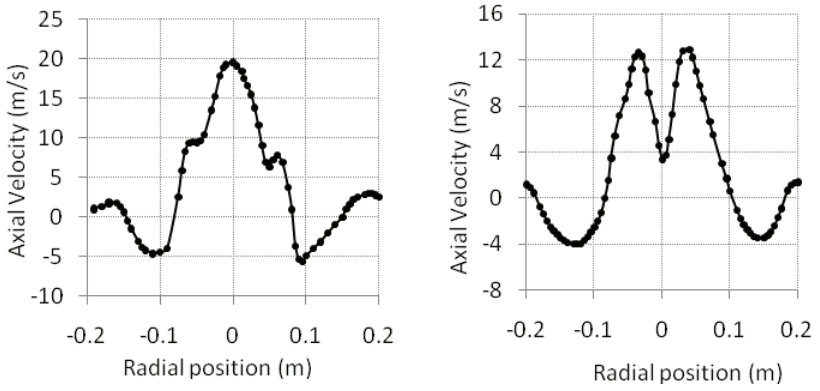


(a) (b)

Fig. 4. Typical axial velocity profile (a) V pattern and (b) W pattern (Adapted from Harasek et al. 2008)

### 4.2 Radial velocity

The radial velocity affects the particle bypass and is an important factor in analyzing the particle collection and losses of efficiency. Frequently the radial velocity is assumed to be of much lesser magnitude than the other components. However, this is valid only in the outer vortex, and especially near the vortex finder, the radial velocity increases rapidly towards the vortex core (Muschelknautz, 1972).

A typical example of radial velocity field is shown in figure 5. The plots are at the center of the cyclone (figure 5a) and at cut of sections B-B and C-C (figure 5b). The radial velocity profile at section D-D of the cyclone (figure 5c) has a helical shape. The axis of the vortex is slightly curved and not aligned with the geometrical axis of the cyclone. It can be seen from figure 5a that the distribution of the radial velocity is positive on one side and negative at the other side. This is due to the non-symmetrical shape of a conventional tangential inlet cyclone. It is also observed that the radial velocity increases sharply towards the vortex core. Alekseenko (1999) suggests that this phenomenon is the result of vortex rotation along the flow, in a helical shape, around the geometric axis of the cyclone. Points A and D in figure 5 show a short circuiting flow that can hinder the cyclone separator performance. Point A is called 'lip leakage". It is located below the rim of the vortex finder where a radial component of velocity flows inward directly to the vortex finder instead of flowing down the outside wall and returning in the central core. Point D is located near the inlet duct and the vortex finder. Just outside the vortex finder the radial velocity indicates an inward flow from the inlet (a negative value) but due to the effect of the centrifugal force around the vortex finder its value rapidly changes to zero and becomes positive. This results in an instability in the cyclone and it may affect the cyclone performance.

### 4.3 Tangential velocity

The flow within a cyclone is dominated by the tangential velocity and strong shear in the radial direction which results in a centrifugal force that determines the particle separation. Subsequently, much discussion within cyclone separator studies is focused on the tangential velocity (Cortes & Gil, 2007).

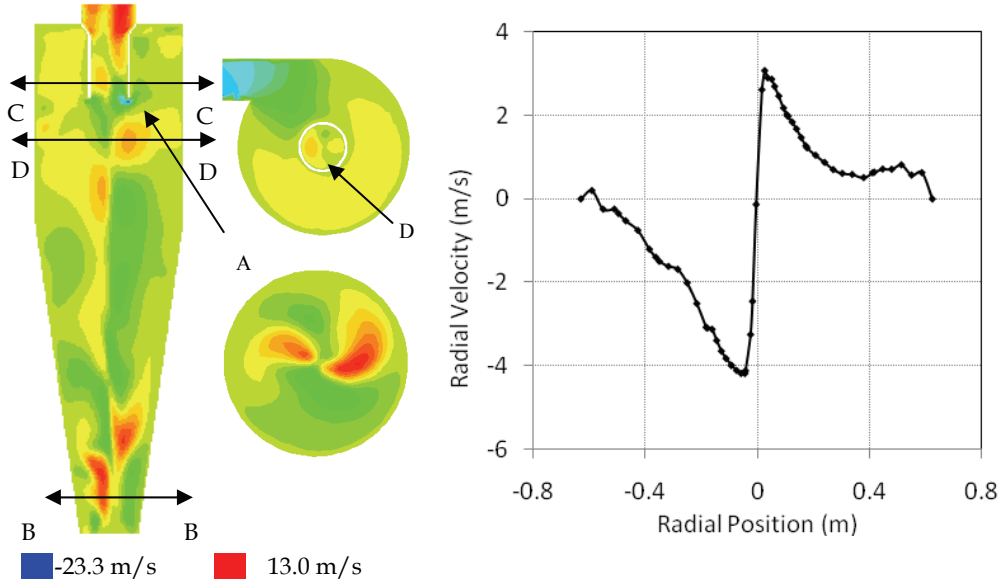


Fig. 5. (a) Contours of radial velocity at a vertical plane (b) Contours of radial velocity at horizontal cut off section B-B and C-C (c) radial velocity profile at section D-D

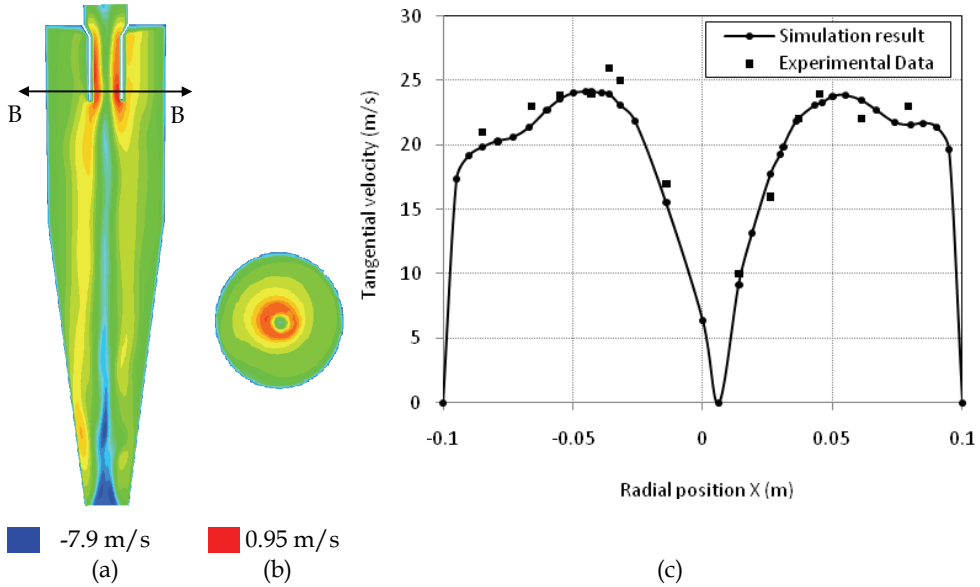


Fig. 6. (a) Contours of tangential velocity at a vertical plane (b) Horizontal cut off section at Line B-B (c) Example of comparison of numerical and experimental results for tangential velocities (Adapted from Wang et al., 2006)

Typical contour plots of the tangential velocity in both vertical and horizontal planes are shown in figures 6a and 6b, respectively. Figure 6c shows comparison of numerical and experimental results for tangential velocities from Wang et al. (2006). The cyclone has an asymmetrical shape and as can be seen from figure 6a, the axis of the cyclone does not exactly coincide with the axis of the vortex. The Rankine vortex can also be visualized. Figure 6b shows the plot of the tangential velocity across horizontal lines. It is observed that the inlet speed is accelerated up but then it decreases when the gas spins down along the cyclone wall. At a certain point flow reversal takes place and the gas flows in the reverse direction to the exit. Before entering the vortex finder, the gas collides with the follow-up flow and velocity decreases sharply. This causes energy loss and pressure drop. The tangential velocity is highly dependent on the geometrical design, wall friction and particle loading. Wang et al. (2006), Wan et al. (2008) and Raoufi et al. (2009) have demonstrated the use of CFD in reasonably predicting the tangential velocity under varied conditions.

The temperature also has an effect on the tangential velocity (Shi et al., 2006). A minor decrease is noticed at the area of the inner vortex with increasing the temperature. The overall and maximum tangential velocity is also decreases on increasing the temperature. As the gas moving toward the vortex finder, the area of inner vortex become narrower and the outer vortex become wider. The main reasons for the changes are that on increasing the temperature the gas density decreases and viscosity increases. Furthermore, the centrifugal force is proportional to the square of the tangential velocity, therefore higher temperature causes the centrifugal force to decrease hence the lower separation efficiency.

### 4.4 Pressure field

The pressure drop across the cyclone is a significant variable since it is directly related to the operating costs. The pressure drop is defined as the difference between the static pressure at the inlet and outlets. Conventional tangential inlet cyclone operations induce a spinning motion that creates radial pressure gradients, which provide a curvature for the gas flow. The particles usually follows these trajectories directed toward the cyclone wall. The Pressure drop within a cyclone is contributed to by both local losses and frictional losses. Local losses include the expansion loss at the inlet and the contraction loss at the outlet while the frictional losses include the swirling loss due to gas to wall friction and the dissipation loss of the dynamic energy of gas.

The total pressure drop, comprising both static and dynamic pressure, decreases on increasing the wall friction coefficient, particle concentration and cyclone length. The combination of the static pressure and the kinetic energy of the vortex is called the total pressure. The viscous dissipation of the kinetic energy in the vortex finder dominates the pressure loss within the cyclone (Dirgo, 1988 and Coker, 1993). Thus the pressure loss is directly proportional to the dynamic pressure. About 40% of the pressure drop is due to the swirl energy losses while the rest is from the sudden expansion at the inlet and the contraction at the outlet duct. Any influence that increases the vortex strength will increase the pressure loss. For example, an increase in the wall friction coefficient will increase the pressure loss as it will decrease the velocity magnitude and will lead to decreased loss in the vortex finder. Similarly, an increase in the wall friction will decrease pressure drop (Hoffman et al. 1992). At increased particle concentration, the tangential velocities will be lower and accordingly will yield a lower pressure drop.

Gimbun et al. (2005) studied the effect of the inlet velocity and particle loading on pressure drop. They compared experimental values by Bohnet (1995) with empirical models by

Shepperd and Lapple (1939), Casal and Martinez (1983), Dirgo (1988), Coker (1993), as well as with CFD predictions using the k-ε model and the RSM model. The result showed that the RSM model produced the closest pressure drop prediction. The k-ε results showed a reasonably good prediction at about 14% -18% deviation. The CFD studies on gas-solid flow in a cyclone separator by Wang et al. (2006) using the RSM model also showed an acceptable agreement with experimental data for Stairmand high efficiency cyclone Hoekstra et al. (1999).

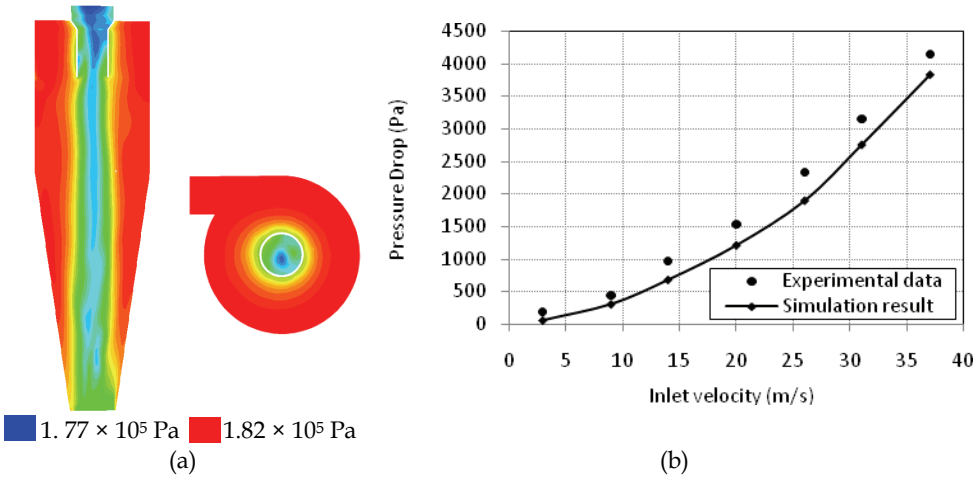


Fig. 7. (a) Contours of total pressure (b) Pressure drop comparison of CFD RSM measurement and experimental data (Stairmand cyclone) for various inlet gas velocities (Adapted from Wang et al., 2009)

Figures 7a and 7b show the contours of the total pressure and the pressure drop comparison between RSM model predictions and experimental data for the Stairmand cyclone at various inlet gas velocities, respectively. The total pressure increases in the radial direction from the the centre to the wall of the cyclone. Flow reversal in a cyclone is due to the low pressure centre. It can be seen from Figure 7b that the CFD simulations underpredict the pressure drop, across the cyclone only the static pressure is considered with the dynamic pressure being neglected. In reality swirl dissipation continues further down the cyclone outlet so that dynamic pressure will be lost without any chance to be recovered. Consequently, the actual pressure drop will be higher.

Any factors that may cause change in the absolute magnitude of the velocity, which in turn changes the strength of the vortex, will affect the pressure drop in the cyclone. Generally, the pressure drop will increase with increasing vortex strength. The pressure drop will decrease with an increase in the wall friction coefficient, particle loading or cyclone length (Yu et al., 1978, Parida & Chand, 1980, Hoffman et al., 1992). When the wall friction coefficient is increased, the swirl in the separation space decreases and causes an increase in the pressure loss. However, it also decreases the absolute velocity magnitude which results in a decreased pressure loss at the vortex finder. The latter effect is always much higher than the first effect and any increase in the wall friction decreases the pressure drop.

Some important processing industries such as pressurized fluidized bed combustion (PFBC), Integrated gasification and combined cycle (IGCC) and Fluid Catalytic Cracking

(FCC) operate at high temperatures and pressures. The operating temperature and pressure will influence the gas density and viscosity and their effect on the drag force. Therefore, for these industries, the operating temperatures and pressures are the important parameters that determine the pressure drop in the cyclone. Shin et al. (2005) (See figure 8) conducted numerical and experimental study on the effect of temperature and pressure on a high efficiency cyclone separator. They found that the pressure drop decreases at a higher pressure and lower temperature. Higher pressures and lower temperatures increase the gas density which in turn creates a higher dynamic pressure hence the higher pressure drop. This trend is confirmed by similar experimental and numerical studies by Gimbun et al. (2005) and Shi et al. (2006)

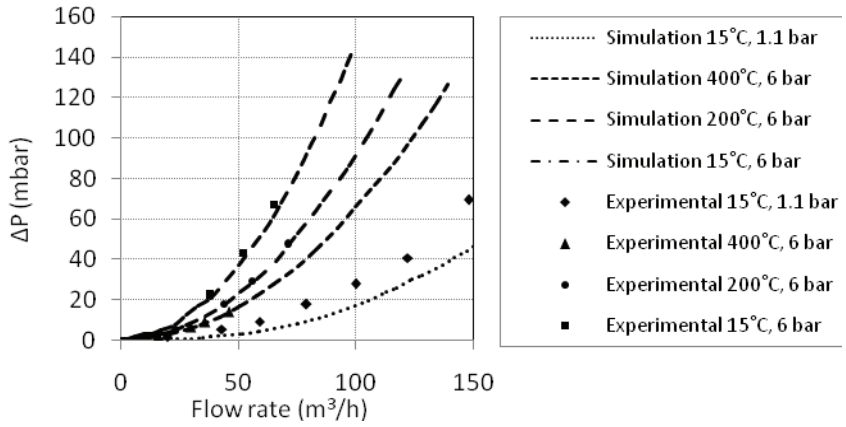


Fig. 8. Comparison of experimental and numerical result for pressure drop at a given flow rate in a elevated pressure and temperature ( Adapted from Shin et al., 2005)

## 5. Collection efficiency

The fraction of solids separated at the outlet is defined as the collection efficiency. Since cyclone separators usually handle various sizes of particles, the efficiencies are defined according to a continuous narrow interval of particular group size particles. The swirling motion within the cyclone separator causes large particles to travel swiftly to the cyclone walls and roll down to the outlet. On the other hand, the smaller particles are often drifted in upward spiral flow due to the slower speed and escape through the gas outlet. This typically yields an S shaped curve for the collection efficiency. Particle collection is the net effect of various forces acting on the particles. It is well known that the collection efficiency is governed by the centrifugal, gravitational and drag forces (Blachmann & Lipmann, 1974). Factors such as the particle-particle and particle-wall interaction also influence the cyclone efficiency. Their effect is not yet fully understood and hence often neglected in empirical modelling. Further, the empirical models are based on the lab scale data. Depending on the operating conditions, the flow inside the cyclone can be laminar, transitional or turbulent for the lab scale equipment. The actual industrial cyclones operate in the turbulent regime where the friction and its corresponding outcomes are significant. Therefore the particle collection efficiency models based on the lab scale data may not accurately predict the collection efficiency for industrial cyclones. At lower mass loading (<5-10 g/m$^3$) the

empirical models perform reasonably well (Cortes and Gil, 2007). Many cyclone separator systems of industrial interest such as the FCC, PFBC and CFBC are well known for handling high particle loadings, where, the interphase and interparticle processes become important and the predictive ability of the conventional models is poor. Numerical studies then become necessary to achieve a better understanding of the cyclone collection efficiency.

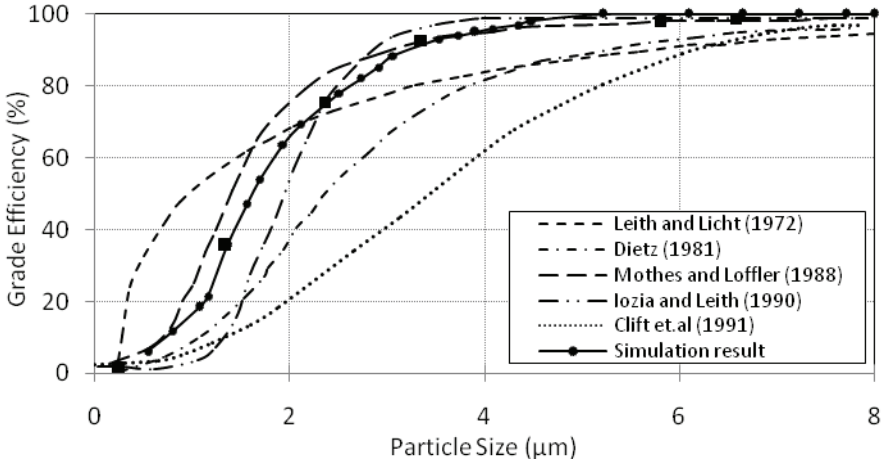


Fig. 9. Collection efficiency model comparison: theoretical, numerical and experimental (Adapted from Zhao et al., 2006)

A typical comparison of relative performance of computational models and conventional models in predicting the cyclone efficiency is shown in figure 9 (Zhao et al. 2006). The collection efficiency in a cyclone with conventional inlet (CI) and a spiral double inlet (DI) configuration is evaluated using the unsteady RANS model with the RSM turbulence model. These predictions are compared with the experimental data and empirical models. Both these profiles follow the S shape with lower collection efficiencies for the smaller particles and almost total capture of larger particles. The comparison also clearly demonstrates the superiority of CFD model over the empirical model in calculating the collection efficiencies. The collection efficiency is a primary measure of the performance of a cyclone separator and depends on the operating conditions and the geometrical characteristics. In the following subsections we look at how these affect the collection efficiencies.

### 5.1 Effect of mass loading, particle diameter and inlet velocity on cyclone efficiency

Qian et al. (2006) investigated the effect of mass loading on the collection efficiency. The results of their simulation are shown in figure 10. The collection efficiency is defined as the ratio of mass flow rate at the inlet and outlet for a converged steady condition. It is clearly evident that the collection efficiency increase on increasing the particle loading. The result is consistent with most of the previous studies (like Stern et al. 1955). Different mass loading for various particle group-sizes affect the grade efficiency differently. Smaller particle group sizes show a higher efficiency increase compared to the larger particle size groups. These findings are also confirmed by the simulation and experimental study by Luo et al. (1999)

and Ji et al. (2009). The increase in cyclone efficiency with solid loading is more pronounced at lower gas velocities (Hoffmann et al. 1991, 1992).

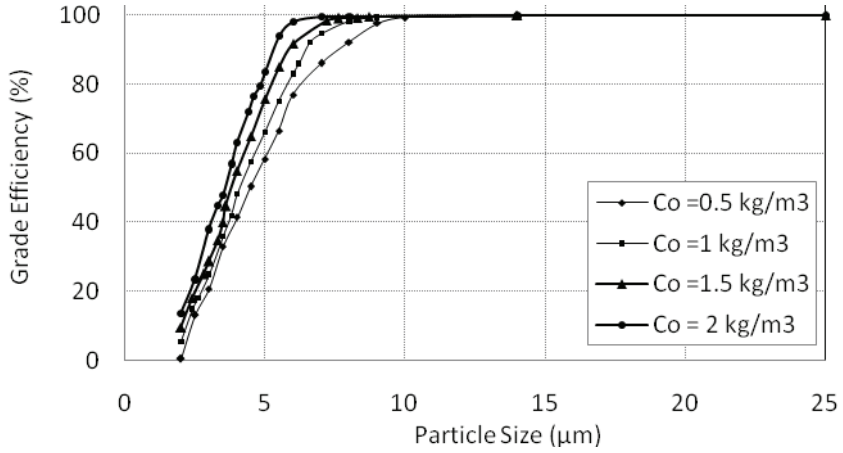


Fig. 10. Separation efficiency simulation result for various inlet particle concentration with constant inlet velocity (Adapted from Qian et al., 2006)

Mass loading effect is usually coupled with the particle diameter. At lower mass loadings, the smaller particles (< 10μm) tend to be dispersed and hauled by the gas flow and escape from the vortex finder at the top of the cyclone separator (Derksen 2003 and Wan et al. 2008). But on increasing the particle mass loading, a sweeping effect of the coarser particle that sweeps away the smaller particles to the cyclone wall is observed. The swept particles then roll down and are collected at the bottom of the cyclone. This effect is also responsible for the formation of agglomerates. Agglomeration causes increased centrifugal force on the smaller particles improving their collection efficiency. Wan et al. (2008) also note that on increasing the particle loading, both the downward flow and the axial velocity at the centre (in upward direction) increase. This aids in higher collection efficiency in the cyclone separator.

The inlet gas velocity also has an effect on the collection efficiency. The effect is also tightly related to the particle mass loading. Figure 11 shows the effect of increasing the inlet gas velocity on the collection efficiency for a given solid loading (Ji et al. 2009). The collection efficiency increases with the inlet gas velocity. For smaller particle sizes (< 10 μm), the increase in the efficiency with respect to the gas velocity is more pronounced. As the particle size increases, the effect of the inlet velocity becomes insignificant. These observations are in line with the experimental work of Fassani et al. (2000) and Hoffmann et al. (1991). The higher inlet velocity, results in the higher tangential velocity, thus leading to a higher centrifugal force and collection efficiency. Patterson and Munz (1989) analyzed the effect of several parameters including the gas temperature (300K - 2000K), inlet gas velocities (3 m/s – 42 m/s) and particle loadings (up to 235.2 g/m$^3$) on the cyclone efficiency. Their analysis showed that there is an increase in the cyclone efficiency especially under high temperature condition.

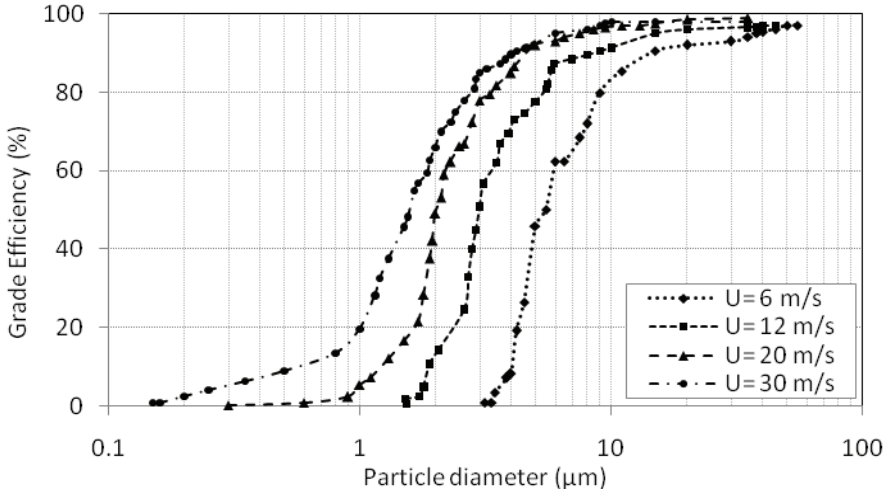


Fig. 11. Grade efficiency for different inlet velocity (Adapted from Ji et al., 2009)

### 5.2 Effect of geometrical configuration on cyclone efficiency

The geometrical configuration is probably the most crucial aspect affecting the performance of a cyclone separator. The cyclone separator performance is sensitive to the smallest of geometrical changes. Through meticulous experimentation, optimal designs of cyclone separators have been proposed. One of the most commonly used designs is the Stairmand high efficiency cyclone (Stairmand 1951). After almost 60 years, this design is still popular since it manages to maintain the velocity profile at every axial point well and achieves very high collection efficiency. The key for Stairmand high efficiency cyclone design lies on the optimal geometrical ratio of cone length to diameter (L/D=4). Unfortunately, it is impossible to always accommodate Stairmand cyclone in the industrial processes, therefore an optimal design best suited for the need has to be explored. Cyclone peripherals like the dipleg and the vortex finder also affect the performance.

Several studies on the effect of dipleg on the cyclone performance have been reported (Hoffmann et al., 1996, Gil et al., 2002, Obermair et al., 2003 and Kaya et al., 2009). Hoffman et al. (1996) found that the L/D ratio of 5.65 is optimal, after this, the collection efficiency starts decreasing. Kaya et al. (2009) extended the effect of dipleg to investigate various inlet velocities and particle diameters for smaller cyclones. They showed that cyclone performance can be improved by adding a correct length of dipleg at the particle outlet. A prolonged cyclone improves the collection efficiency by providing additional space for the separation. According to their results, the optimum dipleg length would be approximately half the height of the cyclone. Placing the vortex end – the location at which the outer vortex changes its direction, exactly at the end of dipleg leads to high collection efficiency. Increasing the length further causes the vortex to fall short and leads to the re-entrainment of particle to the vortex finder thus decreasing the efficiency. Similar observations were made by Gil et al. (2002).

The vortex finder provides another avenue for optimizing the cyclone design. The size of the vortex finder is critical since it determines the inner and outer swirling flow pattern within a

cyclone separator. Concrete methodology is not yet available to optimize the vortex finder. Saltzmann et al. (1984) and Iozia et al. (1989) studied the effect of vortex diameter on the cyclone performance. Kim and Lee (1990) provide information on how the vortex finder and cyclone body diameter affects the cyclone performance. Lim et al. (2004) evaluated different geometries of the vortex finders to optimize the performance. Their results concluded that with smaller vortex finder diameters, the tangential velocity in the inner region of the cyclone increases resulting in a higher collection efficiency. These findings were supported by Raoufi et al. (2009) using CFD modelling.

CFD modelling has opened an avenue for the cost effective optimization of the cyclone geometry. Many geometrical designs have been proposed using CFD studies that can be used to improve the performance of cyclone separators. The list of these modifications include, (i) the use of different inlet types (scroll, helicoidal, axial spiral double inlet and square cyclone inlets) can be found in Cortes and Gil (2007), Wang et al. (1999) and Zhao et al. (2006), (ii) including a long coned (Lee et al., 2006), and (iii) the variation in body and cone height (Xiang et al., 2005).

## 6. Erosion in cyclone separator

The erosion often poses a serious problem in industrial cyclone separators. It is caused by the friction between the particles and the cyclone walls due to the continuous motion of the particles along the cyclone wall. The erosion often leads to a physical damage to the equipment (holes) and costly unscheduled shutdowns. Even pinholes in the wall can disrupt the pressure balance and can cause increased emissions. The eroded wall material may also contaminate the particles collected at the outlet. The erosion occurs due to directional or random impingement of the solid particles and due to friction of the sliding particles against the cyclone wall. Assuming a perfect elasticity, a particle colliding with the cyclone wall will rebound at the same angle (in opposite direction) as it hits the wall, the erosion is minimal at larger angles, however, at very acute angles of impingement, severe erosion results along the cyclone wall circumference. On a flat and ductile target the greatest erosion occurs at around 15° impingement angle (Noppenberger 2000). The erosion is proportional to the kinetic energy of the particles hitting the cyclone wall and the intrinsic strength of the particles. It also depends upon the angle of incidence on the cyclone wall.

At certain specific locations significantly higher erosion occurs compared to other locations, most possibly due to high local velocity which is a function of the particle size and particle density. The high erosion rates are also observed at the inlet. Severe erosion is also observed inside the cylone, however, the there is no consensus on the location of this. Jones et al. (1979) found that the area extending 180$^o$ from the inlet point has most severe erosion and the erosion maxima is observed at angular positions of 105$^o$, 165$^o$, 205$^o$ and 245$^o$ from the tangential inlet. Another study by Youngdahl (1984) found that the highest rate of erosion occurs at 28° and near the lower edge of the inlet stream. Because a detailed velocity and pressure fields and particle trajectories are available from an Eulerian-Lagrangian CFD simulation, it can be used to determine the otherwise impossible locations for likely erosion sites.

Figure 12 shows the erosion map for an industrial cyclone using (a) uniform particle size of 80μm at the inlet and (b) Rosin – Ramler particle size distribution at the inlet with average particle size of 80μm. The results show that the particles follow a distinct path rather than

cluttering on the cyclone walls while swirling down. For the uniform particle size, most severely eroded sites were the top part of the cyclone cylinder (near the inlet) and the cone of the cyclone. This observation is in accordance with the experimental findings of Jones et al. (1979) and Yongdahl et al. (1984). On using a particle size distribution, the most eroded part in the cyclone was at the intersection between the cyclone cylinder and cone. This demonstrates the sensitivity of the erosion to particle size distribution.

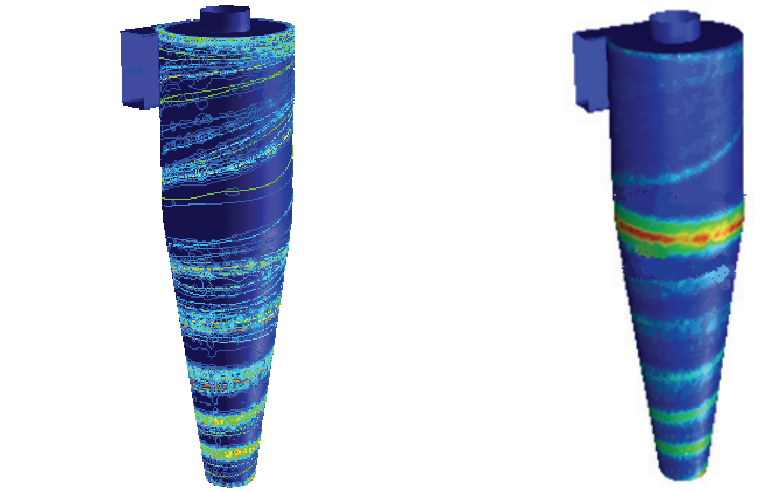


(a) (b)

Fig. 12. (a) Contours of erosion (a) with uniform catalyst size (b) Rosin-Rammler PSD

### 6.1 Effect of particle size distribution on cyclone wall erosion

To investigate the effect of particle size distribution, a wider inlet particle size distribution (1 μm to 160 μm) was simulated using the Lagrangian tracking. The resulting particle trajectories are shown in Figure 13. It is clearly evident that the larger particles are collected at the walls while the smaller particles escape downwards in spiral manner. This is because the drag force on the smaller particles is larger than the centrifugal force preventing their transportation to the cyclone wall. The results show that the particle with sizes < 40 μm escape from the bottom of the cyclone after a certain residence time while the particle with sizes > 60 μm keep spinning around the mid level for significantly longer. Wang et al. (2006) have shown this phenomenon experimentally using ceramic balls. One possible explanation lies in the balance of the centrifugal force versus the gravitational force. As the larger particles roll down the conical part, the centrifugal force on the particle increases because the radius of the cyclone decreases while the tangential velocity of the particle remain almost the same. The larger particles will eventually be collected at the solid outlet due to the particle-particle interaction. However, some of the particles will stay at the cyclone wall. There also appears to be a critical value of the particle diameter below which the particle is not expected to be collected at the outlet. The critical value of particle diameter is related to the cyclone geometry, gas inlet velocity and particle properties.

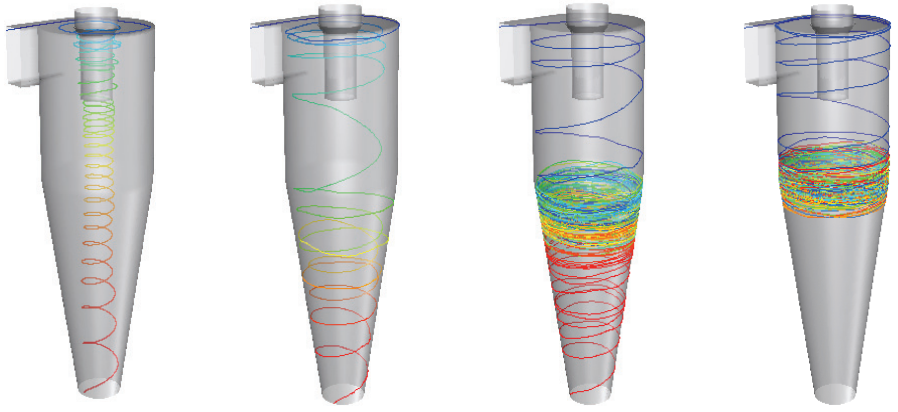

(a) (b) (c) (d)

Fig. 13. Single particle trajectories of size (a) 5 μm b) 20 μm (c) 40 μm (d) >60 μm

### 6.2 Effect of particle mass loading on cyclone wall erosion

The effect of particle mass loading on the average erosion rate at different gas velocities is shown in figure 14. The average of erosion rate gives a global measure of this quantity within the entire cyclone. As expected, at a given gas velocity, the erosion rate decreases with the solid loading. For a given solid loading, however, the average erosion rate increases with gas velocity upto a certain velocity. Beyond this velocity, the erosion rate remains constant or decreases slightly.

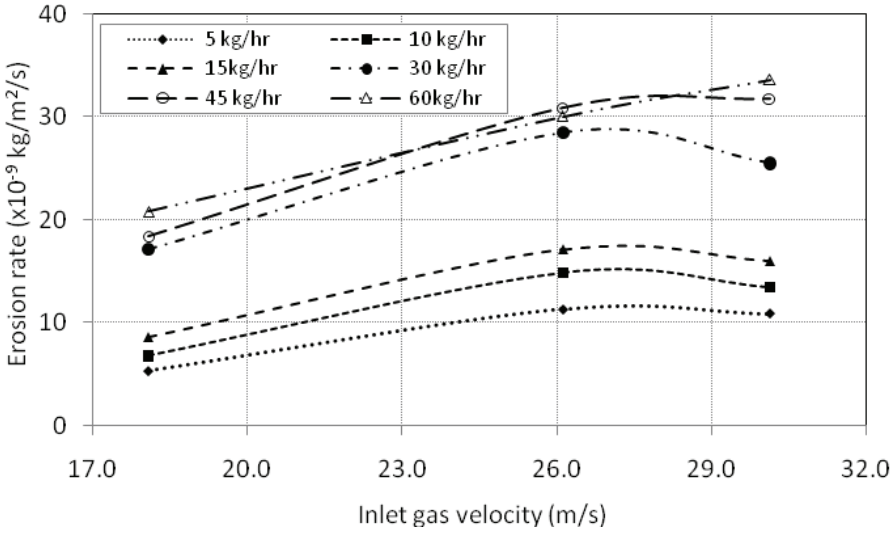


Fig. 14. Comparison of erosion rate with various gas and particle flow rate

At lower gas velocities, lower momentum is imparted by the gas on the particle, which sometimes prevents a second rebound to happen and the particle is forced to stay near the cyclone wall. Consequently, the rate of erosion is lesser at lower velocities. As the gas velocity is increased, the particle rebound is more likely to happen. Since the particle rebounds are not perfectly elastic, it reduces the impact angle gradually after the first rebound, thus increasing the average erosion rate. At even higher gas velocities, the centrifugal force on the particles increases. This makes some particles reach the cyclone wall faster. As a consequence, a layer of slow moving particles is formed that protects the walls from collision by other particles which then reduces the rate of erosion slightly.

## 7. Summary

Due to their simple and robust construction, cyclone separators are widely used in the chemical and process industries. In spite of their simple construction, flow patterns inside cyclones are highly complex and not fully understood. Understanding the flow is critical in accessing their performance and CFD is a useful tool in providing this information. However, due to the very nature of the flow, the application of CFD should be exercised with prudence. In order to accurately resolve the unsteady nature of the flow inside a cyclone, higher order numerical discretization along with unsteady simulation (unsteady RANS or LES) are needed. It also requires a higher order turbulence model (atleast second order like RSM) for the unsteady RANS simulations. For resolving the gas flow field, the LES provides superior results than the RANS approach. However, the cost of LES is prohibitive for the industrial-scale devices. Recent developments turbulence modelling such as the differential RSMs have shown a light of hope to achieve LES level of accuracies at RANS cost. However, the conditions under which the unsteady RANS solver can be used in place of the LES need to be explored.

To obtain the particle flow, the Eulerian-Lagrangian formulation with either one way or two way coupling should be employed. The necessity of capturing the unsteadiness of the gas flow in combination to the flow of poly-disperse particulates demands far superior computational power than what is currently available. Therefore, a considerable progress needs to be made in multiphase flow simulation of cyclones. Factors like interparticle phenomena and the boundary condition at the wall also need a careful attention. The advances in the DEM-CFD coupled simulations will bring new insight in the calculation of highly-loaded cyclones. Nevertheless, the two phase flow simulations have provided some useful insight into the cyclone operations and have provoked to question the existing theories on the particle flow and separation in cyclones.

The enormous computational requirements, even for the minimal modelling of cyclone phenomena, have limited our ability to go beyond a simple understanding of the flow structures, collection efficiency and global design issues. More systematic research for addressing the other important issues, such as reasonable estimates of the cyclone natural length and vortex finder dimensions, is needed. Furthermore, the loss of coherence in the vortex and the ensuing chaotic flow patterns and the effect of swirl-stabilization are some of the other topics that remain unanswered. With increasing computational power, it is envisaged that in the near future we will be able to perform fully resolved simulations on cyclones which will not only answer the above questions but will also advance our knowledge of cyclone operations and even optimize them for specific operational circumstances.

## 8. References


Barth, W. (1956) Design and Layout of the cyclone separator on the basis of new investigation. *Brenn. Warme Kraft, 8*, 1-9.

Blachmann, M. W., Lippmann, M. (1974) Performance characteristic of the multi cyclone aerosol sampler, *Ind Hyg. Ass. J., 35*, 311-326.

Bohnet, M. (1995) Influence of the Gas Temperature on the Separation Efficiency of Aerocyclones, *Chem. Eng. Process,* (34), 151.

Boysan, F., Ayers, W.H., Swithenbank, J. (1982). A fundamental mathematical modeling approach to cyclone design, *Trans. Isntn. Chem. Engrs, 60*, 222-230.

Boysan, F., Ewan, B. C. R., Swithenbank, J., Ayers, W.H. (1983) Experimental and theoretical studies of cyclone separator aerodynamics, *Inst Chem Eng Symp Ser* ,69:305–19.

Bunyawanichakul, P.,Kirkpatrick, M. P., Sargison, J. E., Walker G. J. (2006) Numerical and Experimental Studies of the Flow Field in a Cyclone Dryer, *J Fluids Eng*, 128 (6), 1240

Casal, J. M., Martinez, A. (1983) A better way to calculate cyclone pressure drop. *Chemical engineering., 90*, 99.

Chu, K. W., Wang, B., Yu, A.B., Vince A. (2009) CFD-DEM modeling of multiphase flow in dense medium cyclone. *Powder Tech., 193*(3), 235-247.

Coker, A. K. (1993) Understand cyclone design. *Chemical Engineering Progress, 28*, 51-55.

Cortes, C., Gil, A. (2007) Modeling the particle flow inside cyclone separators. *Progress in energy and combustion Science* (33).

Derksen, J. J., van den Akker, HEA, (2000) Simulation of vortex core precession in a reverse flow cyclone. *AIChE J., 49*, 1359-1371

Derksen, J. J. (2003) Separation performance predictions of a Stairmand high-efficiency cyclone. *AIChE J* (49), 1359-1371.

Derksen, J. J. (2005) Simulations of confined turbulent vortex flow. *Comp Fluids* (34), 301-318.

Derksen, J. J., Sundaresan, S., van der Akker H.E.A. (2006) Simulation of mass loading effects in gas -solid cyclone separators. *Powder Tech., 163*, 59-68.

Dietz, P. W. (1981) Collection efficiency of cyclone separators. *A.I. Ch.E.J, 27*, 888.

Dirgo, J. (1988) Relationships between cyclone dimensions and performance. Havarad University, USA.

Dirgo, J., Leith, D., (Ed.) (1986) Encyclopedia of fluid mechanics, (Vols. 4). Houston: Gulf Publishing Company.

Elghobashi ,S. E. (1994) On predicting particle-laden turbulent flows. *Appl Sci Res;* (52), 309–29.

Gil, A., Corte´s, C., Romeo, L. M., Velilla, J. (2002) Gas-particle flow inside cyclone diplegs with pneumatic extraction. *Powder Tech.* (128), 822-829.

Gimbun, J., Chuah, T.G, Fakhru'l-Razi,A. , Choong, T.S.Y. (2005) The influence of temperature and inlet velocity on cyclone pressure drop: A CFD study. *Chemical engineering and Processing, 44*, 7-12.

Gosman, A. D., Ioannides, E. (1981) Aspect of computer simulation of liquid fuelled combusters. *AIAA paper, 81-0323*.

Grotjans, H., Menter, F.R., Burr, R.C. and Gluck, M., 1999, "Higher Order Turbulence Modelling in Industrial Applications", 4th Int. Symp. on Engineering Turbulence Modeling and Measurement..

Harasek, M., Horvath, A., Jordan, C. (2004) *Investigation of dependence of gas flow on the geometry of cyclonic separators by CFD simulation*. Paper presented at the CHISA 2004 - 16th International Congress of Chemical and Process Engineering.

Harasek, M., Horvath, A., Jordan, C. (2008) Influence of vortex finder diameter on axial gas flow in simple cyclone. *Chemical product and process modeling 3*(1), Article 5.

Hoekstra, A. J., Derksen, J. J., Van Den Akker, H. E. A. (1999) An experimental and numerical study of turbulent swirling flow in gas cyclones. *Chem. Eng. Sci., 54*, 2055-2056.

Hoffmann AC, H Arends, H Sie, (1991), An experimental investigation elucidating the nature of the effect of solids loading on cyclone performance, Filtration & Separation, 28 (3), pp 188-193

Hoffmann, A. C., van Santen A., Allen, R. W. K., Cliff, R. (1992) Effects of geometry and solid loadings on the performance of gas cyclones. *Powder Tech., 70*, 83-91.

Hoffmann, AC; deGroot, M; Hospers, A, (1996), The effect of the dust collection system on the flowpattern and separation efficiency of a gas cyclone, Canadian journal of chemical engineering , 74 (4), pp 464-470.

Hogg, S., Leschziner, M.A. (1989). Computational of highly swirling confined flow with a Reynolds stress turbulence model, *AIAA J* ,1(27), 57–63.

Iozia, D. L. a. L., D. (1989) Effect of cyclone dimensions on gas flow pattern and collection efficiency. *Aerosol Science tech., 10*, 491-500.

Jakirlic, S., Hanjalic, K. (2002). Modelling rotating and swirling turbulent flows: a perpetual challenge. *AIAA J,* 40:1984–96.

Ji, Z., Xiong, Z., Chen, H., Wu, H. (2009) Experimental investigations on a cyclone separator performance at an extremely low particle concentration. *Powder Tech.* (191), 254-259.

Jones, J. L., Arnold, J. M., Youngdahl, C. A. (1979) Erosion rates and patterns of the gas pilot plant's effluent cyclone.

Kaya, F., Karagoz, I. (2009) Numerical Investigation of performance characteristics of a cyclone prolonged with a dipleg. *Che. eng. Journal, 151*, 39-45.

Kim, J. (1990) Experimental study of particle collection by small cyclones, *Aerosol Science tech., 12*, 1003-1015.

Lapple, C. E. (1951). Processes use many collector types, *Chemical engineering,* 58, 144 - 151.

Leith, D., Licht, W. (1972) Collection efficiency of cyclone type particle collector: A new theoretical approach, *A.I.Ch.E Symposium series (Air-1971), 68*, 196-206.

Ma, L., Ingham, D.B ., Wen, X. . (2000). Modelling of the fluid and particle penetration through small sampling cyclones. *J Aerosol Sci* (31), 1097-1119.

Meier, H. F., Mori , M. (1998) Gas–solid flow in cyclones: theEulerian–Eulerian approach. *Comput Chem Eng* , 22(Suppl 1):S641–4.

Meier, H. F., Mori, M. (1999) Anisotropic behavior of the Reynolds stress in gas and gas-solid flows in cyclones. *Powder Tech.*(101), 108-119.

Morsi, S. A., Alexander, A.J., . (1972). An investigation of particle trajectories in two phase flow systems. *Fluid Mech. J., 55*(2), 193-208.

Muschelknautz, E. (1972) Die Berechnung von Zyklonabscheidern fur Gase. *Chem-Ing-Tech* (44), 63-71.

Noppenberger, M. (2000) How to control erosion in FCC cyclone. *World refining, 10*(6), 36-38.

Obermair, S. (2003). *Einfluss der Feststoffaustragsgeometrie auf die Abscheidung und den Druckverlust eines Gaszyklons,* Technical University Graz.

Pant, K., Crowe, C. T., Irving, P. (2002) On the design of miniature cyclone for the collection of bioaerosols. *Powder Tech., 125*, 260-265.

Parida, A., Chand, P. (1980) Turbulent swirl flow with gas-solid flow in cyclone. *Che. Eng. Sci., 35*(4), 949-954.

Patterson, P. A. M., Munz R. J. (1989) Cyclone Collection Efficiencies at Very High Temperatures. *Can. J. Chem. Eng, 37*.

Qian, F., Huang, Z., Chen, G., Zhang, M. (2006) Numerical study of the separation characteristics in a cyclone of different inlet particle concentrations. *Computers and chemical engineering, 31*, 1111-1122.

Raoufi, A., Shams, M., Kanani, H. (2009) CFD analysis of flow field in square cyclones. *Powder Tech.* (191), 349-357.

Saltzmann, B. (1984) Generalized performance characteristics of miniature cyclone for atmospheric particulate sampling. *Am. Ind. Hyg. Assoc. J., 45*, 671-680.

Shalaby, H., Pachler, K., Wozniak, K., Wozniak, G. (2005) Comparative study of the continuous phase flow in cyclone separator using different turbulence models. *International J. of Numerical methods in fluids, 11*(48), 1175-1197.

Shalaby, H., Wozniak, K., Wozniak, G. (2008) Numerical calculation of particle -laden cyclone separator flow using LES. *Eng. app. of Comp. Fluid Mech., 2*(4), 382-392.

Shepherd, C. B., Lapple, C.E. (1939). Flow pattern and pressure drop in cyclone dust collectors. *Ind. Eng. Chem, 31*, 972-984.

Shi, L., Bayless D. J., Kremer G., Stuart B. (2006) CFD Simulation of the Influence of Temperature and Pressure on the Flow Pattern in Cyclones. *Ind. Eng. Chem. Res.*(45), 7667-7672.

Shin, M. S. K., Jang, D. S., Chung, J. D.; Bohnet, M. (2005) Numerical and Experimental Study on a High Efficiency Cyclone Dust Separator for High Temperature and Pressurized Environments, *Appl. Therm. Eng.,* (25), 1821.

Slack, M. D., Prasad, R.O., Bakker, A., Boysan, F. (2000) Advances in cyclones modeling using unstructured grids, *Transactions of the Institution of Chemical engineers,* 78A, 1098.

Sommerfeld, M., Ho, C.H. (2003) Numerical calculation of particle transport in turbulent wall bounded flows. *Powder Tech., 131*, 1-6.

Sproul (1970) Air pollution and its control, New York: Exposition Press.

Stairmand (1951) The design and performance of cyclone separators. *Trans. Isntn. Chem. Engrs, 29*, 356 - 383.

Sturgess, G. J., Syed, S.A. (1985) Calculation of a hollow-cone liquid spray in uniform airstream, *J. Propul. Power* (1)

Swift, P. (1969). Dust Control in Industry. *Steam Heat. Engr., 38*, 453 - 456.

Tengbergen, H. J. (1965) Comparative studies with cyclone, *Staub, 25*(11), 44-49.

Velilla, J. (2005) Study of the flow at a PFBC cyclone dipleg. University of Zaragoza.

Wan, G., Sun, G., Xue, X., Shi, M. (2008) Solids concentration simulation of different size particles in a cyclone separator, *Powder Tech., 183*, 94-104.

Wang, B., Xu, D.L., Chu, K.W., Yu, A.B. (2006) Numerical study of gas solid flow in a cyclone separator, *Applied Mathematical Modeling, 30*, 1326-1342.

Wang, S., Fang, M., Luo, Z., Li, X., Ni, M., Chen K.,. (1999). Instantaneous separation model of a square cyclone,. *Powder Technology* (102), 65-70.

Xiang, R. B., Lee, K.W. (2005) Numerical study of flow field in cyclones of different height. *Che. Eng. Sci., 44*, 877-883.

Youngdahl, C. A. (1984). Nondestructive monitoring of erosive wear in transfer lines and cyclones at synfuels pilot plants, Paper presented at the Corrosion/84, International Corrosion Forum Devoted Exclusively to the Protection and Performance of Materials

Yuu, S., Jotaki T., Tomita, Y., Yoshida, K. (1978) the reduction of pressure drop due to dust loading in a conventional cyclone. *ChE. Eng. Sci., 33*(12), 1573-1580.

Zhao, B., Su, Y., Zhang, J. (2006). Simulation of gas flow pattern and separation efficiency in cyclone with conventional single and spiral double inlet configuration. *Chemical Engineering research and Design, A12* (84), 1158-1165.

# 12

# Prediction of Magnetite Segregation and Coal Partitioning In Dense Medium Cyclone Using Computational Fluid Dynamics Technique

M. Narasimha[1], M. S. Brennan[2], P.N. Holtham[2] and P.K. Banerjee[1]
[1]*R&D Division, TATA Steel, Jamshedpur, Jharkhand 831 007,*
[2]*Julius Kruttschnitt Mineral Research Centre, The University of Queensland, Isles Road, Indooroopilly 4068, Queensland,*
[1]*India*
[2]*Australia*

## 1. Introduction

Dense medium cyclones are designed to partition coal particles based on particle density with the cut density adjusted by adding a finely dispersed heavy medium to the feed and adjusting the feed medium concentration. In a typical DMC, illustrated in Figure 1, a mixture of medium and raw coal enters tangentially near the top of the cylindrical section, thus forming a strong swirling flow. The denser high ash particles move along the wall of

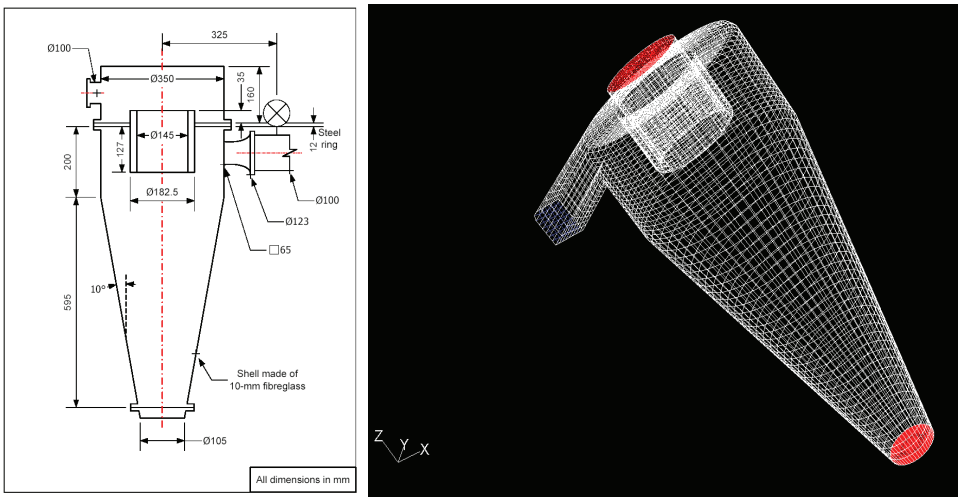


(a) (b)

Fig. 1. (a) Detailed dimensional drawing of the 350 mm DSM dense medium cyclone used for simulations, (b) Grid generated in Gambit.

the cyclone due to the centrifugal force, where the velocity is downward and is discharged through the underflow orifice or the spigot. The lighter low ash coal moves towards the longitudinal axis where a strong up flow exists and passes through the vortex finder to the overflow chamber.

The presence of medium, coal particles, swirl and the fact that DMCs operate in the turbulent regime makes the flow behavior complex and studying the hydrodynamics of DMCs using Computational Fluid Dynamics (CFD) is a valuable aid to understanding their behaviour.

Most of the CFD studies have been conducted for classifying hydrocyclones (Davidson, 1994; Hsieh, 1988; Slack et al 2000; Narasimha et al 2005 and Brennan, 2006). CFD studies of DMCs are more limited (Zughbi et al, 1991, Suasnabar (2000) and Brennan et al, 2003, Narasimha et al (2006)). DMCs and Classifying cyclones are similar geometrically and the CFD approach is the same with both. A key problem is the choice of turbulence model. The turbulence is too anisotropic to treat with a k-e model and this has led some researchers to use the differential Reynolds stress turbulence model. However some recent studies (Slack et al, 2000; Delagadillo and Rajamani, 2005; Brennan, 2006) have shown that the LES technique gives better predictions of the velocities in cyclones and seems to do so on computationally practical grids.

In this paper, CFD studies of multiphase flow in 350mm and 100mm Dutch State Mine (DSM) dense medium cyclone are reported. The studies used FLUENT with 3d body fitted gird and used the mixture model to model medium segregation, with comparisons between Large Eddy Simulation (LES) and Differential Reynolds Stress Model (DRSM) turbulence models. Predictions are compared to measured concentrations by GRT (Gamma ray tomography) and overall simulated performance characteristics using Lagrangian particle tracking for particles were compared to experimental data.

## 2. Model description

### 2.1 Turbulence models

The basic CFD approach was the same as that used by Brennan (2003). The simulations used Fluent with 3d body fitted grids and an accurate geometric model of the 350mm DSM pattern dense medium cyclone used by Subramanian (2002) in his GRT studies. The dimensions of the cyclone are shown in Figure 1a and a view of the grid used in the simulations is shown in Figure 1b. The equations of motion were solved using the unsteady solver and represent a variable density slurry mixture:

$$\frac{\partial \rho_m}{\partial t} + \frac{\partial \rho_m u_{mi}}{\partial x_i} = 0 \tag{1}$$

$$\begin{aligned} &\frac{\partial}{\partial t}\left(\rho_m u_{mi}\right) + \frac{\partial}{\partial x_j}\left(\rho_m u_{mi} u_{mj}\right) = \\ &-\frac{\partial}{\partial x_i} p + \frac{\partial}{\partial x_j}\left(\tau_{\mu,ij} + \tau_{d,ij} + \tau_{t,ij}\right) + \rho_m g_i \end{aligned} \tag{2}$$

The RANS simulations were conducted using the Fluent implementation of the Launder et al (1975) DRSM model with the Launder linear pressure strain correlation and LES

simulations used the Fluent implementation of the Smagorinsky (1966) SGS model. In the DRSM simulations $\tau_{t,ij}$ in equation (2) denotes the Reynolds stresses, whilst in the LES simulations $\tau_{t,ij}$ denotes the sub grid scale stresses. $\tau_{d,ij}$ is the drift tensor and arises in equation (2) as part of the derivation of the Mixture model (Manninenn et al 1996). The drift tensor accounts for the transport of momentum as the result of segregation of the dispersed phases and is an exact term:

$$\tau_{d,ij} = \sum_{p=1}^{n} \alpha_p \rho_p u_{pm,i} u_{pm,j} \tag{3}$$

All equations were discretized using the QUICK option except that Bounded central differencing was used for momentum with the LES. PRESTO was used for Pressure and SIMPLE was used for the pressure velocity coupling. The equations were solved with the unsteady solver with a time step which was typically $5.0 \times 10^{-4}$s for both the DRSM simulations and LES simulations. The LES used the Spectral Synthesiser option to approximate the feed turbulence.

### 2.2 Multiphase modeling – mixture model with lift forces

The medium was treated using the Mixture model (Manninnen et al 1996), which solves the equations of motion for the slurry mixture and solves transport equations for the volume fraction for any additional phases p, which are assumed to be dispersed throughout a continuous fluid (water) phase c:

$$\begin{aligned} &\frac{\partial}{\partial t}\alpha_p + \frac{\partial}{\partial x_i}\left(\alpha_p u_i\right) + \frac{\partial}{\partial x_i}\left(\alpha_p u_{pm,i}\right) = 0 \\ &u_{pm,i} = u_{pi} - u_i \end{aligned} \tag{4}$$

$u_{pm,i}$ is the drift velocity of the p relative to the mixture m. This is related to the slip velocity $u_{pc,i}$, which is the velocity of the p relative to the continuous water phase c by the formulation:

$$\begin{aligned} &u_{pmi} = u_{pci} - \sum_{l=1}^{n} \frac{\alpha_k \rho_k}{\rho_m} u_{lci} \\ &u_{pci} = u_{pi} - u_{ci} \end{aligned} \tag{5}$$

Phase segregation is accounted for by the slip velocity which in Manninen et al's (1996) treatise is calculated algebraically by an equilibrium force balance and is implemented in Fluent in a simplified form. In this work Fluent has been used with the granular options and the Fluent formulation for the slip velocity has been modified where (i) a shear dependent lift force based on Saffman's (1965) expression and (ii) the gradient of granular pressure (as calculated by the granular options) have been added as additional forces. Adding the gradient of granular pressure as an additional force effectively models Bagnold dispersive forces (Bagnold 1954) and is an enhancement over our earlier work (Narasimha et al, 2006).

$$u_{pci} = \frac{d^2{}_p\left(\rho_p - \rho_m\right)}{18 f_{rep}\mu_c} * \left( g_i - \frac{\partial}{\partial t}u_{mi} - u_{mj}\frac{\partial}{\partial x_j}u_{mi} + 0.75\frac{\rho_c}{\rho_p - \rho_m}C_{lp}\varepsilon_{ijk}\omega_{mj}u_{pck} - \frac{1}{\alpha_p\left(\rho_p - \rho_m\right)}\frac{\partial}{\partial x_i}P_{pg} \right) \quad (6)$$

Equation (6) has been implemented in Fluent as a custom slip velocity calculation using a user defined function. frep has been modelled with the Schiller Naumann (1935) drag law but with an additional correction for hindered settling based on the Richardson and Zaki (1954) correlation:

$$f_{rep} = \left(1 + 0.15\,\mathrm{Re}_p{}^{0.687}\right)\alpha_p{}^{-4.65} \quad (7)$$

The lift coefficient has been calculated as

$$C_{lp} = 4.1126\left(\frac{\rho_f d_p{}^2|\omega|}{\mu_c}\right)f_c \quad (8)$$

$f_c$ corrects the lift coefficient using the correlation proposed by Mei (1992).

### 2.3 Medium rheology

The mixture viscosity in the region of the cyclone occupied by water and medium has been calculated using the granular options where the Gidaspow et al (1992) granular viscosity model was used. This viscosity model is similar to the Ishii and Mishima (1984) viscosity model used in earlier work (Narasimha et al 2006) in that it forces the mixture viscosity to become infinite when the total volume fraction of the medium approaches 0.62 which is approximately the packing density and has the effect of limiting the total medium concentration to less than this value. However the Gidaspow et al model (1992) also makes the viscosity shear dependant.

### 2.4 Medium with size distribution

The mixture model was set up with 8 phase transport equations, where 7 of the equations were for medium which was magnetite with a particle density of 4950 kg.m-3 and 7 particle sizes which were; 2.4, 7.4, 15.4, 23.8, 32.2, 54.1 and 82.2 μm. The seventh phase was air, however the slip velocity calculation was disabled for the air phase thus effectively treating the air with the VOF model (Hirt & Nichols 1981). The volume fraction of each modeled size of medium in the feed boundary condition was set so that the cumulative size distribution matched the cumulative size distribution of the medium used by Subramanian (2002) and the total feed medium concentration matched Subramanian's (2002) experimental feed medium concentrations.

### 2.5 Coal particle tracking model

In principle the mixture model can be used to model the coal particles as well as medium but the computational resources available for this work limited simulations using the

mixture model to around 9 phases, and it was impractical to model coal with more than two sizes or densities simultaneously with 6 medium sizes. Thus the Fluent discrete particle model (DPM) was used where particles of a known size and density were introduced at the feed port using a surface injection and the particle trajectory was integrated through the flow field of a multiphase simulation using medium. This approach is the same as that used by Suasnabar (2000).
Fluent's DPM model calculates the trajectory of each coal particle d by integrating the force balance on the particle, which is given by equation (10):

$$\frac{Du_{d,i}}{dt} = k_d\left(u_{m,i} - u_{d,i}\right) + g_i\left(\frac{\rho_d - \rho_m}{\rho_d}\right) \tag{9}$$

$k_d$ is the fluid particle exchange coefficient:

$$k_d = \left(\frac{18\mu_m d_d^2}{\rho_d}\right)\left(\frac{C_D \mathrm{Re}_d}{24}\right) \tag{10}$$

The presence of medium and the effects of medium segregation are incorporated in the DPM simulations because the DPM drag calculation employs the local mixture density and local mixture viscosity which are both functions of the local medium concentration. This intrinsically assumes that the influence of the medium on coal partitioning is a primarily continuum effect. i.e., the coal particles encounter (or "see") only a dense, high viscosity liquid during their trajectory. Further the DPM simulations intrinsically assume that the coal particles only encounter the mixture and not other coal particles and thus assume low coal particle loadings.
To minimize computation time the DPM simulations used the flow field predicted by the LES at a particular time. This is somewhat unrealistic and assumes one way coupling between the coal particles and the mixture.

## 3. Results

### 3.1 Velocity predictions

The predicted velocity field inside the DSM geometry is similar to velocities predicted in DMCs by Suasnabar (2000). Predicted flow velocities in a 100mm DSM body were compared with experimental data (Fanglu and Wenzhen (1987)) and shown in Fig 2(a) and 2(b). Predicted velocity profiles are in agreement with the experimental data of Fanglu and Wenzhen (1987), measured by laser doppler anemometry.

### 3.2 Air core predictions

Figure 3 shows a comparison between the air core radius predicted from LES and DRSM simulations and the air core measured by Subramanian (2002) by GRT in a 350mm DSM body.
In particular Figure 3 shows that the air core position is predicted more accurately by the LES and that the radius predicted by the RSM is smaller than experimental measurements in the apex region. This is consistent with velocity predictions because a lower prediction of the tangential velocity (as predicted by the DRSM) should lead to a thicker slurry/water region for the same slurry/water feed flow rate and therefore a thinner air core. This lends some cautious credibility to the LES velocity predictions.

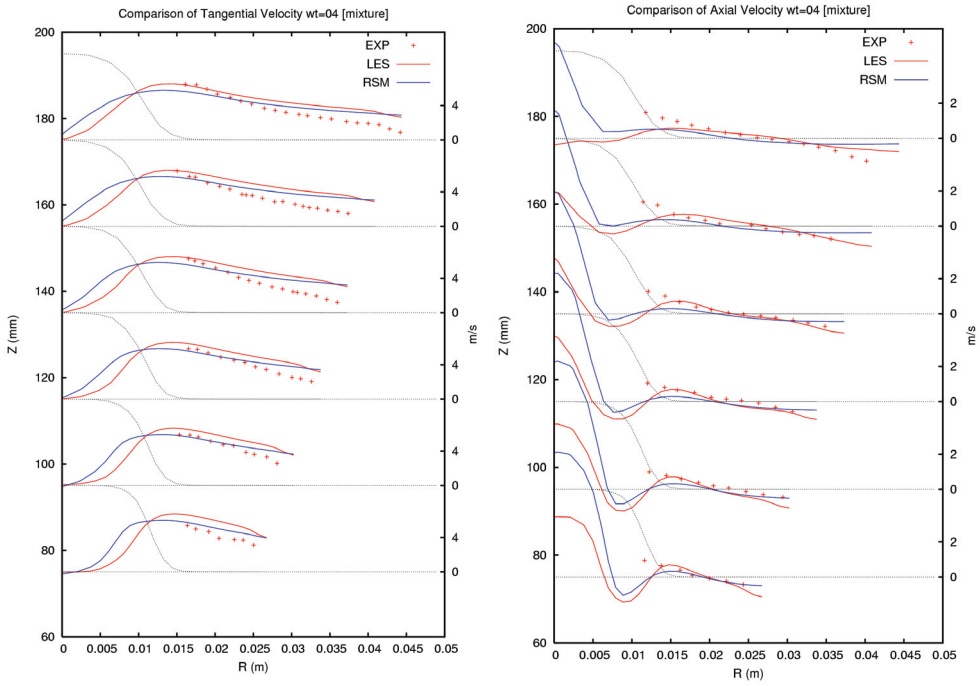


(a) (b)

Fig. 2. Comparison of predicted (a) tangential velocity field, (b) axial velocity field with experimental data (Fanglu and Wenzhen (1987))

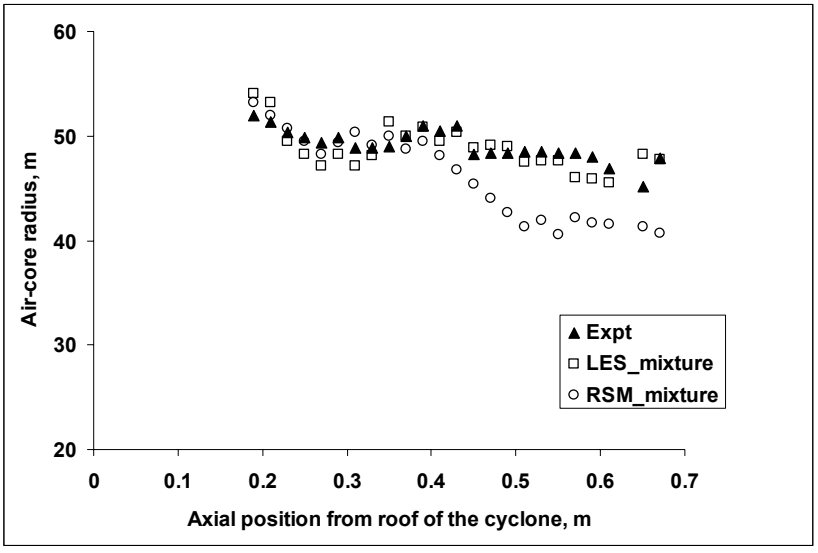


Fig. 3. Comparison between predicted and measured air core positions

### 3.3 Turbulence analysis of two phase flow in DSM body

Using the LES turbulence model, an analysis was made of the two phase (air-water) turbulence in a 350 mm DSM body. Figure 4 shows that in the DSM design, a very high turbulent kinetic energy occurs near the tip of vortex finer. As expected, the sudden transition from the cylindrical body to the conical section is a clear source of turbulent fluctuations down the cyclone body. These fluctuations propagate a very high turbulent kinetic energy near the bottom of the apex zone.

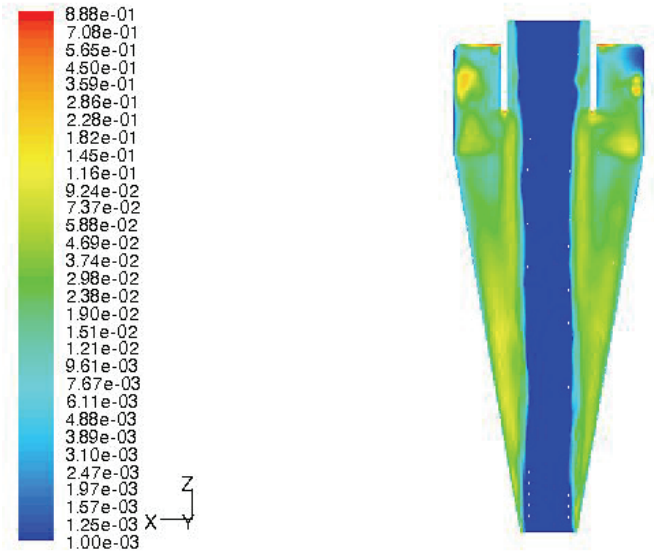


Fig. 4. Predicted turbulent kinetic energy contours in 350 mm DSM body

### 3.4 Prediction of medium segregation using medium feed size distribution, lift forces and viscosity corrections

Figure 5 shows the density profiles predicted by the CFD at steady flow for a feed RD of 1.465 and a feed head of 9Dc (equivalent to a volumetric flow rate of 0.0105 $m^3.s^{-1}$) together with an experimentally measured density profile for the same feed conditions from Subramanian (2002) . Figure 5a shows the density profile using the modelling approach reported in Brennan (2003) and Brennan et al (2003) which is the basic mixture model with DRSM turbulence, Schiller Naumann drag relationship and a single medium size of 30µm, Figure 5b shows the density profile for the latest work which is from am LES using the mixture-granular model, medium with a feed size distribution, Schiller Naumann drag relationship with hindered settling, Lift and Bagnold forces and the Gidaspow et al (1992) granular viscosity law.

Figure 6 is a graphical comparison of the same data shown in Figure 5 at an elevation of 0.27 m and 0.67 m below the top of the cyclone body. 0.27m is the beginning of the apex and 0.67m is the lowest point at which Subramanian (2002) collected data. The predicted overflow and underflow medium densities are listed in Table 1.

The simulations from earlier work (Brennan 2003, Brennan et al 2003) with the basic mixture model, DRSM, single particle size, no lift and viscosity corrections display excessive

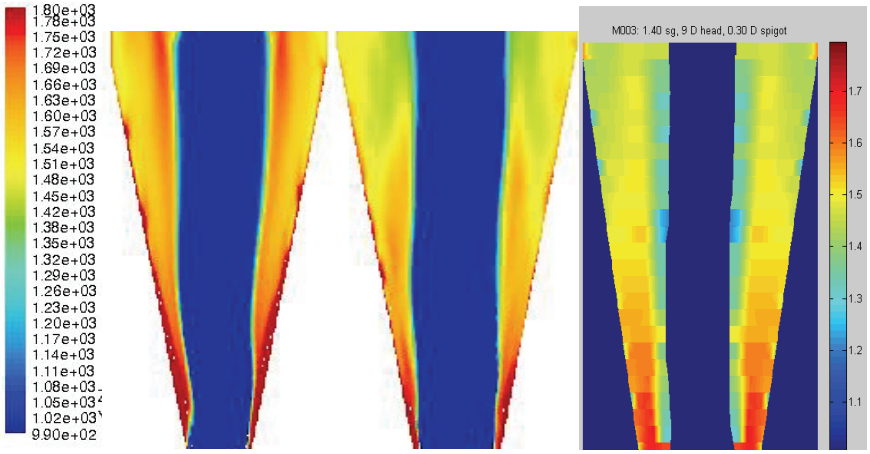


(a) DRSM-Brennan (2003) (b) LES latest work (c) GRT data- Subramanian (2002)

Fig. 5. Comparison between predicted slurry densities (a) DRSM-Mixture from Brennan (2003) (b) LES-Mixture latest work (see text left) (c) Experimental - Subramanian, 2002 for feed RD of 1.465, Feed head = $9D_c$ ($Q_f = 0.0105\ m^{-3}.s^{-1}$); in elevation.

medium segregation although some of the characteristics of the distribution of medium are captured even though the predictions are inaccurate. At both 0.27m and 0.67m the medium concentration is excessive in the centre of the slurry region, and increases to a very large concentration at the wall at 0.67m.

The LES with the mixture model enhancements is much more realistic. The improved accuracy however can be attributed to all of the enhancements. The medium used in Subramanian's (2002) GRT studies contained a significant distribution of sizes between 4 and 40 $\mu m$ and one would expect that the smaller size would not segregate to the same degree as the larger size. Hence modeling the medium size distribution is necessary.

Finally the LES model is an enhancement over the DRSM turbulence model. This is partly because it is believed that it predicts the tangential velocities more accurately but also because LES resolves the larger scale turbulent fluctuations which generate turbulent mixing of the medium and this mixing is resolved because the instantaneous velocities are passed to the slip velocity calculation.

| Turbulence model | Overflow, $kg.m^{-3}$ | Underflow, $kg.m^{-3}$ | Recovery to underflow |
|---|---|---|---|
| DRSM | 1194 | 2232 | 0.256 |
| LES | 1339 | 1978 | 0.175 |
| Experimental | 1375 | 2076 | 0.137 |

Table 1. Predicted Flow densities and recovery to underflow - (a) DRSM-Mixture from Brennan (2003) (b) LES-Mixture latest work, (c) Experimental from Subramanian (2002) (feed RD of 1.465, Feed head = $9D_c$ , $Q_f = 0.0105\ m^{-3}.s^{-1}$)

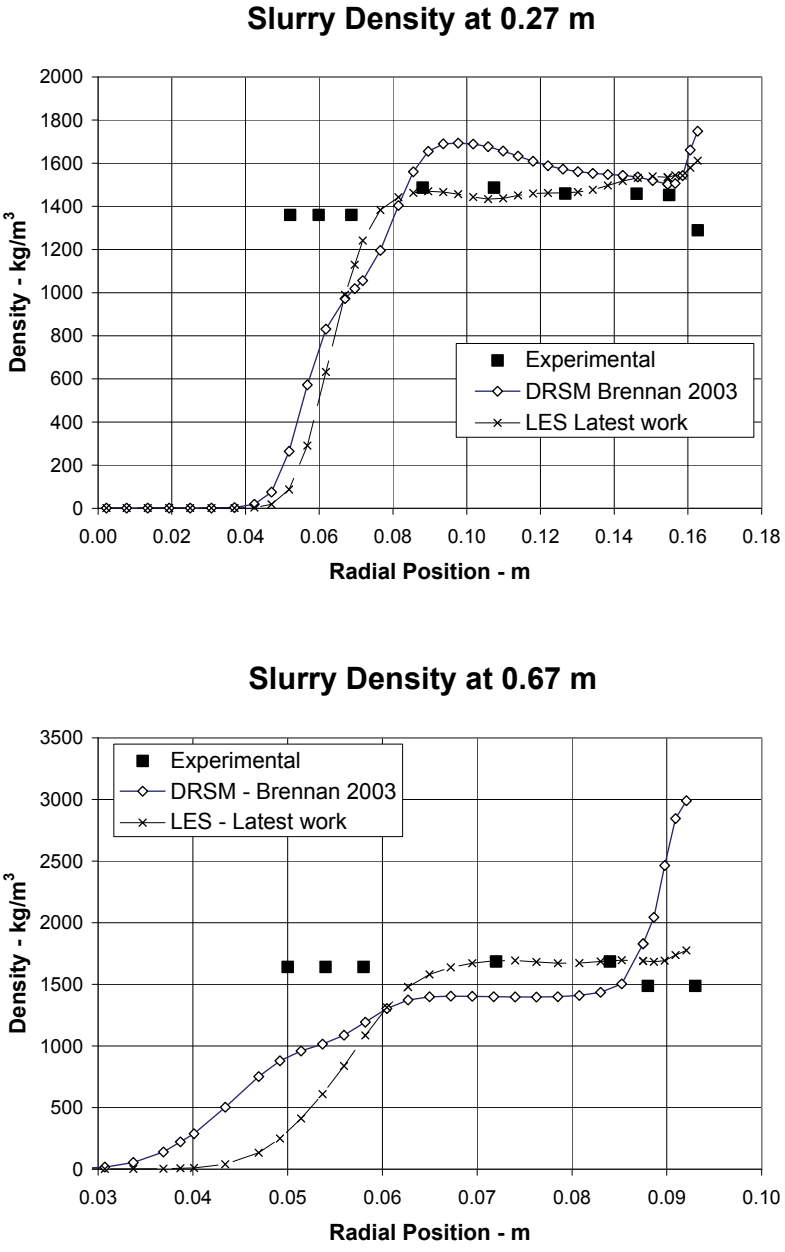


Fig. 6. Comparison between density contours predicted (LES and RSM models) by CFD and those measured by gamma ray tomography (a) at 0.27m, (b) 0.67m from roof of cyclone (Subramanian, 2002) for feed RD of 1.465.

### 3.5 Prediction of Magnetite segregation at different feed slurry densities

Medium segregation was studied with superfine magnetite at three feed solids concentrations (6.12, 7.5 and 11.62 % by volume), corresponding to medium densities of 1245, 1300 and 1465 kg $m^{-3}$. Comparison of density contours between the measured densities of Subramanian (2002) and the medium densities predicted using the modified CFD multi-phase with LES turbulence modified mixture model are shown in Figure 7. The quantitative density comparisons are made in Table 2. The overflow and the underflow densities are predicted well by the LES multi-phase model. Table 2 also shows predictions from the Wood (1990) and Dungilson (1999) models which are empirical models based on a compendium of experimental data for the DSM geometry and these models are close to the experimental values.

| Case | | Dunglison DMC model | Wood DMC model | Experimental values | CFD predictions |
|---|---|---|---|---|---|
| M001 | Feed density, kg.$m^{-3}$ | 1237 | 1237 | 1240 | 1237 |
| | Under flow density, kg.$m^{-3}$ | 1844 | 1725 | 1834 | 1710 |
| | Over flow density, kg.$m^{-3}$ | 1130 | 1114 | 1151 | 1144 |
| | $R_u$, (under flow volumetric fraction) | 0.15 | 0.143 | 0.1304 | 0.157 |
| M002 | Feed density kg.$m^{-3}$ | 1300 | 1300 | 1299 | 1300 |
| | Under flow density, kg.$m^{-3}$ | 1930 | 1769 | 1889 | 1867 |
| | Over flow density, kg.$m^{-3}$ | 1188 | 1182 | 1203 | 1189 |
| | $R_u$, (under flow volumetric fraction) | 0.151 | 0.143 | 0.143 | 0.162 |
| M003 | Feed density, kg.$m^{-3}$ | 1467 | 1467 | 1467 | 1467 |
| | Under flow density, kg.$m^{-3}$ | 2073 | 1868 | 2076 | 1976 |
| | Over flow density, kg.$m^{-3}$ | 1351 | 1366 | 1375 | 1339 |
| | $R_u$ (under flow volumetric fraction) | 0.154 | 0.142 | 0.137 | 0.175 |

Table 2. Comparison of flow densities predicted by CFD (LES-Mixture model) with experimental densities and densities predicted by empirical models. Feed head = 9Dc

From Figure 7, it is observed that an increase in the medium feed concentration increases the density gradient across the radius of cyclone from the air core to the wall of the cyclone. Also the axial medium segregation increases; hence an increase in density differential is expected (see the Figure 8). This effect can be interrelated with changes of medium viscosity in the DMC (He & Laskowski, 1994; Wood, 1990). It is expected that an increase in the feed solids concentration increases the medium viscosity. This increase in slurry viscosity at higher feed medium densities increases the drag on solid particles, which has the effect of reducing the particle terminal velocity, giving the particles less time to settle. This results an increased flow resistance of solid particles and further accumulation of solids near the wall and also at the bottom of the cyclone.

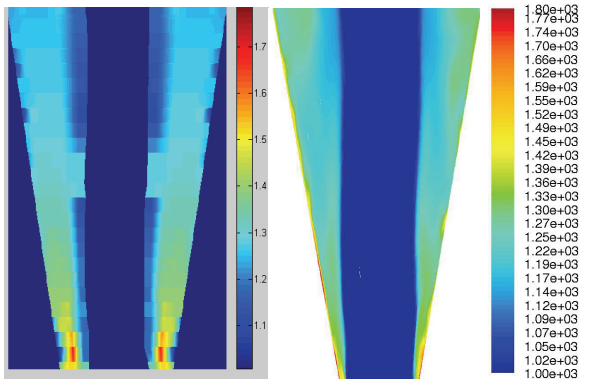


(a) RD@1.245 GRT data (left side) and CFD data (right side

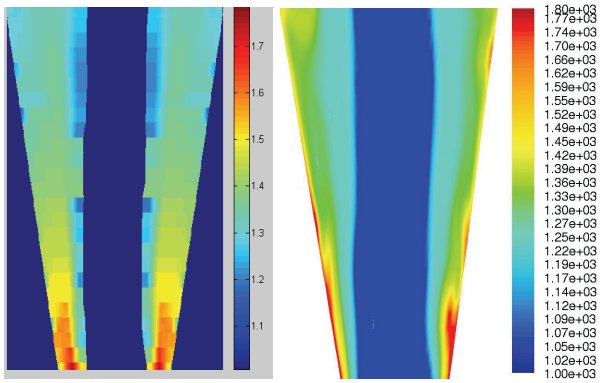


(b) RD@1.3 GRT data (left side) and CFD data (right side)

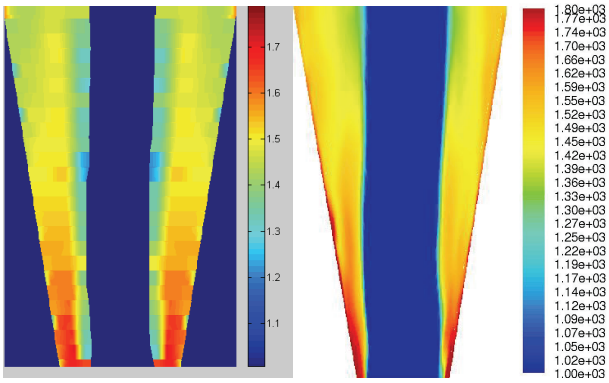


(c) RD@1.465 GRT data (left side) and CFD data (right side)

Fig. 7. Comparison between measured medium density contours (left side) by Subramanian (2002) and predicted medium density contours (right side) by CFD model at different feed medium relative densities (a) RD@1.245, (b) RD@1.3, and (c) RD@1.465 respectively.

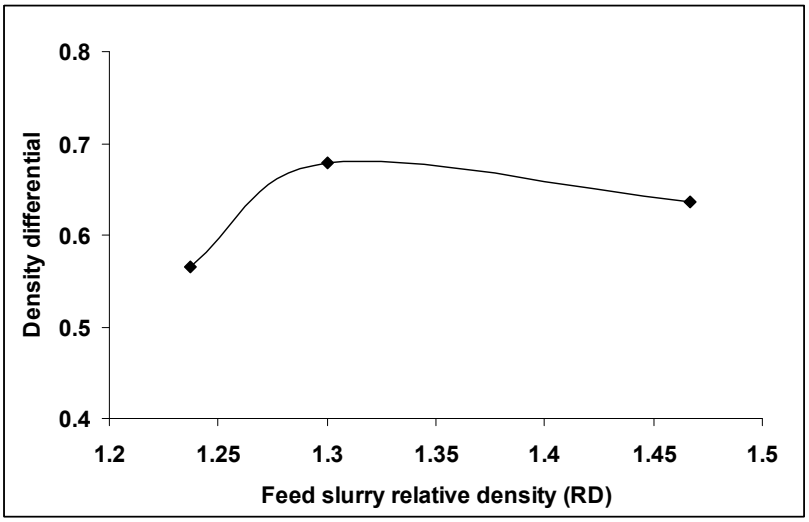


Fig. 8. Predicted density differential at various feed relative densities for superfine magnetite in DSM body

### 3.6 Effect of feed size distribution on medium segregation

The medium properties were modified by changing the particle size distribution. Effect of medium size distribution was investigated. Simulated sizes are given Table 3; the results are shown in Figure 9 and Table 4.

It was observed that reducing $d_{63.2}$ of medium reduces the segregation and density differential. Results are consistent with expected behaviour.

| **Magnetite sample** | $d_{63.2}(\mu m)$ | ***(Rosin-Rammler-Bennett constant) m*** |
|---|---|---|
| Fine | 30.5 | 3.2 |
| Superfine | 20 | 1.6 |
| ultrafine | 17 | 1.45 |

Table 3. Particle size distribution of the tested magnetite samples

| **Magnetite** | **rho_u** | **rho_o** | **diff** |
|---|---|---|---|
| Fine | 2218 | 1267 | 951 |
| Superfine | 1987 | 1339 | 648 |
| ultrafine | 1949 | 1326 | 623 |

Table 4. Predicted density differential for a feed RD@1.465, at feed head = 9 Dc,

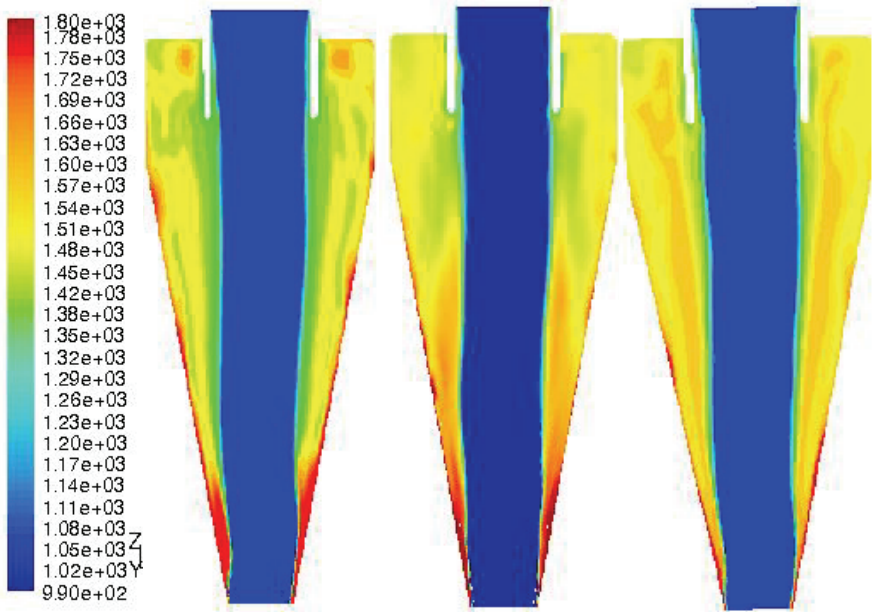


(a) Fine, (b) Superfine, (c) ultra fine

Fig. 9. Contours of medium density for (a) fine, (b) superfine and (c) ultrafine quality in DMC

### 3.7 Prediction of partition curve-pivot phenomena

Coal particles are typically in the range of 1100 and 1800 kg.m$^{-3}$ in density and between 0.5 and 8 mm in size. DPM simulations were conducted where particles in this size range were injected at the feed and tracked. Each DPM simulation was repeated 5 times and 1050 particles were injected per simulation. The outlet stream to which each particle deported was noted and the information used to construct partition curves as function of particle density for given particle sizes. Figure 10 shows the partition curves so generated using a multiphase simulation with a feed RD of 1.2 and a feed head of $9D_c$.

As shown in figure 10, for the first time, the pivot phenomenon, in which partition curves for different sizes of coal pass through a common pivot point, has been successfully modelled using CFD. The predicted pivot parameters deviate slightly from the experimental data. The underflow split ratio and feed RD should be 14% and 1.236 from experimental observations whereas the CFD pivot point represents about 12 % underflow flow ratio and pivot point relative density of 1.215.

This comprehensive CFD model of dense medium cyclone is able to predict the performance of the DSM body reasonably well when compared to float-sink data of -2 +0.5 mm sized coal fraction (Hornsby and Wood 2000) (shown in figure 11). In particular, for the given set of design and operating condition, the predicted Ep value is about 0.075, where as float and sink data represents about 0.0625. The predicted Ep values are close to the experimental values although cut-point predictions deviate slightly. It is believed that the cut-point deviations are due to the interaction between coal particle-particles, which drive the extra resistance forces for the particle separation.

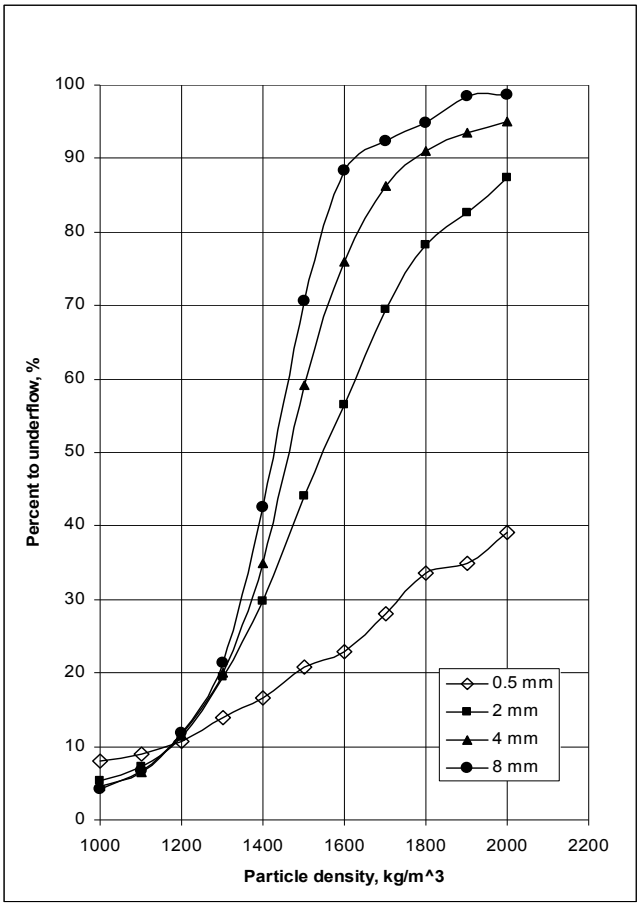


Fig. 10. Predicted size-by-size partition curves in a 350mm DSM cyclone

## 4. Conclusion

A large eddy simulation (LES) coupled with the Mxture Model has been applied to the study of medium segregation in a dense medium cyclone. The Mixture model was modified with corrections for wall lift forces, hindered settling, slurry rheology and particle interactions. Predicted velocity profiles are in agreement with the experimental data of Fanglu and Wenzhen (1987), measured by laser doppler anemometry. The multi-phase mixture model was modified with corrections for wall lift forces, hindered settling, and slurry rheology. Predicted density profiles are close to gamma ray tomography data (Subramanian (2002)) showing a density drop near the wall. At higher feed densities the agreement between the empirical correlations of Dungilson (1998), Wood (1990) and the CFD are reasonably good, but the overflow density from CFD is lower than the empirical model predictions and experimental values. The effect of size distribution of the magnetite has been fully studied. As expected, the ultra-fine magnetite sizes are distributed uniformly

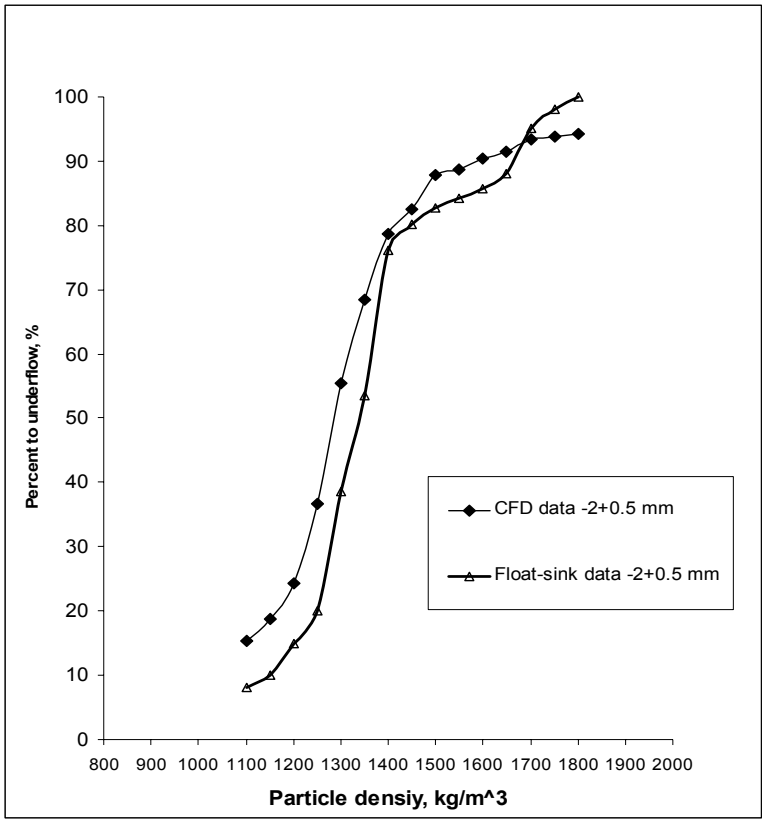


Fig. 11. Comparison of CFD prediction with float-sink data (Hornsby and Wood (2000), feed density RD =1.3 at 9Dc inlet head) in 350mm DSM.

throughout the cyclone. Once correct medium segregation was predicted, the performance characteristics of the DMC on coal were modelled using Lagrangian particle tracking for particles ranging in size from 0.5 to 8 mm. The predicted Ep values are very close to the experimental values although a slight deviation in the cut-point predictions was observed.

## 5. Acknwoledgements

The authors would like to express their sincere thanks to Dr Debashish Bhattacharjee, Direector RD&T, INDIA, TATA Steel groups and Prof. Tim Napier-Munn, Former Director of JKMRC, University of Queensland, Australia for their keen interest and encouragement for undertaking these studies.

## NOMENCLATURE

### Greek symbols

$\alpha$ volume fraction

$\rho$ density kg.m$^{-3}$

$\varepsilon_{ijk}$ permutation tensor
$\tau_{ij}$ stress tensor kg.m$^{-1}$.s$^{-2}$
$\omega_{ij}$ rotation or vorticity vector
$\mu$ viscosity kg.m$^{-1}$.s$^{-1}$

**Other symbols**

$C_d$ drag coefficient
$C_{lp}$ lift coefficient
$d$ particle or phase diameter - m
$D_c$ cyclone diameter – m
$E_p$ cyclone efficiency parameter
$f_{rep}$ drag correction
$F_{lpi}$ lift force on particle - N
$g_i$ gravity - m.s$^{-2}$
$k_d$ fluid particle exchange coefficient
$P_g$ Granular pressure - pa
$Re$ Reynolds number
$t$ time - s
$x_i$ co-ordinate $i$- m
$u_i$ velocity - m.s$^{-1}$

**Subscripts**

$c$ continuous phase
$d$ discrete (coal) phase
$m$ mixture
$p$ particulate (medium) phase

## 6. References

BAGNOLD, R. A., (1954), "Experiments on a gravity free dispersion of large particles in a Newtonian fluid under shear", *Proc. Roy. Soc. London,* A225, 59-63.

BRENNAN, M. S., (2003), "Multiphase CFD simulations of dense medium and classifying hydrocyclones", Proceedings of the 3rd International Conference on CFD in the Minerals and Process Industries, CSIRO Melbourne Australia, 10-12 December 2003, 59-63.

BRENNAN, M.S, SUBRAMANIAN, V.J., RONG, R., HOLTHAM, P.N., LYMAN, G.J., AND NAPIER-MUNN, T.J., (2003), "Towards a new understanding of the cyclone separator", *Proceedings of XXII International Mineral Processing Congress, 29 September – 3 October, 2003, Cape Town, South Africa.*

BRENNAN, M., (2006), "CFD simulations of hydrocyclones with an air core – comparison between large eddy simulations and a second moment closure", *Chemical Engineering Research and Design,* 84A, 495-505

DAVIDSON, M., R., (1994), "A numerical model of liquid-solid flow in a hydrocyclone with high solids fraction", *FED-Vol 185, Numerical Methods in Multiphase Flows, ASME, 29-39.*

DELGADILLO J.A., AND RAJAMANI, R. K., (2005), "A comparative study of three turbulence-closure models for the hydrocyclone problem", *International Journal of Mineral Processing*, 77, 217-230.

FANGLU, G. AND WENZHEN, L., (1987) "Measurement and Study of Velocity Field in Various Cyclones by Use of Laser Doppler Anemometry", *3rd International Conference on Hydrocylones, Oxford, England, 30 September 1987*

GIDASPOW D., BEZBURUAH R, DING J. (1992), "Hydrodynamics of Circulating Fluidized Beds, Kinetic Theory Approach. ",In *Fluidization VII, Proceedings of the 7th Engineering Foundation Conference on Fluidization*, pages 75-82

HIRT, C. W., AND NICHOLS, B. D., (1981), "Volume of fluid (VOF) method for the dynamics of free boundaries", Journal *of Computational Physics*, 39, 201-225.

HORNSBY D., WOOD J. C., (2000), "Long cylinder dense medium cyclones for high near-gravity separations", ACARP project-C3010 report.

HSIEH, K. T., (1988), "*A phenomenological model of the hydrocyclone*", Ph D Thesis, University of Utah.

ISHII, M., AND MISHIMA, K., (1984), "Two-fluid model and hydrodynamic constitutive relations", *Nuclear Engineering and design*, 82, 107-126.

KELSALL, D. F., (1952), "A study of the motion in a hydraulic cyclone", *Transactions of the Institution of Chemical Engineers,* 30, 87-104.

LAUNDER, B.E., REECE, G.J., RODI, W., (1975), "Progress in the development of a Reynolds-stress turbulence closure", *Journal of Fluid Mechanics*, 68, 537-566.

MANNINEN, M., TAIVASSALO V., KALLIO S., (1996), "On the mixture model for multiphase flow", Valtion Teknillinen Tutkimuskeskus, Espoo, Finland.

MEI, R., (1992), "An approximate expression for the shear lift force on a spherical particle at finite Reynolds number", *Int. J. Multiphase flow*, 18, 145-147.

NAPIER-MUNN, T.J., (1990), "The effect of dense medium viscosity on separation efficiency", *Coal Preparation*, 8, 145-165.

NARASIMHA, M., BRENNAN, M. S., HOLTHAM, P. N., (2006), "Numerical Simulation of magnetite segregation in a dense medium cyclone", *Minerals Engineering*, 19, 1034-1047.

NARASIMHA, M., SRIPRIYA, R. AND BANERJEE, P.K., (2005), "CFD modeling of hydrocyclone-prediction of cut size", *International Journal of Mineral Processing, 75(1-2),53-68*

RICHARDSON, J. R., ZAKI, W. N. (1954) Sedimentation and Fluidization: Part I. *Trans. Inst. Chem. Eng*., 32:35-53

SAFFMAN P. G., (1965), "The lift on a small sphere in a slow shear flow", *Journal of Fluid Mechanics*, 22, 385-400.

SCHILLER, L., NAUMANN, Z., Z. (1935), Ver. Deutsch. Ing., 77, 318.

SLACK, M.D., PRASAD, R.O., BAKKER, A., BOYSAN, F., (2000), "Advances in cyclone modeling using unstructured grids", *Transactions of the Institution of Chemical Engineers, Chemical Engineering Research and Design,* 78(A), 1098-1104.

SMAGORINSKY, J., (1963), "General circulation experiments with the primitive equations. I. the basic experiment", *Monthly Weather Review,* 91, 99-164.

SUASNABAR, D.J., (2000), "*Dense Medium Cyclone Performance, Enhancements via computational modeling of the physical process*", PhD Thesis, University of New South Wales.

SUBRAMANIAN, V.J., (2002), "*Measurement of medium segregation in the dense medium cyclone using gamma-ray tomography*", PhD Thesis, JKMRC, University of Queensland.

ZUGHBI, H. D.; SCHWARZ, M.P.; TURNER, W.J. AND HUTTON, W., (1991), "*Numerical and experimental investigations of wear in heavy medium cyclones*", Minerals Engineering, 4, No. ¾, 245-262.

# 13

# Modeling of Turbulent Flows and Boundary Layer

Dr. Srinivasa Rao .P
*C-DAC,*
*India*

## 1. Introduction

Most flows occurring in nature and in engineering applications are turbulent. The boundary layer in the earth's atmosphere is turbulent; jet streams in the upper troposphere are turbulent; cumulus clouds are in turbulent motion. The water currents below the surface of the oceans are turbulent. The Gulf Stream is a turbulent wall-jet kind of flow. The photosphere of the sun and the photospheres of similar stars are in turbulent motion; interstellar gas clouds are turbulent; the wake of the earth in the solar wind is presumably a turbulent wake. Boundary layers growing on aircraft wings are turbulent. The study of turbulence clearly is an interdisciplinary activity, which has a very wide range of applications. In fluid dynamics laminar flow is the exception, not the rule: one must have small dimensions and high viscosities to encounter laminar flow.
Turbulence is the feature of fluid flow but not of fluids. Most of the dynamics of turbulence is the same in all fluids, whether they are liquids or gases, if the Reynolds number of the turbulence is large enough; the major characteristics of turbulent flows are not controlled by the molecular properties of the fluid in which the turbulence occurs. Since the equations of motion are nonlinear, each individual flow pattern has certain unique characteristics that are associated with its initial and boundary conditions. No general solution to the Navier-Stokes equations is known; consequently, no general solutions to problems in turbulent flow are available. Since every flow is different, it follows that every turbulent flow is different, even though all turbulent flows have many characteristics in common. Students of turbulence, of course, disregard the uniqueness of any particular turbulent flow and concentrate on the discovery and formulation of laws that describe entire classes or families of turbulent flows.

## 2. Turbulence

To begin with a question what is turbulence? The Reynolds number of a flow gives a measure of the relative importance of inertia forces and viscous forces. In experiments on fluid systems it is observed that at values below the so-called critical Reynolds number $Re_{cri}$, the flow is smooth and adjacent layers of fluid slide past each other in an orderly fashion. If the applied boundary conditions do not change with time the flow is steady. This regime is called laminar regime. At values of the Reynolds number above $Re_{cri,}$ a complicated series of events takes place which eventually leads to a radical change of the flow character, in the final state the flow behavior is random and chaotic. The motion becomes intrinsically

unsteady even with constant imposed boundary conditions. The velocity and all other flow properties vary in a random and chaotic way. This regime is called turbulent flow.

Turbulence is the state of fluid processing a non regular or irregular motion such that velocity at any point may vary both in magnitude and direction with time. Turbulent motion is also called as serious motion and is accompanied by the formulation of eddies and the rapid interchange of momentum in the fluid. The physical phenomenon of the irregularity or disorderliness is not simply the Turbulence. We do not have a clear-cut or final definition of Turbulence. It can also be stated as the irregular flow of fluid in which various quantities show a random variation with time and space. It is insufficient to define turbulent flow as irregular or chaotic only in time alone or in space alone.

According to von Karman, Turbulence can be generated by fluid flow past solid surfaces or by the flow of layers of fluids at different velocities past or over one another. Turbulence can be distinguished as wall Turbulence and free Turbulence. Wall Turbulence is the Turbulence generated by the viscous effects due to the presence of a solid wall. Free Turbulence is generated by the flow of layers of fluids at different velocities. Why we should study the theory of Turbulence is the another question we must answer. There are many problems of engineering importance such as boundary layer, heat transfer, friction and diffusion of fluids which cannot be estimated correctly without the consideration of Turbulence.

The Figure 1, which depicts a cross-sectional view of a turbulent boundary layer on a flat plate, shows eddies whose length scale is comparable to that of the flow boundaries as well as eddies of intermediate and small size. Particles of fluid which are initially separated by a long distance can be brought close together by the eddying motions in turbulent flows. As a consequence, heat, mass and momentum are very effectively exchanged.

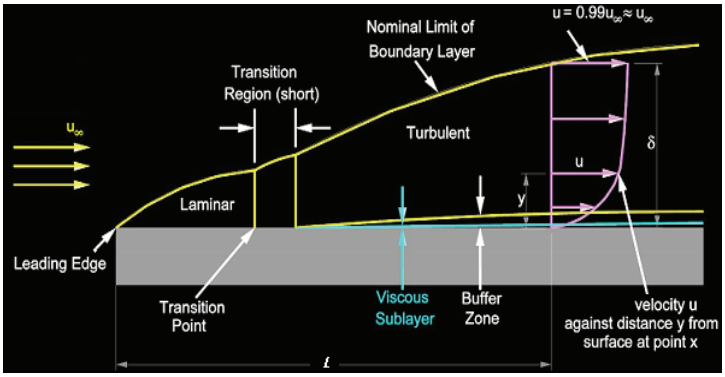


Fig. 1. Turbulent Boundary layer and Viscous Sublayer

For example, a streak of dye which is introduced at a point in a turbulent flow will rapidly break up and be dispersed right across the flow. Such effective mixing gives rise to high values of diffusion coefficients for mass, momentum and heat. The largest turbulent eddies interact with and extract energy from the mean flow by a process called vortex stretching. The presence of mean velocity gradients in sheared flows distorts the rotational turbulent eddies. Suitably aligned eddies are stretched because one end is forced to move faster than the other.

In the fluid flow, if the stress and velocity at a point fluctuate in a random fashion with time. Turbulence sets up greater shear stresses throughout the fluid and causes more

irreversibility or losses. Also the losses vary about 1.7 to 2 power of the velocity in laminar flow, they vary as the first power of the velocity. Turbulent flow occurs when the boundary and initial conditions that are characteristic of the flow led to the spontaneous growth of hydrodynamic instabilities which eventually decay to yield a random statistically fluctuating fluid motion. Now we shall also see that why there is turbulence. The first reason may be the occurrence of strong shear regions in the flow, the presence of wakes or boundary layers; it may be because of separated flow regions or because of Buoyancy flow. Turbulence is characterized by high levels of momentum, heat and mass transport due to turbulent diffusivity. Due to the energy is not supplied continuously in the high shear regions. At slightly higher Reynolds numbers the turbulence primarily gets initiated by the formation of two dimensional vertices and eventually breaks down to a fully three dimensional turbulent flow. If observed figuratively the laminar flow at very low Reynolds number say Re<5, the stream lines are shown in the figure 2; the seams separated and small vortex are shown in the figure 3, though the flow is separated the normal flow parameters would be the same and the stream lines are seen to be more organized and ordered.

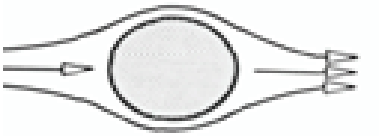

Fig. 2. Re < 5 Laminar attached Steady

Fig. 3. 5 < Re < 40 Laminar Separated Steady

In Figure 4 it is clearly visible that the periodic and laminar separated flow stream lines are getting spread over the spatial scale and over the time period. In the similar way if the flow conditions are further changed to even higher Reynolds number a turbulent wake gets created and the same is shown in the figure 5. The fluid motion becomes turbulent and more chaotic at slightly higher Reynolds number; it is illustrated in the figure 6.

Fig. 4. 40 < Re < 200 Laminar Separated Periodic

Fig. 5. 200 < Re < 350K Turbulent Wake Periodic

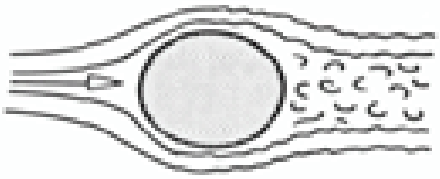

Fig. 6. 350K < Re Turbulent Separation Chaotic

Reynolds was the first person to study the Turbulence experimentally. He used dye experiment to investigate the transition from laminar to turbulent flow. He observed and concluded with his experimental results that transition from laminar to turbulent flow in pipes is occurring at nearly same Reynolds number. He established critical Reynolds number at which laminar regime breaks down to Turbulence for a particular flow conditions. The transition occurs as a result of external disturbances. It is proposed experimentally that there is a definite limit below which all the initial disturbances in the flow will be damped out, and laminar flow becomes stable. The time and space dependent disturbance are analyzed by scientists after Reynolds and in the two dimensional flow plate problems, it is observed that the flow is considered to be stable if the disturbance decay with time. It is very essential to study and understand the nature of Turbulence.
A typical point velocity measurement might exhibit the form shown in Figure below in Fig 7

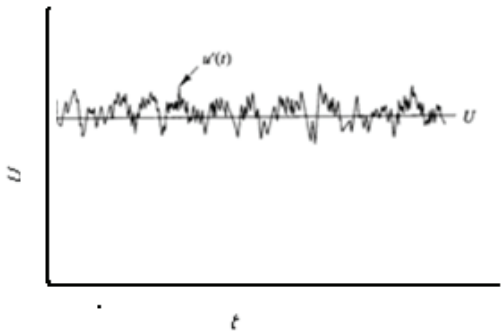


Fig. 7. Point velocities in turbulent flow

The random nature of a turbulent flow precludes computations based on a complete description of the motion of all the fluid particles. Instead the velocity in Figure 1.7 can be decomposed into a steady mean value U with a fluctuating component u'(t) superimposed on it: $U(t) = U + U'(t)$. In general, it is most attractive to characterize a turbulent flow by the mean values of flow properties (U, V, W, P etc.) and the statistical properties of their fluctuations. Even in flows where the mean velocities and pressures vary in only one or two space dimensions, turbulent fluctuations always have a three-dimensional spatial character. Furthermore, visualizations of turbulent flows reveal rotational flow structures, so-called turbulent eddies, with a wide range of length scales.

### 2.1 Characteristics of the turbulent flow

*Highly unsteady*: A plot of velocity as a function of time would appear random to an observer unfamiliar with these flows.

*Irregularity:* It is another characteristic of Turbulence which makes the deterministic approach to Turbulence problems impossible. One should relay on statistical approach.
*Diffusivity:* If the flow pattern is random but does not exhibit spreading of velocity fluctuations through the surrounding fluid then it is not turbulent. The mixing is accomplished by diffusion. This process is also named as turbulent diffusion. The diffusivity of turbulence the single most important feature as far as applications are concerned.
*Three dimensional:* Turbulence is three dimensional and rotational.
*Dissipative:* The turbulent lows are always dissipative. The viscous shear stresses perform deformation work which increases the internal energy of the fluid at the expense of kinetic energy of turbulence.
*Higher Reynolds number:* Turbulence in the fluid flow always occurs at high Reynolds numbers. The instabilities are related to the interaction of viscous terms and non linear inertia terms in the equations of fluid motion.

### 2.2 Transition from laminar to turbulent flow

The initial cause of the transition to turbulence can be explained by considering the stability of laminar flows to small disturbances. A sizeable body of theoretical work is devoted to the analysis of the inception of transition: hydrodynamic instability. In many relevant instances the transition to turbulence is associated with sheared flows. Linear hydrodynamic stability theory seeks to identify conditions which give rise to the amplification of disturbances. Of particular interest in an engineering context is the prediction of the values of the Reynolds numbers at which disturbances are amplified and at which transition to fully turbulent flow takes place. Fig 8 is shown to illustrate the phenomenon. The subject matter is fairly complex but its confirmation has led to a series of experiments which reveal an insight into the physical processes causing the transition from laminar to turbulent flow. Most of our knowledge stems from work on two-dimensional incompressible flows. All such flows are sensitive to two- dimensional disturbances with a relatively long wavelength, several times the transverse distance over which velocity changes take place.

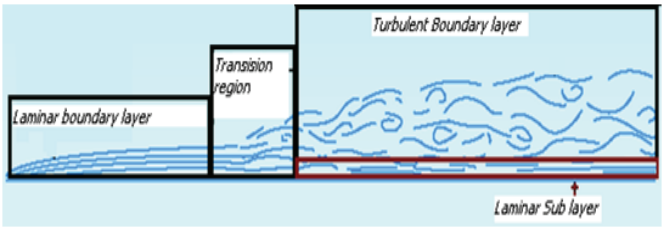


Fig. 8. Transition from Laminar to Turbulent flow

The point where instability first occurs is always upstream of the point of transition to fully turbulent flow. The distance between the points of instability where the Reynolds number equals critical Reynolds and the point of transition depends on the degree of amplification of the unstable disturbances. The point of instability and the onset of the transition process can be predicted with the linear theory of hydrodynamic instability. There is, however, no comprehensive theory regarding the path leading from initial instability to fully turbulent flows. Below we describe the main, experimentally observed, characteristics of three simple flows: jets, flat plate boundary layers and pipe flows.

## 3. General governing equations of fluid flow

The unsteady Navier stokes equations are considered as the governing equations of turbulent flows. These unsteady Navier stokes equations are not easy to solve sometimes next to impossible. The basic Navier-Stokes equations are presented here, as they are the basic equations of fluid flow it becomes essential to the reader to know the equations so that the modifications can easily be understood.

$$\frac{\partial \rho}{\partial t}+\frac{\partial(\rho u)}{\partial x}+\frac{\partial(\rho v)}{\partial y}+\frac{\partial(\rho w)}{\partial z}= \tag{1}$$

$$\begin{aligned}
\rho\left[\frac{\partial v_x}{\partial t}+v_x\frac{\partial v_x}{\partial x}+v_y\frac{\partial v_x}{\partial y}+v_z\frac{\partial v_x}{\partial z}\right] &= -\frac{\partial P}{\partial x}+\mu\left[\frac{\partial^2 v_x}{\partial x^2}+\frac{\partial^2 v_x}{\partial y^2}+\frac{\partial^2 v_x}{\partial z^2}\right] \\
\rho\left[\frac{\partial v_y}{\partial t}+v_x\frac{\partial v_y}{\partial x}+v_y\frac{\partial v_y}{\partial y}+v_z\frac{\partial v_y}{\partial z}\right] &= -\frac{\partial P}{\partial y}+\mu\left[\frac{\partial^2 v_y}{\partial x^2}+\frac{\partial^2 v_y}{\partial y^2}+\frac{\partial^2 v_y}{\partial z^2}\right] \\
\rho\left[\frac{\partial v_z}{\partial t}+v_x\frac{\partial v_z}{\partial x}+v_y\frac{\partial v_z}{\partial y}+v_z\frac{\partial v_z}{\partial z}\right] &= -\rho g\vec{k}-\frac{\partial P}{\partial z}+\mu\left[\frac{\partial^2 v_z}{\partial x^2}+\frac{\partial^2 v_z}{\partial y^2}+\frac{\partial^2 v_z}{\partial z^2}\right]
\end{aligned} \tag{2}$$

The N-S equations are presented as under in the most common form of their practice

$$\begin{aligned}
\rho\frac{Du}{Dt} &= X-\frac{\partial p}{\partial x}+\frac{\partial}{\partial x}\left[\mu\left(2\frac{\partial u}{\partial x}-\frac{2}{3}\,div\,\omega\right)\right]+\frac{\partial}{\partial y}\left[\mu\left(\frac{\partial u}{\partial y}+\frac{\partial v}{\partial x}\right)\right]+\left[\frac{\partial}{\partial z}\left[\mu\left(\frac{\partial \omega}{\partial x}+\frac{\partial u}{\partial z}\right)\right]\right] \\
\rho\frac{Dv}{Dt} &= Y-\frac{\partial p}{\partial x}+\frac{\partial}{\partial y}\left[\mu\left(2\frac{\partial v}{\partial y}-\frac{2}{3}\,div\,\omega\right)\right]+\frac{\partial}{\partial z}\left[\mu\left(\frac{\partial v}{\partial z}+\frac{\partial \omega}{\partial y}\right)\right]+\left[\frac{\partial}{\partial x}\left[\mu\left(\frac{\partial u}{\partial y}+\frac{\partial v}{\partial x}\right)\right]\right] \\
\rho\frac{D\omega}{Dt} &= Z-\frac{\partial p}{\partial x}+\frac{\partial}{\partial z}\left[\mu\left(2\frac{\partial \omega}{\partial z}-\frac{2}{3}\,div\,\omega\right)\right]+\frac{\partial}{\partial y}\left[\mu\left(\frac{\partial \omega}{\partial x}+\frac{\partial u}{\partial z}\right)\right]+\left[\frac{\partial}{\partial y}\left[\mu\left(\frac{\partial v}{\partial z}+\frac{\partial \omega}{\partial y}\right)\right]\right]
\end{aligned} \tag{3}$$

In the form of tensor notation the Navier-Stokes equations is given in the equation [4]

$$\frac{\partial \rho u_i}{\partial t}+\frac{\partial\left(\rho u_i u_j\right)}{\partial x_j}=-\frac{\partial(p)}{\partial x_i}+\frac{\partial}{\partial x_j}\left(\mu\left[\frac{\partial u_i}{\partial x_j}+\frac{\partial u_j}{\partial x_i}\right]\right)-\frac{\partial}{\partial x_i}\left(\tfrac{2}{3}\mu\frac{\partial u_k}{\partial x_k}\right)+S_i \tag{4}$$

Equation of Energy

$$\begin{aligned}
&\frac{\partial(\rho\varepsilon)}{\partial t}+\frac{\partial\left(\rho u_j e\right)}{\partial x_j}=-p\frac{\partial u_j}{\partial x_j}+\frac{\partial}{\partial x_j}\left(k\frac{\partial T}{\partial x_j}\right)+\Phi+S_e \\
&where, \\
&\Phi=\mu\frac{\partial u_i}{\partial x_j}\left(\frac{\partial u_i}{\partial x_j}+\frac{\partial u_j}{\partial x_i}\right)-\tfrac{2}{3}\mu\left(\frac{\partial u_k}{\partial x_k}\right)^2
\end{aligned} \tag{5}$$

If turbulence is entirely irregular and chaotic, it would be inaccessible to any kind of mathematical treatment; instead the irregularity of the turbulence can be described by the laws of probability to a great extent. Through the physics of the turbulence is problem specific, almost all of the situations of the turbulent fluid motion can be mathematically modeled.

Generally the irregular flow would decay if there are no external sources of energy for the continuous generating of turbulence.

The smallest length scale in the study of turbulence is still several orders of magnitude larger than the molecular mean free path. Therefore the continuum approximation is still valid in the study of turbulence. A point here to mention is Navier stokes equations do represent the turbulence without any approximation.

To solve numerically or analytically the full Navier stokes equations we face little difficulty. One such difficulty is computing. For example N-S equation is fineness of spatial and temporal resolution required to represent the smallest length and scales of velocity and pressure fluctuations. Therefore obviously the modern powerful supercomputers also may sometimes fail.

Also when we generally attach a physical problem to solve numerically, there will be eventually round off errors in the methods. Now when we go for finer and finer meshes or grid points the round off errors will accumulate and thereby destroy the accuracy of the solution. However this drawback can be overcome by highly accurate numerical schemes.

Numerical methods for the turbulent flows may be classified as empirical correlations, integral equation, averaging equations. This approach is also known as one point closure which leads to a set of partial differential equations called as Reynolds averaged Navier-stokes (or RANS) equations two-point closure, the Fourier transform equations will be evolved. LES and DNS are the other very important methods. As mentioned above the computation of turbulence is with the determination of time averaged velocity, pressure and temperature profiles and effect of time dependent fluctuations on them. The wall shear stress, heat transfer rates and points of separation could be determined from the time averaged flow properties.

Nevertheless it is quite clear that turbulence is characterized by random fluctuations, the statistical methods are studied extensively rather than deterministic methods. In this approach the time averaging of variables is carried out in order to separate the mean quantities from the fluctuations. As a result of this new unknown variable appears in the governing equations.

Therefore additional equations are needed to close the system, this process is known as turbulence modeling. The turbulence modeling is also known as Reynolds averaged Navier-stokes (or RANS) methods. This approach will help in modeling the large and small scales of turbulence so the requirements of DNS such as refined mesh can be ignored. Large eddy simulation which has become more popular in recent years is actually a compromise between DNS and RANS.

Turbulent flows contain great deal of velocity. It is rotational and moreover three dimensional. Velocity dynamics plays an essential role in the description of turbulent flows. In fact the intensity of turbulence is increased by the mechanism known as vertex stretching, as such the vertex stretching is absent in two dimensional flows.

The instantaneous field fluctuations rapidly in all three spatial dimensions because Turbulence is composed of high level fluctuating vertex. The velocity dynamics also plays an important role in the description of turbulent flows. Turbulent flows always exhibit high

levels of fluctuating vorticity. Turbulent motion is random and irregular, if has a broad range of length scales. It is next to impossible to obtain theoretical solutions by solving three dimensional, time dependent problems. Therefore we are forced to restrict ourselves to go on some averaged quantities; there are two types of averaging procedures.
Conventional time averaging (Reynolds averaging) and Mass – weighed time averaging (Favre averaging). In most of the flow situations the instantaneous values do not satisfy Navier poisson law. There will be additional shear stress due to the turbulence in the fluid flow also to be considered
There are many ways of averaging flow variables such as time averages, spatial averages and mass averages etc.

**Time averages**

Any variable $f$ assumed to be the sum of its mean quantity $\bar{f}$ and its fluctuating part $f'$

$$f(x,t) = \bar{f}(x,t) + f'(x,t)$$

$\bar{f}$ is the time average of $f'$

$$\bar{f}(x,t) = \frac{1}{\Delta t}\int_{t}^{t+\Delta t} f(x,t)dt$$

$$\bar{f}(x,t) = \frac{1}{\Delta t}\int_{t}^{t+\Delta t} f'dt = 0$$

**Spatial Averages**

When the flow variable is uniform on the average such as in homogeneous turbulence,

$$\lim_{\varphi\to\infty}\frac{1}{\varphi}\int_{\varphi} f(x,t)\,d\varphi$$

**Mass Averages:**

The mass average instead of time averages is preferred for compressible flows.

$$F = \bar{f} + f''$$

Where the mean quantity $\bar{f}$ is defined

$$\bar{f} = \frac{\overline{\rho f}}{\rho} = \bar{f} + \frac{\overline{\rho f'}}{\rho}$$

$$\overline{\rho f''} = 0$$

Where as $$\overline{f''} = -\frac{\overline{\rho}\,\overline{f'}}{\overline{\rho}} = 0$$

$\bar{f}$ is known as force fluctuation field.

**Ensemble Averages:**

If N identical experiments are carried out f(x, t) = $f_n$ (x, t) we may determine the average

$$\bar{f}(x,t) = \lim_{N\to\infty} \frac{1}{N} \sum_{n=1}^{N} f_n(x,t)$$

## 4. Reynolds Averaged Navier-Stokes (RANS) equations

As described above, turbulence models seek to solve a modified set of transport equations by introducing averaged and fluctuating components. RANS are time-averaged equations of motion for fluid flow. These equations can be used with approximations based on knowledge of the properties of flow turbulence to give fairly accurate averaged solutions to the Navier–Stokes equations.

For example, Reynolds decomposition refers to separation of the flow variable (like velocity *u*) into the mean (time-averaged) component ( $\bar{u}$ ) and the fluctuating component (*u*′).

Thus the average component is given as

$$u(\mathbf{x},t) = \bar{u}(\mathbf{x}) + u'(\mathbf{x},t)$$

If *f* and *g* are two flow variables, *viz* pressure (*p*), velocity (*u*),density (ρ) and ***s*** is one of the independent variables, independent of space and time then,

$$\bar{\bar{f}} = \bar{f} \;,\; \overline{f+g} = \bar{f} + \bar{g}$$

$$\overline{\bar{f}g} = \bar{f}\bar{g} \;,\; \overline{fg} \neq \bar{f}\bar{g} \text{ and } \overline{\frac{\partial f}{\partial s}} = \frac{\partial \bar{f}}{\partial s}$$

If we consider the incompressible N-S equations now and substitute the average values in the equation then we will be obtaining the new form of equation which can conveniently capture the turbulence to certain flow characteristics' and boundary conditions.

$$\rho\frac{\partial \bar{u}_i}{\partial t} + \rho\frac{\partial \bar{u}_j \bar{u}_i}{\partial x_j} = \rho\bar{f}_i + \frac{\partial}{\partial x_j}\left[-\bar{p}\delta_{ij} + 2\mu\bar{S}_{ij} - \rho\overline{u_i' u_j'}\right] \tag{6}$$

where $\bar{S}_{ij} = \frac{1}{2}\left(\frac{\partial \bar{u}_i}{\partial x_j} + \frac{\partial \bar{u}_j}{\partial x_i}\right)$ is the mean rate of strain tensor

### 4.1 Effect of turbulence on time-averaged Navier-Stokes equations

The critical difference amid visualizations of laminar and turbulent flows is the appearance of eddying motions of a wide range of length scales in turbulent flows. We would need computing meshes of $10^9$ up to $10^{12}$ points to be able to describe processes at all length scales. For instance the direct simulation of a turbulent pipe flow at a Reynolds number of 500000 requires 10 million times faster super computer than CRAY, the fastest supercomputer now in the world.

As the computing power is increasing enormously it may now be possible to track the dynamics of eddies in very simple flows at transitional Reynolds number. The computing requirements for the direct solution of the time dependent Navier-Stokes equations of fully turbulent flows at high Reynolds numbers are truly phenomenal and must await major

developments in computer hardware, in the meantime, engineers need to work on computational procedures which can supply adequate information about the turbulent flow processes, but which can avoid the need to predict the effects of each and every eddy in the flow. We examine the effects of the appearance of turbulent fluctuations on the mean flow properties.

### 4.2 Reynolds equations

First we define the mean Γ of a flow property φ as follows

$$\Gamma = \frac{1}{\Delta t}\int_0^{\Delta t} \varphi(t)\, dt$$

In theory we should take the limit of time interval Δt approaching infinity, but Δt is large enough to hold the largest eddies if it exceeds the time scales of the slowest variations of the property Γ.The general equations of the fluid flow with all kinds of considerations are represented by the Navier stokes equations along with the continuity equation.
The time average of the fluctuations $\overline{\Gamma}'$ is given as

$$\overline{\Gamma}' = \frac{1}{\Delta t}\int_0^{\Delta t} \varphi'(t)\, dt$$

The following rules govern the time averaging of the fluctuating properties used to derive the governing equations of the turbulent fluid flow.

$$\overline{\varphi'} = \overline{\psi'} = 0,\ \overline{\Gamma} = \Gamma_i,\ \frac{\partial \overline{\varphi}}{\partial s} = \frac{\partial \varphi}{\partial s},$$

$$\overline{\int \varphi\, ds} = \int \Gamma\, ds,\ \ \overline{\varphi'} = \overline{\psi'} = \Gamma, \overline{\varphi + \psi} = \Gamma + \Omega \ \text{ and } \ \overline{\varphi\psi} = \Gamma\,\Omega + \overline{\varphi'\psi'}$$

The root mean square of the fluctuations is given by the equation
The kinetic energy associated with the turbulence is

$$\varphi_{rms} = \sqrt{\overline{(\varphi')^2}} = \left[\frac{1}{\Delta t}\int_0^{\Delta t} (\varphi')^2\, dt\right]^{1/2} \qquad k = \frac{1}{2}\left(\overline{u'^2} + \overline{v'^2} + \overline{w'^2}\right)$$

To demonstrate the influence of the turbulent fluctuations on the mean flow, we have to consider the instantaneous continuity and N-S equations.

$$\begin{aligned}
&div\ \mathbf{u} = 0\\
&\frac{\partial u}{\partial t} + div(u\mathbf{u}) = -\frac{1}{\rho}\frac{\partial p}{\partial x} + \nu\ div\ grad\ u\\
&\frac{\partial v}{\partial t} + div(v\mathbf{u}) = -\frac{1}{\rho}\frac{\partial p}{\partial y} + \nu\ div\ grad\ v\\
&\frac{\partial w}{\partial t} + div(w\mathbf{u}) = -\frac{1}{\rho}\frac{\partial p}{\partial z} + \nu\ div\ grad\ w
\end{aligned} \tag{7}$$

The flow variables u and p are to be replaced by their sum of the mean and fluctuating components.

$$\mathbf{u} = \mathbf{U} + \mathbf{u}'; u = U + u';\ v = V + v';\ w = W + w';\ p = P + p'$$

Continuity equation is $div\ \mathbf{U} = 0$

The time averages of the individual terms in the equation are as under

$$\overline{\frac{\partial u}{\partial t}} = \frac{\partial U}{\partial t}; \qquad \overline{div(u\mathbf{u})} = div(U\mathbf{U}) + div\left(\overline{u'\mathbf{u}'}\right)$$

$$\overline{-\frac{1}{\rho}\frac{\partial p}{\partial x}} = -\frac{1}{\rho}\frac{\partial P}{\partial x}; \qquad \overline{v\ div\ grad\ u} = v\ div\ grad\ U$$

Substitution of the average values in the basic derived equation would yield the following momentum conservation equations, the momentum in x- y- and z- directions.

$$\frac{\partial U}{\partial t} + div(U\mathbf{U}) + div\left(\overline{u'\mathbf{u}'}\right) = -\frac{1}{\rho}\frac{\partial P}{\partial y} + v\ div\ grad\ U \tag{8}$$

$$\frac{\partial V}{\partial t} + div(V\mathbf{U}) + div\left(\overline{v'\mathbf{u}'}\right) = -\frac{1}{\rho}\frac{\partial P}{\partial y} + v\ div\ grad\ V \tag{9}$$

$$\frac{\partial W}{\partial t} + div(W\mathbf{U}) + div\left(\overline{w'\mathbf{u}'}\right) = -\frac{1}{\rho}\frac{\partial P}{\partial z} + v\ div\ grad\ W \tag{10}$$

In time-dependent flows the mean of a property at time t is taken to be the average of the instantaneous values of the property over a large number of repeated identical experiments. The flow property cp is time dependent and can be thought of as the sum of a steady mean components and a time-varying fluctuating components with zero mean value; hence p(t) = p + p'(t).

The non zero turbulent stresses usually large compared to the viscous stresses of turbulent flow are also need to be incorporated into the Navier Stokes equations, they are called as the Reynolds equations as shown below in the Euqations [11-13]

$$\frac{\partial U}{\partial t} + div(U\mathbf{U}) = -\frac{1}{\rho}\frac{\partial P}{\partial x} + v\ div\ grad\ U + \left[-\frac{\partial \overline{u'^2}}{\partial x} - \frac{\partial \overline{u'v'}}{\partial y} - \frac{\partial \overline{u'w'}}{\partial z}\right] \tag{11}$$

$$\frac{\partial V}{\partial t} + div(V\mathbf{U}) = -\frac{1}{\rho}\frac{\partial P}{\partial y} + v\ div\ grad\ V + \left[-\frac{\partial \overline{u'v'}}{\partial x} - \frac{\partial \overline{v'^2}}{\partial y} - \frac{\partial \overline{v'w'}}{\partial z}\right] \tag{12}$$

$$\frac{\partial W}{\partial t} + div(W\mathbf{U}) = -\frac{1}{\rho}\frac{\partial P}{\partial z} + \nu\, div\, grad\, W + \left[-\frac{\partial \overline{u'w'}}{\partial x} - \frac{\partial \overline{v'w'}}{\partial y} - \frac{\partial \overline{w'^2}}{\partial z}\right] \quad [13]$$

### 4.3 Modeling flow near the wall

Experiments and mathematical analysis have shown that the near-wall region can be subdivided into two layers. In the innermost layer, the so-called viscous sub layer, as shown in the figure 1 (indicated in blue)the flow is almost laminar-like, only the viscosity plays a dominant role in fluid flow. Further away from the wall, in the logarithmic layer, turbulence dominates the mixing process. Finally, there is a region between the viscous sublayer and the logarithmic layer called the buffer layer, where the effects of molecular viscosity and turbulence are of equal importance. Near a no-slip wall, there are strong gradients in the dependent variables. In addition, viscous effects on the transport processes are large. The representation of these processes within a numerical simulation raises the many problems. How to account for viscous effects at the wall and how to resolve the rapid variation of flow variables which occurs within the boundary layer region is the important question to be answered.

Assuming that the logarithmic profile reasonably approximates the velocity distribution near the wall, it provides a means to numerically compute the fluid shear stress as a function of the velocity at a given distance from the wall. This is known as a 'wall function' and the logarithmic nature gives rise to the well known 'log law of the wall.' Two approaches are commonly used to model the flow in the near-wall region:

The wall function method uses empirical formulas that impose suitable conditions near to the wall without resolving the boundary layer, thus saving computational resources. The major advantages of the wall function approach is that the high gradient shear layers near walls can be modeled with relatively coarse meshes, yielding substantial savings in CPU time and storage. It also avoids the need to account for viscous effects in the turbulence model.

When looking at time scales much larger than the time scales of turbulent fluctuations, turbulent flow could be said to exhibit average characteristics, with an additional time-varying, fluctuating component. For example, a velocity component may be divided into an average component, and a time varying component.

In general, turbulence models seek to modify the original unsteady Navier-Stokes equations by the introduction of averaged and fluctuating quantities to produce the Reynolds Averaged Navier-Stokes (RANS) equations. These equations represent the mean flow quantities only, while modeling turbulence effects without a need for the resolution of the turbulent fluctuations. All scales of the turbulence field are being modeled. Turbulence models based on the RANS equations are known as Statistical Turbulence Models due to the statistical averaging procedure employed to obtain the equations.

Simulation of the RANS equations greatly reduces the computational effort compared to a Direct Numerical Simulation and is generally adopted for practical engineering calculations. However, the averaging procedure introduces additional unknown terms containing products of the fluctuating quantities, which act like additional stresses in the fluid. These terms, called 'turbulent' or 'Reynolds' stresses, are difficult to determine directly and so become further unknowns.

The Reynolds stresses need to be modeled by additional equations of known quantities in order to achieve "closure." Closure implies that there is a sufficient number of equations for all the unknowns, including the Reynolds-Stress tensor resulting from the averaging procedure. The equations used to close the system define the type of turbulence model.

## 5. Turbulance governing equations

As it has been mentioned earlier the nature of turbulence can well be analyzed comprehensively with Navier-stokes equations, averaged over space and time.

### 5.1 Closure problem

The need for turbulence modeling the instantaneous continuity and Navier-Stokes equations form a closed set of four equations with four unknowns' u, v, w and p. In the introduction to this section it was demonstrated that these equations could not be solved directly in the foreseeable future. Engineers are content to focus their attention on certain mean quantities. However, in performing the time-averaging operation on the momentum equations we throw away all details concerning the state of the flow contained in the instantaneous fluctuations. As a result we obtain six additional unknowns, the Reynolds stresses, in the time averaged momentum equations. Similarly, time average scalar transport equations show extra terms. The complexity of turbulence usually precludes simple formulae for the extra stresses and turbulent scalar transport terms. It is the main task of turbulence modeling to develop computational procedures of sufficient accuracy and generality for engineers to predict the Reynolds stresses and the scalar transport terms.

## 6. Turbulence models

A turbulence model is a computational procedure to close the system of flow equations derived above so that a more or less wide variety of flow problems can be calculated adopting the numerical methods. In the majority of engineering problems it is not necessary to resolve the details of the turbulent fluctuations but instead, only the effects of the turbulence on the mean flow are usually sought.

The following are one equation models generally implemented; out of the mentioned three spalart-Allmaras model is used in most of the cases.

- Prandtl's one-equation model
- Baldwin-Barth model
- Spalart-Allmaras model

The Spalart-Allmaras model was designed specifically for aerospace applications involving wall-bounded flows and has been shown to give good results for boundary layers subjected to adverse pressure gradients. It is also gaining popularity for turbo machinery and internal combustion engines also. Its suitability to all kinds of complex engineering flows is still uncertain; it is also true that Spalart-Allmaras model is effectively a low-Reynolds-number model.

In the two equations category there are two most important and predominant models known as k-epsilon, k-omega models. In the k-epsilon model again there are three kinds. However the basic equation is only the k-epsilon, the other two are the later corrections or improvements in the basic model.

### 6.1 K-epsilon models

- Standard k-epsilon model
- Realisable k-epsilon model
- RNG k-epsilon model

Launder and Spalding's the simplest and comprehensive of turbulence modeling are two-equation models in which the solution of two separate transport equations allows the turbulent velocity and length scales to be independently determined.

### 6.2 Standard k-ε model

The turbulence kinetic energy, *k* is obtained from the following equation where as

$$\frac{\partial}{\partial t}(\rho k)+\frac{\partial}{\partial x_i}(\rho k u_i)=\frac{\partial}{\partial x_j}\left[\left(\mu+\frac{\mu_t}{\sigma_k}\right)\frac{\partial k}{\partial x_j}\right]+P_k+P_b-\rho\epsilon-Y_M+S_k$$

rate of dissipation, $\epsilon$ can be obtained from the equation below.

$$\frac{\partial}{\partial t}(\rho\epsilon)+\frac{\partial}{\partial x_i}(\rho\epsilon u_i)=\frac{\partial}{\partial x_j}\left[\left(\mu+\frac{\mu_t}{\sigma_\epsilon}\right)\frac{\partial \epsilon}{\partial x_j}\right]+C_{1\epsilon}\frac{\epsilon}{k}\left(P_k+C_{3\epsilon}P_b\right)-C_{2\epsilon}\rho\frac{\epsilon^2}{k}+S_\epsilon$$

The term in the above equation $P_k=-\rho\overline{u_i'u_j'}\frac{\partial u_j}{\partial x_i}$ represents the generation of turbulence kinetic energy due to the mean velocity gradients.

$P_b=\beta g_i\frac{\mu_t}{\mathrm{Pr}_t}\frac{\partial T}{\partial x_i}$ is the generation of turbulence kinetic energy due to buoyancy and

$Y_M$ Represents the contribution of the fluctuating dilatation in compressible turbulence to the overall dissipation rate

### 6.3 Realisable k- ε model

$$\frac{\partial}{\partial t}(\rho k)+\frac{\partial}{\partial x_j}(\rho k u_j)=\frac{\partial}{\partial x_j}\left[\left(\mu+\frac{\mu_t}{\sigma_k}\right)\frac{\partial k}{\partial x_j}\right]+P_k+P_b-\rho\epsilon-Y_M+S_k$$

$$\frac{\partial}{\partial t}(\rho\epsilon)+\frac{\partial}{\partial x_j}(\rho\epsilon u_j)=\frac{\partial}{\partial x_j}\left[\left(\mu+\frac{\mu_t}{\sigma_\epsilon}\right)\frac{\partial \epsilon}{\partial x_j}\right]+\rho C_1 S\epsilon-\rho C_2\frac{\epsilon^2}{k+\sqrt{\nu\epsilon}}+C_{1\epsilon}\frac{\epsilon}{k}C_{3\epsilon}P_b+S_\epsilon$$

Where $C_1=\max\left[0.43,\frac{\eta}{\eta+5}\right]$, $\eta=S\frac{k}{\epsilon}$, $S=\sqrt{2S_{ij}S_{ij}}$

The realizable *k*- $\epsilon$ model contains a new formulation for the turbulent viscosity. A new transport equation for the dissipation rate, $\epsilon$, has been derived from an exact equation for the transport of the mean-square vorticity fluctuation

In these equations, $G_k$ represents the generation of turbulence kinetic energy due to the mean velocity gradients, and $G_b$ is the generation of turbulence kinetic energy due to buoyancy.

$Y_M$ represents the contribution of the fluctuating dilatation in compressible turbulence to the overall dissipation rate. And some constants *viz* $C_2$ $C_{1\varepsilon}$ and also the source terms $S_k$ and $S_\varepsilon$

### 6.4 RNG k-ε model

The RNG k-ε model was derived using a statistical technique called renormalization group theory. It is similar in form to the standard k-ε model, however includes some refinements

$$\frac{\partial}{\partial t}(\rho k) + \frac{\partial}{\partial x_i}(\rho k u_i) = \frac{\partial}{\partial x_j}\left(\alpha_k \mu_{\text{eff}} \frac{\partial k}{\partial x_j}\right) + G_k + G_b - \rho\epsilon - Y_M + S_k$$

$$\frac{\partial}{\partial t}(\rho\epsilon) + \frac{\partial}{\partial x_i}(\rho\epsilon u_i) = \frac{\partial}{\partial x_j}\left(\alpha_\epsilon \mu_{\text{eff}} \frac{\partial \epsilon}{\partial x_j}\right) + C_{1\epsilon}\frac{\epsilon}{k}(G_k + C_{3\epsilon}G_b) - C_{2\epsilon}\rho\frac{\epsilon^2}{k} - R_\epsilon + S_\epsilon$$

The RNG model has an additional term in its ε equation that significantly improves the accuracy for rapidly edgy flows. The effect of spin on turbulence is included in the RNG model, enhancing accuracy for swirling flows. The RNG theory provides an analytical formula for turbulent Prandtl numbers, while the standard k- ε model uses user-specified, constant values. while the standard k- ε model is a high-Reynolds-number model, the theory provides an analytically-derived differential method for effective viscosity that accounts for low-Reynolds-number effects.

### 6.5 K-ω models

- Wilcox's k-omega model
- Wilcox's modified k-omega model
- SST k-omega model

#### 6.5.1 Wilcox's k-omega model

The K-omega model is one of the most common turbulence models. It is a two equation model that means, it includes two extra transport equations to represent the turbulent properties of the flow. This allows a two equation model to account for history effects like convection and diffusion of turbulent energy.

Kinematic eddy viscosity

$$\nu_T = \frac{k}{\omega}$$

Turbulence Kinetic Energy

$$\frac{\partial k}{\partial t} + U_j \frac{\partial k}{\partial x_j} = \tau_{ij}\frac{\partial U_i}{\partial x_j} - \beta^* k\omega + \frac{\partial}{\partial x_j}\left[(\nu + \sigma^*\nu_T)\frac{\partial k}{\partial x_j}\right]$$

Specific Dissipation Rate

$$\frac{\partial \omega}{\partial t} + U_j \frac{\partial \omega}{\partial x_j} = \alpha\frac{\omega}{k}\tau_{ij}\frac{\partial U_i}{\partial x_j} - \beta\omega^2 + \frac{\partial}{\partial x_j}\left[(\nu + \sigma\nu_T)\frac{\partial \omega}{\partial x_j}\right]$$

The constants are mentioned as under

$$\alpha = \frac{5}{9} \qquad \beta = \frac{3}{40} \qquad \beta^* = \frac{9}{100}$$
$$\sigma = \frac{1}{2} \qquad \sigma^* = \frac{1}{2} \qquad \varepsilon = \beta^*\omega k$$

### 6.5.2 Wilcox's modified k-omega model

Kinematic eddy viscosity

$$\nu_T = \frac{k}{\omega}$$

Turbulence Kinetic Energy

$$\frac{\partial k}{\partial t} + U_j \frac{\partial k}{\partial x_j} = \tau_{ij} \frac{\partial U_i}{\partial x_j} - \beta^* k\omega + \frac{\partial}{\partial x_j}\left[(\nu + \sigma^* \nu_T)\frac{\partial k}{\partial x_j}\right]$$

Specific Dissipation Rate

$$\frac{\partial \omega}{\partial t} + U_j \frac{\partial \omega}{\partial x_j} = \alpha \frac{\omega}{k} \tau_{ij} \frac{\partial U_i}{\partial x_j} - \beta \omega^2 + \frac{\partial}{\partial x_j}\left[(\nu + \sigma \nu_T)\frac{\partial \omega}{\partial x_j}\right]$$

The constants are mentioned as under

$$\alpha = \frac{13}{25} \qquad \beta = \beta_0 f_\beta \qquad \beta^* = \beta_0^* f_{\beta^*} \qquad \sigma = \frac{1}{2} \qquad \sigma^* = \frac{1}{2}$$

$$\beta_0 = \frac{9}{125} \qquad f_\beta = \frac{1+70\chi_\omega}{1+80\chi_\omega} \qquad \chi_\omega = \left|\frac{\Omega_{ij}\Omega_{jk}S_{ki}}{(\beta_0^*\omega)^3}\right| \qquad \beta_0^* = \frac{9}{100} \qquad f_{\beta^*} = \begin{cases} 1, & \chi_k \le 0 \\ \frac{1+680\chi_k^2}{1+80\chi_k^2}, & \chi_k > 0 \end{cases}$$

### 6.6 Standard and SST k- ω models theory

The standard and shear-stress transport k- ω is another important model developed in the recent times. The models have similar forms, with transport equations for k and ω. The major ways in which the SST model differs from the standard model are as follows:

Gradual change from the standard k- ω model in the inner region of the boundary layer to a high-Reynolds-number version of the k- ω model in the outer part of the boundary layer

Modified turbulent viscosity formulation to account for the transport effects of the principal turbulent shear stress. The transport equations, methods of calculating turbulent viscosity, and methods of calculating model constants and other terms are presented separately for each model.

### 6.7 $v^2$-f models

The $v^2$- f model is akin to the standard k-ε model; besides all other considerations it incorporates near-wall turbulence anisotropy and non-local pressure-strain effects. A limitation of the $v^2$- f model is that it fails to solve Eulerian multiphase problems. The $v^2$- f model is a general low-Reynolds-number turbulence model that is suitable to model turbulence near solid walls, and therefore does not need to make use of wall functions.

### 6.7.1 Reynolds stress model (RSM)

The Reynolds stress model is the most sophisticated turbulence model. Abandoning the isotropic eddy-viscosity hypothesis, the RSM closes the Reynolds-averaged Navier-Stokes equations by solving transport equations for the Reynolds stresses, together with an equation for the dissipation rate. This means that five additional transport equations are required in two dimensional flows and seven additional transport equations must be solved in three dimensional fluid flow equations. This is clearly discussed in the following pages. In view of the fact that the Reynolds stress model accounts for the effects of streamline swirl,

curvature, rotation, and rapid changes in strain rate in a more exact manner than one-equation and two-equation models, one can say that it has greater potential to give accurate predictions for complex flows $\rho\overline{u_i'u_j'}$ is known as the transport of the Reynolds stresses

$$\frac{\partial}{\partial t}(\rho\,\overline{u_i'u_j'}) + \frac{\partial}{\partial x_k}(\rho u_k\overline{u_i'u_j'}) = -\frac{\partial}{\partial x_k}\left[\rho\,\overline{u_i'u_j'u_k'} + \overline{p\left(\delta_{kj}u_i' + \delta_{ik}u_j'\right)}\right]$$

$$+ \frac{\partial}{\partial x_k}\left[\mu\frac{\partial}{\partial x_k}(\overline{u_i'u_j'})\right] - \rho\left(\overline{u_i'u_k'}\frac{\partial u_j}{\partial x_k} + \overline{u_j'u_k'}\frac{\partial u_i}{\partial x_k}\right) - \rho\beta(g_i\overline{u_j'\theta} + g_j\overline{u_i'\theta})$$

$$+ \overline{p\left(\frac{\partial u_i'}{\partial x_j} + \frac{\partial u_j'}{\partial x_i}\right)} - 2\mu\overline{\frac{\partial u_i'}{\partial x_k}\frac{\partial u_j'}{\partial x_k}}$$

$$-2\rho\Omega_k\left(\overline{u_j'u_m'}\epsilon_{ikm} + \overline{u_i'u_m'}\epsilon_{jkm}\right) + S_{\text{user}}$$

The first part of the above equation local time derivative and the second term is convection term; the right side of the equation is turbulent and molecular diffusion and buoyancy and stress terms.

### 6.7.2 Large eddy simulation

As it is noted above turbulent flows contain a wide range of length and time scales; the range of eddy sizes that might be found in flow is shown in the figures below. The large scale motions are generally much more energetic than the small ones. Their size strength makes them by far the most effective transporters of the conserved properties. The small scales are usually much weaker and provide little of these properties. A simulation which can treat the large eddies than the small one only makes the sense. Hence the name the large eddy simulation. Large eddy simulations are three dimensional, time dependent and expensive.

LES models are based on the numerical resolution of the large turbulence scales and the modeling of the small scales. LES is not yet a widely used industrial approach, due to the large cost of the required unsteady simulations. The most appropriate area will be free shear flows, where the large scales are of the order of the solution domain. For boundary layer flows, the resolution requirements are much higher, as the near-wall turbulent length scales become much smaller.LES simulations do not easily lend themselves to the application of grid refinement studies both in the time and the space domain. The main reason is that the turbulence model adjusts itself to the resolution of the grid. Two simulations on different grids are therefore not comparable by asymptotic expansion, as they are based on different levels of the eddy viscosity and therefore on a different resolution of the turbulent scales. However, LES is a very expensive method and systematic grid and time step studies are prohibitive even for a pre-specified filter. It is one of the disturbing facts that LES does not lend itself naturally to quality assurance using classical methods. This property of the LES also indicates that (non-linear) multigrid methods of convergence acceleration are not suitable in this application.

The governing equations employed for LES are obtained by filtering the time-dependent Navier-Stokes equations in either Fourier (wave-number) space or configuration (physical) space. The filtering process effectively filters out the eddies whose scales are smaller than

the filter width or grid spacing used in the computations. The resulting equations thus govern the dynamics of large eddies.

A filtered variable is defined by $\overline{\phi}(\mathbf{x}) = \int_{\mathcal{D}} \phi(\mathbf{x}')G(\mathbf{x},\mathbf{x}')d\mathbf{x}'$

When the Navier stokes equations with constant density and incompressible flow are filtered, the following set of equations which are similar to the RANS equations.

$$\frac{\partial \rho}{\partial t} + \frac{\partial}{\partial x_i}(\rho \overline{u}_i) = 0$$

$$\frac{\partial}{\partial t}(\rho \overline{u}_i) + \frac{\partial}{\partial x_j}(\rho \overline{u}_i \overline{u}_j) = \frac{\partial}{\partial x_j}\left(\mu \frac{\partial \sigma_{ij}}{\partial x_j}\right) - \frac{\partial \overline{p}}{\partial x_i} - \frac{\partial \tau_{ij}}{\partial x_j}$$

The continuity equation is linear and does not change due to filtering.

$$\frac{\partial}{\partial x_i}(\rho \overline{u}_i) = 0$$

### 6.8 Example

Wall mounted cube as an example of the LES; the flow over a cube mounted on one wall of a channel. The problem is solved using the mathematical modeling and the Reynolds number is based on the maximum velocity at the inflow. The inflow is fully developed channel flow and taken as a separate simulation, the outlet condition is the convective condition as given above. No-slip conditions all wall surfaces. The mesh is generated in the preprocessor and the same is exported to the solver. The time advancement method is of fractional step type. The convective terms are treated solved by Runge-Kutta second order method in time. The pressure is obtained by solving poisson equation.

The stream lines of the time averaged flow in the region close to the wall is observed. The simulation post processed results and plots are presented. The stream line of the time-averaged flow in the region is depicting the great deal of information about the flow. The

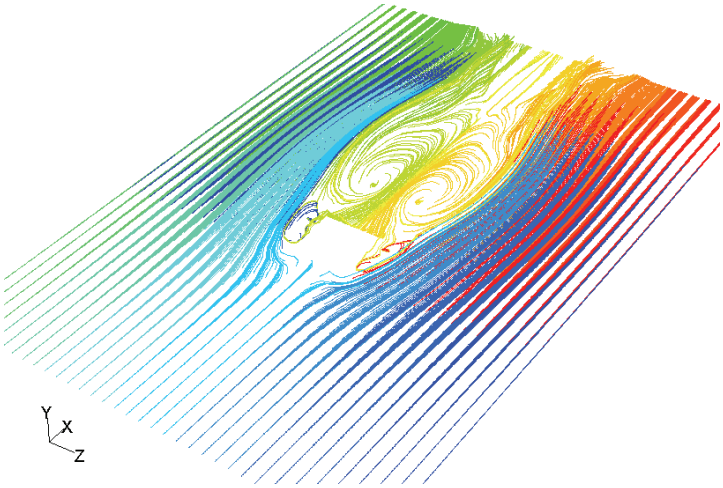


Fig. 9. Stream Lines from the top view

Figure 9 is showing the stream lines and it is clearly visible that the flow is not separated at the incoming and if it is closely observed that there is a secondary separation and reattachment in the flow just afterwards. There are two areas of swirling flow which are the foot prints of the vortex. Almost all the features including the separation zone and also horseshoe vortex.
It is significant to note down that the instantaneous flow looks very different than the time averaged flow.; the arch vortex does not exit in and instantaneous since; there are vortices in the flow but they are almost always asymmetric as shown in the figure figure 10. Indeed, the near-symmetry of figure 10 is an indication that the averaging time is long enough.
Performance of such a simulation has more practical importance and experimental support to such mathematical modeling would help to understand the real time problems.

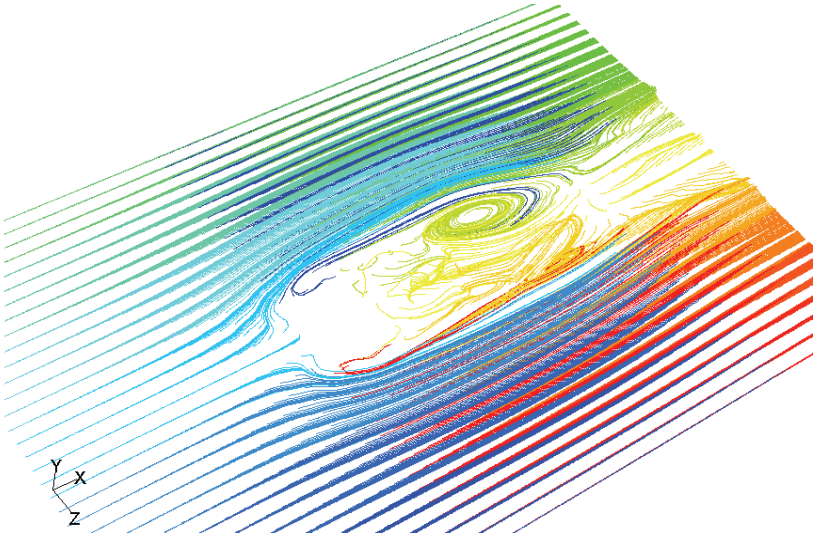


Fig. 10. Stream lines in the region close to the cube to trace the large eddies

## 7. Direct Numerical Simulation (DNS)

A direct numerical simulation (DNS) is a simulation of fluid flow in which the Navier-Stokes equations are numerically solved without any turbulence model. This means that the whole range of spatial and temporal scales of the turbulence must be resolved. Closure is not a problem with the so-called direct numerical simulation in which we numerically produce the instantaneous motions in a computer using the exact equations governing the fluid. Since even when we now perform a DNS simulation of a really simple flow, we are already overwhelmed by the amount of data and its apparently random behavior. This is because without some kind of theory, we have no criteria for selecting from it in a single lifetime what is important.
DNS using high-performance computers is an economical and mathematically appealing tool for study of fluid flows with simple boundaries which become turbulent. DNS is used to compute fully nonlinear solutions of the Navier-Stokes equations which capture important phenomena in the process of transition, as well as turbulence itself. DNS can be

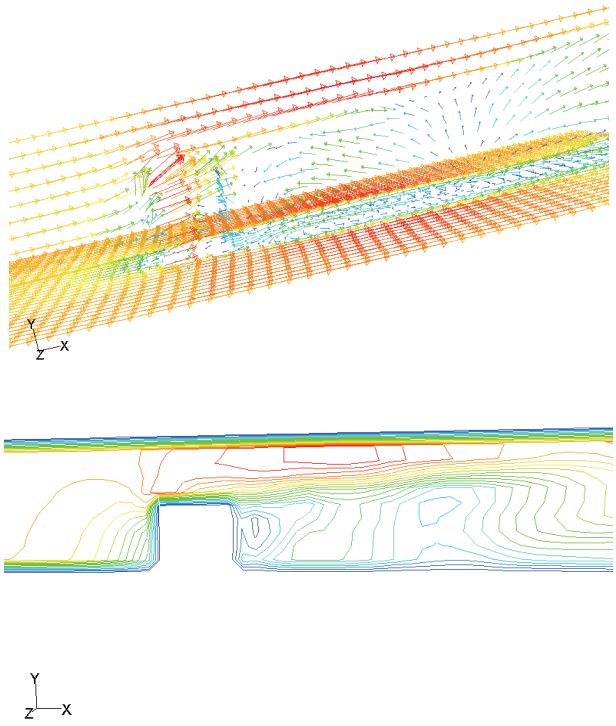


Fig. 11. Vector plots and the stream lines over the cube

used to compute a specific fluid flow state. It can also be used to compute the transient evolution that occurs between one state and another. DNS is mathematical, and therefore, can be used to create simplified situations that are not possible in an experimental facility, and can be used to isolate specific phenomena in the transition process.

All the spatial scales of the turbulence must be resolved in the computational mesh, from the smallest dissipative scales known as Kolmogorov scales, up to the integral scale L, and the kinetic energy.

Kolmogorov scale, η, is given by

$$\eta = (\nu^3/\varepsilon)^{1/4}$$

where ν is the kinematic viscosity and ε is the rate of kinetic energy dissipation.

$Nh > L$, so that the integral scale is contained within the computational domain, and also $h \leq \eta$, so that the Kolmogorov scale can be resolved

Since

$$\varepsilon \approx u'^3/L$$

where $u'$ is the root mean square of the velocity, the previous relations imply that a three-dimensional DNS requires a number of mesh points $N^3$ satisfying

$$N^3 \geq \mathrm{Re}^{9/4} = \mathrm{Re}^{2.25}$$

where Re is the turbulent Reynolds number:

$$\mathrm{Re} = \frac{u'L}{\nu}$$

The memory storage requirement in a DNS grows very fast with the Reynolds number. In addition, given the very large memory necessary, the integration of the solution in time must be done by an explicit method. This means that in order to be accurate, the integration must be done with a time step, Δt, small enough such that a fluid particle moves only a fraction of the mesh spacing *h* in each step. That is,

$$C = \frac{u'\Delta t}{h} < 1$$

*C* is here the Courant number
The total time interval simulated is generally proportional to the turbulence time scale τ given by

$$\tau = \frac{L}{u'.}$$

Combining these relations, and the fact that *h* must be of the order of η, the number of time-integration steps must be proportional to $L/\eta$. By other hand, from the definitions for Re, η and *L* given above, it follows that

$$\frac{L}{\eta} \sim \mathrm{Re}^{3/4}$$

and consequently, the number of time steps grows also as a power law of the Reynolds number.
The contributions of DNS to turbulence research in the last decade have been impressive and the future seems bright. The greatest advantage of DNS is the stringent control it provides over the flow being studied. It is expected that as flow geometries become more complex, the numerical methods used in DNS will evolve. However, the significantly higher numerical fidelity required by DNS will have to be kept in mind. It is expected that use of non-conventional methodologies (e.g. multigrid) will lead to DNS solutions at an affordable cost, and that development of nonlinear methods of analysis are likely to prove very productive.

## 8. The Detached Eddy Simulation model (DES)

In an attempt to improve the predictive capabilities of turbulence models in highly separated regions, Spalart proposed a hybrid approach, which combines features of classical RANS formulations with elements of Large Eddy Simulations (LES) methods. The concept has been termed Detached Eddy Simulation (DES) and is based on the idea of covering the boundary layer by a RANS model and switching the model to a LES mode in detached regions. Ideally, DES would predict the separation line from the underlying RANS model, but capture the unsteady dynamics of the separated shear layer by resolution of the developing turbulent structures. Compared to classical LES methods, DES saves orders of magnitude of computing power for high Reynolds number flows. Though this is due to the moderate costs of the RANS model in the boundary layer region, DES still offers some of the advantages of an LES method in separated regions.

## 9. Final remarks

This chapter provides a first glimpse of the role of turbulence in defining the wide-ranging features of the flow and of the practice of turbulence modeling. Turbulence is a phenomenon of great complexity and has puzzled engineers for over a hundred years. Its appearance causes radical changes to the flow which can range from the favorable to the detrimental. The fluctuations associated with turbulence give rise to the extra Reynolds stresses on the mean flow. What makes turbulence so difficult to attempt mathematically is the wide range of length and time scales of motion even in flows with very simple boundary conditions. It should therefore be considered as truly significant that the two most widely applied models, the mixing length and k-ε models, succeed in expressing the main features of many turbulent flows by means of one length scale and one time scale defining variable. The standard k-ε model still comes highly recommended for general purpose CFD computations. Although many experts argue that the RSM is the only feasible way forward towards a truly general purpose standard turbulence model, the recent advances in the area of non-linear k-e ε models are very likely to re- revitalize research on two-equation models.
Large eddy simulation (LES) models require great computing resources and are used as general purpose tools. Nevertheless, in simple flows LES computations can give values of turbulence properties that cannot be measured in the laboratory owing to the absence of suitable experimental techniques. Therefore LES models will increasingly be used to guide the development of classical models through comparative studies. Although the resulting mathematical expressions of turbulence models may be quite complicated it should never be forgotten that they all contain adjustable.
DNS data is extensively used to evaluate LES results which are an order of magnitude faster to obtain. The availability of this detailed flow information has certainly improved our understanding of physical processes in turbulent flows which thus emphasizes the importance of DNS in present scientific research. Due to the very good correlation between the DNS results and the experimental data, DNS has become synonymous with the term "Numerical Experiment". CFD calculations of the turbulence should never be accepted without the validation with the high quality experiments.

# 14

# Computational Flow Modeling of Multiphase Mechanically Agitated Reactors

Panneerselvam Ranganathan[1] and Sivaraman Savithri[2]
[1]*Department of Geo Technology, Delft University of Technology, 2628 CN Delft,*
[2]*Computational Modeling & Simulation, National Institute for Interdisciplinary Science & Technology (CSIR), Thiruvananthapuram, Kerala,*
[1]*The Netherlands*
[2]*India*

## 1. Introduction

Mixing and dispersion of solids and gases in liquids in mechanically agitated reactors is involved in about 80% of the operations in the chemical industries, including processes ranging from leaching and complete dissolution of reagents to suspension of catalysts and reaction products, such as precipitates and crystals (Smith, 1990). This is one of the most widely used unit operations because of its ability to provide excellent mixing and contact between the phases.

An important aspect in the design of solids suspension in such reactors is the determination of the state of full particle suspension, at which point no particle remains in contact with the vessel bottom for more than 1 sec. Such a determination is critical because until such a condition is reached the total surface area of the particles is not efficiently utilized, and above this speed the rate of processes such as dissolution and ion exchange increases only slowly (Nienow, 1968).

Despite their widespread use, the design and operation of these agitated reactors remain a challenging problem because of the complexity encountered due to the three-dimensional (3D) circulating and turbulent multiphase flow in the reactor. Mechanically agitated reactors involving solid–liquid flows exhibit three suspension states: complete suspension, homogeneous suspension and incomplete suspension, as depicted in Figure 1 (Kraume, 1992).

A suspension is considered to be complete if no particle remains at rest at the bottom of the vessel for more than 1 or 2 sec. A homogeneous suspension is the state of solid suspension, where the local solid concentration is constant throughout the entire region of column. An incomplete suspension is the state, where the solids are deposited at the bottom of reactor. Hence, it is essential to determine the minimum impeller speed required for the state of complete off-bottom suspension of the solids, called the critical impeller speed. It is denoted by $N_{js}$ for solid suspension in the absence of gas and by $N_{jsg}$ for solid suspension in the presence of gas. A considerable amount of research work has been carried out to determine the critical impeller speed starting with the pioneering work of Zwietering (1958) who

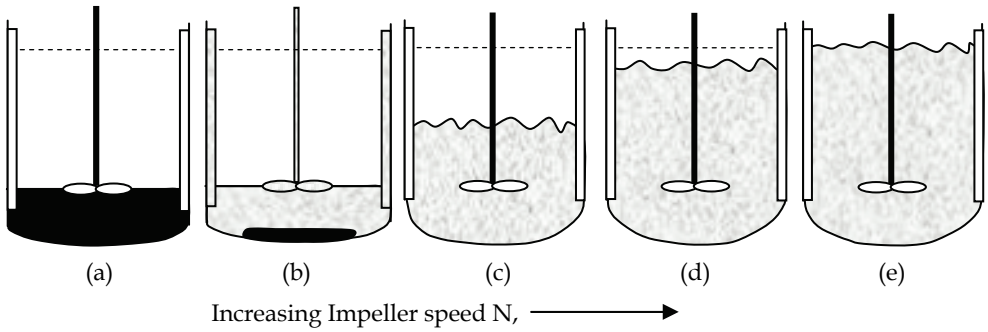


Fig. 1. Flow regimes of liquid–solid stirred reactor (Kraume, 1992)

proposed a correlation for the minimum impeller speed for complete suspension of solids on the basis of dimensional analysis of the results obtained from over a thousand experiments. Since then, numerous papers on determination of critical impeller speed for different operating conditions and different types of impellers have been published (Bohnet and Niesmak, 1980; Chapman et al., 1983a; Kraume, 1992) for liquid–solid stirred reactors, and a few of them (Zlokarnik & Judat, 1969; Chapman et al., 1983b; Warmoeskerken et al., 1984; Nienow et al., 1985; Bujalski et al., 1988; Wong et al., 1987; Frijlink et al., 1990; Rewatkar et al., 1991; Dylag & Talaga, 1994; Dutta & Pangarkar, 1995; Pantula & Ahmed, 1998; Zhu & Wu, 2002) have been extended towards the development of correlations for the critical impeller speed for gas–liquid–solid stirred reactors.

According to the literature, in general, $N_{jsg}$ is always greater than $N_{js}$. Zlokarnik and Judat (1969) have reported that approximately 30% higher impeller speed over $N_{js}$ is required to ensure the resuspension of solid, when gas is introduced. This is due to the reduction in impeller pumping capacity. The reason for the reduction in impeller power in three-phase agitated reactor system has been extensively studied in the literature. Chapman et al. (1983b) explained the decreased liquid pumping capacity and power input on the basis of the sedimentation phenomena. Warmoeskerken et al. (1984) explained the decrease in impeller power due to the formation of gas-filled cavities behind the impeller blades. Rewatkar et al. (1991) reported that the reduction in the impeller power in the three-phase system is due to the formation of solid fillet at the center and along the periphery of the vessel bottom and the formation of gas-filled cavities behind the impeller. Tables 1 & 2 show empirical correlations developed by various authors for the determination of critical impeller speed from their own experimental data for solid–liquid and gas–solid–liquid mechanically agitated reactors.

The critical impeller speed for liquid–solid and gas–liquid–solid mechanically agitated reactors depend on several parameters, such as particle settling velocity, impeller design, impeller diameters and sparger design, and its location. The selection of impeller type is an important consideration for simultaneous solid suspension and gas dispersion with minimum power requirement in such reactors. In the literature, various authors (Chapman et al., 1983b; Frijlink et al., 1990; Rewatkar et al., 1991; Pantula & Ahmed, 1998) have studied the performance of different types of impellers for a solid suspension in a stirred tank for various ranges of operating conditions and concluded that the pitched blade turbine with

downward pumping (PBTD) is more favorable at lower gassing rates and disc turbine (DT) and pitched blade turbine with upward pumping (PBTU) is more favorable at higher gassing rate.

| Authors | Experimental system used | Empirical Correlation |
|---|---|---|
| Zweitering (1958) | Impeller type = Propeller, Disc and 2-paddle<br>T = 0.154–1.0 m<br>D = 0.06–0.26 m<br>C = 0.051E-02–0.076E-02 m<br>Particle density = 2500 kg /m$^3$<br>Dp = 125–850 μm<br>Solid loading = 0.34–3.4 wt % | $N_{js} = \frac{S\gamma^{0.1} dp^{0.2} \left(\frac{g\Delta\rho}{\rho_l}\right)^{0.45}}{D^{0.85}} x^{0.13}$ |
| Nienow (1968) | Impeller type = 6-DT<br>T = 0.14m<br>D = 0.0364, 0.049, 0.073<br>Dp =153–9000 μm<br>Particle density =530–1660 kg/m$^3$<br>Solid loading = 0.1–1.0 wt % | $N_{js} = \frac{(\Delta\rho/\rho_l)^{0.43} dp^{0.21}}{D^{2.25}} x^{0.12}$ |
| Narayanan et al. (1969) | Impeller type = 8-Paddle<br>T = 0.114,0.141 m<br>D = 0.036–0.057 m<br>Particle density =140–1600 kg/m$^3$<br>Dp =106–600 μm<br>Solid loading = 2.5–20 wt % | $N_{js} = \frac{0.9v}{2T - D}\left(\frac{T}{D}\right)^2$<br>$v = \sqrt{\left(2g\left(\rho_p - \rho_l\right)\left(\frac{2dp}{3\rho_p} + \frac{X_s H_{sl}}{\rho_p + H_{sl}\rho_l}\right)\right.}$ |
| Raghava Rao et al. (1988) | Impeller type = 6-DT, 6-PTD, 6-PDU<br>T= 0.3–0.15 m<br>D = 0.175–0.58 m<br>C = 0.5T– 0.167T<br>W/D = 0.25–0.4<br>Particle density = 1520 kg/m$^3$<br>Solid loading = 0–50 wt %<br>Dp =100–2000 μm | $N_{js} = \frac{f\gamma^{0.1}\left(\frac{g\Delta\rho}{\rho_l}\right)^{0.45} X^{0.1} dp^{0.11} T^{0.31}}{D^{1.16}}$ |
| Takahashi et al. (1993) | T = 0.1–0.58 m<br>Impeller type = 6-DT<br>D = 0.05–0.29 m<br>C = 0.0125-0.0725 m<br>Dp = 50–5000 μm<br>Particle density=1049–3720 kg/m$^3$<br>Solid concentration = 0.1–2 vol. % | $N_{js} \propto \frac{\mu^{0.1}\left(\frac{g\Delta\rho}{\rho_l}\right)^{0.34} X^{0.22} dp^{0.023}}{D^{0.54}}$<br>$N_{js} \propto \frac{\mu^{0.1}\left(\frac{g\Delta\rho}{\rho_l}\right)^{0.38} X^{0.17} dp^{0.05}}{D^{0.6}}$ |

| | | |
|---|---|---|
| Rieger and Ditl (1994) | Impeller type = pitched six blade turbines with 45°<br>T= 0.2, 0.3, 0.4 m<br>D= T/3<br>C = 0.5D<br>Dp = 0.18–6 mm<br>Particle density = 1243 kg/m$^3$<br>Solid concentration= 2.5, 10 vol. % | $N_{js} \propto (\Delta\rho/\rho_l)^{0.5} D^{-0.5}$<br>$N_{js} \propto (\Delta\rho/\rho_l)^{0.5} d_p^{0.3} D^{-0.8}$<br>$N_{js} \propto \Delta\rho^{0.42} \rho_l^{-0.58} \mu^{0.16} D^{-0.73}$<br>$N_{js} \propto \Delta\rho^{0.42} \rho_l^{-0.58} \mu^{0.16} d_p^{0.25} D^{-0.99}$ |
| Ibrahim & Nienow (1996) | Impeller type = 6-DT, 6-FDT, 6-PDT<br>T = 0.292,0.33 m<br>D = 0.065–0.102<br>Particle density = 2500 kg/m$^3$<br>Dp = 110 µm<br>Solid concentration = 0.5 vol % | $N_{js} = \frac{S\gamma^{0.1} dp^{0.2} \left(\frac{g\Delta\rho}{\rho_l}\right)^{0.45}}{D^{0.85}} x^{0.13}$ |
| Armenante & Nagamine (1998) | Impeller type = 6-DT, 6-FBT, 6-PTD, HE-3<br>T= 0.188–0.584 m<br>D= 0.0635–0.203m<br>Particle density = 2500 kg/m$^3$<br>Dp =60–300 µm<br>Solid concentration = 0.5 vol % | $N_{js} = \frac{S\gamma^{0.1} dp^{0.2} \left(\frac{g\Delta\rho}{\rho_l}\right)^{0.45}}{D^{0.13}} x^{0.13}$ |
| Bujalski et al. (1999) | Impeller type = A310, A315<br>T= 0.29 m<br>D= 0.10–0.12 m<br>Particle density=1350–500kg/m$^3$<br>Dp = 100–1000 µm<br>Solid concentration = 0–40% | $N_{js} = \frac{S\gamma^{0.1} dp^{0.2} \left(\frac{g\Delta\rho}{\rho_l}\right)^{0.45}}{D^{0.85}} x^{0.13}$ |
| Sharma & Shaikh (2003) | Impeller type: 4,6-PTD<br>T= 0.15–1.21 m<br>D= 0.0535-0.348 m<br>Particle density=1390–635kg/m$^3$<br>Dp = 130–850 µm<br>Solid concentration =1.55–2 vol.% | $N_{js} = \frac{S\gamma^{0.1} dp^{0.2} \left(\frac{g\Delta\rho}{\rho_l}\right)^{0.45}}{D^{-2.0}} x^{0.13}$ |
| Dohi et al. (2004) | Impeller type = Maxblend, PTD Fullzone,Pfaudler<br>T= 0.2–0.8 m<br>D= 0.42T–0.53T m<br>Particle density = 2500 kg/m$^3$<br>Dp = 187–810 µm<br>Solid concentration =0–30 by vol.% | $N_{js} = \frac{S\gamma^{0.1} dp^{0.2} \left(\frac{g\Delta\rho}{\rho_l}\right)^{0.45}}{D^{-0.85}} x^{0.13}$ |

Table 1. Empirical correlations for the critical impeller speed from the literature for solid–liquid mechanically agitated reactors

Another criterion which is also used for assessing the quality of solids suspension is the degree of homogeneity of suspension. Einenkel (1979), suggested the variance of solid concentration as a measure of homogeneity of the solids suspension, which is defined as

$$\sigma^2 = \frac{1}{n}\sum_{1}^{n}\left(\frac{C}{\overline{C}} - 1\right)^2 \quad (1)$$

| References | Experimental system used | Empirical correlation |
|---|---|---|
| Chapman et al.(1983b) | tank diameter = 0.29–1.83 m,<br>Impeller type = DT, PBTD and PBTU and marine propeller<br>impeller clearance = T/4<br>solid loading = 0.34–50 wt %<br>particle density = 1050– 2900 kg /m$^3$<br>particle diameter = 100–2800 µm<br>air flow rate = 0–32 mm/s<br>sparger type = ring, pipe, conical and concentric rings | $\Delta N_{js} = N_{jsg} - N_{js}$<br>$= kQ_v$<br>where k=0.94 |
| Nienow et al.(1985) | tank diameter = 0.45 m<br>impeller type = Disc turbine<br>impeller diameter = 0.225 m<br>impeller clearance = 0.1125 m<br>particle type = glass beads<br>particle diameter = 440–530 µm | $\Delta N_{js} = N_{jsg} - N_{js}$<br>$= kQ_v$<br>where k=0.94 |
| Wong et al.(1987) | tank diameter = 0.29 m<br>impeller type = Propeller, Disc and Pitched turbine<br>impeller diameter = 0.06–0.26 m<br>impeller clearance = 0.051– 0.076 m<br>particle density = 2514–8642 kg /m$^3$<br>particle diameter = 200–1200 µm<br>air flow rate = 0–2 vvm | $\Delta N_{js} = N_{jsg} - N_{js}$<br>$= kQ_v$<br>where k=2.03 for DT,<br>k=4.95 for PBTD |
| Rewatkar et al.(1991) | tank diameter = 0.57–1.5 m,<br>impeller type = RT, PBTD and PBTU<br>impeller diameter = 0.175T–0.58T m<br>impeller clearance = T/3<br>particle diameter = 100–2000 µm<br>air flow rate = 0–32 mm/s<br>Solid loading = 0.34–50 wt %<br>sparger type = ring, pipe, conical and concentric rings | $\Delta N_s = 132.7 V_{s\infty}^{0.5} D^{-1.67} T V_g$<br>where $\Delta N_s = N_{jsg} - N_{sp}$<br>$N_{sp}$= critical impeller speed for solid suspension in the presence of sparger<br>$N_{jsg}$= critical impeller speed for suspension in gas-liquid-solid system<br>$V_{s\infty}$= terminal setting velocity of particle |

| | | |
|---|---|---|
| Dylag and Talaga (1994) | tank diameter = 0.3 m and ellipsoidal bottom<br>impeller type = DT and PBTD<br>impeller clearance = 0.5D<br>particle density = 2315 kg /m3<br>particle diameter = 0.248–0.945 mm<br>air flow rate = 1.5–22.5 mm/s<br>solid loading = 2–30 wt % | For DT<br>$\frac{N_{jsg}D^2\rho_c}{\eta_c} = 18.95\times10^4\left(\frac{v_G D\rho_g}{\eta_g}\right)^{0.15} X^{0.15}\left(\frac{d_p}{D}\right)^{0.20}$<br>For PBTD<br>$\frac{N_{jsg}D^2\rho_c}{\eta_c} = 17.55\times10^4\left(\frac{v_G D\rho_g}{\eta_g}\right)^{0.31} X^{0.15}\left(\frac{d_p}{D}\right)^{0.20}$ |

Table 2. Empirical correlations for the critical impeller speed from the literature for gas–solid– liquid mechanically agitated reactors

Bohnet and Niesmak (1980) used the square root of variance, which corresponds to the standard deviation of the concentration profile (σ). Kraume, (1992) used another measure to evaluate the homogeneity of suspension which is based on the cloud height. The suspension is said to be homogeneous when the solid concentration is uniform throughout the tank. When the slurry height or cloud height becomes equal to 0.9H, the state of suspension is said to be homogeneous where H refers to the height of the reactor. Even though the suspended slurry height or cloud height is not an absolute measure of homogeneity, it may be useful for comparing the identical slurries.

During the last few decades, various models have been proposed for quantifying the solid suspension from the theoretical power requirement. Kolar (1967) presented a model for solid suspension based on energy balance, that all the power is consumed for suspending the solids and that the stirred tank is hydrodynamically homogeneous. Baldi et al. (1978) proposed a new model for complete suspension of solids where it is assumed that the suspension of particles is due to turbulent eddies of certain critical scale. Further it is assumed that the critical turbulent eddies that cause the suspension of the particles being at rest on the tank bottom have a scale of the order of the particles size, and the energy transferred by these eddies to the particles is able to lift them at a height of the order of particle diameter. Since their hypothesis related to the energy dissipation rate for solid suspension to the average energy dissipation in the vessel by employing modified Reynolds number concept, it gave good insight into the suspension process compared to other approaches. Chudacek (1986) proposed an alternative model for the homogeneous suspension based on the equivalence of particle settling velocity and mean upward flow velocity at the critical zone of the tank which leads to the constant impeller tip speed criterion, but this is valid only under conditions of geometric and hydrodynamic similarity. Shamlou and Koutsakos (1989) introduced a theoretical model based on the fluid dynamics and the body force acting on solid particles at the state of incipient motion and subsequent suspension. Rieger and Ditl (1994) developed a dimensionless equation for the critical impeller speed required for complete suspension of solids based on the inspection analysis of governing fluid dynamic equations. They observed four different hydrodynamic regimes based on the relative particle size and Reynolds number values.

Although the available correlations in the literature are of great importance from an operational view-point, they do not provide a clear understanding of the physics underlying the system. From a physical standpoint, the state of suspension of solid particles in the reactor is completely governed by the hydrodynamics and turbulence prevailing in the reactor. Only a few studies (Guha et al., 2007; Spidla et al., 2005 (a,b); Aubin et al., 2004) have been made to understand the complex hydrodynamics of such complicated stirred reactors. Even though in the recent past, both invasive and non invasive experimental measurement techniques have been reported in the literature, a systematic experimental study to characterize the solid hydrodynamics in mechanically agitated reactors can hardly be found in the literature.

For this reason, computational fluid dynamics (CFD) has been promoted as a useful tool for understanding multiphase reactors (Dudukovic et al., 1999) for precise design and scale up. Although much experimental effort has been focused on developing correlations for just-suspension speed, CFD simulations offer the only cost-effective means to acquire the detailed information on flow and turbulence fields needed for realistic distributed-parameter process simulations. The RANS-based CFD approach is the most widely used approach for the multiphase phase flow simulation of such reactors. In the literature, CFD based simulations have been used to predict the critical impeller speed for a solid suspension in a liquid–solid stirred tank reactor (Bakker et al., 1994; Micale et al., 2000; Barrue et al., 2001; Sha et al., 2001; Kee and Tan, 2002; Montante & Magelli 2005; Khopkar et al., 2006; Guha et al., 2008) by employing the Eulerian–Eulerian approach, and this prediction have been extended to the case of gas–liquid–solid stirred tank reactors. Recently Murthy et al. (2007) carried out CFD simulations for three-phase stirred suspensions. The effect of tank diameter, impeller diameter, type, location, size, solid loading and superficial gas velocity on the critical impeller speed was investigated by them using the standard deviation approach. The solid loading in their study varied from 2–15% by weight. But most of the industrial applications, especially hydrometallurgical applications, involve high density particles with high concentration. Moreover, it has been reported in the literature (Khopkar et al., 2006; van der Westhuizen & Deglon, 2008) that it is difficult to quantify the critical impeller just based on the standard deviation approach alone.

Hence, the objective of this work is to carry out the CFD simulation based on the Eulerian multi-fluid approach for the prediction of the critical impeller speed for high density solid particles with solid loading in the range of 10–30% by weight. CFD Simulations were carried out using the commercial package ANSYS CFX-10. Since any CFD simulation has to be validated first, the CFD simulations have been validated with those reported in the literature (Guha et al., 2007; Spidla et al., 2005; Aubin et al., 2004) for solid–liquid agitated reactors. After the validation, the CFD simulations have been extended for gas–liquid–solid mechanically agitated contactor to study the effects of impeller design, impeller speed, particle size and gas flow rate on the prediction of critical impeller speed based on both the standard deviation approach and cloud height criteria, and the simulation results were compared with our experimental results.

## 2. CFD modeling

### 2.1 Eulerian multiphase model

Even though CFD models have shown to be successful in simulating single-phase flow generated by impeller(s) of any shape in complex reactors (Ranade, 2002), the complexity of

modeling increases considerably for multiphase flows because of various levels of interaction of different phases. Two widely used modeling methods for multiphase flows are Eulerian–Eulerian or two fluid approach and Eulerian–Lagrangian approach. In Eulerian–Lagrangian approach, trajectories of dispersed phase particles are simulated by solving an equation of motion for each dispersed phase particle. Motion of the continuous phase is modeled using a conventional Eulerian framework. Depending on the degree of coupling (one–way, two–way or four–way), solutions of both phases interact with each other. But this approach can only be used for multiphase systems with a low solid volume fraction (≤ 5%) because of the tremendous computational need. In Eulerian–Eulerian approach, the dispersed phase is treated as a continuum. All phases 'share' the domain and may interpenetrate as they move within it. This approach is more suitable for modeling dispersed multiphase systems with a significant volume fraction of dispersed phase (>10%). But the coupling between different phases is incorporated in this approach by developing suitable interphase transport models. The computational details along with merits and demerits of these two approaches are given in the book by Ranade (2002).

For the present work, the liquid–solid/gas–liquid–solid flows in mechanically agitated contactor are simulated using Eulerian multi-fluid approach. Each phase is treated as a different continuum which interacts with other phases everywhere in the computational domain. The share of the flow domain occupied by each phase is given by the volume fraction. Each phase has its own velocity, temperature and physical properties. In this work, both gas and solid phases are treated as dispersed phases and the liquid phase is treated as continuous. The motion of each phase is governed by respective Reynolds averaged mass and momentum conservation equations. The general governing equations are given below:

**Continuity equation:**

$$\frac{\partial}{\partial t}\left(\epsilon_k \rho_k\right) + \nabla.\left(\rho_k \epsilon_k \vec{u}_k\right) = 0 \tag{2}$$

where $\rho_k$ is the density and $\epsilon_k$ is the volume fraction of phase k (liquid, gas or solid) and the volume fraction of the all phases satisfy the following condition:

$$\sum_k \epsilon_k = 1 \tag{3}$$

**Momentum Equations:**

$$\frac{\partial}{\partial t}.\left(\rho_k . \epsilon_k . \vec{u}_k\right) + \nabla.\left(\rho_k . \epsilon_k . \vec{u}_k \vec{u}_k\right) - \nabla.\left(\epsilon_k \mu_{eff,k}\left(\nabla \vec{u}_k + \left(\nabla \vec{u}_k\right)^T\right)\right) = -\epsilon_k . \nabla P + \rho_k . \epsilon_k . \vec{g} + F \tag{4}$$

where $\mu_{eff,k}$ is the phase viscosity, P is the pressure, g is the gravitational acceleration and F stands for time averaged interface force between different phases and are discussed in detail below.

**Interphase transport models**

There are various interaction forces such as the drag force, the lift force and the added mass force etc. during the momentum exchange between the different phases. But the main interaction force is due to the drag force caused by the slip between the different phases. Recently, Khopkar et al. (2003, 2005) studied the influence of different interphase forces and reported that the effect of the virtual mass force is not significant in the bulk region of

agitated reactors and the magnitude of the Basset force is also much smaller than that of the inter-phase drag force. Further they also reported that the turbulent dispersion terms are significant only in the impeller discharge stream. Very little influence of the virtual mass and lift force on the simulated solid holdup profiles was also reported by Ljungqvist and Rasmuson (2001). Hence based on their recommendations and also to reduce the computational time, the interphase drag force and turbulent dispersion force are considered in this work.

**Solid-liquid mechanically agitated reactor**

For this case, the liquid phase is treated as a continuous phase and the solid phase is treated as a dispersed phase. The corresponding momentum equations are
Liquid phase (continuous phase)

$$\frac{\partial}{\partial t}.\left(\rho_l.\in_l.\vec{u}_l\right)+\nabla.\left(\rho_l.\in_l.\vec{u}_l\vec{u}_l\right)=-\in_l.\nabla P+\nabla.\left(\in_l \mu_{eff,l}\left(\nabla\vec{u}_l+\left(\nabla\vec{u}_l\right)^T\right)\right)+\rho_l\in_l\vec{g}+\vec{F}_{D,ls}+\vec{F}_{TD} \quad (5)$$

Solid phase (dispersed solid phase)

$$\begin{aligned}&\frac{\partial}{\partial t}.\left(\rho_s.\in_s.\vec{u}_s\right)+\nabla.\left(\rho_s.\in_s.\vec{u}_s\vec{u}_s\right)=\\&-\in_s.\nabla P-\nabla P_s+\nabla.\left(\in_s \mu_{eff,s}\left(\nabla\vec{u}_s+\left(\nabla\vec{u}_s\right)^T\right)\right)+\rho_s.\in_s.\vec{g}-\vec{F}_{D,ls}-\vec{F}_{TD}\end{aligned} \quad (6)$$

where the interphase drag force between the liquid and solid phases is represented by the equation

$$\vec{F}_{D,ls}=C_{D,ls}\frac{3}{4}\rho_l\frac{\in_s}{d_p}\left|\vec{u}_s-\vec{u}_l\right|\left(\vec{u}_s-\vec{u}_l\right) \quad (7)$$

where the drag coefficient proposed by Brucato et al. (1998) is used viz.,

$$\frac{C_{D,ls}-C_{D0}}{C_{D0}}=8.67\times10^{-4}\left(\frac{d_p}{\lambda}\right)^3 \quad (8)$$

where, $d_p$ is the particle size and $\lambda$ is the Kolmogorov length scale, $C_{D0}$ is the drag coefficient in stagnant liquid which is given as

$$C_{D0}=\frac{24}{Re_p}\left(1+0.15Re_p^{\,0.687}\right) \quad (9)$$

where $Re_p$ is the particle Reynolds number.
The turbulent dispersion force is the result of the turbulent fluctuations of liquid velocity which approximates the diffusion of the dispersed phase from higher region to lower region. The following equation for the turbulent dispersion force derived by Lopez de Bertodano (1992) is used for the present simulation and is given by

$$\vec{F}_{TD}=-C_{TD}\rho_l k_l\nabla\in_l \quad (10)$$

where $C_{TD}$ is a turbulent dispersion coefficient, and is taken as 0.1 for the present investigation.

**Gas-liquid-solid mechanically agitated reactor**

For this case, the liquid phase is treated as a continuous phase and both the gas and the solid phases are treated as dispersed phases. The interphase forces considered for this simulation are the drag forces between liquid and solid, and liquid and gas and the turbulent dispersion force. The corresponding momentum equations are
Gas phase (dispersed fluid phase)

$$\frac{\partial}{\partial t}.\left(\rho_g . \in_g .\vec{u}_g\right) + \nabla.\left(\rho_g . \in_g .\vec{u}_g\vec{u}_g\right) = - \in_g .\nabla P + \nabla.\left(\in_g \mu_{eff,g}\left[\nabla\vec{u}_g + \left(\nabla\vec{u}_g\right)^T\right]\right) + \rho_g . \in_g .\vec{g} - \vec{F}_{D,lg} \quad (11)$$

Liquid phase (continuous phase)

$$\begin{aligned}&\frac{\partial}{\partial t}.\left(\rho_l . \in_l .\vec{u}_l\right) + \nabla.\left(\rho_l . \in_l .\vec{u}_l\vec{u}_l\right) = \\ &- \in_l .\nabla P + \nabla.\left(\in_l \mu_{eff,l}\left[\nabla\vec{u}_l + \left(\nabla\vec{u}_l\right)^T\right]\right) + \rho_l \in_l \vec{g} + \vec{F}_{D,lg} + \vec{F}_{D,ls} + \vec{F}_{TD}\end{aligned} \quad (12)$$

Solid phase (dispersed solid phase)

$$\begin{aligned}&\frac{\partial}{\partial t}.\left(\rho_s . \in_s .\vec{u}_s\right) + \nabla.\left(\rho_s . \in_s .\vec{u}_s\vec{u}_s\right) \\ &= - \in_s .\nabla P - \nabla P_s + \nabla.\left(\in_s \mu_{eff,s}\left[\nabla\vec{u}_s + \left(\nabla\vec{u}_s\right)^T\right]\right) + \rho_s . \in_s .\vec{g} - \vec{F}_{D,ls} - \vec{F}_{TD}\end{aligned} \quad (13)$$

The drag force between the solid and liquid phases and the turbulent dispersion force are the same as given by equations (7–9 ). The drag force between the gas and liquid phases is represented by the equation

$$\vec{F}_{D,lg} = C_{D,lg}\frac{3}{4}\rho_l\frac{\in_g}{d_b}\left|\vec{u}_g - \vec{u}_l\right|\left(\vec{u}_g - \vec{u}_l\right) \quad (14)$$

where the drag coefficient exerted by the dispersed gas phase on the liquid phase is obtained by the modified Brucato drag model (Khopkar et al., 2003), which accounts for interphase drag by microscale turbulence and is given by

$$\frac{C_{D,lg} - C_D}{C_D} = 6.5\times10^{-6}\left(\frac{d_p}{\lambda}\right)^3 \quad (15)$$

where $C_D$ is the drag coefficient of single bubble in a stagnant liquid and is given by

$$C_D = Max\left(\frac{24}{Re_b}\left(1 + 0.15Re_b^{\,0.687}\right), \frac{8}{3}\frac{Eo}{Eo+4}\right) \quad (16)$$

where Eo is Eotvos number, $Re_b$ is the bubble Reynolds number and they are given by

$$Re_b = \frac{\left|\vec{u}_l - \vec{u}_g\right| d_b}{\nu_l} \quad (17)$$

$$Eo = \frac{g\left(\rho_l - \rho_g\right)d_b^{\,2}}{\sigma} \tag{18}$$

**Closure law for turbulence**

In the present study, the standard k-ε turbulence model for single phase flows has been extended for turbulence modeling of two/three phase flows in mechanically agitated contactors. The corresponding values of $k$ and $\varepsilon$ are obtained by solving the following transport equations for the turbulence kinetic energy and turbulence dissipation rate.

$$\frac{\partial\left(\in_l \rho_l k_l\right)}{\partial t} + \nabla.\left(\in_l \left(\rho_l \vec{u}_l k_l - \left(\mu + \frac{\mu_{tl}}{\sigma_k}\right)\Delta k_l\right)\right) = \in_l \left(P_l - \rho_l \varepsilon_l\right) \tag{19}$$

$$\frac{\partial\left(\in_l \rho_l \varepsilon_l\right)}{\partial t} + \nabla.\left(\in_l \rho_l \vec{u}_l k_l - \left(\mu + \frac{\mu_{tl}}{\sigma_\varepsilon}\right)\Delta \varepsilon_l\right) = \in_l \frac{\varepsilon_l}{k_l}\left(C_{\varepsilon 1} P_l - C_{\varepsilon 2}\rho_l \varepsilon_l\right) \tag{20}$$

where $C_{\varepsilon 1}$=1.44, $C_{\varepsilon 2}$ =1.92, $\sigma_k$=1.0, $\sigma_\varepsilon$ =1.3 and $P_l$, the turbulence production due to viscous and buoyancy forces, is given by

$$P_l = \mu_{tl}\nabla\vec{u}_l.\left(\nabla\vec{u}_l + \nabla\vec{u}_l^{\,T}\right) - \frac{2}{3}\nabla.\vec{u}_l\left(3\mu_{tl}\nabla.\vec{u}_l + \rho_l k_l\right) \tag{21}$$

For the continuous phase (liquid phase) the effective viscosity is calculated as

$$\mu_{eff,l} = \mu_l + \mu_{T,l} + \mu_{tg} + \mu_{ts} \tag{22}$$

where $\mu_l$ is the liquid viscosity, $\mu_{T,l}$ is the liquid phase turbulence viscosity or shear induced eddy viscosity, which is calculated based on the k-ε model as

$$\mu_{T,l} = c_\mu \rho_l \frac{k^2}{\varepsilon} \tag{23}$$

$\mu_{tg}$ and $\mu_{ts}$ represent the gas and solid phase induced turbulence viscosity respectively and are given by

$$\mu_{tg} = c_{\mu p}\rho_l \in_g d_b \left|\vec{u}_g - \vec{u}_l\right| \tag{24}$$

$$\mu_{ts} = c_{\mu p}\rho_l \in_s d_p \left|\vec{u}_s - \vec{u}_l\right| \tag{25}$$

where $C_{\mu p}$ has a value of 0.6.
The effective viscosities of dispersed phases (gas and solid) are calculated as

$$\mu_{eff,g} = \mu_g + \mu_{T,g} \tag{26}$$

$$\mu_{eff,s} = \mu_s + \mu_{T,s} \tag{27}$$

where $\mu_{T,g}$ and $\mu_{T,s}$ are the turbulence viscosity of gas and solid phases respectively. The turbulent viscosity of the gas phase and the solids phase is related to the turbulence viscosity of the continuous liquid phase and are given by equations (28) and (29)

$$\mu_{T,g} = \frac{\rho_g}{\rho_l}\mu_{T,l} \tag{28}$$

$$\mu_{T,s} = \frac{\rho_s}{\rho_l}\mu_{T,l} \tag{29}$$

**Closure law for solids pressure**

The solids phase pressure gradient results from normal stresses resulting from particle–particle interactions, which become very important when the solid phase fraction approaches the maximum packing. This solid pressure term is defined based on the concept of elasticity, which is described as a function of elasticity modulus and solid volume fraction. The most popular constitutive equation for solids pressure as given by Gidaspow (1994) is

$$\nabla P_s = G(\epsilon_s)\nabla \epsilon_s \tag{30}$$

where G ($\varepsilon_s$) is the elasticity modulus and it is given as

$$G(\epsilon_s) = G_0 \exp\left(c(\epsilon_s - \epsilon_{sm})\right) \tag{31}$$

as proposed by Bouillard et al. (1989), where $G_0$ is the reference elasticity modulus, c is the compaction modulus and $\epsilon_{sm}$ is the maximum packing parameter.

### 2.2 Impeller rotation modeling

Flows in baffled stirred reactors are modeled by different approaches, which are basically classified into four types (Ranade, 2002). They are black box approach, sliding mesh approach, multiple reference frame or inner–outer approach and computational snapshot approach. The black box approach is basically a steady state approach which requires boundary conditions like mean velocity and turbulence characteristics on the impeller swept surface, and these parameters need to be determined experimentally. This approach cannot be extended easily to multiphase systems since experimental values cannot be obtained accurately and hence this approach cannot be used as a design tool. In the sliding mesh approach, full transient simulations are carried out using two grid zones. One grid zone is attached to the stationary baffles and reactor wall and the other zone is attached to the rotating impeller. The detailed geometry of the impeller needs to be modeled and the impeller blades are modeled as solid rotating walls. The boundary between the two zones should be chosen in such a way that it is greater than the impeller radius but less than the inner edges of the baffles. General transport equations are used for both the zones. This method was first applied to flow in stirred tank by Perng and Murthy (1992). Since this approach is capable of generating a priori predictions, this approach can be used as a design tool. But since this approach requires tremendous computational power, this approach is not widely used as a design tool.

Inner–outer approach or multiple reference frame (MFR) approach, approximates the unsteady flow in stirred vessels. In both the approaches, a fictitious cylindrical zone with radius larger than that of impeller blades and smaller than the inner tip of the baffles and height sufficient to include the entire impeller region is defined. Only difference between inner–outer approach and MFR approach is inner and outer zones overlap in the inner–

outer approach, whereas in the MRF approach there is no overlap. Here also the full geometry needs to be modeled and the impeller blades are modeled as walls. In the MRF approach, flow characteristics of the inner region are solved using a rotating framework. These results are used to provide boundary conditions for the outer region after azimuthal averaging where the flow is solved using a stationary frame work. Solution of outer region is used to provide boundary condition for the inner region. This method was originally introduced by Luo et al. (1994). The inner-outer approach was introduced by Brucato et al. (1994).The fourth approach is called computational snapshot approach which was first proposed by Ranade (1994). This approach is based on taking a snapshot of flow in stirred vessels with a fixed relative position of blades and baffles. In this approach also, the whole solution domain is divided into two regions like in MRF approach, but the time derivative terms in the inner region are approximated in terms of spatial derivatives. The impeller blades are modeled as solid walls and flow is simulated using a stationary framework for a specific blade position. Appropriate sources are specified to consider the impeller rotation. If necessary, simulations are carried out at different blade positions to obtain ensemble-averaged results over different blade positions.

In this work, the MFR approach is used for simulating the impeller rotation. In the MFR approach, the computational domain is divided into an impeller zone (rotating reference frame) and a stationary zone (stationary reference frame). The interaction of inner and outer regions is accounted for by a suitable coupling at the interface between the two regions where the continuity of the absolute velocity is implemented. In this work, the boundary between inner and outer region is located at position of r/R=0.6.

## 3. Numerical methodology

The commercial CFD software ANSYS CFX-10 is used for the steady state hydrodynamic simulation of multiphase flows in the mechanically agitated contactor. Steady state simulations are performed for different types of impellers, agitation speeds, particle diameter, solid concentration and air flow rate. The details of the reactor geometry used for CFD simulation and the operating parameters are given in Table 3.

| Reference | Impeller type | Geometry | Physical Properties | Operating conditions |
|---|---|---|---|---|
| Guha et al.(2007) | 6-DT | T=H=0.2 m<br>D/T=1/3,<br>C/T=1/3 | Liquid: $\rho$ = 1000 kg/m$^3$,<br>Solid: $\rho$ = 2500 kg/m$^3$,<br>$d_p$ = 300 μm | Solid conc. =7 vol%<br>$N_{js}$=1200 rpm |
| Spidla et al.(2005 a, b) | 6-PBTD and 4-A315 | T=H=1.0 m<br>D/T=1/3,<br>C/T=1/3 | Liquid: $\rho$ = 1000kg/m$^3$,<br>Solid: $\rho$ = 2500kg/m$^3$,<br>$d_p$ = 350 μm | Solid conc. =10 vol%<br>$N_{js}$ = 267 rpm |
| Our experiment | 6-DT and 4-PBTD | T=H=0.25 m<br>For DT,<br>D = 0.1m,<br>For PBTD,<br>D=0.125 m<br>C/T=0.0625 m | Liquid: $\rho$ = 1000 kg/m$^3$,<br>Solid: $\rho$ = 4200 kg/m$^3$,<br>$d_p$ =125, 180, 230 μm<br>Gas: Air | Solid conc. =30 wt%<br>$N_{js}$ = 330–520 rpm<br>Air flow = 0–1.0 vvm |

Table 3. Tank design parameters and physical properties

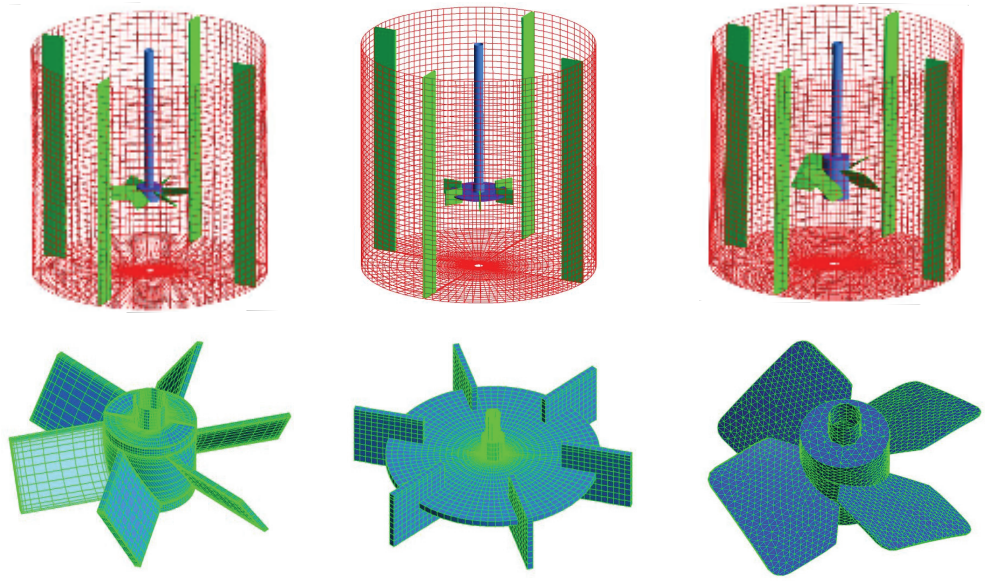

(a) 6 blade Pitched Turbine (b) 6 blade Rushton turbine (c) 4 blade A315 hydrofoil

Fig. 2. Typical geometry and mesh used in the CFD simulation

Due to the symmetry of geometry, only one-half of the agitated contactor is considered as the computational domain and is discretised using block structured grids, which allows finer grids in regions where higher spatial resolutions are required. The blocks are further divided into finer grids. The computational domain is discretised by using ICEM CFD software. Figure 2 depicts a typical mesh used for the numerical simulation. The numerical solutions of set of governing equations described in earlier sections consists of the following steps: (a) translations of partial differential equations into their discretised form in the form of liner algebraic equations (b) using suitable algorithm to handle the various interactions and couplings (c) finally solve the resulting algebraic equations. The discrete algebraic governing equations are obtained by the element based finite volume method. The second order equivalent to high-resolution discretisation scheme is applied for obtaining algebraic equations for momentum, volume fraction of individual phases, turbulent kinetic energy and turbulence dissipation rate. Pressure–velocity coupling was achieved by the Rhie-Chow algorithm (1982). No-slip boundary conditions are applied on the tank walls and shaft. The free surface of tank is considered as the degassing boundary condition. Initially the solid particles are distributed in a homogeneous way inside the whole computational domain. The governing equations are solved using the advanced coupled multi grid solver technology of ANSYS CFX-10. The criteria for convergence is set as $1 \times 10^{-4}$ for the RMS residual error for all the governing equations. The RMS (Root Mean Square) residual is obtained by taking all of the residuals throughout the domain, squaring them, taking the mean, and then taking the square root of the mean for each equation.

## 4. Numerical results

### 4.1. Solid suspension in solid–liquid mechanically agitated reactor

CFD simulation of liquid–solid mechanically agitated contactor is undertaken in this study to verify quantitatively the solid suspension characteristics since this is the vital parameter for predicting the performance of this type of reactor. One way of checking the quality of solid suspension is by evaluating the extent of off-bottom suspension i.e., critical impeller speed for just suspended state. Another way is to map the concentration profiles of solids in such reactors to determine the extent of solid distribution i.e., solid suspension height.

#### 4.1.1 Off-bottom suspension

Generally Zwietering criteria (the impeller speed at which the particles do not remain stationary at the bottom of the vessel for more than 2 s) is used for characterising the off-bottom suspension. But incorporating Zwietering criteria is difficult in the Eulerian–Eulerian approach of the present CFD simulation. Hence the method proposed by Bohnet and Niesmak (1980), which is based on the value of standard deviation, is used in the present study for the prediction of critical impeller speed. This standard deviation method was also successfully employed for liquid–solid suspension by Khopkar et al. (2006). It is defined as

$$\sigma = \sqrt{\frac{1}{n}\sum_{i=1}^{n}\left(\frac{C_i}{C_{avg}} - 1\right)^2} \tag{32}$$

where $n$ is the number of sampling locations which is used for measuring the solid holdup. The increase in the degree of homogenisation (better suspension quality) is manifested in the reduction in the value of the standard deviation. The standard deviation is broadly divided into three ranges based on the quality of suspension. For uniform suspension the value of the standard deviation σ is found to be smaller than 0.2 ($\sigma<0.2$), for just suspended condition the value of the standard deviation is between 0.2 and 0.8 ($0.2<\sigma< 0.8$) and for an incomplete suspension the standard deviation value is greater than 0.8 ($\sigma > 0.8$). But it is very difficult to exactly find the critical impeller speed required for the just suspended state from the values of the standard deviation. These difficulties were also cited in literature (Khopkar et al., 2006, van der Westhuizen & Deglon 8). Hence we have also used another criterion which is based on the solid suspension height i.e., cloud height ($H_{cloud}= 0.9H$) along with the standard deviation method. Kraume (1992) used these two criteria to determine the critical impeller speed in liquid–solid suspension. For the present study, both these criteria have been used to evaluate the quality of solid suspension and to determine the critical impeller speed.

CFD simulations have been carried out for the reactor configuration of Spidla et al. (2005a) for three different impeller types. Figure 3 shows the variation of the standard deviation values with respect to the impeller speed for DT, PBTD and A315 hydrofoil impeller. The standard deviation value decreases with an increase in impeller speed for all the impellers. Figure 4 depicts the predicted cloud height for various impeller rotational speeds (4.0, 4.45, and 5.0 rps) for the PBTD impeller. Figure 5 depicts the predicted cloud height for various impeller rotational speeds (3.5, 4.1, and 4.7 rps) for the A315 hydrofoil impeller. It can be

seen clearly from these figures that there is an increase in the cloud height with an increase in the impeller speed. Similar observations were also reported by Khopkar et al. (2006).

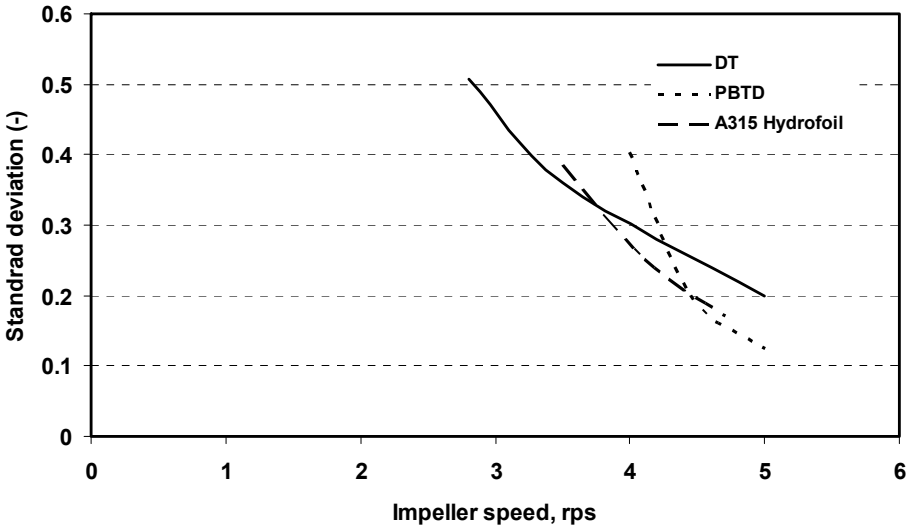


Fig. 3. Standard deviation values obtained from CFD with respect to impeller rotational speed for DT, PBTD and A315 hydrofoil impeller (particle size of 350 μm with solids loading of 10 vol. %)

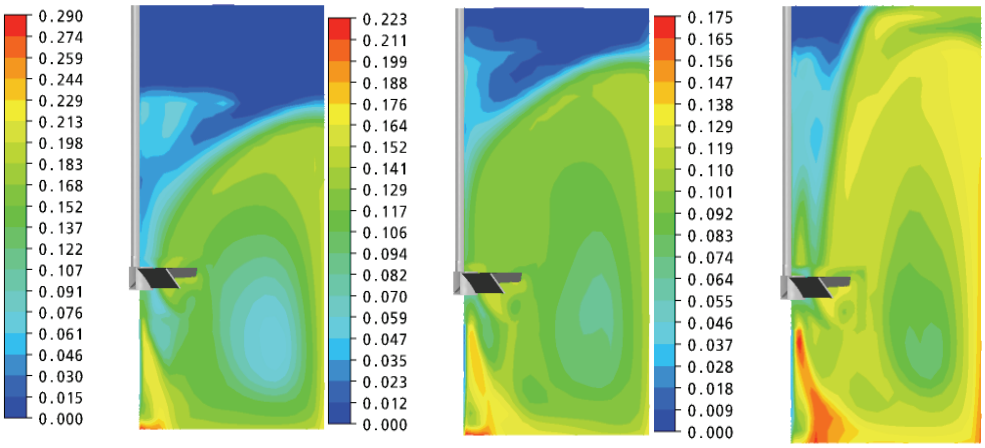


(a) 4 rps ($H_s$/H=0.8) (b) 4.45 rps ($H_s$/H=0.9) (c) 5 rps ($H_s$/H=1.0)

Fig. 4. Cloud height predicted by CFD simulation for PBTD impeller at different rotational speeds (particle size of 350 μm with solid loading of 10 vol. %)

The values of the standard deviation and cloud height obtained by CFD simulation along with experimental values for the three types of impellers are presented in Table 4. Based on

these two criteria, it is found that the critical impeller speed required for 6-PBTD is 4.45 rps which agrees very well with the experimental observation. It has to be noted again that both these criteria have to be satisfied for the determination of the critical impeller speed.

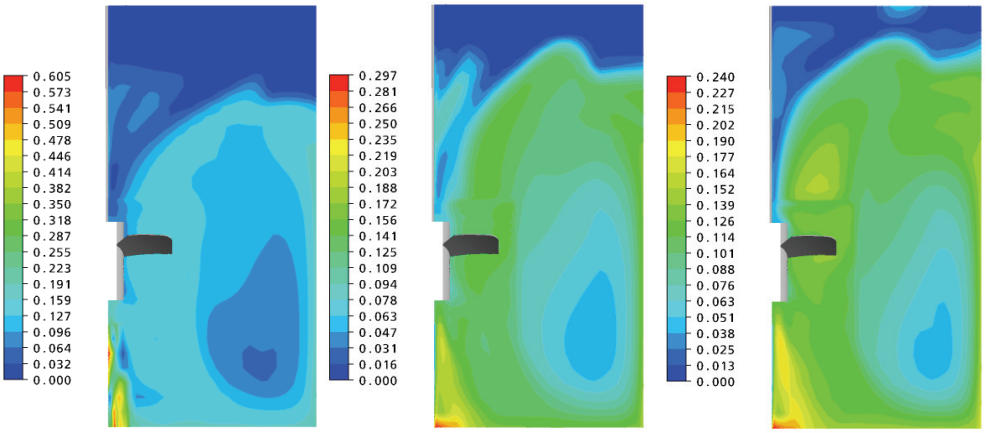


(a) 3.5 rps ($H_s/H$=0.8) (b) 4.1 rps ($H_s/H$=0.88) (c) 4.7rps ($H_s/H$=1.0)

Fig. 5. Cloud height predicted by CFD simulation for A315 hydrofoil impeller at different rotational speeds (particle size of 350 μm with solid loading of 10 vol. %)

| Type of impeller | Critical impeller speed, rps | | Standard deviation, σ | Cloud height |
|---|---|---|---|---|
| | Experimental (rps) | CFD (rps) | | |
| DT | - | 3.5 | 0.36 | 0.90 |
| PBTD | 4.45 | 4.45 | 0.21 | 0.91 |
| A315 hydrofoil | - | 4.1 | 0.25 | 0.88 |

Table 4. Effect of impeller type on the quality of suspension (particle size of 350 μm with solid loading of 10 vol. %)

#### 4.1.2 Power number comparison

The comparison of different types of impellers with regard to their suspension ability is investigated in terms of power number. The power consumption is calculated as the product of torque on the impeller blades and the angular velocity. This is then used for the estimation of power number which is expressed as follows:

$$N_P=2\pi NT/\rho_s N^3 D^5 \tag{33}$$

where torque ($T$) exerted on all blades was computed from the total momentum vector, which is computed by summing the cross products of the pressure and viscous forces vectors for each facet on the impeller with the moment vector.

The predicted values of power number are compared with experimental data and are shown in Table 5. It can be observed that the values predicted by CFD simulations agree reasonably

well with the experimental values. It can also be seen from the table that the suspension performance in terms of power number is different for different impeller designs. The lowest power consumption was observed for A315 hydrofoil impeller and highest for Rushton turbine impeller. This indicates that the impeller which directs the flow downward having mainly axial component and has the least power number is most energy efficient.

| Impeller type | Power number | |
|---|---|---|
| | Experimental | CFD |
| 6-Rushton turbine | 6.0 | 5.1 |
| 6-PBTD | 1.67 | 1.55 |
| 4- A315 Hydrofoil downward | 1.5 | 1.37 |

Table 5. Experimental and predicted values of Power number

### 4.2 Solid suspension in gas–solid–liquid mechanically agitated reactor

The critical impeller speed for gas–liquid–solid mechanically agitated contactor obtained by CFD simulation based on the criteria of both standard deviation approach and cloud height is validated with our experimental data. The bubble size distribution in the mechanically agitated reactor depends on the design and operating parameters and there is no experimental data available for bubble size distribution. It has been reported by Barigou and Greaves (1992) that their bubble size distribution is in the range of 3.5–4.5 mm for the higher gas flow rates used in their experiments. Also in the recent simulation study on a gas–liquid stirred tank reactor carried out by Khopkar et al. (2005) a single bubble size of 4 mm was assumed. Since the gas flow rates used in our experiments are also in the same range, a mean bubble size of 4 mm is assumed for all our simulations.

#### 4.2.1 Off-bottom suspension

CFD simulations have been carried out for 6 blade Rushton turbine impeller (DT) and 4 blade pitched blade turbine with downward pumping (PBTD) at different impeller speeds. The air flow rate for this simulation is 0.5 vvm and the solid phase consists of ilmenite particles of size 230 μm and the solid loading is 30% by weight. Figure 6 shows the variation of the standard deviation value with respect to impeller speed for DT and PBTD. The value of standard deviation decreases with increase in impeller speed for both the impellers. Figure 7 depicts the predicted cloud height for the three impeller rotational speeds (7.83, 8.67, and 9.5 rps) for DT and Figure 8 shows the predicted cloud height for PBTD for three different impeller speeds (6.3, 7.13, and 7.97 rps). It can be seen clearly from these figures that there is an increase in the cloud height with an increase in the impeller rotational speed. Similar observations were also reported by Khopkar et al. (2006). The values of standard deviation and cloud height obtained by CFD simulation along with experimental values for both the type of impellers are presented in Table 6. Based on these two criteria, it is found that the critical impeller speed required for DT is 8.67 rps and for PBTD is 7.13 rps which agrees very well with the experimental observation. It has to be noted again that both the criteria have to be satisfied for critical impeller speed determination.

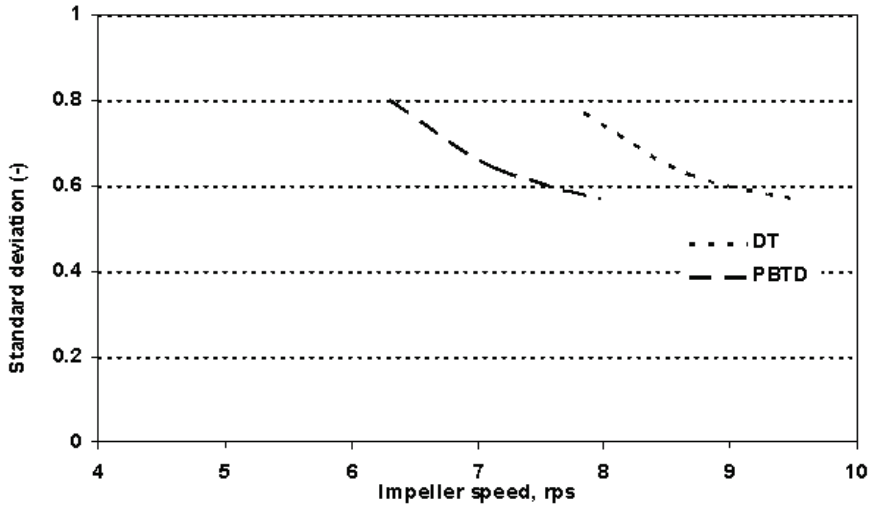


Fig. 6. Variation of standard deviation values with respect to the impeller speed for DT and PBTD

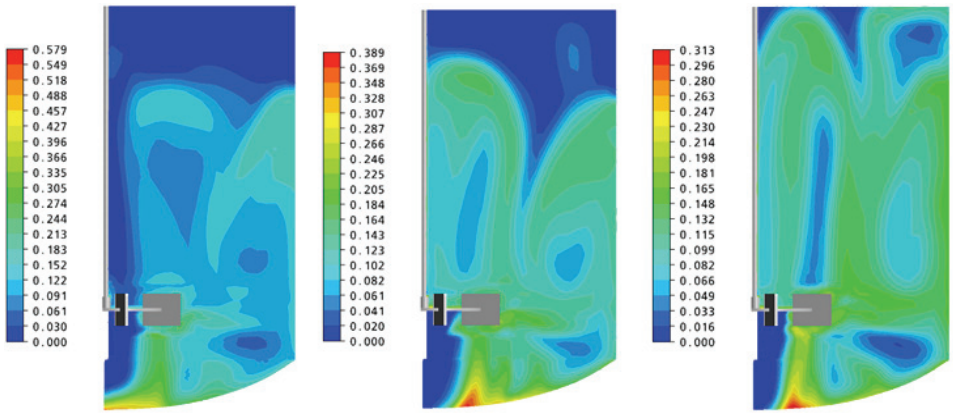


Fig. 7. CFD prediction of cloud height with respect to the impeller speed for DT (gas flow rate = 0.5 vvm, particle size = 230 μm & particle loading = 30 wt.%)

#### 4.2.1 Effect of particle size

It has been reported in the literature that the critical impeller speed depends on the particle size. Hence, CFD simulations have been carried out for three different particle sizes *viz,* 125 μm, 180 μm and 230 μm at the solid loading of 30 % by wt. and a gas flow rate of 0.5 vvm with both DT and PBTD type impellers. From the CFD simulation, the standard deviation

and cloud height values are also obtained and they are shown in Table 7. It can be seen clearly that critical impeller speed predicted by CFD simulation based on the criteria of standard deviation and solid cloud height agrees very well with the experimental data.

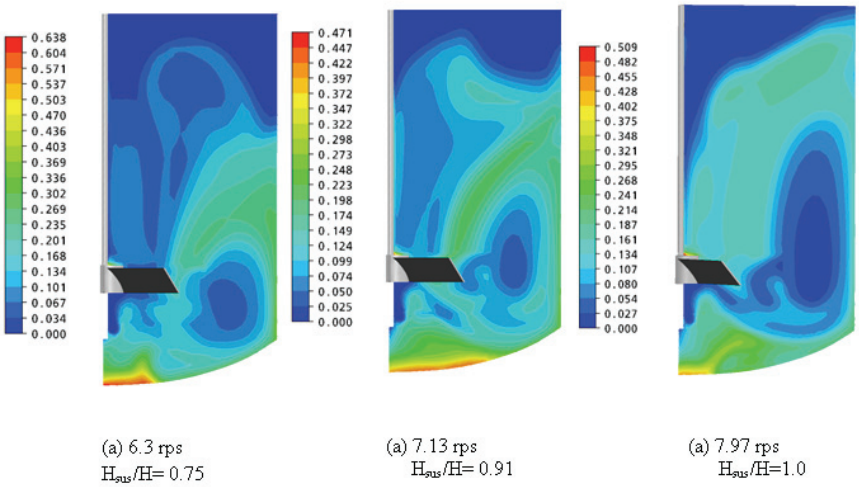


Fig. 8. CFD prediction of cloud height with respect to the impeller speed for PBTD (gas flow rate = 0.5 vvm, particle size =230 μm & particle loading =30 wt %)

| Type of impeller | Critical impeller speed, rps | | Standard deviation, σ | Cloud height |
|---|---|---|---|---|
| | Experimental | CFD simulation | | |
| DT | 8.67 | 8.67 | 0.66 | 0.90 |
| PBTD | 7.13 | 7.13 | 0.64 | 0.91 |

Table 6. Effect of impeller type on quality of suspension (gas flow rate =0.5 vvm, particle size = 230 μm, & particle loading = 30 wt %)

| Particle diameter (μm) | (DT) | | | | PBTD | | | |
|---|---|---|---|---|---|---|---|---|
| | Critical impeller speed, rps | | Standard deviation, σ | Cloud height | Critical impeller speed, rps | | Standard deviation, σ | Cloud height |
| | Experimental | CFD | | | Experimental | CFD | | |
| 125 | 5.67 | 5.67 | 0.50 | 0.90 | 5.42 | 5.42 | 0.46 | 0.91 |
| 180 | 6.25 | 6.92 | 0.75 | 0.89 | 5.77 | 6.0 | 0.62 | 0.88 |
| 230 | 8.67 | 8.67 | 0.66 | 0.90 | 7.13 | 7.13 | 0.64 | 0.91 |

Table 7. Effect of particle size on quality of suspension (gas flow rate = 0.5 vvm & particle loading 30 = wt %)

### 4.2.2 Effect of air flow rate

CFD simulations have further been carried out to study the effect of air flow rate on the critical impeller speed for gas–liquid–solid mechanically agitated contactor. Figure 9 shows the comparison of CFD predictions with the experimental data on critical impeller speed for both the type of impellers at various gas flow rates (0 vvm, 0.5 vvm and 1. 0 vvm). The values of the standard deviation and cloud height with respect to the impeller speed for different gas flow rates with different type of impellers are shown in Table 8. It can be observed that CFD simulation is capable of predicting the critical impeller speed in terms of standard deviation value and cloud height with an increase in gas flow rate for both types of impellers. Figure 10 shows solid volume fraction distribution predicted by CFD at the critical impeller speed for the solid loading of 30 % by wt. and particle size of 230 μm with different air flow rates (0, 0.5, 1.0 vvm).

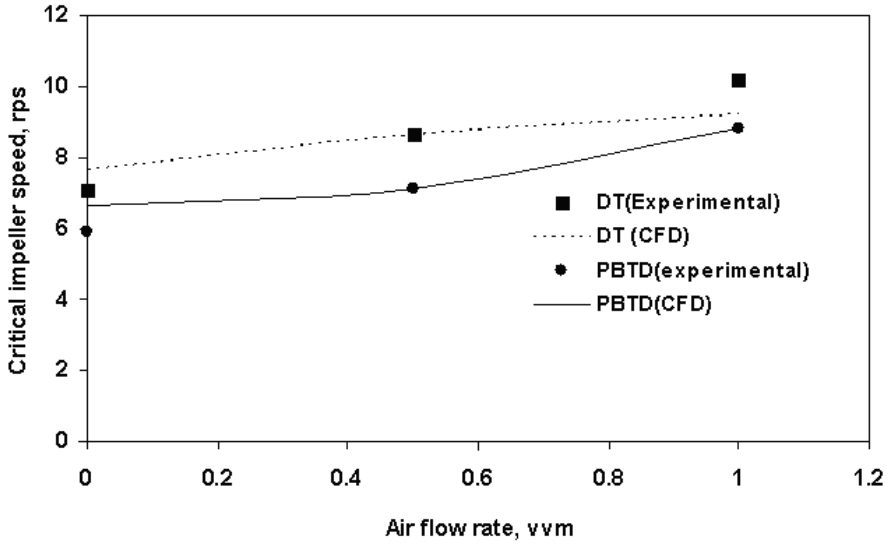


Fig. 9. Effect of air flow rate on Critical impeller speed for different impellers (particle size= 230 μm & particle loading = 30 wt %)

| Air flow rate (vvm) | DT | | | | PBTD | | | |
|---|---|---|---|---|---|---|---|---|
| | Critical impeller speed, rps | | Standard deviation, σ | Cloud height | Critical impeller speed, rps | | Standard deviation, σ | Cloud height |
| | Experimental | CFD | | | Experimental | CFD | | |
| 0 | 7.17 | 7.67 | 0.80 | 0.89 | 5.5 | 6.67 | 0.80 | 0.90 |
| 0.5 | 8.67 | 8.67 | 0.66 | 0.90 | 7.13 | 7.13 | 0.64 | 0.91 |
| 1.0 | 10.2 | 9.2 | 0.66 | 0.90 | 8.82 | 8.82 | 0.71 | 0.93 |

Table 8. Effect of air flow rate on quality of suspension for different type of impellers (particle size = 230 μm & particle loading = 30 wt. %)

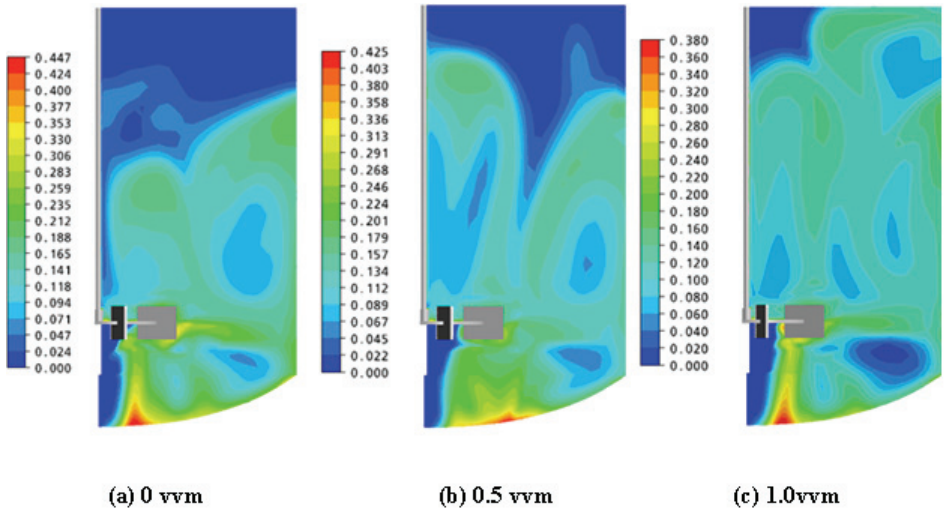


Fig. 10. Effect of air flow rate on solid concentration distribution for DT by CFD simulations at the critical impeller speed (a) 0 vvm (b) 0.5 vvm (c) 1. 0 vvm (particle size =230 μm and particle loading = 30 wt. %)

Figure 11 shows the variation of standard deviation value with respect to the impeller speed. It can be seen that the reduction rate of standard deviation value in ungassed condition is more with increasing impeller speed when compared with gassed condition. Similarly for the case of higher gas flow rate, the reduction rate in the standard deviation value is much lower compared to lower gas flow rate. This is due to the presence of gas which reduces both turbulent dispersion and fluid circulation action of the impeller.

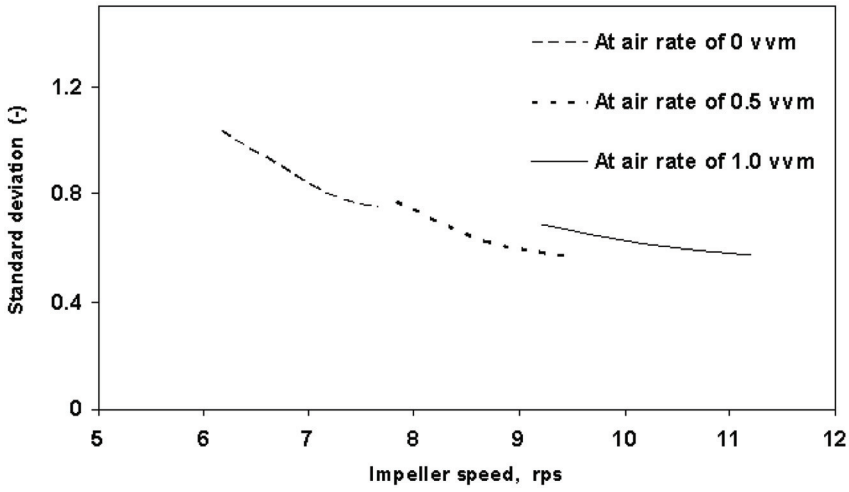


Fig. 11. Effect of gas flow rate on the standard deviation value for different impeller speeds of DT (particle size= 230 μm &particle loading= 30 wt.%)

## 5. Conclusions

In this present work, Eulerian multi-fluid approach along with standard k-ε turbulence model has been used to study the solid suspension in liquid-solid and gas–liquid–solid mechanically agitated contactor. CFD predictions are compared quantitatively with literature experimental data (Spidla et al., 2005a,b) in terms of critical impeller speed based on the criteria of standard deviation method and cloud height in a mechanically agitated contactor. An adequate agreement was found between CFD prediction and the experimental data. The numerical simulation has further been extended to study the effect of impeller design (DT, PBTD and A315 Hydrofoil), impeller speed and particle size (200–650 μm) on the solid suspension in liquid–solid mechanically agitated contactor.

For gas–liquid–solid flows, the CFD predictions are compared quantitatively with our experimental data in terms of critical impeller speed based on the criteria of standard deviation method and cloud height in a mechanically agitated contactor. An adequate agreement was found between CFD prediction and experimental data. The numerical simulation has further been extended to study the effect of impeller design (DT, PBTD), impeller speed, particle size (125–230 μm) and air flow rate (0–1.0 vvm) on the prediction of critical impeller speed for solid suspension in gas–liquid–solid mechanically agitated contactor.

## Nomenclature

| | |
|---|---|
| $c$ | solid compaction modulus |
| $C_{avg}$ | average solid concentration |
| $C_i$ | instantaneous solid concentration |
| $C_{D,ls}$ | drag coefficient between liquid and solid phase |
| $C_{D,lg}$ | drag coefficient between liquid and gas phase |
| $C_D$ | drag coefficient in turbulent liquid |
| $C_{D0}$ | drag coefficient in stagnant liquid |
| $C_{TD}$ | turbulent dispersion coefficient |
| $C_\mu, \sigma_k, \sigma_\varepsilon, C_{\varepsilon 1}, C_{\varepsilon 2}$ | coefficient in turbulent parameters |
| $C_{\mu p}$ | coefficient in particle induced turbulence model |
| $D$ | impeller diameter, m |
| $d_b$ | bubble mean diameter, m |
| $d_p$ | particle mean diameter, m |
| $Eo$ | Eotvos number |
| $F_{TD}$ | turbulent Dispersion Force, N |
| $F_{D,lg}$ | interphase drag force between liquid and gas, N |
| $F_{D,ls}$ | interphase drag force between liquid and solid, N |
| $g$ | acceleration due to gravity, m / s$^2$ |
| $G(\epsilon_s)$ | solid elastic modulus |
| $G_0$ | reference elasticity modulus |
| $H_{cloud}$ | Cloud height, m |
| $k$ | the turbulence kinetic energy, m$^2$/s$^2$ |
| $n$ | number of sampling locations |
| $N$ | impeller speed, rpm |
| $N_{js}$ | critical impeller speed for just suspended, rpm |

| | |
|---|---|
| $N_{jsg}$ | critical impeller speed in the presence of gas, rpm |
| $N_P$ | Power number |
| $N_q$ | Pumping number |
| P | Power, W |
| P | liquid-phase pressure, kg/ $m^1$ $s^2$ |
| $P_s$ | solids pressure, kg /m $s^2$ |
| $P_\alpha$ | turbulence production due to viscous and buoyancy forces |
| $Q_g$ | gas flow rate, vvm |
| R | radial position, m |
| $Re_b$ | bubble Reynolds number |
| $Re_p$ | particle Reynolds number |
| T | Tank height, m |
| $\vec{u}_g$ | local gas phase velocity vector, m/s |
| $\vec{u}_l$ | local liquid phase velocity vector, m/s |
| $\vec{u}_s$ | local solid phase velocity vector, m/s |
| z | axial position, m |

### Greek letters

| | |
|---|---|
| $\in_l, \in_g, \in_s$ | liquid, gas and solid volume fraction respectively |
| $\in_{sm}$ | maximum solid packing parameter |
| ε, $\varepsilon_l$ | liquid phase turbulence eddy dissipation, $m^2/s^3$ |
| $\rho_g$ | gas density, kg/$m^3$ |
| $\rho_l$ | liquid density, kg/$m^3$ |
| $\rho_s$ | density of solid phase, kg/ $m^3$ |
| $\Delta\rho$ | density difference between liquid and gas, kg/$m^3$ |
| $\Delta N_{js}$ | Difference in critical impeller speed, rpm |
| $\mu_{eff,c}$ | continues phase effective viscosity, kg /m $s^2$ |
| $\mu_{eff,d}$ | dispersed phase effective viscosity, kg /m $s^2$ |
| $\mu_c$ | continuous viscosity, kg /m $s^2$ |
| $\mu_d$ | dispersed phase viscosity, kg /m $s^2$ |
| $\mu_{td}$ | dispersed phase induced turbulence viscosity, kg /m $s^2$ |
| $\mu_{\tau,c}$ | continuous phase turbulent viscosity, kg /m $s^2$ |
| σ | standard deviation value for solid suspension |

### Subscripts and superscripts

| | |
|---|---|
| k | phase |
| s | solid phase |
| l | liquid phase |
| g | gas phase |
| eff | effective |
| max | maximum |
| DT | Disc turbine |
| PBTD | Pitched blade turbine downward pumping |
| PBTU | Pitched blade turbine upward pumping |
| rpm | revolution per minute |
| vvm | volume of gas per volume of liquid per minute |

## 6. References

Armenante, P.M., Nagamine, E.U., 1998. Effect of low off-bottom impeller clearance on the minimum agitation speed for complete suspension of solids in stirred tanks. Chemical Engineering Science 53, 1757–1775.

Baldi, G., Conti, R., Alaria, E., 1978. Complete suspension of particles in mechanically agitated vessels. Chemical Engineering Science 33, 21–25.

Bakker, A., Fasano, J.B., Myers, K.J., 1994. Effects of flow pattern on the solids distribution in a stirred tank. Institution of Chemical Engineering Symposium Series 136, 1–8.

Barrue, H., Bertrand, J., Cristol, B., Xuereb, C., 2001. Eulerian simulation of dense solid–liquid suspension in multi-stage stirred vessel. Journal of Chemical Engineering Japan. 34, 585–594.

Barigou, M., Greaves, M., 1992. Bubble size distribution in a mechanically agitated gas–liquid contactor. Chemical Engineering Science 47, 2009–2025.

Bohnet, M., Niesmak, G., 1980. Distribution of solids in stirred suspension. General Chemical Engineering 3, 57-65.

Bouillard, J.X., Lyczkowski, R.W., Gidaspow, D., 1989. Porosity distribution in a fluidised bed with an immersed obstacle. A.I.Ch.E. Journal 35, 908–922.

Brucato, A., Ciofalo, M., Grisafi, F., Micale, G., 1994. Complete numerical simulation of flow fields in baffled stirred vessels: the inner-outer approach. Institution of Chemical Engineering Symposium Series 136, 155–162.

Brucato, A., Grisafi, F., Montante, G., 1998. Particle drag coefficient in turbulent fluids. Chemical Engineering Science 53, 3295–3314.

Bujalski, W., Konno. M., Nienow, A.W., 1988. Scale-up of 45° pitch-blade agitators for gas dispersion and solid suspension. Proceeding of 6th European Conference on Mixing, Italy, 389–398.

Bujalski, W., Takenaka, K., Paolini, S., Jahoda, M., Paglianti, A., Takahashi, K., Nienow, A.W., Etchells, A.W., 1999. Suspension and liquid homogenization in high solids concentration stirred chemical reactors. Chemical Engineering Research and Design 77, 241–247.

Chapman, C.M., Nienow, A.W., Cooke, M., Middleton, J.C., 1983a. Particle–gas–liquid mixing in stirred vessels, part I: particle–liquid mixing. Chemical Engineering Research and Design 61a, 71–81.

Chapman, C.M., Nienow, A.W., Cooke, M.; Middleton, J.C. 1983b. Particle–gas–liquid mixing in stirred vessels, part III: three-phase mixing. Chemical Engineering Research and Design 61a, 167–181.

Chudacek, M.W., 1986. Relationships between solids suspension criteria, mechanism of suspension, tank geometry, and scale-up parameters in stirred tanks. Industrial and Engineering Chemistry Fundamentals 25, 391–401.

Dohi, N., Takahashi, T., Minekawa, K., Kawase, Y., 2004. Power consumption and solid suspension performance of large-scale impellers in gas–liquid–solid three-phase stirred tank reactors. Chemical Engineering Journal 97, 103–114.

Dutta, N.N., Pangarkar, V.G., 1995. Critical impeller speed for solid suspension in multi-impeller three-phase agitated contactors. The Canadian Journal of Chemical Engineering 73, 273–283.

Dudukovic, M.P., Larachi, F., Mills, P.L., 1999. Multiphase Reactor–Revisited. Chemical Engineering Science 54, 1975–1995.

Dylag, M., Talaga, J., 1994. Hydrodynamics of mechanical mixing in a three-phase liquid-gas-solid System. International Chemical Engineering 34, 539–551.

Einenkel, W.G., 1979. Description of fluid dynamics in stirred tanks. VDI Forschungsheft No. 595.

Frijlink, J.J., Bakker, A., Smith, J.M., 1990. Suspension of solid particles with gassed impellers. Chemical Engineering Science 45, 1703–1718.

Gidaspow, D., 1994. Multiphase Flow and Fluidisation: Continuum and Kinetic Theory Descriptions. Academic Press, San Diego.

Guha, D., Ramachandran, P.A., Dudukovic, M.P., 2007. Flow field of suspended solids in a stirred tank reactor by Lagrangian tracking. Chemical Engineering Science 62, 6143–6154

Guha, D., Ramachandran, P.A., Dudukovic, M.P., Derksen, J.J., 2008. Evaluation of large eddy simulation and Euler–Euler CFD Models for solids flow dynamics in a stirred tank reactor. A.I.Ch.E. Journal, 54, 766–778.

Ibrahim, S., Nienow, A. W., 1996. Particle suspension in the turbulent regime: the effect of impeller type and impeller/vessel configuration. Chemical Engineering Research and Design 74a, 679–688.

Kee, N.C.S., Tan, R.B. H., 2002. CFD simulation of solids suspension in mixing vessels. The Canadian Journal of Chemical Engineering 80, 1–6.

Khopkar, A.R., Aubin, J., Xureb, C., Le Sauze, N., Bertrand, J. and Ranade, V.V., 2003. Gas–liquid flow generated by a pitched blade turbine: PIV measurements and CFD simulations. Industrial and Engineering Chemistry Research, 42, 5318–5332.

Khopkar, A.R., Rammohan, A.R., Ranade, V.V., Dudukovic, M.P., 2005. Gas–liquid flow generated by a Rushton turbine in stirred vessel: CARPT/CT measurements and CFD simulations. Chemical Engineering Science 60, 2215–2229.

Khopkar, A.R., Kasat, G.R., Pandit, A.B. and Ranade, V.V., 2006, Computational fluid dynamics simulation of the solid suspension in a stirred slurry reactor. Industrial and Engineering Chemistry Research 45, 4416–4428.

Kolar, V., 1967. Contribution to the theory of suspension and dissolution of granular solids in liquids by means of mechanically mixed liquids. Collection of Czechoslovak Chemical Communications 32, 526–534.

Kraume, M., 1992. Mixing times in stirred suspension. Chemical Engineering and Technology 15, 313–318.

Ljungqvist, M., Rasmuson, A., 2001. Numerical simulation of the two-phase flow in an axially stirred vessel. Chemical Engineering Research and Design 79, 533–546.

Lopez de Bertodano, M., 1992. Turbulent Bubbly Two-Phase Flow in a Triangular Duct. Ph.D. Thesis, Rensselaer Polytechnic Institute, Troy, New York.

Luo, J. Y., Issa, R. I. and Gosman, A. D., 1994. Prediction of impeller-induced flows in mixing vessels using multiple frames of reference. Institution of Chemical Engineers Symposium Series 136, 549–556.

Micale, G., Montante, G., Grisafi, F., Brucato, A., Godfrey, J., 2000. CFD simulation of particle distribution in stirred vessels. Chemical Engineering Research and Design 78, 435–444.

Montante, G., Magelli, F., 2005. Modeling of solids distribution in stirred tanks: Analysis of simulation strategies and comparison with experimental data. International Journal of Computational Fluid Dynamics 19, 253–262.

Murthy, B.N., Ghadge, R.S., Joshi, J.B., 2007. CFD simulations of gas–liquid–solid stirred reactor: Prediction of critical impeller speed for solid suspension. Chemical Engineering Science 62, 7184–7195.

Narayanan, S., Bhatia, V.K., Guha, D.K., Rao, M.N., 1969. Suspension of solid by mechanical agitation. Chemical Engineering Science 24, 223–230.

Nienow, A.W., 1968. Suspension of solid particles in turbine agitated baffled vessel. Chemical Engineering Science 23, 1453–1459.

Nienow, A.W., Konno. M., Bujalski, W., 1985. Studies on three-phase mixing: A review and recent results. Proceeding of 5th European Conference on Mixing, Wurzburg, Germany, 1–12.

Pantula, P.R.K., Ahmed, N., 1998. Solid suspension and gas hold-up in three phase mechanically agitated reactors. Proceedings of the 26th Australian Chemical Engineering Conference (Chemiea 98), Port Douglas, Australia.

Perng, C.Y., Murthy, J.Y., 1993. A moving-deforming mesh technique for the simulation of flow in mixing tanks. A.I.Ch.E. Symposium Series. 89 (293), 37–41.

Ranade, V.V., Van den Akker, H.E.A., 1994. A computational snapshot of gas-liquid flow in baffled stirred reactors. Chemical Engineering Science 49, 5175–5192.

Ranade, V. V. Computational Flow Modelling for Chemical Reactor Engineering; Academic Press: New York, 2002.

Raghava Rao, K.S.M.S., Rewatkar, V.B., Joshi, J.B., 1988. Critical impeller speed for solid suspension in mechanically agitated contactors. A.I.Ch.E Journal 34, 1332–1340.

Raw, M. J., 1994. A Coupled Algebraic Multigrid Method for the 3-D Navier Stokes Equations. Proceedings of the 10th GAMM-Seminar, Notes on Numerical Fluid Mechanics 49, 204.

Rieger, F., Ditl. P., 1994. Suspension of solid particles. Chemical Engineering Science 49, 2219–2227.

Rewatkar, V.B., Raghava Rao, K.S.M.S., Joshi, J.B., 1991. Critical impeller speed for solid suspension in mechanically agitated three-phase reactors. 1. Experimental part. Industrial and Engineering Chemistry Research 30, 1770–1784.

Rhie, C.M., Chow, W.L., 1982. A numerical study of the turbulent flow past an isolated airfoil with trailing edge separation. AIAA Journal 21, 1525–1532.

Sharma, R.N., Shaikh, A.A., 2003. Solids suspension in stirred tanks with pitched blade turbines. Chemical Engineering Science 58, 2123–2140.

Sha, Z., Palosaari, S., Oinas, P., Ogawa, K., 2001. CFD simulation of solid suspension in a stirred tank. Journal of Chemical Engineering of Japan 34, 621–626.

Shamlou, P.A., Koutsakos, E., 1989. Solids suspension, distribution in liquids under turbulent agitation, Chemical Engineering Science 44, 529–542.

Smith, J. M., 1990. Industrial Needs for Mixing Research. Transactions of Institution of Chemical Engineering 68, 3–6.

Spidla, M., Sinevic, V., Jahoda, M., Machon, V., 2005a. Solid particle distribution of moderately concentrated suspensions in a pilot plant stirred vessel. Chemical Engineering Journal 113, 73–82.

Spidla, M., Sinevic, V., Machon, V., 2005b. Effect of baffle design on the off-bottom suspension characteristics of axial-flow impellers in a pilot-scale mixing vessel. Chemical and Biochemical Engineering Quarterly 19, 333–340.

Takahashi, K., Fujita, H., Yokota, T., 1993. Effect of size of spherical particle on complete suspension speed in agitated vessels of different scale. Journal of Chemical Engineering of Japan 26, 98–100.

van der Westhuizen, A.P., Deglon, D.A., 2008. Solids suspension in a pilot-scale mechanical flotation cell: A critical impeller speed correlation. Mineral Engineering 21, 621–629.

Warmoeskerken, M.M.C.G., van Houwelingen, M.C., Frijlink, J.J., Smith, J.M., 1984. Role of cavity formation in stirred gas–liquid–solid reactors. Chemical Engineering Research and Design 62, 197–200.

Wong, C.W., Wang, J.P. Haung, S.T., 1987. Investigations of fluid dynamics in mechanically stirred aerated slurry reactors. The Canadian Journal of Chemical Engineering 65, 412–419.

Zlokarnik, N.W., Judat, P., 1969. Tubular and propeller stirrers–an effective stirrer combination for simultaneous gassing and suspending. Chemie Ingenieur Technik 41, 1270–1277.

Zhu, Y., Wu, J., 2002. Critical impeller speed for suspending solids in aerated agitation tanks. The Canadian Journal of Chemical Engineering 80, 1–6.

Zwietering, T.N., 1958. Suspending of solid particles in liquid by agitators. Chemical Engineering Science 8, 244–253.

# 15

# Computational Fluid Dynamics Methods for Gas Pipeline System Control

Vadim Seleznev
*Physical and Technical Center*
*Sarov, Nizhny Novgorod Region,*
*Russia*

## 1. Introduction

At the present level of development of long, branched gas transmission networks (GTN), solving the problems of improving safety, efficiency and environmental soundness of operation of industrial pipeline systems calls for the application of methods of numerical simulation. The development of automated devices for technical inspection and process control, and availability of high-performance computer hardware have created a solid technical basis to introduce numerical simulation methods into the industrial practice of GTN analysis and operation. One of the promising approaches for numerical analysis of GTN operating is the development and application of high-accuracy computational fluid dynamics (CFD) simulators of modes of gas mixture transmission through long, branched pipeline systems (CFD-simulator) (Seleznev, 2007).

Actually, a CFD-simulator is a special-purpose software simulating, in "online" and "real time" modes with a high similarity and in sufficient detail, the physical processes of gas mixture transmission through a particular GTN. The development of a CFD-simulator focuses much attention to correctness of simulation of gas flows in the pipelines and to the impact produced by operation of relevant GTN gas pumping equipment (including gas compressor unit (GCU), valves, gas pressure reducers, etc.) and the environment upon the physical processes under study.

From the standpoint of mathematical physics, a CFD-simulator performs numerical simulation of steady and transient, non-isothermal processes of a gas mixture flow in long, branched, multi-line, multi-section gas pipeline network. Such simulation is aimed at obtaining high-accuracy estimates of the actual distribution (over time and space) of fluid dynamics parameters for the full range of modes of gas mixture transmission through the specific GTN in normal and emergency conditions of its operation, as well as of the actual (temporal) distribution of main parameters of GTN equipment operation, which can be expressed as functional dependencies on the specified controls on the GTN and corresponding boundary conditions. Theoretically, the high-accuracy of estimates of gas flow parameters is achieved here due to (Seleznev et al., 2005): (1) minimization of the number and depth of accepted simplifications and assumptions in the mathematical modeling of gas flows through long, branched, multi-section pipelines and gas compressor stations (CS) on the basis of adaptation of complete basic fluid dynamics models, (2) minimization of the number and depth of accepted simplifications and assumptions in the

construction of a computational model of the simulated GTN, (3) improving methods for numerical analysis of the constructed mathematical models based upon results of theoretical investigation of their convergence and evaluation of possible errors of solution, (4) taking into account the mutual influence of GTN components in the simulation of its operation, (5) detailed analysis and mathematically formal description of the technologies and supervisor procedures for management of gas mixture transport at the simulated GTN, (6) automated mathematic filtration of occasional and systemic errors in input data, etc.

Input information required for work of a CFD-simulator is delivered from the Supervisory Control and Data Acquisition System (SCADA-system) operated at the simulated GTN.

CFD-simulator's operating results are used for on-line control of the specific GTN, as well as in short-term and long-term forecasts of optimal and safe modes of gas mixture transport subject to fulfillment of contractual obligations. Also, a CFD-simulator is often used as base software for a hardware and software system for prevention or early detection of GTN failures.

For better illustration of the material presented in this chapter, but without loss of generality, further description of a CFD-simulator will be based on a sample pipeline network of a gas transmission enterprise. For the purpose of modeling, natural gas is deemed to be a homogenous gas mixture. A CFD-simulator of a gas transmission enterprise's GTN is created by combining CS mathematical models into a single model of the enterprise's pipeline system, by applying models of multi-line gas pipelines segments (GPS) (Seleznev et al., 2007). At that, in accordance with their process flow charts, the CS models are created by combining of GCU, dust catcher (DC) and air cooling device (ACD) models by applying mathematical models of connecting gas pipelines (CGP).

In a CFD-simulator, the control of simulated natural gas transmission through the GTN is provided by the following control commands: alteration of shaft rotation frequency of centrifugal superchargers (CFS) of GCU or their startup/shutdown; opening or closing of valves at a CS and valve platforms of multi-line GPS; alteration of the rates of gas consumption by industrial enterprises and public facilities; alteration of the gas reduction program at reduction units; alteration of the operation program at gas distributing stations; change in the program of ACD operating modes, etc. Therefore, simulated control in a CFD-simulator adequately reflects the actual control of natural gas transmission through pipeline networks of the gas transmission enterprise.

Generally, a CFD-simulator can be divided into three interrelated components (elements) (Seleznev et al., 2007). Each of these components is an integral part of the CFS-simulator.

The first system element is a computational scheme of a gas transmission enterprise pipeline system built on the basis of typical segments representing minimum distinctions from a comprehensive topology of an actual system considering the arrangement of valves, the system architecture, laying conditions, the process flow scheme of the system's CS, etc. The second component is a database containing input and operative (current) data on time-dependent (owing to valves operation) system topology, pipeline parameters, process modes and natural gas transmission control principles for an actual gas transmission enterprise. The third component of a CFD-simulator is a mathematical software which operates the first two CFD-simulator elements.

The mathematical software includes (in addition to the computation core) a user interface environment imitating the operation of actual control panels located at gas transmission enterprises control centers in a visual form familiar to operators. This provides for faster training and, for the operator, easier adaptation to the CFD-simulator.

## 2. Simulation of multi-line GPS by CFD-simulator

Multi-line GPS are long, branched, multi-section pipelines. For numerical evaluation of parameters of steady and transient, non-isothermal processes of the gas mixture flow in multi-line GPS, a CFD-simulator uses a model developed by tailoring the full set of integral fluid dynamics equations to conditions of the gas flow through long branched pipeline systems. Transform of the 3D integral problem to an equivalent one-dimensional differential problem is implemented by accepting the minimum of required simplifications and projecting the initial system of equations onto the pipeline's geometrical axis. At that, a special attention is given to the adequacy of simulation of pipeline junction nodes where the 3D nature of the gas flow is strongly displayed.

In order to improve the accuracy of the simulations, it is reasonable to use the CFD-simulator in the "online" and "real time" modes for the numerical analysis of the given processes. There are two mathematical models of fluid flow through branched pipeline: heat-conductive model of pipeline junction and nonconductive model of pipeline junction. These models were developed by S. Pryalov and V. Seleznev at the turn of the century. These alternatives differ in a way of simulation of gas heat transfer within pipeline junction. The principle underlying the simulations is to observe the major conservation laws as strictly as possible. In practice the simultaneous implementation of the models makes it possible to find an accurate solution in short time.

The basis for the mathematical models of fluid flow through branched pipeline was the geometrical model of a junction (fig. 1) proposed by S. Pryalov (Seleznev et al., 2005). In this model, volume ${}^{(0)}V$ can be depicted as a right prism with base area $S_{base}$ and height $H$ (see fig. 1a). For the prism lateral surface with linear dimensions ${}^{(n)}\delta$, true is the following relation: ${}^{(n)}\delta = {}^{(n)}f/H$, where ${}^{(n)}f$ is the cross-sectional area of the pipe adjacent to the junction core ${}^{(0)}V$. It should be noted that the summarized volume of the joint is equal to $V = \bigcup_{n=0}^{N} {}^{(n)}V$, where ${}^{(n)}V$, $n = 1,\ldots,N$, is the volume of an infinitely small section of the pipe adjacent to the junction core ${}^{(0)}V$ (see fig. 1b). The prism base area can be represented as follows: $S_{base} = \varsigma_{base}\,{}^{(1)}\delta^2$, where $\varsigma_{base}$ is the factor depending on the prism base geometry only. Now volume ${}^{(0)}V$ can be determined by the following formula: ${}^{(0)}V = HS_{base} = H\varsigma_{base}\left({}^{(1)}f/H\right)^2 = \varsigma_{base}\,{}^{(1)}f^2/H$, which means that $\lim_{H\to\infty} {}^{(0)}V = \lim_{H\to\infty}\left[\varsigma_{base}\,{}^{(1)}f^2/H\right] = 0$. The application of this geometrical model enabled us to approximate compliance with mass, momentum and energy conservation laws at the pipelines junction.

Simplifications and assumptions used to construct the heat-conductive model of pipeline junction include the following: (1) when gas mixture flows join together, pressure can change with time, but at each time step it will have the same value at the boundaries of the pipeline junction, (2) the simulations take account of «downwind" heat and mass exchange due to heat conduction and diffusion, (3) in the pipeline junction, the gas mixture instantaneously becomes ideally uniform all over the pipeline junction volume ${}^{(0)}V$ (see fig. 1b), (4) effects of gas mixture viscosity in the pipeline junction (inside the volume ${}^{(0)}V$) can be ignored, (5) there are no heat sources in ${}^{(0)}V$ (inside the volume ${}^{(0)}V$), (6) pipeline diameters near the pipeline junction are constant.

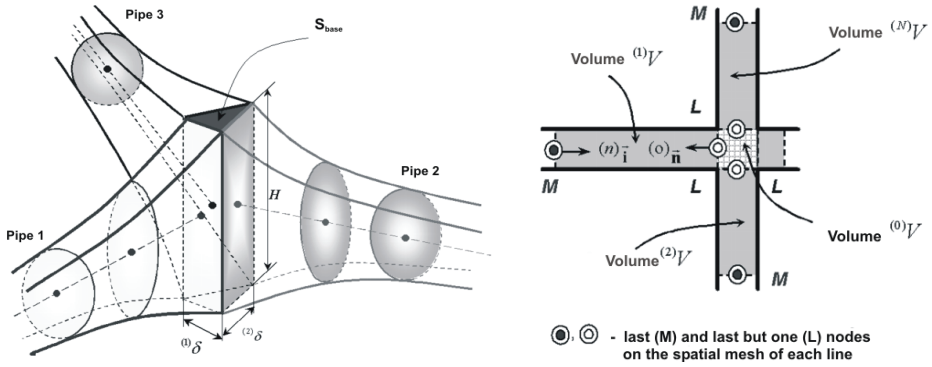


a) b)

Fig. 1. A schematic of a pipeline junction (a – 3D drawing; b – diagram)

Then, the heat-conductive fluid dynamics model of a transient, non-isothermal, turbulent flow of a viscous, chemically inert, compressible, heat-conductive, multi-component gas mixture through multi-line GPS which consist of pipes of round cross-sections and rigid rough heat-conductive walls is represented in the following way (Seleznev et al., 2005):

- for each pipe adjacent to the junction node

$$\frac{\partial(\rho f)}{\partial t}+\frac{\partial}{\partial x}(\rho w f)=0; \tag{1}$$

$$\frac{\partial}{\partial t}(\rho Y_m f)+\frac{\partial}{\partial x}(\rho Y_m w f)-\frac{\partial}{\partial x}\left(\rho f D_m \frac{\partial Y_m}{\partial x}\right)=0,\ m=\overline{1,N_S-1},\ Y_{N_S}=1-\sum_{m=1}^{N_S-1}Y_m; \tag{2}$$

$$\frac{\partial(\rho w f)}{\partial t}+\frac{\partial(\rho w^2 f)}{\partial x}=-f\left(\frac{\partial p}{\partial x}+g\rho\frac{\partial z_1}{\partial x}\right)-\frac{\pi}{4}\lambda\rho w|w|R; \tag{3}$$

$$\begin{aligned}&\frac{\partial}{\partial t}\left[\rho f\left(\varepsilon+\frac{w^2}{2}\right)\right]+\frac{\partial}{\partial x}\left[\rho w f\left(\varepsilon+\frac{w^2}{2}\right)\right]=-\frac{\partial}{\partial x}(pw f)-\rho w f g\frac{\partial z_1}{\partial x}-\\&-p\frac{\partial f}{\partial t}+Q f+\frac{\partial}{\partial x}\left(kf\frac{\partial T}{\partial x}\right)-\Phi(T,T_{\text{am}})+\frac{\partial}{\partial x}\left(\rho f\sum_{m=1}^{N_S}\varepsilon_m D_m\frac{\partial Y_m}{\partial x}\right);\end{aligned} \tag{4}$$

- for each of the junction nodes

$$\frac{\partial\rho}{\partial t}+\sum_{n=1}^{N}{}^{(n)}\Theta\left(\frac{\partial(\rho w)}{\partial x}\right)^{(n)}=0; \tag{5}$$

$$\begin{aligned}&\frac{\partial(\rho Y_m)}{\partial t}+\sum_{n=1}^{N}\left(\frac{\partial(\rho Y_m w)}{\partial x}\right)^{(n)}\Theta-\sum_{n=1}^{N}\left[\frac{\partial}{\partial x}\left(\rho D_m\frac{\partial Y_m}{\partial x}\right)\right]^{(n)}\Theta=0,\\&m=\overline{1,N_S-1};\quad {}^{(n)}Y_{N_S}=1-\sum_{m=1}^{N_S-1}{}^{(n)}Y_m;\end{aligned} \tag{6}$$

$$ {}^{(n)}\left(\frac{\partial(\rho w)}{\partial t}\right)+{}^{(n)}\left(\frac{\partial\left(\rho w^2\right)}{\partial x}\right)=-{}^{(n)}\left(\frac{\partial p}{\partial x}\right)-g\rho\,{}^{(n)}\left(\frac{\partial z_1}{\partial x}\right)-0.25\,{}^{(n)}\left(\frac{\lambda\rho w|w|}{R}\right),\ n=\overline{1,N}; \tag{7} $$

$$ \begin{aligned} &\frac{\partial(\rho\varepsilon)}{\partial t}+\sum_{n=1}^{N}{}^{(n)}\left(\frac{\partial(\rho\varepsilon w)}{\partial x}\Theta\right)=-\sum_{n=1}^{N}{}^{(n)}\left(p\frac{\partial w}{\partial x}\Theta\right)+0.25\sum_{n=1}^{N}{}^{(n)}\left(\frac{\lambda\,\rho\,|w|^3\,\Theta}{R}\right)+\\ &+Q+\sum_{n=1}^{N}{}^{(n)}\left(\left[\frac{\partial}{\partial x}\left(k\frac{\partial T}{\partial x}\right)\right]\Theta\right)-\sum_{n=1}^{N}{}^{(n)}\left(\frac{\Phi(T,T_{\text{am}})}{f}\Theta\right)+\sum_{n=1}^{N}\sum_{m=1}^{N_S}{}^{(n)}\left(\left[\frac{\partial}{\partial x}\left(\rho\varepsilon_m D_m\frac{\partial Y_m}{\partial x}\right)\right]\Theta\right); \end{aligned} \tag{8} $$

$$ {}^{(n)}T={}^{(\xi)}T,\quad \varepsilon={}^{(n)}\varepsilon={}^{(\xi)}\varepsilon,\quad {}^{(n)}\left(\varepsilon_m\right)={}^{(\xi)}\left(\varepsilon_m\right),\quad \rho={}^{(n)}\rho={}^{(\xi)}\rho,\quad {}^{(n)}p={}^{(\xi)}p, $$

$$ {}^{(n)}k={}^{(\xi)}k,\quad {}^{(n)}\left(D_m\right)={}^{(\xi)}\left(D_m\right),\quad Y_m={}^{(n)}\left(Y_m\right)={}^{(\xi)}\left(Y_m\right),\quad {}^{(n)}\left(z_1\right)={}^{(\xi)}\left(z_1\right) $$

$$ \text{for any } n,\xi\in\overline{1,N} \text{ and } m\in\overline{1,N_S}; \tag{9} $$

$$ \sum_{n=1}^{N}{}^{(n)}\left(wfs\right)=0;\quad \sum_{n=1}^{N}{}^{(n)}\left(\frac{\partial T}{\partial x}fs\right)=0;\quad \sum_{n=1}^{N}{}^{(n)}\left(\frac{\partial Y_m}{\partial x}fs\right)=0; \tag{10} $$

$$ {}^{(n)}S=\begin{cases} 1,\ if\left({}^{(0)}\vec{\mathbf{n}}\cdot{}^{(n)}\vec{\mathbf{i}}\right)<0; \\ -1,\ if\left({}^{(0)}\vec{\mathbf{n}}\cdot{}^{(n)}\vec{\mathbf{i}}\right)>0; \end{cases}\quad {}^{(n)}\Theta=\frac{{}^{(n)}V}{V}=\frac{{}^{(n)}f_L\,{}^{(n)}\gamma}{\sum_{k=1}^{N}\left({}^{(k)}f_L\,{}^{(n)}\gamma\right)},\ 0<{}^{(n)}\Theta<1,\ \sum_{n=1}^{N}{}^{(n)}\Theta=1; \tag{11} $$

- equation of state (EOS) and additional correlations:

$$ p=p\left(\{S_{\text{mix}}\}\right);\ \ \varepsilon=\varepsilon\left(\{S_{\text{mix}}\}\right);\ \ k=k\left(\{S_{\text{mix}}\}\right);\ \ \varepsilon_m=\varepsilon_m\left(\{S_{\text{mix}}\}\right),\ \ D_m=D_m\left(\{S_{\text{mix}}\}\right),\ \ m=\overline{1,N_S}; $$

$$ T_1=T_2=\ldots=T_{N_S}=T, \tag{12} $$

where $\rho$ is the density of the gas mixture; $f$ is the flow cross-sectional area of pipeline; $t$ is time (marching variable); $x$ is the spatial coordinate over the pipeline's geometrical axis (spatial variable); $w$ is the projection of the pipeline flow cross-section averaged vector of the mixture velocity on the pipeline's geometrical axis (on the assumption of the developed turbulence); $Y_m$ is a relative mass concentration of the m component of the gas mixture); $D_m$ is a binary diffusivity of component m in the residual mixture; $N_S$ is the number of components of the homogeneous gas mixture; $p$ is the pressure in the gas mixture; $g$ is a gravitational acceleration modulus; $z_1$ is the coordinate of the point on the pipeline's axis, measured, relative to an arbitrary horizontal plane, upright; $\pi$ is the Pythagorean number; $\lambda$ is the friction coefficient in the Darcy – Weisbach formula; $R=\sqrt{f/\pi}$ is the pipe's internal radius; $\varepsilon$ is specific (per unit mass) internal energy of the gas mixture; $Q$ is specific (per unit volume) heat generation rate of sources; $k$ is thermal conductivity; $T$ is the temperature of gas mixture; $\varepsilon_m$ is specific (per unit mass) internal energy of the $m$ component; $T_m$ is the temperature of the $m$ component; $N$ is the number of pipes

comprising one junction (see (5–11)); ${}^{(n)}s$, ${}^{(n)}\Theta$ are auxiliary functions (re ${}^{(0)}\vec{\mathbf{n}}$, ${}^{(n)}\vec{\mathbf{i}}$ see fig. 1b below); $\{S_{\text{mix}}\}$ is a set of parameters of gas mixture. Function $\Phi(T, T_{\text{am}})$ is defined by the law of heat transfer from the pipe to the environment and expresses the aggregate heat flow through the pipe walls along perimeter $\chi$ of the flow cross-section with area $f$ ($\Phi(T, T_{\text{am}}) > 0$ is cooling), $T_{\text{am}}$ is the ambient temperature. To denote the relationship of a value to the pipe numbered by $n$, we use a parenthesized superscript on the left side of the value, e.g.: ${}^{(n)}\rho$. In equations (1–12), we use physical magnitudes averaged across the pipeline's flow cross-section. The set of equations (1–12) is supplemented by the boundary conditions and conjugation conditions. As conjugation conditions it is possible to specify boundary conditions simulating a complete rupture of the pipeline and/or its shutoff, operation of valves, etc.

As was stated above, the energy equations (4) and (8) comprise function $\Phi(T, T_{\text{am}})$ describing the heat exchange between the environment and natural gas in the course of its pipeline transmission. The space-time distribution of function $\Phi(T, T_{\text{am}})$ is defined, in the CFD-simulator, at specified time steps of the numerical analysis of parameters of the transient mode of gas transmission by solving a series of conjugate 2D or 3D problems of heat exchange between the gas flow core and the environment (Seleznev et al., 2007).

Simulation of steady processes of gas mixture flow through multi-line GPS is a less complicated task compared to (1–12). These models can be easily derived by simplifying the set of equations (1–12).

When simulating the gas mixture flow through real multi-line GPSs, one uses meshes with a spatial cell size of 10m to 10,000m. As a result, a smooth growth (or decrease) of temperature in a span of about $10^{-5}m$ will be simulated as a temperature jump. Difference "upwind" equations make it possible to find a solution, which is quite adequate for the process at issue, almost without any impact on the convergence and accuracy of the resulting solution. On the contrary, the schemes that use the principles of central differences as applied to this process can yield solutions with difference oscillations. This may impair the accuracy of such simulations.

To overcome this drawback, S. Pryalov and V. Seleznev in 2008 suggested using the nonconductive model of pipeline junction. Downwind (and upwind) heat conduction and diffusion in this model are ignored. There will be a temperature discontinuity on gas mixture transition through the pipeline junction node, but this dependence will be monotone along each pipeline.

The list of additional simplifications in setting up the nonconductive model of pipeline junction includes only one item: the model ignores the downwind heat and mass exchange in the gas mixture due to heat conduction and diffusion. The temperature of the gas mixture at the outlet boundaries of inlet pipelines is defined only by the mixture flow parameters (mainly, by the temperature) inside these pipelines.

As there is no downwind heat transfer mechanism from the volume ${}^{(0)}V$ to the inlet pipelines, the temperature of the gas mixture at these boundaries may differ from the temperature inside the volume ${}^{(0)}V$. On the other hand, the outlet boundaries of the inlet pipelines are also boundaries of the volume ${}^{(0)}V$. For this reason, it does not seem to be correct to say that the mixture is uniformly intermixed all over the volume.

Thus, the nonconductive model of pipeline junction of a transient, non-isothermal, turbulent flow of a viscous, chemically inert, compressible, multi-component gas mixture through

multi-line GPS which consist of pipes of round cross-sections and rigid rough heat-conductive walls contains equations (1), (3), (7), (11) and the following equations:

- for each pipe adjacent to the junction node

$$\frac{\partial}{\partial t}\left(\rho Y_m f\right)+\frac{\partial}{\partial x}\left(\rho Y_m w f\right)=0,\ m=\overline{1,N_S-1},\ Y_{N_S}=1-\sum_{m=1}^{N_S-1}Y_m; \tag{13}$$

$$\begin{aligned}&\frac{\partial}{\partial t}\left[\rho f\left(\varepsilon+\frac{w^2}{2}\right)\right]+\frac{\partial}{\partial x}\left[\rho w f\left(\varepsilon+\frac{w^2}{2}\right)\right]=\\&=-\frac{\partial}{\partial x}\left(pwf\right)-\rho w f g\frac{\partial z_1}{\partial x}-p\frac{\partial f}{\partial t}+Qf-\Phi\left(T,T_{\text{am}}\right);\end{aligned} \tag{14}$$

- for each of the junction nodes

$$\begin{aligned}&\sum_{n\in\mathbb{C}_{\text{IN}}}\left\{\frac{\partial}{\partial t}\left[\rho\left(p_{\text{Joint}},\ {}^{(n)}T,\ \left\{{}^{(n)}Y_m\middle|m=\overline{1,N_s}\right\}\right)\right]{}^{(n)}\Theta\right\}+\\&+\frac{\partial}{\partial t}\left[\rho\left(p_{\text{Joint}},\ T_{\text{Joint}},\ \left\{Y_{m,\text{Joint}}\middle|m=\overline{1,N_s}\right\}\right)\right]\sum_{n\in\mathbb{C}_{\text{OUT}}}{}^{(n)}\Theta+\\&+\sum_{n=1}^{N}\left\{\frac{\partial}{\partial x}\left[\rho\left(p_{\text{Joint}},\ {}^{(n)}T,\ \left\{{}^{(n)}Y_m\middle|m=\overline{1,N_s}\right\}\right){}^{(n)}w\right]{}^{(n)}\Theta\right\}=0;\end{aligned} \tag{15}$$

$${}^{(n)}\left(\frac{\partial}{\partial t}\left(\rho Y_m f\right)\right)+{}^{(n)}\left(\frac{\partial}{\partial x}\left(\rho Y_m w f\right)\right)=0,\ m=\overline{1,N_S-1},\ Y_{N_S}=1-\sum_{m=1}^{N_S-1}Y_m,\ n\in\mathbb{C}_{\text{IN}}; \tag{16}$$

$$Y_{m,\text{ Joint}}=\sum_{n\in\mathbb{C}_{\text{IN}}}{}^{(n)}\left(\rho|w|fY_m\right)\Big/\sum_{n\in\mathbb{C}_{\text{IN}}}{}^{(n)}\left(\rho|w|f\right),\ m=\overline{1,N_S}; \tag{17}$$

$$\begin{aligned}&{}^{(n)}\left(\frac{\partial}{\partial t}\left[\rho\left(\varepsilon+\frac{w^2}{2}\right)\right]\right)+{}^{(n)}\left(\frac{\partial}{\partial x}\left[\rho w\left(\varepsilon+\frac{w^2}{2}\right)\right]\right)=\\&=-{}^{(n)}\left(\frac{\partial\left(pw\right)}{\partial x}\right)-{}^{(n)}\left(\rho w g\frac{\partial z_1}{\partial x}\right)+{}^{(n)}Q-{}^{(n)}\left(\frac{\Phi\left({}^{(n)}T,\ {}^{(n)}T_{\text{am}}\right)}{f}\right),\ n\in\mathbb{C}_{\text{IN}};\end{aligned} \tag{18}$$

$$h_{\text{Joint}}=\sum_{n\in\mathbb{C}_{\text{IN}}}{}^{(n)}\left(\rho|w|hf\right)\Big/\sum_{n\in\mathbb{C}_{\text{IN}}}{}^{(n)}\left(\rho|w|f\right);\ n\in\begin{cases}\mathbb{C}_{\text{IN}}\in\overline{1,N}, & if\ \ {}^{(n)}\left(ws\right)\geq 0;\\ \mathbb{C}_{\text{OUT}}\in\overline{1,N}, & if\ \ {}^{(n)}\left(ws\right)<0;\end{cases} \tag{19}$$

$$T_{\text{Joint}}=T\left(p_{\text{Joint}},\ \varepsilon_{\text{Joint}},\ \left\{Y_{m,\text{Joint}}\middle|m=\overline{1,N_s}\right\}\right);\quad \rho_{\text{Joint}}=\rho\left(p_{\text{Joint}},\ T_{\text{Joint}},\ \left\{Y_{m,\text{Joint}}\middle|m=\overline{1,N_s}\right\}\right); \tag{20}$$

$$\varepsilon_{\text{Joint}}=h_{\text{Joint}}-p_{\text{Joint}}/\rho_{\text{Joint}};\quad \sum_{n\in\mathbb{C}_{\text{IN}}}{}^{(n)}\left(\rho|w|f\right)=\sum_{n\in\mathbb{C}_{\text{OUT}}}{}^{(n)}\left(\rho|w|f\right); \tag{21}$$

$$ {}^{(n)}p = p_{\text{Joint}},\ n=\overline{1,N};\quad {}^{(n)}\rho = \rho_{\text{Joint}},\ n\in\mathbb{C}_{\text{OUT}};\quad {}^{(n)}T = T_{\text{Joint}},\ n\in\mathbb{C}_{\text{OUT}};\quad {}^{(n)}\varepsilon = \varepsilon_{\text{Joint}},\ n\in\mathbb{C}_{\text{OUT}}; $$

$$ {}^{(n)}Y_m = Y_{m,\text{Joint}},\ n\in\mathbb{C}_{\text{OUT}},\ m=\overline{1,N_S};\quad {}^{(n)}(z_1) = {}^{(\xi)}(z_1) \text{ for any } n,\xi\in\overline{1,N}; \tag{22} $$

- equation of state:

$$ h=\varepsilon+p/\rho;\ \ p=p\left(\rho,\ T,\ \left\{Y_m\middle|m=\overline{1,N_s}\right\}\right),\ \rho=\rho\left(p,\ T,\ \left\{Y_m\middle|m=\overline{1,N_s}\right\}\right); \tag{23} $$

$$ \varepsilon=\varepsilon\left(p,\ T,\ \left\{Y_m\middle|m=\overline{1,N_s}\right\}\right),\ \ T=T\left(p,\ \varepsilon,\ \left\{Y_m\middle|m=\overline{1,N_s}\right\}\right), \tag{24} $$

where the subscript "Joint" means that the physical parameter of the gas mixture belongs to the pipeline junction (i.e. to the volume ${}^{(0)}V$); $h_{\text{Joint}}$ is enthalpy of the gas mixture in the pipeline junction.

The numerical analysis of the mathematical models (1–12) and (1, 3, 7, 11, 13–24) under consideration will be carried out by hybrid algorithm. It comprises Integro-Interpolation Method by A. Tikhonov and A. Samarsky (IIM) (Russian analog of the Finite Volume Method) (Tikhonov & Samarsky, 1999) and Lagrangian Particle Method by Pryalov (LPM).

To illustrate the parametric classes used for the difference equations in IIM, it is possible to present the class of the difference equations for a mathematical model of the non-isothermal transient motion of a multi-component gas mixture through a GPS line (see (1–4, 12)) (Seleznev, 2007):

$$ \left[(\rho F)^{(-S)}\right]_{\overset{t}{+}} + \left(\rho_{(-R)}w_{(0.5)}f_{(0.5)}\right)_{\overset{x}{+}}^{(\sigma,\theta)} = 0; \tag{25} $$

$$ \begin{aligned} &\left[(\rho F)^{(-S)}\left(Y_m\right)^{(-S)}\right]_{\overset{t}{+}} + \left(\rho_{(-R)}w_{(0.5)}f_{(0.5)}\left(Y_m\right)_{(-R)}\right)_{\overset{x}{+}}^{(\sigma,\theta)} - \\ &-\left[\left(\rho f D_m\right)_{(-R)}\delta\left(Y_m\right)^a\right]_{\overset{x}{+}}^{(\sigma,\theta)} = 0,\quad m=\overline{1,N_S-1},\quad Y_{N_S}=1-\sum_{m=1}^{N_S-1}Y_m; \end{aligned} \tag{26} $$

$$ \begin{aligned} &\left[(\rho F)^{(-S)}w^{(-S)}\right]_{\overset{t}{+}} + \left(\rho_{(-R)}w_{(0.5)}f_{(0.5)}w_{(-R)}\right)_{\overset{x}{+}}^{(\sigma,\theta)} = \\ &= -\left(B^-\gamma^-p_{\overline{x}} + B^+\gamma^+p_x\right)^{(\sigma,\theta)} - g\left[\rho\left(B^-\gamma^-\left(z_1\right)_{\overline{x}} + B^+\gamma^+\left(z_1\right)_x\right)\right]^{(\sigma,\theta)} - \frac{\pi}{4}\left(\lambda\rho|w|r\right)^{(\sigma,\theta)}w^{(\sigma,\theta)}; \end{aligned} \tag{27} $$

$$ \begin{aligned} &\left[(\rho F)^{(-S)}\varepsilon^{(-S)}\right]_{\overset{t}{+}} + \left(\rho_{(-R)}w_{(0.5)}f_{(0.5)}\varepsilon_{(-R)}\right)_{\overset{x}{+}}^{(\sigma,\theta)} + K_t\left(\rho F\frac{w^2}{2}\right) + K_x\left(\rho w f\frac{w^2}{2}\right)^{(\sigma,\theta)} = \\ &= -\left(p_{(-R)}w_{(0.5)}f_{(0.5)}\right)_{\overset{x}{+}}^{(\sigma,\theta)} - g\left[\rho\left(B^-\gamma^-\left(z_1\right)_{\overline{x}} + B^+\gamma^+\left(z_1\right)_x\right)\right]^{(\sigma,\theta)}w^{(\sigma,\theta)} - p^{(\sigma,\theta)}\left[F^{(-S)}\right]_{\overset{t}{+}} + \\ &+ \left(QF\right)^{(\sigma,\theta)} + \left[\left(kf\right)_{(-R)}\delta T^a\right]_{\overset{x}{+}}^{(\sigma,\theta)} - \phi^{(\sigma,\theta)} + \sum_{m=1}^{N_S}\left[\left(\rho D_m f\right)_{(-R)}\left(\varepsilon_m\right)_{(-R)}\delta\left(Y_m\right)^a\right]_{\overset{x}{+}}^{(\sigma,\theta)}; \end{aligned} \tag{28} $$

$$ \varepsilon_m=\varepsilon_m\left(\left\{S_{\text{mix}}\right\}\right),\ m=\overline{1,N_S};\ \ T_1=T_2=\ldots=T_{N_S}=T;\ \ p=p\left(\left\{S_{\text{mix}}\right\}\right);\ \ \varepsilon=\varepsilon\left(\left\{S_{\text{mix}}\right\}\right); \tag{29} $$

$$k = k\left(\{S_{\text{mix}}\}\right);\ \ D_m = D_m\left(\{S_{\text{mix}}\}\right),\ m = \overline{1, N_S}, \tag{30}$$

where $F$, $B^+$, $B^-$ are the expressions approximating $f$; $r$ is the expression approximating $R$ (the type of these expressions is defined upon selection of a particular scheme from the class of schemes); $s^a, s^b, r^a, r^b$, $\sigma$, $\theta$ are parameters of the class of schemes (e.g., by specifying $s^a = s^b = 1$, $r^a = r^b = 0,5$, $\sigma = 1$, $\theta = 0$, a two-layer scheme with central differences is selected from the class of scheme, and by specifying $s^a = s^b = 1$, $r^a, r^b$ is according to the principles of "upwind" differencing, $\sigma = 1$, $\theta = 0$ is a two-layer "upwind" scheme); $K_t$ and $K_x$ are the differential-difference operators of functions $\left(0.5\rho F w^2\right)$ and $\left(0.5\rho w f w^2\right)$ over time and space, respectively (the type of these operators is defined upon selection of a particular scheme from the class of schemes); $\phi^{(\sigma,\theta)}$ is a difference expression approximating function $\Phi\left(T, T_{\text{am}}\right)$. The difference equations (25–30) are supplemented by difference expression of initial and boundary conditions, as well as of conjugation conditions.

To record the parametric class of the difference equations (25–30), we used notations of a non-uniform space-time mesh $\left\{x_i, t_j\right\}$, where $x_i$ and $t_j$ are coordinates of the mesh node numbered $i$ over space, and $j$, over time, $i, j \in Z$, $Z$ being a set of nonnegative integers.

To explain the notations, it is expedient to consider an individual computational cell containing the node $\left\{x_i, t_j\right\}$ (mesh base node) and bounded by straight lines $x = x_i^a$, $x = x_i^b$, $t = t_j^a$ and $t = t_j^b$ ($x_{i-1} \le x_i^a \le x_i$, $x_i \le x_i^b \le x_{i+1}$, $t_{j-1} \le t_j^a \le t_j$, $t_j \le t_j^b \le t_{j+1}$, $x_i^a \ne x_i^b$, $t_j^a \ne t_j^b$). Let us introduce the so-called weighing parameters:

$$r_i^a = \frac{x_i^a - x_{i-1}}{x_i - x_{i-1}} = \frac{x_i^a - x_{i-1}}{h_i};\quad r_i^b = \frac{x_i^b - x_i}{x_{i+1} - x_i} = \frac{x_i^b - x_i}{h_{i+1}};\quad s_j^a = \frac{t_j^a - t_{j-1}}{t_j - t_{j-1}} = \frac{t_j^a - t_{j-1}}{\tau_j};\quad s_j^b = \frac{t_j^b - t_j}{\tau_{j+1}},$$

where $h_i = x_i - x_{i-1}$ and $h_{i+1} = x_{i+1} - x_i$ are steps "backward" and "forward" over the space coordinate for the $i$ node; $\tau_j = t_j - t_{j-1}$ and $\tau_{j+1} = t_{j+1} - t_j$ are steps "backward" and "forward" over the time coordinate on the $j$ time layer; $\alpha_i = h_{i+1}/h_i$ and $\beta_j = \tau_{j+1}/\tau_j$ are mesh parameters characterizing non-uniformity of the space and time mesh. To describe mesh function $y = y(x,t)$, the system (25–30) used the following notations:

$$y_i^j = y\left(x_i, t_j\right);\quad y_i = y_i(t) = y\left(x_i, t\right);\quad y^j = y^j(x) = y\left(x, t_j\right).$$

Where there was applied the quadratic approximation

$$y(x,t) = a_i^{y-}(t)x^2 + b_i^{y-}(t)x + c_i^{y-}(t),\ x \in \left[x_{i-1}, x_i\right],$$
$$y(x,t) = a_i^{y+}(t)x^2 + b_i^{y+}(t)x + c_i^{y+}(t),\ x \in \left[x_i, x_{i+1}\right],$$

the system used the following notations:

$$\delta y(x,t) = \frac{\partial y}{\partial x} = 2a_i^{y-}(t)x + b_i^{y-}(t),\ x \in \left[x_{i-1}, x_i\right];\quad \delta y(x,t) = \frac{\partial y}{\partial x} = 2a_i^{y+}(t)x + b_i^{y+}(t),\ x \in \left[x_i, x_{i+1}\right];$$

$$\left(\delta y^a\right)_i^j = 2a_i^{y-}\left(t_j\right)x^a + b_i^{y-}\left(t_j\right);\quad \left(\delta y^b\right)_i^j = 2a_i^{y+}\left(t_j\right)x^b + b_i^{y+}\left(t_j\right).$$

Also, the system (25–30) used the following index-free notations:

$$y = y_i^j,\ \ h = h_i,\ \ \alpha = \alpha_i,\ \ \tau = \tau_j,\ \ \beta = \beta_j,\ \ x = x_i,\ \ t = t_j,\ \ \widehat{y} = y_i^{j+1},\ \ \breve{y} = y_i^{j-1},\ \ y(+1) = y_{i+1}^j,$$

$$y(-1) = y_{i-1}^j,\ \ r^a = r_i^a,\ \ r^b = r_i^b,\ \ s^a = s_j^a,\ \ s^b = s_j^b,\ \ i, j \in Z;\ \ y^{(a)} = ay + (1-a)\breve{y};$$

$$y_{(b)} = by + (1-b)y(-1);\ \ y^{(a,b)} = a\widehat{y} + (1-a-b)y + b\breve{y};\ \ y^{(-S)} = s^a y + (1-s^a)\breve{y};$$

$$y^{(+S)} = s^b \widehat{y} + (1-s^b)y;\ \ y_{(-R)} = r^a y + \left(1-r^a\right)y(-1);\ \ y_{(+R)} = r^b \cdot y(+1) + \left(1-r^b\right)y;$$

$$y_{(-R)}(+1) = y_{(+R)};\ \ y_{(+R)}(-1) = y_{(-R)};\ \ \widehat{y}^{(-S)} = y^{(+S)};\ \ \breve{y}^{(+S)} = y^{(-S)};\ \ \Delta t^- = t - t^a = (1-s^a)\tau;$$

$$\Delta t^+ = t^b - t = s^b \widehat{\tau} = \beta s^b \tau;\ \ \Delta x^- = x - x^a = (1-r^a)h;\ \ \Delta x^+ = x^b - x = r^b h(+1) = \alpha r^b h;$$

$$\Delta t = t^b - t^a = \Delta t^+ + \Delta t^- = (1-s^a)\tau + s^b \widehat{\tau} = (1-s^a)\tau + \beta s^b \tau;$$

$$\Delta x = x^b - x^a = \Delta x^+ + \Delta x^- = (1-r^a)h + r^b h(+1) = (1-r^a)h + \alpha r^b h;$$

$$\gamma^- = \Delta x^- / \Delta x = (1-r^a)h \Big/ \left[(1-r^a)h + r^b h(+1)\right] = (1-r^a) \Big/ \left[(1-r^a) + \alpha \cdot r^b\right];$$

$$\gamma^+ = \Delta x^+ / \Delta x = r^b h(+1) \Big/ \left[(1-r^a)h + r^b h(+1)\right] = \alpha \cdot r^b \Big/ \left[(1-r^a) + \alpha \cdot r^b\right];,$$

$$\delta y^a(+1) = \delta y^b;\ \ \delta y^b(-1) = \delta y^a;\ \ y_x = \left[y(+1) - y\right]/h(+1);\ \ y_{\bar{x}} = \left[y - y(-1)\right]/h;$$

$$y_{\bar{x}}(+1) = y_x;\ \ y_x(-1) = y_{\bar{x}};\ \ y_{\underset{+}{t}} = \left[\widehat{y} - y\right]/\Delta t;\ \ y_{\underset{+}{x}} = \left[y(+1) - y\right]/\Delta x.$$

LPM is illustrated by the example of solution of energy equation from gas dynamics equations set for a single-component gas transmitted through an unbranched pipeline. Imaginary Lagrange particles are distributed along the pipeline. They are considered weightless. This allows them to move together with the fluid. Due to the small size, each particle can instantaneously acquire the temperature of the ambient fluid. Thus, by tracking the motion of such Lagrange particles along with the fluid and their temperature, one can analyze the process of heat transfer through multi-line GPSs. Energy equation is easy to derive by simplifying and transforming equation (4) accounting for (1-3), (12) and (23). The simplified equation will have the following form:

$$\frac{\partial h}{\partial t} + w\frac{\partial h}{\partial x} = \frac{w}{\rho}\frac{\partial p}{\partial x} + \frac{1}{\rho}\frac{\partial p}{\partial t} + \frac{\lambda |w|^3}{4R} - \frac{\Phi\left(T, T_{\text{am}}\right)}{f\rho} \quad \text{or} \quad \frac{Dh}{Dt} = G\left(x,\, t,\, T(h)\right), \tag{31}$$

where

$$G\left(x,\, t,\, T\right) = \frac{w}{\rho}\frac{\partial p}{\partial x} + \frac{1}{\rho}\frac{\partial p}{\partial t} + \frac{\lambda |w|^3}{4R} - \frac{\Phi\left(T, T_{\text{am}}\right)}{f\rho}; \tag{32}$$

$D\xi/Dt = \partial\xi/\partial t + w\,\partial\xi/\partial x$ is a derivative of an arbitrary function $\xi$ over $t$ in the direction

$$dx/dt = w(x,t). \tag{33}$$

This direction is called characteristic, and the equation is called the equation of characteristic direction. The second equation in (31) is called the characteristic form of the first equation in (31) or the differential characteristic relation. From the physical standpoint, the derivative $Dh/Dt$ corresponds to the substantial derivative, and the solution of equation (33) defines the coordinate of the continuum particle (in our case, the spatial coordinate of the fluid flow cross section) at each time.

Considering the known thermodynamic relationship

$$dh = c_p dT - \mu c_p dp, \tag{34}$$

where $c_p$ is specific heat capacity at constant pressure; $\mu$ is the Joule-Thomson factor, equation (31) can be transformed as follows:

$$\frac{DT}{Dt} = \left(\mu + \frac{1}{\rho c_p}\right)\frac{Dp}{Dt} + \frac{\lambda|w|^3}{4Rc_p} - \frac{\Phi(T, T_{\text{am}})}{f\rho c_p}. \tag{35}$$

Equation (35) is satisfied along each characteristic curve (33). These curves per se describe the trajectory of fluid particles. In other words, these equations describe the change in the fluid temperature for each cross section of the transported product flow.

When implementing the LPM, fluid flow parameters (such as pressure and velocity) are obtained using a difference scheme, while the gas temperature distribution is obtained based on the analysis of the Lagrange particle motion. For each particle, equation (35) is solved. The form of this equation enables such simulations, because it corresponds to the change in time of the temperature at each cross section of the fluid flow. Within this problem statement (which is Lagrangian with respect to each particle), equation (35) transforms into an ordinary differential equation (ODE) relative to the marching variable:

$$\frac{dT}{dt} - \left(\mu + \frac{1}{\rho c_p}\right)\frac{dp}{dt} = \frac{\lambda|w|^3}{4Rc_p} - \frac{\Phi(T, T_{\text{am}})}{f\rho c_p}. \tag{36}$$

Numerical analysis of ODE (36) can be carried out using different ODE solution procedures, for example, the known Runge – Kutta method with an adjustable accuracy of solution. As initial temperature of Lagrange particles one uses respective values from the defined initial conditions (i.e., for each Lagrange particle, its temperature is assumed equal to the fluid temperature at the location of the given particle).

As particles move together with the fluid flow towards the outlet pipe boundary, one needs to introduce new Lagrange particles at the inlet boundary at some regular intervals. The initial temperature of each introduced particle should be defined based on the boundary conditions related to the inlet boundary of the given pipe. The Lagrange particles that leave the pipe are deleted. As applied to the inlet boundaries of the outlet pipelines of each

junction node, the temperature of the introduced particles should be defined in accordance with equations (10) and (12).
Since LPM for solving the energy equation is not related immediately to the finite difference mesh used to solve the continuity and momentum equations, this mesh has almost no effect on the accuracy of the method proposed. Thus, high-accuracy computed values of gas temperature are obtained without mesh refinement, and this leads to a considerable speedup of computations.
Also, as there is no direct relationship between LMP and the finite difference mesh, the method is free of artificial viscosity and computational dispersion (Fletcher, 1988). As a result, LPM yields solutions without "scheme smoothing" of temperature fronts, which is consistent with actual physical processes. This makes such simulations more credible than the simulations, in which the energy equation is solved using difference schemes.

## 3. Simulation of a CS by CFD-simulator

The principal task of mathematical simulation of stable and safe operation of a CFS is to determine physical parameters of gas at the CFS outlet on the basis of the known values of gas flow parameters at the CFS inlet. To construct a 1D mathematical model of a CFS in a CFD-simulator, we used a well-known polytropic model of a CFS developed by A. Stepanov. The model is based on the combination of analytical dependencies for polytropic fluid dynamics processes and empirical characteristics obtained for each CFS during its full-scale testing.
When simulating steady modes of CS operation, an isothermal model is used for description of the gas flow in a CGP and DC, and an isobaric model – for description of the gas flow in an ACD. The power drive is simulated by specifying an analytical dependency of the capacity at the CFS shaft on energy expenditures. Such approach provides for the simplicity of the conjugation of models and a high, from the practical standpoint, veracity of simulation.
As was noted above, a CFD-simulator of a particular CS is a result of combining GCU, ACD and DC models, by application of CGP models, into a single integral network model of the CS in accordance with the process flow charts of the actual CS (fig. 2).
As proposed by V. Seleznev (Kiselev et al., 2005), in order to determine parameters of steady modes of natural gas transmission through a CS, generally, it is necessary to solve a system of nonlinear algebraic equalities under simple constraints on unknown variables. The system includes the law of conservation of gas masses at CGP branching points and one of the group of equations representing either conditions for conservation of mass flow rate at inlet and outlet CGPs in one branch, or conditions for equality of natural gas heads in parallel branches, where a branch is a segment of a pipeline system, which comprises an inflow (inlet) CGP, CFS and an outflow (outlet) CGP (see fig. 2).
As independent decision variables we used fractions of a mass flow rate of natural gas transmitted through separate branches of a CS, ratios of compression by compressor shops and ratios of compression by GCUs working as the first stage of transmitted gas compression at compressor shops. Such a set of variables allowed to reduce the problem dimension and narrow the range of search for problem solution, by more accurate specification of constraints on variables. This allowed to considerably save running time.

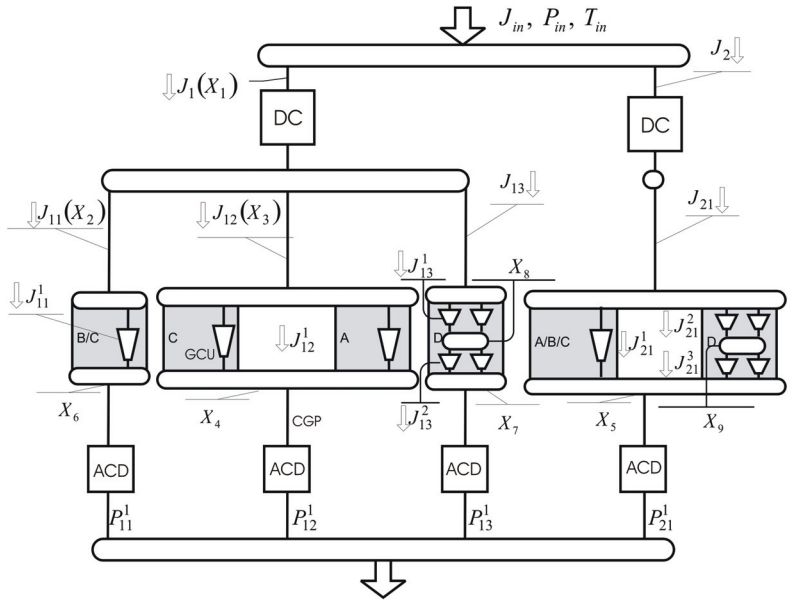


Fig. 2. The scheme of decision independent variables assignment for on-line technological analysis of gas transmission through CS

The mathematical model for the CS scheme presented in fig. 2 can be written as follows:

$$\begin{cases} P_{11}^1\left(J_{in},P_{in},T_{in},J_1\left(X_1\right),J_{11}\left(X_2\right),X_6\right)-P_{12}^1\left(J_{in},P_{in},T_{in},J_1\left(X_1\right),J_{12}\left(X_3\right),X_4\right)=0; \\ P_{12}^1\left(J_{in},P_{in},T_{in},J_1\left(X_1\right),J_{12}\left(X_3\right),X_4\right)-P_{13}^1\left(J_{in},P_{in},T_{in},J_1\left(X_1\right),J_{13},X_8,X_7\right)=0; \\ P_{13}^1\left(J_{in},P_{in},T_{in},J_1\left(X_1\right),J_{13},X_8,X_7\right)-P_{21}^1\left(J_{in},P_{in},T_{in},J_2,J_{21},X_9,X_5\right)=0; \\ J_{11}\left(X_2\right)-J_{11}^1\left(X_6\right)=0; \qquad J_{12}\left(X_3\right)-J_{12}^1\left(X_4\right)=0; \qquad J_{13}-J_{13}^1\left(X_8\right)=0; \\ J_{13}^1\left(X_8\right)-J_{13}^2\left(X_8,X_7\right)=0; \quad J_{21}-J_{21}^1\left(X_5\right)-J_{21}^2\left(X_9\right)=0; \quad J_{21}^2\left(X_9\right)-J_{21}^3\left(X_9,X_5\right)=0; \\ 0<X_i<1, \quad i=\overline{1,3}; \qquad \varepsilon_{\max}^1<X_j<\varepsilon_{\max}^{shop}, \quad j=\overline{4,7}; \qquad \varepsilon_{\min}^1<X_k<\varepsilon_{\max}^1, \quad k=\overline{8,9}, \end{cases} \tag{37}$$

where $P_{11}^1$, $P_{12}^1$, $P_{13}^1$, $P_{21}^1$ are the natural gas pressure at the outlet of each of the CS branches, $J_{in}$, $P_{in}$, $T_{in}$ are the natural gas flow rate, pressure and temperature at the CS inlet, $J_1$, $J_2$ are the natural gas mass flow rates through "branches I", $J_{11}$, $J_{12}$, $J_{13}$, $J_{21}$ are the natural gas mass flow rates through "branches II", $X_6$, $X_4$, $X_7$, $X_5$ are the ratios of compression for compressor shops, $X_8$, $X_9$ are the ratios of compression for GCU groups of the first stages of compressor shops, $\varepsilon_{\min,\max}^1$ is a minimal/maximal ratio of compression for GCU groups of the first stage, $\varepsilon_{\max}^{shop}$ is the maximal ratio of compression for compressor shops.

To assure a safe mode of CS operation, it is required to observe the following restrictions on: maximal volumetric capacity $Q_j$ of each operating CFS; frequency $u_j$ of the CFS shaft rotation; maximal capacity $N_j$ of the CFS drive; maximal outlet pressure $P_j$ of the CFS, which is determined by the pipe's strength; maximal temperature $T_j$ at the CFS outlet,

which is determined by the insulating coating; the lower value of pressure at the outlet of each CFS, related to the requirements to maintain pressure at major gas tapping and boundary gas pipeline points. These restrictions can be formulated as one-sided and two-sided weak inequality:

$$\left\{Q_j^{\min} \le Q_j(\vec{X}) \le Q_j^{\max};\ u_j^{\min} \le u_j \le u_j^{\max};\ N_j(\vec{X}) \le N_j^{\max};\ P_j^{\min} \le P_j(\vec{X}) \le P_j^{\max};\ T_j(\vec{X}) \le T_j^{\max}\right\}, \quad (38)$$

where index $j = 1,\ldots,M$ means the number of CFS. Also, it is necessary to comply with restrictions on: positions of operational points at the CFS performance curves, related to surge-free operation requirements; conditions related to CFS drive's stable operation; etc. Compliance with the latest restrictions can only be analyzed in the process of a detailed simulation of the mode of gas transmission through the CS.

The system of nonlinear algebraic inequalities (38) describes technological, operating and design constraints on CS equipment operation. When formulating the constraints in a CFD-simulator, a maximum consideration is given to the specifics of the CS process flow chart and the modes of its operation, including a possibility of surging in "CFS – Adjacent CGP" (Seleznev & Pryalov, 2007).

The resultant system (37, 38) represents a generalized system of nonlinear algebraic equalities and inequalities. One of the methods to solve the system of nonlinear algebraic equalities and inequalities is the well-known Interior Point Method, which, in a CFD-simulator, is implemented by statement and solution of an equivalent problem of mathematical optimization (Dennis & Schnabel, 1988). The equivalent optimization problem is solved by the method of modified Lagrange functions. If no solution can be found, the possibility of failure occurrence is admitted. The method we use makes it possible to identify constraints which are not complied with and to evaluate the extent of such non-compliance.

## 4. Simulation of a GTN by CFD-simulator

Industrial application of CFD-simulators in the gas industry is shown by the example of two acute problems: cutting down the power costs for natural gas transportation through pipeline networks; finding out the reasons for discrepancy between estimates of supplied gas volume by seller and consumer. To resolve these problems, one should be able to simulate the processes of GTN operation in a credible way. Let us consider the GTN simulation algorithm of S. Pryalov as applied to a fragment of a hypothetical CS (fig. 3).

In this CS fragment, three GCUs are combined in parallel into a group by means of a CGP. Fig. 3a uses the following notations: $P, T$ – pressure and temperature of the gas (the double number subscripts indicate that the physical parameters of the natural gas flow are attributed to the CFS inlet or outlet with a respective number; parameters at the CS inlet are denoted with the lower index "$in$"); $J_i,\ i = 1,2,3,$ – gas mass flow in the CS pipeline branch with its own number; $n_i,\ i = 1,2,3,$ – speed of the $i$-th CFS shaft; $\xi$ – friction factor for CGP (the double number subscripts indicate that the quantity is attributed to a certain CGP).

Let us conventionally isolate one (the second from the top in fig. 3a) CS branch (fig. 3b): between points **A** and **B**. In this case, it is assumed that respective boundary conditions are defined at the branch inlet and outlet points. Such boundary conditions can include:

pressure $P_A$ and temperature $T_A$ at the branch inlet, and pressure $P_B$ and heat flux $q_B$ (or temperature $T_B$) at the branch outlet (note that generally speaking these quantities are functions of time).

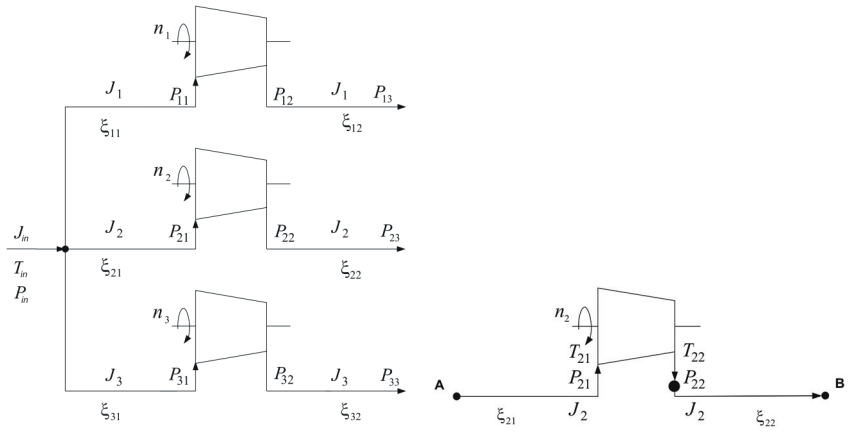


Fig. 3. A diagram of a hypothetical CS (a) and a diagram for the branch point A to point B (b)

The value of the mass flow rate through the CFS $J = J_2^{\mathrm{CFS}} = J_2^{\mathrm{CFS}}(t)$ in this case is a solution of a non-linear algebraic equation (lower indices of pressures are the same as in fig. 3):

$$\Psi_2(J) = P_{22}^{\mathrm{CFS}}(J) - P_{22}^{\mathrm{CGP}}(J) = 0, \tag{39}$$

where $P_{22}^{\mathrm{CFS}}(J) = \varepsilon_2\left(P_{21}^{\mathrm{CGS}}(J),\ T_{21}^{\mathrm{CGS}}(J),\ J\right) \cdot P_{21}^{\mathrm{CGS}}(J)$ is pressure at the CFS outlet; $\varepsilon_2\left(P_{21}^{\mathrm{CGS}}(J),\ T_{21}^{\mathrm{CGS}}(J),\ J\right)$ is gas compression rate produced by the CFS and computed in the CFD-simulator using a semi-empirical CFS model (Seleznev & Pryalov, 2007); $P_{21}^{\mathrm{CGS}}(J)$ and $T_{21}^{\mathrm{CGS}}(J)$ are the outlet pressure and temperature of the inlet CGP from the simulations of the gas flow parameters in the given pipeline, in which boundary conditions at its outlet include the target mass flow $J$ and heat flux conservation at the outlet of the inlet CGP; $P_{22}^{\mathrm{CGS}}(J) = P_{22}^{\mathrm{CGS}}\left(J,\ T_{22}^{\mathrm{CFS}}(J)\right)$ is inlet pressure of the inlet CGP from the simulations of the gas flow parameters in the given pipeline, in which boundary conditions at its outlet include the target mass flow $J$ and gas temperature equal to the gas temperature $T_{22}^{\mathrm{CFS}}(J)$ at the CFS outlet.

The functions in this equation are determined numerically by using the CFD-simulator at each step of the iterative solution of equation (39). Therefore, the target distributions of the fluid dynamics parameters of both CGPs and operating parameters of the GCU are obtained automatically in the course of solving equation (39).

Equation (39) in the CFD-simulator is solved numerically using the well-known modified Newton procedure, in which equation (39) is solved by iterations using a finite-difference Jacobian approximation. In the paper (Dennis & Schnabel, 1988) the authors show that this method preserves its q-quadratic convergence of the classical Newton procedure for solving

non-linear algebraic equations provided that the finite-difference step length is chosen properly.

For simulations of transient CS operation conditions, the computational model of a hypothetical CS fragment (see fig.3a) will comprise sub-models of an inlet CGP, three CFSs and an outlet CGP. The inlet CGP includes pipelines from the point of transported gas flow entry into the CS to the points of the gas flow entry into each CFS. The outlet CGP includes pipelines from the points of gas flow exit from each CFS to the point of gas flow exit from the CS. These inlet and outlet CGPs in this case are branched, multi-line pipelines, which are simulated by models (1–12) or (1, 3, 7, 11, 13–24). It is assumed that boundary conditions at the transported gas flow inlet/outlet points of the CS are defined in accordance with the principles described above. Here, the values of the mass flow rate through each CFS, $J_i^{\mathrm{CFS}} = J_i^{\mathrm{CFS}}(t)$ (where $i = \overline{1,N}$, $N$ is the number of CFSs in the group), constitute a solution to the set of non-linear algebraic equations:

$$\Psi_i(J_i) = P_{i2}^{\mathrm{CGP}}(J_i) - P_{i2}^{\mathrm{CFS}}(J_i) = 0, \quad i = \overline{1,N}. \tag{40}$$

The notations used in (40) are similar to those used in equation (39). The subscripts of pressures correspond to the indices shown in fig. 3.

The target distributions of the fluid dynamics parameters of the CGPs and operating parameters of the GCU equipment are obtained automatically by numerical simulation of equations (40) (as a result of using the CFD-simulator for solving this set of equations to determine the values of its constituent functions).

Numerical solution of equations (40) in industrial application of the CFD-simulator is performed by known quasi-Newton methods. In the first line, one can recommend using the modified Broyden method (Dennis & Schnabel, 1988) as one of the best performing extensions of the classical secant method to the case of numerical solution of non-linear algebraic equations. This method can have q-superlinear local convergence with an r-order of $2^{1/2N}$.

It is not difficult to extend the above method to the whole GTN. In this case, equations (40) instead of the mass flow rates through the CFSs will contain the mass flow rates through the CS as a whole. By analogy with simulations of gas transportation through an individual CS, due to the use of the CFD-simulator, target distributions of parameters for the whole multi-line GPS and operating parameters of GCU, CFS, DC and ACD are obtained automatically by numerical simulation of modified equations (40) by the quasi-Newton methods.

## 5. Optimization of gas transmission expenditures using CFD-simulator

To avoid too many technical details without loss of generality, here we consider GTNs with serially connected CSs (fig. 4).

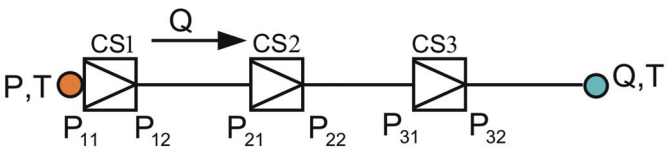


Fig. 4. A diagram of a hypothetical GTN of serially connected compressor stations

Fig. 4 uses the following notations: $P, T, Q$ – pressure, temperature and volumetric flow rate. The symbols CS1, CS2 and CS3 in fig. 4 are used in the diagram to designate CSs with their serial number. The double number subscripts indicate that the physical parameters of the natural gas flow are associated with the inlet or outlet of the CS with a respective serial number. The horizontal lines between the CSs in the diagram show multi-line GPSs. The flow direction in fig. 4 is from left to right. The GTN diagram is typical of many gas transportation companies. As an example one can mention GTNs of Tomsktransgas, Russia, and SPP, a.s., Slovakia.

The energy criterion of reduced expenses for failure-free natural gas transportation through GTNs has the following form: One should obtain calculated estimates of GTN equipment controls corresponding to minimum costs of integral energy costs related to transient conditions of gas transportation through the GTN in a given time interval subject to compliance with gas specifications at GTN control points and, at the same time, observance of applicable restrictions to ensure safe and environmentally sound operation of the GTN.

In such a criterion, estimates of the cost function for integral energy expenditures are made using the CFD-simulator. For this purpose, the CFD-simulator features functional dependencies of energy carrier consumption in GCUs on the power consumption at CFS shafts for all GCUs of the GTN. Note that plotting distributions of energy carrier consumption in GCUs over time in the CFD-simulator belongs to GTN performance monitoring procedures and is one of its standard functions (Seleznev & Pryalov, 2007). If the energy carrier consumption and the price of these energy carriers are known, it will be easy for a gas transportation company to calculate their total cost.

The requirement of compliance with gas specifications at GTN control points within the criterion is consistent with the requirement for gas transportation companies to fulfill their contractual obligations. The requirement of compliance with restrictions to ensure GTN safety and environmental soundness comes to the observance of process, performance, design and other restrictions as applied to the operation of the GTN equipment. These restrictions can be formalized mathematically as a set of simple constraints on the target values of the GTN equipment controls and a set of non-linear weak two-sided (and/or one-sided) algebraic inequalities. Function values in these inequalities (GTN equipment operating data and fluid dynamics parameters of the gas flow in the network) are calculated using the CFD-simulator.

In practice, in implementing the criterion mathematically, one usually seeks a local minimum of the function of integral expenses subject to given constraints. This is primarily related to the complexity (and, as a rule, polymodality) of the target function, complexity of the constraint functions and uncertainties in input data coming to the CFD-simulator from SCADA systems.

An optimization algorithm for transient GTN operation conditions was developed by V. Seleznev in 2003. It provides for preliminary predictive simulations, using the CFD-simulator, of physical parameters of the gas flow through the GTN for a given time interval based on the predefined history of GTN operation and gas flow parameters at the GTN boundaries. The value of the function of energy (or financial) expenses for gas transportation through the GTN, which is related immediately to the operating parameters of its equipment and gas flow parameters, is calculated at each time step of this simulation. Thus, during the predictive simulations, the time dependence of expenses is automatically generated for a so-called non-optimized prediction.

Setting up an optimized prediction for the given time interval in a general case consists in the definition of time laws for the GTN equipment controls to reduce the costs of natural gas transportation. Target controls should first of all include regulation of the CFS shaft speed in the whole GTN. The speed regulation for all CFSs can result in shutdowns or starts of individual GCUs. The list of involved GCUs, including valve status data, are called the CS configuration (or configuration of the GTN as a whole).

As has been already mentioned above, energy (or financial) expenses at a given time point $t$ depend on the status $\vec{\mathbf{u}}(t)$ of the whole package of GTN gas pumping equipment. These expenses will be represented in the form of a non-linear algebraic cost function, $Z\left(t, \vec{\mathbf{u}}(t)\right)$. It is evident that total expenses for the prediction period $[0, T]$ will be an integral, $\int_0^T Z\left(t, \vec{\mathbf{u}}(t)\right) dt$. From the mathematical viewpoint, minimizing the costs of natural gas transportation through the GTN over the predicted period comes to the minimization of the area of the 2D figure $\mathbf{\Phi}$ shown in fig. 5.

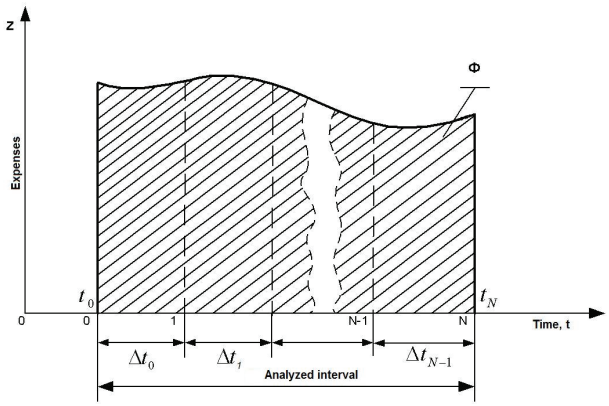


Fig. 5. Initial function of gas transportation expenses in the analyzed interval (prediction period)

Mathematically, this can be represented in the following way:

$$J(\vec{\mathbf{u}}) = \int_0^T Z\left(t, \vec{\mathbf{u}}(t)\right) dt \to \min, \quad t \in [0, T], \quad \vec{\mathbf{u}}(t) \in U(t) \subset R^m, \tag{41}$$

given that

$$\begin{aligned} \vec{\mathbf{W}}\left(t, \vec{\mathbf{u}}(t)\right) \in \Omega = \Big\{ \vec{\mathbf{W}} \in R^k : \left(w_{\min}^{specified}\right)_j \le w_j\left(t, \vec{\mathbf{u}}(t)\right) \le \left(w_{\max}^{specified}\right)_j, \ j = \overline{1, l}; \\ w_j\left(t, \vec{\mathbf{u}}(t)\right) \le \left(w_{\max}^{specified}\right)_j, \ j = \overline{l+1, k} \Big\}, \end{aligned} \tag{42}$$

where $U(t)$ is a given set to define the type of constraints related to the limited availability of control resources (simple constraints on the control quantities); $m$ is the number of

controls used for optimization; $\vec{\mathbf{W}}\left(t,\vec{\mathbf{u}}(t)\right)=\left(w_1\left(t,\vec{\mathbf{u}}(t)\right),...,w_k\left(t,\vec{\mathbf{u}}(t)\right)\right)^T$ is a given algebraic constraint vector-function; $k$ is the total number of constraints in the form of two-sided and one-sided weak algebraic inequalities used for optimization; $\vec{\mathbf{w}}_{\min}^{specified}\in R^l$ and $\vec{\mathbf{w}}_{\max}^{specified}\in R^k$ are given vectors of the minimum and maximum permissible values to implement the constraints; $l$ is the number of constraints in the form of two-sided weak algebraic inequalities used for optimization; $R^m$ is the Euclidean $m$-dimensional vector space; $R^k$ is the Euclidean $k$-dimensional vector space; $R^l$ is the Euclidean $l$-dimensional vector space.

The first $l$ rows of the vector-function $\vec{\mathbf{W}}\left(t,\vec{\mathbf{u}}(t)\right)$ describe process, design, environmental and other constraints on the GTN operating conditions. The rest of the constraint vector-function rows provide stabilization of the programmed status and GTN operating conditions. Stabilization of a given programmed status and GTN operating conditions here means maintaining true paths of GTN operating and gas flow parameters in some neighborhood of expected paths. Examples of such GTN parameters are gas pressures at the GTN boundaries, which should be strictly controlled in accordance with contractual obligations of the gas company. Thus, problem (41, 42) includes additional conditions, $w_j\left(t,\vec{\mathbf{u}}(t)\right)\le\left(w_{\max}^{specified}\right)_j$, $j=\overline{l+1,k}$, which will constrain the deviation of computed paths of specified parameters from their programmed paths. Algebraic functions in these constraints are generally modules of discrepancies between computed and programmed paths.

The technology of natural gas transportation through GTNs provides for stepwise variation of the GTN equipment controls (for example, individual GCUs or their groups) in time. Therefore, in setting up an optimal prediction of expenses, one should map a grid $t_0$, $t_1$,..., $t_N$ onto the analyzed interval $[0,T]$ (see fig. 5) in such a way as to provide constant control of the GTN equipment within the time interval $(t_i,\ t_{i+1})$, $i=\overline{0,\ N-1}$, (fig. 6a), i.e: $\vec{\mathbf{u}}(t)=\vec{\mathbf{u}}^i=const$, $t\in(t_i,t_{i+1})$, $\vec{\mathbf{u}}^i\in U(t)$. To simplify the problem definition (without loss of generality), we assume conventionally that the step $\Delta t=t_{i+1}-t_i$, $i=0,\ ...\ ,N-1$, is constant all over the prediction period.

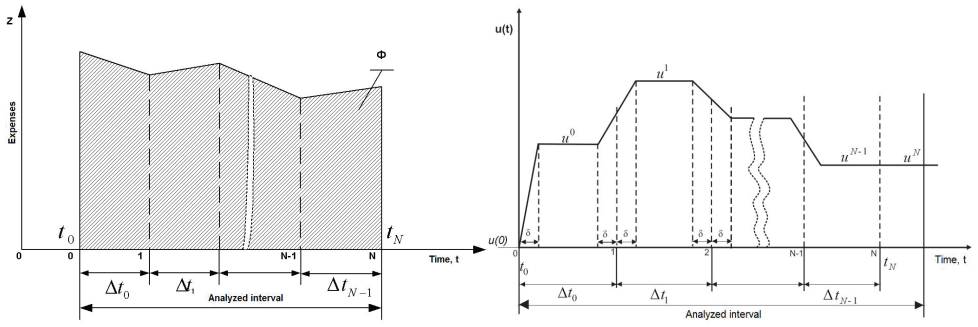


Fig. 6. Approximation sequence for the cost function

Given this, the function of the GTN equipment status will be represented as follows (fig .6a):

$$u_j(t)=\begin{cases}\dfrac{t-t_0}{\delta}\left(u_j^0-u_j(0)\right)+u_j(0), & t\in[0,\delta);\\ u_j^i, & t\in\left[t_i+\delta,t_{i+1}-\delta\right);\\ \dfrac{t-\left(t_{i+1}-\delta\right)}{2\delta}\left(u_j^{i+1}-u_j^i\right)+u_j^i, & t\in\left[t_{i+1}-\delta,t_{i+1}+\delta\right),\end{cases} \tag{43}$$

where $i=0,...,N-1$; $j=1,...,m$; $u_j(0)$ is a known value of the initial control at the initial time, $u_j^N=u_j^{N-1}$; the spacing $\delta$ is chosen empirically. In industrial applications the function of the GTN equipment status is often a function of shaft speed variation for all CFSs.
It is difficult to calculate the integral of expenses (41) in the constructed optimization model (41–43) analytically. Therefore, this integral is calculated numerically. The widely known method of trapezoids is considered quite acceptable as applied to this case, i.e. (fig .6b):

$$J(\vec{\mathbf{u}})=\int_0^T Z\left(t,\vec{\mathbf{u}}(t)\right)dt\approx 0.5\Delta t\,Z_0\left[\vec{\mathbf{u}}(t_0)\right]+\Delta t\sum_{i=1}^{N-1}Z_i\left[\vec{\mathbf{u}}(t_0+i\cdot\Delta t)\right]+0.5\Delta t\,Z_N\left[\vec{\mathbf{u}}(t_N)\right]. \tag{44}$$

Thus, for some set of discrete controls $\left(\vec{\mathbf{u}}^0,\vec{\mathbf{u}}^1,\ldots,\vec{\mathbf{u}}^{N-1}\right)^T$, formula (44) allows calculating the quality functional $J\left(\vec{\mathbf{u}}^0,\vec{\mathbf{u}}^1,\ldots,\vec{\mathbf{u}}^{N-1}\right)$.

Hence, the problem of finding an optimal control (41–43) can be replaced with an equivalent problem of nonlinear programming with respect to independent vectors $\left(\vec{\mathbf{u}}^0,\vec{\mathbf{u}}^1,\ldots,\vec{\mathbf{u}}^{N-1}\right)^T$:

$$\tilde{J}\left(\vec{\mathbf{u}}^0,\vec{\mathbf{u}}^1,\ldots,\vec{\mathbf{u}}^{N-1}\right)=0.5\,Z_0\left[\vec{\mathbf{u}}^0\right]+\sum_{i=1}^{N-1}Z_i\left[\vec{\mathbf{u}}^i\right]+0.5\,Z_N\left[\vec{\mathbf{u}}^{N-1}\right]\to\min, \tag{45}$$

subject to the conditions (considering (43)):

$$\vec{\mathbf{u}}^i\in U=\left\{\vec{\mathbf{u}}\in R^m:\ \max\left[u^{i-1}-\eta_{constr},\ u_{\min}^{specified}\right]_j\le u_j^i\le\min\left[u^{i-1}+\eta_{constr},\ u_{\max}^{specified}\right]_j,\ j=\overline{1,m}\right\},\quad i=\overline{1,N-1}; \tag{46}$$

$$\vec{\mathbf{W}}_i\left(\vec{\mathbf{u}}^0,\vec{\mathbf{u}}^1,\ldots,\vec{\mathbf{u}}^{N-1}\right)\in\Omega=\left\{\vec{\mathbf{W}}_i\in R^k:\ \left(w_{\min}^{specified}\right)_j\le w_j^i\left(\vec{\mathbf{u}}^0,\vec{\mathbf{u}}^1,\ldots,\vec{\mathbf{u}}^{N-1}\right)\le\left(w_{\max}^{specified}\right)_j,\ j=\overline{1,l};\ w_j^i\left(\vec{\mathbf{u}}^0,\vec{\mathbf{u}}^1,\ldots,\vec{\mathbf{u}}^{N-1}\right)\le\left(w_{\max}^{specified}\right)_j,\ j=\overline{l+1,k}\right\},\quad i=\overline{1,N}, \tag{47}$$

where $\vec{\mathbf{u}}_{\min}^{specified}\in\mathbb{R}^m$ and $\vec{\mathbf{u}}_{\max}^{specified}\in\mathbb{R}^m$ are given vectors of the minimum and maximum values of control parameters (as a rule, these vectors are time-independent); $\vec{\boldsymbol{\eta}}_{constr}\in\mathbb{R}^m$ is a given constraint on the maximum step of a single *j*-th control change in time. The numerous constrains in (47) are attributed to the requirement that variation of GTN operating parameters on transition from one time layer to the next one should be smooth. One should be reminded here that calculations of expenses $Z_i\left(\vec{\mathbf{u}}^i\right)$ for gas transportation through the GTN are enabled by the CFD-simulator.

In industrial applications for optimal predictions, knowing the optimal control path is more critical than knowing the minimum value of the quality functional. Therefore, it is reasonable to transform the problem statement (45) in the following way:

$$\hat{J}\left(\vec{\mathbf{u}}^1,\ldots,\vec{\mathbf{u}}^{N-1}\right)=\sum_{i=1}^{N}\mathrm{Z}_i\left(\vec{\mathbf{u}}^i\right)\to\min,\quad\text{where }\vec{\mathbf{u}}^N=\vec{\mathbf{u}}^{N-1}. \tag{48}$$

To solve the problem of general non-linear programming (46–48), we use the method of modified Lagrange functions (Vasilyev, 2002). In accordance with this method, the modified target function of the optimized problem being solved is a sum of initial target function (48) and formalized constrains (47) weighted in a special way (by means of Lagrange multipliers and penalties). An equivalent task of searching for the minimum value of the modified target function subject to simple constraints on variables (46) is fulfilled using modified varied metrics algorithms (Vasilyev, 2002) or modified conjugate gradient algorithms (Vasilyev, 2002), which are resistant to the error accumulation in the course of arithmetic operations.

If the choice of the GTN configuration is considered as an additional control, one will have to introduce additional constraints into the optimization problem to represent process bans on frequent changes of GTN configurations during gas transportation. The choice of the GTN configuration does not require fundamental changes in the optimization approach or algorithm for transient conditions of gas transportation through the GTN.

The above approach to the construction of optimal prediction for gas transportation through the GTN can be easily extended to the CS or group of GCUs.

## 6. Numerical monitoring of gas distribution discrepancy using CFD-simulator

Numerical monitoring of the discrepancy is based on a statement (for a specified time gap) and numerical solution of identification problem of a physically proved quasi-steady gas dynamics mode of natural gas transmission through specified gas distribution networks.

In large communities, natural gas is supplied to the consumers using medium or low pressure ring mains, being several dozen kilometers long. Gas from the supplier is transmitted to such mains through a GTN after its pressure is reduced by means of a system of gas reducers installed at inlet gas distribution stations (GDSs) (fig. 7). Major parameters of gas supplied by the gas transportation company to the seller are also measured at the GDS outlets. Here, major parameters of natural gas include its flow rate, pressure and temperature.

Gas from inlet GDSs is delivered to the ring main via the CGP network of the gas seller. Consumers receive gas from the ring mains through outlet CGPs leading from the ring main to the consumer. The length of the CGPs can range from several hundred meters to several kilometers. In the first approximation, each consumer is considered independent and provided with gas through one CGP, which is completely associated with the consumer (called "associated CGP" as the text goes). Consumer independence means that the consumer's gas cannot be delivered to other consumers.

Thus, the gas distribution network (GDN) under consideration comprises inlet CGPs from inlet GDSs, a ring main and associated CGPs. In fig. 7, the GDN under consideration is shown with gray color.

If the GDN operates properly, the seller seeks to sell the whole amount of gas received from the supplier. An exception in this case is natural gas forcedly accumulated in the GDN.

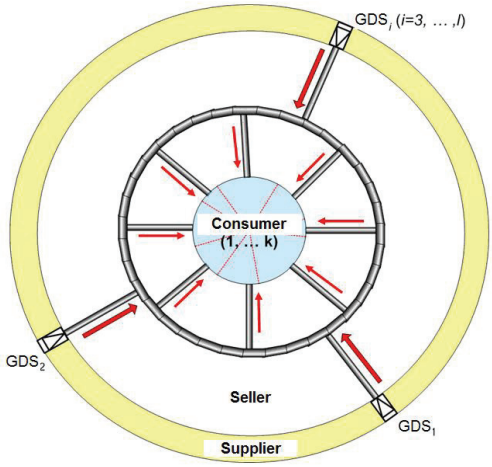


Fig. 7. A diagram of the GDN under consideration

For settlement of accounts, consumers submit reports to the seller, in which they indicate estimated volumes of received gas. These reports are usually generated either by processing the consumers' field flow meter readings or by simplified calculations based on the rates formally established for the given category of consumers. Verification of data provided by the consumers consists in the comparison of their estimates with data obtained by processing the seller's flow meter readings in compliance with current guidelines.

The central difficulty in such verification is that the amount of field measurements of supplied gas that can be used as a reliable basis is rather limited in the present-day gas industry. Such a situation results in occasional discrepancies (especially during the heating season) in analyzing the volume of natural gas supplied to the consumers. The total discrepancy over a given time period is determined as a difference between two estimates of the gas volume. The first estimate represents the total gas volume actually received during the time period in question as reported by all consumers, and the second estimate, the total volume of natural gas delivered by the supplier to the seller less the gas volume accumulated in the GDN.

One of the most promising ways to resolve the above problem is to use the CFD-simulator. For this purpose, the following problem setup can be used for numerical monitoring of gas distribution discrepancy using CFD-simulator.

Input data: layout chart of the GDN; sensor locations in the GDN, where gas parameters are measured; given time interval of GDN operation; results of field measurements of gas parameters in the GDN in the given time interval; actual (or nameplate) errors of instruments used to measure gas parameters; data on received gas volumes as reported by each consumer for the given time interval.

Target data: (1) physically based gas flow parameters in the GDN in the given time interval having a minimum discrepancy compared to respective field measurement data at identification points and providing the closest possible agreement between calculated flow rate values at the outlet of each associated CGP and corresponding reported values (further as the text goes, this mode will be called "the identified gas flow"); (2) associated CGPs with underreported gas volumes as against the identified gas flow; (3) calculated estimates of

discrepancies between gas volumes delivered in the given time interval through each associated CGP as an arithmetic difference between the calculated gas volume corresponding to the identified gas flow and the reported value; (4) calculated estimates of discrepancies between gas volumes delivered in the given time interval through each inlet GDS as an arithmetic difference between the calculated gas volume corresponding to the identified gas flow and the reported value.

Correct simulation of item 1 in the problem statement makes it possible to obtain credible information on physically consistent space-time distributions of flow rates, pressures and temperatures for the gas flow, which is most reasonable for the given time interval with the given field measurement data. Convergence of calculated and reported gas flow values for individual consumers increases the level of objectivity of numerical analysis, as it seeks to maintain the highest possible trust in the data on received gas volumes reported by the consumers.

It follows from the above problem statement that numerical monitoring of gas distribution discrepancy under items 2–4 in the list of target values in essence consists in performing straightforward arithmetic operations with output data of item 1. Therefore, special attention below will be paid to the algorithm of this calculation. This algorithm was proposed by V. Seleznev in 2008. In the first approximation, we consider the process of gas flow through the GDN to be steady-state.

In order to calculate non-isothermal steady-state gas flow parameters in the GDN under consideration, the following boundary conditions of "Type I" need to be specified: pressure, temperature and composition are defined at the outlet of each inlet GDS; mass flow rate and gas temperature are defined at the outlet of each associated CGP.

Using the CFD-simulator with the given boundary conditions and fixed GDN characteristics, one can unambiguously determine physically based spatial distributions of calculated estimates of steady-state GDN operation parameters (Seleznev et al., 2007). Spatial distributions of parameters here mean their distributions along the pipelines.

A diagram of identification locations is generated on the given layout of sensor locations in the GDN. The preferred location of each identification point should correspond to the key requirement: a considerable change in the fluid dynamics conditions of GDN operation should be accompanied by considerable changes in the gas parameters actually measured at this point. The distribution of identification points over the GDN diagram should be as uniform as possible. An identification point can be located both inside the GDN and at its boundaries. At each identification point, different combinations of major gas flow parameters can be measured. These combinations can be varied for every identification point.

The process of finding the identified gas flow comes to the statement and solution of the problem of conditional optimization:

$$\left\| \vec{\mathbf{f}}_{\text{calc}}\left(\vec{\mathbf{X}}\right) - \vec{\mathbf{f}}_{\text{meas}}^{\text{const}} \right\|_L \to \min_{\vec{\mathbf{X}} \in \Omega \subset R^n}, \tag{49}$$

where $\|\ldots\|_L$ is the vector norm, the type of which is determined by the value of the parameter $L$, $(L = 0, 1, 2)$ (see below); $\vec{\mathbf{f}}_{\text{calc}}\left(\vec{\mathbf{X}}\right)$, $f_{\text{calc}} : R^n \to R^m$, is the vector-function of calculated estimates of controlled transported gas variables at the identification points in the $m$-dimensional Euclidean space $R^m$ (these calculated estimates are obtained using the CFD-simulator); $\vec{\mathbf{f}}_{\text{meas}}^{\text{const}} \in R^m$ is a given vector of measured values of controlled transported gas variables at the identification points; $m$ is the number of given identification points in the

GDN diagram; $\vec{\mathbf{X}} \in \Omega \subset R^n$ is the vector of independent controlled variables in the $n$-dimensional Euclidean space $R^n$;

$$\vec{\mathbf{X}} \in \Omega = \left\{ \vec{\mathbf{X}} \in R^n : \quad \vec{\mathbf{a}} \le \vec{\mathbf{X}} \le \vec{\mathbf{b}}; \quad \left\| \vec{\mathbf{q}}_{\text{calc}}^{\text{GDS}} \left( \vec{\mathbf{X}} \right) - \vec{\mathbf{q}}_{\text{meas\_GDS}}^{\text{const}} \right\|_0 \le t_{\text{flow\_rate}}^{\text{GDS}} \right\}; \tag{50}$$

$\vec{\mathbf{a}} \in R^n$ and $\vec{\mathbf{b}} \in R^n$ are correctly defined vectors setting limits in simple constraints for the range of admissible variation of the vector of independent controlled variables (see below); $n$ is the number of independent controlled variables (see below); $\|\ldots\|_0$ is the cubic vector norm (e.g., $\left\| \vec{\mathbf{Y}} \right\|_0 = \max\limits_{1 \le i \le n} |y_i|$, $\vec{\mathbf{Y}} \in R^n$ ); $\vec{\mathbf{q}}_{\text{calc}}^{\text{GDS}} \left( \vec{\mathbf{X}} \right)$, $q_{\text{calc}}^{\text{GDS}} : R^n \to R^l$, is the vector function of calculated estimates of mass flow rates through inlet GDSs in the $l$-dimensional Euclidean space $R^l$ (these calculated estimates are obtained using the CFD-simulator); $\vec{\mathbf{q}}_{\text{meas\_GDS}}^{\text{const}} \in R^l$ is a given vector of measured mass flow rates at GDS outlets; $l$ is the number of GDSs; $t_{\text{flow\_rate}}^{\text{GDS}} = const$ is a given upper estimate of actual (nameplate) absolute error of flow meters installed at the inlet GDSs. The constraint in the form of a one-sided weak inequality in (50) formalizes the assumption that the probability of gas underdelivery by the supplier is small. Components $x_i$ of the vector of independent controlled variables here mean some boundary conditions of "Type I" specified in the simulations of steady-state fluid dynamics conditions using the CFD-simulator. As practice shows, problem (49, 50) can be solved successfully, if as components of the vector of independent variables one uses an integrated set of mass flow rates at outlet boundaries of associated CGPs $\left( x_i,\ i = \overline{1,\ k} \right)$ and pressures at outlet GDSs $\left( x_i,\ i = \overline{k+1,\ n},\ \ n = k + l \right)$, where $k$ is the number of associated CGPs.

Components $\left( a_i,\ b_i,\ i = \overline{1,\ k} \right)$ (see (50)) establish the ranges for controlled variables, the size of which is largely attributed to the degree of the seller's actual trust in a certain consumer. The following conditions should be necessarily observed:

$$a_i + t_{\text{flow\_rate}}^{\text{cons}} < \left[ q_{cons}^{const} \right]_i < b_i - t_{\text{flow\_rate}}^{\text{cons}}, \quad i = \overline{1,\ k}; \quad a_i + t_{\text{flow\_rate}}^{\text{cons}} < \left[ x_0 \right]_i < b_i - t_{\text{flow\_rate}}^{\text{cons}}, \quad i = \overline{1,\ k}; \tag{51}$$

$$\sum_{i=1}^{k} \left[ x_0 \right]_i = \sum_{i=1}^{k} \left\{ \left[ q_{\text{cons}}^{\text{const}} \right]_i + \left[ \Delta q_{\text{sell}}^{\text{const}} \right]_i \right\} = \sum_{j=1}^{l} \left[ q_{\text{meas\_GDS}}^{\text{const}} \right]_j, \tag{52}$$

where $\vec{\mathbf{q}}_{\text{cons}}^{\text{const}} \in R^k$ is a given vector of mass flow rates at outlet boundaries of associated CGPs; $t_{\text{flow\_rate}}^{\text{cons}} = const$ is a given upper estimate of the actual (nameplate) absolute error of flow meters installed at outlet boundaries of associated CGPs; $\vec{\mathbf{X}}_0 \in R^n$ is the starting point of the conditional optimization problem; $\Delta \vec{\mathbf{q}}_{\text{sell}}^{\text{const}} \in R^k$ is the increment vector for reported mass flow rates at outlet boundaries of associated CGPs, which is chosen by the gas seller depending on the degree of trust in a certain consumer. Fulfillment of conditions (51) is a guaranty for the consumers that the discrepancy analysis will necessarily account for their reported values of received gas volumes. Constraints (52) serve to implement quasi-steady-state operating conditions of the pipeline network of interest from the very starting point of the conditional optimization problem. The values of remaining components $\left( a_i,\ b_i,\ \ i = \overline{k+1,\ n} \right)$ are generally defined in accordance with conditions:

$$a_i + t^{\text{GDS}}_{\text{pressure}} < \left[x_0\right]_i < b_i - t^{\text{GDS}}_{\text{pressure}}, \quad i = \overline{k+1,\, n}; \quad \left[x_0\right]_i = \left[p^{\text{const}}_{\text{meas\_GDS}}\right]_{i-k}, \quad i = \overline{k+1,\, n}, \tag{53}$$

where $\vec{\mathbf{p}}^{\text{const}}_{\text{meas\_GDS}} \in R^l$ is a given vector of measured pressures in the GDS; $t^{\text{GDS}}_{\text{pressure}}$ is a given upper estimate of the actual (nameplate) absolute error of pressure gauges installed in the GDS. As a result of fulfillment of conditions (51) and (53), the starting point of optimization problem (49, 50) will be the inner point with respect to simple constraints on controlled variables, which by far extends the range of methods that can be used for conditional minimization.

Thus, based on (51–53):

$$\begin{aligned} a_i &< \left\{\min\left(\left[x_0\right]_i - t^{\text{cons}}_{\text{flow\_rate}};\ \left[q^{\text{const}}_{\text{cons}}\right]_i - t^{\text{cons}}_{\text{flow\_rate}}\right),\ i = \overline{1,\, k};\ \left[p^{\text{const}}_{\text{meas\_GDS}}\right]_{i-k} - t^{\text{GDS}}_{\text{pressure}},\ i = \overline{k+1,\, n}\right\}; \\ b_i &> \left\{\max\left(\left[x_0\right]_i + t^{\text{cons}}_{\text{flow\_rate}};\ \left[q^{\text{const}}_{\text{cons}}\right]_i + t^{\text{cons}}_{\text{flow\_rate}}\right),\ i = \overline{1,\, k};\ \left[p^{\text{const}}_{\text{meas\_GDS}}\right]_{i-k} + t^{\text{GDS}}_{\text{pressure}},\ i = \overline{k+1,\, n}\right\}. \end{aligned} \tag{54}$$

Problem (49–54) can take different forms depending on the type of the vector norm chosen in (49). For example, if we choose the cubic vector norm ($L$=0), we come to a discrete minimax problem with constraints in the form of one-sided weak inequalities and simple constraints on independent controlled variables:

$$\max_{1 \le i \le m} \left| \left[f_{\text{calc}}\left(\vec{\mathbf{X}}\right)\right]_i - \left[f^{\text{const}}_{\text{meas}}\right]_i \right| \to \min_{\vec{\mathbf{X}} \in \Omega \subset R^n}. \tag{55}$$

Solution to (55) provides so-called uniform agreement between calculated estimates of gas flow parameters and their measured values. Choosing the octahedron vector norm ($L$=1) transforms initial problem (49–54) into a general non-linear programming problem represented in the following way:

$$\begin{cases} \sum\limits_{i=1}^{m} \left| \left[f_{\text{calc}}\left(\vec{\mathbf{X}}\right)\right]_i - \left[f^{const}_{изм}\right]_i \right| \to \min, \\ \vec{\mathbf{X}} \in \Omega^* = \left\{ \vec{\mathbf{X}} \in R^n :\ \vec{\mathbf{a}} \le \vec{\mathbf{X}} \le \vec{\mathbf{b}};\ \left| \left[q^{\text{GDS}}_{\text{calc}}\left(\vec{\mathbf{X}}\right)\right]_j - \left[q^{\text{const}}_{\text{meas\_GDS}}\right]_j \right| - t^{\text{GDS}}_{\text{flow\_rate}} \le 0,\quad j = \overline{1,l} \right\}. \end{cases} \tag{56}$$

Choosing the Euclidean vector norm ($L$=2) in (49) results in the statement of a new conditional optimization problem, which is almost equivalent to (50-54, 56):

$$\sqrt{\sum_{i=1}^{m} \left( \left[f_{\text{calc}}\left(\vec{\mathbf{X}}\right)\right]_i - \left[f^{\text{const}}_{\text{meas}}\right]_i \right)^2} \to \min_{\vec{\mathbf{X}} \in \Omega^*}. \tag{57}$$

Solution of (50-54, 57) provides root-mean-square agreement between calculated estimates of gas flow parameters and their measured values. It should be stressed here that statement (50-55) is stricter than (50-54, 57).

Problems (50-55), (50-54, 56) and (50-54, 57) can be solved numerically using the method of modified Lagrange functions (Vasilyev, 2002), which is quite suitable for this purpose. Note that in practice the time of numerical solution of (50-54, 57) in most cases is much shorter than the time of numerical solution of problems (50–55) or (50-54, 56).

To choose a certain type of the target function in problem (49, 50), a series of numerical experiments were conducted and more than a hundred applied tasks were simulated. The

best (in terms of the accuracy/runtime ratio) results in simulating the identification problem (49, 50) were obtained using target function (57).

Based on the above considerations, in order to provide efficiency and improved accuracy of industrial applications, it is reasonable to propose the following algorithm for finding the identified gas flow in the GDN at the initial stage:

**Step 1.** Define the starting point $\vec{\mathbf{X}}_0 \in R^n$ in accordance with conditions (52) and (53). Define the vectors $\vec{\mathbf{a}}$ and $\vec{\mathbf{b}}$ in simple constraints according to (54).

**Step 2.** Solve optimization problem (50-54, 57). Results of its numerical solution become input data in searching for the conditional minimum at Step 4.

**Step 3.** Analyze correctness of solution results from Step 2. The correctness criterion in this case is the condition of necessary fulfillment of all constraints in problem (50-54, 57). If this criterion is satisfied, proceed to Step 4. If not, extend the variation range of independent variables with subsequent transition to Step 2, i.e. $\left(\left\{\vec{\mathbf{a}},\ \vec{\mathbf{b}}\right\} \Rightarrow \left\{\vec{\mathbf{a}}^*,\ \vec{\mathbf{b}}^*\right\}\right)$. Usually, the range extension algorithm used here is heuristic and bases on the experience gained in the course of actual simulations.

**Step 4.** Find numerical solution to problem (50–55) from the starting point, obtained at Step 2, by the method of modified Lagrange functions. Execution of Step 4 makes it possible to reduce or completely eliminate individual local peaks in discrepancy between calculated estimates and measured values, which may appear at Step 2.

**Step 5.** Analyze correctness of the results obtained at Step 4, i.e. check the necessary fulfillment of all constraints in problem (50–55). If the correctness criterion is not fulfilled, solution of Step 3 is assumed to be the target solution.

**Step 6.** The vector of controlled variables corresponding to the optimal solution at Step 5, is designated as $\vec{\mathbf{X}}_{\text{init}}$, with $\vec{\mathbf{X}}_{\text{init}} \in \Phi \subset R^n$. The found fluid dynamics conditions of GDN operation is taken as the **primary fluid dynamics mode.** Its calculated parameters have uniform (i.e. strictest) agreement with respective measured values.

At the final stage of identification, the primary fluid dynamics mode is corrected within the available measured information, in order to minimize possible discrepancies between calculated and reported estimates of gas volumes transmitted through each associated CGP in the given time interval. This stage is legal by nature, because given the limited amount of measured data the gas seller has no right to accuse the consumer a priori of deliberate misrepresentation of reported received gas volumes. This stage consists in the solution of the general nonlinear programming problem:

$$
\begin{cases}
\left\| \vec{\mathbf{q}}_{\text{calc}}^{\text{cons}}\left(\vec{\mathbf{X}}\right) - \vec{\mathbf{q}}_{\text{cons}}^{\text{const}} \right\|_2 \to \min, \\
\vec{\mathbf{X}} \in \Theta = \left\{ \vec{\mathbf{X}} \in R^n :\ a_i^{**} \le x_i \le b_i^{**},\quad i = \overline{1,\ k}; \right. \\
\qquad \left[ p_{\text{init\_GDS}}^{\text{const}} \right]_i - t_{\text{pressure}}^{\text{GDS}} \le x_i \le \left[ p_{\text{init\_GDS}}^{\text{const}} \right]_i + t_{\text{pressure}}^{\text{GDS}},\quad i = \overline{k+1,\ n}; \\
\qquad \left| \left[ f_{\text{calc}}^{\text{ident}}\left(\vec{\mathbf{X}}\right) \right]_s - \left[ f_{\text{init\_ident}}^{\text{const}} \right]_s \right| - t_{\text{pressure}}^{\text{ident}} \le 0,\quad s = \overline{1,\ h}; \\
\qquad \left. \left| \left[ q_{\text{calc}}^{\text{GDS}}\left(\vec{\mathbf{X}}\right) \right]_j - \left[ q_{\text{meas\_GDS}}^{\text{const}} \right]_j \right| - t_{\text{flow\_rate}}^{\text{GDS}} \le 0,\quad j = \overline{1,\ l} \right\},
\end{cases}
\tag{58}
$$

where $\vec{\mathbf{q}}_{\text{calc}}^{\text{cons}}\left(\vec{\mathbf{X}}\right)\subset\vec{\mathbf{X}}$, $\left[q_{\text{calc}}\left(x\right)\right]_i=x_i$, $i=\overline{1,k}$, is the vector function of calculated mass flow rates for outlet boundaries of associated CGPs in the $k$-dimensional Euclidean space $R^k$; $\vec{\mathbf{p}}_{\text{init\_GDS}}^{\text{const}}\in R^l$ is a given vector of GDS pressure corresponding to the primary fluid dynamics mode at $\vec{\mathbf{X}}_{\text{init}}\in R^n$; $\vec{\mathbf{f}}_{\text{calc}}^{\text{ident}}\left(\vec{\mathbf{X}}\right)$, $f_{\text{calc}}^{\text{ident}}:R^n\to R^h$, is the vector function of calculated estimates of controlled variables at inner identification points in the $h$-dimensional Euclidean space $R^h$ (these calculated estimates are obtained using the CFD-simulator); $\vec{\mathbf{f}}_{\text{init\_ident}}^{\text{const}}\in R^h$ is a given vector of controlled variables at inner identification points corresponding to the primary fluid dynamics mode at $\vec{\mathbf{X}}_{\text{init}}\in R^n$; $h$ is a given number of inner identification points; $t_{\text{pressure}}^{\text{ident}}=const$ is a given upper estimate of the actual (nameplate) absolute error of pressure gauges at inner identification points.

The first group of simple constraints on the controlled variables in (58) is partly redundant. It assures that numerical search for solutions in industrial applications is always performed in the domain of practically significant results. The second group of simple constraints and the second group of one-sided weak inequality constraints in problem (58) account for the imperfectness of corresponding existing instruments in favor of consumers. The first group of one-sided weak inequality constraints in (58) formalizes the demand for the closest possible uniform agreement between calculated estimates and reported volumes of gas received by each consumer.

Problem (58) can be solved using modified Lagrange functions (Vasilyev, 2002). As a starting point here we use $\vec{\mathbf{X}}_{\text{init}}\in R^n$. The target result of the simulation should necessarily be correct, i.e. it should fulfill all simple constraints and inequality constraints of problem (58). Otherwise, the primary fluid dynamics mode is taken as a solution to (58).

The simulation outcome of optimization problem (58) is the final solution to the problem of finding the identification gas flow in the GDN. The target identified gas flow is completely defined by the vector $\vec{\mathbf{X}}_{\text{ident}}\in\Theta\subset R^{n+1}$, corresponding to the optimal solution of problem (58), and is characterized by the fulfillment of the following conditions: (1) calculated gas flow parameters at each identification point should be as close as possible to corresponding field measurement data; (2) calculated estimates of gas volumes supplied to the GDN in a given time interval should correspond to the supplier-reported values within actual (nameplate) absolute errors of the flow meters installed in the GDS; (3) calculated estimates of gas volumes received by each consumer in the given time interval should be as uniformly close as possible to the values reported by the consumers.

## 7. Conclusion

The methods and approaches described in this chapter have been developed during the past fifteen years. These methods demonstrated their efficiency as applied to simulations for Gazprom, Russia, and SPP, a.s., Slovakia (Seleznev et al., 2005). These methods apply to pipeline systems for transportation of liquid and gas-liquid products. They are rather efficient in analysis and prevention of accidents (Aleshin & Seleznev, 2004).

The approach presented in this article for high-accuracy numerical analysis of operating parameters of industrial pipeline networks using CFD-simulators is based on adaptation of the full system of equations of fluid dynamics to conditions of transient, non-isothermal

processes of the flow of gas mixtures in actual GTNs. The adaptation applies the rule of minimization of the number and depth of accepted simplifications and assumptions. The high accuracy of analysis of industrial pipeline networks operating parameters is understood here as the most reliable description and prediction of actual processes in a GTN, which are achievable due to the present level of development of mathematical modeling and technical monitoring methods and available computer hardware. Development and operation of CFD-simulators in solving industrial problems of improving safety, efficiency and environmental soundness of pipeline network operation can be regarded as one of the promising trends of industrial application of the state-of-the-art computational mechanics methods.

In the past few years, the proposed approach to the numerical monitoring of natural gas delivery through gas distribution networks has proved to be well-performing in industrial applications for discrepancy analysis of natural gas deliveries to large and medium-size consumers. This approach can be implemented even on standard personal computers.

Future development of the methods discussed will be largely focused on their applications in high accuracy analysis and control of multi-phase fluid transportation.

## 8. References


Aleshin, V. V. & Seleznev, V. E. (2004). Computation technology for safety and risk assessment of gas pipeline systems, *Proceedings of the Asian International Workshop on Advanced Reliability Modeling (AIWARM'2004)*, pp. 443–450, ISBN 981-238-871-0, Hiroshima, Japan, August 2004, World Scientific Publishing Co. Pte. Ltd., London.

Dennis, J. E. Jr. & Schnabel, R. B. (1988). *Numerical Methods for Unconstrained Optimization and Ninlinear Equations,* Prentice-Hall Inc., ISBN 0-13-627216-9, New Jersy.

Fletcher, C. A. J. (1988). *Computational Techniques for Fluid Dynamics. Fundamental and General Techniques,* Springer-Verlag, ISBN 3-540-18151-2, Berlin.

Kiselev, V. V.; Seleznev, V. E. & Zelenskaya, O. I. (2005). Failure forecast in engineering systems by searching for the inner points of system of algebraic equalities and inequalities, *Proceedings of the European Safety and Reliability Conference (ESREL 2005)*, Vol. 2, pp. 1773–1776, ISBN 0-415-38343-9, Tri City (Gdyna – Sopot – Gdansk), Poland, June 2005, Taylor & Francis Group, London.

Seleznev, V. E.; Aleshin, V. V. & Klishin, G. S. & Il'kaev, R. I. (2005). *Numerical Analysis of Gas Pipelines: Theory, Computer Simulation, and Applications,* KomKniga, ISBN 5-484-00352-0, Moscow.

Seleznev, V. (2007). Numerical simulation of a gas pipeline network using computational fluid dynamics simulators. *Journal of Zhejiang University SCIENCE A*, Vol. 8, No. 5, pp.755–765, ISSN 1673-565X (Print); ISSN 1862-1775 (Online)

Seleznev, V. & Pryalov, S. (2007). Numerical forecasting surge in a piping of compressor shops of gas pipeline network. Journal of Zhejiang University SCIENCE A, Vol. 8, No. 11, pp.1770–1783, ISSN 1673-565X (Print); ISSN 1862-1775 (Online)

Seleznev, V. E.; Aleshin, V. V. & Pryalov, S. N. (2007). *Mathematical modelling of pipeline networks and channel systems: methods, algorithms, and models,* MAX Press, ISBN 978-5-317-02011-8, Moscow. *(In Russian)*

Tikhonov, A. N. & Samarsky, A. A. (1999). Equations of Mathematical Physics, Moscow State University Publisher, ISBN 5-211-04138-0, Moscow. *(In Russian)*

Vasilyev, F. P (2002). *Methods for Optimization*, Factorial Press, ISBN 5-88688-05-9, Moscow. *(In Russian)*

# 16

# A Preconditioned Arbitrary Mach Number Scheme Applied to Rotating Machinery

Chunhua Sheng
*The University of Toledo*
*U.S.A.*

## 1. Introduction

It is well known that the compressible flow equations face difficulties at low Mach numbers due to the large ratio of the acoustic and convective time scales, which leads to an ill-conditioned system when solving low-speed or incompressible flows. The time-dependent system of the Euler and Navier-Stokes equations exhibits stiffness that is strongly dependent on the Mach number and the Reynolds number. In this regard, Briley et al. (Briley et al., 1983) first introduced the preconditioning method using a simple constant preconditioning matrix added to a non-dimensional form of the isoenergetic equations. This generally improved convergence for a test case with reference Mach number Mr = 0.05 using the ADI factorization scheme in primitive variables. However, when applying this preconditioning to rotating flows in either fixed or rotating frame formulation, Sheng, et al. (Sheng & Wang, 2006; Wang & Sheng, 2005) observed the instability of the scheme due to the large variation of rotating speeds across the computational domain. Furthermore, it was found that the convergence of the preconditioned equations is sensitive to the selection of the reference Mach number, especially in rotating flows with a wide range of radial speeds and physical time scales. It was later proved using the Fourier footprint analysis (Wang & Sheng, 2005) that the eigensystem of the compressible governing equations can be significantly affected by both free stream and rotating speeds in rotating flows. A modified preconditioning scheme was thus proposed (Sheng & Wang, 2006; Wang & Sheng, 2005), in which both the global reference Mach number and the rotating Mach number are considered in the formulation of the preconditioning matrix. In general, this modified preconditioning scheme has improved the convergence and accuracy of compressible flows in subsonic, transonic and supersonic Mach number regimes. In this study, the modified preconditioning is further investigated and validated for predicting incompressible viscous flows in rotating machinery, such as a marine propeller P5168.

One of the most important characters for marine propellers is the cavitation observed in high speed flows, which is of vital importance because of the damage of metal surfaces and degradation of performance of lifting surfaces. It is also a source of high-frequency noise in connection with acoustic detection of ships and submarines. Cavitation would take place when the local pressure drops to the vapor pressure. Therefore, accurate prediction of the velocity and pressure field is essential for understanding the process of cavitation inception and improving the hydrodynamic performance of the marine propeller. Since the condition for cavitation inception is related to the tip-vortex location, strength, convection, cavitation

position on the propeller surface, and the minimum pressure location. The present study will investigate these important flow characteristics using modified preconditioning scheme, and compare the computed hydrodynamics characters of P5168 with the LDV measurement (Chesnakas & Jessup, 1998).

## 2. Preconditioned method

### 2.1 Governing equations

The governing equations for solving the hydrodynamic flow in the present study are based on an unsteady three-dimensional Reynolds-averaged Navier-Stokes equations, coupled with the one-equation turbulent model of Spalart and Allmaras (Spalart & Allmaras, 1991). The unsteady compressible equations are cast in a rotating Cartesian coordinates with a rotational speed of Ω, and are written in terms of absolute velocities. It represents a system of conservation laws for a control volume that relates the rate of change of a vector of node-based average state variables to the flux through the volume surface. The following reference quantities are chosen to normalize the flow variables and equations: density, $\rho_r$; velocity, $U_r$; temperature, $T_r$; pressure, $\rho_r U_r^2$; length, $L_r$; time, $L_r/U_r$; energy and enthalpy, $C_p T_r$. The non-dimensional conservative form of the governing equations can be written in integral form as

$$\frac{d}{dt}\int_\Omega Q dV + \oint_{\partial\Omega} F(Q)\cdot\hat{n} dA = \int_\Omega S(Q) dV \tag{1}$$

The above equation can also be written in terms of primitive variables by introducing a transformation matrix $M = \partial Q / \partial q$, where $Q=(\rho, \rho u, \rho v, \rho w, \rho e_t)$, and $q = (\rho, u, v, w, p)$. The governing equations in primitive variables are

$$M\frac{d}{dt}\int_\Omega q dV + \oint_{\partial\Omega} F(q)\cdot\hat{n} dA = \int_\Omega S(q) dV \tag{2}$$

The projected normal flux vector to the face of a control volume is given as

$$F\cdot\hat{n} = \begin{bmatrix} \rho\Theta \\ \rho u\Theta + n_x p - (n_x\tau_{xx} + n_y\tau_{xy} + n_z\tau_{xz}) \\ \rho v\Theta + n_y p - (n_x\tau_{yx} + n_y\tau_{yy} + n_z\tau_{yz}) \\ \rho w\Theta + n_z p - (n_x\tau_{zx} + n_y\tau_{zy} + n_z\tau_{zz}) \\ \rho h_t\Theta - n_t E_c p - (\gamma-1)M_r^2(\vec{u}\cdot(\vec{\tilde{\tau}}\cdot\hat{n})) + Q_n \end{bmatrix} \tag{3}$$

where $E_c = (\gamma-1)M_r 2$ is an Eckert number. Θ is the relative velocity in the normal direction of the control surface in a rotating frame.Let Ω×r be the speed of the control volume at position r, Θ is given as

$$\Theta = \vec{u}\cdot\hat{n} - \times r\cdot\hat{n} = n_x u + n_y v + n_z w + n_t \tag{4}$$

The viscous stresses in the flux vector are given as

$$\tau_{xx} = \mu\frac{2}{3}\left(2\frac{\partial u}{\partial x} - \frac{\partial v}{\partial y} - \frac{\partial w}{\partial z}\right) \qquad \tau_{xy} = \tau_{yx} = \mu\frac{2}{3}\left(\frac{\partial u}{\partial y} + \frac{\partial v}{\partial x}\right)$$

$$\tau_{yy} = \mu\frac{2}{3}\left(2\frac{\partial v}{\partial y} - \frac{\partial u}{\partial x} - \frac{\partial w}{\partial z}\right) \qquad \tau_{xz} = \tau_{zx} = \mu\frac{2}{3}\left(\frac{\partial u}{\partial z} + \frac{\partial w}{\partial x}\right)$$

$$\tau_{zz} = \mu\frac{2}{3}\left(2\frac{\partial w}{\partial z} - \frac{\partial u}{\partial x} - \frac{\partial v}{\partial y}\right) \qquad \tau_{yz} = \tau_{zy} = \mu\frac{2}{3}\left(\frac{\partial v}{\partial z} + \frac{\partial w}{\partial y}\right)$$

and the heat flux term is

$$Q_n = -\frac{\mu}{\mathrm{Re}\,P_r}\left(\hat{n}\cdot\nabla T\right) \tag{5}$$

where $\mu$ is the viscosity, $Pr$ is the Prandt number, and Re is the Reynolds number based on the reference values.

Since the governing equations are cast in the rotating coordinate system, body forces (Coriolis and centrifugal forces) are added in the momentum equations as a source term due to the non-inertial reference frame, which can be expressed as

$$S = \begin{bmatrix} 0 \\ \rho w\Omega_y - \rho v\Omega_z \\ \rho u\Omega_z - \rho w\Omega_x \\ \rho v\Omega_x - \rho u\Omega_y \\ 0 \end{bmatrix} \tag{6}$$

The formulation of the governing equations in a rotating frame provides advantages for faster convergence in unsteady flows and a more stable solution without the unsteady effects of the grid motion. Furthermore, the above formulation can be easily restored into the ones in the fixed frame by setting the rotational speed Ω to zero in Eq. (6), making the body force source term disappear from the governing equations. All other relations, including the equation of state, remain the same under the current formulation. Using the absolute velocity components to represent the formulation in rotating frame offers great flexibility for solving the governing equations in both unsteady mode (fixed frame) and steady mode (rotating frame).

### 2.2 Preconditioned equations

In order to solve flows from essentially incompressible regime to supersonic Mach number, a preconditioning matrix $\Gamma_q^{-1}$ is introduced into the time derivative terms of the compressible governing equations, which can be expressed as

$$M\Gamma_q^{-1}\frac{\partial}{\partial t}\int_\Omega q dV + \oint_{\partial\Omega} F\cdot\hat{n}dA = \int_\Omega S dV \tag{7}$$

where $\Gamma_q^{-1}$ is a constant diagonal matrix that only depends on the reference Mach number $M_r$

$$\Gamma_q^{-1} = diag\left[1,\ \ 1,\ \ 1,\ \ 1,\ \ 1/\beta(M_r)\right] \tag{8}$$

The selection of preconditioning parameter $\beta(M_r)$ will be discussed in the following section. The finite–volume scheme needs the approximation of both inviscid and viscous fluxes on the face of a control volume. In order to develop characteristic–based flux formulation, the eigensystem of the preconditioned equations needs to be derived.
The preconditioned Eq. (7) can also be expressed as

$$\frac{\partial q}{\partial t} + a_\Gamma \frac{\partial q}{\partial x} = \Gamma_q M^{-1} S \tag{9}$$

where $a_\Gamma = \Gamma_q a = \Gamma_q M^{-1} A M$ is the system matrix for preconditioned equations, and $A$ is the flux Jacobian matrix with respect to conservative variables $Q$. The system matrix for the three–dimensional Euler equations is

$$a_\Gamma = \begin{bmatrix} \Theta & \rho n_x & \rho n_y & \rho n_z & 0 \\ 0 & \Theta & 0 & 0 & \frac{n_x}{\rho} \\ 0 & 0 & \Theta & 0 & \frac{n_y}{\rho} \\ 0 & 0 & 0 & \Theta & \frac{n_z}{\rho} \\ 0 & \beta\rho c^2 n_x & \beta\rho c^2 n_y & \beta\rho c^2 n_z & \beta\Theta \end{bmatrix} \tag{10}$$

The eigenvalues of $a_\Gamma$ are

$$\lambda^{(1)} = \lambda^{(2)} = \lambda^{(3)} = \Theta,\ \lambda^{(4)} = \Theta\beta^+ + \sigma,\ \lambda^{(5)} = \Theta\beta^+ - \sigma \tag{11}$$

where $\sigma = \sqrt{(\Theta\beta^-)^2 + \beta c^2}$, $\beta^\pm = (1 \pm \beta)/2$. A nonsingular set of right eigenvectors for $a_\Gamma$ is given by

$$R = \begin{bmatrix} n_x & n_y & n_z & \frac{\rho(\Theta\beta^- + \sigma)}{\beta c^2} & -\frac{\rho(\Theta\beta^- - \sigma)}{\beta c^2} \\ 0 & -n_z & n_y & n_x & -n_x \\ n_z & 0 & -n_x & n_y & -n_y \\ -n_y & n_x & 0 & n_z & -n_z \\ 0 & 0 & 0 & -\rho(\Theta\beta^- - \sigma) & \rho(\Theta\beta^- + \sigma) \end{bmatrix} \tag{12}$$

where $\Psi = \rho\Theta(1-\beta)/\beta c^2$, and $c^\pm = \dfrac{\Theta\beta^\pm \pm \sigma}{2\sigma}$

### 2.3 Preconditioning parameter

From the above equations, it is seen that the eigenvalues and eginevectors of the system matrix have been modified due to the introduction of a preconditioned matrix. If the preconditioning parameter $\beta$ is selected as one, no preconditioning is applied to the governing equations, and thus the original set of eigenvalues for compressible flowsis restored.

Briley, et al. (Briley et al., 2003) suggested that a global constant preconditioning parameter is evaluated based on the reference Mach number as:

$$\beta = \min\left(1, M_r^2\right) \tag{13}$$

where the reference Mach number should represent the global flow property for the problem being solved. For a steady and non–rotating flow, the above choice provided well–behaved eigenvalues in all characteristic waves, and thus improved the convergence and accuracy for solutions up to nearly incompressible Mach number (Briley et al., 2003). However, it was found that such a preconditioning may cause instability for low Mach number rotating flows, such as the case of a marine propeller P5168 presented here. In rotating machinery, the flow filed is complicated with secondary swirling flow structures due to the high-speed rotating elements. It is thus rational to consider the speed of rotating element in determining the preconditioning parameter. In this work the modified preconditioning parameter is employed for flows aimed at unsteady flows in rotating machinery:

$$\beta = \min\left(1, M_r^2 + \alpha M_\Omega^2\right) \tag{14}$$

where $M_\Omega$ is evaluated based on the rotational reference speed, and $\alpha$ is a scalar factor to tune the rotational Mach number in the preconditioned scheme. Numerical tests conducted in the previous work (Sheng & Wang, 2006; Wang & Sheng, 2005) indicated that the value of $\alpha$ should be in the range of 0.5~1.0 in order to achieve the optimal convergence and accuracy in preconditioned solutions. In the following, an analysis of the Fourier footprint for the eigensystem of the two-dimensional Euler equations provides evidences for the modification of the preconditioning parameter in low Mach number rotating flows.

### 2.4 Fourier footprint analysis

Fourier analysis is a useful tool for inspecting analytical and numerical solutions of the partial differential equations of mathematical physics. It is used to investigate the accuracy related to the approximation of hyperbolic equations and characteristics of all frequency modes of the discretized equation system (Vichnevetsky & Bowles, 2005). Euler equation is a pure hyperbolic system in which Fourier analysis finds its full power. The Euler Fourier footprint reveals the characters of error propagation and damping of all modes produced by the numerical discretization. The Fourier footprint of a given spatial discretization scheme is obtained by inserting the discrete Fourier transforms in the semi-discrete equation of the finite-volume governing equations. Detailed analytical formulation of the eigenvalues of Fourier footprint of the preconditioned Euler equation can be found in the reference (Wang, 2005).

In terms of Von Neumann stability analysis (O'Brien et al., 1951), the convective part of numerical solutions of hyperbolic equations corresponds to the extent of the Fourier footprints along the imaginary axis, and the dissipation component corresponds to the extent of the negative real axis. In Fig. 1 (a) for a low Mach number non-rotating flow at Mr = 0.01, there exists large disparity among phase velocities of convective waves (in red and black colors) and acoustic waves (in blue and green colors), which is visually indicated by the extension of the imaginary part of Fourier footprints. The group velocity, which describes the propagation of transient errors, is approximately equal to the amplitude of the

sinusoid that defines the imaginary component in the plots. Thus, the damping and propagation of transient errors are much less effective for the convective waves, especially for low frequency modes. For this non-rotating flow, the preconditioned system with $\beta = M_r^2$ equalized the real parts of the complex eigenvalues among all wave families, and rescaled the real and imaginary components to the same order of magnitude as indicated in Fig. 1 (b). Figure 2 presents the Euler Fourier footprint for the same low Mach number flow, but with a rotating Mach number $M_\Omega = 0.1$. Without preconditioning, large disparity still remains among the convective and acoustic wave speeds in the same order of non-rotating flow, see Fig.2 (a). When the original preconditioning parameter is used ( $\beta = M_r^2$ ) for Mach number relative to a rotating frame of $M_\Omega = 0.1$, as shown in Fig. 2(b), the real part extensions of Fourier footprints in all wave families are properly rescaled, and the damping effects of the high frequency error modes are well balanced between acoustic and convective waves. However, there are more footprints collapsed to the origin so that neither damping nor propagation of those low frequency modes is possible, and the system will not converge.

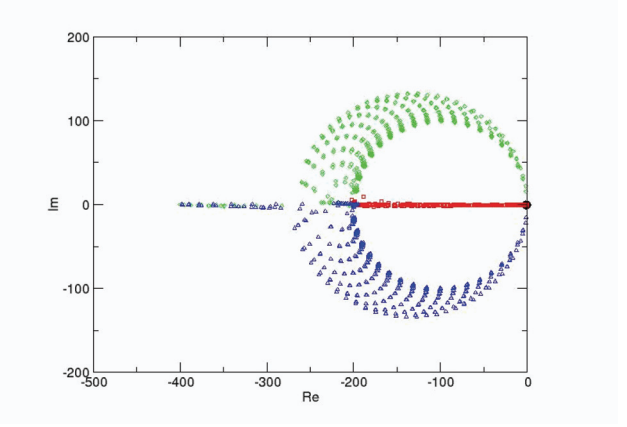


(a) $\beta$=1

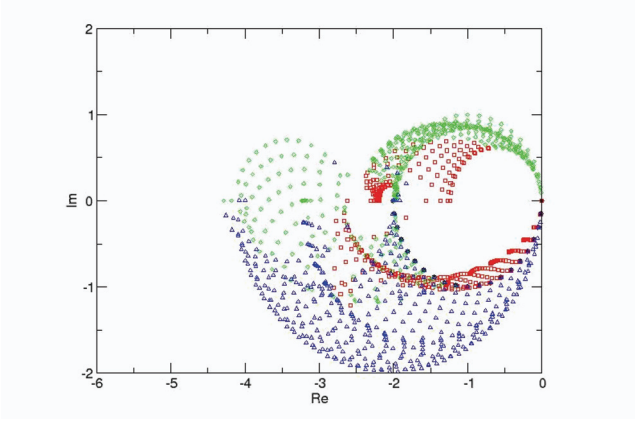


(b) $\beta = M_r^2$

Fig. 1. Fourier Footprint of 1st Order Euler Operator for Non-Rotating Flow at $M_r = 0.01$ .

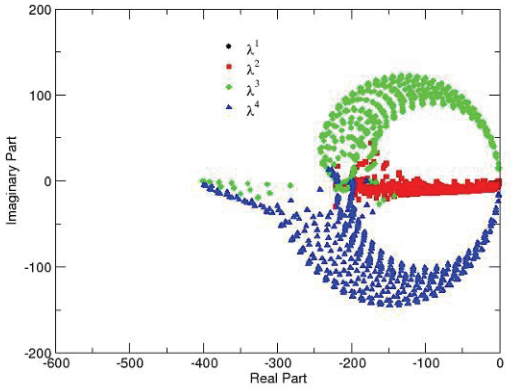


(a) $\beta = 1$

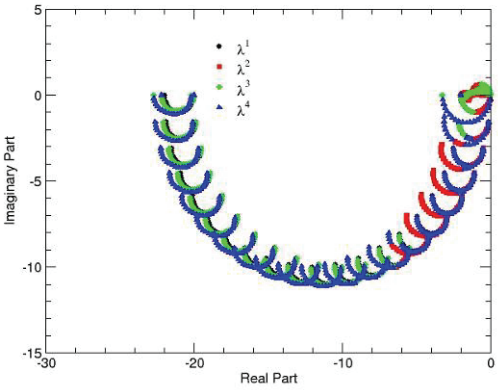


(b) $\beta = M^2_r$

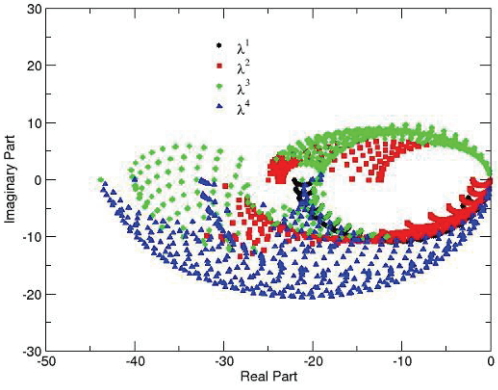


(c) $\beta = M^2_r + M^2_\Omega$

Fig. 2. Fourier Footprint of 1st Order Euler Operator for Rotating Flow at $M_r$=0.01, $M_\Omega$=0.1

This may explain the reason why the original preconditioning showed instability for low Mach number rotating flows. Using a modified a modified preconditioning parameter as $\beta$ $M_r^2 + M_\Omega^2$ proposed here, the extensions along the negative real axis for all wave modes are clustered to the same order of magnitude, as indicated in Fig. 2(c). In addition, the imaginary parts of the complex eigenvalues are mostly away from the negative real axis. The propagation properties are thus maintained at the ordinary levels so that the low frequency error modes can rapidly propagate out of the computational domain. The convergence of the Euler system is thus improved.

## 3. Discretization scheme

The preconditioned governing equations are discretized using a finite volume formulation. This is done by dividing the computational domain into a finite number of elements, from which control volumes are formed that surround each vertex in the mesh. The flow variables are stored at the vertices of the element. The preconditioned governing Eq. (7) or (9) is then numerically integrated over the closed boundaries of control volumes surrounding each node, and the preconditioning matrix $\Gamma_q^{-1}$ is applied to the convective (inviscid) term only through modifying the system matrix. The diffusive (viscous) term of the governing equations remains unchanged. The discretized form of the Navier-Stoles governing equations over a control volume can be written as:

$$\mathrm{M}\Gamma_q^{-1}\frac{\Delta q_i}{\Delta t}\Delta V_i + \sum_{j=1}^{nj}\left(\left(\hat{F}\cdot\vec{n}\right)_j \Delta A_j\right) = S_i \Delta V_i \tag{15}$$

where $\hat{F}$ is the numerical flux vector evaluated on the face of the control volume. The subscript i denotes the vertex, and j=(1,… nj) denotes the jth surface of the control volume V surrounding the vertex i .

### 3.1 Convective flux evaluation

The convective numerical flux of preconditioned governing equations is calculated using in a formula similar to Roe's flux, as proposed by Briley, et al. (Briley et al., 2003). Consider the surface j of a control volume whose left and right states are denoted by L and R, the numerical flux projected onto the surface j can be written as:

$$\hat{F}\cdot\vec{n} = \frac{1}{2}\left(F(q_L)+F(q_R)\right) - \frac{1}{2}\hat{M}\Gamma_q^{-1}\left|\hat{a}_\Gamma\right|\left(q_R - q_L\right) \tag{16}$$

where $F(q_L)$ and $F(q_R)$ are the convective fluxes evaluated at the left and right state of the surface. $|\hat{a}_\Gamma|$ is the preconditioned system matrix with positive eigenvalues. The system matrix is evaluated using the following averaged primitive variables $\hat{q}$ on the surface of a control volume:

$$\hat{q} = \frac{1}{2}\left(q_L + q_R\right) \tag{17}$$

Since the eigensystem and the flux are evaluated using the above averaged variables instead of Roe variables, the current approach is considered to be an extension of the Roe flux approximation.

In the above Eq. (16) quantities $q_L$ and $q_R$ are the values of the primitive variables on the left and right side of the face of the control volume. For a first-order accurate differencing, quantities $q_L$ and $q_R$ are set equal to the value at the vertices lying on either side of the face. For the second-order scheme, these face values (*j*) are computed with a Taylor series expansion about the central node (*i*) of the control volume

$$q_j = q_i + \nabla q_i \cdot \Delta r \tag{18}$$

where r is the vector that extends from the central node to the midpoint of each edge, and $\nabla q$ is the first derivatives of the primitive variables at node and is evaluated with an un-weighted least-squares procedure (Anderson et al., 1995).

### 3.2 Diffusive flux evaluation

Since the local state can be found from the reconstructed solutions at the vertex of each edge, the essence of computing the viscous fluxes is finding the gradients of the velocity vector and the temperature at the midpoints of the interface. A directional derivative approach for viscous gradients has been developed by Hyams (Hyams, 2002). In the present work, a normal derivatibbe approach is presented.

Introducing two unit tangential vectors $\hat{m}$ , $\hat{l}$ that are orthogonal to the unit normal vector $\hat{n}$ on the surface of a control volume

$$\hat{m} = \left( \frac{n_y - n_z}{n_m}, \frac{n_z - n_x}{n_m}, \frac{n_x - n_y}{n_m} \right)^T \tag{19}$$

$$\hat{l} = \left( \frac{n_y n_s - 1}{n_m}, \frac{n_y n_s - 1}{n_m}, \frac{n_z n_s - 1}{n_m} \right)^T \tag{20}$$

Where

$$n_m = \sqrt{(n_y - n_z)^2 + (n_z - n_x)^2 + (n_x - n_y)^2} \tag{21}$$

$$n_s = n_x + n_y + n_z$$

It is easy to verify that unit vectors are orthogonal to each other. The components of any gradient can be expressed in terms of derivatives in $\hat{m}$ , $\hat{l}$ , $\hat{n}$ directions.

$$\begin{aligned} \frac{\partial \phi}{\partial x} &= \frac{\partial \phi}{\partial n} n_x + \frac{\partial \phi}{\partial m} m_x + \frac{\partial \phi}{\partial l} l_x \\ \frac{\partial \phi}{\partial y} &= \frac{\partial \phi}{\partial n} n_y + \frac{\partial \phi}{\partial m} m_y + \frac{\partial \phi}{\partial l} l_y \\ \frac{\partial \phi}{\partial z} &= \frac{\partial \phi}{\partial n} n_z + \frac{\partial \phi}{\partial m} m_z + \frac{\partial \phi}{\partial l} l_z \end{aligned} \tag{22}$$

The derivatives in the normal direction $\hat{n}$ can be approximated by

$$\frac{\partial \phi}{\partial n} \approx \frac{\phi_2 - \phi_1}{ds} \tag{23}$$

where $\phi_1$ and $\phi_2$ are the values of the interest at two vertices of an edge, and ds is the length of an edge. It is seen that this formula guaranties positivity of the operator, and second-order accuracy can be achieved if the direction of the edge is in concurrence with the normal direction of the face. The tangential derivatives are evaluated by projecting the averaging value of the two gradients at the nodes of an edge in $\hat{m}$, $\hat{l}$ directions, respectively,

$$\frac{\partial \phi}{\partial m} \approx \frac{1}{2}\left(\nabla \phi_1 + \nabla \phi_2\right) \cdot \hat{m} \tag{24}$$

$$\frac{\partial \phi}{\partial l} \approx \frac{1}{2}\left(\nabla \phi_1 + \nabla \phi_2\right) \cdot \hat{l} \tag{25}$$

where $\nabla \phi_1$ and $\nabla \phi_2$ are the gradients evaluated at two nodes of the edge using a weighted least square procedure (Anderson, et al., 1995). The key point here is to make sure that these tangential derivatives are positive as well. Because a positive scheme satisfies the local maximum principle such that the solution is bounded by its surrounding neighboring vertices, a limiter is incorporated into the gradients in Eq. (22) to ensure the positivity of the tangential derivatives. A positive scheme for viscous discretization is thus achieved.

### 3.3 Temporal discretization

The temporal discretization is considered with an implicit Euler method for the system of governing equations. A general expression is available for the temporal discretization, which is given as:

$$\mathrm{M}\Gamma_q^{-1} \frac{\Delta q_i^n - \dfrac{\theta}{1+\theta}\Delta q_i^{n-1}}{\Delta t} + \frac{1}{\Delta V_i} \sum_{j \in N(0)} (\hat{F} \cdot \vec{n})_j^{n+1} \Delta A_j = S_i^{n+1} \tag{26}$$

where $\Delta q_i^n = q_i^{n+1} - q_i^n$, $\Delta q_i^{n-1} = q_i^n - q_i^{n-1}$. $\Delta t$ is the time step increment between steps n and n+1, and $\Delta V$ is the control volume. $\hat{F}$ denotes both inviscid and viscous fluxes. Subscript i and j denote the indices of the central node and the dual faces that compose of the control volume. A first order accuracy time Euler implicit scheme is given by the choice $\theta = 0$. Correspondingly, a second order time accurate Euler implicit scheme is given by $\theta = 1$.

### 3.4 Newton's method

The above nonlinear system of Eq. (26) is solved by Newton's method, which yields a linear system of equations at each time step. The use of Newton's method allows relatively large time step to be used in numerical computations, a considerable savings compared to the explicit method, in particular fro the unsteady time-accurate problems. Denote

$$\mathrm{N}\left(q_i^{n+1}\right) = \mathrm{M}\Gamma_q^{-1} \frac{\Delta q_i^n - \dfrac{\theta}{1+\theta}\Delta q_i^{n-1}}{\Delta t} + \frac{1}{\Delta V_i} \sum_{j \in N(0)} (\hat{F} \cdot \vec{n})_j^{n+1} \Delta A_j - S_i^{n+1} = 0 \tag{27}$$

The Newton's method solves the following equation:

$$\mathrm{N}'\left(q_i^{n+1,m}\right)\left(q_i^{n+1,m+1}-q_i^{n+1,m}\right)=-\mathrm{N}\left(q_i^{n+1,m}\right) \tag{28}$$

where m = 1,2,3 ... are the Newton steps, with $q_i^{n+1,0}=q_i^n$. $\mathrm{N}'\left(q_i^{n+1,m}\right)$ is the Jacobian matrix of Eq. (27), that is

$$\mathrm{N}'\left(q_i^{n+1}\right)=\mathrm{M}\Gamma_q^{-1}\frac{I}{\Delta t}+\frac{1}{\Delta V_i}\sum_{j\in N(0)}\frac{\partial(\hat{F}\cdot\vec{n})_j^{n+1}}{\partial q_i^{n+1}}\Delta A_j-\frac{\partial S_i^{n+1}}{\partial q_i^{n+1}} \tag{29}$$

In the above Eq. (29), the first term on the right hand side is the contribution from the unsteady time derivative of q, the second term is the contribution from the steady state residual (both inviscid and viscous) of the governing equations, and the third comes from the source term in the rotating reference frame. The flux Jacobian of the steady state residual can be evaluated by an approximate method. Consider the matrix $\hat{M}\Gamma_q^{-1}\left|\hat{a}_\Gamma\right|$ in Eq. (16) as a local constant, the approximate flux Jacobian for the inviscid flux can be written as

$$\sum_{j\in N(0)}\frac{\partial(\hat{F}\cdot\vec{n})_j^{n+1}}{\partial q^{n+1}}\Delta A_j=\sum_{j\in N(0)}\frac{\partial(\hat{F}\cdot\vec{n})_j^{n+1}}{\partial q_L^{n+1}}\Delta A_j+\sum_{j\in N(0)}\frac{\partial(\hat{F}\cdot\vec{n})_j^{n+1}}{\partial q_R^{n+1}}\Delta A_j \tag{30}$$

$$\frac{\partial(\hat{F}\cdot\vec{n})_j^{n+1}}{\partial q_L^{n+1}}=\frac{1}{2}\left(\frac{\partial(F(q_L))^{n+1}}{\partial q_L^{n+1}}+\hat{M}\Gamma_q^{-1}\left|\hat{a}_\Gamma\right|\right)$$

$$\frac{\partial(\hat{F}\cdot\vec{n})_j^{n+1}}{\partial q_R^{n+1}}=\frac{1}{2}\left(\frac{\partial(F(q_R))^{n+1}}{\partial q_R^{n+1}}-\hat{M}\Gamma_q^{-1}\left|\hat{a}_\Gamma\right|\right)$$

A similar method is used to evaluate the viscous flux Jacobian by taking the derivatives of discretized viscous flux formulation.

### 3.5 Gauss-Seidel relaxation

The nonlinear system of equations is linearized by Newton's method, which results in a sparse system of equations at each time. The solution of the sparse system of equations is obtained by a relaxation scheme in which $\Delta q^{n+1,m}$ is obtained through a sequence of iterations, $\{\Delta q^{n+1,m}\}^i$, which converge to $\Delta q^{n+1,m}$. There are several variations of classic relaxation procedures that have been used in the past for solving this linear system of equations (Coirier, 1994; Anderson, 1992; Batina, 1990). In this work, a symmetric implicit Gauss–Seidel procedure as described in (Batina, 1990) is used. To clarify the scheme, the system matrix is first written as a linear combination of matrices representing the diagonal, upper triangular, and lower triangular parts at each time step

$$[A]=[D+U+L] \tag{31}$$

where

$$[\mathrm{D}]=\mathrm{M}\Gamma_q^{-1}\frac{I}{\Delta t}+\frac{1}{\Delta V}\sum_{j\in N(0)}\frac{\partial\hat{F}_j^{n+1}}{\partial q^{n+1}}\Delta A_j-\frac{\partial S}{\partial q^{n+1}}$$

$$[\mathrm{U}]=\frac{1}{\Delta V}\sum_{j\in N_U(0)}\frac{\partial \hat{F}_j^{n+1}}{\partial q^{n+1}}\Delta A_j$$

$$[\mathrm{L}]=\frac{1}{\Delta V}\sum_{j\in N_L(0)}\frac{\partial \hat{F}_j^{n+1}}{\partial q^{n+1}}\Delta A_j$$

Let $\{R^{n+1}\}$ be the vector of unsteady residuals, and $\{\Delta q^{n+1}\}$ represents the change in the dependent variables, the symmetric Gauss–Seidel relaxation can be written as the following two–step process:

$$[L+D]\left\{\Delta q^{n+1,m}\right\}^{i+1/2}+[U]\left\{\Delta q^{n+1,m}\right\}^{i}=\left\{R^{n+1,m}\right\} \tag{32}$$

$$[D+U]\left\{\Delta q^{n+1,m}\right\}^{i+1}+[L]\left\{\Delta q^{n+1,m}\right\}^{i+1/2}=\left\{R^{n+1,m}\right\} \tag{33}$$

In the forward pass, $\{\Delta q\}^{i+1/2}$ are obtained with the previously updated $\{\Delta q\}^{i}$, which were set to zero at the initial stage. In the backward pass, $\{\Delta q\}^{i+1}$ are obtained with the most recent value of $\{\Delta q\}^{i+1/2}$ from the previous pass. Normally eight symmetric Gauss–Seidel sub-iterations are adequate at each time step.

## 4. Turbulence model

Several turbulence closure models have been developed for high-Reynolds number flows. One of them is the Spalart-Allmaras one-equation turbulence model (Spalart & Allmaras, 1991), which formulates a transport equation for the turbulence Reynolds number, and is the only one used in the present study. From the original Spalart-Allmaras formulation, a transport equation for the turbulence Reynolds number $\tilde{v}=\rho\mu_t/f_{v2}$ (working variable) is expressed as

$$\frac{\partial \tilde{\nu}}{\partial t}+\vec{U}\cdot\nabla\tilde{\nu}=c_{b1}\left(f_{r1}-f_{t2}\right)\tilde{S}\tilde{\nu}-\frac{1}{\mathrm{Re}}\left[c_{w1}f_w-\frac{c_{b1}}{k^2}f_{t2}\right]\left[\frac{\tilde{\nu}}{d}\right]^2$$

$$+\frac{1}{\sigma\,\mathrm{Re}}\left\{\nabla\cdot\left[\left(\tilde{\nu}+(1+c_{b2})\tilde{\nu}\right)\nabla\tilde{\nu}\right]-c_{b2}\tilde{\nu}\nabla\cdot\left(\nabla\tilde{\nu}\right)\right\}=0 \tag{34}$$

where the first and second terms on the right hand side of Eq. (34) is the source production, and the third term is the turbulence dissipation. Constants in Eq. (34) can be found in the original paper (Spalart & Allmaras, 1991).

## 5. Characteristic-based boundary conditions

In order to compute internal and external flows at arbitrary Mach numbers, four commonly used characteristic–based boundary conditions have been developed (Sheng & Wang, 2003), including far field boundary, inflow boundary based on total conditions or mass flow, outflow boundary based on back pressure, and impermeable wall. The characteristic variables are derived based on preconditioned system matrix in order to be consistent with

interior point treatment. To solve the governing equations in a rotating frame, a source term is included which should be implicitly integrated into the characteristic boundary conditions. In the following, characteristic-based boundary conditions are provided for completeness.

### 5.1 Far field

The preconditioned system matrix can be diagonalized as $a_\Gamma = R\Lambda_\Gamma R^{-1}$, where $\Lambda_\Gamma$ is a diagonal matrix made up of the eigenvalues of $a_\Gamma$, and $R$ and $R^{-1}$ are matrices whose columns and rows are the right and left eigenvectors of $a_\Gamma$, respectively. Multiplying both side of the Eq. (9) by $R_0^{-1}$ gives the following characteristic relations in one dimensional space

$$\frac{\partial W}{\partial t} + \Lambda_\Gamma \frac{\partial W}{\partial x} = R^{-1}\Gamma_q M^{-1} S \tag{35}$$

where $W = R_0^{-1} q$ is the characteristic variables with the subscript 0 denoting a reference value. The following relation is valid along the characteristic line:

$$dx / dt = \lambda_\Gamma$$

$$\frac{dW}{dt} = R_0^{-1}\Gamma_q M^{-1} S$$

$$W_b = W_r + R_0^{-1}\Gamma_q M^{-1} S_b \Delta t \tag{36}$$

where subscript *b* denotes a point on the boundary, and subscript *r* denotes an appropriate reference point depending on the sign of the eigenvalues on the boundary. Five characteristic variables for the three-dimensional preconditioned system are

$$w^1 = \left(\rho - p / \beta c_0^2\right) n_x - \left(\Theta - n_t\right)\psi_0 n_x - w n_y + v n_z \tag{37}$$

$$w^2 = \left(\rho - p / \beta c_0^2\right) n_y - \left(\Theta - n_t\right)\psi_0 n_y - u n_z + w n_x \tag{38}$$

$$w^3 = \left(\rho - p / \beta c_0^2\right) n_z - \left(\Theta - n_t\right)\psi_0 n_z - v n_x + u n_y \tag{39}$$

$$w^4 = \frac{p}{2\rho_0 \sigma_0} + \left(\Theta - n_t\right) c_0^+ \tag{40}$$

$$w^5 = \frac{p}{2\rho_0 \sigma_0} + \left(\Theta - n_t\right) c_0^- \tag{41}$$

where

$$\psi_0 = \rho_0 \Theta_0 (1 - \beta) / \beta c_0^2$$

$$c_0^{\pm} = \frac{\Theta\beta^{\pm} \pm \sigma_0}{2\sigma_0}$$

The direction of propagation of five characteristic waves is determined by the sign of each associated eigenvalue. Since all boundary faces have an positive outward pointing normal with the current unstructured grid topology, a negative sign of the eigenvalue means that the related characteristic wave propagates from the free stream to the boundary nodes, and the reference value is the free stream value; while a positive sign of the eigenvalue means that the characteristic wave propagates from the interior of the computational domain to the boundary, so the reference value should be taken from the interior node. The primitive variables at the boundary are then computed by solving the following equations:

$$q_b = R_0 W_r + \Gamma_q M^{-1} S \Delta_t \tag{42}$$

### 5.2 Inflow

For internal flows in rotating machineries, total conditions (total pressure Pt, total temperature Tt) are usually given at the inlet, along with the flow angle $(\phi_x, \phi_y, \phi_z)$. Denote the inflow velocity as $U_b$, then the following relations exist

$$\rho_b = \frac{\gamma M_r^2 P_t}{T_t}\left(1 - \frac{\gamma - 1}{2T_t} M_r^2 U_b^2\right)^{\frac{1}{\gamma - 1}} \tag{43}$$

$$p_b = P_t\left(1 - \frac{\gamma - 1}{2T_t} M_r^2 U_b^2\right)^{\frac{\gamma}{\gamma - 1}} \tag{44}$$

$$u_b = U_b \cos\phi_x \tag{45}$$

$$v_b = U_b \cos\phi_y \tag{46}$$

$$w_b = U_b \cos\phi_z \tag{47}$$

Since there are six unknowns ($\rho_b$, $p_b$, $u_b$, $v_b$, $w_b$, $U_b$) out of the above five equations, one more relation is required to solve the equations. For the subsonic inflow, all eigenvalues except $\lambda^{(4)}$ are negative. The fourth characteristic relation that propagates from the interior field to the boundary is used

$$w_b^{(4)} = w_i^{(4)} + \left[R_0^{-1}\Gamma_q M^{-1} S_b \Delta t\right]^{(4)} \tag{48}$$

or

$$\frac{p_b}{2\rho_0\sigma_0} + \left(\Theta - n_t\right)_b c_0^{+} = \frac{p_i}{2\rho_0\sigma_0} + \left(\Theta - n_t\right)_i c_0^{+} + \left[R_0^{-1}\Gamma_q M^{-1} S_b \Delta t\right]^{(4)} \tag{49}$$

An alternate way to specify the inflow boundary conditions is to use the total temperature $T_t$, mass flow rate $\dot{m}$, and the inflow angle $\alpha = (\phi_x, \phi_y, \phi_z)$. Equations (43), (44), and (48) are replaced by the following three equations:

$$\dot{m} = \rho_b U_b \tag{50}$$

$$T_t = T_b + \frac{\gamma - 1}{2} M_r^2 U_b^2 \tag{51}$$

$$p_b = \frac{\rho_b T_b}{\gamma M_r^2} \tag{52}$$

All flow variables at the boundary are obtained by solving the above equations.

### 5.3 Outflow

Characteristic variable boundary conditions are applied to outflows as well. For the subsonic outflow, the first four eigenvalues $\lambda^{(1,2,3,4)}$ are positive and the fifth eigenvalue $\lambda^{(5)}$ is negative. Flow variables at the boundary are connected with the interior values through the first four characteristic relations. The fifth relation is replaced by the static pressure at the exit

$$\left(\rho_b - p_b / \beta c_0^2\right) n_x - \left(\Theta - n_t\right)_b \psi_0 n_x - w_b n_y + v_b n_z =$$

$$\left(\rho_i - p_i / \beta c_0^2\right) n_x - \left(\Theta - n_t\right)_i \psi_0 n_x - w_i n_y + v_i n_z + \left[R_0^{-1} \Gamma_q M^{-1} S_b \Delta t\right]^{(1)} \tag{53}$$

$$\left(\rho_b - p_b / \beta c_0^2\right) n_y - \left(\Theta - n_t\right)_b \psi_0 n_y - u_b n_z + w_b n_x =$$

$$\left(\rho_i - p_i / \beta c_0^2\right) n_y - \left(\Theta - n_t\right)_i \psi_0 n_y - u_i n_z + w_i n_x + \left[R_0^{-1} \Gamma_q M^{-1} S_b \Delta t\right]^{(2)} \tag{54}$$

$$\left(\rho_b - p_b / \beta c_0^2\right) n_z - \left(\Theta - n_t\right)_b \psi_0 n_z - v_b n_x + u_b n_y =$$

$$\left(\rho_i - p_i / \beta c_0^2\right) n_z - \left(\Theta - n_t\right)_i \psi_0 n_z - v_i n_x + u_i n_y + \left[R_0^{-1} \Gamma_q M^{-1} S_b \Delta t\right]^{(3)} \tag{55}$$

$$\frac{p_b}{2\rho_0 \sigma_0} + \left(\Theta - n_t\right)_b c_0^+ = \frac{p_i}{2\rho_0 \sigma_0} + \left(\Theta - n_t\right)_i c_0^+ + \left[R_0^{-1} \Gamma_q M^{-1} S_b \Delta t\right]^{(4)} \tag{56}$$

$$p_b = p_e \tag{57}$$

The boundary values ($\rho_b$, $p_b$, $u_b$, $v_b$, $w_b$) are solved by the above equations.

For a supersonic outflow case, the fifth eigenvalue $\lambda^{(5)}$ is positive, and no characteristic waves can propagate from downstream to the upstream. The last equation (57) is replaced by the fifth characteristic relation (58) where characteristic variables come from the interior field:

$$\frac{p_b}{2\rho_0 \sigma_0} + \left(\Theta - n_t\right)_b c_0^- = \frac{p_i}{2\rho_0 \sigma_0} + \left(\Theta - n_t\right)_i c_0^- + \left[R_0^{-1} \Gamma_q M^{-1} S_b \Delta t\right]^{(5)} \tag{58}$$

### 5.4 Impermeable wall

For impermeable surfaces, the specified condition is that of no flow past perpendicular to the surface, i.e., $\Theta_b = 0$. The remaining boundary conditions are found from the following characteristic relations:

$$\begin{aligned}&\left(\rho_b - p_b / \beta c_0^2\right) n_x - w_b n_y + v_b n_z = \\ &\left(\rho_i - p_i / \beta c_0^2\right) n_x - \Theta_i \psi_0 n_x - w_i n_y + v_i n_z + \left[R_0^{-1} \Gamma_q M^{-1} S_b \Delta t\right]^{(1)}\end{aligned} \tag{59}$$

$$\begin{aligned}&\left(\rho_b - p_b / \beta c_0^2\right) n_y - u_b n_z + w_b n_x = \\ &\left(\rho_i - p_i / \beta c_0^2\right) n_y - \Theta_i \psi_0 n_y - u_i n_z + w_i n_x + \left[R_0^{-1} \Gamma_q M^{-1} S_b \Delta t\right]^{(2)}\end{aligned} \tag{60}$$

$$\begin{aligned}&\left(\rho_b - p_b / \beta c_0^2\right) n_z - v_b n_z + u_b n_y = \\ &\left(\rho_i - p_i / \beta c_0^2\right) n_z - \Theta_i \psi_0 n_z - v_i n_z + u_i n_y + \left[R_0^{-1} \Gamma_q M^{-1} S_b \Delta t\right]^{(3)}\end{aligned} \tag{61}$$

$$\frac{p_b}{2\rho_0 \sigma_0} = \frac{p_i}{2\rho_0 \sigma_0} + \Theta_i c_0^+ + \left[R_0^{-1} \Gamma_q M^{-1} S_b \Delta t\right]^{(4)} \tag{62}$$

$$u_b n_x + v_b n_y + w_b n_z = -n_t \tag{63}$$

It is noticed that the first four characteristic relations (59) through (62) can be obtained by setting $\Theta_b = 0$ in Eqs. (53) through (56). It is also worth noting that in all above boundary conditions, the source term contributions are added to the equations implicitly.

## 6. Results

To validate the new preconditioned algorithm for low Mach number flows in rotating machinery, application of a hydrodynamic flow about the David Taylor marine propeller P5168 is performed in this study. This is a five-bladed, controllable–pitch propeller (Fig. 3) with a design advance coefficient of J = 1.27. The diameter of the propeller is 0.4027m. The 3-D LDV tip-vortex flow field measurement was conducted by Chesnakas and Jessup (Chesnakas & Jessup, 1998) in the CDNSWC 36-inch water tunnel. Four different advance coefficients were measured with detailed velocity data behind the propeller. The numerical simulations were conducted under the four advance ratios corresponding to the experiment. The body-fitted mixed-element anisotropic unstructured mesh was generated using the Advancing-Front Local Reconnection (AFLR) grid generation technique (Marcum, 2001). The far field boundary of the computational domain extends to 3.5 blade diameters in both upstream and downstream, and 1.5 blade diameters in the radial direction. The unstructured mesh contains 3.825 million nodes and 12.182 million elements. For the viscous gird used in this work, the y+ distribution is less than 1.5 over the solid bodies to provide a good viscous sublayer resolution. In addition to the fine grid region over all the viscous surfaces for achieving good boundary layer resolution, a number of interior faces were created downstream in the domain along blade wake paths to refine the volume grid in order to capture the fine details of the flow field in the downstream of the propeller. Those

interior faces are transparent to the flow solver with no physic boundary conditions required. As moving further beyond the shaft rear face, the computational mesh becomes coarse to reduce the computational costs. The spatial variation of grid resolution is expected to affect the accuracy of the numerical simulations and its influence will be assessed in the investigation of the simulation results. Computation domain was partitioned into 64 sub-domains for parallel computations.

The velocity measurements were performed by Chesnakas and Jessup (Chesnakas & Jessup, 1998) in the water tunnel, and is used in this work for code validation. Detailed flow conditions for the simulation cases are summarized in Table 1. The characteristic based far-field boundary condition is applied to the far-field boundary with implicit treatment of the source terms. The no-slip boundary conditions are applied to the propeller blade and shaft

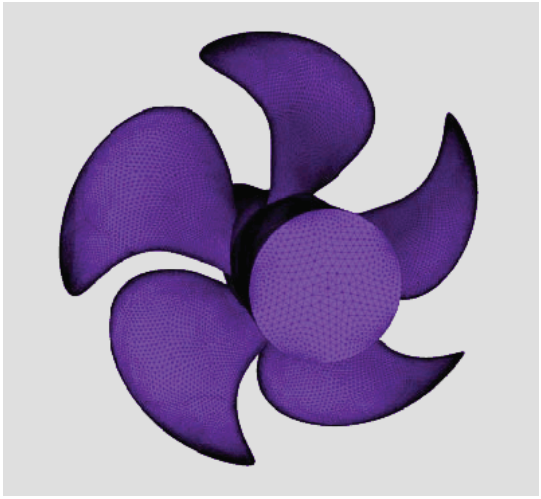

Fig. 3. Marine Propeller 5168 and Surface Mesh

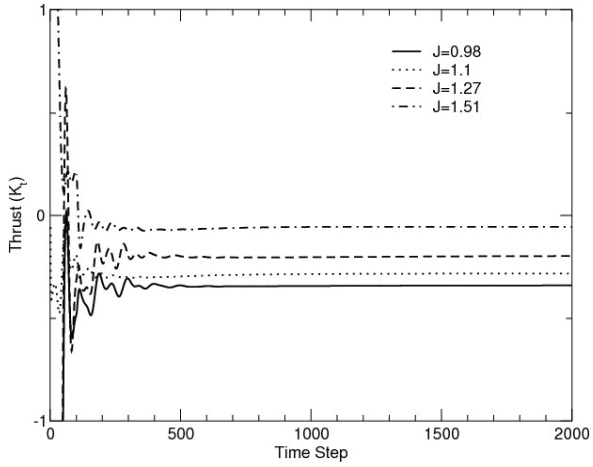


Fig. 4. Convergence History of Propeller Thrust

| Advance Coefficient J=V/nD | Free Stream V(m/s) | Rotational Speed RPM | Tip Velocity $V_{tip}$ (m/s) | Tip Mach Number $M_{tip}$ | Reynolds Number Re (106) |
|---|---|---|---|---|---|
| 0.98 | 7.893 | 1200 | 25.302 | 0.0744 | 3.14 |
| 1.1 | 10.705 | 1450 | 30.574 | 0.0899 | 4.26 |
| 1.27 | 11.081 | 1300 | 27.411 | 0.0806 | 4.41 |
| 1.51 | 11.730 | 1150 | 24.248 | 0.0713 | 4.64 |

Table 1. Simulation Flow Conditions of P5168 Propeller

surfaces in the rotating frame. All solid surfaces are assumed to be adiabatic, i.e., no heat fluxes across the solid surfaces. The Reynolds number is based on the free stream speed and the diameter of the propeller. The reference Mach number $M_r = 0.1$ is selected for all the cases based on the free stream condition. The preconditioning parameter is estimated by the modified scheme as $\beta = M_r^2 + M_\Omega^2$, in which $M_\Omega$ is set equal to the propeller tip Mach number listed in Table 1 for each case. This seems to provide the best accuracy and convergence. Due to the adoption of the relative rotating frame, flows of the rotating propeller can be considered as steady problems. The local time stepping is used in all the simulations with CFL number of 10. One Newton's iteration and eight Gauss-Seidel sub-iterations are used at each time step. Simulations are initiated from a uniform flow, and converged steady solutions are achieved in less than 1000 iterations. Fig. 4 shows the simulation history of the computed propeller thrust coefficient to demonstrate the convergence at each advance ratio of the propeller.

### 6.1 Propeller performance

The propeller has been open-water tested in the CDNSWC towing basin, where the cavitation inception conditions are related to either thrust loading (KT) or tunnel velocity (J). The numerical simulations are performed under the same four advance ratios J=0.98, 1.1, 1.27, 1.51 that have been tested in the water tunnel. The computed thrust and torque on the propeller are calculated by integrating the pressure over the propeller surfaces. The thrust and torque coefficients are defined as

$$K_T = \frac{thrust}{\rho n^2 D^4}, \qquad K_Q = \frac{torque}{\rho n^2 D^5} s$$

where ρ is the flow density, n is the rate of revolutions in the unit of revolution per second, and D is the propeller diameter. Fig. 5 shows that computed thrust and torque coefficients for the P5168 propeller agree well with experiment in all advance ratios. Results obtained by the current preconditioning method seem to provide excellent predictions of the propeller thrust and torque comparing with the experimental data.

### 6.2 Circumferentially averaged velocity

The measured and computed circumferentially averaged velocities at two downstream locations (x/R=0.2386 and 0.8378) are shown in Fig. 6. The filled symbols are measured values and unfilled symbols are computed values. Predicted axial and tangential velocities match the experiment quietly well, although a slight underestimated radial velocity is seen in Fig. 6 (c). This is related to the prediction of tip-vortex flow in the downstream of the

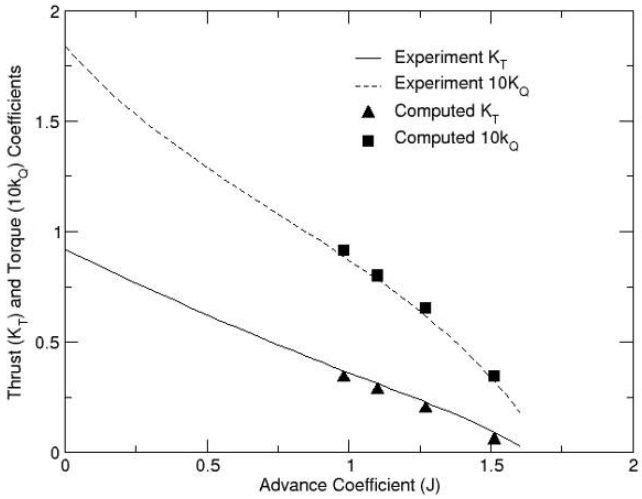


Fig. 5. Comparison of Predicted and Measured Propeller Thrust and Torque

propeller, which will be discussed in the following section. However, the overall trend in velocity distributions are well captured in the computation, including in the blade tip-vortex region at r/R=1.0. The computed results showed favorable agreement with the experimental data.

### 6.3 Mean velocity contours

To further investigate the tip-vortex flow generated by the propeller, the computed contours of the axial, radial, and tangential velocity components in the rotating frame at a stream-wise location of x/R = 0.2386 are presented in Fig. 7. The tip vortices generated by the blade tip are clearly visible in both the computation and the experiment, where the vortex core is represented as blue "spokes" in the plot of low velocity. There is a flow circulation around the tip vortex, as well as the radial velocity generated by the blade wake. The strong asymmetry of the vortex can be seen here. It also indicates that the current preconditioned scheme does capture the general feature of the tip-vortex flow. The axial and radial velocity components (Fig. 7(a) and (b)) showed a good agreement regarding the locations of tip vortices between the computation and measurement. However, the numerical diffusion was observed in the current second-order discretization scheme in the vortex core region, as predicted vortex strength appeared not as strong as what was measured in the experiment. To improve the prediction accuracy in the vortex core region, an adaptively refined mesh or a higher-order spatial discretization scheme (Sheng & Wang, 2009) is necessary. Nevertheless, the modified preconditioning method was proved to provide stable and reasonably accurate predictions to the hydrodynamic viscous flows in rotating machinery, which would otherwise impossible to achieve with the original preconditioning method, not to mention the compressible flow solver.

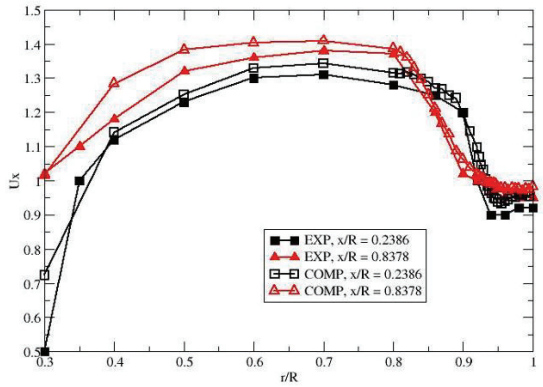


(a) Axial Velocity

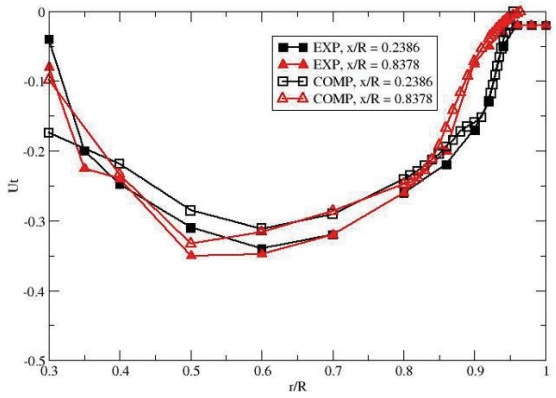


(b) Tangential Velocity

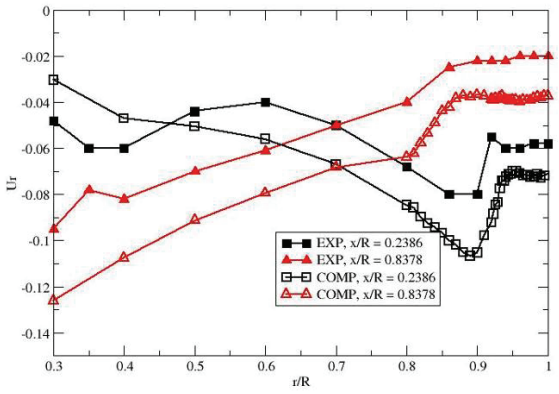


(c) Radial Velocity

Fig. 6. Comparison of Computed and Measured circumferentially Averaged Velocities

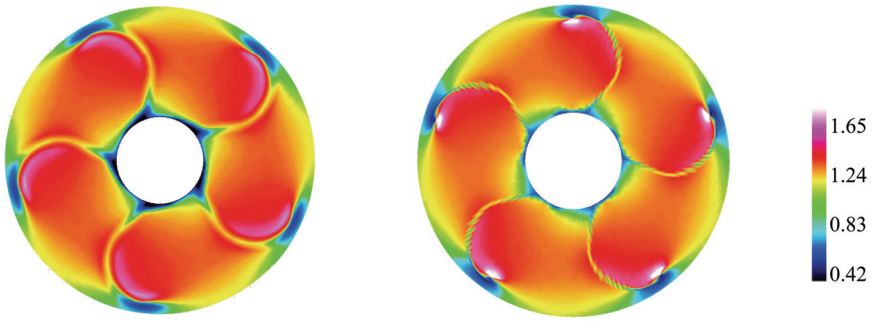


(a) Axial Velocity

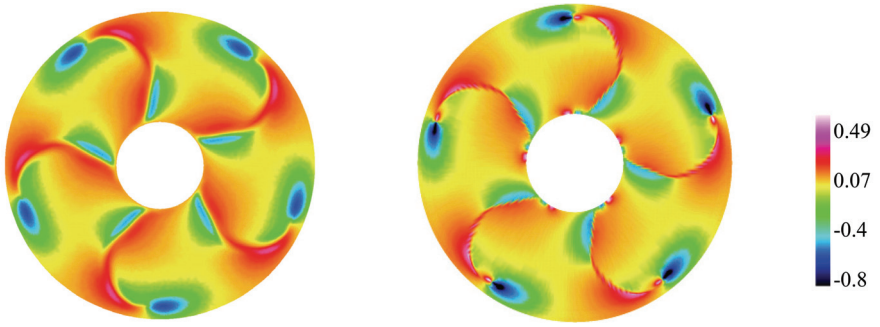


(b) Radial Velocity

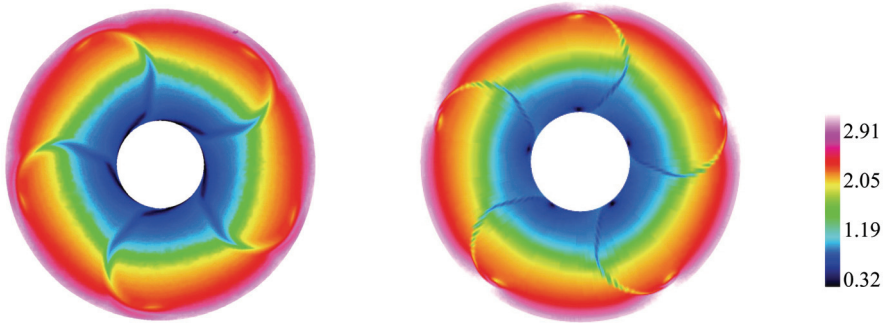


(c) Tangential Velocity

Computed Experiment

Fig. 7. Comparison of Computed and Measured Mean Velocity Contours at x/R=0.2386

### 6.4 Tip-vortex trajectory

The tip vortex trajectory was predicted and compared with the experiment measurements. An approximate approach to locate the tip vortex core location is to limit the search for a minimum pressure within the region of the known vortex indicated by a swirl parameter. The physical interpretation for this criterion is given by Jeong and Hussain (Jeong & Hussain, 1995). Within the vortex core, pressure tends to have a local minimum on the axis of a circulatory or swirling motion when the centrifugal force is balanced by the pressure force, which is strictly true only in a steady inviscid planar flow. Using this method, the tip-vortex trajectories were identified from computed flows at the advance ratio of J=1.1. Fig. 8 compared the predicated radial locations of the tip vortex with the experimental observation. In the experiment, the tip vortex was tracked from the blade tip to an axial location of approximately one diameter downstream where x/R=2.0. The current simulation conducted in this study can predict the tip vortex radial trajectory accurately up to a limited distance downstream, due to the grid coarsening in the downstream of the propeller. As shown in Fig. 8, the predicted tip-vortex trajectory is tracked to the location about only one radius downstream at x/R=1.0 before dissipated into the flow field. The largest disagreement between the prediction and the experiment measurement occurs at the last station of x/R=1.0. Beyond that point it appeared to be difficult to trace the tip vortex as it has completely smeared out in the flow field. Examination of the grid resolution of the propeller indicated a finer grid resolution only coving a limited distance in the downstream of the propeller. The grid cells became very coarser as moving beyond the shaft rear surface at station x/R=0.69. Fig. 9 clearly demonstrated the tip vortex convection which is quickly dissipated due to the limited grid resolution. As discussed in the previous section, a refined computational mesh and a higher-order discretization scheme may reduce the numerical dissipation of this vortical flow, although the computational costs would be significantly higher.

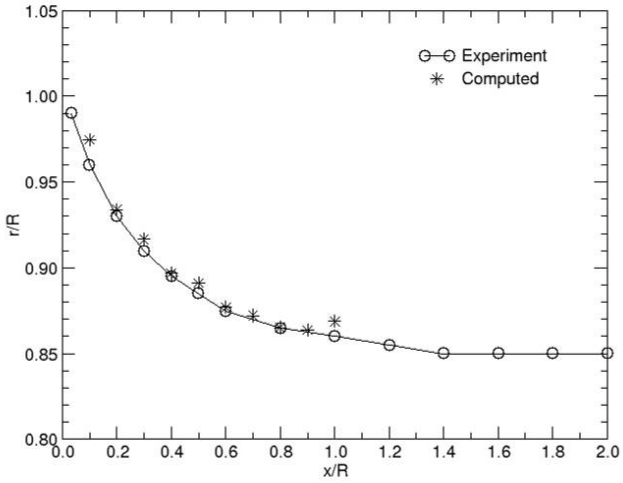


Fig. 8. Propeller 5168 Tip Vortex Radial Trajectory

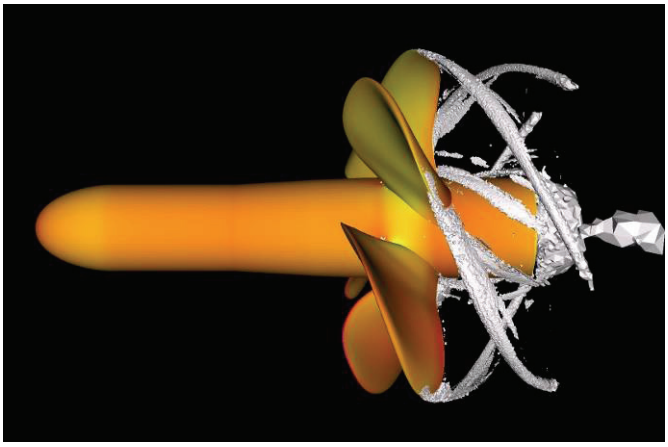

Fig. 9. Computed Tip Vortex Visualized by Swirl Parameter

### 6.5 Tip vortex convection and decay

Another way to trace the tip vortex of the propeller is to use a non-dimensional parameter termed intrinsic swirl parameter $\tau$ (Berdahl & Thompson, 1993), which calculates the velocity gradient tensor over the computational domain. The intrinsic swirl indicates the tendency for the fluid to swirl about a local point, and is more effective to represent the vortical motion in the flow field. In regions where the swirl parameter approaches to zero ($\tau \to 0$), the fluid convects too rapidly to be captured in swirling motion, while in region where $\tau > 0$, the fluid does not move quickly enough and is trapped in a swirling motion. Fig. 10 compares the tip vortex strength under the four advance coefficients. The intrinsic swirl contours are visualized on six downstream stations of x/R=[0.1, 0.6] with an equal spacing of 0.1. Streamlines are generated from the shaft rear surface at x/R=0.69. The core regions of blade tip vortices are evident by the largest magnitude of swirl parameter. It clearly shows the rapid decay of the tip vortices and the separation of vortices from the wake as the flow moves downstream. The swirl parameter values at the vortex core on selected stream-wise stations are extracted and presented in Fig. 11. The simulation results indicated that vortex strength varied strongly with advance coefficient. At a high loading (lower advance ratio values, J=0.98 and 1.10), strong tip vortices are observed over a longer distance downstream. The tip vortices are very weak at J=1.27 and eventually disappeared at J=1.51. It is noticed that the decreasing of the intrinsic swirl under the advance coefficients of J=1.27 and 1.51 is not monotonic as x/R goes beyond 0.4, where the swirl parameter even increases at further downstream stations. Further investigation found that the locations of high swirl centers at station x/R=0.5, 0.6 under J=1.27 and 1.51 occur in a much finer grid region, which was originally generated for the purpose of capturing the propeller wake. Therefore, the non-physical behaves of the swirl parameter appear in Fig. 11 are due to the variation of grid resolution. The simulation results are qualitatively consistent with the experimental measurements.

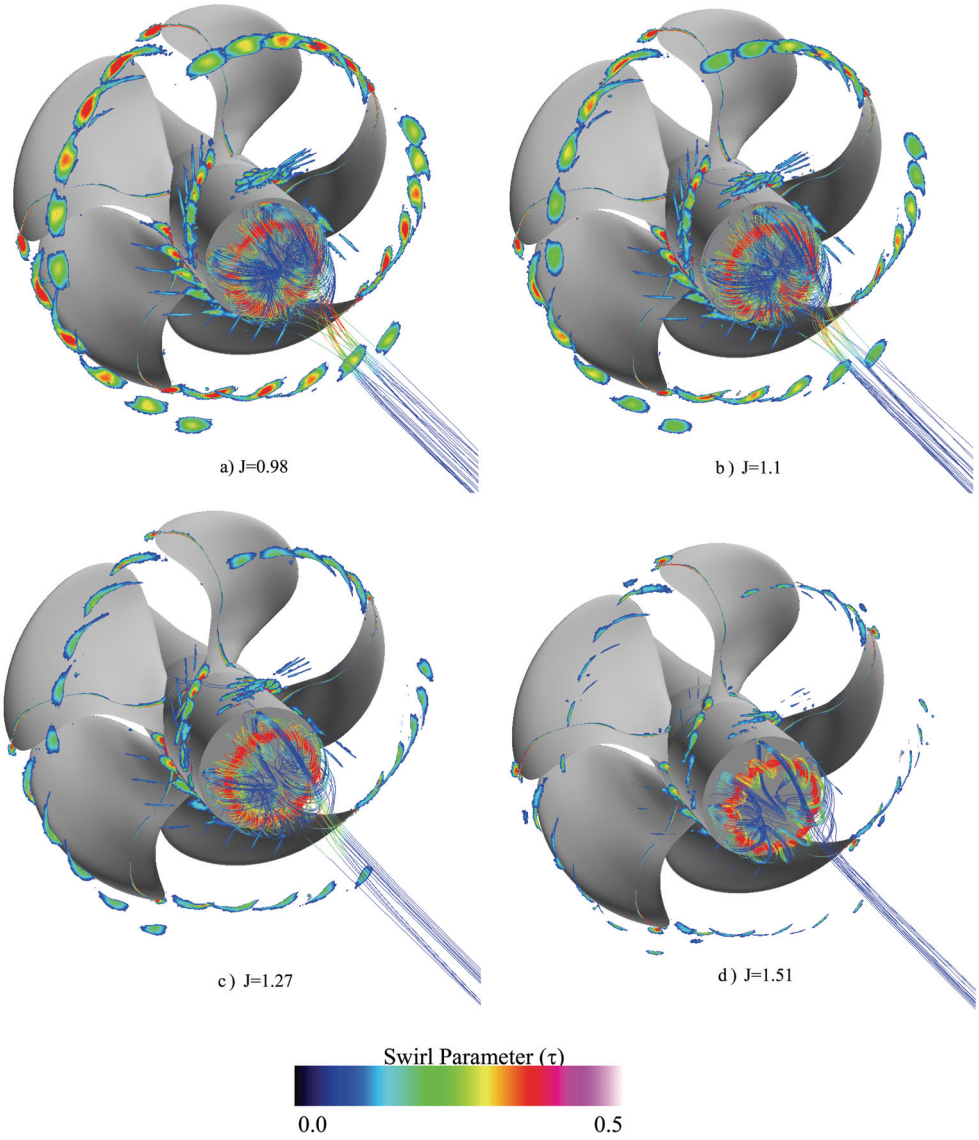


Fig. 10. Predicted Wakes and Tip Vortices vs. Advance Coefficient

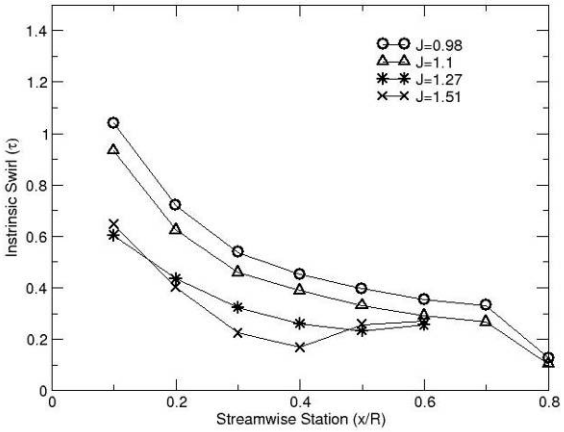


Fig. 11. Tip Vortex Decay vs. Advance Coefficient J

### 6.6 Tip-vortex attachment

The water tunnel experiment also observed suction-side tip vortex attachment occurred aft of the blade tip over certain range of tested advance ratio. The locations of the tip vortex attachment on the five blades showed minor variation from blade to blade, and their average radial location has been estimated. In the open-water experiment at an advance ratio of J=0.98, this average location was estimated at the blade trailing edge of 0.99R radius, while at J=1.1, the attachment point was moved aft to 0.998R radius of the trailing edge. From the current computed results, the iso-surface of swirl parameter $\tau$=1.0 is generated to visualize the tip vortex structure as shown in Fig. 12. The iso-surface is shaded by static

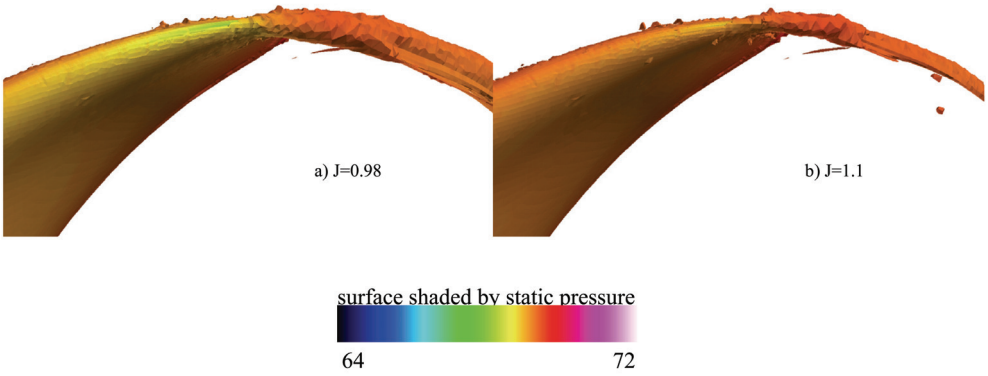


Fig. 12. Blade Suction Side Tip Vortex Attachment.

pressure. The propeller geometry is not plotted in the figure, but the tip region of the propeller blade is seen clearly, which is actually the swirl iso-surface in the blade boundary layer. At the blade tip, the attachment occurs aft a local minimum pressure center at the trailing edge. The iso-surface of the swirl parameter indicated that the tip vortex attachment occurs at the trail edge on the blade suction side between 0.994R-0.999R. The variation of the attachment points at J=0.98 and J=1.1 are not distinguishable except that the local minimum pressure center upstream the attachment location has lower pressure at J=0.98 and originates stronger tip vortex. The current simulations correctly captured the tip-vortex attachment observed in the experiment, which is important for the improved understanding of the cavitation inception of the marine propeller.

## 7. Conclusion

A modified preconditioning method was investigated and validated in the prediction of hydrodynamic viscous flows for marine propeller P5168. The preconditioning parameter is based on the reference Mach number and rotating Mach number to provide stable and accurate solutions for low Mach number flows in rotating machinery, while the original preconditioning method failed to provide converged solutions in the case presented in this study. The predicted overall propeller performance, circumferentially averaged velocities, mean velocity contours, tip-vortex trajectory and decay at blade downstream stations are validated against the experimental data. The comparison between the computation and the experiment indicates that the current preconditioned solver was able to capture the general features of the tip vortex generated by the propeller. In particular, the predicted thrust and torque coefficients at several advance ratios matched well with the open-water experimental data. However, the current numerical simulation showed a quick decay of the tip vortex in the propeller downstream, due to a lack of enough grid resolution. Future studies include using adaptive grid technique to locally refine the computational mesh in the vortex core region, and a higher-order spatial discretization schemes to further reduce the numerical diffusion in the solver.

## 8. Acknowledgements

The author wishes to thank Qiuying Zhao of The University of Toledo and Xiao Wang of High Performance Computing Collaboratory at Mississippi State University for helping processing the simulation data and formatting the manuscript.

## 9. References

Anderson, W.K. (1992). Grid Generation and Flow Solution Method for Euler Equations on Unstructured Grids, NASA Technical Report TM– 4295, April 1992.

Anderson, W.K.; Rausch, R.D., & Bonhaus, D. L. (1995). Implicit/Multigrid Algorithms for Incompressible Turbulent Flows on Unstructured Grids, AIAA Paper 95–1740, June 1995.

Berdahl, C. H. and Thompson, D. S., (1993). Eduction of Swirling Structure using the Velocity Gradient Tensor, *AIAA J.*, vol. 31, no. 1, (January 1993), 97-103.

Briley, W.R., and McDonald, H., and Shamroth, S.J., (1983). A Low Mach Number Euler Formulation and Application to Time Iterative LBI Schemes, *AIAA J.*, 21 (10), (1983),1467–1469.

Briley, W.R., Tayler, L.K., and Whitfield, D.L., (2003). High–Resolution Viscous Flow Simulations at Arbitrary Mach Number, *Journal of Computational Physics*, 184(1), (2003), 79-105.

Chesnakas, C.J., and Jessup, S.D., (1998). Cavitation and 3–D LDV Tip–Flowfield Measurements of Propeller 5168, *CRDKNSWC*/HD–1460–02, (May 1998), Carderock Division, Naval Surface Warfare Center.

Chen, J.P.; Ghosh, A.R., Sreenivas, D., & Whitfield, D.L. (1997). Comparison of Computations Using Navier–Stokes Equations in Rotating and Fixed Coordinates for Flow Through Turbomachinery, AIAA Paper No.97–0878, AIAA 35th Aerospace Sciences Meeting and Exhibit, Reno, NV, January 6–10, 1997.

Choi, D., & Merkle, C.L. (1985). Application of Time–Iterative Schemes to Incompressible Flow, AIAA J., 23 (10):1518–1524, 1985.

Choi, D., & Merkle, C.L. (1993). Application of Preconditioning to Viscous Flows, J. Comp. Physics, 105:207–223, 1993.

Chorin, A.J. (1967). A Numerical Method for Solving Incompressible Viscous Flow Problems, J. Comp. Physics, 2:12–26, 1967.

Coirier, W.J. (1994). An Adaptively–Refined, Cartesian, Cell–Based Scheme for the Euler and Navier–Stokes Equations, NASA Technical Memorandum 106754, NASA Lewis Research Center, October 1994.

Hyams, D.G. (2000), An Investigation of Parallel Implicit Solution Algorithms for Incompressible Flows on Unstructured Topologies, Ph.D. Dissertation, Mississippi State University, May 2000.

Hageman, L.A. and Young, D.M., (1981). *Applied Iterative Methods*, 1981, Academic Press, New York.

Jeong, J. and Hussain, F., (1995). On the Indentification of a Vortex, *Journal of Fluid Mechanics*, Vol. 285, (1995), 69-94.

Marcum, D. L., (2001). Efficient Generation of High Quality Unstructured Surface and Volume Grids, *Engineering with Computers*, Vol. 17, No. 3, (2001), 211-233.

O'Brien, G.G., Hyman, M.A., and Kaplan, S., (1951), A Study of the Numerical Solution of Partial Differential Equations, *Journal of Mathematics and Physics*, Vol 29, No. 4, (1951), 223-249.

Sheng, C., and Wang, X., (2006). A Global Preconditioning Method for Low Mach Number Viscous Flows in Rotating Machinery, GT2006-91189, *Proceedings of ASME Turbo Expo 2006*, 8-11 May 2006, Barcelona, Spain.

Sheng, C., and Wang, X., (2003). Characteristic Variable Boundary Conditions for Arbitrary Mach Number Algorithm in Rotating Frame, AIAA-2003-3976, *Proceedings of the 16th AIAA Computational Fluid Dynamics Conference*, June 23-26, 2003, Orlando, FL.

Sheng, C. and Wang, X., (2009). Aerodynamic Analysis of a Spinning Missile with Dithering Canards Using a High Order Unstructured Grid Scheme, AIAA-2009-1090, *47th AIAA Aerospace Sciences Meeting*, 5-8 January 2009, Orlando, Florida.

Spalart, P., and Allmaras, S., (1991). A One-Equation Turbulence Model for Aerodynamic Flows, AIAA Paper 92-0439, January 1991.

Vichnevetsky, R., and Bowles, J.B., (1982). *Fourier Analysis of Numerical Approximations of Hyperbolic Equations*, 1982.

Wang, X. and Sheng, C., (2005). Numerical Study of Preconditioned Algorithm for Rotational Flows, *17th AIAA Computational Fluid Dynamics Conference*, June 6–9, 2005, Toronto, Ontario, Canada

Wang, X., (2005). A Preconditioned Algorithm for Turbomachinery Viscous Flow Simulation. Ph.D. Dissertation, Mississippi State University, December 2005.

# 17

# Modelling Hydrodynamic Drag in Swimming using Computational Fluid Dynamics

Daniel A. Marinho[1,2], Tiago M. Barbosa[2,3], Per L. Kjendlie[4], Narendra Mantripragada[2,5], João P. Vilas-Boas[6,7], Leandro Machado[6,7], Francisco B. Alves[8], Abel I. Rouboa[9,10] and António J. Silva[2,11]

[1]*University of Beira Interior. Department of Sport Sciences (UBI, Covilhã)*
[2]*Research Centre in Sports, Health and Human Development (CIDESD, Vila Real)*
[3]*Polytechnic Institute of Bragança. Department of Sport Sciences (IPB, Bragança)*
[4]*Norwegian School of Sport Sciences. Department of Physical Performance (Oslo)*
[5]*IIT Kharagpur. Department of Aerospace Engineering (Mumbai)*
[6]*University of Porto, Faculty of Sport (FADEUP, Porto)*
[7]*Centre of Research, Education, Innovation and Intervention in Sports (CIFI2D, Porto)*
[8]*Technical University of Lisbon. Faculty of Human Kinetics (FMH-UTL, Lisbon)*
[9]*University of Trás-os-Montes and Alto Douro. Department of Engineering (UTAD, Vila Real)*
[10]*Research Centre and Technologies of Agro-environment and Biological Sciences (CITAB, Vila Real)*
[11]*University of Trás-os-Montes and Alto Douro. Department of Sport Sciences, Exercise and Health (UTAD, Vila Real)*
[1,2,3,6,7,8,9,10,11]*Portugal*
[4]*Norway*
[5]*India*

## 1. Introduction

In the sports field, numerical simulation techniques have been shown to provide useful information about performance and to play an important role as a complementary tool to physical experiments. Indeed, this methodology has produced significant improvements in equipment design and technique prescription in different sports (Kellar et al., 1999; Pallis et al., 2000; Dabnichki & Avital, 2006). In swimming, this methodology has been applied in order to better understand swimming performance. Thus, the numerical techniques have been addressed to study the propulsive forces generated by the propelling segments (Rouboa et al., 2006; Marinho et al., 2009a) and the hydrodynamic drag forces resisting forward motion (Silva et al., 2008; Marinho et al., 2009b).

Although the swimmer's performance is dependent on both drag and propulsive forces, within this chapter the focus is only on the analysis of the hydrodynamic drag. Therefore, this chapter covers topics in swimming drag simulation from a computational fluid dynamics (CFD) perspective. This perspective means emphasis on the fluid mechanics and

CFD methodology applied in swimming research. One of the main aims for performance (velocity) enhancement of swimming is to minimize drag forces resisting forward motion, for a given trust. This chapter will concentrate on numerical simulation results, considering the scientific simulation point-of-view, for this practical implication in swimming.
In the first part of the chapter, we introduce the issue, the main aims of the chapter and a brief explanation of the CFD methodology. Then, the contribution of different studies for swimming using CFD and some practical applications of this methodology are presented. During the chapter the authors will attempt to present the CFD data and to address some practical concerns to swimmers and coaches, comparing as well the numerical data with other experimental data available in the literature.

## 2. Fluid mechanics and CFD methodology

### 2.1 Background

CFD is a branch of fluid mechanics that solves and analyses problems involving a fluid flow with computer-based simulations. CFD methodology consists of a mathematical model that replaces the Navier-Stokes equations with discretized algebraic expressions that can be solved by iterative computerized calculations. The Navier–Stokes equations describe the motion of viscous non-compressible fluid substances. These equations arise from applying Newton's second law to fluid motion, together with the assumption that the fluid stress is the sum of a diffusing viscous term (proportional to the gradient of velocity), plus a pressure term. A solution of the Navier–Stokes equations is called a velocity field or flow field, which is a description of the velocity of the fluid at a given point in space and time. CFD methodology is based on the finite volume approach. In this approach, the equations are integrated over each control volume. It is required to discretize the spatial domain into small cells to form a volume mesh or grid, and then apply a suitable algorithm to solve the equations of motion. In addition, CFD analyses complements testing and experimentation, reducing the total effort required in the experimental design and data acquisition.
In the early days of its application, CFD was quite difficult to use. It was only applied by a few high technological level companies, in the Aerospatiale Engineering or in some specific scientific research areas. It became obvious that its application had to assume a user friendly interface and to progress from a heavy and difficult computation to practical, flexible, intuitive and quick software. Therefore, the following step was to transform CFD in a new set of commercial software to be used in different applications and to improve the user interface.
Presently, this tool is used in the solution of complex engineering problems involving fluid dynamics and it is also being extended to the study of complex flow regimes that define the forces generated by animal species in self propulsion.
The basic steps of CFD analysis are:

1. Problem identification and pre-processing: (i) define the modelling goals, (ii) identify the domain to model, (iii) design and create the grid.
2. Solver execution: (i) set up the numerical model, (ii) compute and monitor the solution.
3. Post-Processing: (i) examine the results; (ii) consider revisions to the model.

### 2.2 Advantages and limitations

CFD can be used to predict fluid flow, heat and mass transfer, chemical reactions and related phenomena by solving the set of governing mathematical equations. The results of

CFD analyses can be relevant in conceptual studies of new designs, detailed product development, troubleshooting and redesign.
Lyttle and Keys (2006) referred that CFD can provide the answers into many complex problems that have been unobtainable using physical testing techniques. One of its major benefits is to quickly answer many "*what if*" type questions. It is possible to test many variations until one arrives at an optimal result, without physical/experimental testing. CFD could be seen as bridging the gap between theoretical and experimental fluid dynamics. CFD can be applied in several research fields, such as: architecture, engineering, medicine, and sports. For example, with this methodology it is possible to: (i) study the aerodynamics of a racing car before it being constructed; (ii) to study the air flow inside the ventilation system of a park station; (iii) to simulate situations where a fire takes place or; (iv) to analyse the ventilation and the acclimatisation of a specific building, such as an hospital, where the quality of the air is quite important.
CFD was developed to model any flow filed provided the geometry of the object is known and some initial flow conditions are prescribed. CFD is based on the use of computers to solve mathematical equation systems. However, it is essential to apply the specific data to characterize the study conditions. The scientific knowledge, the computational program which solves the equation system representing the problem, the kind of computer that executes the defined calculations in the numerical program and the person who verifies and analyses the obtained results must also be taken in account.
In this sense, one must consider that the CFD analyses can have some inaccurate results if there is not thorough study of the specific situation. The inserted data should not have wide-ranging estimation. On the other hand, the available computational resources can be insufficient to obtain results with the necessary precision. Previous to any simulation the flow situation must be very well analysed and understood, followed by the careful analysis of the obtained results.

### 2.3 Validity, reliability, accuracy

CFD studies are becoming more and more popular. However, a main concern still persists. Can the numerical data be comparable with experimental research? Are the numerical results accurate enough to be meaningful and therefore have ecological validity? For sport scientists who work in close connection with coaches and athletes this question is important in order to give good, appropriate and individual feed-backs for practitioners.
Several studies with different scopes attempted to verify the validity and accuracy of CFD. This numerical tool has been validated as being feasible in modelling complicated biological fluid dynamics, through a series of stepwise baseline benchmark tests and applications for realistic modelling of different scopes for hydro and aerodynamics of locomotion (Liu, 2002).
In bioscience, Yim et al. (2005) described in detail critical aspects of this methodology including surface reconstruction, construction of the volumetric mesh, imposition of boundary conditions and solution of the finite element model. Yim et al. (2005) showed the validity of the methodology *in vitro* and *in vivo* for experimental biology. Barsky et al. (2004) have also demonstrated good agreement between the numerical and experimental data on tethered DNA in flow. Moreover, Gage et al. (2002) reported that computational techniques coupled with experimental verification can offer insight into model validity and showed promise for the development of accurate three-dimensional simulations of medical procedures.

In engineering one can cite, for example, Venetsanos et al. (2003) illustrated an application of CFD methods for the simulation of an actual hydrogen explosion occurred in a built up area of central Stockholm, Sweden, in 1983. The subsequent simulation of the combustion adopted initial conditions for mean flow and turbulence from the dispersion simulations, and calculated the development of a fireball. This data provided physical values that were used as a comparison with the known accident details to give an indication of the validity of the models. The simulation results were consistent with both the reported near-field damage to buildings and persons and with the far-field damage to windows.
In sports, some tests have been performed to compare the numerical results with experimental results also. A combined CFD and experimental study on the influence of the crew position on the bobsleigh aerodynamics was conducted by Dabnichki and Avital (2006). The experimental results obtained in a wind tunnel suggested that the adopted computational method is appropriate and yields valid results. In aquatic sports, there is a lack of studies comparing experimental and CFD data. However, CFD was developed to be valid and accurate in a large scope of fluid environments, bodies and tasks, including sports. So, it is usually assumed that CFD has ecological validity even for swimming research.
Another important concern is that of CFD reliability. In experimental tests, the input data are not always the same and thus the outputs will vary. However, the numerical simulations allow having always the same input conditions and therefore the same outputs.

## 3. Hydrodynamic drag

### 3.1 Definition

Swimming is characterized by the intermittent application of a propulsive force (thrust) to overcome a velocity-dependent water resistance (hydrodynamic drag). The thrust is generated by a combination of arm, leg and body movements and lead to variations of thrust and velocity. Different fluctuations in thrust, drag and velocity among different techniques and different level of skills contribute to the highly variable performance in swimming. Swimming performance can be studied by analysing the interaction of propelling and resistive forces. In this sense, a swimmer will only enhance performance by minimizing resistive forces that act on the swimming body at a given velocity and/or by increasing the propulsive forces produced by the propelling segments. Furthermore, a third performance enhancing factor would be to do this with a minimal enhancement of physiological or energetic costs.
Hydrodynamic drag can be defined as an external force that acts in the swimmer's body parallel but in the opposite direction of his movement direction. This resistive force is depending on the anthropometric characteristics of the swimmer, on the characteristics of the equipments used by the swimmers, on the physical characteristics of the water field, and on the swimming technique (Vilas-Boas, 1996).
The hydrodynamic drag resisting forward motion ($D$) can be expressed by the Newtonian equation:

$$D = \tfrac{1}{2}\ C_D\, \rho\, S\, v^2 \tag{1}$$

where: $\rho$ represents the fluid density, $C_D$ represents the drag coefficient, $S$ represents the projection surface of the swimmer and $v$ represents the swimming velocity.
The total drag consists of the frictional, form and wave drag components. Frictional drag is depending on water viscosity and generates shear stress in the boundary layer. The intensity

of this component is due to the wetted surface area of the body, the characteristics of this surface and the flow conditions inside the boundary layer. Form drag is the result of a pressure differential between the front and the rear of the swimmer, depending on the velocity, the density of water and the cross sectional area of the swimmer. Near the water surface, due to the interface between two fluids of different densities, the swimmer is constrained by the formation of surface waves leading to wave drag (Toussaint & Truijens, 2005).

It is accepted that frictional drag is the smallest component of total drag, especially at higher swimming velocities. However, this drag component should not be disregarded in elite level swimmers. In this sense, issues such as sports equipments, shaving and the decrease of immersed body surface should be taken into account. In addition, form and wave drag represent the major part of total hydrodynamic drag, thus swimmers must emphasize the most hydrodynamic postures during swimming (Toussaint, 2006; Marinho et al., 2009b).

The evaluation of the intensity of the hydrodynamic drag during swimming represents an important aim in swimming biomechanics. Drag determined by towing a non-swimming subject through the water (passive drag) has been studied for a long time (Karpovich, 1933). Passive drag analysis does not consider the drag that the swimmer creates when he produces thrust to overcome the drag, i.e., during actual swimming (active drag). Nevertheless, passive drag seems to be a simple way to investigate the contribution of each drag component to total drag. In addition, passive drag could be used to evaluate drag during parts of the swimming event, namely during the gliding after starts and turns, when the swimmer is "passively" gliding underwater.

### 3.2 Minimizing drag after start and turns

Minimizing the hydrodynamic drag should be a main concern during swimming. After the push-off during turns and after the block start, the swimmer travels underwater. The first part of this underwater swimming is usually performed without any movements of the propelling segments. Indeed, Lyttle and Keys (2006) reported that at velocities higher than 2.40 m/s it is more efficient for the swimmer to maintain a streamline position than to initiate underwater kicking. This situation is due to the swimmer creating more active drag than propulsion while kicking compared to remaining in a streamlined posture, leading to wasted energy and/or negative acceleration of the swimmer. According to these statements, Lyttle and Keys (2006) suggested that it may be more beneficial to maintain a streamlined position during gliding.

In this sense, the evaluation of the hydrodynamic drag during gliding after starts and turns represents an important question to be addressed. The position of the body segments, such as the head (Zaidi et al., 2008) and the arms (Marinho et al., 2009b), but also different postures adopted during the underwater gliding (Marinho et al., 2009c) have been evaluated using CFD.

Zaidi et al. (2008) evaluated the effect of the head position on hydrodynamic performance, analysing three head positions: (i) head aligned with the body, (ii) a lower head position, and (iii) a higher head position. These three situations were numerically analysed with the swimmer completely submerged in a prone position. Flow velocities of 1.40, 2.20 and 3.10 m/s were used during the simulations. The main results showed that the head position adopted during the gliding should be a main concern of swimmers, since it alters the flow around the body. The head position aligned with the body presented around 20 % less drag

than the other two positions for velocities of 2.20 and 3.10 m/s. For a velocity of 1.40 m/s, the difference is small, although the drag force for the lower head and higher head positions is higher than in the aligned head position. It was also interesting to note that the higher head position presented higher values than the lower head position for the three different flow velocities. The numerical results show that the position of the head plays a very important role for high swimming velocities. They reveal that the position of the head has a noticeable effect on the hydrodynamic performances, strongly modifying the wake around the swimmer. Based on a two-dimensional analysis, Zaidi et al. (2008) proposed an optimal position of the head of a swimmer in underwater swimming. However, restrictions inherent to the use of a two-dimensional steady flow model to investigate a really unsteady three-dimensional flow must be kept in mind when analyzing these results.

Marinho et al. (2009b) attempted to analyze the underwater phase after start and turns in a specific technique. In fact, in breaststroke, the first part of the underwater phase is performed with the arms extended at the front of the body, whereas the second gliding is performed with the arms aside the trunk. Therefore, Marinho et al. (2009b) developed a three-dimensional model representing a male adult swimmer in these two gliding positions. The simulations were carried-out with the model placed at a water depth of 0.90 m with flow velocities from 1.60 to 2.0 m/s. The drag coefficient of the position with the arms extended at the front presented lower values than the position with the arms aside the trunk. In fact, the model with the arms at the front of the body presented about 60 % of the hydrodynamic drag values of the position with the arms aside the trunk. It was also interesting to notice that the friction drag component was very similar in both body positions. The pressure drag component was the responsible for the differences between the models, suggesting that the streamlined position with the arms extended at the front of the body lead to decreasing the negative hydrodynamic effects of the human body morphology, especially near the head and shoulders of the swimmer. For the breaststroke underwater phase after start and turns, it was concluded that the first glide, performed with the arms at the front, must be emphasized in relation to the second glide, performed with the arms along the trunk. Vilas-Boas et al. (2009) attempted to analyse the same situations but through inverse dynamics. This procedure was based on the experimental velocity to time gliding curve and the swimmers' inertia performed during the first and second gliding positions of the breaststroke underwater stroke. We were very pleased to observe similar results obtained through CFD and through inverse dynamics. Regarding drag coefficient, Vilas-Boas et al. (2009) reported that the position with the arms at the front (position adopted during the first gliding) presented about 65 % of the drag coefficient values of the position with the arms aside the trunk (position adopted during the second gliding).

Another interesting research concerning the underwater gliding and the most advantageous postures to improve performance was conducted by Marinho et al. (2009c). These authors developed four two-dimensional models to analyse this phase: (i) a ventral position with the arms at the front of the model, (ii) a ventral position with the arms aside the trunk, (iii) a dorsal position with the arms at the front, and (iv) a lateral position with the arms at the front. All these body positions can be used in high level events during the underwater gliding. The four selected postures can be applied to a real swimming situation after the starts and turns, as: the gliding phase in front crawl, butterfly and the first gliding in breaststroke (prone position with the arms extended at the front), the second gliding in

breaststroke (prone position with the arms aside the trunk), the gliding in backstroke (dorsal position with the arms extended at the front) and, in some techniques/phases during the gliding in front crawl (lateral position with the arms extended at the front). Marinho et al. (2009c) found that the body postures with the arms extended at the front presented lower drag values than the body posture with the arms aside the trunk. Furthermore, the lateral position was the one in which the drag force was lower. The prone and the dorsal positions (both with the arms extended at the front) presented similar values. Thus, the position with the arms extended at the front (perhaps performed in a lateral position) must be the one adopted after stars and turns. Nevertheless, this issue demands further research using three-dimensional CFD models.

Although the aim of Bixler et al. (2007) study was not the evaluation of different body postures during gliding, this research represented an important contribution to CFD validation in swimming research. Bixler et al. (2007) studied the accuracy of CFD analysis of the passive drag of a male swimmer in a submerged streamlined position. The authors compared the drag force of a real swimmer, a three-dimensional model of this swimmer and a real mannequin based on the digital model. Bixler et al. (2007) found drag forces determined from the digital model using the CFD approach to be within 4 % of the values assessed experimentally for the mannequin, although the mannequin drag was found to be 18 % smaller than the real swimmer drag. Indeed, the Bixler et al. (2007) study has underlined the validity and accuracy of CFD approach in swimming research.

As mentioned above, Lyttle and Keys (2006) studied the underwater phase in swimming. However, contrarily to the previous mentioned studies, these authors were able to perform a CFD analysis providing limb movement. This movement was completed by breaking the limb movements down into discrete time steps and having the package solve the flow field for that position before moving on to the next position. The volume mesh was also updated at each time step with the previous flow field being the starting point at the next time step. Therefore, the authors were able to evaluate two different dynamic dolphin kicking techniques used also during the underwater phase: (i) a large/slow kick (0.54 m of kick amplitude and 2.27 Hz of kick frequency), and (ii) a small/fast kick (0.42 m of kick amplitude and 2.63 Hz of kick frequency). Lyttle and Keys (2006) simulated velocities of 1.50, 2.18 and 2.40 m/s and reported that both kicking techniques have a similar effect at 2.40 m/s. For velocities lower than 2.40 m/s the large/slow kick appears more effective, with about 4 % better efficiency at 2.18 m/s and about 18 % more efficiency at 1.50 m/s. Although these data showed that the large/slow kick has produced better results, one should be aware that these results are based only on the two kicking patterns analyzed and can not be generalized to the large number of possible kicking patterns used by the swimmers. Lyttle and Keys (2006) also showed the benefits of using a modelling approach in the area of technique modification strategies. To illustrate the capabilities of the CFD approach, various simulations were carried-out by varying ankle movement in order to examine the effects on the swimmer's net thrust. The main results showed that while the swimmer is travelling at 2.18 m/s, a $10^{o}$ increase in ankle plantar flexion created a 16.4 N greater peak propulsive force during the kick cycle. However, with $10^{o}$ more dorsi-flexion, the peak drag increased by 31.4 N, showing that increasing ankle flexibility will increase the efficiency of the stroke. Nevertheless, this information should be carefully read, since this analysis referred to a specific male swimmer.

### 3.3 Tandem effects

The tandem concept in swimming is related to situations where a swimmer displaces himself immediately behind another. During swimming events, these tandem effects do not occur since swimmers performed alone in their own lane. However, in open water competitions this situation is very common. Furthermore, during swimming training, due to time and space issues, several swimmers train in the same lane, performing significant parts of total swimming volume "in roundabout" (Silva et al., 2008).

Some experimental studies reported that the distance between swimmers significantly influences the energy cost of the swimmer submitted to the suction effect (Bassett et al., 1991; Hausswirth et al., 1999, 2001; Chatard and Wilson, 2003) and it helps proper technique maintenance when fatigue appears (Chollet et al., 2000). Hence, CFD analysis of the tandem effects on drag force represented an opportunity to help swimmers and coaches improving training sets and also improving performance. Another important aim is to clearly understand the hydrodynamic differences of swimming in the front of the group or behind another.

Silva et al. (2008) aimed to determine the effect of tandem distance on the drag coefficient in swimming. A k-epsilon turbulent model was implemented in the commercial code Fluent® and applied to the fluid flow around two swimmers in a tandem situation. CFD simulations were conducted for various distances between swimmers (from 0.50 to 8.0 m) and swimming velocities (from 1.60 to 2.0 m/s). Silva et al. (2008) computed the drag coefficient for each of the distances and velocities. As expected, these authors found that the relative drag coefficient of the back swimmer was lower (about 56 % of the leading swimmer) for the smallest inter-swimmer distance (0.50 m). This value increased progressively until the distance between swimmers reached 6.0 m, where the relative drag coefficient of the back swimmer was about 84 % of the leading swimmer. Due to some limitations of this study, mainly the simulation domain having small dimensions, it was not possible to numerically accomplish one aim of this study: to determine the distance in which both swimmers performed in the same hydrodynamic conditions, i.e., the distance in which the drag coefficient of the back swimmer is equal to the drag coefficient of the leading swimmer. In fact, for distances higher than 6.0 m, the values of the drag coefficient of the back swimmer remained constant. In this sense, to calculate the distances in which the drag coefficient of the back swimmer's equalled the value of the leading swimmer, a fitting of the drag coefficient curves of the back swimmer was carried out (according to a polynomial function of the values found until the 6.0 m distance). Silva et al. (2008) indicated that the drag coefficient of the back swimmer was equal to that of the leading swimmer at distances ranging from 6.45 to 8.90 m, depending on flow velocity, concluding that these distances allow the swimmers to be in the same hydrodynamic conditions during training and competitions. Regarding specific swimming training sets, Silva et al. (2008) suggested that the back swimmer must start swimming only when the leading swimmer reaches a 10 m distance from the starting wall, rather than the 5 m distance commonly used in training. Nevertheless, concerning open water competitions, the athletes could take important advantages of swimming in a drafting situation.

Although the important findings of the study of Silva et al. (2008), it presented some limitations that should be improved in future studies. The model used during the CFD simulations was a two-dimensional model and the analysis was performed with the model totally submerged. Further studies are needed to evaluate these tandem effects with more realistic models (three-dimensional models) and with the models at the water surface. The

inclusion of the interface between air and water seems to be an important concern to be accomplished in the future. Additionally, movements of the propelling segments can be added to the simulations.

Although the most common tandem effects are related to queue displacements, it has been reported that lateral side effects can also be observed during swimming (Janssen et al., 2009). For instance, during competitions it is usual to observe competitors swimming near the lane rope, in a lateral position and a little bit behind the swimmer of the near lane. It is supposed that this option can benefit the swimmer that follows in this lateral and behind position. However, in a recent experimental study, Janssen et al. (2009) reported that at the side of a passive lead swimmer, passive drag was significantly increased by 9 %, and at the side of an active lead swimmer it increased by 8 %. This is in opposition to the significantly reduction of passive drag observed behind a passive lead swimmer (20 %) and behind an active lead swimmer (9 %). Therefore, it should be interesting to perform a similar procedure using CFD methodology.

### 3.4 Form, friction and wave drag components

The contribution of form, friction and wave drag components to total drag during swimming is an interesting topic in sports biomechanics. Data available from several experimental studies show some difficulties involved in the evaluation of the contribution of each drag component. However, CFD has the advantage of allowing the computation of these drag components, letting the user to perform the desired simulations and to know exactly what is the intensity of form, friction and wave drag in different swimming simulation situations (Bixler et al., 2007).

Nevertheless, to the best of our knowledge, there is no CFD studies that have been able to compute wave drag in swimming. In fact, CFD studies in swimming were only able to analyse form and friction drag components, since the models were placed underwater. Bixler et al. (2007) simulated a human body placed at a water depth of 0.75 m, Zaidi et al. (2008) positioned the model 1.50 m below the water surface, whereas Marinho et al. (2009b) used a model at a water depth of 0.90 m. These distances were experimentally proven to be sufficient to exclude the wave drag component from the simulations (Lyttle et al., 1999; Vennell et al., 2006). Therefore, it seems very interesting to improve CFD simulations, including the analysis of hydrodynamic drag when wave drag is a real phenomenon. To achieve this purpose the inclusion of the air and water in the same computational domain is required.

Bixler et al. (2007) found that friction drag represented about 25 % of total drag when the swimmer is gliding underwater; stating that although form drag was dominant, friction drag should be taken in consideration by swimmers and coaches. Zaidi et al. (2008) also found an important contribution of friction drag to the total drag. These authors, used a two-dimensional model with the head in different positions, and found that friction drag represented about 20 % of the total drag. In the study of Zaidi et al. (2008) it was very interesting to note that the position with the head aligned with the body presented lower form and friction drag values than the lifted up head position and the lowered head position. Although the lifted up and lowered head positions presented similar values of friction drag, the lifted up position presented higher form drag values than the lowered head position, showing that the lifted up head position lead to a higher pressure gradient around the swimmer during the gliding.

Marinho et al. (2009b), when analysing two different gliding postures, found a bit lower values of friction drag. However, these authors reported contributions of 13 % and 8 % for the friction drag component in the position with the arms extended at the front and in the position with the arms along the trunk, respectively. Nevertheless, Marinho et al. (2009b) showed that differences in the drag force between these two body positions were only related to different form drag values. Indeed, the absolute values of friction drag were about the same in the two gliding positions. Thus, this finding underlined the idea that the so-called streamline position allowed decreasing the pressure gradient around the swimmer body during the underwater gliding.
It is important to emphasize that, if the swimmer model was at the water surface, rather than gliding underwater, the contribution of each drag component is expected to be different. For instance, one should be aware that in this situation wetted area would be lower, thus decreasing friction drag.

### 3.5 Equipments

The influence in performance of the equipments used during swimming is not a clear issue and, usually, the methodological design involved during the experiments lead to some difficulties in the data analysis.
However, the numerical analysis with CFD can be a good approach to overcome this problem. For instance, different human body models can be tested wearing different swimsuits, fins, paddles, caps, goggles, to evaluate the effects in hydrodynamic drag.
The most known application of CFD in swimming research is probably the numerical analysis of different types of swimsuits and the testing procedures that lead to the development of new swimsuit models (Fluent, 2004). These data suggest that the polyurethane generation of swimsuits can significantly improve performance due to the reduction in hydrodynamic drag.
It is usually accepted that drag-reducing suits can reduce skin friction, with an effect similar to shaving (Sharpe & Costill, 1998; Pendergast et al., 2006). Nevertheless, Mollendorf et al. (2004) revealed that total drag decreased by 3 % to 10 % mostly due to decreased form drag in textile suits. These experimental data suggest that the water flow was tripped by frictional drag, remained attached to the swimmer body, thus decreasing form drag (Polidori et al., 2006; Marinho et al., 2009b). Pendergast et al. (2006) stated that studies of the effects of a drag reducing textile suit on active drag at low to moderate velocities failed to show a clear benefit, although at the fastest velocity the textile suit reduced the drag of some swimmers (Sanders et al., 2001; Toussaint et al., 2002). Other authors used physiological approaches, and the results were controversial as well (Starling et al., 1995; Roberts et al., 2003). All these data suggests that CFD can represent an additional solution to clear this issue and help swimmers improve their performance. CFD has the advantage to show the water flow around the swimmer body, allowing understanding if the water really remained attached to the body. Moreover, an important issue that has not been systematically evaluated is the compression effects due to swimsuits. The compression of the body may decrease the area projected in the frontal plane, being this variable a major determinant of form drag. Furthermore, the advantage of swimsuits upon wobbling body masses represent an important opportunity to future research in this field, especially after the FINA changing rules regarding swimsuits to 2010 swimming events.
Another interesting concern is related to the flow visualization around the fins. Swimmers wearing fins can swim much faster than without this device. Research on the flow

characteristics around the fins still needs more attention (Tamura et al., 2002). On the other hand, the effects on hydrodynamic drag by wearing different fin types (e.g., on size and/or flexibility) and with different kick movements can allow enhanced performance during training sets with fins and also during fin swimming events.
Following this line of research, effects of different caps and goggles can be tested using numerical simulation techniques. The effects of different swimming pools on drag (depth, width lane, number of lanes, lane ropes, and lane position) should also be attempted in the near future.

## 4. Future research in swimming using CFD

Throughout this chapter, several future ideas have been presented to improve the application of CFD in swimming research. One of our major aims is to be able to evaluate biomechanical situations that can be used by coaches and swimmers to swim faster and, thus to enhance performance. Therefore, the effective evaluation of active drag should be one of the first concerns in future studies using CFD. At this point, it seems important to analyse the intensity of active drag in the four competitive strokes within a wide range of swimming velocities. On the other hand, CFD can compute the contribution of friction, form and wave drag components to total drag. This issue will only be possible if the simultaneous simulation of the interface between air and water within the same CFD domain is achieved.
The tandem issues also represent a significant matter that can be more deeply understood. If the above mentioned questions are solved, one can simulate several current tandem situations that occur during training but also during competitions, as in open-water events where tandem situations are common. Rear and lateral positions occur in this type of events and the lateral position (in an adjacent lane) can also be possible in swimming events, thus its effects on hydrodynamic drag must be quantified.
As mentioned above, the analysis of the effects of different equipments and facilities on hydrodynamic drag seems to be an interesting and an important issue to be dealt in future studies.

## 5. Conclusion

During this chapter, the authors attempted to present some important studies that have been conducted in swimming research using CFD. Although there are some limitations of these studies, it seems that this numerical tool should not be disregarded. CFD can be used to evaluate several hydrodynamic issues, hence helping swimmers moving faster. In the current work some issues regarding the effect of hydrodynamic drag on swimming performance were discussed. We believe that we were able to show the practical applications of CFD to swimmers and their coaches.
Moreover, several questions to be addressed in future investigations were reported. These concerns represent an important step forward to bridge the gap between theory and practice, allowing even more the scientific knowledge to be available to swimmers and coaches.

## 6. Acknowledgement

This work was supported by the Portuguese Government by Grants of the Science and Technology Foundation (PTDC/DES/098532/2008).

## 7. References

Barsky, S.; Delgado-Buscalioni, R. & Coveney, P.V. (2004). Comparison of molecular dynamics with hybrid continuum-molecular dynamics for a single tethered polymer in a solvent. *Journal of Chemical Physics*, 121, 2403-2411.

Bassett, D.R.; Flohr, J.; Duey, W.J.; Howley, E.T. & Pein, R.L. (1991) Metabolic responses to drafting during front crawl swimming. *Medicine and Science in Sports and Exercise*, 23, 6, 744-747.

Bixler, B. & Schloder, M. (1996). Computational fluid dynamics: an analytical tool for the 21st century swimming scientist. *Journal of Swimming Research*, 11, 4-22.

Bixler, B.; Pease, D. & Fairhurst, F. (2007). The accuracy of computational fluid dynamics analysis of the passive drag of a male swimmer. *Sports Biomechanics*, 6, 81-98.

Chatard, J.C. & Wilson, B. (2003). Drafting distance in swimming. *Medicine and Science in Sports and Exercise*, 35, 7, 1176-1181.

Chollet, D.; Hue, O.; Auclair, F.; Millet, G. & Chatard, J.C. (2000). The effects of drafting on stroking variations during swimming in elite male triathletes. *European Journal of Applied Physiology*, 82, 5-6, 413-417.

Dabnichki, P. & Avital, E. (2006). Influence of the position of crew members on aerodynamics performance of two-man bobsleigh. *Journal of Biomechanics*, 39, 2733-2742.

Fluent (2004). Speedo goes for gold with CFD. *Fluent News*, 13, 1, 4-6.

Gage, K.L.; Gartner, M.J.; Burgreen, G.W. & Wagner, W.R. (2002). Predicting membrane oxygenator pressure drop using computational fluid dynamics. *Artificial Organs*, 26, 600-607.

Hausswirth, C.; Lehenaff, D.; Dreano, P. & Savonen, K. (1999). Effects of cycling alone or in a sheltered position on subsequent running performance during a triathlon. *Medicine and Science in Sports and Exercise*, 31, 4, 599-604.

Hausswirth, C.; Vallier, J.M.; Lehenaff, D.; Brisswalter, J.; Smith, D.; Millet, G. & Dreano, P. (2001). Effect of two drafting modalities in cycling on running performance. *Medicine and Science in Sports and Exercise*, 33, 3, 485-492.

Janssen, M.; Wilson, B.D. & Toussaint, H.M. (2009). Effects of drafting on hydrodynamic and metabolic responses in front crawl swimming. *Medicine and Science in Sports and Exercise*, 41, 4, 837-843.

Karpovich, P. (1933). Water resistance in swimming. *Research Quarterly*, 4, 21-28.

Kellar, W.P.; Pearse, S.R.G. & Savill, A.M. (1999). Formula 1 car wheel aerodynamics. *Sports Engineering*, 2, 203-212.

Liu, H. (2002). Computational biological fluid dynamics: digitizing and visualizing animal swimming and flying. *Integrative and Comparative Biology*, 42, 1050-1059.

Lyttle, A. & Keys, M. (2006). The application of computational fluid dynamics for technique prescription in underwater kicking. *Portuguese Journal of Sport Sciences*, 6, Suppl. 2, 233-235.

Lyttle, A.D.; Blanksby, B.A.; Elliott, B.C. & Lloyd, D.G. (1999). Optimal depth for streamlined gliding, In: *Biomechanics and Medicine in Swimming VIII*, K.L. Keskinen, P.V. Komi & A.P. Hollander (Eds.), 165-170. Gummerus Printing, Jyvaskyla.

Marinho, D.A.; Rouboa, A.I.; Alves, F.B.; Vilas-Boas, J.P.; Machado, L.; Reis, V.M. & Silva, A.J. (2009a). Hydrodynamic analysis of different thumb positions in swimming. *Journal of Sports Science and Medicine*, 8, 1, 58-66.

Marinho, D.A.; Reis, V.M.; Alves, F.B.; Vilas-Boas, J.P.; Machado, L.; Silva, A.J. & Rouboa, A.I. (2009b). The hydrodynamic drag during gliding in swimming. *Journal of Applied Biomechanics*, 25, 3, 253-257.

Marinho, D.A.; Carvalho, F.; Barbosa, T.M.; Reis, V.M.; Alves, F.; Rouboa, A. & Silva, A.J. (2009c). The determination of drag in the gliding phase in swimming, In: *Proceedings of the 27th International Conference on Biomechanics in Sports*, R. Anderson, D. Harrison & I. Kenny (Eds.), 620. University of Limerick, Limerick.

Mollendorf, J.C.; Termin, A.C.; Oppenheim, E. & Pendergast, D.R. (2004). Effect of swim suit design on passive drag. *Medicine and Science in Sports and Exercise*, 36, 6, 1029-1035.

Pallis, J.M.; Banks, D.W. & Okamoto, K.K. (2000). 3D computational fluid dynamics in competitive sail, yatch and windsurfer design, In: *The Engineering of Sport: Research, Development and Innovation*, F. Subic & M. Haake (Eds.), 75-79. Blackwell Science, Oxford.

Pendergast, D.R.; Capelli, C.; Craig Jr, A.B.; di Prampero, P.E.; Minetti, A.E.; Mollendorf1, J.; Termin, A. & Zamparo, P. (2006). Biophysics in swimming. *Portuguese Journal of Sport Sciences*, 6, Suppl. 2, 185-189.

Polidori, G.; Taiar, R.; Fohanno, S.; Mai, T.H. & Lodini, A. (2006). Skin-friction drag analysis from the forced convection modeling in simplified underwater swimming. *Journal of Biomechanics*, 39, 2535-2541.

Roberts, B.S.; Kamel, K.S.; Hedrick, C.E.; MLean, S.P. & Sharpe, R.L. (2003). Effect of Fastskin suit on submaximal freestyle swimming. *Medicine and Science in Sports and Exercise*, 35, 519-524.

Rouboa, A.; Silva, A.; Leal, L.; Rocha, J. & Alves, F. (2006). The effect of swimmer's hand/forearm acceleration on propulsive forces generation using computational fluid dynamics. *Journal of Biomechanics*, 39, 1239-1248.

Sanders, R.B.; Rushall, H., Toussaint, H., Steager, J. & Takagi, H. (2001). Bodysuit yourself but first think about it. *American Swimming Magazine*, 5, 23-32.

Sharpe, R.L. & Costill, D.L. (1998). Influence of body hair removal on physiological responses during breaststroke swimming. *Medicine and Science in Sports and Exercise*, 21, 576–80.

Silva, A.J.; Rouboa, A.; Moreira, A.; Reis, V.; Alves, F.; Vilas-Boas, J.P. & Marinho, D. (2008). Analysis of drafting effects in swimming using computational fluid dynamics. *Journal of Sports Science and Medicine*, 7, 1, 60-66.

Starling, R.D.; Costill, D.; Trappe, T.A.; Jozsi, A.C.; Trappe, S.W. & Goodplaster, B.H. (1995). Effect of swimming suit design on the energy demands of swimming. *Medicine and Science in Sports and Exercise*, 27, 1086–1089.

Tamura, H.; Nakazawa, Y.; Sugiyama, Y.; Nomura, T. & Torii, N. (2002). Motion analysis and shape evaluation of a swimming monofin. *The Engineering Sports*, 4, 716-724.

Toussaint, H.B. (2006). Technology applied to optimise training for improving of front crawl performance. *Portuguese Journal of Sport Sciences*, 6, Suppl. 2, 205-210.

Toussaint, H. & Truijens, M. (2005). Biomechanical aspects of peak performance in human swimming. *Animal Biology*, 55, 1, 17-40.

Toussaint, H.M.; Truijens, M.J.; Elzinga, M.J.; van de Ven, A.; de Best, H.; Snabel, B. & de Groot, G. (2002). Effect of a Fast-skin "body" suit on drag during front crawl swimming. *Sport Biomechanics*, 1, 1–10.

Venetsanos, A.G.; Huld, T.; Adams, P. & Bartzis, J.G. (2003). Source, dispersion and combustion modelling of an accidental release of hydrogen in an urban environment. *Journal of Hazardous Materials*, 105, 1-3, 1-25.

Vennell, R.; Pease, D.L. & Wilson, B.D. (2006). Wave drag on human swimmers. *Journal of Biomechanics*, 31, 664-671.

Vilas-Boas, J.P. (1996). *Bases Mecânicas da Natação*. Faculty of Sport Sciences and Physical Education of Porto University, Porto.

Vilas-Boas, J.P.; Costa, L.; Fernandes, R.; Ribeiro, J.; Figueiredo, P.; Marinho, D.; Silva, A.; Rouboa, A. & Machado, L. (2009). Determination of the drag coefficient during the first and second glide positions of the breaststroke underwater stroke. *Journal of Applied Biomechanics*, in press.

Yim P.; Demarco, K.; Castro, M.A. & Cebral, J. (2005). Characterization of shear stress on the wall of the carotid artery using magnetic resonance imaging and computational fluid dynamics. *Studies in Health Technology and Informatics*, 113, 412-442.

Zaidi, H.; Taiar, R.; Fohanno, S. & Polidori, G. (2008). Analysis of the effect of swimmer's head position on swimming performance using computational fluid dynamics. *Journal of Biomechanics*, 41, 1350-1358.

# 18

# Hydrodynamic Behavior of Flow in a Drinking Water Treatment Clarifier

Wen-Jie Yang[1], Syuan-Jhih Wu[2], Yu-Hsuan Li[2], Hung-Chi Liao[1], Chia-Yi Yang[2], Keng-Lin Shih[2] and Rome-Ming Wu[3a,b]*
[1]*graduate student, Department of Chemical and Materials Engineering,*
[2]*undergraduate student, Department of Chemical and Materials Engineering,*
[3a]**associate professor, Department of Chemical and Materials Engineering,*
[3b]*Energy and Opto-Electronic Materials Research Center,*
*Tamkang University, Tamsui, Taipei County,*
*Taiwan*

## 1. Introduction

Over 50% drinking water was supplied to the Taiwan's public by sludge blanket clarifiers (Chen *et al*., 2003; Lin *et al*., 2004). The sludge blanket performs dual functions as a filter as well as a particle coagulator. Coagulation, the chemistry-based treatment stage, controls the characteristics of the generated sludge layer, whereas sedimentation, the hydrodynamic treatment stage, controls sludge layer stability. The existence of a sludge blanket in clarifiers is thereby essential to produce quality effluent water. In addition, the flow dynamics is an important parameter for the design of clarifiers.

The use of solids flux theory continues in many studies in the design and operation of sludge treatment processes (Takacs *et al*., 1991; Daigger, 1995; Wett, 2002). Ekama and Marais (2004) gave a survey on the development of one dimensional (1D) settler modeling. Although application of solids flux theory is good for studying the performance of clarifiers, it does not adequately describe the effect of hydrodynamic behavior in clarifiers (Narayanan *et al*., 2000). Computational fluid dynamics (CFD) has shown to be a powerful tool for resolving complex practical problems in engineering. (Hsu et al., 2007; Videla et al., 2008; Lin et al., 2008; Tao et al., 2008; Yang et al., 2007) Therefore some studies attempted to simulate full clarifiers via CFD (Deininger *et al*., 1998; Burger *et al*., 2005; Fan et al., 2007). Recently Wu *et al*. (2007) simulated flow pattern in a clarifier with porous medium as sludge blanket by 3D CFD. The first work to utilize a 3D, multiphase flow simulation for a clarifier is by Wu *et al*. (2008). Weiss *et al*. (2007) utilized non-Newtonian flow to model a circular secondary clarifier and showed that viscosity of sludge dominates the flow in clarifier. This study attempts to improve clarifier effluent quality by altering its geometric construction. The simulation is based on the sludge blanket clarifier at the Bansin Water Treatment Plant, Taiwan.

Bansin Water Treatment Plant (BWTP) is in Banchiao City, Taipei County, Taiwan. About every 20 minutes sludge blanket overturns somewhere and effluent solid flux increases. The turbidity of the clarified water is generally too high to produce quality clean water after

sand filtering. In this work, four types of constructions of clarifiers are simulated by 3D, multiphase flow model to improve clarifier effluent quality. *Type A* is the conventional clarifier used in BWTP. *Type B* changes inlet pipe to a large one (1.6 folds). *Type C* changes reaction well angle from $120^0$ to $90^0$. *Type D* changes reaction well angle from $120^0$ to $60^0$. As shown in previous research (Yang *et al.*, 2008) that, the velocity of suspension in the reaction well is one of the factors affecting the quality of water discharge, so the improved method of *Type B* is expected to slow the velocity of flow by enlarging diameter of inlet pipe. The improvement method of *Type C* is the angle of $90^0$ of reaction cover. It is hoped that the backflow could be limited within the reaction well, so that the residence time of suspension in the reaction well can be increased. The improved method for *Type D* reverses the whole reaction cover, so the water quality may not deteriorate for reason of easy outflow of the suspension from the reaction well.

## 2. Geometry and meshes

Figure 1 indicates the geometry of the sludge blanket clarifier. The clarifier is 19×19×5.5 $m^3$, with an impeller with 16 blades and diameter of 3 m. The impeller is located in center top of the clarifier. The inlet pipe is 0.9 m in diameter. The inlet pipe is connected to a draft tube 2.4 m in diameter. The inlet water velocity was typically operated at 0.34 m/s. The draft tube comprises the first reaction zone. The second reaction zone is outside the first reaction zone and inside a reaction well with upper and lower diameters of 8 and 13 m, respectively. The reaction well is 3.8 m high. Figure 2 shows all grids in the clarifier.

## 3. Governing equations and boundary conditions

### 3.1 Conservation equations.

Volume fractions represent the space occupied by each phase, and the laws of conservation of mass and momentum are satisfied by each phase individually. The volume of phase $q$, $V_q$, is defined by

$$V_q = \int_V \alpha_q dV \tag{1}$$

where $\alpha$ is phase volume fraction occupied by each phase, and

$$\sum_{q=1}^{n} \alpha_q = 1 \tag{2}$$

The effective density of phase $q$ is

$$\hat{\rho}_q = \alpha_q \rho_q \tag{3}$$

where $\rho_q$ is the physical density of phase $q$. In this work, only water and solid phases are considered.

The continuity equation for phase $q$ is

$$\frac{\partial}{\partial t}(\alpha_q \rho_q) + \nabla \bullet (\alpha_q \rho_q \vec{v}_q) = \sum_{p=1}^{n} (\dot{m}_{pq} - \dot{m}_{qp}) \tag{4}$$

where $\vec{v}_q$ is the velocity of phase $q$ and $\dot{m}_{pq}$ characterizes the mass transfer from the $p$ to $q$ phase, and $\dot{m}_{qp}$ characterizes the mass transfer from phase $q$ to phase $p$, hence $\dot{m}_{pq} = -\dot{m}_{qp}$ and $\dot{m}_{pp} = 0$.
The momentum balance for water phase $w$ yields

$$\frac{\partial}{\partial t}(\alpha_w \rho_w \vec{v}_w) + \nabla \bullet (\alpha_w \rho_w \vec{v}_w \vec{v}_w) = -\alpha_w \nabla P + \nabla \bullet \overline{\overline{\tau}}_w + \alpha_w \rho_w \vec{g} + (\vec{R}_{sw} + \dot{m}_{sw}\vec{v}_{sw} - \dot{m}_{ws}\vec{v}_{ws}) \tag{5}$$

where $P$ is the pressure shared by all phases, and $\overline{\overline{\tau}}_w$ is the water phase stress-strain tensor

$$\overline{\overline{\tau}}_w = \alpha_w \mu_w (\nabla \vec{v}_w + \nabla \vec{v}_w^T) + \alpha_w (\lambda_w - \frac{2}{3}\mu_w) \nabla \cdot \vec{v}_w \bar{\bar{I}} \tag{6}$$

Here $\mu_w$ and $\lambda_w$ are the shear and bulk viscosity of water phase, $\vec{R}_{sq}$ is an interaction force between water and solid phases. $\vec{v}_{sw}$ is the interphase velocity, defined as follows. If $\dot{m}_{sw} > 0$, $\vec{v}_{sw} = \vec{v}_s$; if $\dot{m}_{sw} < 0$, $\vec{v}_{sw} = \vec{v}_w$.
The momentum balance for solid phase $s$ yields

$$\frac{\partial}{\partial t}(\alpha_s \rho_s \vec{v}_s) + \nabla \bullet (\alpha_s \rho_s \vec{v}_s \vec{v}_s) = -\alpha_s \nabla P - \nabla p_s + \nabla \bullet \overline{\overline{\tau}}_s + \alpha_s \rho_s \vec{g} + (\vec{R}_{ws} + \dot{m}_{ws}\vec{v}_{ws} - \dot{m}_{sw}\vec{v}_{sw}) \tag{7}$$

where $p_s$ is the solids pressure. For granular flows in the compressible regime, a solids pressure is calculated independently and used for the pressure gradient term, $\nabla p_s$, in the granular-phase momentum equation.
The solids stress tensor contains shear and bulk viscosities arising from particle momentum exchange due to translation and collision. The collisional and kinetic parts are added to give the solids shear viscosity. The solids bulk viscosity accounts for the resistance of the granular particles to compression and expansion.

### 3.2 Phase interactions.

$\vec{R}_{ws}$ depends on the friction, pressure, cohesion, and other effects, and is subject to the conditions that $\vec{R}_{sw} = -\vec{R}_{ws}$ and $\vec{R}_{ww} = \vec{R}_{ss} = 0$.
FLUENT uses a simple interaction term of the following form:

$$\vec{R}_{sw} = K_{sw}(\vec{v}_s - \vec{v}_w) \tag{8}$$

where $K_{sw}(= K_{ws})$ is the interphase momentum exchange coefficient. The fluid-solid exchange coefficient $K_{sw}$ can be written in the following general form:

$$K_{sw} = \frac{\alpha_s \rho_s f}{\tau_s} \tag{9}$$

where $\tau_s$, the particulate relaxation time, is defined as

$$\tau_s = \frac{\rho_s d_s^2}{18\mu_w} \tag{10}$$

where $d_s$ is the diameter of particles of phase $s$.

For the Syamlal-O'Brien model (1989),

$$f = \frac{C_D \operatorname{Re}_s \alpha_w}{24 v_{r,s}^2} \tag{11}$$

where the drag function and relative Reynolds number have the following forms:

$$C_D = (0.63 + \frac{4.8}{\sqrt{\operatorname{Re}_s / v_{r,s}}})^2 \tag{12}$$

$$\operatorname{Re}_s = \frac{\rho_w d_s \left| \vec{v}_s - \vec{v}_w \right|}{\mu_w} \tag{13}$$

This model is based on measurements of the terminal velocities of particles in fluidized or settling beds. $v_{r,s}$ is the terminal velocity correlation for the solid phase (Garside and Al-Dibouni, 1977):

$$v_{r,s} = 0.5\left( \alpha_w^{4.14} - 0.06 \operatorname{Re}_s + \sqrt{(0.06 \operatorname{Re}_s)^2 + 0.12 \operatorname{Re}_s \left( 2\alpha_w^{2.65} - \alpha_w^{4.14} \right) + \alpha_w^{8.28}} \right) \tag{14}$$

Lift forces act on a particle mainly due to velocity gradients in the primary-phase flow field. The lift force will be more significant for larger particles. Thus, the inclusion of lift forces is not appropriate for closely packed particles or for very small particles. When a secondary phase *p* accelerates relative to the primary phase *q*, the inertia of the primary phase mass encountered by the accelerating particles exerts a virtual mass force on the particles. The virtual mass effect is significant when the secondary pahse density is much smaller than the primary phase density. Therefore virtual mass force is not either considered in this work. In order to make the calculation simple, the acting force between water and particle is dominated by the drag force, which is shown in the $\vec{R}_{sw}$ term. The other relatively strong acting forces, such as combination between particle and particle by coagulant, can be reflected in the viscosity of solid phase.

### 3.3 Boundary conditions.

The boundary conditions are as follows:

$$\vec{v}_s = \vec{v}_w = \vec{V} \text{ at inlet pipe} \tag{15a}$$

$$\alpha_s = 0.005 \text{ at inlet pipe} \tag{15b}$$

$$\vec{v}_s = \vec{v}_w = 0 \text{ , at walls} \tag{15c}$$

$$P = 0, \text{ at water/air surface} \tag{15d}$$

Equation (15a) and (15b) state that the inlet suspension is moving at a constant speed and has a solid volume fraction equal to 0.005. Equation (15c) describes no slip boundary

conditions for water and solid phases. Equation (15d) describes the gauge pressure at the water surface (top of the clarifier) is zero.

The computational fluid dynamics program FLUENT 6.1 (Fluent Inc., USA) solved the governing equations, together with the associated boundary conditions, using hybrid mesh volumes generated by GAMBIT. This work uses three groups of meshes of different quantities (1 million, 2 million, 2.5 million) for calculation. The relative error of the solid volume fraction at the overflow is smaller than 10%. Therefore the numbers of mesh volumes in the whole clarifier are used about 2,500,000. The calculations were carried out with maximum relative error of $10^{-4}$ in fluid velocity evaluation.

## 4. Results and discussion

### 4.1 Velocity vector of water flow.

Figure 3 plots the velocity vector of water in the clarifier (inlet velocity = 0.3 m/s, impeller rotation speed = 0.3 rad/s). When inlet water is flowing into the draft tube, it is sucked to the top of the clarifier, owing to the rotating impeller. Then it goes down along the inside of the well and separates into two streams. One stream inside the well makes a strong cycling flow (#1) in the secondary reaction well, the other stream rises along the wall of the clarifier, to water surface, and descends along the outside of the reaction well, making another weaker cycling flow (#2). Although this cycling flow (#2) is weaker than (#1), it is still a strong density current that the flocs will be elutriated, leading to an average 20 minutes overturn as reported in Chen *et al.* (2003). An idea is to treat the flocs into a strong and dense blanket.

## 5. Comparison with Bansin Water Treatment Plant (BWTP)

Bansin Water Treatment Plant (BWTP) adopted 16 sludge blanket clarifiers to treat its raw water. This type of clarifier is used by many regions to produce drinking water, but relevant references are very few. Figure 4 is a comparison between observation in BWTP and CFD results. An observer stood beside the clarifier, recorded which areas sludge blanket was floating. Thus in figures 4(a)-(d), blue color means that water surface is clean; while yellow color indicates that sludge suspension was on that surface. Figures 4(a)-(d) were the observation results at 0 s, 600 s, 900 s, and 1200 s. Figures 4(e)-(h) were volume fraction contours calculated by FLUENT at 2400 s, 3000 s, 3300 s, and 3600 s. The patterns are similar between BWTP observation and numerical calculation and that sludge overturns from edge and corner every 20 minutes. Circular clarifier might be a solution to solve this problem.

### 5.1 Twophase flow.

Figure 5 reveals the contour of volume fraction of solid phase of Eulerian two phase flow as time evolves. The primary phase is water phase, the secondary phase is solid phase with particle size 10 μm and density 1,005 kg/m$^3$. As time goes by, the solid particles were sucked from the draft tube to the top of the impeller, descends along the reaction well inside, be full of the whole reaction well, and overflow to the reaction well outside, making a relatively stable blanket at the bottom of the clarifier, and a dynamic upward particles' surface. Compared with figures 5a to 5c, it is obviously shown that as time passes, the

particles boundary becomes higher (white dash line), i.e., many particles rise and the loading of the following fast filtration becomes heavy.

In order to enunciate the geometric effects on the stability of the sludge blanket, the other three types (*Type B*, *Type C*, and *Type D*) of constructions of clarifiers were studied. Comparing with these figures it is shown that after 3600s' operation, the lowest particle concentration at the effluent surface happens at the *Type B* construction, the large inlet pipe.

As shown in Figure 6a, the increase of the caliber size of inlet pipes decelerate the fluid, thus, the intensity of backflow formed is smaller than the original structure (Fig. 3). The flow-up velocity outside of the reaction well is relatively small, and the volume fraction of particles carried upward by fluids is small as well. Finally, the quality of water discharge is favorable.

As shown in Figure 6b, the angle of the reaction well is a right angle, which is equivalent to an impinge flow when the suspension flows downward along the inside of the reaction well and approaches the bottom of the clarifier. The effective backflow cannot be formed, thus, the particles are prone to flow out of the reaction well to raise the concentration. In Figure 6c, it is expected that the suspension will be surrounded by the reversed reaction cover, thus preventing the particles from flowing out of the reaction well. However, a backflow zone is produced at the top of reaction well (as compared to the backflow zone appeared in the middle section of the reaction well in the original structure, Fig. 3). The upper backflow field at this position will hamper the backflow of the suspension under the reaction well so that it does not backflow into the reaction well, but leaving the reaction well. Thus, the concentration of the suspension outside the reaction well is raised.

Effluent upflow velocity (EUV) is proposed as an important parameter affecting clarifier performance (Narayanan *et al*., 2000). In this simulation work, effluent solid flux can be calculated in advance. The effluent solid flux is displayed in figure 7. For *Type A* and *Type B*, effluent solid flux increase steadily; while for *Type C* and *Type D*, effluent solid flux increase saw-toothed. This might due to the squeezed backflow in top of the reaction well causing unstable flow field outside the reaction well. Before 2500s, effluent solid flux is less than 0.05 kg/m$^2$-s except for *Type D*. After 2500s, effluent solid flux is increasing dramatically. It is suggested that BWTP could drain sludge away per hour according to this simulation work. At almost all the 3000s' operations, the effluent solid flux is the lowest in *Type B* construction.

## 6. Conclusions

Blanket floc volumetric concentration is an important parameter in understanding the performance of sludge blanket clarifiers. 3D simulations of a clarifier using four different geometric constructions were studied in this work. From the simulation results of effluent solid flux, it is suggested that under the same daily throughput the large inlet pipe can reduce the flow velocity in the clarifier, hence reduce effluent solid flux and improve the quality of water. According to this simulation results, it is recommended that BWTP has to make large inlet pipe to obtain good quality water under the same daily throughput, or obtain large daily throughput under the same quality water.

The simulation results can only be interpreted qualitatively and not quantitatively since only hydrodynamic behavior is considered. Further work should concern the chemical

based treatment, i.e., coagulation of flocs in clarifier. Nevertheless, the simulation results can show tendencies in the flow pattern due to changes in clarifier construction.

## 7. Acknowledgment

The authors would like to thank the National Science Council of the Republic of China, Taiwan, for financially supporting this research under Contract No. NSC 96-2221-032-020.

## 8. References

Burger, R., K. H. Karlsen, and J. D. Towers, "Mathematical Model and Numerical Simulation of the Dynamics of Flocculated Suspensions in Clarifier-Thickeners," *Chem. Eng. J.*, 111, 119 (2005).

Chen, L. C., S. S. Sung, W. W. Lin, D. J. Lee, C. Huang, R. S. Juang, and H. L. Chang, "Observations of Blanket Characteristics in Full-Scale Floc Blanket Clarifiers," *Water Sci. and Tech.*, 47, 197 (2003).

Daigger, D. T. "Development of Refined Clarifier Operating Diagrams using An Updated Settling Characteristics Database," *Water Environ. Res.*, 67, 95 (1995).

Deininger, A.,E. Holthausen, and P. A. Wilderer, "Velocity and Solids Distribution in Circular Secondary Clarifiers: Full Scale Measurements and Numerical Modeling," *Water Res.*, 32, 2951 (1998).

Ekama, G. A. and P. Marais, "Assessing the Applicability of the 1D Flux Theory to Full-Scale Secondary Settling Tank Design with a 2D Hydrodynamic Model," *Water Res.*, 38, 495 (2004).

Fan, L., N. Xu, X. Ke, and H. Shi, "Numerical Simulation of Secondary Sedimentation Tank for Urban Wastewater," *J. Chin. Inst. Chem. Eng.*, 38, 425 (2007).

Garside, J. and M. R. Al-Dibouni, "Velocity-Voidage Relationships for Fluidization and Sedimentation," *Ind. Eng. Chem. Process Design and Develop.*, 16, 206 (1977).

Hsu, J. P., S. C. Yang, and J. C. Chen, "Drag on Two Co-axial Rigid Spheres Moving Normal to A Plane: Newtonian and Carreau Fluids," *J. Chin. Inst. Chem. Eng.*, 38, 409 (2007).

Lin, W. W., S. S. Sung, L. C. Chen, H. Y. Chung, C. C. Wang, R. M. Wu, D. J. Lee, C. Huang, R. S. Juang, X. F. Peng, and H. L. Chang, "Treating High-Turbidity Water Using Full-Scale Floc Blanket Clarifiers," *J. Environ. Eng.-ASCE*, 130, 1481 (2004).

Lin, J. S., C. J. Tsai, K. L. Tung, H. C. Chiang, "Thermophoretic Particle Deposition Efficiency in Turbulent Tube Flow," *J. Chin. Inst. Chem. Eng.*, 39, 281 (2008).

Narayanan, B., S. G. Hough, and R. J. Ooten, "New Hypothesis for Secondary Clarifier Performance under Hydraulically Limited Conditions," *Water Environ. Res.*, 72, 116 (2000).

Syamlal, M. and T. J. O'Brien, "Computer Simulation of Bubbles in a Fluidized Bed," *American Institute of Chemical Engineering Symposium Series*, 85, 22 (1989).

Takacs, I., G. G. Patry, and D. Nolasco, "A Dynamic Model of the Clarification-Thickening Process," *Water Res.*, 25, 1263 (1991).

Tao, T., X. F. Peng, A. Su, D. J. Lee, "Modeling Convective Drying of Wet Cake," *J. Chin. Inst. Chem. Eng.*, 39, 287 (2008).

Videla, A. R., C. L. Lin, and J. D. Miller, "Simulation of Saturated Fluid Flow in Packed Particle Beds-The Lattice-Boltzmann Method for the Calculation of Permeability from XMT Images," *J. Chin. Inst. Chem. Eng.*, 39, 117 (2008).

Weiss, M., B. G. Plosz, K. Essemiani, and J. Meinhold, "Suction-Lift Sludge Removal and Non-Newtonian Flow Behaviour in Circular Secondary Clarifiers: Numerical Modeling and Measurements," *Chem. Eng. J.*, 132, 241 (2007).

Wett, B. "A Straight Interpretation of the Solids Flux Theory for a Three-Layer Sedimentation Model," *Water Res.*, 36, 2949 (2002).

Wu, R. M., T. H. Lee, W. J. Yang, "Study of Water Treatment Clarifier," *Tamkang J. of Sci. and Eng.*, 10, 317 (2007).

Wu, R. M., T. H. Lee, and W. J. Yang, "Study of Flow in a Blanket Clarifier Using Computational Fluid Dynamics," *J. Environ. Eng.-ASCE*, 134, 443 (2008).

Yang, W. J., C. C. Wang, R. Y. Hsu, and R. M. Wu, "Two-Phase Flow Simulation of Reactor Clarifiers," *J. Chin. Inst. Chem. Eng.*, 39, 275 (2008).

Yang, Z., X. F. Peng, D. J. Lee, and A. Su, "Reynolds Number-Dependent Permeability of Wastewater Sludge Flocs," *J. Chin. Inst. Chem. Eng.*, 38, 135 (2007).

## 9. Nomenclature

| | |
|---|---|
| $C_D$ | drag coefficient, - |
| $K$ | interphase momentum exchange coefficient, - |
| $d_s$ | diameter of particle, m |
| $f$ | correlation factor, - |
| $\vec{g}$ | acceleration of gravity, m/s$^2$ |
| $\dot{m}_{pq}$ | mass transfer from $p$ to $q$ phase, kg/m$^3$-s |
| $P$ | pressure, N/m$^2$ |
| $p_s$ | solid pressure, N/m$^2$ |
| $Re_s$ | Reynols number, - |
| $\vec{R}$ | water/solid interaction, N/m$^2$ |
| $V$ | volume of each phase, m$^3$ |
| $v_{r,s}$ | terminal velocity correlation, - |
| $\vec{v}$ | water/solid velocity, m/s |
| α | volume fraction, - |
| μ | shear viscosity, kg/m-s |
| λ | bulk viscosity, kg/m-s |
| $\rho$ | density, kg/m$^3$ |
| $\hat{\rho}$ | effective density, kg/m$^3$ |
| $\tau_S$ | particulate relaxation time, s |
| $\bar{\bar{\tau}}$ | stress tensor, N/m$^2$ |

**Subscripts**

| | |
|---|---|
| $w$ | water phase |
| $s$ | solid phase |

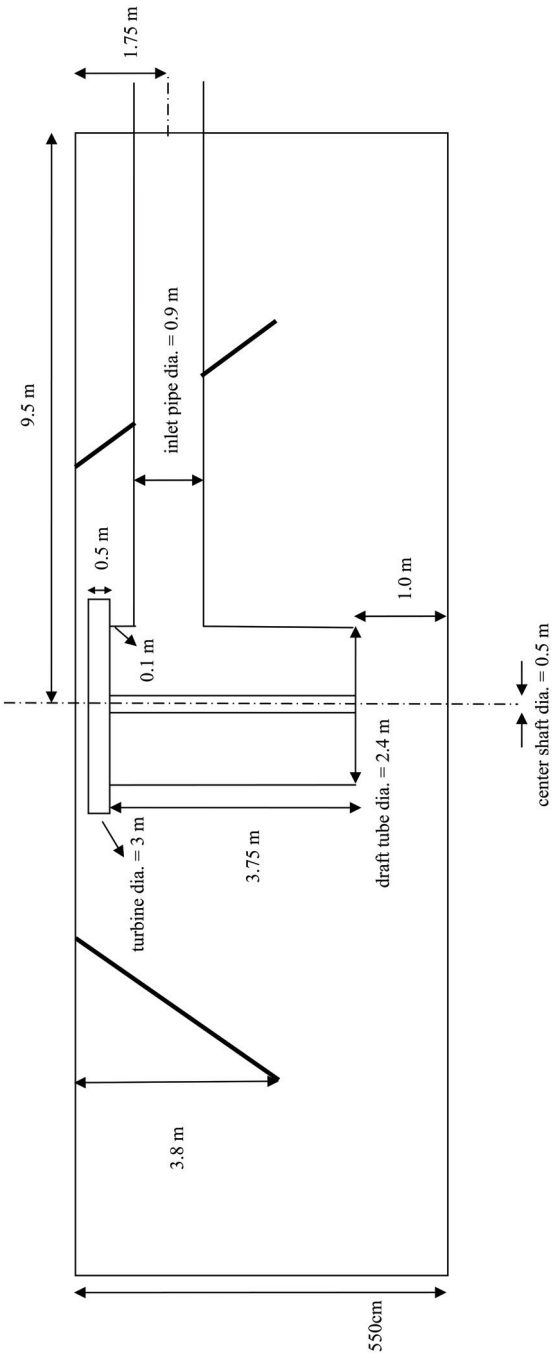


Fig. 1. Geometry of the clarifier

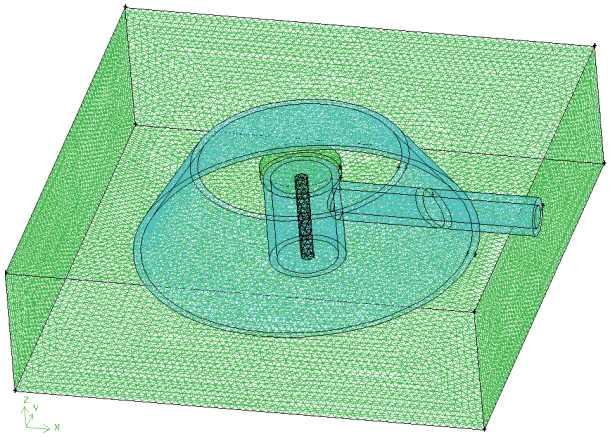

(a)

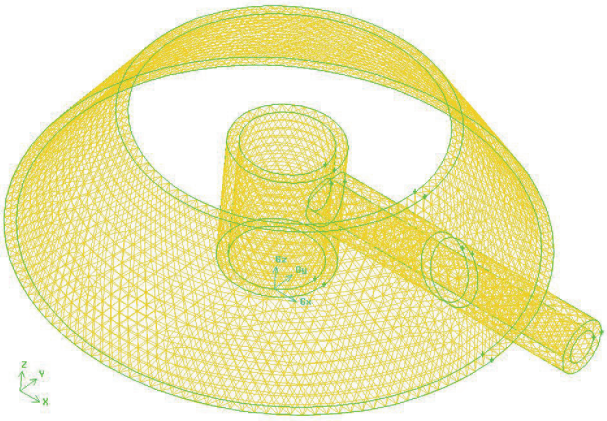

(b)

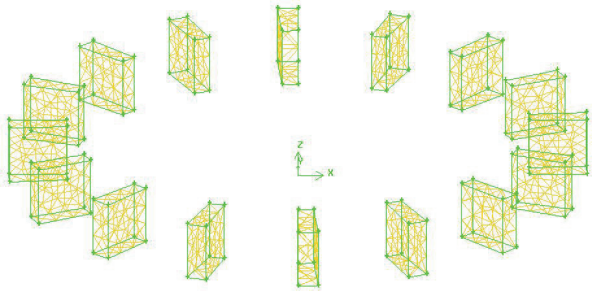

(c)

Fig. 2. Meshes of the clarifier (a) whole clarifier (b) reaction well, inlet pipe, and draft tube (c) blades

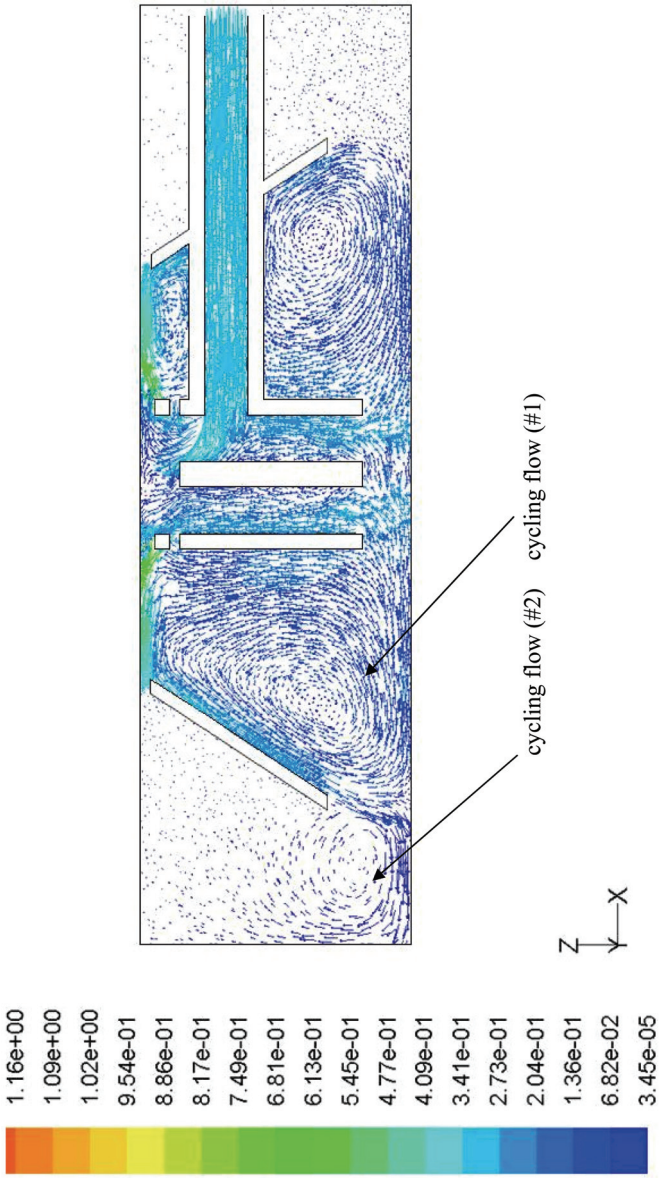


Fig. 3. Velocity vector of water flows (inlet velocity = 0.3 m/s, impeller rotation speed = 0.3 rad/s)

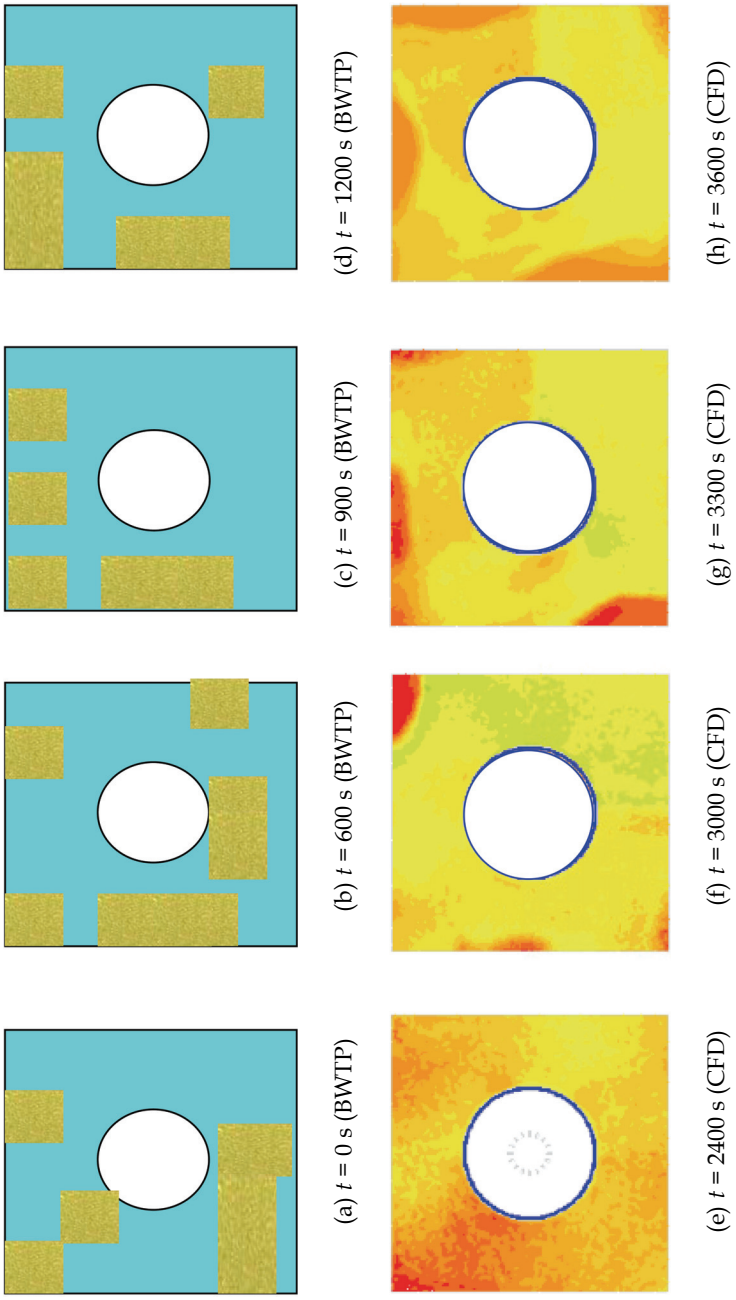


Fig. 4. Contour of solid volume fraction on water surface (a) $t$ = 0 s (BWTP) (b) $t$ = 600 s (BWTP) (c) $t$ = 900 s (BWTP) (d) $t$ = 1200 s (BWTP) (e) $t$ = 2400 s (CFD) (f) $t$ = 3000 s (CFD) (g) $t$ = 3300 s (CFD) (h) $t$ = 3600 s (CFD)

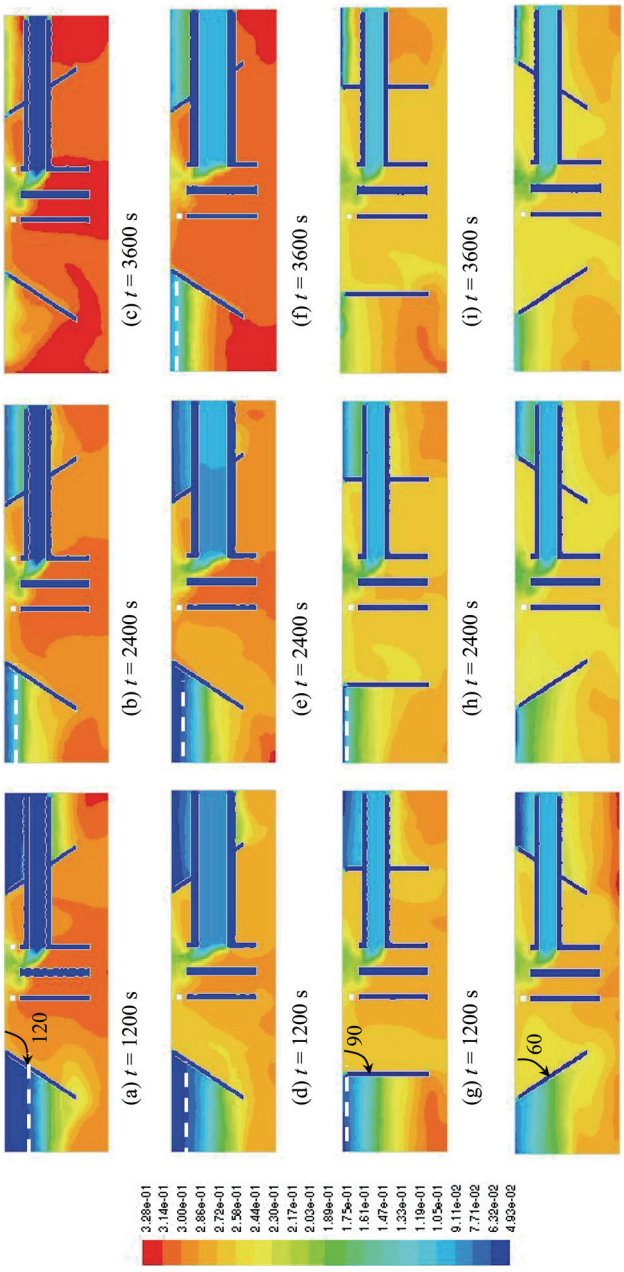


Fig. 5. Contour of solid volume fraction in clarifier (a) *Type A*, *t* = 1200 s (b) *Type A*, *t* = 2400 s (c) *Type A*, *t* = 3600 s (d) *Type B*, *t* = 1200 s (e) *Type B*, *t* = 2400 s (f) *Type B*, *t* = 3600 s (g) *Type C*, *t* = 1200 s (h) *Type C*, *t* = 2400 s (i) *Type C*, *t* = 3600 s (j) *Type D*, *t* = 1200 s (k) *Type D*, *t* = 2400 s (l) *Type D*, *t* = 3600 s

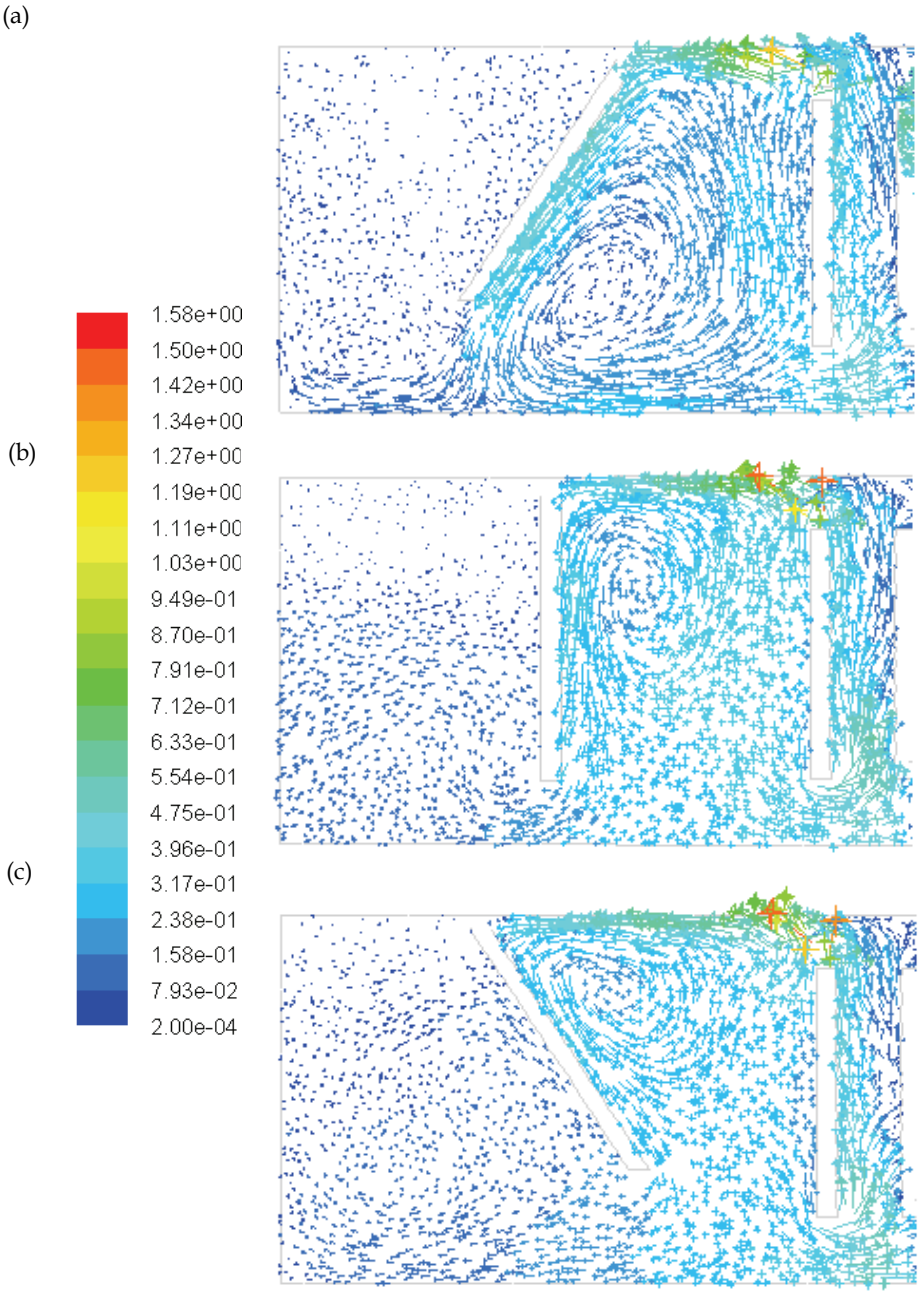


Fig. 6. Velocity vector of water flows (inlet velocity = 0.3 m/s, impeller rotation speed $\omega$ = 0.3 rad/s). (a) *Type B* (b) *Type C* (c) *Type D*

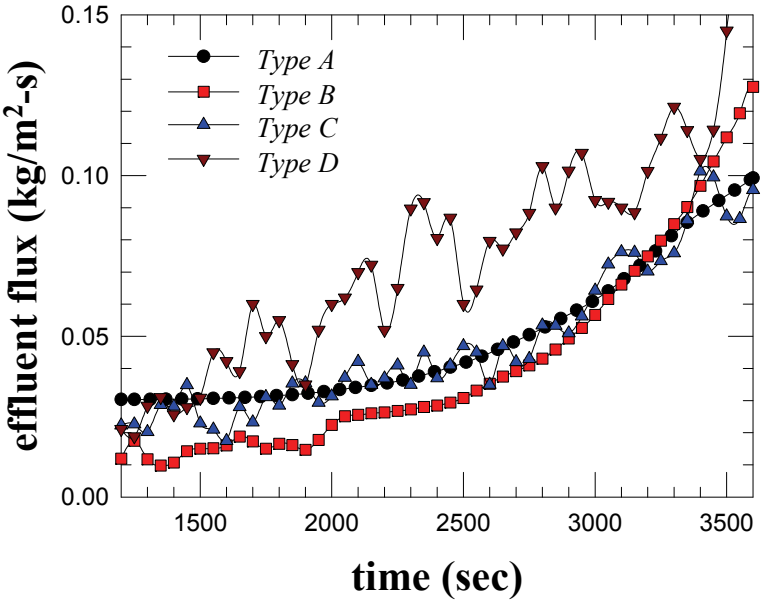


Fig. 7. Effluent solid flux of four constructions of clarifiers